

Executive Summary

WABAMUN AREA CO₂ SEQUESTRATION PROJECT (WASP)

Authors

Rob Lavoie

David Keith

Rev.	Date	Description	Prepared by
1	December 23, 2009	Executive Summary	Rob Lavoie and David Keith
2	January 7, 2010	Executive Summary	Rob Lavoie, David Keith and WASP team members

Background

The geologic storage of carbon dioxide (CO₂) could enable Canada to exploit its fossil energy resources while simultaneously managing its CO₂ emissions. Developing cost-effective, environmentally sound and publicly acceptable CO₂ storage depends on building the public's understanding of the long-term safety and storage capacity for underground CO₂ storage. Knowledge must be in the public domain, because only then can it assure policy makers, regulatory agencies and the public that these operations are safe and that CO₂ has been permanently removed from the atmosphere. Both safety and capacity are important. Without assurances for environmental safety, storage makes little sense and without public confidence, sufficient storage capacity will not be made available to make a meaningful impact in economy-wide CO₂ emissions removal. If these situations exist, it makes little sense to invest in scaled-up storage capacity.

The WASP study was conducted by a group of 16 University of Calgary (U of C) researchers and industry consultants over a period of 16 months from March 2008 to August 2009. The study performed a comprehensive characterization of large-scale CO₂ storage opportunities over a large 5000 km² area (Figure 1) in central Alberta. It also analyzed potential risks. As a benchmark, the project examined the feasibility of storing 20 Mt-CO₂/year over 50 years. This gigaton-scale storage project is more than ten times larger than the commercial projects that are currently under review. It fills a gap between the province-wide capacity estimates (which do not involve site-specific studies of geology, flow and geomechanics) and the detailed commercial studies now being performed for individual CO₂ storage projects. Unlike commercial projects, this study is a public non-confidential project lead by the U of C in cooperation with Alberta Geological Survey.

A number of large stationary CO₂ emitters are located in central Alberta with cumulative CO₂ emissions of 30 Mt annually. This includes four coal-fired power generation plants in the Wabamun Lake area, which is located southwest of Edmonton. Emissions from these plants range from 3 to 6 Mt-CO₂/year. Although significant CO₂ storage capacity exists in depleted oil and gas reservoirs within the Wabamun area, these may not be available in the near future because most of the reservoirs are still producing. Moreover, the large Pembina Cardium oil fields located just south of the Wabamun Lake area are now producing through the assistance of mature waterflood systems and many are in the initial stages of investigating the use of CO₂ as a miscible flooding agent to further enhance oil recovery (EOR). Commercial scale use of CO₂ for this purpose is still a few years away and until then, these pools will require only pilot-scale volumes of CO₂ for reservoir characterization and testing purposes. As a result, CO₂ storage in deep saline aquifers is a likely near-future scenario for large scale CO₂ sequestration. While it is certainly possible to move CO₂ from the Wabamun area to distant storage locations, it is of considerable interest to public policy makers to determine if large-scale storage is feasible in the immediate vicinity of the power plants.

Early in the study, the Nisku aquifer was selected as the primary target for CO₂ sequestration. About a quarter (12 townships over the top northeast diagonal) of this area has current oil and gas exploration and production activity occurring in the Nisku formation, and represent a less desirable location for CO₂ injection in the short term. The remaining 38 townships were assessed as a possible repository for current CO₂ storage. Wells drilled in the area over the past 50 to 60 years enabled the study team to access geological and petroleum engineering information. Data was available primarily from two sources: public domain databases and oil and gas seismic data for the study area.

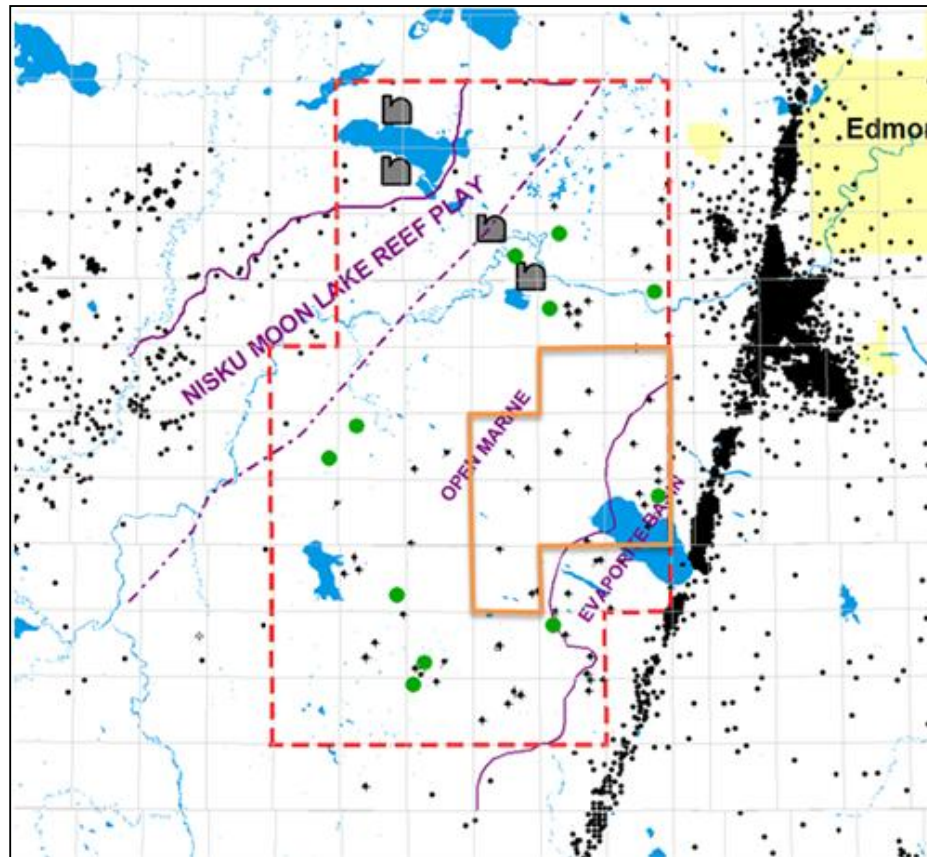


Figure 1: WASP Study Area

The WASP study was unusual in the aerial extent of the study area and the 1 Gt-CO₂ notional target for CO₂ injection. This scale raised new challenges with respect to available data. The most difficult challenges were as follows:

1. Only 96 wells (an average of 2 wells per township) have penetrated the Nisku aquifer's primary geological horizon.
2. Only two of these wells are active. One serves as a water source well and the other as a water injection well. Both are used in an up-hole waterflood operation. With so few wells, the team's ability to obtain fluid samples or use pressure measurements to test large-scale connectivity within the Nisku aquifer was limited.
3. Seismic data was plentiful, however, it was acquired for a variety of purposes over many decades. This resulted in the data being heterogeneous, which necessitated careful re-interpretation to maximize its value for characterizing the Nisku aquifer. In addition, the depth, thickness, and impedance contrast of the formation makes it a challenging target for seismic analysis.
4. Available core samples are very old (30 to 60 years) and not appropriate for geomechanical experimentation.
5. Well tests with limited duration were conducted using old pressure-measurement technology.
6. The Nisku is a marine carbonate reservoir, which makes the application of geo-statistical tools more difficult than for clastic sedimentary formations.

The challenge of sparse data relative to large study areas is likely to be inherent in any gigaton-scale CO₂ storage study. The WASP team exploited existing Nisku data to develop a range of models that were used to make initial assessments regarding favourable locations for further assessments. Uncertainties can be reduced in local areas, if reservoir evaluations for specific injection locations are performed. The WASP study has provided recommendations for prospective locations for CO₂ storage within the WASP study area, as well as site-specific evaluation methodologies (see the impedance analysis of the Geophysical Analysis and the porosity and permeability estimations in the Geological Modelling sections).

In addition to site-specific results, the WASP study has generated insights into how to manage large-scale CO₂ storage studies that aim to simultaneously evaluate secure large-scale storage while identifying prospective locations for storage sites.

Geological Characterization of the Nisku Aquifer for CO₂ Sequestration

Although other geological formations in the Wabamun Lake area have CO₂ storage capability, the Nisku aquifer was selected because of its depth, good reservoir qualities, and lack of oil and gas plays in the area of interest. The Nisku formation also scored well on the delicate balance between the availability of data (number of penetrating wells) and the risk of well leakage. One other deep reservoir, the Basal Cambrian sandstone, exists below the WASP study area. Unfortunately this horizon suffers from a lack of well penetration and associated data. Therefore, the WASP evaluation was limited to the Nisku aquifer.

Findings from the study include the following.

1. Mean porosities for the Nisku interval range from 3 to 5%, with localized zones in excess of 10%. These findings were determined from available core analyses and petro-physical wireline logs.
2. Permeability from core measurements (air permeabilities) yielded a median of 10 mD, but values are strongly heterogeneous with some intervals having values in excess of 1000 mD.
3. Geostatistical methods successfully made use of the more abundant wireline log information to create best-efforts-basis mapping of the distribution, connectivity, and size of the better porosity/permeability intervals. New statistical correlations were exploited between wireline resistivity and conductivity measurements, and porosity and permeability values were determined using core analyses. These correlations were then used to estimate porosity and permeability when core data was unavailable. Although these correlations are informative, further research is necessary for validation. This work is described in detail in this report (see Using Resistivity/Conductivity to Estimate Permeability in the Geological Modelling section).
4. Zones of high porosity (8% or higher) found from logs were distributed unequally in depth, with the lower third of the reservoir showing a higher than expected number of high permeability zones. Unfortunately, most of the core samples were only available for the upper third of the interval. This highlights the importance of using analyses that derive porosity/permeability data from wireline measurements.
5. A geostatistical method using “Geo-bodies” or “objects” was successfully employed to model the connectivity of high and lower porosity and permeability regions. Statistical information about geo-body distribution was gathered from satellite imagery of modern analogs for the Nisku aquifer. A large amount of uncertainty remains about the nature and extent of high porosity/permeability zones within the Nisku interval.

6. Geological models were generated and exported successfully for use in fluid-flow simulators. These simulators suggest potentially good injection volume capability is available in the Nisku aquifer (see summary of numerical modelling results below).

Geophysical Characterization of the Nisku Aquifer

The study area was explored using vintage surface seismic data that had been acquired as hydrocarbon exploration over many decades. The WASP team had access to approximately 200 seismic lines (2432 km total length) and seven 3D seismic volumes (419 km² total area). The datasets have varying acquisition and processing specifications. Therefore prior to interpretation, inversion and attribute analysis, two primary steps were taken. One was data calibration and the second amplitude normalization. While a catalog of seismic data was made covering the entire WASP region, detailed analyses was concentrated on the proposed CO₂ injection region.

The following are the most important findings.

1. There was no sign of faulting in the WASP study area.
2. The time structure map for the Nisku aquifer is smooth and consistent with the NE-SW regional dip orientation.
3. Several localized anomalies were detected in the focus area. The WASP team concluded that these were probably caused by dissolution (karsting) in the overlying Wabamun formation that occurred while it was near the surface. These locations should be avoided until further characterization can be completed to establish the level of connectivity between the Nisku and the Wabamun formations as a result of these features.
4. Several favourable zones of low acoustic impedance and high bulk porosity were identified in the study area. Ambiguity remains around how much the increase in shale content has impacted these measurements. Nevertheless, these zones are prospective as high permeability/porosity possibilities.
5. The use of surface seismic as a method of mapping the development of a Nisku CO₂ plume was difficult because of the thin nature of the Nisku formation. Therefore, other methods of monitoring CO₂ movement within the formation will be necessary.

Geochemical Characterization of the Nisku Aquifer for CO₂ Sequestration

The WASP study has compiled a baseline of geochemistry data for the Nisku formation using public domain data. This information was used in the geochemical modelling of the CO₂ injected into the Nisku formation over a 50-year period. The key findings of this model are as follows.

1. Nisku bines are “sour” in that they contain potentially significant concentrations of dissolved H₂S.
2. Small amounts of dolomite and calcite will be dissolved and/or precipitated in the reservoir. According to the simplified model, mineral trapping will likely only play a minor role in CO₂ sequestration.
3. For sulfur-containing species, there are no significant observable differences in the chemical or mineralogical reactions between H₂S and non-H₂S containing aquifers.
4. A further significant finding is the potential for H₂S to be exsolved into the advancing pure CO₂ plume. This point is discussed further in the reservoir modelling section below.

5. ToughReact is a 1D reservoir simulator with full geochemistry and was used to study the injection process. Please note that the differences between the results from ToughReact and the reservoir modelling sub-group have not been resolved. The preliminary results of the ToughReact simulations are as follows.
 - a. Between 34% (after 1 year) and 56% (after 50 years) of the injected CO₂ that dissolves in the brine will convert to bicarbonate (HCO₃⁻) in a process called “solubility trapping”.
 - b. Approximately 26 times more CO₂ will be sequestered in the brine compared to mineral trapping.
 - c. CO₂ injection will likely create a dehydrated region around the injection wellhead with the radius increasing from ~ 20 m after 1 year to 140 m after 50 years.

Reservoir Modelling of the Nisku Aquifer for CO₂ Sequestration

A number of reservoir models are discussed in this report. They range from generic assessments of CO₂ plume development using Nisku parameters to a full 3D areal model of the entire Nisku aquifer that assesses the long-term fate of a large scale 20 Mt/yr over 50 years CO₂ injection project. The following are the most important results from the reservoir modelling activity.

1. The primary limit to CO₂ storage capacity in the Nisku is the buildup of pressure at the injection wells. On the 50-year injection timescale, the entire WASP study area will be pressurized, so one cannot treat individual injection operations independently.
2. Although the large-scale pressure field is controlled by the total rate of injection into the Nisku, the pressure at the injection wells will be substantially higher than the large-scale background pressure. It is a requirement that injection well pressure be below fracture pressure, which will provide the first order of constraint on storage volumes.
3. Methods to increase near-well injectivity can significantly reduce near-well pressure and increase overall storage capacity. For example, horizontal injection wells and the use of modern methods to stimulate these wells (i.e., controlled multiple vertical fractures), can increase total storage capacity by ~ 50% while maintaining a given maximum wellbore pressure.
4. Available pore space is not a significant limitation in the 50-year scenario with no brine production.
5. The CO₂ saturation plumes associated with large-scale multiple injection projects do not show interference and are limited to radii of about 4 or 5 km, assuming injection rates of 0.25 to 0.5 Mt/yr/well.
6. Managing reservoir pressure by removing brine from the Nisku formation may substantially increase overall storage capacity.
7. H₂S dissolved in the Nisku aquifer brine may pose an additional risk when the gas front passes by existing wells. Maximum H₂S saturation in the gas phase is located at the leading edge of the advancing CO₂ plume; and the composition of the gas at the edge can be dominated by H₂S even for relatively low-dissolved H₂S concentrations in the brine. This is an important and unique finding for the WASP study that underscores the importance of proper geochemical characterization of the formation fluids prior to initiating a CO₂ sequestration project. Knowledge of these phenomena enables engineers to properly plan for the existence of H₂S in potential produced fluids associated with future plume management programs.

One of the most significant finding is that plume pressure management will be required to increase CO₂ storage capacity in large-scale CO₂ sequestration projects. Members of the WASP team have previously published studies on the engineering methods needed to “manage” the placement of CO₂ plumes to mitigate the saturation plume radius using methods that force CO₂ dissolution. It is almost a certainty that these approaches will eventually be required once many large scale CO₂ sequestration projects are underway and competing for aquifer storage space. If these methods are employed and they involve brine production from a target reservoir, it will be very important to be aware of any increase in H₂S concentrations in the advancing CO₂ plume.

Geomechanical Data Analysis of the Nisku Aquifer for CO₂ Sequestration

In-situ stress fields for the subsurface of the Wabamun CO₂ storage area where established based on existing analyses. These analyses provided guidance for determining maximum injection pressure and acted as boundary conditions for further geomechanical modelling efforts.

A table of geomechanical properties for the subsurface at the Wabamun CO₂ storage area was created. Well logs were used to establish dynamic deformation properties (Young’s modulus, Poisson’s ratio and bulk modulus) and correlations were used to determine static deformation properties. The unconfined compressive strength (UCS) was established for each lithology based on correlations with log properties. The created database was used as input data for the geomechanical modelling component of the WASP study. The lower sedimentary succession within the Nisku aquifer and Calmar cap rock is very competent stiff rock.

When new cores become available from future drilled CO₂ sequestration wells, it will be important to perform a modern suite of geomechanical tests on these samples. For example, tri-axial laboratory tests are recommended to confirm the accuracy of the UCS correlations for the site and to adjust the dynamic-to-static conversion factors. Because of the age of the existing cores, they are not suitable for this kind of laboratory analysis.

Geomechanical Modelling of the Nisku Aquifer for CO₂ Sequestration

Potential surface heaving and hydraulic-induced fracturing because of a large scale CO₂ injection project were investigated using GEOSIM, a state-of-the-art coupled flow and geomechanical modelling program. Injection of CO₂ into the Nisku aquifer (premised on bottom hole injection pressures being below fracture pressures) is not likely to cause any significant surface heave or environmental impact associated with surface deformation.

Injection of CO₂ above the fracture pressure will have the potential to increase well injectivity, but may also fracture the caprock. This underscores the importance of acquiring detailed laboratory geomechanical fracture tests on fresh caprock core samples.

Also of significant importance is the need to determine the thermal impact of cold CO₂ injection on the reduction in fracture pressure. Indications from the reported work suggest that cold CO₂ injection may significantly reduce the fracture pressure, while improving the containment of the fracture to the injection zone and reducing the likelihood of fracturing the caprock. This is of particular concern/interest for any large scale commercial CO₂ sequestration projects.

Well Integrity Review of Existing Wells Penetrating the Nisku Aquifer

After a thorough review of the existing wells penetrating the Nisku aquifer, only 4 of the 27 wells in the WASP focus area (smaller region highlighted by an orange boundary in Figure 1) were deemed to require remediation work. This is a welcomed outcome relative to original concerns that abandoned wells drilled through the Nisku aquifer would require significant remediation. More details are reported in the Well Integrity section of this report.

The cost of a properly designed and constructed vertical CO₂ injection well is around \$1.3 million CAD. The oil and gas industry already drills and completes this class of well with good results and integrity.

Based on the results of the literature review conducted for the WASP study on the impact of injecting cold CO₂, there is some concern relating to thermal and pressure cycling effects on cement sheath integrity for future CO₂ injection wells. More experimentation using scale models and in-situ testing is needed to fully assess these issues.

Risk Based Leakage Model for the WASP Study

Golder and Associates developed a probabilistic analytical simulator capable of evaluating alternative leakage scenarios associated with legacy wells in multiple formations. The intent of developing this model was to provide a tool that would help with the prioritization of site characterization needs by reducing the overall uncertainty in the ultimate performance of a potential carbon capture site (CCS) site.

Results generated by the model are preliminary. More site-specific information would be necessary to fully utilize the model to establish risk levels that are meaningful for specific projects.

WASP CO₂ Monitoring Measurement and Verification Recommendations

This section of the report is intended to provide a specific set of recommendations relative to a full scale CO₂ sequestration project (i.e., 1 Mt/yr single CO₂ injector). Several stages of development are recommended before an actual full-scale CO₂ injection site is started. In addition, a set of specific monitoring requirements should be implemented for each stage of development.

Given that it was concluded in the geophysical analysis section that surface 3D monitoring of the movement of a CO₂ plume would not be useful, the need to drill monitoring wells (or recomplete existing wells) is stressed. Monitoring wells could be designed as information sources for small CO₂ sequestration projects, and could later be converted to brine injectors or producers for plume management for larger-scale CO₂ sequestration projects.

Although 3D geophysical monitoring of plume movement within the Nisku formation may not be feasible, monitoring of potential CO₂ leakage to the formations above the Nisku (i.e., Wabamun and Banff) may be possible, and would be a sensitive way to detect CO₂ movement. This would ensure the integrity of CO₂ stored in the Nisku. The extent to which baseline surveys are needed to use this method still needs to be resolved.

Full Commercial Scale Economic Summary

The cost for storing large quantities of CO₂ was addressed by developing cost models that reflected several simulated injection scenarios. The storage capacity was evaluated for a time period of 50 years for each injection well development scenario: vertical or horizontal injection wells with or without fractures to stimulate injection. The total volume of stored CO₂ was in the range of 210 to 430 million tonnes. These development scenarios assumed the use of ten vertical injection wells or ten horizontal fracture stimulated wells respectively. The cost model objective was to evaluate only the sequestration costs, which included all costs encountered from the wellhead down into the formation, as well as the costs for a monitoring program. The cost of capturing, pressurizing, and transporting CO₂ to the injection site was not included in the model.

The overall cost for the storage project was in the range of \$700 million CAD for the injection scenario with ten vertical injection wells, and up to \$1.1 billion CAD for the scenario with 10 horizontal hydraulically fractured injection wells. All values are stated in 2009 dollars. The average cost for storing a ton of CO₂ was estimated to be in the range of \$2.7 to \$3.4 CAD/ton depending on the type of injection well used. The lowest cost per ton was obtained using horizontal fracture stimulated wells, which also gave the largest amount of stored CO₂. The largest portion of the costs involved monitoring, which accounted for about 75% of the total cost. In addition, 4D seismic acquisition made up the majority of the monitoring costs.

Conclusion and Recommendations

The most important conclusion of this first phase of the WASP studies is that the Nisku aquifer continues to represent a viable location for the long-term sequestration of CO₂. All available public domain data (and a significant amount of industry seismic data) were used to arrive at this conclusion. Straight CO₂ injection without intentionally managing reservoir pressures (i.e., through brine production and re-injection into a different aquifer or location) will ultimately limit the capacity for CO₂ storage. In the case of the WASP study area, that limitation would be in the range of 0.25 to 0.40 Gt of cumulative CO₂ injection. However, this is a very conservative estimate of the total capacity for the Nisku aquifer's ability to accept CO₂. The total capacity for a "managed" project where net brine withdrawal is used to mitigate the increase in aquifer pressure could easily be 2, 3 or more times this conservative capacity estimate. In other words, the WASP study has identified the lower boundaries of the Nisku formation's storage capacity.

Future studies will need to go further to explore pressure and CO₂ saturation management of the injection plume. This would likely be accomplished with strategically located brine injection and production wells designed to accelerate solution and saturation trapping of CO₂ while maintaining a net total voidage replacement ratio of 1.0 (i.e., an equal reservoir volume withdrawal of fluids relative to the reservoir volume of injected CO₂). This will prevent average reservoir pressure from exceeding the initial pressure at the start of the project. Of course this assumes availability of capacity for re-injection of excess brine production into a suitable brine aquifer either above, below, or adjacent to the aquifer where the CO₂ is being sequestered.

Recommendations for Future WASP Studies

The following is a list of recommendations for future WASP studies.

1. Brine compositions in the WASP database are based on simple sampling methods that do not preserve dissolved gases. Consequently, bottomhole sampling or sampling through surface separators, is required to determine reservoir compositions of dissolved gases. Proper planning of a CO₂ storage project relies on this information.
2. Available seismic data has not been typically shot with the saline aquifer (in this case the Nisku formation) as the primary target. Coverage and vintage issues are also a factor that has limited the options for interpretation and modelling. New seismic programs specifically targeting the Nisku aquifer in the vicinity of a planned CO₂ sequestration site would be useful for the following reasons:
 - a. for verification of what is currently being interpreted as karst features to assess the possibility that these features represent possible leakage paths,
 - b. for verification of low impedance (higher porosity zones) within the Nisku formation, and
 - c. to establish a baseline enabling future seismic to monitor movement of CO₂ to formations above the Nisku in the event of a breach of the cap rock or well seals.
3. Available core from the cap rock (Calmar formation shale) and underlying seal (Ireton formation. shale) are not adequate because of their age—often more than 30 years old and of a highly desiccated nature. Proper geomechanical analysis requires fresh core samples.
4. Various in-situ test programs are needed to assess the geothermal effects on fracturing of reservoir and cap rock and actual leakage rates through compromised cement behind casing and/or poor abandonment. Intentionally designed test wells and testing sites are vital.
5. Pressure management of the injection plume is critical. To that end, DSTs and core samples need to be taken from aquifers that are above and below the target sequestration site. Early on in the development of saline aquifer sequestration sites, characterization needs to address seal quality as much as the actual injection reservoir. Carefully planned and designed vertical pressure transient interference tests to determine the effective vertical permeability are vital for modelling of vertical CO₂ plume movement and evolution.
6. The deepest potential sequestration formations, such as the Basal Cambrian formation sandstone in the WASP region, also need to be appraised as potential CO₂ containers. The lack of financial incentives to explore these possibilities could result in better injection targets being overlooked.

The first phase of the WASP project was about characterization—determining what data is available, interpreting and integrating that data, and predicting system behavior during and after large-scale injection. The next phases of WASP will focus on acquiring data to compensate for the deficiencies listed above. A set of recommended test programs for wells intentionally drilled as test wells and/or CO₂ injectors will be identified and mathematically modelled. The analysis of these tests will facilitate improvements in the design of future large-scale CO₂ sequestration projects. As the rapidly growing industry for the geological storage of CO₂ is nascent, it is necessary and appropriate to define the strategies now to deal with data deficiencies specific to these projects.

Data Integration, Petrophysics, and Geomodelling

Wabamun Area CO₂ Sequestration Project (WASP)

Authors

Chris L. Eisinger

Jerry L. Jensen

Rev.	Date	Description	Prepared by
11	December 22, 2009	WASP Static Earth Model: Final Report	Chris Eisinger & Jerry Jensen

Table of Contents

INTRODUCTION.....	7
Area Of Interest	7
Geological Setting.....	7
Nisku Deposition And Lithofacies	10
1. DATA	14
1.1 Wells	14
1.2 Core	14
1.3 Wireline Geophysical Logs	16
1.4 Seismic Data.....	16
1.5 Mineralogy	16
1.6 Drill Stem Tests.....	17
2. PETROPHYSICS.....	19
2.1 Well Logs	19
2.2 Porosity Estimation	20
2.2.1 Core.....	20
2.2.2 Acoustic Wireline Logs	21
2.2.3 Density And Neutron Wireline Logs	22
2.2.4 Resistivity Wireline Logs	25
2.2.5 Porosity—Summary	27
2.3 Permeability Estimation	27
2.3.1 Core.....	27
2.3.2 Well Tests.....	28
2.3.3 Analysis Of Production Data	29
2.3.4 Using Resistivity/Conductivity To Estimate Permeability	29
2.3.5 Permeability—Summary.....	31
2.4 Nisku Lithofacies Distinction	31
3. GEOMODELLING.....	34
3.1 Structural And Stratigraphic Grid	34
3.2 Depositional Grid	34
3.3 Upscaling Well Logs	36
3.4 Variogram Analysis.....	36
3.5 Permeability Estimates	37
3.6 Pixel-Based Modelling	38
3.6.1 Kriging	38
3.6.2 Sequential Gaussian Simulation (Sgs).....	40
3.7 Object-Based Modelling.....	42
3.7.1 Nisku Enhanced Poro-Perm Objects	43
3.8 Model Validation	47
3.9 Summary.....	47
CONCLUSIONS.....	47
ACKNOWLEDGEMENTS	48
REFERENCES.....	49

APPENDIX 1: WELLS (NISKU)	51
APPENDIX 2: WELL CORES (WASP AREA)	54
APPENDIX 3: WIRELINE GEOPHYSICAL LOGS.....	55
APPENDIX 4: DRILL STEM TESTS	59
APPENDIX 5: FORMATION WATER RESISTIVITY	61
APPENDIX 6: POROSITY AND PERMEABILITY (INBOARD PLATFORM MARGIN)	62

List of Tables

Table 1: Summary of DST analyses from Nisku interval in WASP region.....	18
Table 2: Vertical grid divisions for Nisku model.	36
Table 3: Geometry of enhanced porosity and permeability objects. All distributions are triangular between minimum, mean, and maximum.	44
Table 4: Division of objects based on vertical interval, enhanced regions, and classes. The percent of total volume objects occupy is a controlled parameter subjectively estimated. IBM = inboard margin, OM = open marine.	45
Table 5: Minimum potential storage capacity for Nisku reservoir using WASP boundary. Actual volumes will be larger as aquifer extends to the northwest and southeast of study area. Mean permeability (k) is significantly larger for the object model as isolated grid cells containing high values affect the result.	47

List of Figures

Figure 1: The WASP study area (red outline) and locations of four large power plants. Black circles show wells that penetrate the Nisku Formation. Purple lines mark important depositional boundaries of the Upper Devonian. The study area has an areal extent of approximately 5000 km ²	8
Figure 2: Geologic cross-section of the Western Canada Sedimentary Basin (Wright et al., 1994) showing Paleozoic interval of interest (yellow box). Stratigraphic column (modified from Bachu and Bennion, 2008) shows distribution of aquifers and aquitards. The target formation is the Upper Devonian Nisku carbonate.	9
Figure 3: The top image shows a conceptual cross-section through the Nisku formation in the WASP study area. Red areas indicate larger expected porosity and vertical blue columns represent existing well cores. Most cores sample the upper portion of Nisku, where porosity is thought to be poorer. The map shows the outline of the entire study area (dashed red) and a high-grade focus area for seismic interpretation (solid orange). NE-SW cross-section line correlates with the above figure.	10
Figure 4: Isopach map (thickness) of Nisku carbonate (from SCG Ltd). Thickest portion is near the edge of shelf reef play with most areas between 50 and 100 m thick.	11
Figure 5: Sample of typical hypersaline facies. Dolomitic mudstone to grainstone with anhydrite plugging are evident.	12
Figure 6: Samples of open marine facies of Devonian Nisku Fm. Typical carbonate (top) versus carbonate with exceptional porosity and permeability (bottom). High porosity example (bottom) shows evidence of abundant Amphipora. Core photos courtesy of SCG Ltd.	13
Figure 7: Distribution of available well cores from the Nisku. Core analyses from existing (5 wells) and newly acquired (8 wells) data sets.	15
Figure 8: Available 2D and 3D seismic data for WASP study. Map (top) shows distribution relative to study area (green) and high-grade focus area (HGFA) (purple). For further information refer to geophysics chapter of report.	17
Figure 9: Distribution of DSTs within WASP study area (green circles).	18
Figure 10: Core porosity data and sample locations.	20
Figure 11: Cross-plot of core porosity estimates versus acoustic log estimates. Larger circles represent mean values for each well (shown in different colours).	21
Figure 12: Porosity determinations from acoustic and density-neutron wireline logs. Locations for samples shown on right.	22
Figure 13: Distribution of deep resistivity and conductivity logs in WASP area. Yellow circles indicate wells with coincident density-neutron logs.	25
Figure 14: Relationship between deep resistivity data and porosity based on Archie's Law. Cementation factor (m) likely between 2 and 3.	26
Figure 15: Intervals of enhanced porosity (<10 ohm-m [blue] and <5 ohm-m [red]) are shown on a cross-section of deep resistivity logs. There is a concentration of higher porosity zones in lower third of Nisku interval.	26
Figure 16: Core permeability measurements (kMax) from the 13 wells with Nisku sampling.	27
Figure 17: Core-measured permeability × thickness (from 7 wells).	28

Figure 18: Relationship between maximum conductivity (from wireline logs) and permeability thickness from core (green circles) and DSTs (pink circles). The cause(s) for the two wells with (kh)DST = 0.3 mD-m to have different behaviour than other wells could not be determined. Open red circle shows water production well (F1/11-29-045-02W5/00) based on known max conductivity measurement and estimate of flow rate. 29

Figure 19: Cumulative distribution function (CDF) of wells based on Cmax (above). Dashed line indicates the equivalent of a ~1 D-m flow capacity threshold. 30

Figure 20: Green circles on map indicate locations of >2 D-m potential flow-capacity wells. 31

Figure 21: Conceptual model showing distribution of open marine facies (blue) and hypersaline facies (yellow) along an NW-SE cross section of WASP area. 32

Figure 22: CDF of sonic wireline data for two recognized Nisku facies—open marine (blue) and hypersaline (yellow). 33

Figure 23: CDF of deep resistivity wireline data for two recognized Nisku facies—open marine (blue) and hypersaline (yellow). 33

Figure 24: Modelled horizons derived from location of formation tops as identified in well logs. Green—Wabamun (carbonate), Pink—Graminia (shale), Purple—Blue Ridge (carbonate), Brown—Calmar (shale), Blue—Nisku open marine (carbonate), Yellow—Nisku hypersaline (carbonate). Red box shows approximate area of Figure 27 below. Vertical exaggeration = 25. 35

Figure 25: Cross-section of Nisku open marine reservoir model showing vertical and horizontal grid spacing. Note vertical division in 3 zones (blue, green, and red) representing potentially differing flow regimes within reservoir. 35

Figure 26: Sample vertical variogram analysis for porosity in the open marine facies of the Nisku reservoir. Vertical range = 27 m, nugget = 0.22. Grey squares show calculated semivariance at a given correlation distance. Blue line represents experimental variogram (gaussian) that was modelled. 36

Figure 27: Porosity-permeability cross plot. Manually fitted line (black) manually overestimates permeability when $\phi > 4\%$ 37

Figure 28: Sample output of ordinary kriging algorithm for porosity of the open marine facies of the Nisku (based on resistivity-derived porosity). 39

Figure 29: Distribution of available 3D acoustic impedance data used for collocated cokriging. 40

Figure 30: Five SGS realizations for Nisku open marine facies porosity (top) and permeability (bottom). 41

Figure 31: A three-dimensional model realization for porosity and permeability of the Nisku reservoir. 42

Figure 32: Generalized workflow for facies attributes (as inferred from satellite imagery) of modern carbonate analogs to be used in generating object-based models. 43

Figure 33: Two regions with higher probability for enhanced porosity and permeability objects based on conceptual modelling of regional deposition. Inboard margin (IBM) (dark blue) and open marine (light blue). 44

Figure 34: Example of object geometries and distributions for object-based modelling for three Nisku intervals in WASP area. Yellow—background Nisku; blue—better porosity and permeability; turquoise—best porosity and permeability. 46

Figure 35: Examples of flow property modelling based on object-models. Porosity (left) scaled 0 to 15% and permeability (right) scaled 1 to 1000 mD. 46

INTRODUCTION

In order to properly assess the storage capacity, injectivity, and confinement of potential deep-saline aquifers in the Wabamun region it is critical to construct a static geological model that characterizes the Nisku aquifer with sufficient accuracy. The model, presented in this section of the report, provides a working understanding of potential repositories, traps, and sealing mechanisms that will be needed to design and implement a CO₂ injection project in the area of interest. As with most geocellular models, it incorporates geological information (stratigraphy, facies mapping, and structure) with estimates of critical flow parameters (e.g., porosity and permeability) at all locations. This model serves as the basis for the fluid flow simulations—a key exercise in predicting the potential for CO₂ injection and storage in the targeted aquifers.

Area of Interest

The Wabamun Area Sequestration Project (WASP) includes a region southwest of Edmonton, Alberta (Figure 1) with a total areal extent of approximately 5034 km². The area of interest (AOI) encompasses 60 townships (57.9 km × 96.6 km) of predominantly agricultural and recreational land. Four major coal-burning power plants are located in the northern portion of the study area (Figure 1) with more than 4000 MW total generating capacity between them. The AOI for WASP is expanded from a region previously identified as a potential site for geological storage of CO₂ (Hitchon, 1996; Michael et al., 2006; Michael et al., 2009).

Geological Setting

The sedimentary sequence for the WASP study area can be divided into Cretaceous and pre-Cretaceous (i.e., Mississippian, Devonian, and Cambrian) units, corresponding with an initial long period of passive margin deposition (blue-green layers on Figure 2), followed by the formation of a deep foreland basin (yellow layers on Figure 2). The combined Cretaceous and pre-Cretaceous intervals can be greater than 1500 m thick in the area of interest. The Paleozoic sequence is marine carbonate and shale dominated with passive margin sandstones found in the Cambrian basal unit. Cretaceous formations are mostly siliciclastics—sandstones, siltstones, and shales. All of the beds dip gently from NE-SW approximately 0.5 degrees on average through the study area.

In selecting aquifers most suitable for CO₂ injection, some key criteria are: (1) aquifer depth; the aquifer needs to be sufficiently deep to allow pressures and temperatures necessary for CO₂ to exist as a super critical fluid (i.e., 31.1°C and 7.8 MPa), but not so deep as to have little permeability (reservoir quality); (2) proximal barriers; there should exist multiple impermeable and low-permeability horizons (i.e., aquitards and aquicludes) between the target aquifer and the surface to minimize leakage risk; and (3) interference with existing activities; there should be no impact on existing hydrocarbon production. Using these simple criteria, the best aquifer targets in the WASP area are the Paleozoic passive-margin carbonates and basal Cambrian sandstones. A saline aquifer, the Devonian Nisku (Figure 2), is of particular interest as its depth, thickness, and stratigraphic configuration appear to be well suited for CO₂ injection and storage.

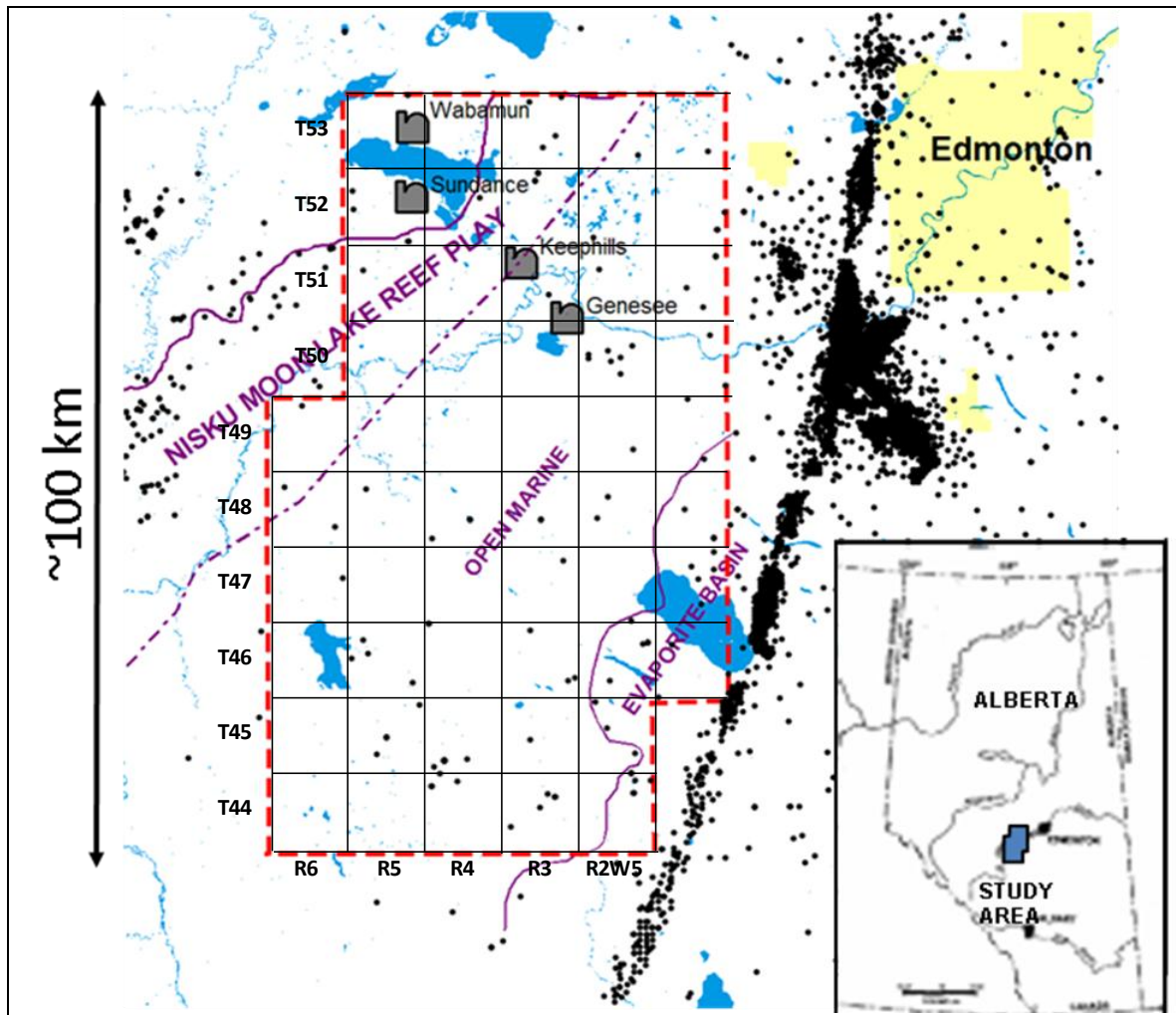
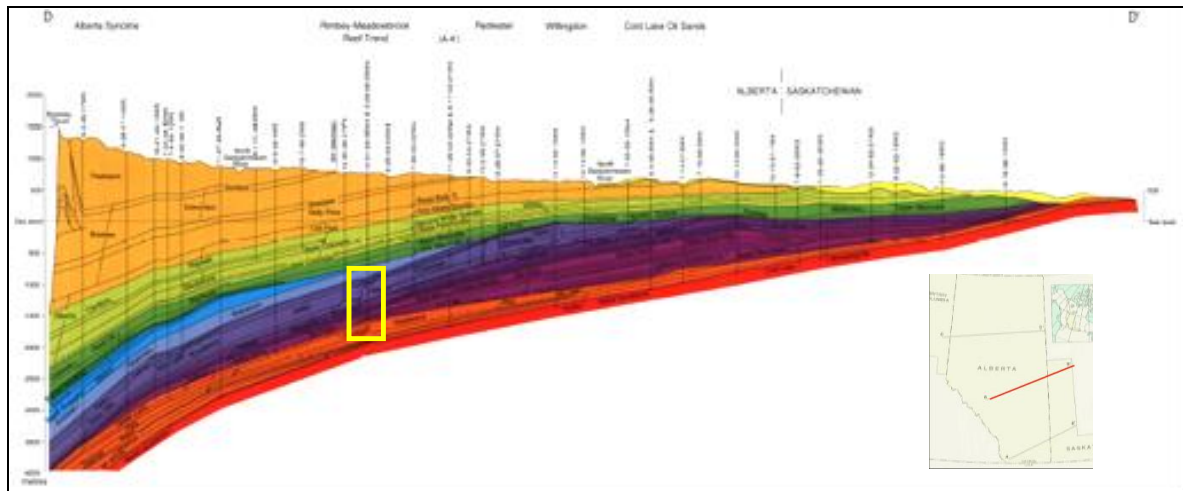


Figure 1: The WASP study area (red outline) and locations of four large power plants. Black circles show wells that penetrate the Nisku Formation. Purple lines mark important depositional boundaries of the Upper Devonian. The study area has an areal extent of approximately 5000 km².



(Wright et al., 1994)

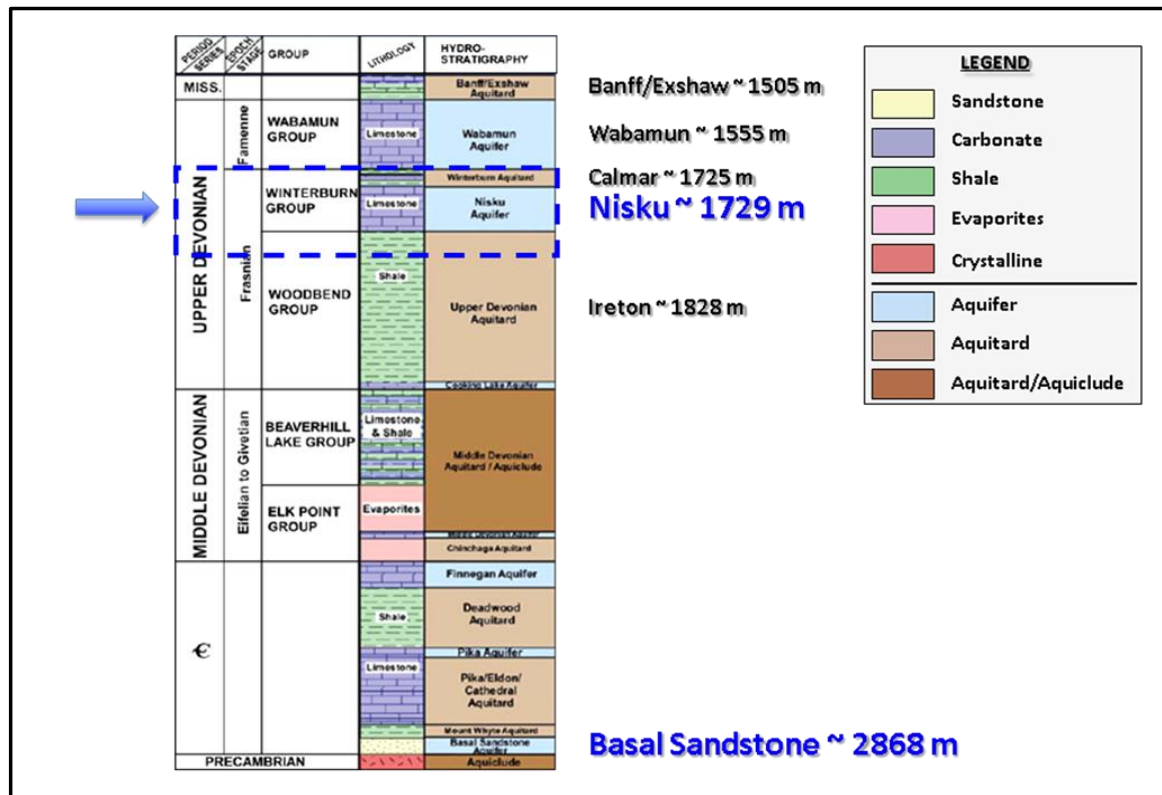


Figure 2: Geologic cross-section of the Western Canada Sedimentary Basin (Wright et al., 1994) showing Paleozoic interval of interest (yellow box). Stratigraphic column (modified from Bachu and Bennion, 2008) shows distribution of aquifers and aquitards. The target formation is the Upper Devonian Nisku carbonate.

Nisku Deposition and Lithofacies

Nisku deposition is part of the Winterburn Group after the last phase of the Woodbend Group sequence when the Western Canada Sedimentary Basin was nearly filled with shales and carbonates. The Nisku interval represents a strong marine transgression with carbonate ramp deposition dominant (Switzer et al., 1994). Indications suggest a late stage regressive episode as well, but deposition was diminished during this time in the area of interest (Switzer et al., 1994).

The WASP region includes open marine and more shallow, hypersaline carbonate ramp deposits within the Nisku stratigraphic interval (Figure 3). Thickness of the Nisku carbonate accumulation is shown in Figure 4, ranging from 40 m near the eastern boundary of the study area to over 100 m closer to the shelf margin. Basinward are hydrocarbon bearing pinnacle reefs (Zeta Pinnacle Trend) and shelf margin reefs (Moon Lake Build-Ups). These mark the western boundary of the potential injection aquifer. The eastern boundary is delineated by the transition from open marine carbonate facies to lower permeability hypersaline rocks of a paleo-evaporite basin (Figure 3).

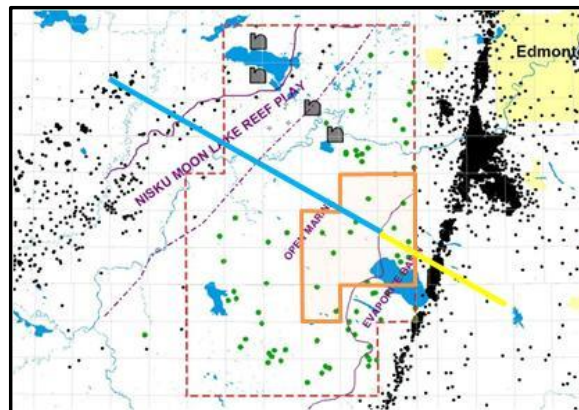
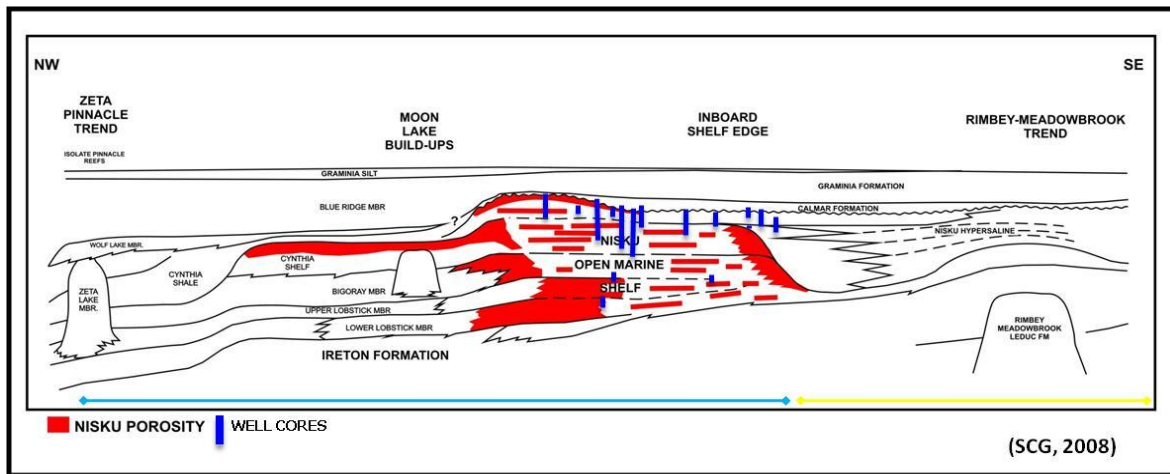


Figure 3: The top image shows a conceptual cross-section through the Nisku formation in the WASP study area. Red areas indicate larger expected porosity and vertical blue columns represent existing well cores. Most cores sample the upper portion of Nisku, where porosity is thought to be poorer. The map shows the outline of the entire study area (dashed red) and a high-grade focus area for seismic interpretation (solid orange). NE-SW cross-section line correlates with the above figure.

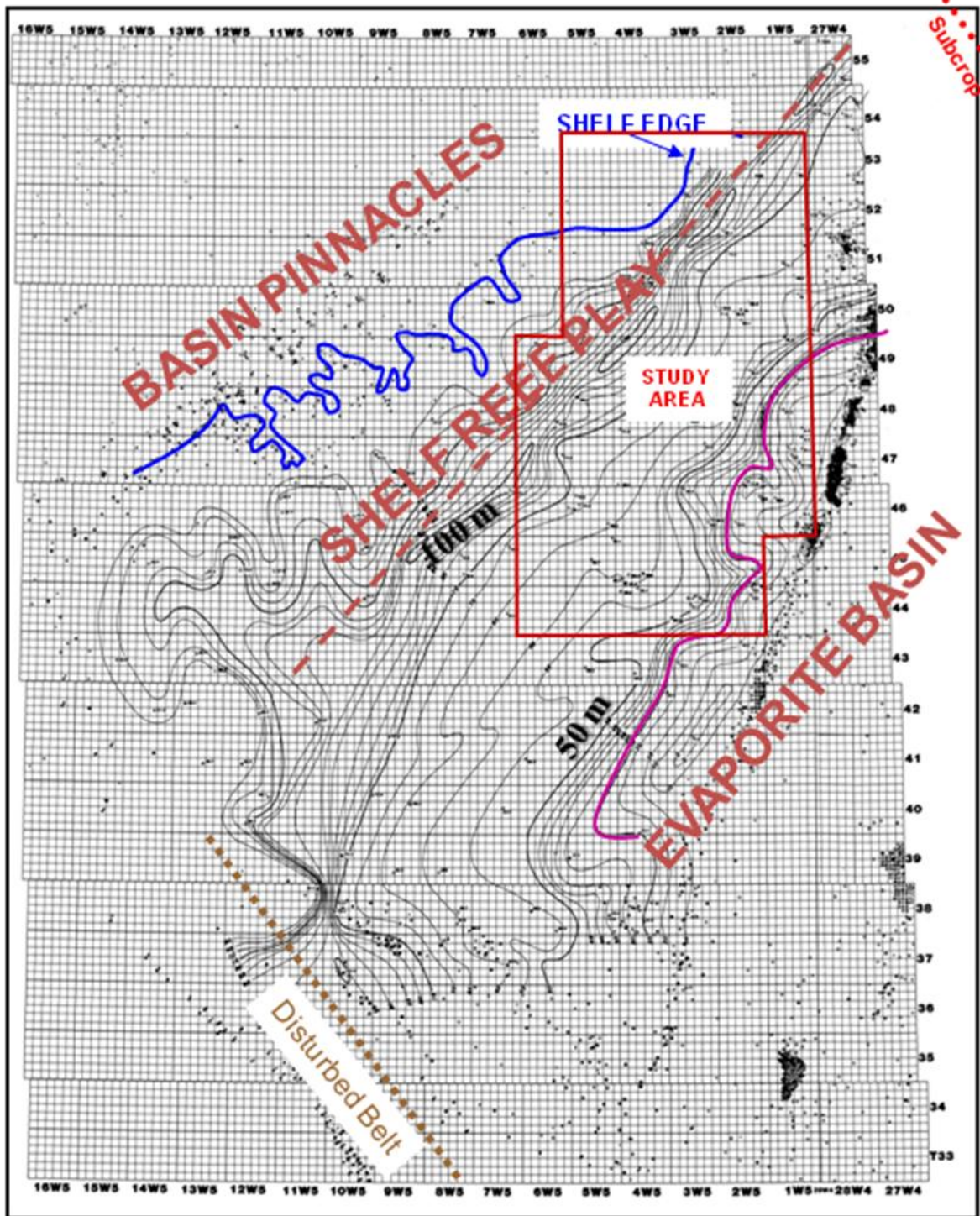


Figure 4: Isopach map (thickness) of Nisku carbonate (from SCG Ltd). Thickest portion is near the edge of shelf reef play with most areas between 50 and 100 m thick.

For the WASP study, two facies assemblages were recognized from the limited core available: an undifferentiated open marine carbonate and a hypersaline carbonate mudstone. The hypersaline facies (Figure 5) is comprised of dolomitic mudstone to grainstone with occasional moldic porosity and very limited *Amphipora* present. Abundant anhydrite and fine-grained silt and shale stringers reduce the permeability significantly. Measurements of core permeability are less than 5 mD and porosity is typically less than 2%. The open marine facies (Figure 6) includes dolomitic mudstone to boundstone lithologies. Vuggy and moldic porosity can be observed in some intervals. Anhydrite plugging is limited. *Stromatoporoids* and *Amphipora* are common, with less frequent corals and brachiopods also observed. From core measurements, porosities are typically between 3 and 5%, and permeabilities are between 5 and 15 mD. In more exceptional cases, porosity exceeds 12%, with permeability in the range of several Darcys.

The Nisku shelf is underlain by Ireton Fm. shales and overlain by fine-grained clastics of the Calmar Formation—a persistent, low-permeability shale unit typically between 5 and 12 m thick. Above the Calmar Fm. is the Graminia Fm. (including the Blue Ridge Member), which collectively with the Calmar comprise the Winterburn aquitard (Figure 2).

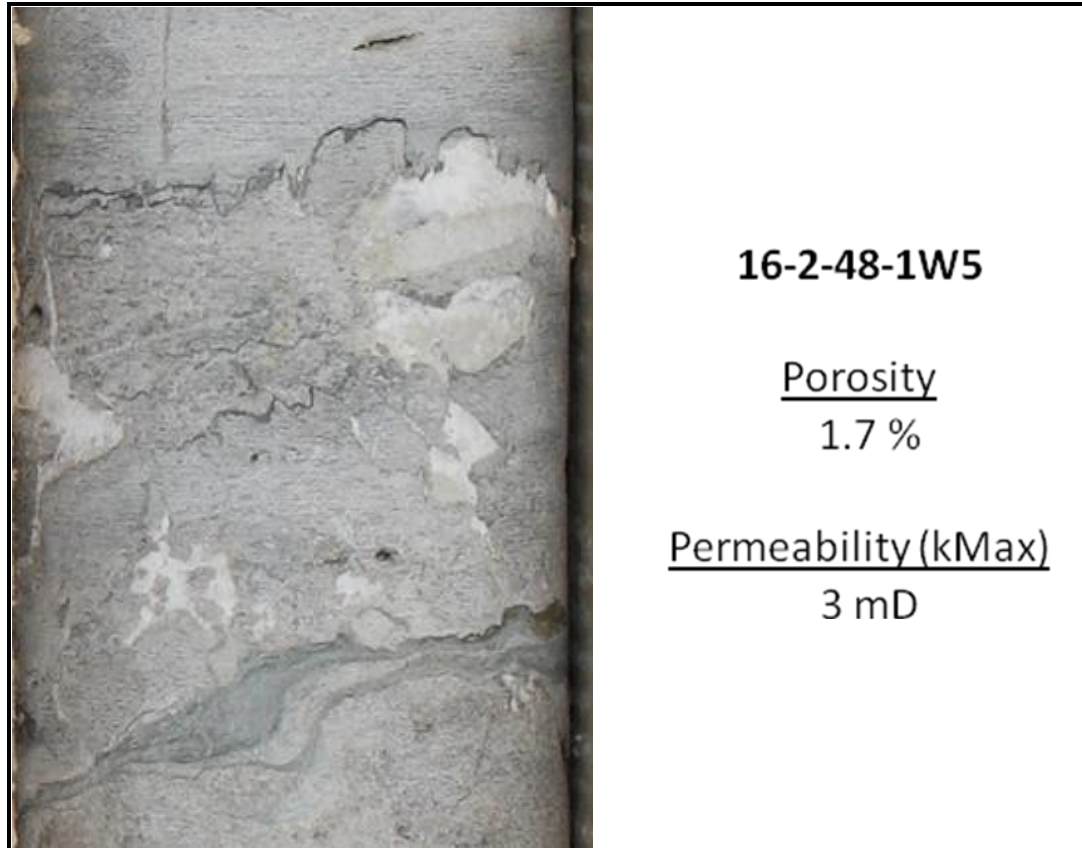


Figure 5: Sample of typical hypersaline facies. Dolomitic mudstone to grainstone with anhydrite plugging are evident.

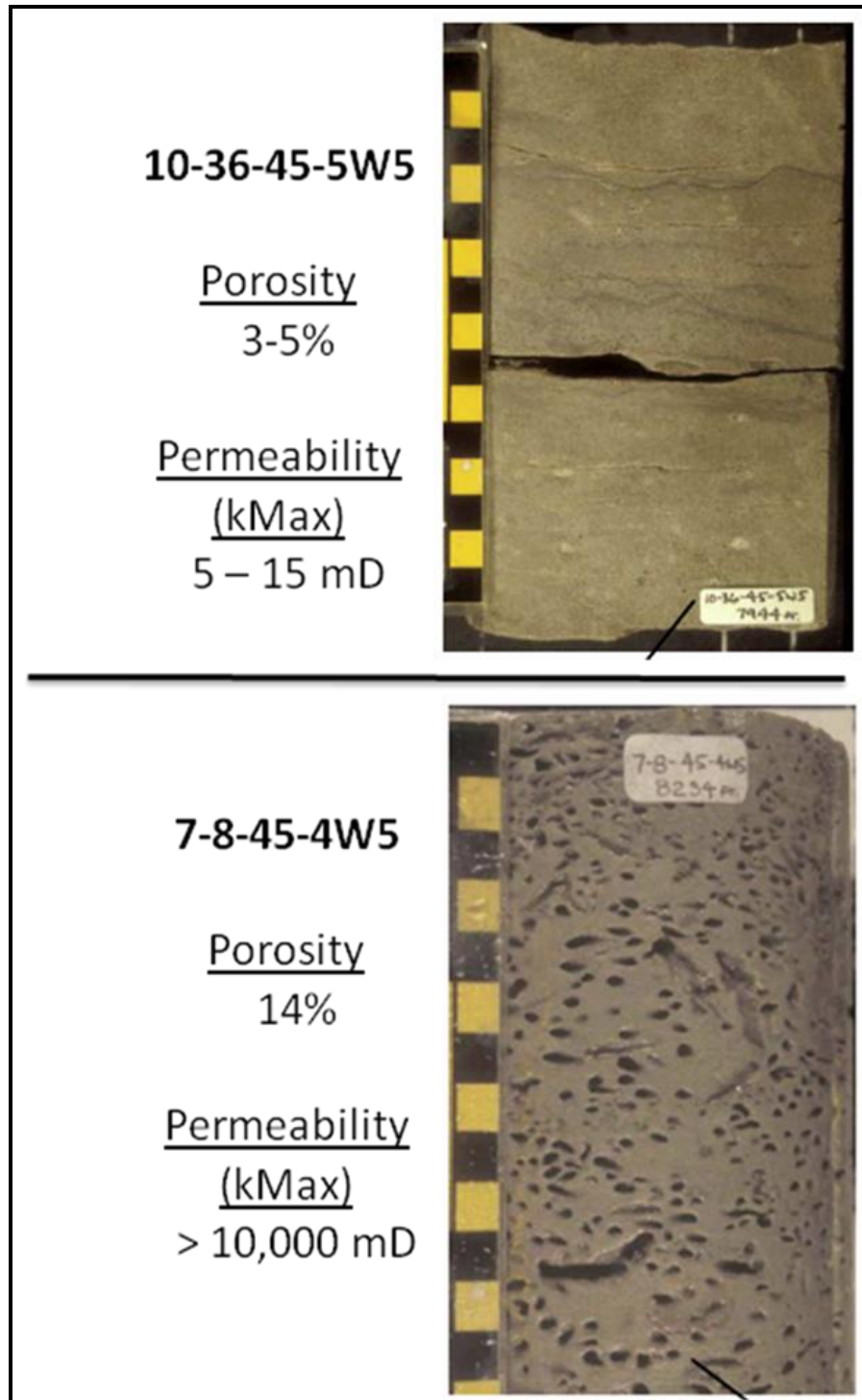


Figure 6: Samples of open marine facies of Devonian Nisku Fm. Typical carbonate (top) versus carbonate with exceptional porosity and permeability (bottom). High porosity example (bottom) shows evidence of abundant Amphipora. Core photos courtesy of SCG Ltd.

1. DATA

The static earth model comprises characterizations of facies, porosity (ϕ), and permeability (k) in the WASP study area. The static model then feeds into dynamic models for fluid flow and geomechanical simulation. Information used for creation of the static earth model includes:

- Data from 96 wells that penetrate the Nisku within the WASP AOI.
- Wireline geophysical logs of varying vintage, from the 1950s to recent suites.
- Routine core analyses and lithological descriptions for 13 wells in the study area. Special core analyses for select samples.
- Processed and raw geophysical data.
- Drill stem tests (DSTs) of generally poor quality.
- Petrographic studies, both publicly available and newly completed for this study.

All core, geophysical, seismic, geomechanical, geochemical, and other relevant data sets used for this study are collected in a digital database maintained with the Energy and Environmental Systems Group (EESG) at the University of Calgary.

The distribution of these sparse data presents a challenge for accurate modelling in the inter-well zones (Figure 7). Cored wells only cover approximately 10% of the WASP area, and inter-well distances are on the order of ~0.5 km to >20 km.

1.1 Wells

For each well drilled, information is provided about the location and depth, the historical status of operation, and in some cases, well casing and completion. Production data are scarce for the Nisku interval as very few wells have produced. One notable exception is a currently active water-production well (F1/11-29-045-02W5/00), which has data recorded since January 2003. A list of wells and selected information are provided in Appendix 1. The entire database is available digitally in the WASP project archives.

1.2 Core

Thirteen wells that include core for some portion of the Nisku interval in the AOI (see Figure 7 and Appendix 2) were logged. Cores are typically 1", 3", or 4" diameter, and represent a small portion of the Nisku interval, usually <20 m. Prior to this study five wells included core with routine core analysis. For this project, cores from eight additional wells were sent for routine analyses. Core plugs provided measurements of porosity, permeability, and in most cases grain density. Two of these wells were outside the study area (Figure 7). Special core analyses (directional permeability and compressibility measurements) were obtained for a subset of collected cores.

All available cored sections were logged by SCG Ltd. and are stored at the ERCB's Core Research Centre in Calgary, Alberta. Core descriptions and photographs are available in the WASP project archives.

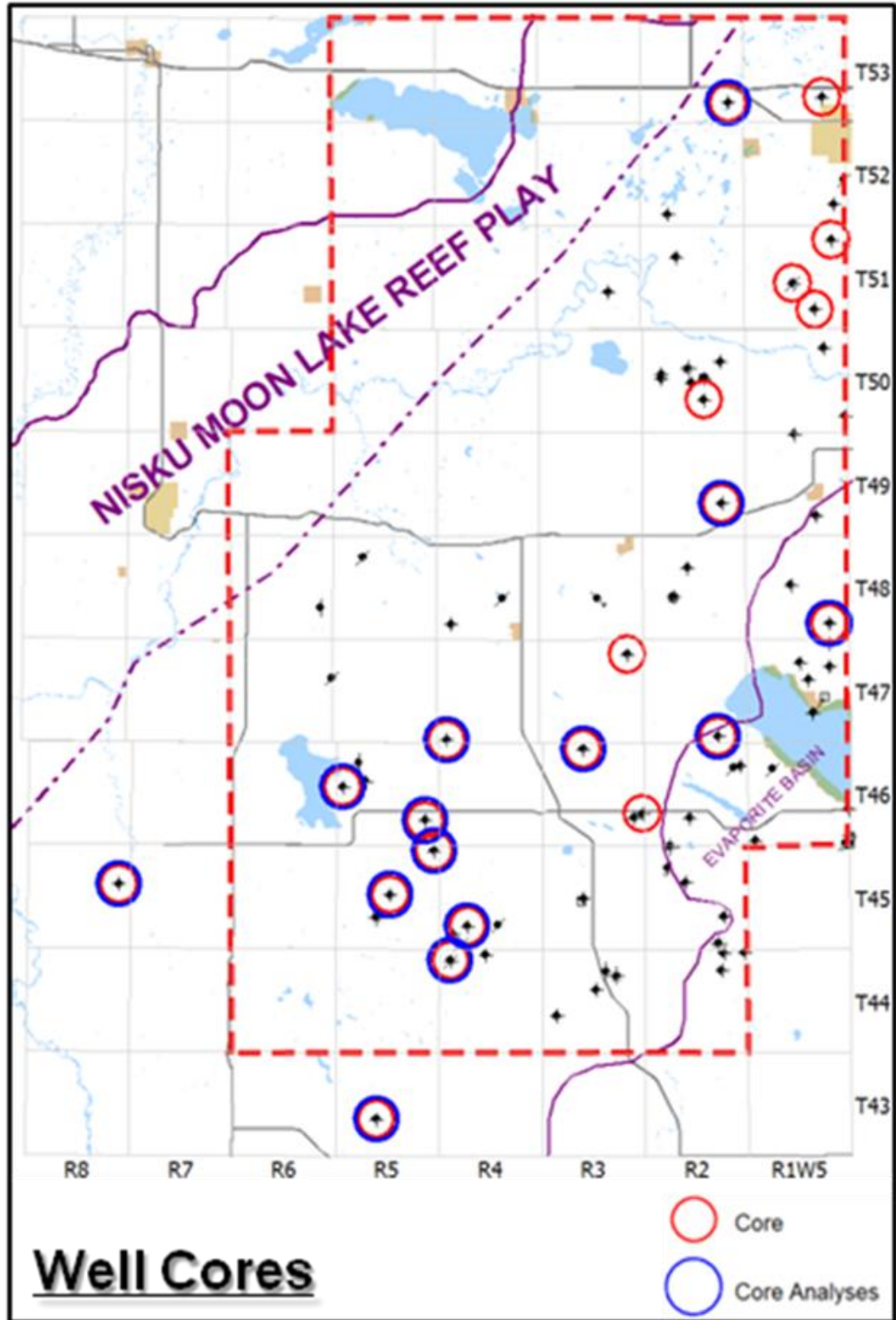


Figure 7: Distribution of available well cores from the Nisku. Core analyses from existing (5 wells) and newly acquired (8 wells) data sets.

1.3 Wireline Geophysical Logs

Logs exist for 93 of the 96 wells in the study area. Log type and quality largely depend on the vintage:

Number of Wells	Vintage	Types of Available Logs
35	Pre-1960	SP, resistivity
34	1960–1980	resistivity, porosity
24	Post-1980	full suite

Of these 93 wells, digitized logs for 79 wells were used in the analysis and interpretation (see Appendices 1 and 3). Wells drilled into the Moon Lake play (17 in total) were excluded so as to avoid mischaracterizing reservoir properties in areas away from this play. An additional two wells that penetrate the Nisku outside the study were also used for modelling as they allowed core calibration in lower Nisku intervals. Of the digitized logs, depth sampling intervals varied between 0.1 m, 0.15 m, 0.2 m, 0.5 m, and 0.6 m. All digitized logs were re-sampled at 0.5 m or 0.6 m.

A critical step before petrophysical analysis is quality control of the digitized wells—this involves checks for unit consistency and accuracy, depth shifting (where possible), and general comparisons with the raster copies for errors in scaling and/or digitization. All of the available logs were imported into the Schlumberger modelling software for analysis.

Stratigraphic picks were made by SCG Ltd. geologists, primarily based on geophysical logs with Nisku facies distinctions influenced by core observations and facies isopach mapping. All stratigraphic picks were individually verified to assure consistency in mapped surfaces.

1.4 Seismic Data

The availability of seismic data is shown in Figure 8. There are a total of 199 2D lines, and seven 3D volumes acquired between 1980 and 2003. Data processing and interpretation was focused on a subset region (purple outline in Figure 8 map). This region was selected based on available seismic data, proximity to potential point source emitters, and a general understanding of the area geology. While this data set provides useful coverage in the focus area, more 3D volumes are needed for a seismic characterization of the entire WASP AOI.

Seismic data have a number of valuable characterization roles. In addition to basic interpretations of the Nisku structure via seismic travel time and amplitude, it is also possible to use other attributes, such as acoustic impedance, to examine the physical nature of the Nisku interval for insight regarding physical properties of the rock.

Seismic 3D volumes were incorporated for use in the geomodelling process. Detailed information on seismic processing and interpretation is described in the full report by Alshuhail et al.

1.5 Mineralogy

A mineralogical evaluation of select core samples was completed. Analysis methods include XRD, XRF, and electron microprobe, as well as standard petrographic assessment. Details and results of this work are presented in the geochemistry section of the full report.

1.6 Drill Stem Tests

Twenty-two DSTs of generally poor quality have been recorded for the Nisku aquifer (Figure 9). The details of these measurements are available in Appendix 4. The recorded DST measurements were difficult to use for a number of reasons including no (or low) resolution of data, erroneous reservoir pressures and temperatures, ‘stair-stepping’ of data points, and erratic pressure plot derivatives. Quality of the DSTs was subjective based on an assessment of data points for a given DST, as well as a rating system devised by Hydro-Fax Resources Ltd.

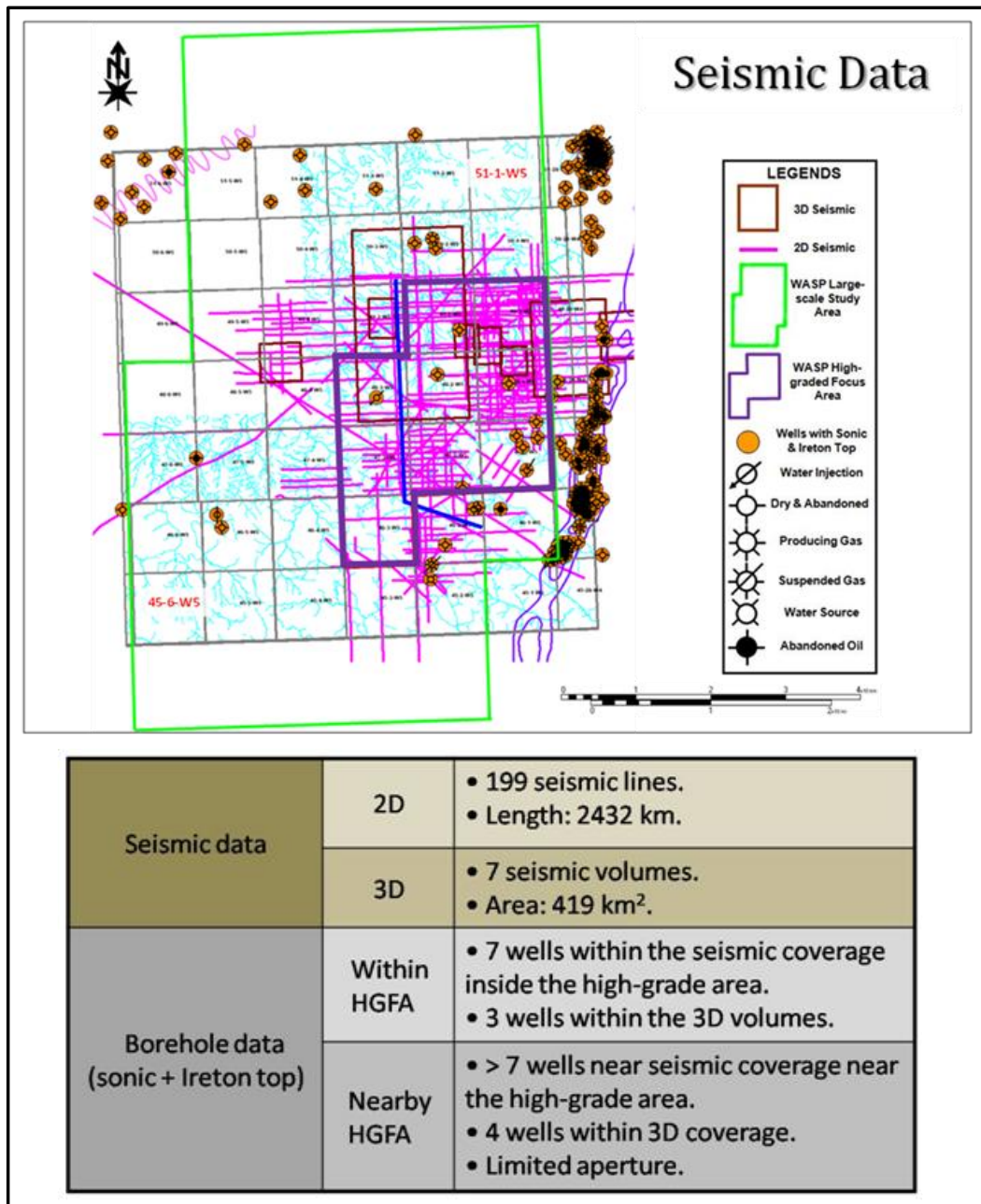


Figure 8: Available 2D and 3D seismic data for WASP study. Map (top) shows distribution relative to study area (green) and high-grade focus area (HGFA) (purple). For further information refer to geophysics chapter of report.

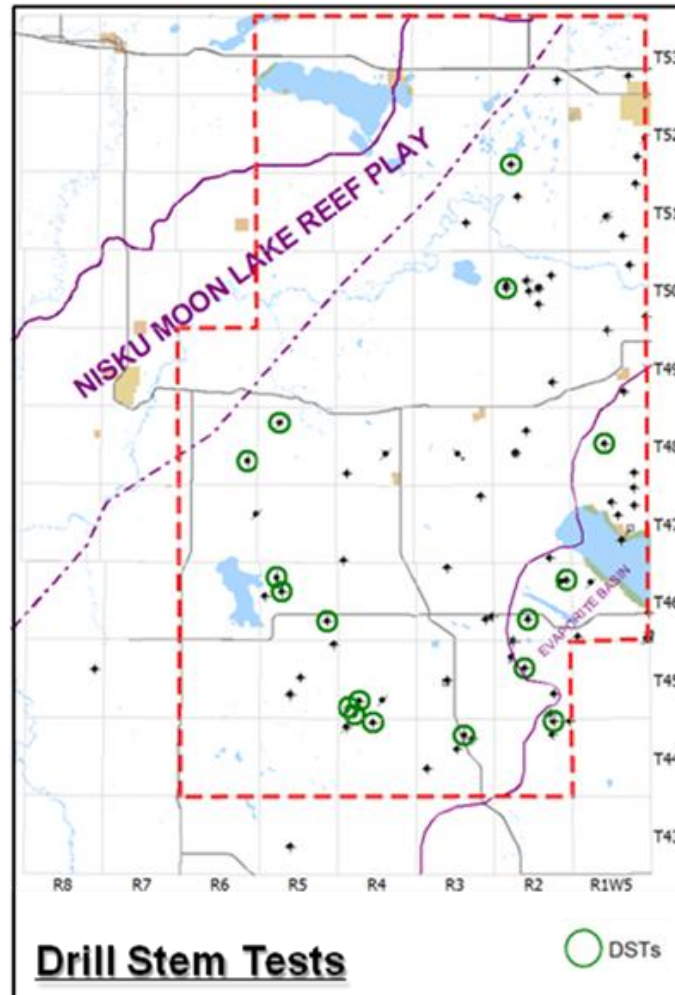


Figure 9: Distribution of DSTs within WASP study area (green circles).

Analyses of DST data are useful for assessing potential reservoir pressures, behavior over time, and most importantly providing estimates of flow capacity (i.e., permeability \times thickness). Horner plot analysis was used to estimate these parameters. A summary of the analyses are described in Table 1 and Appendix 4. Additionally, DST estimates of flow capacity can be used as a rough validation tool for gauging the accuracy of static earth models used for flow simulation. DSTs targeted only limited intervals of the Nisku Fm. (Appendix 4).

Table 1: Summary of DST analyses from Nisku interval in WASP region.

Description	Results
Number of DSTs	22 (18 for k estimation)
Quality	poor to mediocre
Permeability (k) est. (mD)	<0.01 – 74
Permeability thickness (kh) est.(mD-m)	<.1 – >700
Initial reservoir pressure est. (kPa)	~15,000 – >21,000
Fluid recovery column (m)	114– 1963

2. PETROPHYSICS

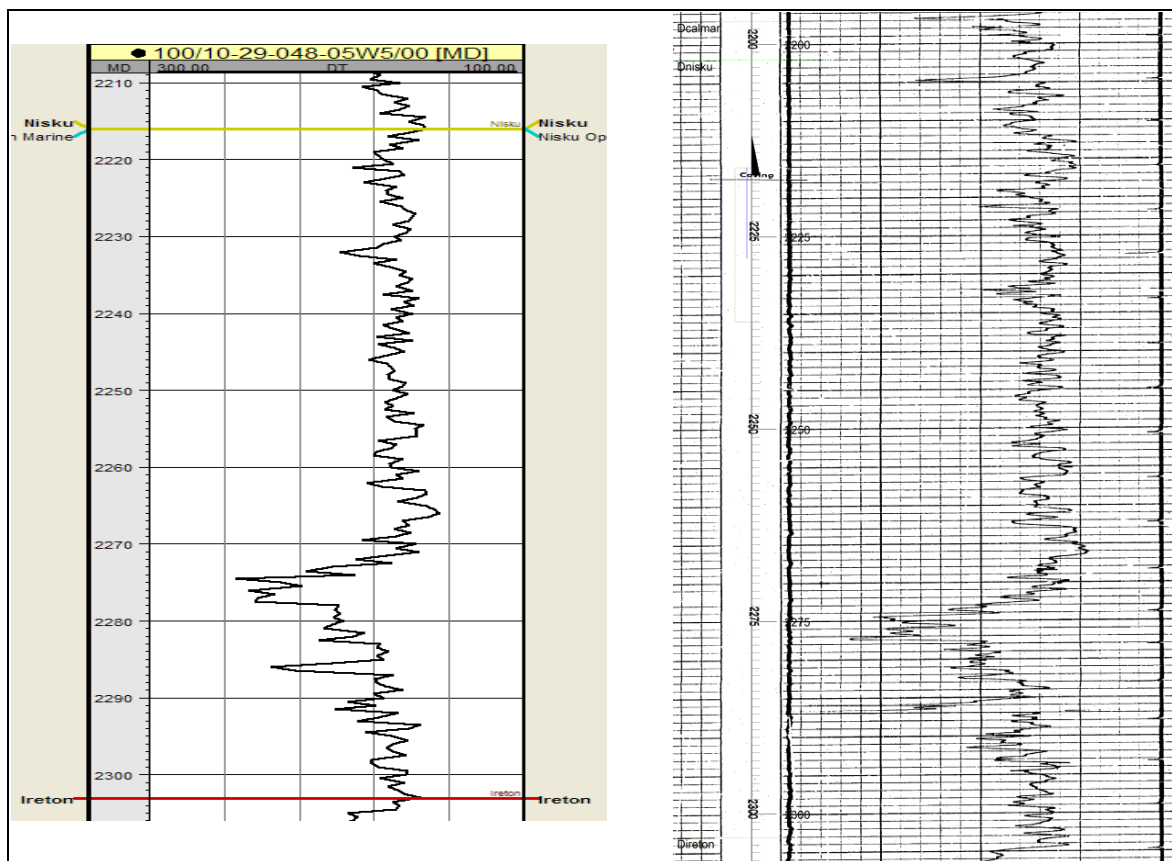
With limited data from direct geological sampling (i.e., core and cuttings), wireline geophysical well logs provide a critical source of information for characterizing the reservoir of interest. The logging process, while providing a complete vertical view of the target interval, requires a significant degree of interpretation in order to provide the necessary data for geological modelling and flow simulation.

For the Nisku Formation in the Wabamun study area, a wide range of logs have been acquired during the past 60 years (see Appendix 3). Many of these logs were recorded digitally, but at a variety of sampling intervals (e.g., 0.5 m, 0.2 m, and 0.15 m). Calibration of these data is critical, as is quality control to ensure reliability and accuracy.

Described in this section are the general steps followed for quality control and calibration of well logs. Then an analysis of porosity measurements will be presented, followed by the techniques developed for estimating permeability.

2.1 Well Logs

Digitized wireline logs were imported into Schlumberger's Petrel geomodelling software. Effort was taken to ensure the digitized well logs were imported in consistent units (metric) and that digital values matched the raster-based logs for the intervals of interest. In some cases the scaling of digital well logs needed to be corrected. An example comparison between digitized and original raster sonic-log for the Nisku interval is shown below:



Depth shifting was performed where coincident core was available (Appendix 1). The principal method was to compare the depths of core porosity with log porosity, and shift the former to the match the latter. Accuracy of 0.3 metres or less was the objective.

2.2 Porosity Estimation

For traditional oil and gas exploration, porosity is usually estimated quantitatively from sonic, density, and neutron wireline data. Resistivity (or conductivity) measurements are more often used for semi-quantitative estimation only. In the case of deep saline aquifers, resistivity may provide useful quantitative estimates due to the assumed 100% water saturated formation environment.

Sensitivities to porosity in carbonate lithologies is not straight forward, although it is generally assumed that acoustic methods are more sensitive to separate-vug porosity, whereas neutron and density logs estimate total porosity.

2.2.1 Core

Petrophysical data obtained from core measurements are normally considered to be accurate and are used to calibrate log data. With limited coverage of the Nisku interval, core provides only a rough estimate of key physical parameters for the entire reservoir, and necessarily needs to be supported by the available wireline data

A summary of the core porosity data, obtained for 13 wells (Appendix 2), is shown in Figure 10. The data are mostly from the less porous, uppermost parts of the open marine facies.

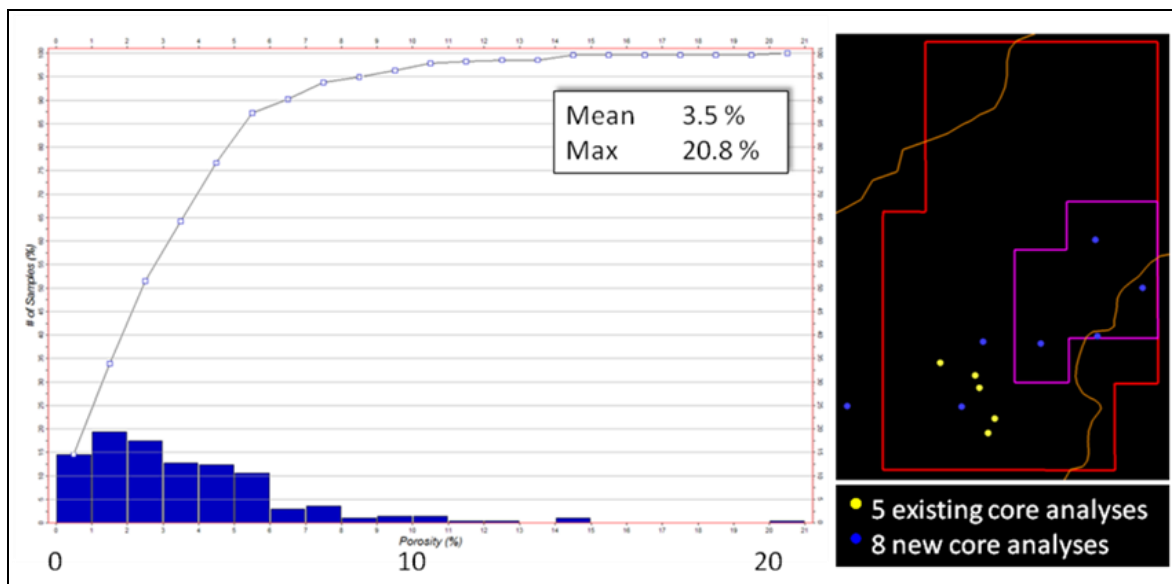


Figure 10: Core porosity data and sample locations.

2.2.2 Acoustic Wireline Logs

The capacity to transmit sound waves varies with lithology and rock texture, in particular porosity. For the WASP study, there exist 32 wells with sonic logs available (Figure 11). Porosity was quantitatively calculated from these data assuming the relationship of Wyllie et al. (1956):

$$\phi_s = \frac{\Delta t - \Delta t_{ma}}{\Delta t_L - \Delta t_{ma}}$$

Where ϕ_s = porosity; Δt = tool measured interval transit time; Δt_{ma} = transit time of matrix material; and Δt_L = transit time of interstitial fluid. The assumed values for the Nisku carbonate are $\Delta t_{ma} = 143 \mu\text{sec/m}$ (suitable for a dolomite) and for the Nisku aquifer fluid, $\Delta t_L = 623 \mu\text{sec/m}$.

In the cored intervals, the vast majority of samples included mostly interparticle porosity with occasional moldic porous zones. The separate-vug porosity was generally less than a few percent of the total porosity, so the Wyllie time-average could provide useful estimates (Lucia, 2007). On comparison of the core porosity and ϕ_s (Figure 11), the sonic porosity tends to overestimate core porosity. This may be caused by anhydrite in the cored intervals, which has a larger transit time (164 $\mu\text{sec/m}$) than that assumed for ϕ_s .

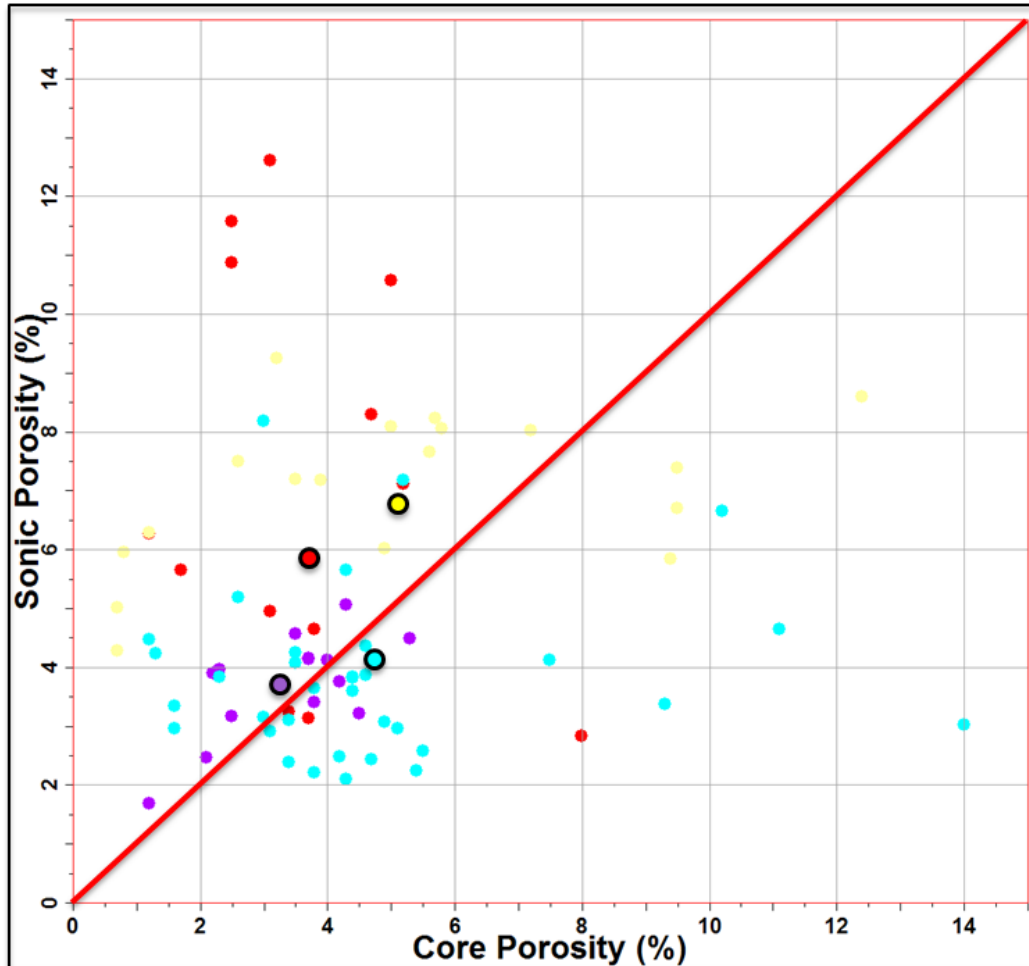


Figure 11: Cross-plot of core porosity estimates versus acoustic log estimates. Larger circles represent mean values for each well (shown in different colours).

2.2.3 Density and Neutron Wireline Logs

Porosity is commonly calculated from a combination of estimates made using neutron and density logs. The general form in water-bearing formations is:

$$\phi_{DN} = \left(\frac{\phi_D + \phi_N}{2} \right)$$

where ϕ_D = density porosity (lithology corrected) and ϕ_N = neutron porosity (lithology corrected).

For WASP, there were 13 wells containing coincident density and neutron logs (Figures 12 and 13). In addition to estimates of porosity the density-neutron combination is an important lithology indicator (Figure 13), suggesting most of the samples for the Nisku are dolostone. There are also occasional occurrences of limestone and silty-mudstones.

The ϕ_s values are less variable than the density-neutron porosities (Figure 12). Possible reasons include:

- 1) the amount of moldic and vuggy porosity is highly variable and larger overall than revealed in core, so that, as in Figure 14, the sonic underestimates the total porosity in vuggy portions of the reservoir;
- 2) the density-neutron porosity estimates are more robust to anhydrite than the sonic; and/or
- 3) more wells in the hypersaline facies are logged with sonic than density-neutron and the hypersaline has smaller porosity than the open marine facies.

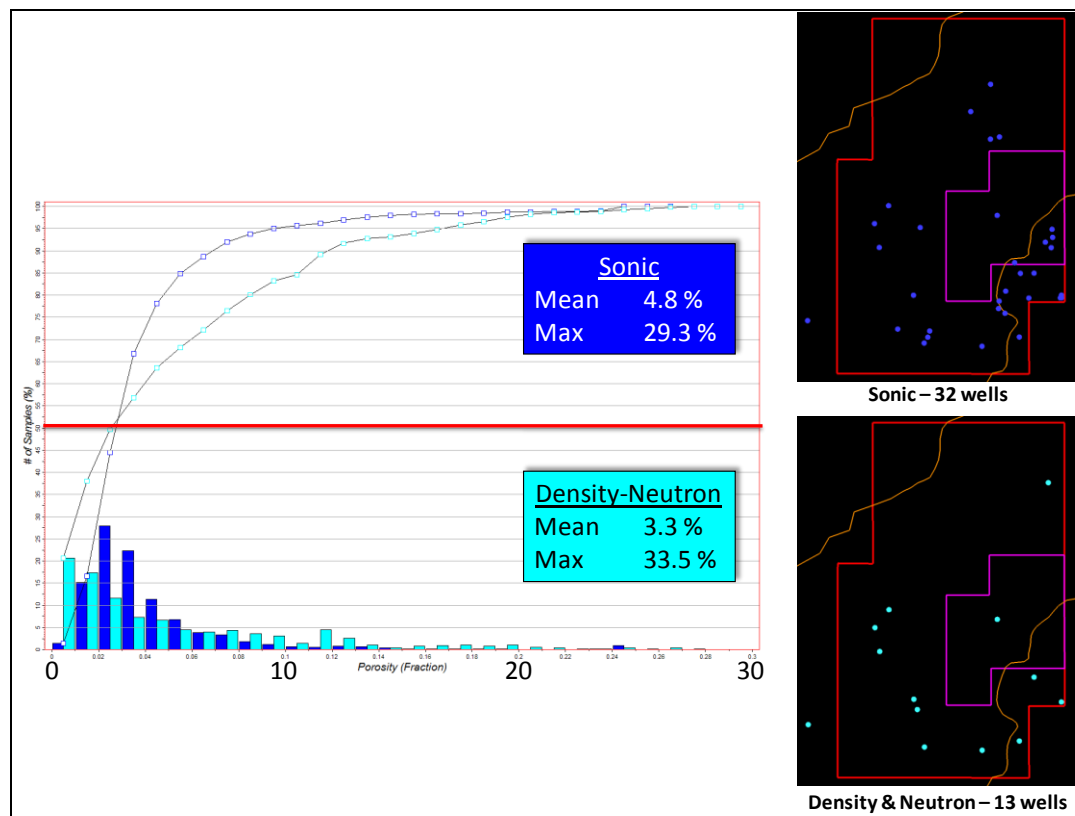


Figure 12: Porosity determinations from acoustic and density-neutron wireline logs. Locations for samples shown on right.

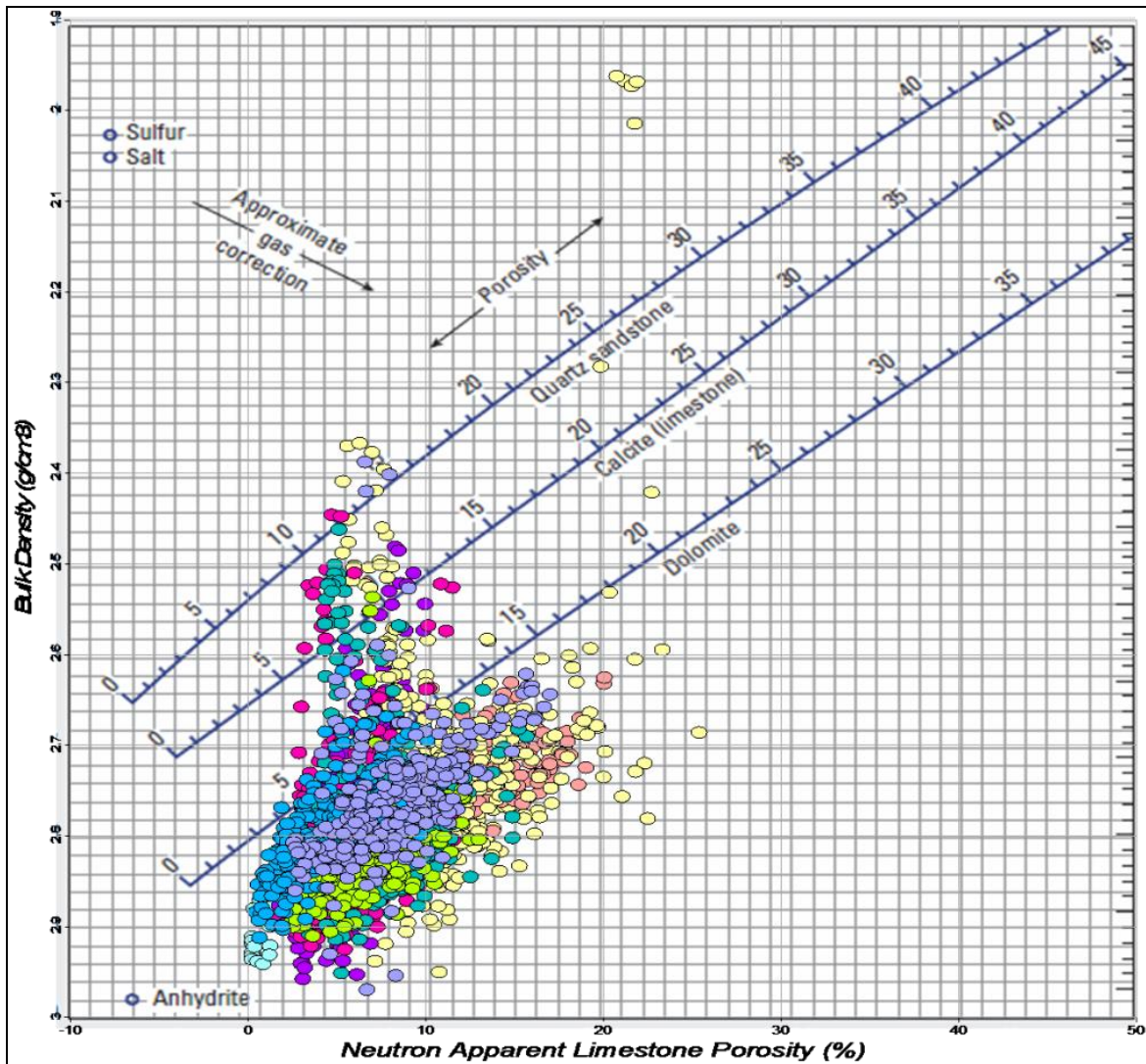


Figure 13: Porosity and lithology determination from bulk density and compensated neutron logs. Nine of the 13 neutron logs used for this plot were run prior to 1986, so the dolomite response line for these logs is more curved concave up than the one shown here.

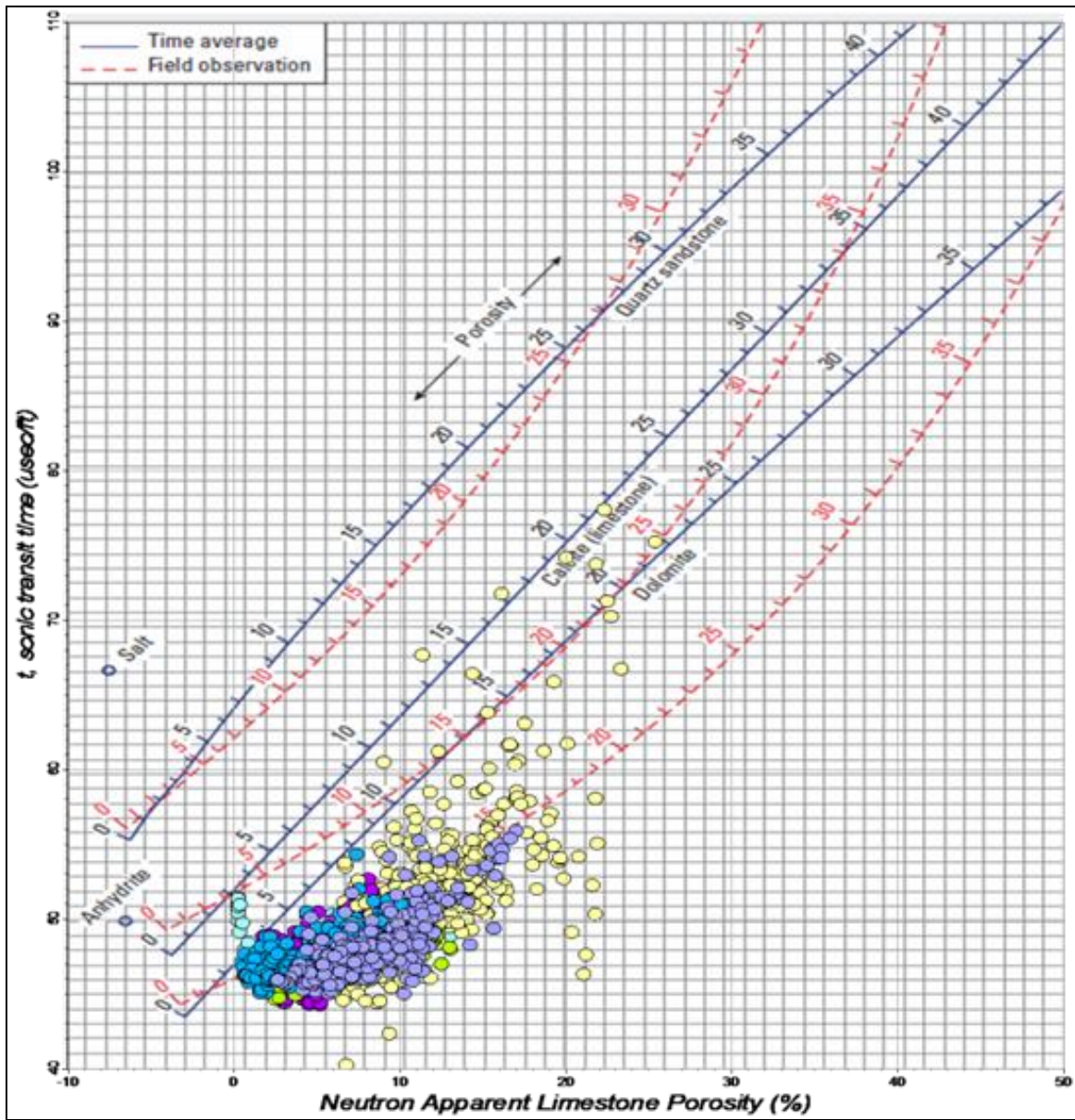


Figure 14: Porosity determination from acoustic and compensated neutron logs.

2.2.4 Resistivity Wireline Logs

There are just over 50 wells which have deep resistivity or conductivity logs distributed over a more extensive portion of the WASP study region (Figure 15). While resistivity logs were run to find hydrocarbons, they also have a potential quantitative utility in describing porosity and permeability in the case of saline aquifers.

Archie (1942) proposed that in 100% water-saturated rocks, porosity depends on rock resistivity (R_o), water resistivity (R_w), and the pore geometry/cementation factor (m):

$$\phi^{-m} = \frac{R_o}{R_w}$$

This relationship is valid for a deep-saline aquifer because S_w is at unity. The formation water resistivity (R_w) was established to be 0.029 ohm-m based on direct measurements from a water source well (11-29-045-02W5) in the Nisku and other R_w measurements collected during drilling (Appendix 5). R_o was estimated using the deepest resistivity measurement available in the log suite (e.g., deep induction). No environmental corrections were applied to the resistivity log values.

Using wireline measurements from deep induction and density-neutron logs, it was observed that $2 < m < 3$ (Figure 16). A similar range for m is obtained using core porosities (Figure 16). This range is consistent with values of m obtained in other carbonate formations (e.g., Lucia, 2007, p. 72). Once a range of values for m is established, porosities may be estimated from the deep resistivity log measurements. For example, at 10 ohm-m, estimates of porosity range from 5.3% to 10.5% (Figure 16).

Assuming $m = 2.5$, resistivity thresholds were established to map out potentially good porosity intervals (Figure 17). For this particular cross-section of wells, lower resistivity zones that have $\phi > 8\%$ appear most common in the lower third of the Nisku stratigraphic interval, with fewer zones in the upper third and very few zones in the middle third.

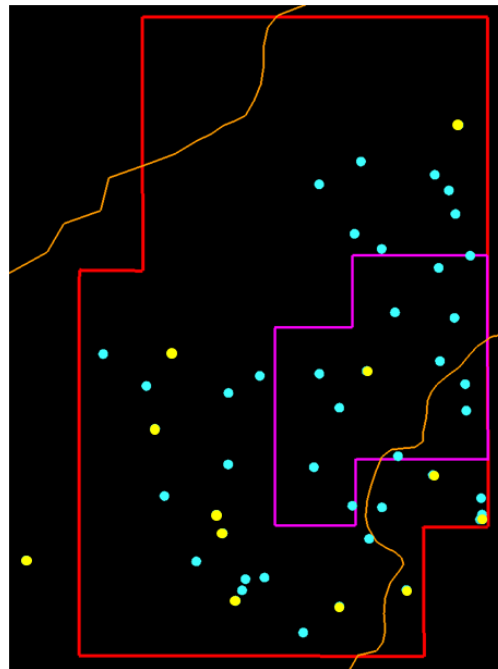


Figure 13: Distribution of deep resistivity and conductivity logs in WASP area. Yellow circles indicate wells with coincident density-neutron logs.

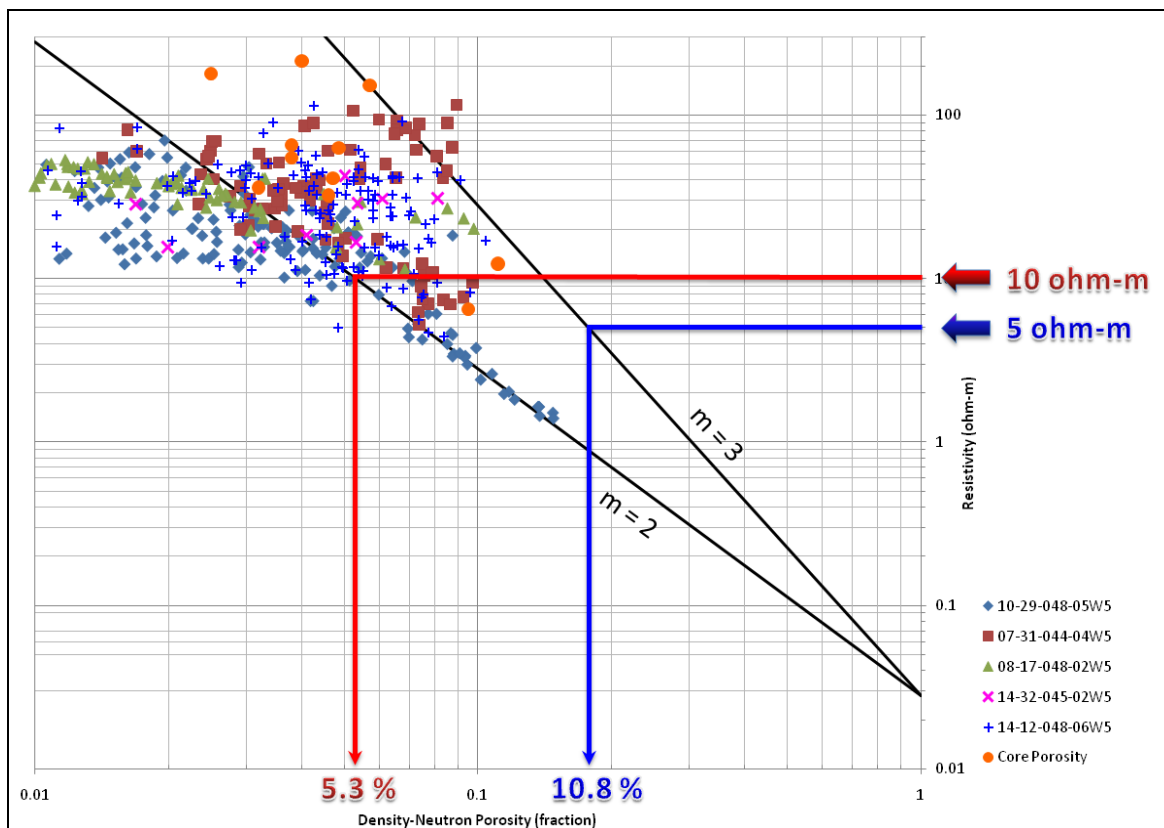


Figure 14: Relationship between deep resistivity data and porosity based on Archie's Law. Cementation factor (m) likely between 2 and 3.

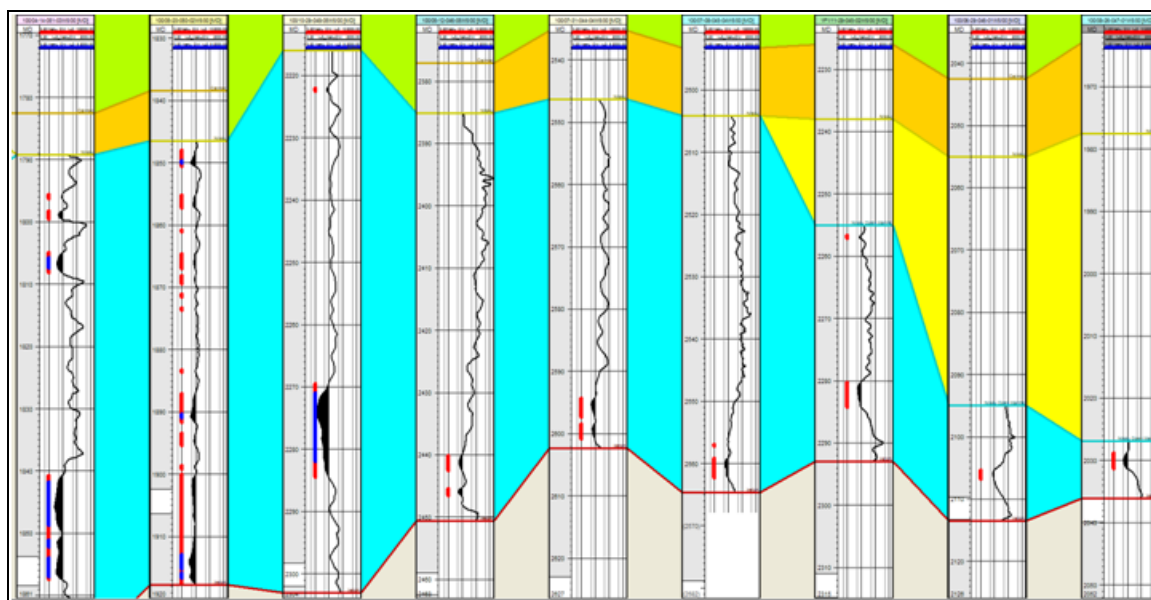


Figure 15: Intervals of enhanced porosity (<10 ohm-m [blue] and <5 ohm-m [red]) are shown on a cross-section of deep resistivity logs. There is a concentration of higher porosity zones in lower third of Nisku interval.

2.2.5 Porosity—Summary

- Resistivity-based porosity prediction is a useful way to use wireline resistivity logs, which are more numerous than sonic, density, and neutron logs.
- Cementation factor (m) appears variable between 2 and 3.
- The porosity-resistivity relationship suggests:
 - (1) <10 ohm-m correlates with > 5% porosity
 - (2) <5 ohm-m correlates with > 8% porosity
- Analysis of resistivity logs for select wells suggest:
 - (1) Areas located in central portion of Nisku platform have potentially good porosity.
 - (2) Porosity enhancement towards the base of Nisku formation.

2.3 Permeability Estimation

Permeability is a critical flow parameter for quantifying the potential for CO₂ injectivity. Despite its importance, there are relatively few permeability assessments for the Nisku. Permeability data exist for the limited core samples acquired, but not necessarily at reservoir conditions. Some variable-quality DSTs are also available, along with production data from well F1/11-29-045-02W5/00 and oil fields in the Leduc trend north east of the AOI. All these data have been analyzed to develop flow capacity estimates.

2.3.1 Core

A histogram of core permeability measurements suggests core-scale permeabilities are highly variable (Figure 18). The lower and upper values observed are likely to reflect measurement limitations as well as the intrinsic permeability of the rock. These were obtained from 13 wells with core collected from the Nisku (Appendix 2). The median permeability is nearly 10 mD, although these data represent a small fraction of the total Nisku interval. Core kh for 7 wells from the uppermost Nisku (Figure 19) suggests potential aquitard qualities—more than 75% of the measurements are below 10 mD-m.

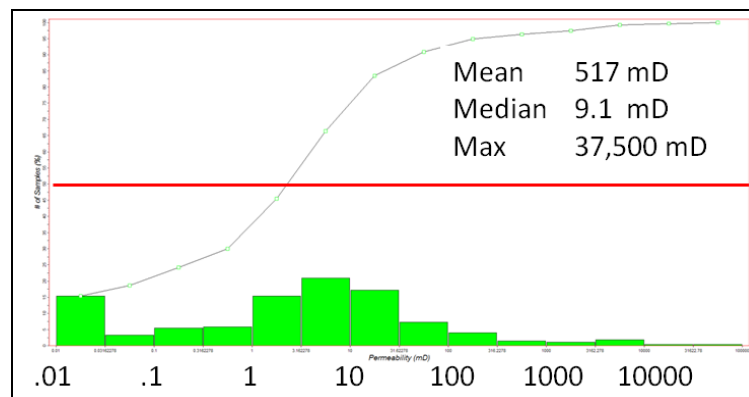


Figure 16: Core permeability measurements (kMax) from the 13 wells with Nisku sampling.

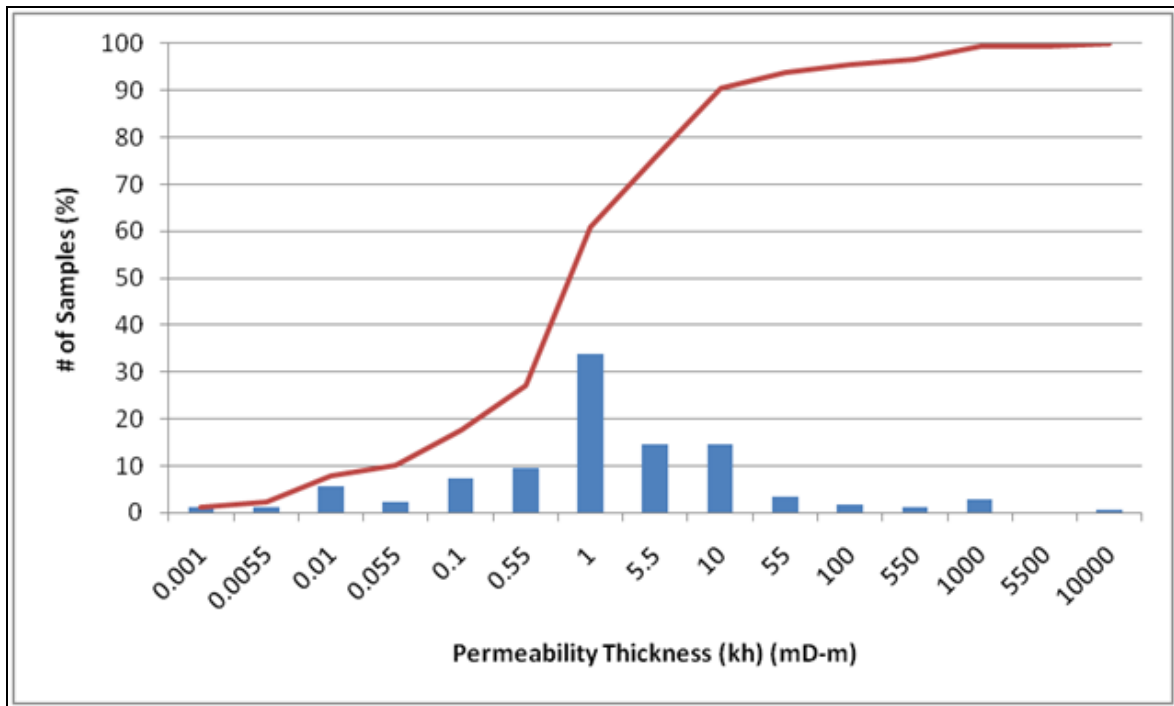


Figure 17: Core-measured permeability × thickness (from 7 wells).

2.3.2 Well Tests

DST measurements provide estimates of permeability at a scale larger than those provided in core plug measurements. The data, while of questionable quality, can provide a gross validation of flow capacity potential for a given well and the aquifer in general.

For individual well tests, the following permeability-thicknesses (kh) were estimated using a horner plot analysis method:

Well Location	kh (mD.m)
100/02-21-048-01W5/00	204
100/04-20-050-02W5/00	153
100/05-12-046-05W5/00	<1
100/06-05-045-04W5/00	16
100/07-08-045-04W5/00	293
100/10-09-046-02W5/00	99
100/10-14-053-03W5/00	3
100/10-20-046-05W5/00	69
100/10-27-044-03W5/00	35

Well Location	kh (mD.m)
100/10-33-044-04W5/00	68
100/13-36-053-03W5/00	99
100/14-21-045-02W5/00	719
100/14-21-045-02W5/00	6
100/14-29-046-05W5/00	<1
100/15-35-044-02W5/00	<1
102/16-06-045-04W5/00	16
102/16-06-045-04W5/00	13

2.3.3 Analysis of Production Data

The Nisku formation provides aquifer support for a number of oil fields to the northeast along the Rimbey-Leduc trend (RLT). Analysis of the production for several fields, detailed in the section on aquifer material balance, indicates the flow capacity of the Nisku in the north east may be approximately 200 to 500 mD-m. Using these values to evaluate flow capacity in the AOI, however, requires caution because of the change in depositional environment from the RLT to the open marine facies in the AOI. The two wells in the study area closest to the aquifer supported plays, 02-21 and 04-20 (see list above), have kh values at the minimum range established from material balance estimations.

The water production well, F1/11-29-045-02W5/00, has reported production capabilities of 1000 m³ per day. Assuming a 10 cm radius wellbore and 10% pressure drop to produce a flow of 1000 m³ per day, we estimate the formation flow capacity to be approximately 3000 md-m.

2.3.4 Using Resistivity/Conductivity to Estimate Permeability

Since electrical flow and fluid flow share the same governing equations, it appears possible to use electrical conductivity measurements from wireline to predict hydraulic conductivity. Several studies have confirmed this use of electrical measurements (e.g., Archie, 1950; Jackson et al., 1998; Ball et al., 1997), although most of the reports concern core-scale relationships. The length of the current path through the formation is directly related to the shape, diameter, and sorting of the grains, geometric packing arrangement, and degree of matrix cementation. All of these factors also affect the formation permeability.

Here, we assessed the maximum electrical conductivity (C_{max}) observed in a well to predict that particular well's flow capacity. Core, DST, and production well kh values compared to wireline C_{max} suggest that a useful relationship may exist for the Nisku (Figure 20).

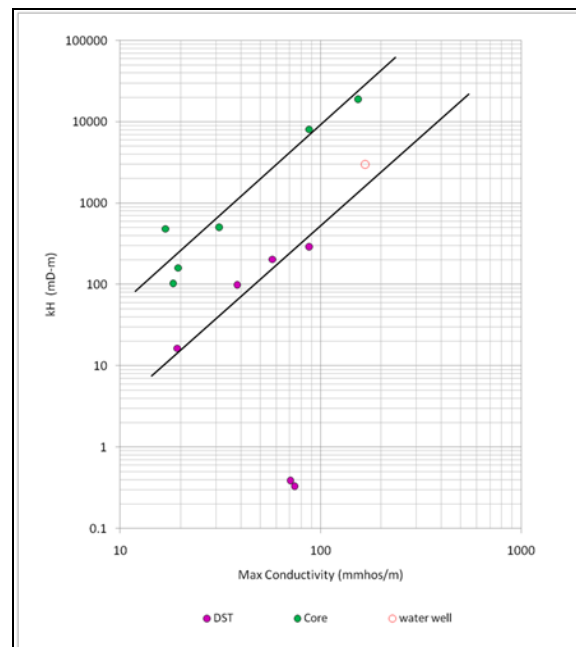


Figure 18: Relationship between maximum conductivity (from wireline logs) and permeability thickness from core (green circles) and DSTs (pink circles). The cause(s) for the two wells with (kh)DST = 0.3 mD-m to have different behaviour

than other wells could not be determined. Open red circle shows water production well (F1/11-29-045-02W5/00) based on known max conductivity measurement and estimate of flow rate.

Core-based kh is larger than the DST and production values (Figure 20) by about a factor of 20. This is reasonable, since we expect locally enhanced permeability seen in core to be limited in lateral extent. The DST and production values will be affected by connectivity beyond the near-wellbore region. The lines of Figure 20 represent speculative C_{max} - kh relationships and have not been tested through either theory or statistical analysis.

From the C_{max} -(kh)_{prod} relationship (lower line of Figure 20), we can estimate flow capacity values, which represent the volumes investigated by DSTs and the production well. A cumulative distribution function of estimated flow capacities can be calculated for every well with useable electrical wireline measurements (Figure 21). For the WASP area, nearly 30% of wells have the potential for greater than 1 D-m, with several wells in two areas possibly having $kh > 2$ D-m (Figure 22). Simulation studies (see flow simulation chapter for more information) suggest that a minimum of 1 D-m is required for adequate injection capacity. The location of these wells might therefore indicate possible regions within the larger WASP area that would make good injection sites.

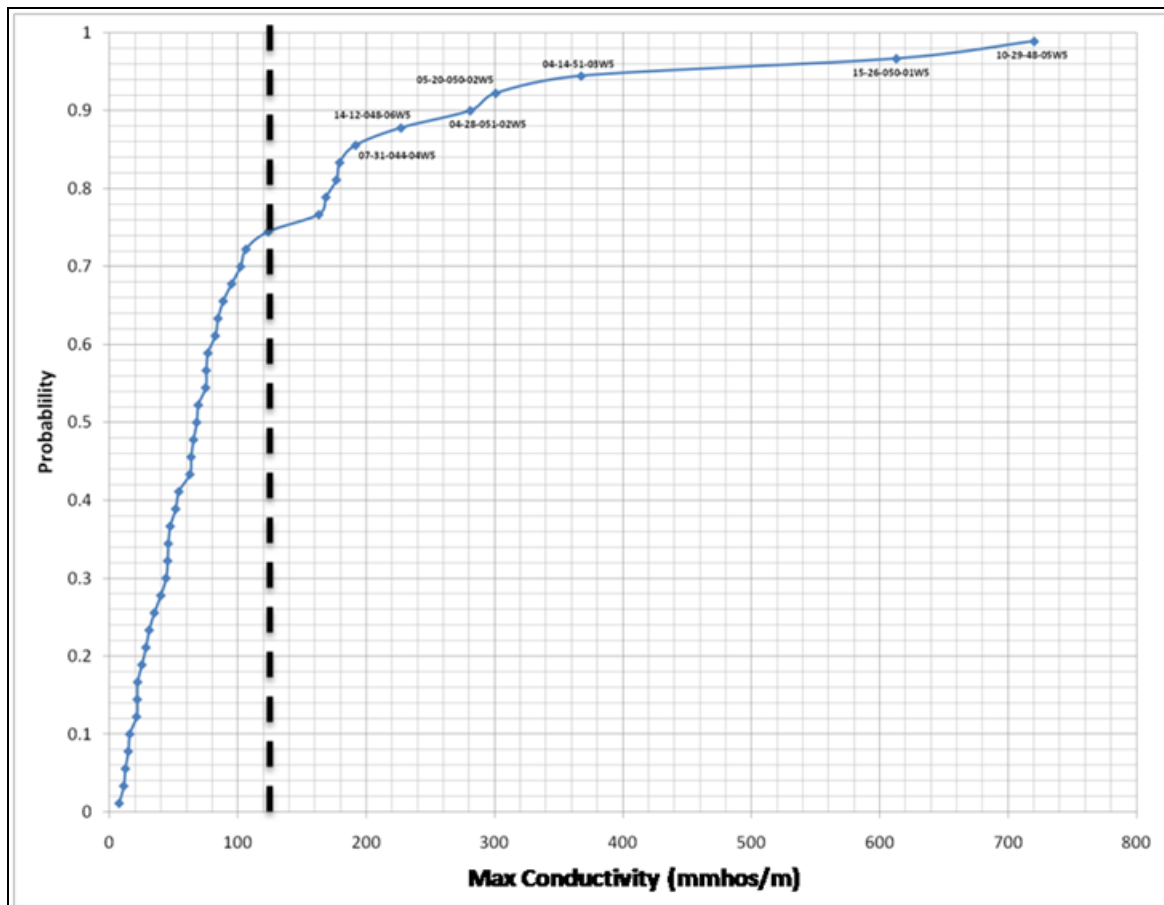


Figure 19: Cumulative distribution function (CDF) of wells based on C_{max} (above). Dashed line indicates the equivalent of a ~ 1 D-m flow capacity threshold.

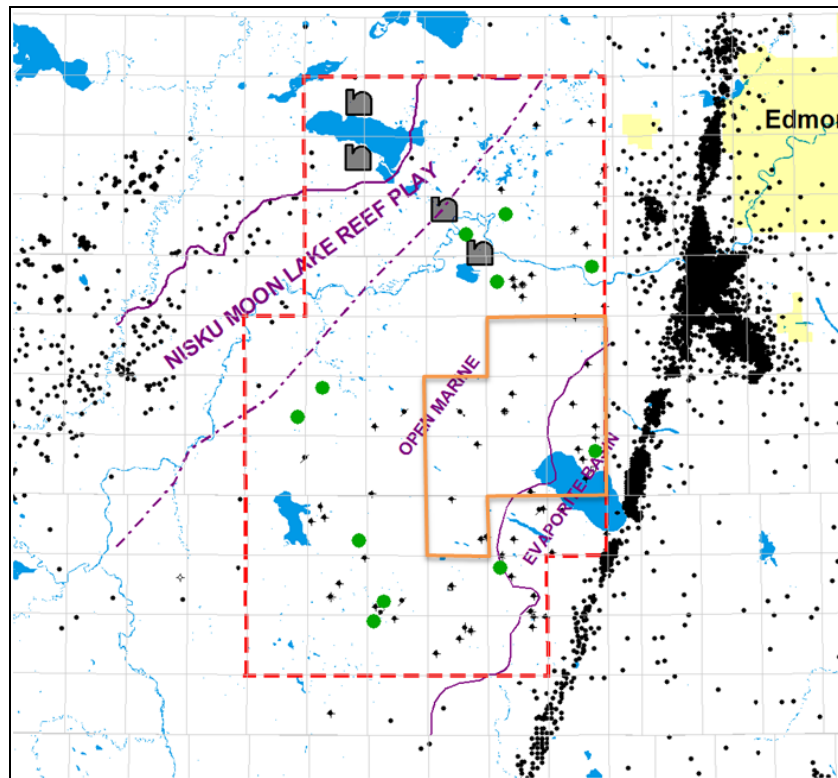


Figure 20: Green circles on map indicate locations of >2 D-m potential flow-capacity wells.

2.3.5 Permeability—Summary

- Wireline resistivity appears to provide a useful flow capacity predictor.
- A minimum electrical conductivity of 150 mhos/m is needed for one Darcy-metre flow capacity to exist for a volume typical of a DST or short-term production test.
- Wireline conductivities suggest that approximately 25% of wells have Darcy-metre flow capacity. These wells are distributed throughout the AOI.
- Two areas in particular show very good flow capacity potential (> 2 Darcy-metres).

2.4 Nisku Lithofacies Distinction

Distinguishing facies within the Nisku carbonate was challenging with very limited core available. The open marine and hypersaline facies were the only two distinctly recognized units (Figure 23), based primarily upon a limited fossil assemblage and presence of more abundant anhydrite in the hypersaline facies. On wireline logs, the distinction between these two facies was difficult to recognize.

A thorough petrophysical analysis of these two facies allows questions important for assessing the suitability for CO₂ injection to be addressed:

- 1) Is there a quantitative distinction between Nisku open marine and hypersaline facies in wireline log data?
- 2) Is the hypersaline facies suitable for CO₂ storage?
- 3) Do wells close to hypersaline/open marine interface show an increased porosity potential?

To address these questions, cumulative distribution functions that aggregate all of the available sonic (Figure 24) and resistivity (Figure 25) data were produced. A significant difference is manifest, with acoustic and resistivity data both suggesting better porosity in the open marine facies. The two facies have a similar abundance of low porosity but, at porosities > 7% ($\Delta t > 53.8 \mu\text{s}/\text{ft}$), the open marine shows a greater probability of higher-porosity regions. This suggests that the open marine facies has a better prospect as an injection target than the hypersaline facies. While there may be some zones of enhanced porosity in the hypersaline rocks, these are likely to be isolated and have poor connectivity.

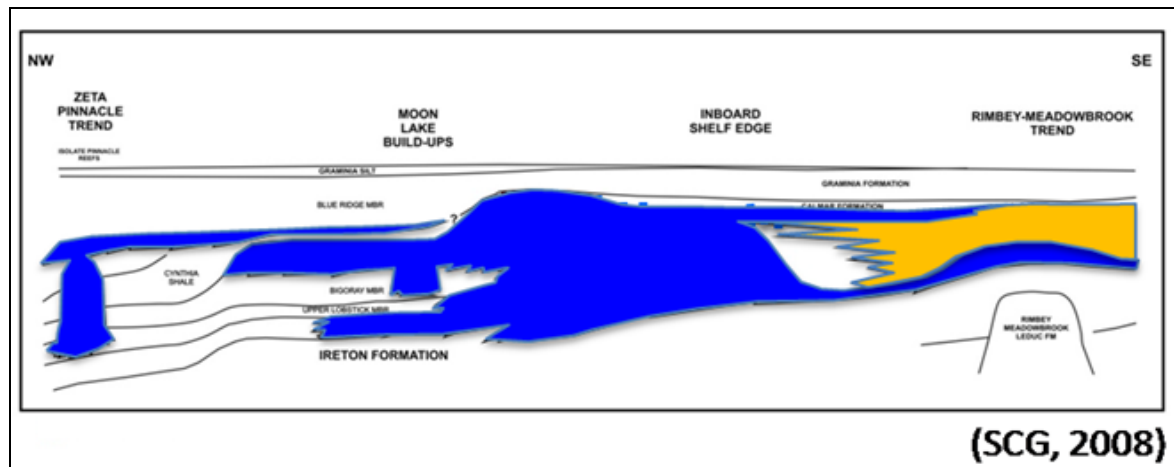


Figure 21: Conceptual model showing distribution of open marine facies (blue) and hypersaline facies (yellow) along an NW-SE cross section of the WASP area.

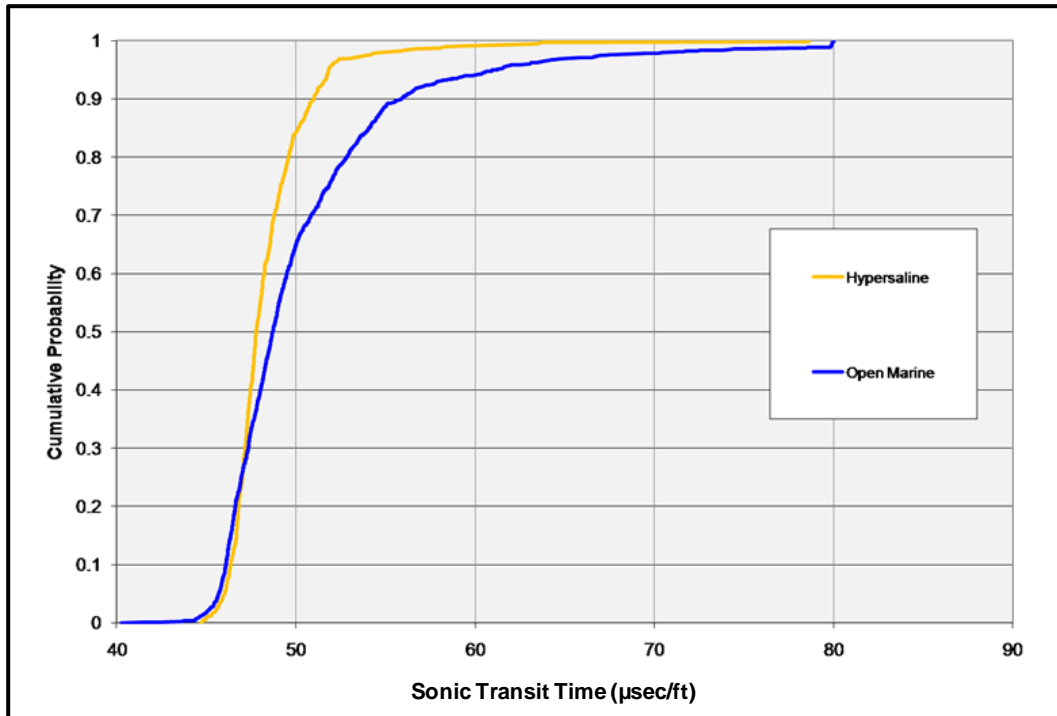


Figure 22: CDF of sonic wireline data for two recognized Nisku facies—open marine (blue) and hypersaline (yellow).

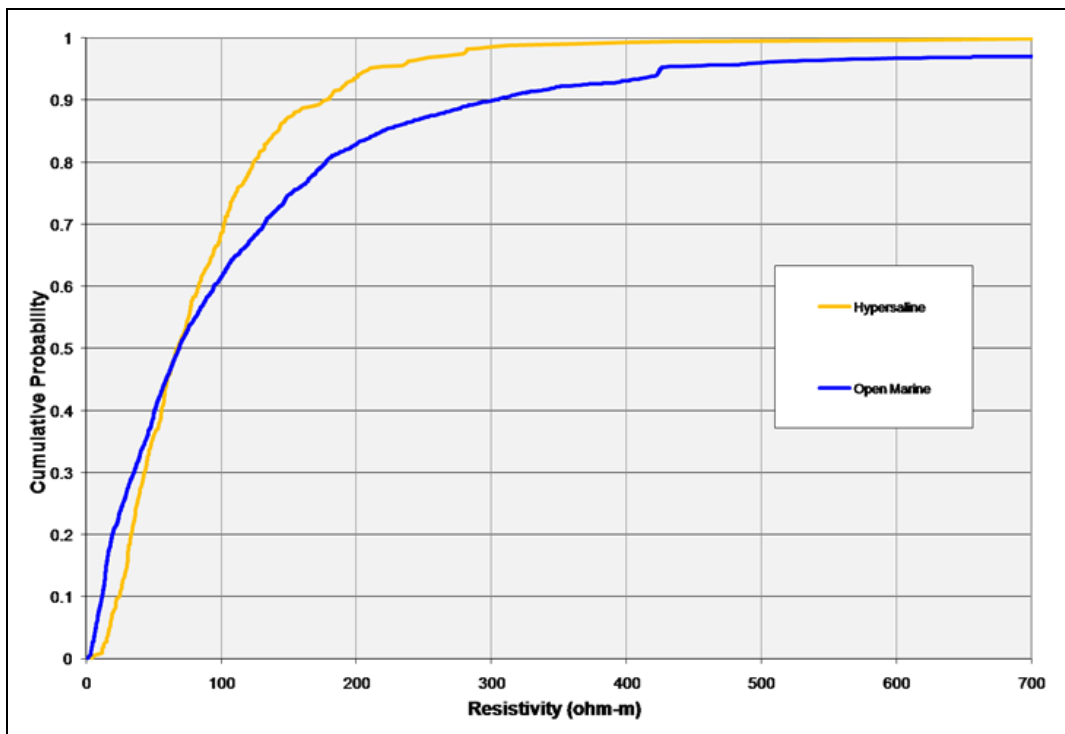


Figure 23: CDF of deep resistivity wireline data for two recognized Nisku facies—open marine (blue) and hypersaline (yellow).

3. GEOMODELLING

Reservoir modelling is necessary to assess the potential capacity of the Nisku aquifer and how fluids will behave during and after CO₂ injection. The reservoir model is an attempt to accurately portray a complex, heterogeneous system using an indirect and incomplete data suite comprising measurements from the forementioned tools. Our main goal is to create accurate models of Nisku aquifer geometry and flow properties consistent with available data and at a scale suitable for the simulation of large-scale fluid injection.

Geostatistics, the statistics and modelling of properties in space and time, provides the estimation techniques that allow the incomplete picture of the potential WASP aquifer to become more complete. Interpretation requiring subjective modelling decisions is critical for capturing the best estimate of geological continuity. While geological detail is usually complex, not all information is necessary for understanding the most significant forces that control subsurface flow.

The workflow for building the Nisku geocellular model was hierarchical given the variable scales of heterogeneity in the reservoir and the different scales of the data collected. The general sequence was to:

- 1) Establish horizons and any structural features using wireline log and seismic data in order to build a 3D stratigraphic grid.
- 2) Construct the depositional grid (i.e., the geostatistical framework).
- 3) Generate petrophysical models for porosity and permeability using a suite of geostatistical methods.
- 4) Upscale the geocellular model (when necessary) and export for reservoir simulation.

When facies property modelling is used, it is also necessary to generate the geometry and distribution of key facies and then populate the facies with petrophysical properties.

The two modelling approaches used for the Nisku characterization were traditional pixel-based methods and object-based (boolean) modelling. Important steps in the workflow will be presented here.

3.1 Structural and Stratigraphic Grid

It is necessary to first establish the reservoir boundary and internal horizons. For the WASP study the boundary was selected based on the region of possible injection and included 54 townships. Formation horizons were identified for approximately 95 wells, and included picks for the tops of the Ireton, Nisku, Calmar, Blue Ridge, Graminia, and Wabamun formations. Additionally, a boundary was established for the Nisku open marine and hypersaline facies, where possible to recognize on wireline geophysical logs. A convergent interpolation method (Taylor series projection with minimum curvature used for smoothing) was used to create the surfaces for the Nisku reservoir envelope (Figure 26). As no major faults were recognized in the zone, the stratigraphy of the reservoir has a simple geometry.

3.2 Depositional Grid

From the stratigraphic grid, a cartesian grid was created for the Nisku reservoir. This grid provides the geostatistical framework for any subsequent property and petrophysical modelling. For this

study the x and y cell dimensions were fixed at 500 m × 500 m (Figure 27) to satisfy computational constraints of modelling the large region of WASP while at the same time providing some reasonable level of geological continuity. All data—well paths, well logs, and seismic data—were conditioned to the cartesian grid once it had been generated. The vertical layering of the grid was set at 30 layers divided unevenly between the 3 zones (Table 2 and Figure 27). The association between the stratigraphic and depositional grid are essentially one to one between each cell.

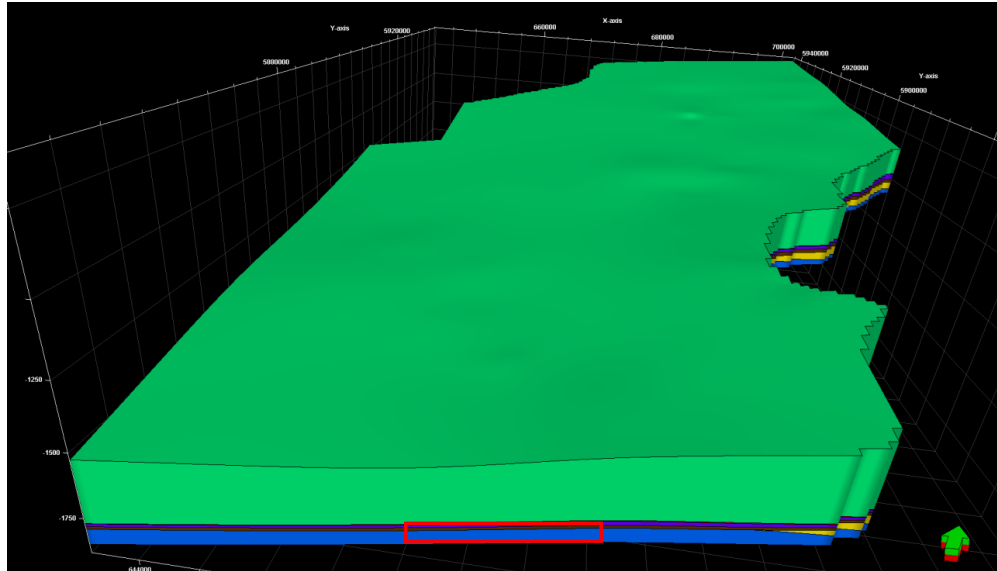


Figure 24: Modelled horizons derived from location of formation tops as identified in well logs. Green—Wabamun (carbonate), Pink—Graminia (shale), Purple—Blue Ridge (carbonate), Brown—Calmar (shale), Blue—Nisku open marine (carbonate), Yellow—Nisku hypersaline (carbonate). Red box shows approximate area of Figure 27 below. Vertical exaggeration = 25.

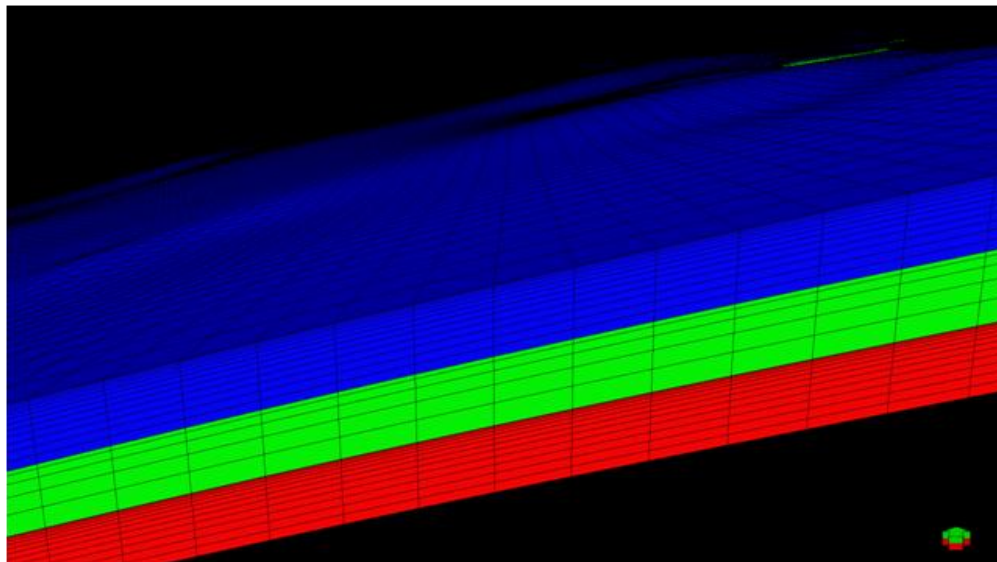


Figure 25: Cross-section of Nisku open marine reservoir model showing vertical and horizontal grid spacing. Note vertical division in 3 zones (blue, green, and red) representing potentially differing flow regimes within reservoir.

Table 2: Vertical grid divisions for Nisku model.

Vertical Layer	Average Thickness (m)	Zone
1–13	1.72	Upper
14–18	4.46	Middle
19–30	1.86	Lower

Vertical grid spacing was designated based upon geological interpretation of wireline logs. As enhanced porosity and permeability zones appear to exist more frequently in the upper and lower thirds of the reservoir, these vertical intervals benefit from a finer vertical resolution when computational constraints are a concern during flow simulation. The upscaling of flow properties is greatly affected by the choice of vertical grid spacing.

3.3 Upscaling Well Logs

Wireline logs were upscaled using an arithmetic average for porosity determination and using a harmonic average for vertical permeability (when appropriate). Logs were treated as lines where each sample value is weighted by a factor proportional to its interval.

3.4 Variogram Analysis

Variogram analysis establishes the geological continuity in porosity and permeability for the Nisku reservoir. An assumption is made, however, that the nature of these petrophysical properties is homogeneous at some scale. An experimental variogram was calculated and characteristics interpreted (Figure 28).

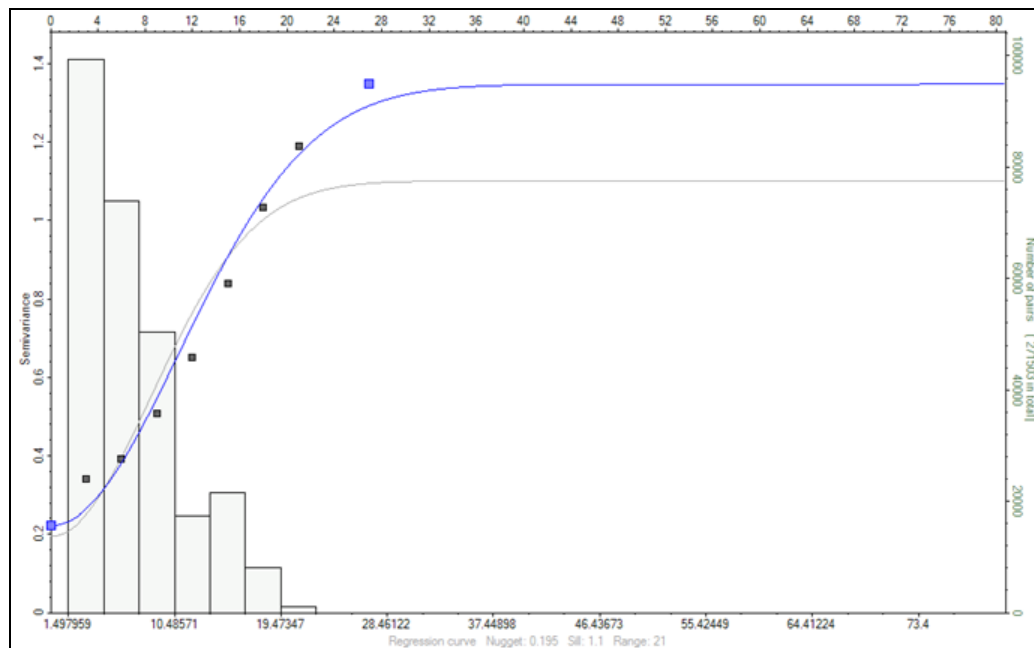


Figure 26: Sample vertical variogram analysis for porosity in the open marine facies of the Nisku reservoir. Vertical range = 27 m, nugget = 0.22. Grey squares show calculated

semivariance at a given correlation distance. Blue line represents experimental variogram (gaussian) that was modelled.

Modelling the variogram allows the ranges and nuggets to be determined, which in turn are critical input parameters for estimation and stochastic simulation. The 3D numerical model is dependent on the specific-variogram algorithm that is selected (Caers, 2005). Here, we used both laterally isotropic (e.g., for kriging) and anisotropic (e.g., for SGS and object-based) semivariograms depending on the modelling objective. Spherical experimental variograms were used for lateral correlation, while gaussian variograms were used in the vertical direction.

3.5 Permeability Estimates

A three-dimensional model of permeability is critical for reservoir characterization and flow simulation. For CO₂ injection, permeability is the most significant variable for controlling total injectivity (see flow simulation section of this report). Data from cores are the typical source of permeability information—which for the WASP study are greatly limited in number and spatial distribution.

A traditional approach for permeability estimation is from porosity using a fitted line (Figure 29) based upon core data. This method has some major drawbacks including poor correlation between porosity and permeability in the data set, few samples from a limited portion of the total Nisku reservoir interval, permeabilities that have the same spatial covariance as porosity, and any existing core permeability data will not be used for populating the static geologic model.

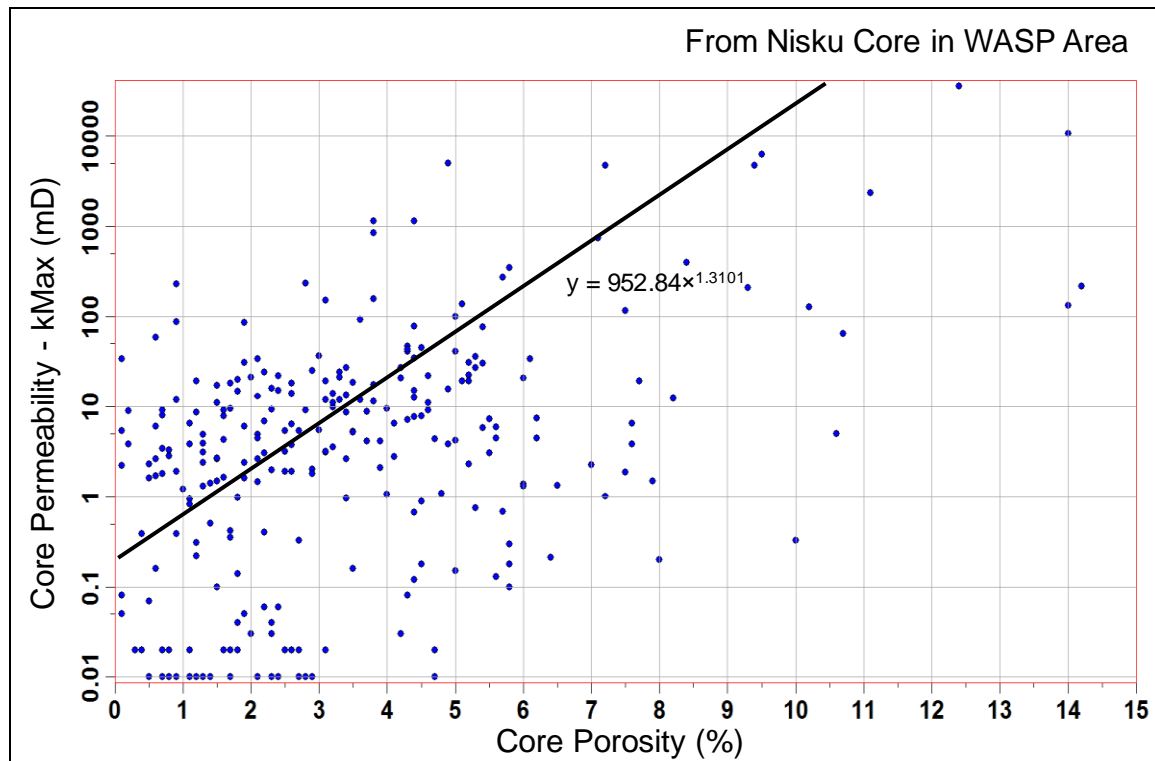


Figure 27: Porosity-permeability cross plot. Manually fitted line (black) manually overestimates permeability when $\phi > 4\%$.

Thus an alternative approach to permeability estimation was employed. Using the maximum conductivity, C_{\max} , for an observed interval versus the permeability times thickness (kh) from core and DST data (Figure 20), permeability could be estimated for two scenarios. Using core data, an optimistic scenario:

- $kh = 0.3307 \cdot C_{\max}^{2.2268}$

and DST data, a pessimistic scenario:

- $kh = 0.0211 \cdot C_{\max}^{2.1973}$

C_{\max} was evaluated at the same interval as the vertical grid spacing (h) in order to determine an appropriate permeability value to populate the grid. These values were then used in a conditional simulation (similar to porosity) to create a three-dimensional model of permeability. Porosity was used as the secondary variable in a colocated co-kriging process.

Results from both methods for permeability estimation were used in the flow simulations.

3.6 Pixel-based Modelling

3.6.1 Kriging

A standard geostatistical method for simulating the distribution of porosity and permeability deterministically is to use a kriging algorithm.

Kriging relies on the spatial relationships as described in the variogram for a particular data set. For this technique to be useful, it requires sufficient knowledge of the modelled phenomenon, uncertainty at the unsampled locations to be minimized, and the context of the data to be well understood. These criteria are not, however, well satisfied with the available data for the Nisku in the WASP area.

In the case of the open marine facies for the Nisku, variogram analysis for porosity data from resistivity logs shows the vertical range to be ~14 m, whereas in the horizontal directions the correlations distance were assumed to be large at 5 km. With large interwell distances, it is difficult to assess this.

The result of kriging (Figure 30) does not capture the heterogeneity of the system and was not pursued as a viable modelling option. The “bull’s-eye effect”, as areas away from known samples will adopt the mean value for porosity (0.052), is driven by the well locations and is not expected to reflect the true porosity distribution of the reservoir. Also, the heterogeneous nature of reservoir is not captured, for example, we would expect to see regions of enhanced porosity in the interwell regions for this open marine facies.

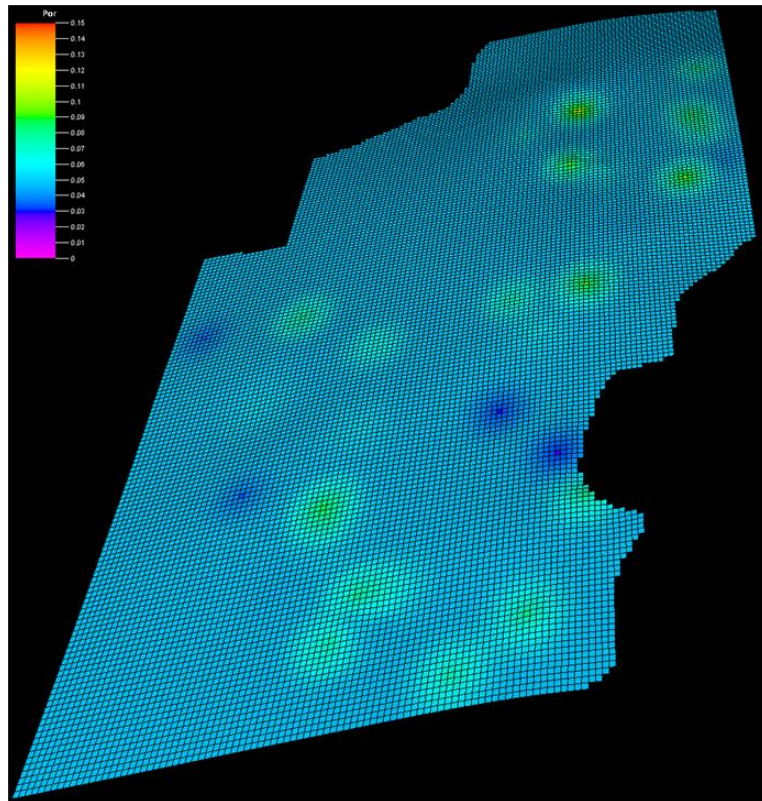


Figure 28: Sample output of ordinary kriging algorithm for porosity of the open marine facies of the Nisku (based on resistivity-derived porosity).

3.6.2 Sequential Gaussian Simulation (SGS)

Another conventional approach is to use a stochastic (probabilistic) method which better recognizes uncertainty and incorporates a factor of randomness (Srivastava, 1994). SGS sacrifices some certainty for greater detail. For the WASP area Nisku, this modelling method can provide a more realistic distribution of porosities and permeabilities.

For SGS simulations seismic estimates of acoustic impedance were included as a secondary variable for collocated cokriging (Figure 31). While areally incomplete, the available impedance data were cokriged with a correlation factor of ~ 0.45 (based on estimates of upscaled cells and normal transform of the data).

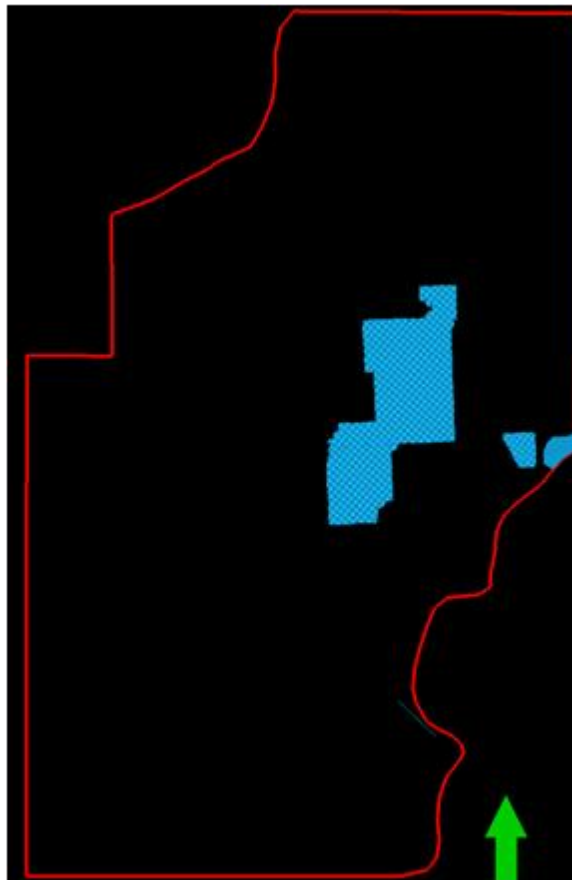


Figure 29: Distribution of available 3D acoustic impedance data used for collocated cokriging.

The semivariogram properties were modelled to be anisotropic:

Range

Major horizontal direction (N 30 E)	8 km
Minor horizontal direction (N 60 W)	5 km
Vertical direction	22 m

Nugget

0.203

A trend (N 30 E) was included to reflect alignment of enhanced porosity regions parallel to the paleo-shoreline during upper Devonian deposition. The major and minor correlation ranges (8 and 5 km) were chosen to be suitably large enough considering the lack of data. The vertical range was derived from analysis of the vertical variogram.

Of the fifty realizations generated, five were selected for fluid simulation (Figure 32). The porosity and log of permeability results for all realizations have a gaussian distribution. A sample porosity and permeability model is shown in Figure 33. While the realizations developed through SGS methods are qualitatively useful for illustrating potential porosity and permeability distributions in the Nisku open marine facies, quantitatively the constraints for geometries of flow pathways over the entire studied region are poor—a consequence of limited data. Injectivity volumes (as determined through simulation) provide a useable scale-of-magnitude calculation, but there is still a large degree of uncertainty regarding the overall flow connectivity within and between model layers using this method.

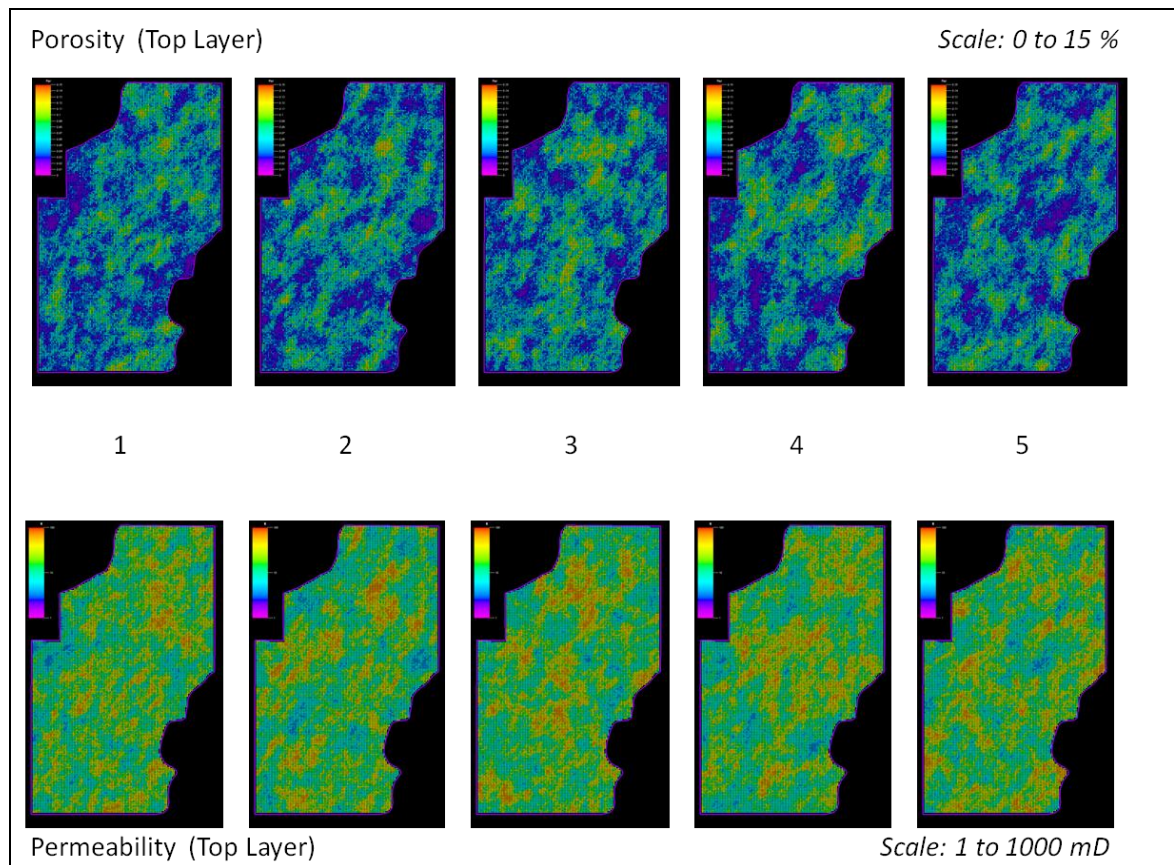


Figure 30: Five SGS realizations for Nisku open marine facies porosity (top) and permeability (bottom).

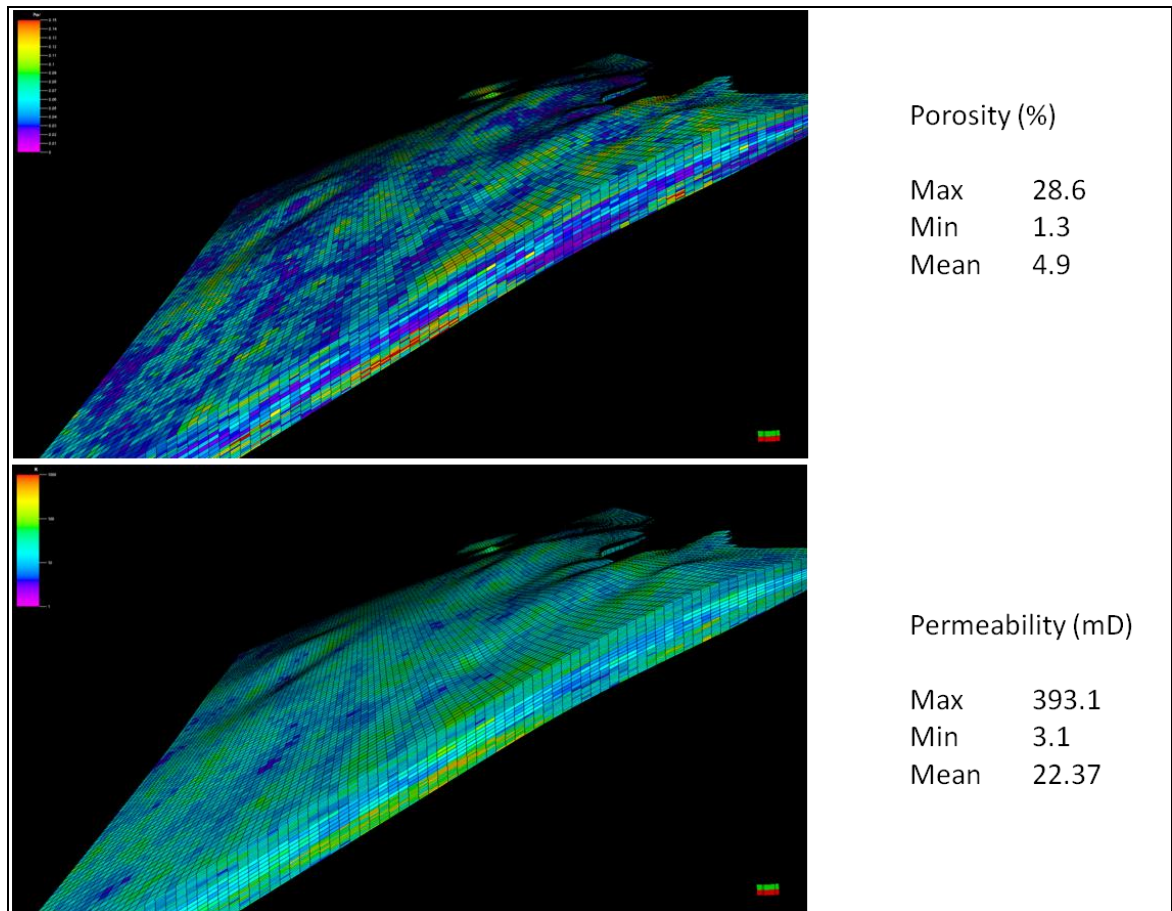


Figure 31: A three-dimensional model realization for porosity and permeability of the Nisku reservoir.

3.7 Object-based Modelling

The distribution and shape of depositional facies in the Nisku carbonate has a critical influence on the heterogeneity of flow properties. Object-modelling (also known as ‘Boolean’ modelling) provides a method for incorporating plausible and quantifiable three-dimensional facies geometries into the static earth model. This method can provide more plausible geological shapes than cell-based methods, but it is also more difficult to constrain the models to the actual wireline log and/or seismic data sets (Caers, 2005).

Already in common use for clastic-systems such as fluvial and submarine channels (e.g., Holden et al, 1998; North, 1996), an objects approach to geomodelling may also have application to carbonate systems—especially in cases where larger reservoir areas are being characterized. The dimensions of facies elements (e.g., reefs, aprons, and shoals), however, need to be quantified in terms of distribution and geometry—thickness, width, aspect ratio, sinuosity, etc. Object parameters may come from outcrop analog studies and/or well-log data (Seifert and Jensen, 2000; North, 1996). To our knowledge, the application of this method has seen limited use for carbonate systems.

The WASP region includes a large area of Nisku carbonate platform deposition. Within that area, a significant challenge is to reasonably quantify the shape and density for potential reef systems and

associated facies (i.e., the objects). From a flow-properties perspective, these objects can represent zones of enhanced porosity and permeability. For this study, constraining them to real-world dimensions was done primarily through modern platform analogs that have been mapped via satellite imagery.

3.7.1 Nisku Enhanced Poro-Perm Objects

The nature of reefal build-ups that may occur in areas away from known producing reef-trends is not well known. In trying to predict the density and dimensions of better zones of porosity and permeability throughout the WASP area, a great deal of uncertainty is involved. Studies that include these types of measurements from outcrops or wireline data of the Nisku are rare (e.g., Atchley et al., 2002).

As an alternative approach, modern carbonate facies analogs as classified from satellite imagery may provide some reasonable quantitative constraints (Harris and Kolwalik, 1994; Andrefouet et. al, 2001; Andrefouet et. al, 2003; Bachtel, 2005). This method has been developed primarily during the past decade as higher resolution, multi-spectral remote sensing data have become easier to obtain and process.

For this study, work by Harris and Vlaswinkel (2008) was used to help select values that would be reasonable for carbonate-object geometry and scale. The methods for classifying facies are described in their paper. The analysis provides attribute data for reef associated facies obtained from platform groups based on shape and size (Harris and Vlaswinkel, 2008). Of particular interest are dimensions for partially aggraded reef and apron facies, which were likely to be a common depositional occurrence in the setting of the Nisku platform for the WASP area. Figure 34 shows the workflow for how information from attributes obtained from satellite imagery is used for object modelling.

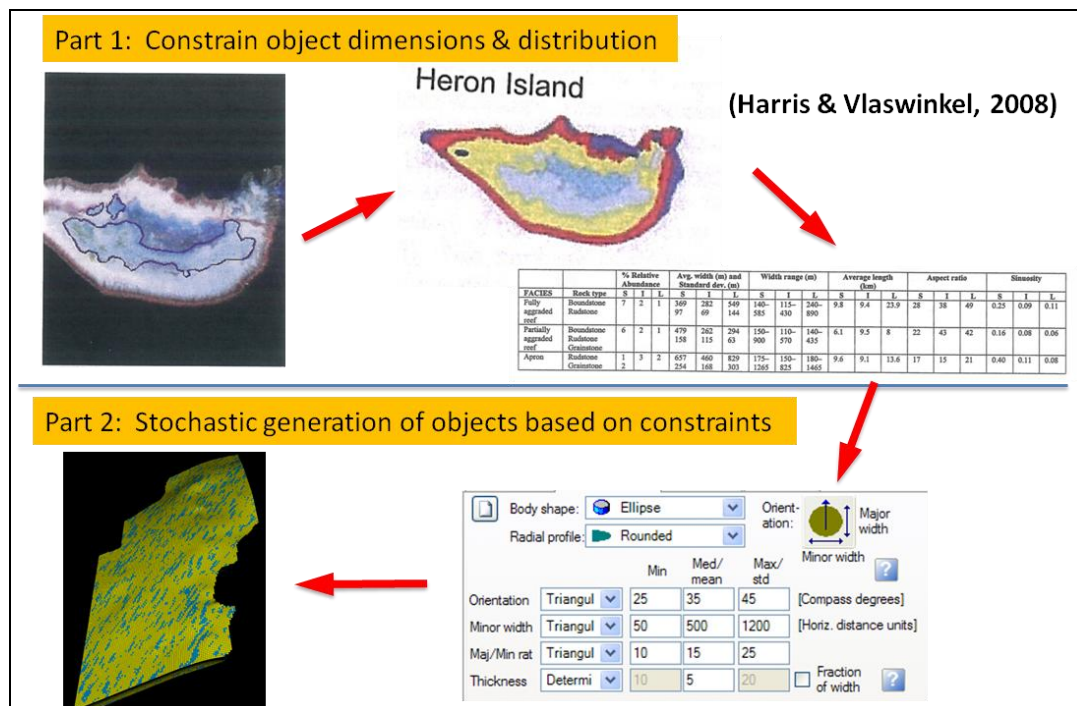


Figure 32: Generalized workflow for facies attributes (as inferred from satellite imagery) of modern carbonate analogs to be used in generating object-based models.

The parameters used for geometry of the objects are shown in Table 3. Lateral distribution of these objects was subjective, based upon conceptual understandings of the Nisku carbonate platform in the WASP study area (see Figures 3 and 35). Two zones, or fairways, were imposed on the model to reflect a greater likelihood of higher porosity and permeability with better connectivity (Figure 35 and Table 4). There is some uncertainty, however, as to the existence of better porosity and permeability along the inboard margin (Figure 35). Appendix 6 discusses this uncertainty.

The vertical distribution of objects was variable depending on the Nisku zone interval being modelled (Figure 27 and Table 4). All objects were populated stochastically in the system, yet still conditioned to existing wireline log data.

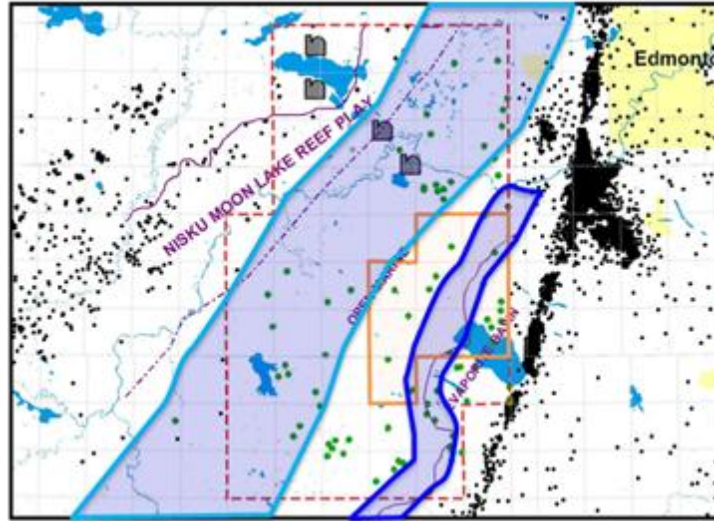


Figure 33: Two regions with higher probability for enhanced porosity and permeability objects based on conceptual modelling of regional deposition. Inboard margin (IBM) (dark blue) and open marine (light blue).

Table 3: Geometry of enhanced porosity and permeability objects. All distributions are triangular between minimum, mean, and maximum.

Enhanced Porosity Class		Minimum (m)	Mean (m)	Maximum (m)
Better	Orientation (Azimuth)	25	35	45
	Major Width	50	500	1200
	Maj/Min Ratio	1	5	7
	Thickness	0.5	5	10
Best	Orientation (Azimuth)	25	35	45
	Major Width	20	300	800
	Maj/Min Ratio	1	5	7
	Thickness	0.1	2	6

Table 4: Division of objects based on vertical interval, enhanced regions, and classes. The percent of total volume objects occupy is a controlled parameter subjectively estimated. IBM = inboard margin, OM = open marine.

Vertical Zone	Enhanced Porosity Object Fairways	Enhanced Porosity Class	% of Total Model Volume
Upper	IBM	Better	3
	IBM	Best	0.5
	OM	Better	7
	OM	Best	1
Middle	IBM	Better	1
	IBM	Best	0.1
	OM	Better	4
	OM	Best	0.5
Lower	IBM	Better	1
	IBM	Best	0.1
	OM	Better	25
	OM	Best	11

Porosities and permeabilities for objects were determined based on the distribution as determined from wireline conductivity (or resistivity) measurements for two classes of enhanced porosity and permeability zones:

- 1) Better — 8% porosity (normal dist. & 1 std.) and 30 md (log-normal dist & 1 std.)
- 2) Best — 14% porosity (normal dist. & 1 std.) and 200 md (log-normal dist & 1 std.)

Normal distributions were used for populating object flow properties and SGS modelling was used for baseline carbonate cells. In both cases, modelled flow parameters were constrained to wireline log and seismic-based acoustic impedance data where available.

Several iterations of object distributions were generated (Figure 36), and each was then geostatistically populated with flow properties (Figure 37). The final model outcome was a combination of strong geologic interpretation and traditional geostatistical methods constrained to available data.

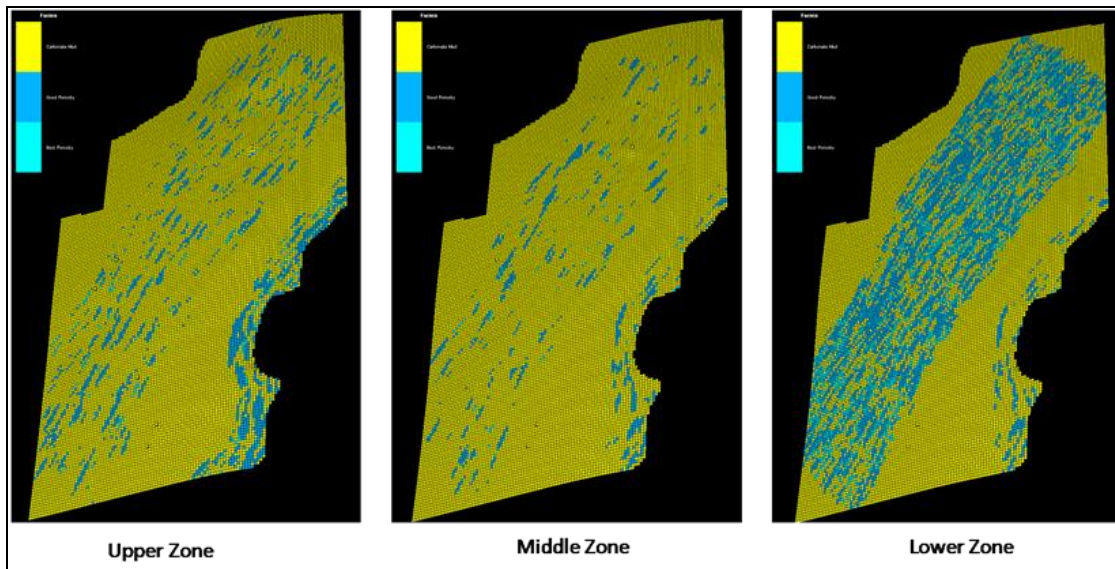


Figure 34: Example of object geometries and distributions for object-based modelling for three Nisku intervals in WASP area. Yellow—background Nisku; blue—better porosity and permeability; turquoise—best porosity and permeability.

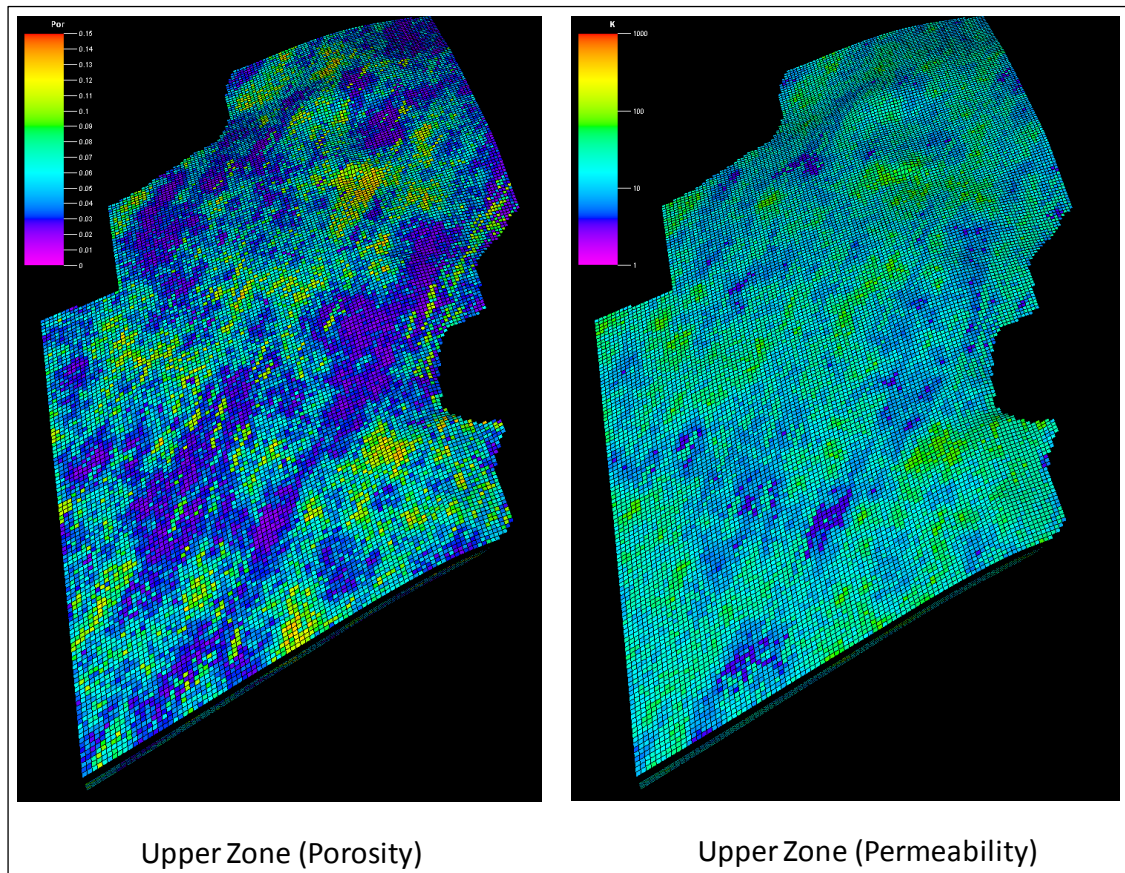


Figure 35: Examples of flow property modelling based on object-models. Porosity (left) scaled 0 to 15% and permeability (right) scaled 1 to 1000 mD.

3.8 Model Validation

Results of both the object- and pixel-based models still require validation. For example, flow simulations of some DSTs could be compared to the field DSTs to assess whether permeability and larger-scale connectivity are adequately captured in the models. Simulation of the water production well could also reveal which models provide the observed deliverabilities along the inboard margin region. Nonetheless, a qualitative inspection suggests a more accurate portrayal of mid-to large-scale reservoir heterogeneity from the object method.

Table 5: Minimum potential storage capacity for Nisku reservoir using WASP boundary. Actual volumes will be larger as aquifer extends to the northwest and southeast of study area. Mean permeability (k) is significantly larger for the object model as isolated grid cells containing high values affect the result.

	Bulk Volume (10⁶ m³)	Pore Volume (10⁶ m³)	Mean ϕ (%)	Mean k (mD)
Homogeneous	305,348	15,267	5.0	30
SGS (50 realizations)	305,348	15,258	4.9	1
Homogeneous	305,348	15,267	5.0	30

3.9 Summary

An accurate representation of the Nisku reservoir is difficult with limited data and measurements. None-the-less, realistic estimates of reservoir capacity and fluid flow behaviour can be made through geomodelling. For the WASP study, probabilistic or object-based methods appear to provide the best order-of-magnitude volume approximations (Table 5) and allow variations in connectivity to be examined through fluid simulation. A synthesis of all the model data suggests pore volumes for the Nisku using the WASP boundary will be between 15 and 17 km³, however the real storage potential will be much larger as the aquifer extends far to the northeast and southwest of the study area. Qualitatively, the potential flow pathways appear most realistic in an object-based model that allows more geologic interpretation to be included. Further, targeted injection of fluids into the lowest most interval of the Nisku may provide the most benefit. Validation of the models through simulated DSTs are necessary. Further, systematic model sensitivity analysis and subsequent fluid simulation of those models would be useful.

CONCLUSIONS

The available core analyses and petrophysical evaluation of wireline logs indicate mean porosities for the Nisku interval to between 3 and 5%, with localized zones in excess of 10%. Permeability from core measurements shows the median to be 10 mD, but also with recorded values in excess of several Darcys. In trying to map the distribution, size, and connectivity of these better porosity-permeability intervals, wireline logs were used.

Resistivity and conductivity measurements appear to be a useful estimation tool for both ϕ and k. With a known formation resistivity factor, an assumption of near unity water saturation, and estimates of porosity from core/petrophysical data, the Archie cementation factor was established to be between 2 and 3. Zones with porosity greater than 8% were more often in the lower third of the reservoir interval. Flow capacities, estimated using a relationship between maximum conductivity and permeability thickness from core and DST data, were up to several Darcy-metres in the best cases. The flow capacity is greater than 1 D-m for 25% of the wells with available wireline data

using this method. Connectivity on the reservoir scale is more difficult to evaluate, but production data from wells in nearby hydrocarbon plays suggest 500 mD-m flow capacities.

The goal of geomodelling is to create an accurate representation of the reservoir flow properties for use in fluid injection simulations. To that end, a model framework was created to represent the Nisku reservoir, measured property data were integrated into that framework, and then geostatistical techniques were utilized to populate the model in areas that were unknown. By targeting a deep saline aquifer, reservoir measurements (both direct and indirect) are greatly limited. Deterministic methods are not very useful for modelling a region of this size. Probabilistic methods, e.g., SGS, do a better job, but do not capture the heterogeneity as constrained by the conceptual understanding of the depositional history of the Nisku. A less common approach using objects in a Boolean-model workflow allows the target reservoir to be more realistically modelled for connectivity. This method, however, requires the geometry and distribution of higher porosity and permeability zones to be well understood, which for this study was done through a reported analysis of modern analogs mapped with satellite imagery. There still remains a lot of uncertainty as to the nature and extent of high porosity-permeability zones within the targeted injection interval.

The static-earth models were exported for use in fluid-flow simulations (discussed in the flow simulation chapter). The petrophysical analysis and geomodelling suggests potentially good injection volume and flow capacity in the Nisku assuming the best interval and laterally extensive zones are targeted. Seismic data will be invaluable in this process. Another concern is the fracture pressure of the reservoir, which requires detailed geomechanical understanding and a well integrated model of the caprock—in this case the formations of the Winterburn aquitard. The geological model created here can be used as part of this process. Finally, it is necessary to validate the static models for accuracy. This can be done using simulated DSTs and by regenerating models when new data become available.

ACKNOWLEDGEMENTS

We greatly appreciate the financial support of NSERC and AERI, with additional funding from TransAlta, TransCanada, ARC Energy Trust, Penn West Energy Trust, Epcor, Enbridge, ConocoPhillips Canada, Encana, StatOilHydro Canada, Total Canada, Computer Modelling Group, and Golder Associates. We also thank Highpine Oil & Gas for sharing wireline log data and Schlumberger for software access and support. Frank Stoakes and Katrine Foellmer of SCG Ltd. provided invaluable help with geological interpretation and guidance.

REFERENCES

- Andrefouet, S., Claereboudt, M., Matsakis, P., Paget, J., and Dufour, P., 2001, Typology of atoll rims in Tuamotu Archipelago (French Polynesia) at landscape scale using SPOT HRV images: *Intl. Journal of Remote Sensing*, 22, 987–1004.
- Andrefouet, S., Kramer, P., Torres-Pulliza, D., Joyce, K.E., Hochberg, E.J., Garza-Perez, R., Mumby, P.J., Riegl, B., Yamano, H., White, W.H., Zubia, M., Brock, J.C., Phinn, S.R., Naseer, A., Hatcher, B.G., and Muller-Karger, F.E., 2003, Multi-site evaluation of IKONOS data for classification of tropical coral reef environments: *Remote Sensing of the Environment*, 88, 128–143.
- Archie, G.E., 1942, The electrical resistivity log as an aid in determining some reservoir characteristics: *Am. Inst. Min. Metall. Engineers Transactions*, 146, 54–62.
- Archie, G.E., 1950, Introduction to petrophysics of reservoir rocks: *Bull. Am. Ass. Petrol. Geol.*, 34, 943–961.
- Atchley, S., and McMurray, M., 2002, Devonian (Frasnian) Leduc- and Nisku-equivalent outcrops near Canmore, Alberta: 1-D outcrops as a guide to subsurface stratal architecture: *Am. Ass. Petrol. Geol. Annual Conv.*, Houston, Texas.
- Bachtel, S.L., 2005, Platform-scale facies distributions using Landsat data from isolated carbonate platforms: methods to constrain lateral facies continuity for geologic modelling: *Am. Ass. Petrol. Geol. Annual Conv.*, Calgary, Alberta.
- Bachu, S., and Bennion, B., 2008, Effects of in-situ conditions on relative permeability characteristics of CO₂-brine systems: *Environ Geol*, 54, 8, 1707–1722.
- Ball, L.D., Corbett, P.W.M., Jensen, J.L., and Lewis, J.J.M., 1997, The role of geology in the behavior and choice of permeability predictors: *SPE Formation Evaluation*, 12, 1, 32–39.
- Caers, J., 2005, *Petroleum Geostatistics*: Soc. for Petro. Eng., Richardson, Texas, 88 p.
- Harris, P.M., and Kolwalik, W.S., eds., 1994, *Satellite Images of Carbonate Depositional Settings: Examples of Reservoir- and Exploration-scale Geologic Facies Variation*: *Am. Ass. Petrol. Geol., Methods in Exploration Series*, 11, 147 p.
- Harris, P.M., and Vlaswinkel, B., 2008, Modern isolated carbonate platforms: Templates for quantifying facies attributes of hydrocarbon reservoirs: *Soc. for Sed. Geol. Special Pub.*, 89, 323–341.
- Hitchon, B., 1996, *Aquifer Disposal of Carbon Dioxide*: Geoscience Publishing Ltd., Sherwood Park, Alberta, 165 p.
- Holden, L., Hauge, R., Skare, O., and Skorstad, A., 1998, Modelling fluid reservoirs with object models: *Mathematical Geology*, 30, 5, 473–496.
- Michael, K., Bachu, S., Buschkuehle, B.E., Haug, K., Grobe, M., and Lytviak, A.T., 2006, Comprehensive characterization of a potential site for CO₂ geological storage in central Alberta, Canada: *Proceedings, CO₂SC Symposium*, Berkeley, California, 4 p.
- Michael, K., Bachu, S., Buschkuehle, B.E., Haug, K., and Talman, S., 2009, Comprehensive characterization of a potential site for CO₂ geological storage in central Alberta, Canada: *Carbon*

Dioxide Sequestration in Geological Media – State of the Art (M. Grobe, J. Pashin and R. Dodge, eds.), AAPG Studies in Geology 59, 227–240.

North, C.P., 1996, The prediction and modelling of subsurface fluvial stratigraphy *in* Advances in Fluvial Dynamics and Stratigraphy, P.A. Carling and M.R. Dawson (eds.): John Wiley & Sons, New York, 395–508.

Jackson, P.D., Harvey, P.K., Lovell, M.A., Gunn, D.A., Williams, C.G., and Flint, R.C., 1998, Measurement scale and formation heterogeneity: effects on the integration of resistivity data: Geological Society Special Publication, 136, 261–272.

Lucia, J.F., 2007, Carbonate Reservoir Characterization: An Integrated Approach: Springer, Berlin, 336 p.

SCG Ltd., Stoakes Consulting Group, 2009, personal communication.

Seifert, D. and Jensen, J.L., 2000, Object and pixel-based reservoir modelling of a braided fluvial reservoir: *Mathematical Geology*, 32, 5, 581–603.

Srivastava, R.M., 1994, An overview of stochastic methods for reservoir characterization in AAPG Computer Applications in Geology No. 3, Stochastic Modelling and Geostatistics: Principles, Methods and Case Studies, J.M. Yarus and R.L. Chambers (eds): American Association of Petroleum Geologists, Tulsa, OK, 3–16.

Switzer, S.B., Holland W.G., Christie, D.S., Graf, G.C., Hedinger, A.S., McAuley, R.J., Wierzbicki, R.A., and Packard, J.J., 1994, Devonian Woodbend - Winterburn strata of the Western Canada Sedimentary Basin *in* Geological Atlas of the Western Canada Sedimentary Basin, G.D. Mossop and I. Shetsen (comp.): Canadian Society of Petroleum Geologists and Alberta Research Council, Special Report 4.

Wright, G.N., McMechan M.E., and Potter, D.E.G., 1994, Structure and architecture of the Western Canada Sedimentary Basin *in* Geological Atlas of the Western Canada Sedimentary Basin, G.D. Mossop and I. Shetsen (comp.): Canadian Society of Petroleum Geologists and Alberta Research Council, Special Report 4.

Wylie, M. R., Gregory, A. R., and Gardner, L. W., 1956, Elastic wave velocities in heterogeneous and porous media: *Geophysics*, 21, 41–70.

APPENDIX 1: WELLS (NISKU)

UWI	Drilling Completed	TVD (m)	Formation@TD	BH Temp. (°C)	Core	Canstrat
100/03-16-043-05W5/00	06/07/1954	3080.3	Dbvrh_lk	?	Y	
100/14-26-044-02W5/00	11/28/1985	2630	Dbvrhl_lk	74		
100/15-35-044-02W5/00	02/16/1988	2938	Cdeadwood	76		Y
100/16-36-044-02W5/00	01/19/1991	2600	Dbvrhl_lk	70		
100/01-18-044-03W5/00	04/14/1985	2792	Dbvrhl_lk	59		Y
100/12-22-044-03W5/00	05/05/1953	2659.4	Dduvernay	73		Y
100/06-26-044-03W5/00	08/08/1978	2412	Dnisku	71		
100/10-27-044-03W5/00	11/23/1977	2420.1	Direton	69		
100/07-31-044-04W5/00	10/03/1974	2631.9	Direton	67	Y	
100/10-33-044-04W5/00	04/07/1975	2578.6	Direton	46		
100/06-02-045-02W5/00	11/10/1977	2779.8	Delk_pt	78		Y
100/15-11-045-02W5/00	02/16/1954	2596.9	Dduvernay	79		Y
100/14-21-045-02W5/00	08/26/1960	2580.4	Dbvrhl_lk	71		Y
1F1/11-29-045-02W5/00	11/27/2002	2321	Direton	?		
100/14-32-045-02W5/00	07/13/1997	2632	Direton	66		
100/14-16-045-03W5/00	01/14/2006	2443	Direton	?		
100/06-05-045-04W5/00	02/13/1975	2592.3	Direton	66		
102/16-06-045-04W5/00	08/06/1975	2947.4	Dbvrhl_lk	72		
100/07-08-045-04W5/00	03/17/1976	2567.9	Dnisku	69	Y	Y
100/06-10-045-04W5/00	12/28/1985	2510	Dnisku	64		
100/14-09-045-05W5/00	08/20/1997	3100	Dbvrhl_lk	93		
100/04-22-045-05W5/00	08/05/1954	3159.3	Delk_pt	93	Y	Y
100/10-36-045-05W5/00	02/05/1976	2514.6	Direton	73	Y	
100/11-24-045-08W5/00	08/25/1978	3150	Dbvrhl_lk	?	Y	
100/01-01-046-01W5/00	08/10/1983	2258.8	Dleduc	68		
100/02-01-046-01W5/00	11/07/1987	2284	Dleduc	66		
100/09-01-046-01W5/00	02/12/1972	2272.9	Dleduc	85		
104/06-06-046-01W5/00	08/21/2004	2484	Direton	72		
100/01-13-046-01W5/00	03/26/1953	2283	Dcook_lk	69		Y
100/06-29-046-01W5/00	10/09/1984	2460	Dbvrhl_lk	68		
100/10-09-046-02W5/00	01/28/1966	2790.7	Delk_pt	87		Y
100/10-25-046-02W5/00	07/30/1966	2690.2	Delk_pt	64		Y
102/12-25-046-02W5/00	06/21/1996	2545	Dbvrhl_lk	81		
100/11-12-046-03W5/00	02/10/1953	2560	Direton	71		
100/16-12-046-03W5/00	01/02/1948	2746.6	Dduvernay	76	Y	Y
100/11-33-046-03W5/00	01/15/1953	2564.9	Dduvernay	74	Y	Y
100/05-12-046-05W5/00	06/13/1978	2481	Direton	76	Y	Y
100/06-19-046-05W5/00	09/11/1958	2865.1	Dbvrhl_lk	85	Y	Y
100/10-20-046-05W5/00	10/29/1978	2565	Dwoodbend	75		
100/14-29-046-05W5/00	06/26/1993	2515	Direton	79		
100/09-10-047-01W5/00	04/17/1987	2311.5	Direton	71		
100/10-22-047-01W5/00	09/23/1964	2539	Dbvrhl_lk	72		Y

UWI	Drilling Completed	TVD (m)	Formation@TD	BH Temp. (°C)	Core	Canstrat
100/08-26-047-01W5/00	10/08/1973	2362.2	Dbvrhl_lk	71		
100/12-27-047-01W5/00	01/02/1965	2401.8	Dbvrhl_lk	63		
100/16-35-047-01W5/00	06/18/1973	2293.6	Dbvrhl_lk	74		
100/06-02-047-02W5/00	07/16/1961	2516.1	Dbvrhl_lk	80		Y
100/04-36-047-03W5/00	04/26/1949	2562.8	Dcook_lk	77	Y	Y
100/02-06-047-04W5/00	02/21/1955	3092.2	Cdeadwood	104	Y	Y
100/09-24-047-06W5/00	09/21/1991	2723	Dduvernay	69		
100/16-02-048-01W5/00	10/31/1952	2286	Dduvernay	62	Y	Y
100/02-21-048-01W5/00	02/12/1962	2286	Dbvrhl_lk	61		Y
100/08-17-048-02W5/00	10/17/1984	2050	Dnisku	69		
100/02-28-048-02W5/00	01/17/1955	2348.2	Direton	68		Y
100/06-15-048-03W5/00	09/14/1959	2674.6	Dgilwood	67		
100/16-06-048-04W5/00	08/18/1959	2874.3	Cambrian	71		
100/08-15-048-04W5/00	05/07/1956	2560	Dbvrhl_lk	71		Y
100/10-29-048-05W5/00	07/14/1979	2355	Direton	80		
102/14-12-048-06W5/00	04/04/1989	2414	Direton	70		
100/14-29-048-06W5/00	05/27/1954	3146.1	Cambrian	76	Y	Y
100/04-11-049-01W5/00	11/12/1950	2128.7	Dduvernay	62		
100/16-33-049-01W5/00	02/22/1954	2102.5	Dcook_lk	41		
100/15-11-049-02W5/00	08/13/1950	2263.1	Dduvernay	76		Y
100/07-33-049-06W5/00	04/18/1978	2322.6	Direton	72		
100/16-01-050-01W5/00	07/06/1952	2083.6	Dduvernay	82		
100/15-26-050-01W5/00	09/06/1949	1981.2	Dduvernay	54		
100/15-10-050-02W5/00	02/09/1948	2040.6	Direton	71	Y	
100/16-16-050-02W5/00	12/02/1960	2295.1	Dbvrhl_lk	63		
100/04-20-050-02W5/00	12/21/1958	1942.2	Direton	56		
100/05-20-050-02W5/00	09/09/1965	2247.6	Dbvrhl_lk	61		
100/10-21-050-02W5/00	08/19/1997	1900	Direton	64		
100/02-22-050-02W5/00	02/26/1955	2581	Dbvrhl_lk	46		Y
100/02-26-050-02W5/00	08/13/1954	2243.3	Dbvrhl_lk	63		Y
100/04-11-051-01W5/00	04/11/1950	2042.8	Dduvernay	?	Y	Y
100/09-16-051-01W5/00	10/04/1954	2088.5	Dduvernay	61	Y	
100/04-36-051-01W5/00	05/01/1948	2128.7	Dcook_lk	?	Y	
100/04-28-051-02W5/00	03/11/1950	2183.6	Dcook_lk	57		Y
100/04-14-051-03W5/00	07/23/1963	1905	Direton	56		
100/05-08-051-04W5/00	06/24/1978	2077	Direton	59	Y	
100/04-14-051-04W5/00	06/24/1978	2057.4	Direton	55	Y	
100/01-34-051-04W5/00	11/09/1978	2060	Direton	54		
100/02-29-051-05W5/00	03/24/1994	2128	Dnisku	50	Y	
100/03-12-052-01W5/00	09/02/1981	2072	Dbvrhl_lk	60		
100/09-13-052-01W5/00	07/20/1949	1830	Direton	64		
100/10-05-052-02W5/00	01/08/1968	2920	preCamb	76		Y
100/04-34-052-03W5/00	02/07/1952	2103.1	Dduvernay	51	Y	
100/11-34-052-03W5/00	01/11/1998	1815	Dnisku	46		
100/15-23-052-04W5/00	02/15/1982	1960	Direton	47	Y	Y
100/05-01-052-05W5/00	08/26/1973	2133.6	Direton	57	Y	Y

UWI	Drilling Completed	TVD (m)	Formation@TD	BH Temp. (°C)	Core	Canstrat
100/16-18-052-05W5/00	05/26/1956	2797.1	Delk_pt	74	Y	Y
100/08-30-052-05W5/00	09/17/1984	2714	Cambrian	65		
100/04-31-052-05W5/00	09/24/1978	2090	Direton	70	Y	
100/07-11-053-01W5/00	08/08/1949	1966.3	Dduvernay	59	Y	
100/04-12-053-02W5/00	11/28/1950	1981.2	Dduvernay	60	Y	Y
100/10-10-053-03W5/00	02/25/1974	1956.8	Direton	53	Y	
100/10-14-053-03W5/00	01/15/1976	1876	Direton	53		
100/07-33-053-03W5/00	10/31/1961	1868.4	Direton	46		
100/13-36-053-03W5/00	07/05/1978	1853.2	Direton	50	Y	
100/13-36-053-05W5/00	06/11/1949	2067.8	Direton	63		

Table Legend

Blue Wells out of WASP study area
Yellow Wells in Moon Lake play

Formation abbreviations

Cambrian → Cambrian
 Cdeadwood → Deadwood
 Dbvrh_lk → Beaverhill Lake
 Dcook_lk → Cooking Lake
 Dduvernay → Duvernay
 Delk_pt → Elk Point
 Dgilwood → Gilwood
 Direton → Ireton
 Dleduc → Leduc
 Dnisku → Nisku
 Dwoodbend → Woodbend
 PreCamb → Pre-Cambrian

APPENDIX 2: WELL CORES (WASP AREA)

CPA Format Well ID	Date Drilling Completed	Core Analysis	Logged	Reported Depth Interval (ft)	Total Core (ft)	ERCB
100/07-31-044-04W5/00	10/03/1974	Y	Y	8497–8516	19	5B/4"/W
100/07-08-045-04W5/00	03/17/1976	Y	Y	8215–8275	58	16B/4"/W
100/04-22-045-05W5/00	08/05/1954	Y (new)	Y	8460–8594	194	27B/3"/W
100/10-36-045-05W5/00	02/05/1976	Y	Y	7933–7983	50	28B/4"/W
100/16-12-046-03W5/00	01/02/1948	N	Y	7319–7339 and 7408–7419	31	2B/2"/W
100/11-33-046-03W5/00	01/15/1953	Y (new)	Y	7215–7351	136	27B/3"/A
100/05-12-046-05W5/00	06/13/1978	Y	Y	7831–7891	60	13B/3"/R
100/06-19-046-05W5/00	09/11/1958	Y	Y	8054–8078	24	5B/3"/R
100/06-02-047-02W5/00	07/16/1961	Y (new)	Y	6841–6876 and 6908–6921	48	7B/3"/W, 3B/3"/W
100/04-36-047-03W5/00	04/26/1949	N	Y	6990–7034	44	1B/1"/W
100/02-06-047-04W5/00	02/21/1955	Y (new)	Y	7642–7753	111	24B/3"/R
100/16-02-048-01W5/00	10/31/1952	Y (new)	Y	6120–6135 and 6137–6186	34	13B/3"/W
100/15-11-049-02W5/00	08/13/1950	Y (new)	Y	6129–6155 and 6260–6278	44	6B/3"/W, 4B/3"/W
100/15-10-050-02W5/00	02/09/1948	N	Y	6040–6094	54	3B/1"/W
Outside Study Area						
100/03-16-043-05W5/00	06/07/1954	Y (new)	Y	8878-8974	96	18B/3"/W
100/11-24-045-08W5/00	08/21/1978	Y (new)	Y	8965-9012	47	10B/3"/W
Notes						
1. Complete core analysis data available in WASP project archives.						
2. Whole core photos available for the following wells:						
<ul style="list-style-type: none"> • 100/04-22-045-05W5/00 • 100/16-02-048-01W5/00 • 100/15-11-049-02W5/00 						

APPENDIX 3: WIRELINE GEOPHYSICAL LOGS

UWI	Wireline Geophysical Logs
100/14-26-044-02W5/00	S (295.8 ~ 2618.3m);DILL (1780.0 ~ 2628.1m);FLUID L (281.0 ~ 2630.0m)
100/15-35-044-02W5/00	S (1400.0 ~ 2584.0m);CS (450.0 ~ 2580.0m);CN-LD (875.0 ~ 2590.0m);DIL (450.0 ~ 2591.0m);C-VOL (450.0 ~ 2590.0m);HR-DIP (2150.0 ~ 2600.0m);SWF (1400.0 ~ 2584.0m);FT (2150.0 ~ 2584.0m);BHTV (2189.1 ~ 2236.0m);CP (430.0 ~ 2938.0m);CS (2575.0 ~ 2920.0m);CN-LD (2575.0 ~ 2933.0m);DIL (2575.0 ~ 2932.0m)
100/16-36-044-02W5/00	S (403.9 ~ 2596.8m);CNFD (1600.0 ~ 2600.0m);DILL (403.9 ~ 2598.6m);CP (390.0 ~ 2219.0m)
100/01-18-044-03W5/00	CS (327.0 ~ 2778.0m);CN-LD (413.3 ~ 2790.8m);DISF (413.3 ~ 2790.3m);C-VOL (413.0 ~ 2780.0m);FLUID L (2730.0 ~ 2792.0m);FLUID L (398.0 ~ 2792.0m)
100/12-22-044-03W5/00	ES (180.4 ~ 2659.4m);LL (180.4 ~ 2659.4m)
100/06-26-044-03W5/00	SONIC (260.0 ~ 2410.0m);DIL (260.0 ~ 2411.0m);PERF (1850.0 ~ 2000.0m);ND-LITH (260.0 ~ 2412.0m)
100/10-27-044-03W5/00	SONIC (248.4 ~ 2415.8m);DIL (248.4 ~ 2415.8m);CB (1524.0 ~ 1975.1m);COLLAR (1850.0 ~ 1890.0m);TRACE L (1825.0 ~ 1905.0m);ND-LITH (248.4 ~ 2417.1m)
100/07-31-044-04W5/00	SONIC (265.2 ~ 2627.1m);DIL (265.2 ~ 2628.3m);GR-CORR (2000.0 ~ 2143.0m);ND-LITH (1066.8 ~ 2629.8m)
100/10-33-044-04W5/00	SONIC (271.3 ~ 2578.6m);DIL (271.3 ~ 2578.0m);ND-LITH (2042.2 ~ 2578.6m)
100/06-02-045-02W5/00	SONIC (1676.4 ~ 2779.2m);NEUT (457.2 ~ 2286.0m);DIL (461.8 ~ 2778.6m);CB (1676.4 ~ 1995.2m);GR (1714.2 ~ 1791.8m);PERF (1801.4 ~ 1856.2m);IND-LOG (1767.0 ~ 1804.0m);ND-LITH (461.8 ~ 2779.8m);GR (1730.0 ~ 1789.7m)
100/15-11-045-02W5/00	ES (188.1 ~ 1430.4m);ML (655.3 ~ 1429.5m);ES (1430.4 ~ 2596.0m);ML (1798.3 ~ 2286.0m)
100/14-21-045-02W5/00	IE (274.3 ~ 2576.2m);ML (670.6 ~ 2578.0m);SONIC (274.3 ~ 2574.3m)
1F1/11-29-045-02W5/00	
100/14-32-045-02W5/00	CS (329.0 ~ 2457.0m);CN-LD (329.0 ~ 2470.0m);GRN-COL (1696.0 ~ 2618.1m);DIL (329.0 ~ 2472.5m);GR-CORR (1550.0 ~ 1700.0m);COLLAR (1783.0 ~ 1840.0m);MUD-HYD (1765.0 ~ 2625.0m);GR-CORR (1800.0 ~ 1855.0m);COLLAR (1796.0 ~ 1866.0m);MUD-HYD (1840.0 ~ 2645.0m);GR-CORR (1600.0 ~ 1866.0m);COLLAR (1837.0 ~ 1840.0m);COLLAR (1764.4 ~ 1836.3m);COLLAR (1772.6 ~ 1842.0m);COLLAR (1642.8 ~ 1699.9m)
100/14-16-045-03W5/00	ML (2368.5 ~ 2484.0m);CS (456.0 ~ 815.0m);D-S-S-I (2368.5 ~ 2473.0m);CN-LD (2368.5 ~ 2492.5m);C-VOL (456.0 ~ 815.0m);ML (2324.0 ~ 2430.0m);CN-LD (2324.0 ~ 2437.0m);DIL (2324.0 ~ 2439.6m)
100/06-05-045-04W5/00	SONIC (265.2 ~ 2590.8m);GRN-COL (1825.0 ~ 2165.0m);DIL (267.3 ~ 2584.4m);CB (2450.0 ~ 2568.0m);GR-CORR (2040.0 ~ 2100.0m);PERF (2510.0 ~ 2550.0m);COLLAR (2475.0 ~ 2563.4m);ND-LITH (2072.6 ~ 2590.8m);GR-CORR (1825.0 ~ 2165.0m);COLLAR (2470.0 ~ 2515.0m)
102/16-06-045-04W5/00	SONIC (284.4 ~ 2597.2m);DIL (286.2 ~ 2595.7m);ND-LITH (2036.1 ~ 2597.2m);SONIC (2499.4 ~ 2946.2m);DIL (2499.4 ~ 2945.0m)
100/07-08-045-04W5/00	SONIC (270.7 ~ 2562.8m);NEUT (1219.2 ~ 2564.6m);LL (270.7 ~ 2564.0m);DEN (1219.2 ~ 2564.6m);CP (2447.5 ~ 2464.9m);CP (2011.7 ~ 2058.6m);CP (1798.3 ~ 1857.5m);CP (1210.1 ~ 1259.1m);CP (198.1 ~ 251.8m)
100/06-10-045-04W5/00	S (393.3 ~ 2505.8m);CNFD (393.3 ~ 2508.7m);DILL (393.3 ~ 2509.1m);GR-CB (164.0 ~ 2114.0m);COLLAR (2025.0 ~ 2115.0m)
100/14-09-045-05W5/00	ML (511.0 ~ 3056.0m);CS (511.0 ~ 3041.0m);CN-LD (511.0 ~ 3056.0m);DIL (511.0 ~ 3058.0m);TEMPL (749.0 ~ 1401.1m);GR-CB (1994.0 ~ 2171.0m);COLLAR (1998.0 ~ 2168.0m);CP (2142.0 ~ 2639.0m)

UWI	Wireline Geophysical Logs
100/04-22-045-05W5/00	IE (214.9 ~ 1341.7m);ML (1182.6 ~ 1339.6m);NEUT (30.5 ~ 3158.3m);IE (1341.7 ~ 1670.9m);ML (1339.6 ~ 1670.0m);NEUT (1158.2 ~ 1325.0m);IE (1670.9 ~ 2388.4m);ML (1182.6 ~ 2387.2m);IE (2388.4 ~ 3159.3m);ML (2387.2 ~ 3158.3m)
100/10-36-045-05W5/00	DIL (250.9 ~ 2514.6m);ND-LITH (579.1 ~ 2514.6m);CP (359.7 ~ 1926.9m);CP (1702.0 ~ 1772.7m);CP (1325.9 ~ 1379.5m);CP (1039.4 ~ 1098.5m);CP (155.4 ~ 192.0m)
100/01-01-046-01W5/00	SONIC (240.0 ~ 2253.0m);DIL (240.0 ~ 2255.0m);CB (1500.0 ~ 2256.3m);PERF (2195.0 ~ 2255.6m);COMP (2191.2 ~ 2252.3m);COLLAR (2192.0 ~ 2248.0m);DIR (240.0 ~ 2224.0m);CI (~ 232.0m);ND-LITH (240.0 ~ 2255.0m);COLLAR (2197.0 ~ 2244.0m)
100/02-01-046-01W5/00	CS (970.0 ~ 2283.2m);CNFD (246.0 ~ 2283.0m);DISF (246.0 ~ 2283.2m);C-VOL (246.0 ~ 2283.0m);COLLAR (2192.9 ~ 2256.0m);COLLAR (2204.0 ~ 2249.0m)
100/09-01-046-01W5/00	IE (234.1 ~ 2266.8m);SONIC (234.1 ~ 2265.3m);DIR (234.1 ~ 2266.8m);DIP (234.1 ~ 2266.8m)
104/06-06-046-01W5/00	CS (346.0 ~ 2170.2m);CN-LD (346.0 ~ 2178.7m);DIL (346.0 ~ 2181.7m);C-VOL (346.0 ~ 2178.7m);CS (2194.0 ~ 2470.5m);CN-LD (2194.0 ~ 2479.0m);DIL (2194.0 ~ 2482.0m);C-VOL (2194.0 ~ 2479.0m)
100/01-13-046-01W5/00	ES (194.5 ~ 2283.0m)
100/06-29-046-01W5/00	CS (395.0 ~ 983.0m);CNFD (395.0 ~ 992.0m);DISF (395.0 ~ 983.0m);GR-CB (1650.0 ~ 1750.0m);COLLAR (1693.0 ~ 1755.0m);CLITH (625.0 ~ 981.0m);CP (2285.0 ~ 2356.0m);CS (750.0 ~ 2448.0m);CNFD (750.0 ~ 2448.0m);CN-LD (750.0 ~ 2448.0m);DISF (750.0 ~ 2458.0m);COLLAR (1645.0 ~ 1683.0m);COLLAR (875.0 ~ 940.0m);COLLAR (875.0 ~ 910.0m);COLLAR (1570.0 ~ 1700.0m);COLLAR (874.0 ~ 1685.0m)
100/10-09-046-02W5/00	IE (1767.8 ~ 2790.7m);SONIC (284.4 ~ 1833.1m);DIL (204.8 ~ 1830.9m);PERF (1783.1 ~ 1840.1m);SONIC (1767.8 ~ 2789.8m)
100/10-25-046-02W5/00	IE (278.3 ~ 2690.2m);SONIC (278.3 ~ 2690.2m)
102/12-25-046-02W5/00	CS (884.0 ~ 2531.6m);CN-LD (1550.0 ~ 1800.0m);DIL (342.0 ~ 2543.1m);GR-CORR (1670.1 ~ 1749.2m);CP (1875.0 ~ 2545.0m);MUD-HYD (1550.0 ~ 2545.0m);GR-CORR (900.0 ~ 1774.0m)
100/11-12-046-03W5/00	ES (199.6 ~ 2560.0m);ML (609.6 ~ 2316.5m)
100/16-12-046-03W5/00	ES (171.6 ~ 2703.3m)
100/11-33-046-03W5/00	ES (180.7 ~ 2564.9m)
100/05-12-046-05W5/00	SONIC (458.7 ~ 2481.0m);DIL (17.7 ~ 459.3m);CI (~ 454.2m);ND-LITH (17.7 ~ 461.5m);DIL (458.7 ~ 2481.0m);ND-LITH (458.9 ~ 2481.0m)
100/06-19-046-05W5/00	IE (182.0 ~ 2863.3m);ML (899.2 ~ 2223.2m);MLL (2223.2 ~ 2864.5m)
100/10-20-046-05W5/00	SONIC (258.0 ~ 2563.0m);DIL (259.0 ~ 2562.0m);ND-LITH (1740.0 ~ 2563.5m)
100/14-29-046-05W5/00	S (400.0 ~ 2499.6m);CNFD (400.0 ~ 2494.3m);DIL (400.0 ~ 2508.5m)
100/09-10-047-01W5/00	ML (422.0 ~ 2077.0m);CS (2767.0 ~ 3101.0m);CN-LD (430.0 ~ 2070.0m);DISF (2769.0 ~ 3113.0m);DIRS (149.0 ~ 3115.0m);DIP (1775.0 ~ 2770.0m);CS (382.0 ~ 2076.0m);DISF (382.0 ~ 2076.0m);DIRS (10.0 ~ 2770.0m)
100/10-22-047-01W5/00	IE (242.3 ~ 2423.8m);SONIC (755.9 ~ 2423.8m);DIP (2057.4 ~ 2421.9m)
100/08-26-047-01W5/00	SONIC (247.5 ~ 2361.9m);DIL (247.5 ~ 2360.7m)
100/12-27-047-01W5/00	IE (245.7 ~ 2401.5m);SONIC (518.2 ~ 2401.2m);DIL (245.7 ~ 1006.8m);DEN (518.2 ~ 1007.1m);PERF (609.6 ~ 903.1m);FT (723.6 ~ 723.6m);FAL (1005.8 ~ 2399.1m)
100/16-35-047-01W5/00	SONIC (247.5 ~ 2290.9m);DIL (247.5 ~ 2290.0m);DEN (548.6 ~ 1981.2m)
100/06-02-047-02W5/00	IE (253.3 ~ 2514.6m);ML (253.3 ~ 2515.5m);SONIC (944.9 ~ 2513.7m);NEUT (1859.3 ~ 1950.7m);CAL (~ 1984.2m);FT (1718.8 ~ 1719.4m)
100/04-36-047-03W5/00	ES (185.9 ~ 2561.8m)
100/02-06-047-04W5/00	ES (203.0 ~ 3092.2m);ML (1051.6 ~ 3092.2m)

UWI	Wireline Geophysical Logs
100/09-24-047-06W5/00	CS (2246.1 ~ 2709.3m);CN-LD (2246.1 ~ 2709.3m);DISF (382.6 ~ 2247.8m);CP (2200.0 ~ 2724.0m);CS (382.6 ~ 2236.3m);CN-LD (800.0 ~ 2249.9m);DISF (2236.1 ~ 2720.5m)
100/16-02-048-01W5/00	ES (182.3 ~ 2286.0m)
100/02-21-048-01W5/00	IE (231.6 ~ 2286.0m);ML (231.6 ~ 2286.0m);SONIC (231.6 ~ 2284.8m);GR (1493.5 ~ 1573.4m);PERF (1521.0 ~ 1574.0m)
100/08-17-048-02W5/00	S (371.3 ~ 2046.2m);CNFD (1399.8 ~ 2048.8m);DILL (371.3 ~ 2049.8m);DIRS (397.0 ~ 2050.0m);DIP (1717.6 ~ 2053.5m);CP (300.0 ~ 1579.0m)
100/02-28-048-02W5/00	ES (190.5 ~ 2348.2m);ML (457.2 ~ 1188.7m);NEUT (61.0 ~ 2347.6m);CAL (579.1 ~ 1585.0m)
100/06-15-048-03W5/00	ES (1740.7 ~ 2672.5m);ML (823.0 ~ 1740.4m);NEUT (1859.3 ~ 2671.3m);DEN (~ 1737.4m);FT (1515.8 ~ 1515.8m)
100/16-06-048-04W5/00	IE (184.1 ~ 2873.0m);ML (670.6 ~ 2873.7m);SONIC (184.1 ~ 2872.1m)
100/08-15-048-04W5/00	ES (185.9 ~ 2559.7m);ML (701.0 ~ 1955.6m);NEUT (1554.5 ~ 2559.7m);MLL (1950.7 ~ 2237.2m);TEMP (304.8 ~ 1595.6m);CAL (701.0 ~ 1862.3m);GR-CORR (900.0 ~ 1335.0m)
100/10-29-048-05W5/00	SONIC (20.0 ~ 2215.6m);DIL (458.0 ~ 2218.0m);CB (800.0 ~ 2204.0m);GR-CB (950.0 ~ 1038.0m);GR (800.0 ~ 2204.0m);GR (975.0 ~ 1041.7m);ND-LITH (458.0 ~ 2217.6m);SONIC (2170.0 ~ 2350.0m);DIL (2217.5 ~ 2352.0m);ND-LITH (240.0 ~ 2351.0m)
102/14-12-048-06W5/00	S (384.8 ~ 2039.8m);CNFD (384.8 ~ 2039.0m);DISF (1450.0 ~ 2039.8m);GR-CB (100.0 ~ 1159.0m);GR-CORR (1000.0 ~ 1125.0m);DIP (2075.0 ~ 2414.0m);CP (2062.0 ~ 2414.0m);S (2039.0 ~ 2407.8m);CNFD (2039.0 ~ 2504.5m);DISF (2039.0 ~ 2413.7m);GR-CORR (1060.0 ~ 1115.0m)
100/14-29-048-06W5/00	ES (186.2 ~ 3115.4m);ML (853.4 ~ 3063.2m);NEUT (30.5 ~ 3145.8m);GRN-COL (795.0 ~ 1112.0m);GR-CORR (810.0 ~ 867.0m);COLLAR (325.0 ~ 350.0m)
100/04-11-049-01W5/00	ES (178.0 ~ 2128.7m)
100/16-33-049-01W5/00	ES (180.7 ~ 1491.7m)
100/15-11-049-02W5/00	ES (186.8 ~ 2262.5m)
100/07-33-049-06W5/00	IE (240.8 ~ 2322.6m);IEL (240.8 ~ 2329.0m);GRN-CB (1495.0 ~ 1835.2m);CNFD (241.0 ~ 2329.0m);TEMPL (15.0 ~ 1100.0m);GR-CB (1495.0 ~ 1835.2m);GR (1694.0 ~ 1836.0m);COLLAR (1728.0 ~ 1834.9m);ND-LITH (241.1 ~ 2322.6m);CP (290.0 ~ 1945.0m);COLLAR (290.0 ~ 331.0m);COLLAR (840.0 ~ 905.0m)
100/16-01-050-01W5/00	ES (189.9 ~ 2083.6m)
100/15-26-050-01W5/00	ES (185.9 ~ 1981.2m)
100/15-10-050-02W5/00	ES (77.7 ~ 2040.3m)
100/16-16-050-02W5/00	IE (223.4 ~ 2292.7m);ML (548.6 ~ 1583.1m);SONIC (1524.0 ~ 2291.2m);COMP (10.0 ~ 80.0m)
100/04-20-050-02W5/00	IE (236.5 ~ 1940.1m);ML (457.2 ~ 1941.9m);NEUT (15.2 ~ 1942.2m);COLLAR (10.0 ~ 90.0m);NEUT (1249.7 ~ 1562.4m);COLLAR (10.0 ~ 48.0m)
100/05-20-050-02W5/00	IE (228.6 ~ 2246.1m);SONIC (1310.6 ~ 2245.8m);DIP (1295.4 ~ 2243.6m);MS (1615.4 ~ 1950.7m)
100/10-21-050-02W5/00	ML (1260.0 ~ 1552.4m);ML-EL (402.0 ~ 1558.2m);CS (402.0 ~ 1555.8m);CNFD (402.0 ~ 1568.7m);DIL (402.0 ~ 1567.9m);ML-EL (1590.0 ~ 1887.8m);CS (1557.2 ~ 1884.5m);CNFD (1557.2 ~ 1898.1m);DIL (1557.2 ~ 1896.9m)
100/02-22-050-02W5/00	ES (184.7 ~ 1483.2m);ML (502.9 ~ 1289.9m);TEMP (182.9 ~ 843.4m);CAL (182.9 ~ 812.6m);GR (30.5 ~ 1081.1m);DIR (27.4 ~ 1084.8m)
100/02-26-050-02W5/00	ES (190.2 ~ 2243.3m);ML (426.7 ~ 1481.3m);CAL (190.2 ~ 1481.3m)
100/04-11-051-01W5/00	ES (185.9 ~ 2040.9m)
100/09-16-051-01W5/00	ES (190.2 ~ 2087.3m);ML (1341.1 ~ 1522.5m);NEUT (1417.3 ~ 1470.1m);COLLAR (273.3 ~ 1429.7m)
100/04-36-051-01W5/00	NLR

UWI	Wireline Geophysical Logs
100/04-28-051-02W5/00	ES (184.7 ~ 2182.4m)
100/04-14-051-03W5/00	IE (200.3 ~ 1905.0m);SONIC (200.3 ~ 1888.8m)
100/05-08-051-04W5/00	ML (229.8 ~ 1933.7m);DIL (229.5 ~ 1931.8m);ND-LITH (229.5 ~ 1933.0m);DIL (1889.8 ~ 2073.6m);ND-LITH (1889.8 ~ 2074.5m)
100/04-14-051-04W5/00	SONIC (235.9 ~ 1936.7m);DIL (235.9 ~ 1936.7m);DIP (1524.0 ~ 1889.8m);ND-LITH (1295.4 ~ 1937.3m);CP (1463.0 ~ 1516.1m);SONIC (1889.8 ~ 2057.4m);DIL (1889.8 ~ 2056.8m);ND-LITH (1889.8 ~ 2057.4m);CP (1036.3 ~ 1073.5m);CP (152.4 ~ 190.8m)
100/01-34-051-04W5/00	ML (231.0 ~ 2060.0m);DIL (231.0 ~ 2060.0m);COLLAR (10.0 ~ 132.0m);ND-LITH (200.0 ~ 1831.0m);CP (1734.0 ~ 1786.0m);CP (1300.0 ~ 1340.0m);CP (585.0 ~ 643.5m);CP (150.0 ~ 189.5m)
100/02-29-051-05W5/00	CS (360.0 ~ 2028.0m);CN-LD (360.0 ~ 2039.0m);DISF (360.0 ~ 2037.3m);TEMPL (10.0 ~ 1153.1m);CB-VD (300.0 ~ 660.0m);GR-CORR (1996.7 ~ 2030.3m);COLLAR (2008.2 ~ 2032.9m);CAS-COL (2008.2 ~ 2032.9m);CS (2041.0 ~ 2120.5m);CN-LD (2041.0 ~ 2115.0m);DISF (2041.0 ~ 2122.0m);CAS-COL (1030.5 ~ 1153.1m)
100/03-12-052-01W5/00	DIL (352.0 ~ 2072.0m);ND-LITH (352.0 ~ 2063.0m);CLOOK (1150.0 ~ 1525.0m);CP (1225.0 ~ 1300.0m);CP (250.0 ~ 302.0m)
100/09-13-052-01W5/00	ES (183.8 ~ 1830.0m)
100/10-05-052-02W5/00	IE (291.4 ~ 2918.8m);ML (291.4 ~ 2919.4m);SONIC (291.4 ~ 2919.4m)
100/04-34-052-03W5/00	ES (183.8 ~ 2103.1m)
100/11-34-052-03W5/00	CNFD (260.0 ~ 1808.5m);DIL (260.0 ~ 1808.5m);CP (375.0 ~ 1500.0m);CP (230.0 ~ 1815.0m)
100/15-23-052-04W5/00	SONIC (347.5 ~ 1945.7m);DIL (347.5 ~ 1954.5m);DIR (361.8 ~ 1930.9m);MS (1450.0 ~ 1508.6m);ND-LITH (347.5 ~ 1954.0m)
100/05-01-052-05W5/00	SONIC (214.6 ~ 2132.4m);DIL (214.6 ~ 2131.2m);DEN (1524.0 ~ 2132.4m);GR (1127.8 ~ 1269.2m)
100/16-18-052-05W5/00	ES (9.1 ~ 2797.1m);ML (670.6 ~ 1691.6m);ML (1630.7 ~ 2773.7m)
100/08-30-052-05W5/00	CS (426.3 ~ 2700.8m);CNFD (1190.0 ~ 1680.0m);DISF (426.3 ~ 2713.8m);DIF-CNS (8.0 ~ 426.5m);CAL (8.0 ~ 426.5m);CS (426.3 ~ 2700.8m);CNFD (1190.0 ~ 1680.0m);DISF (426.3 ~ 2713.8m);CLOOK (1400.0 ~ 1680.0m);CP (1600.0 ~ 2007.0m)
100/04-31-052-05W5/00	ML (462.0 ~ 1946.7m);SONIC (462.0 ~ 1946.0m);NEUT (1400.0 ~ 1700.0m);CNFD (462.0 ~ 1046.6m);DISF (462.0 ~ 1945.5m);CB (1400.0 ~ 1700.0m);PERF (1550.0 ~ 1625.0m);COLLAR (27.0 ~ 70.0m);ML (1946.5 ~ 2088.5m);CS (1946.5 ~ 2088.5m);CNFD (1964.5 ~ 2088.5m);DISF (141.0 ~ 2087.5m)
100/07-11-053-01W5/00	ES (186.8 ~ 1965.4m)
100/04-12-053-02W5/00	ES (184.7 ~ 1981.2m)
100/10-10-053-03W5/00	SONIC (190.5 ~ 1956.5m);DIL (190.5 ~ 1955.3m);ND-LITH (1341.1 ~ 1956.5m)
100/10-14-053-03W5/00	SONIC (196.9 ~ 1871.5m);NEUT (196.9 ~ 1873.3m);LL (196.9 ~ 1873.6m);DEN (196.9 ~ 1873.3m);CP (1554.5 ~ 1697.7m);CP (1249.7 ~ 1310.6m);CP (624.8 ~ 669.3m);CP (91.4 ~ 157.9m)
100/07-33-053-03W5/00	IE (184.1 ~ 1867.8m);ML (640.1 ~ 1768.8m);SONIC (184.1 ~ 1865.4m);FT (1513.6 ~ 1514.9m)
100/13-36-053-03W5/00	SONIC (201.4 ~ 1852.0m);DIL (201.4 ~ 1853.2m);ND-LITH (600.0 ~ 1852.8m);CP (486.2 ~ 500.8m);CP (388.6 ~ 406.0m);CP (342.9 ~ 358.5m);CP (175.3 ~ 191.1m);CP (45.7 ~ 54.6m)
100/13-36-053-05W5/00	ES (187.1 ~ 2067.2m)
100/03-16-043-05W5/00	(SCH, Rm=0.370@190F); ES (184.7 ~ 2073.2m); ML (1280.2 ~ 2072.0m); NEUT (15.2 ~ 3080.3m); ES (2073.2 ~ 3080.3m); ML (2164.1 ~ 3080.3m)
100/11-24-045-08W5/00	(DRA, Rm=0.280@95C); SONIC (456.0 ~ 3150.0m); DIL (456.0 ~ 3150.0m); CI (~ 442.0m); IND-LOG (30.5 ~ 481.6m); ND-LITH (456.0 ~ 3150.0m)
Table Legend	Formation abbreviations

UWI		Wireline Geophysical Logs
Blue	Wells out of WASP study area	List of log abbreviations available in WASP project archives.
Yellow	Wells in Moon Lake play	

APPENDIX 4: DRILL STEM TESTS

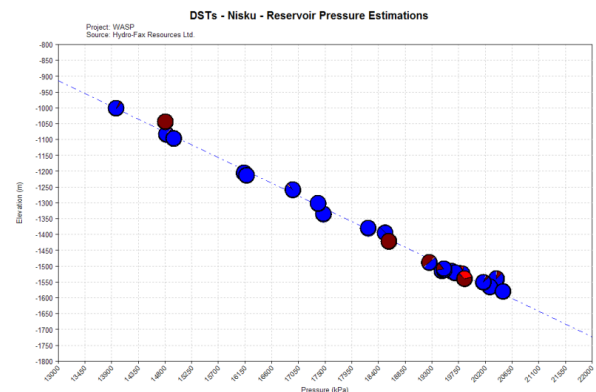
Recorded Measurements

(Source: Hydro-Fax Resources Ltd.)

Well Location	DST #	Test Date	Core?	BH Temp (°C)	BH Temp Source	Salinity (ppm)	Hydrofax Quality Assess.	Hydrofax Rated Perm	Recovery (m)
100/02-21-048-01W5/00	6	02/05/62		74.4	DST	125000	B	High	1136.9
100/04-20-050-02W5/00	4	12/18/58		51.1	DST	125000	D	High	1356.4
100/05-12-046-05W5/00	2	06/15/78	Y	70	Est.	135000	B	Average	128.1
100/06-05-045-04W5/00	4	02/16/75		77.8	DST	200000	A	Really High	951.1
100/07-08-045-04W5/00	3	03/15/76	Y	62.8	DST	200000	A	High	1756
100/10-05-052-02W5/00	3	12/19/67		56.7	DST	135000	A	Excellent	1310.7
100/10-09-046-02W5/00	4	01/17/66		72.2	DST	135000	B	Really High	320
100/10-14-053-03W5/00	4	01/20/76		70	Est.	135000	B	Really High	1355.4
100/10-20-046-05W5/00	6	11/04/78		70	Est.	135000	F	Low	1719
100/10-25-046-02W5/00	3	07/17/66		60	DST	135000	A	High	1498.7
100/10-27-044-03W5/00	7	11/30/77		76.7	DST	150000	B	High	1962.9
100/10-29-048-05W5/00	5	07/16/79		70	Est.	135000	A	High	1300
100/10-33-044-04W5/00	1	04/08/75		70	Est.	200000	A	High	1770.9
100/10-33-044-04W5/00	3	04/11/75		70	Est.	200000	A	Really High	417.6
100/13-36-053-03W5/00	1	07/06/78	Y	42	DST	135000	A	Excellent	1267
100/14-21-045-02W5/00	2	08/19/60		82.2	DST	135000	B	High	1585
100/14-21-045-02W5/00	3	08/28/60		70	DST	135000	D	High	521.2
100/14-29-046-05W5/00	2	06/27/93		95	DST	135000	F	Low	114
100/15-35-044-02W5/00	2	02/03/88		71.3	DST	135000	C	Average	367
102/14-12-048-06W5/00	3	04/05/89		77.7	DST	135000	A	Excellent	1690
102/16-06-045-04W5/00	1	07/27/75		80.6	DST	200000	A	Really High	541.6
102/16-06-045-04W5/00	3	08/09/75		87.8	DST	200000	A	Really High	823

Hydrofax Ratings

Code	Quality Status	Permeability
A	Very good test	High to Excellent
B	Good test	Average to Relatively High
C	Fair test	Relatively Low to Average
D	OK test	Relatively Poor
E	Poor	Tight
F	Very poor test	Very Low to Low
G	Recovery data only	No reliable data



WASP Project DST Analysis

Well Location	k (mD)	kh (mD.m)	s*	p* (kPa)	m (kPa/cycle)	Quality Assess.	Reason	Form.	Interval (m KB)	
100/02-21-048-01W5/00	39.201	203.84	-4.696	14908		Poor	Stair-stepping	Dnisku	1878.5	1883.7
100/04-20-050-02W5/00	10.041	1.53E+02	-4.524	15054		Poor		Dnisku	1854.7	1869.9
100/05-12-046-05W5/00	0.011	0.33	-0.247	19094		Mediocre		Dnisku	2383.5	2414
100/06-05-045-04W5/00	1.078	16.39	-0.822	19798	6086.87	Poor	PPD erratic	Dnisku	2519.5	2534.7
100/07-08-045-04W5/00	19.264	292.82	-4.286	19661		Poor	Stair-stepping	Dnisku	2507	2522.2
100/10-05-052-02W5/00	N/A	N/A	N/A	14054		Poor	No resolution	Dnisku	1740.4	1758.7
100/10-09-046-02W5/00	9.335	98.96	30.925	16883	411.42	Mediocre	Pressure Low	Dnisku	2220.5	2231.1
100/10-14-053-03W5/00	0.671	3.09	-3.957	15329		Mediocre	Pressure Low	Dnisku	1780	1784.6
100/10-20-046-05W5/00	3.45	68.99	-3.485	20208		Poor	PPD erratic	Dnisku	2460	2480
100/10-25-046-02W5/00	N/A	N/A	N/A	N/A		Poor	No resolution	Dnisku	2121.4	2129
100/10-27-044-03W5/00	1.122	34.57	-3.337	18487		Poor	PPD erratic	Dnisku	2339.6	2370.4
100/10-29-048-05W5/00	N/A	N/A	N/A	18337		Poor	No resolution	Dnisku	2215.9	2236
100/10-33-044-04W5/00	2.818	68.47	-3.379	19676		Poor	Too Few Points	Dnisku	2511.6	2535.9
100/10-33-044-04W5/00	0.349		-2.108	21646		Poor	Low resolution	Dnisku	2510.6	2514.3
100/13-36-053-03W5/00	14.107	98.75	-5.334	14086		Poor	Stair-stepping / Low Pressure	Dnisku	1759	1766
100/14-21-045-02W5/00	74.125	719.01	-4.96	17559		Poor	Poor resolution	Dnisku	2246.4	2256.1
100/14-21-045-02W5/00	0.328	5.81	0.391	17335		Poor	Poor resolution	Dnisku	2216.2	2233.9
100/14-29-046-05W5/00	0.003	0.03	-0.645	7282		Poor	Pressure Low / Temp High	Dnisku	2470	2480
100/15-35-044-02W5/00	0.011	0.39	-1.037	17111		Mediocre		Dnisku	2185	2219
102/14-12-048-06W5/00	N/A	N/A	N/A	18972		Poor	No resolution	Dnisku	2300	2335
102/16-06-045-04W5/00	0.865	15.83	-1.456	19896		Interm.	2nd slope used for p*	Dnisku	2525.3	2543.6
102/16-06-045-04W5/00	0.89	13.08	-1.304	19702		Poor	Low resolution	Dnisku	2522.5	2537.2

Notes

1. Quality assessment based on number and distribution of recorded values for estimation of reservoir pressure and permeability using Horner plot analysis method.
2. DST data available in WASP project archives.

APPENDIX 5: FORMATION WATER RESISTIVITY

UWI	Resistivity	Resistivity Temp	Rw @ 70 °C	log Rw	Well Name
100/02-28-048-02W5/00	0.1	25	0.0508	-1.2940	TEXACO SOCONY WARBURG A-2-28
100/02-28-048-02W5/00	0.1	25	0.0508	-1.2940	TEXACO SOCONY WARBURG A-2-28
100/04-20-050-02W5/00	0.07	25	0.0356	-1.4489	TEXACO TELFORDVILLE 4-20-50-2
100/05-20-050-02W5/00	0.09	72	0.0920	-1.0364	MIDWEST TELFORDVILLE 5-20-50-2
100/05-20-050-02W5/00	0.06	72	0.0613	-1.2125	MIDWEST TELFORDVILLE 5-20-50-2
100/10-05-052-02W5/00	0.08	20	0.0363	-1.4403	HOME CPOG BRIGHTBANK 10-5-52-2
100/10-14-053-03W5/00	0.07	25	0.0356	-1.4489	AMOCO B-2 WABAMUN LAKE 10-14-53-3
100/07-33-053-03W5/00	0.08	20	0.0363	-1.4403	M.W. GAS WABAMUN 7-33-53-3
100/07-33-053-03W5/00	0.08	20	0.0363	-1.4403	M.W. GAS WABAMUN 7-33-53-3
100/13-36-053-03W5/00	0.06	25	0.0305	-1.5158	HOME ALBERTA BEACH 13-36-53-3
1F1/11-29-045-02W5/00	0.056	25	0.0285	-1.5458	KETCH RES WROSES 11-29-45-2
		Median =	0.0363	-1.4403	
		Average =	0.0449	-1.3743	

UWI	Date Sampled	Depth Interval (m)		Na	Ca	Mg	Cl	Bicarb	Sulfate	TDS (calc)
100/02-28-048-02W5/00	01/05/1955	1956.8	2026.9	45309	11089		88830	500	500	146228
100/02-28-048-02W5/00	01/04/1955	1956.8	1964.1	27378	8332		56272	550	500	93032
100/04-20-050-02W5/00	12/18/1958	1854.7	1870.0		16930		118419	317	377	
100/05-20-050-02W5/00	10/10/1965	1847.4	1853.5	24953	3376	1152	46581	1037	840	77939
100/05-20-050-02W5/00	10/02/1965	1847.4	1853.5	44047	9688	1934	89689	813	720	146891
100/10-05-052-02W5/00	12/29/1967	1740.4	1758.7	47218	10250	2255	96600	600	785	157708
100/10-14-053-03W5/00	01/20/1976	1780.0	1784.6	46138	11340	1417	95014	513	24	154446
100/07-33-053-03W5/00	10/17/1961	1581.6	1589.5	43493	7928	2168	86850	366	487	141292
100/07-33-053-03W5/00	10/22/1961	1746.5	1751.1	41102	8834	2168	83955	497	1481	138037
100/13-36-053-03W5/00	07/05/1978	1759.0	1766.0	45018	10890	2193	94200	361	942	153604

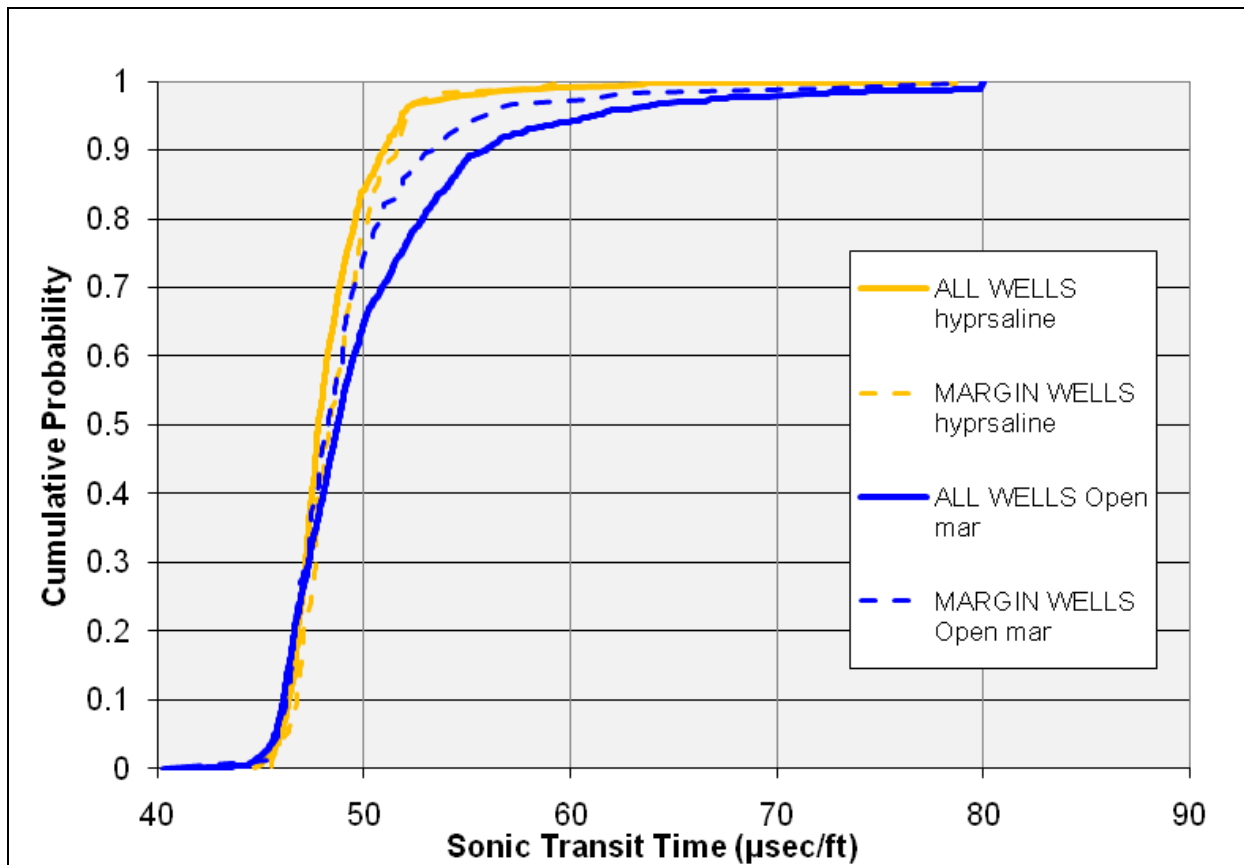
Source: GeoFluids database at IHS Energy and well-file information for 1F1/11-29-045-02W5/00. For more complete water chemistry information, see the geochemistry portion of the full report.

APPENDIX 6: POROSITY AND PERMEABILITY (INBOARD PLATFORM MARGIN)

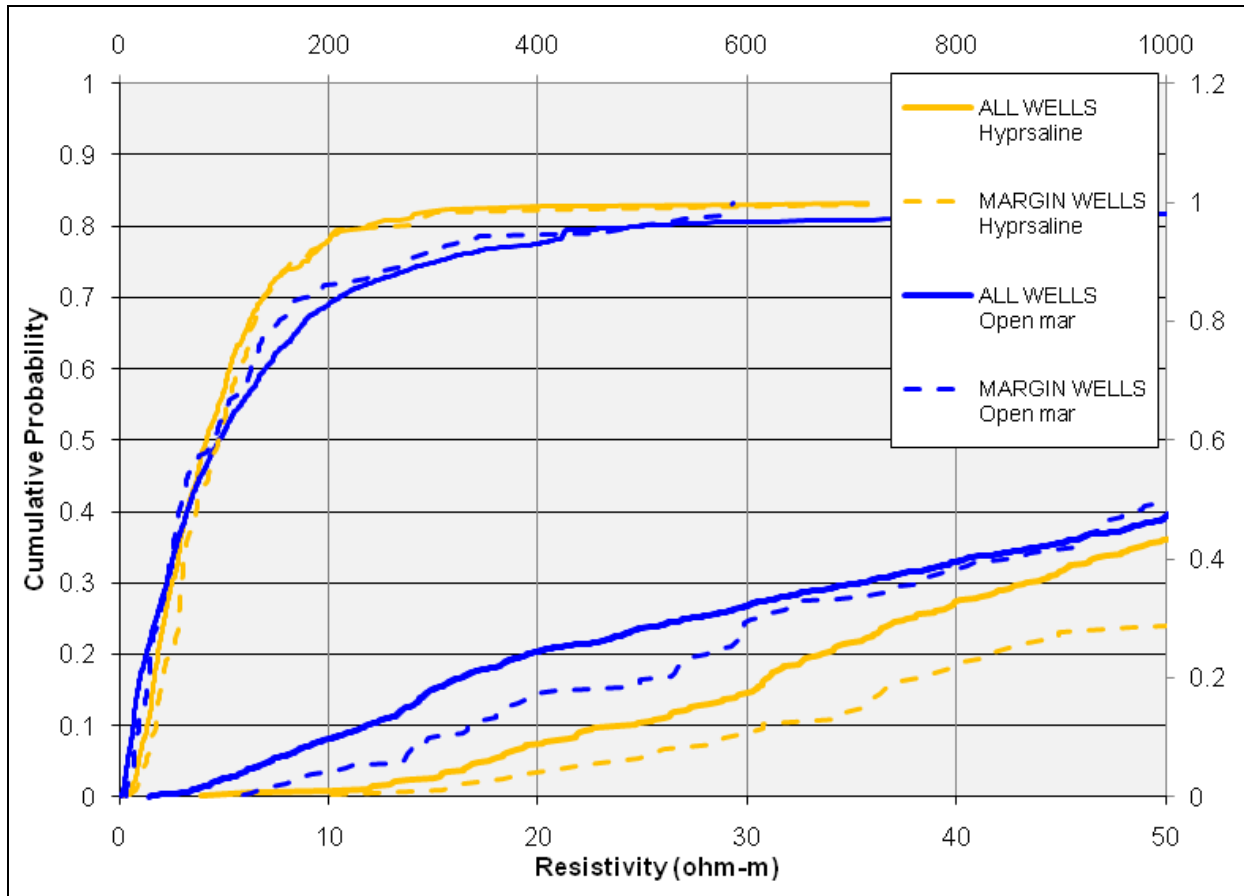
Based on a conceptual understanding of the depositional setting for Nisku carbonates within the WASP study boundary (Figure 1 in text) and direct evidence (core observations) outside the study area, it is thought that the inboard margin of the upper Nisku should include zones of enhanced porosity and permeability. The inboard edge marks the eastern boundary of marine-based deposition for the Nisku and is a transitional zone into evaporate/hypersaline facies of the Nisku abundant to the southeast of the study area (Figure 1). More intense wave action and generally energetic conditions favourable for reef growth were thought to have been present during the upper Devonian along this inboard edge (Figure 1 and Figure 3 in text for reference). As there are limited direct observations via core, the next best option is an analysis of existing wireline data specifically comparing wells that are thought to be located along this edge versus wells which are well away from this edge.

Our assessment of the sonic data (see graph below) suggests:

The sonic transit times along the inboard edge are NOT necessarily better for targeting enhanced porosity zones in the open marine facies relative to the entire population of wells. For the hypersaline facies location is irrelevant to log response.



For resistivity log data the interpretation is the same (see plot below; upper set of curves uses the top and right axes; lower set of curves uses lower and left axes).





UNIVERSITY OF
CALGARY

Energy &
Environmental
Systems

EES

iseee



Energy and Environmental Systems Group

Institute for Sustainable Energy, Environment and Economy (ISEEE)

Geochemistry

Wabamun Area CO₂ Sequestration Project (WASP)

Authors

Maurice Shevalier

Michael Nightingale

Bernhard Mayer

Rev.	Date	Description	Prepared by
1	January 4, 2010	Geochemical Analysis of WASP Study Area	Dr. Bernhard Mayer

Table of Contents

INTRODUCTION.....	5
DISCUSSION	6
1. Baseline Geochemistry of Nisku Fluids and Gases: Chemical and Isotopic Composition.....	6
1.1 Data Sources	6
1.2 Regional Baseline Geochemistry.....	12
1.2.1 Chemical Composition	12
1.2.2 Isotopic Composition.....	18
1.3 Geochemistry of Fluids and Gases from the Water Source Well	21
2. MINERALOGY.....	22
2.1 Sample Selection and Methods	22
2.2 Bulk Chemical Composition	23
2.3 Microscopy	24
2.4 Quantitative Mineralogy	30
3. GEOCHEMICAL MODELLING.....	30
3.1 SOLMINEQ88	30
3.2 H ₂ S Saturation Modelling	31
3.3 ToughReact Modelling	32
3.3.1 Problem Setup	32
3.3.2 Results	35
3.3.3 Key Findings and Implications	41
4. SUMMARY	43
REFERENCES.....	44

List of Tables

Table 1: pH, total dissolved solids, and major ion concentrations for fluids in the Nisku Formation obtained from the ERCB data base.	9
Table 2: Isotopic composition of water, sulfate, dissolved sulfide, and dissolved inorganic carbon in samples from the Nisku Formation surrounding the WASP study area; data from [5].	10
Table 3: Water and gas compositional data for samples from well 100/11-29-045-02W5. Data provided by Conoco-Phillips.....	11
Table 4: Gas composition, water chemistry and isotopic composition of water, dissolved constituents and gases of samples obtained from well 100/11-29-045-02W5 in summer 2008.	11
Table 5: Bulk Chemical Composition of Individual Core Samples (Ni = Nisku, C = Calmar).	23
Table 6: Carbon isotope ratios of Nisku carbonates.	23
Table 7: Average Composition of Nisku Formation Calcite (wt%).	25
Table 8: Average Composition of Nisku Formation Dolomite (wt%).	26
Table 9: Quantitative Mineral Composition (wt%).....	30
Table 10: Saturation Indices for common minerals found in the Nisku formation, the Calmar caprock and the Ireton bottom-rock.	31
Table 11: Hydrogeological parameters for the Nisku carbonate formation.	33
Table 12: Initial mineral volume fractions and possible secondary minerals used in the ToughReact simulations.	34
Table 13: Initial total dissolved chemical species concentrations used in the ToughReact simulations.	34
Table 14: Parameters for calculating kinetic rate constants of minerals used in the simulations [20].....	35
Table 15: Injection time of CO ₂ and radius of dehydrated region for both H ₂ S and non-H ₂ S aquifers.....	41
Table 16: Injection time of CO ₂ and amount of CO ₂ stored as HCO ₃ in the reservoir waters for both H ₂ S and non-H ₂ S aquifers.....	41

List of Figures

Figure 1: Study area of the WASP project located in central Alberta.....	7
Figure 2a: WASP contour plots of total dissolved solids (TDS).....	12
Figure 2b: WASP contour plots of pH values.	13
Figure 3a: WASP contour plots of sodium concentrations.	14
Figure 3b: WASP contour plots of chloride concentrations.	15
Figure 4a: WASP contour plots showing calcium concentrations.	16
Figure 4b: WASP contour plots showing HCO ₃ concentrations.	17
Figure 5a: Contour plots showing $\delta^{13}\text{C-HCO}_3$ values for Nisku fluids sampled in the vicinity of the WASP study area.....	18
Figure 5b: Contour plots showing $\delta^{34}\text{S-SO}_4$ values for Nisku fluids sampled in the vicinity of the WASP study area.....	19
Figure 6: Contour plot of $\delta^{34}\text{S-S}^{2-}$ values obtained from [5].	20
Figure 7: Gas concentration versus sampling date for four gases from well 100/11-29-045-02W5.	21
Figure 8: Photomicrograph of the Calmar Formation.	24
Figure 9: Photomicrograph of the Nisku Formation (Sample W12).....	25
Figure 10: Photomicrograph of Zoned Dolomites (Sample W2).....	26
Figure 11: Photomicrograph of Nisku Open Marine Facies (Sample W6).	27
Figure 12: Photomicrograph of Nisku Hyper-Saline Facies (Sample W7).	27
Figure 13: Photomicrograph of Nisku Sample W3.	28
Figure 14: Photomicrograph of Nisku Anhydrite (Sample W4).....	29
Figure 15: pH of aquifer as a function of radial distance after initiation of CO ₂ injection for both non-H ₂ S and H ₂ S aquifers.	36
Figure 16: HCO ₃ concentration as a function of radial distance after initiation of CO ₂ injection for both non-H ₂ S and H ₂ S aquifers.....	36
Figure 17: Ca concentration as a function of radial distance after initiation of CO ₂ injection for both non-H ₂ S and H ₂ S aquifers.	37
Figure 18: Mg concentration as a function of radial distance after initiation of CO ₂ injection for both non-H ₂ S and H ₂ S aquifers.	37
Figure 19: Dolomite mineral abundance as a function of radial distance after initiation of CO ₂ injection for both non-H ₂ S and H ₂ S aquifers.	38
Figure 20: Calcite mineral abundance as a function of radial distance after initiation of CO ₂ injection for both non-H ₂ S and H ₂ S aquifers.	38
Figure 21: Change in volume fraction of magnesite as a function of radial distance after initiation of CO ₂ injection for both non-H ₂ S and H ₂ S aquifers.	39
Figure 22: Amount of CO ₂ sequestered in the reservoir in all mineral forms as a function of radial distance after initiation of CO ₂ injection for both non-H ₂ S and H ₂ S aquifers.....	40
Figure 23: Changes in the porosity of the reservoir as a function of radial distance after initiation of CO ₂ injection for both non-H ₂ S and H ₂ S aquifers.	40

INTRODUCTION

Carbon capture and storage (CCS) is a promising approach for reducing anthropogenic CO₂ emissions to the atmosphere as a means of mitigating future impacts of human-induced climate change [1]. Successful CCS projects should demonstrate that the injected CO₂ is safely and securely sequestered in the chosen reservoir. It is not only important to demonstrate that CO₂ has been stored, but also desirable to evaluate how much CO₂ is sequestered in soluble, ionic or mineral form. Geochemical monitoring programs are an excellent tool for tracing the movement and the fate of the injected CO₂ in the reservoir and to assess the nature and effectiveness of the storage mechanisms [e.g., 2].

The injected CO₂ first dissolves in the water to become an aqueous species, i.e., CO_{2(aq)}. Once in this form the CO_{2(aq)} can undergo a number of reactions with the fluids and minerals present in the reservoir. These include:

1. reaction with the formation water [3];
2. reaction with carbonate minerals present in the reservoir [3];
3. reaction with carbonate and silicate minerals present in the reservoir [4].

In the first reaction, CO_{2(aq)} will react with water as follows [3]:



This trapping of CO_{2(aq)}, **solubility trapping**, will result in changes of geochemical parameters that can be monitored, i.e., there will be a decrease in the pH of the water due to the disassociation of H₂CO₃ and changes in the isotopic composition of the HCO₃⁻ dependant on the isotopic composition of the injected CO₂.

In the second reaction, the carbonic acid reacts with carbonate minerals that may be present in the reservoir as shown below [3]:



The net reaction is as follows:



In this reaction sequence a carbonate mineral, such as calcite, reacts with the carbonic acid, which is formed by the dissolution of CO_{2(aq)} in water resulting in the formation of two moles of HCO₃⁻ for each mole of CO_{2(aq)}. This is known as **ionic trapping** and is a very stable and secure form of storage since the CO_{2(aq)} is now in trapped as a dissolved species in solution. This reaction results in an increase in the concentrations of Ca²⁺ and HCO₃⁻, which can be monitored geochemically. Further, there will be changes in the carbon isotope ratio of HCO₃⁻. These changes will be governed not only by the isotopic composition of the injected CO₂ but also by the isotopic composition of the carbonate minerals.

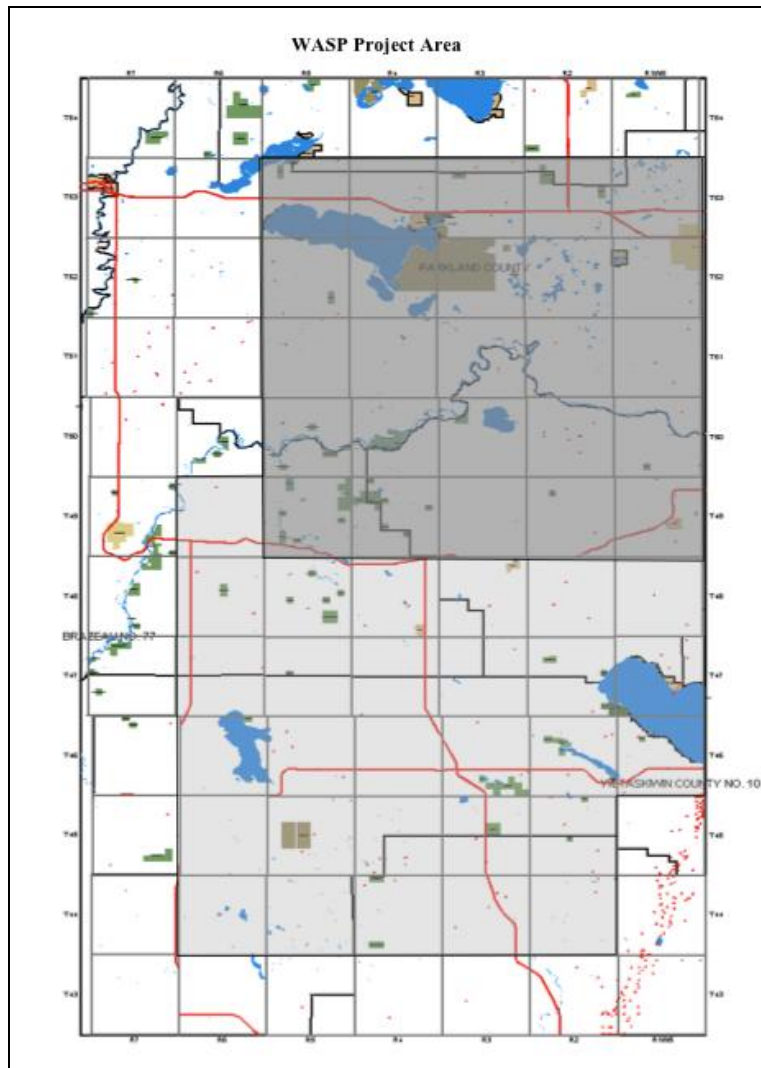


Figure 1: Study area of the WASP project located in central Alberta.

The chemical data available for the Nisku formation waters from the ERCB data base are subject to a number of potential inaccuracies and inaccurate analyses must be identified and removed [6]. Contamination associated with drilling, completion and production methods, incorrect sampled intervals, multiple tested intervals, data entry errors, and multiple entries are the most common forms of error. The following culling methods are modified from those described by Bachu et al. [6]. Data entries with analyses missing any of the major ions Na, Cl, Ca and alkalinity, were ignored, as well as those collected from production locations down-stream of the separators (facilities where water-oil or water-gas mixtures are separated). Waters with densities less than 1, pH less than 4 or greater than 10, and those with lab analysis dates more than 1 month after sample collection dates were also culled. Data entry errors were identified by calculating charge balances, with imbalances of greater than 5% being culled. Contamination by drilling mud, acid washes or washes from cement jobs were determined by cross-plotting the various cations and anions and by reviewing the recovery descriptions. Duplicate analyses, and analyses from larger test intervals, multiple intervals, and incorrect intervals were removed by scrutinizing the individual well samples.

The remaining geochemical analyses were used to map the distribution of water chemistry that is considered to be representative of the Nisku aquifer. There were 40 wells in the ERCB data base within the WASP study area that had pH values and major ion geochemistry for the reservoir fluids that were considered representative for the Nisku formation. Table 1 summarizes the available chemical parameters for Nisku fluids from these 40 wells.

The ERCB data base does not contain any data on the isotopic composition of reservoir fluids. The Ph.D. thesis of Graham Simpson [5] completed at the University of Calgary in 1999 summarizes information on the isotopic composition of fluids and dissolved constituents in the Nisku Formation. None of the samples described in [5] were obtained from within the WASP study area. However, since this thesis contains the only known source of high quality isotopic data from the Nisku formation it was viewed as important to review the isotopic composition of Nisku fluids in the surroundings of the WASP study area. A total of 33 wells from the thesis were used in this study. Table 2 lists the wells and summarizes the isotopic composition of water ($\delta^2\text{H}$, $\delta^{18}\text{O}$), sulfate ($\delta^{34}\text{S-SO}_4$), sulfide ($\delta^{34}\text{S-S}^{2-}$) and dissolved inorganic carbon ($\delta^{13}\text{C-HCO}_3$).

Table 1: pH, total dissolved solids, and major ion concentrations for fluids in the Nisku Formation obtained from the ERCB data base.

Location	pH	Sodium (mg/L)	Calcium (mg/L)	Magnesium (mg/L)	Chloride (mg/L)	Bicarbonate (mg/L)	Sulfate (mg/L)	TDS Calculated (mg/L)
10-08-044-01W5	7.6	38538	7581	1314	75164	130	1969	124696
07-31-044-04W5	6.8	43976	16657	1798	101250	732	1187	165600
07-31-044-04W5	7.3	48254	16235	1712	106832	254	1141	208610
10-33-044-04W5	6.5	57592	17778	1968	124750	771	1132	203991
10-33-044-04W5	6.5	53936	17017	2065	118625	762	355	192760
15-11-045-01W5	7.5	57064	12835	2114	116232	110	765	189120
05-23-045-01W5	7.4	36701	7384	1025	70430	595	2530	118665
11-24-045-01W5	7.9	56694	11956	2313	114724	180	708	186575
11-24-045-01W5	6.5	55704	12852	3206	117242	465	678	190147
14-21-045-02W5	7.1	38983	10699	1452	82000	255	1560	134949
06-05-045-04W5	6.6	52281	14695	1968	110705	880	1585	182114
16-06-045-04W5	6.6	54368	16536	2248	118400	844	1068	193464
16-06-045-04W5	7.7	42505	12472	2770	93000	1050	2848	154645
16-06-045-04W5	6.6	42712	12412	1409	88900	1296	3124	149853
16-06-045-04W5	6.1	55032	19499	2649	126250	759	574	204763
07-08-045-04W5	7.3	61617	17257	2479	132400	602	80	214435
04-22-045-05W5	7.4	8080	2030	344	14233	1510	2642	28839
04-22-045-05W5	6	56860	19092	2910	129250	702	430	209244
10-36-045-05W5	7.4	57397	17448	1723	122823	458	1214	201963
10-25-046-02W5	7.3	49136	14104	1461	103574	532	1188	170476
16-12-046-03W5		57800	15030	200	115060	940	940	190270
05-12-046-05W5	8.2	27504	7399	1061	55200	522	4214	95900
06-19-046-05W5	6.8	43121	16720	2772	102000	330	2701	167644
04-36-047-03W5	7.4	21647	7339	1005	48833	115	535	79474
02-06-047-04W5	9.2	44155	14832	1876	98011	166	1451	161012
02-28-048-02W5	6.6	27378	8332		56272	550	500	93032
02-28-048-02W5	7.3	45309	11089		88830	500	500	146228
14-12-048-06W5	6.2	43600	11430	2768	102000	498	634	163383
15-11-049-02W5	7.2	42000	8610	870	81500	456	1021	134457
15-11-049-02W5	6.7	35400	8260	708	70300	525	808	116001
15-11-049-02W5	7.2	42000	8610	870	81500	456	1021	134457
02-29-051-05W5	6.2	39000	7940	1580	84700	717	604	136453
09-13-052-01W5	7.4	36645	8534	1873	76247	216	948	124463
10-05-052-02W5	5.9	47218	10250	2255	96600	600	785	157708
10-14-053-03W5	6.2	46138	11340	1417	95014	513	24	154446
07-33-053-03W5	6.7	43493	7928	2168	86850	366	487	141292
07-33-053-03W5	6.8	41102	8834	2168	83955	497	1481	138037
13-36-053-03W5	7.5	45018	10890	2193	94200	361	942	153604

Table 2: Isotopic composition of water, sulfate, dissolved sulfide, and dissolved inorganic carbon in samples from the Nisku Formation surrounding the WASP study area; data from [5].

Location	$\delta^{18}\text{O}$ in H_2O (‰)	$\delta^2\text{H}$ in H_2O (‰)	$\delta^{34}\text{S}$ in SO_4 (‰)	$\delta^{34}\text{S}$ in S^{2-} (‰)	$\delta^{13}\text{C}$ in HCO_3 (‰)
15-6-40-23W4	7.8	-55	21.9	16.4	-7.1
10-31-39-23W4	6.5	-52	21.6	20.2	-2.7
12-9-41-23W4	8.2	-43	23.0	19.5	-10.1
13-9-41-23W4	7.5	-49	22.5	19.1	-9.0
8-35-48-12W5	-13.6	-133	22.9		0.9
5-1-40-24W4	3.3	-65	22.9	15.3	-4.3
14-32-13-16W4	-8.8	-88	25.0	16.1	-2.9
14-19-15-16W4	-9.6	-93	24.7	12.5	-8.3
16-4-14-16W4	-9.3	-99	27.7	23.5	-2.4
7-10-56-24W4	-3.9	-81	45.4	18.7	-6.0
16-10-56-24W4	-4.8	-80	48.5	20.4	
16-3-56-24W4	-4.7	-78	47.9	19.4	-6.8
4-10-56-24W4	-4.0	-72	45.9	20.7	-6.9
4-21-57-24W4	-5.1	-84	46.0	15.7	-6.4
2-23-36-20W4	-4.4	-75	24.2	14.7	
11-23-35-20W4	-4.4	-83	23.6	13.2	-7.0
13-3-35-20W4	-4.1	-76	22.5	14.5	-7.5
2-27-37-20W4	-3.5	-71	23.6	13.4	-3.9
9-11-36-20W4	-3.9	-79	25.8		-4.8
16-16-41-2W5	5.1	-48	22.5	16.0	-2.1
10-15-38-24W4	7.6	-50	21.2	18.4	-5.1
12-23-38-24W4	6.0	-54	21.1	16.4	-9.7
3-14-38-24W4	8.1	-54	21.5	19.9	-3.4
10-14-38-24W4	9.3	-53	24.0	18.6	-5.0
7-5-31-27W4	8.8	-49	25.8	17.5	-4.3
5-32-36-21W4	2.5		22.6		-9.6
10-15-29-11W4	1.5	-65	23.5	18.4	-9.2
6-11-29-24W4	0.9	-66	23.3	16.4	
10-14-29-24W4	7.2	-46	22.7	15.0	-15.9
6-9-34-26W4	0.9		24.7	24.8	-12.1
14-27-33-26W4	1.3		27.2	27.4	-13.2
12-11-49-12W5	-13.9	-129	22.7		0.5
4-21-42-23W4	6.6	-56	24.6	15.3	-7.7

Another source of data was from water and gas samples collected from the only known water well completed in the Nisku formation in the study area in 2003 and 2004 (well 100/11-29-045-02W5). These samples were collected when the well first went into production and compositional data were determined by commercial laboratories. The chemical compositions of gases and fluids are summarized in Table 3.

Table 3: Water and gas compositional data for samples from well 100/11-29-045-02W5. Data provided by Conoco-Phillips.

Description	03/01/25	03/01/27	03/06/03	03/08/29	04/12/13	08/06/19	08/09/10
CO ₂ (mole %)	0.09	0.05	4.41	5.89	3.07	5.00	
H ₂ S (mole %)	0.60	0.60	29.23	49.26	8.80	36.01	
N ₂ (mole %)	97.08	97.46	2.57	1.51	3.92	1.31	
CH ₄ (mole %)	0.36	0.24	61.44	41.26	79.89	55.32	
Ethane (mole %)	0.34	0.15	1.69	1.26	2.66	1.66	
Propane (mole %)	0.69	0.29	0.23	0.25	0.47	0.37	
pH	6.90		6.70				7.10
Na (mg/L)	51230		53450				55150
K (mg/L)	3370		3450				3720
Ca (mg/L)	15290		15290				15430
Mg (mg/L)	2550		2160				2130
Sr (mg/L)	671		705				884
Cl (mg/L)	122707		123068				117743
HCO ₃ (mg/L)	576		479				315
SO ₄ (mg/L)	390		387				577
H ₂ S (aq) (mg/L)	560		660				177
TDS (mg/L)	197344		199649				196004

In June and September 2008, additional fluid and gas samples were collected from the source water well (100/11-29-045-02W5). The gas composition, water chemistry and isotopic composition of water, dissolved constituents and gases were determined at the University of Calgary and results are summarized in Table 4.

Table 4: Gas composition, water chemistry and isotopic composition of water, dissolved constituents and gases of samples obtained from well 100/11-29-045-02W5 in summer 2008.

Description	Value	Description	Value
pH	6.43	S ²⁻ (mg/L)	171
Total Alkalinity (mg/L)	577	Total Dissolved Solids (mg/L)	197074
Na (mg/L)	55150	Electrical Conductivity (mS/cm)	129
Ca (mg/L)	15430	δ ³⁴ S in SO ₄ (‰)	22.9
K (mg/L)	3720	δ ³⁴ S in S ²⁻ (‰)	16.1
Mg (mg/L)	2129	δ ¹³ C in HCO ₃ (‰)	-8.2
Sr (mg/L)	884	CH ₄ (mole %)	55.32
Mn (mg/L)	0.51	CO ₂ (mole %)	5.00
Si (mg/L)	12.0	H ₂ S (mole %)	36.01
Cl (mg/L)	117743	δ ¹³ C in CO ₂ (‰)	-7.0
SO ₄ (mg/L)	470	δ ³⁴ S in H ₂ S (‰)	16.1

1.2 Regional Baseline Geochemistry

The data summarized in Tables 1 and 2 were plotted and contoured over the WASP area (Figures 2–7). The black dots on the maps represent the locations of the wells for which data were available. The large red dot shows the location of the water source well (100/11-29-045-02W5). Data for fluids and gases from this well were not used for contouring.

1.2.1 Chemical Composition

Figure 2 shows the maps for total dissolved solids (TDS) and pH. The TDS map indicates high TDS values in the Nisku formation varying from less than 125,000 mg/L to more than 200,000 mg/L. There is a NE-SW gradient across the study area with high TDS values in the SW exceeding 200,000 mg/L and TDS values decreasing below 125,000 mg/L towards the NE. Fluids from the water source well had constant TDS values between 196,000 and 200,000 mg/L between 2003 and 2008 (Tables 3 and 4).

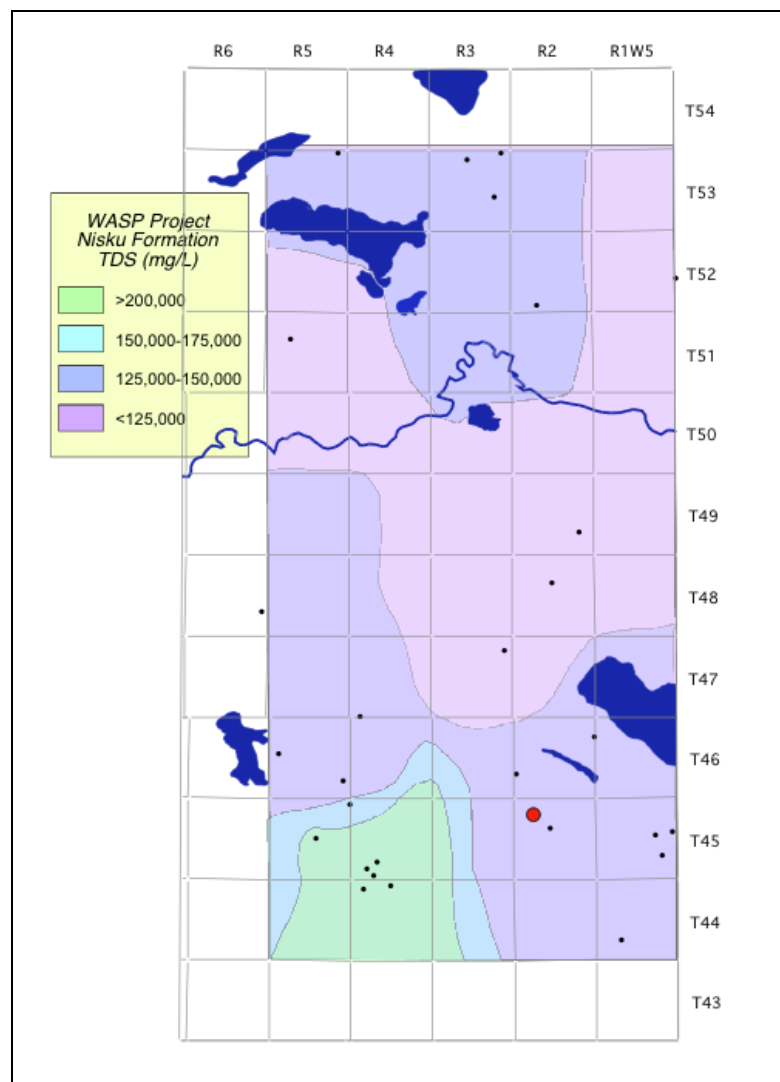


Figure 2a: WASP contour plots of total dissolved solids (TDS).

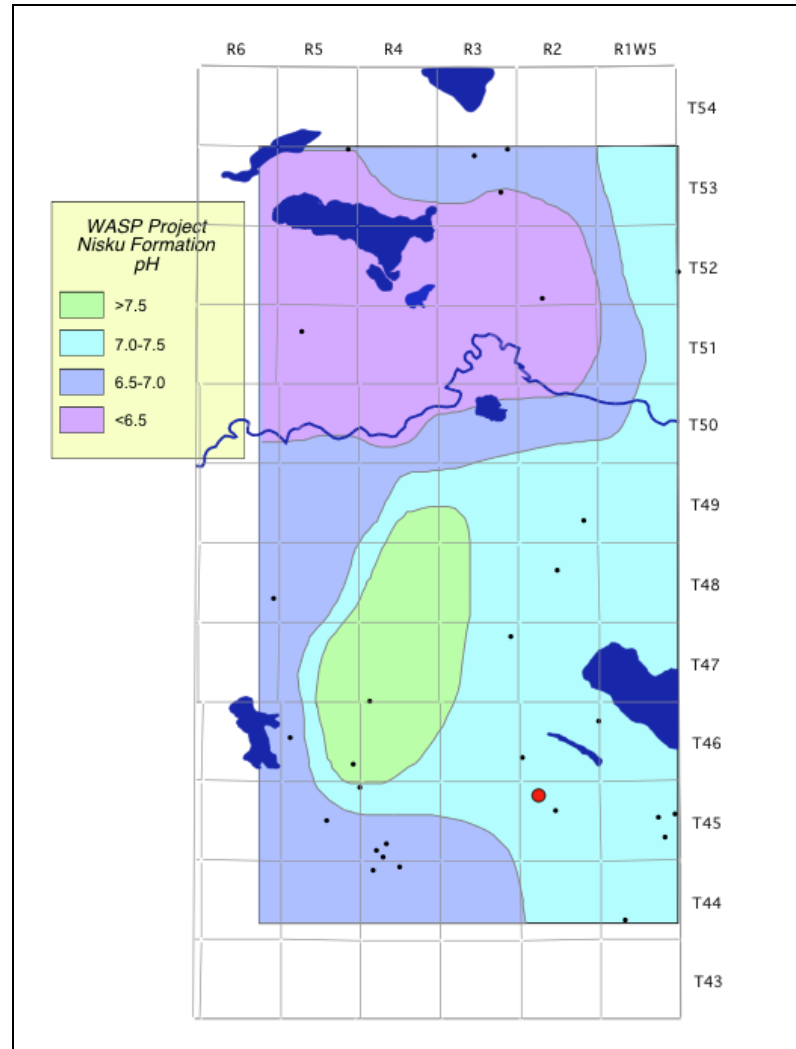


Figure 2b: WASP contour plots of pH values.

The pH map shows near neutral pH values across the study area (Figure 2) consistent with the measured pH value of 6.4 for fluids from the water source well (Table 4). The measured pH may be slightly biased towards higher values if samples were not preserved for dissolved sulphide, a very reactive species. When $H_2S_{(gas)}$ degasses from the sample the pH will increase towards a neutral value.

The fluid samples are Na-Cl brines and Figure 3 shows contour maps for sodium and chloride concentrations. Both of these maps show the same NE-SW concentration gradient as the TDS map. Na concentrations range from more than 55,000 mg/L in the SW to less than 50,000 mg/L in the central and northern part of the study area and Cl concentrations vary from more than 120,000 mg/L in the SW to less than 100,000 mg/L elsewhere. Fluids from the water source well had sodium concentrations between 51,000 and 55,000 mg/L and chloride concentrations between 118,000 and 123,000 mg/L (Table 3).

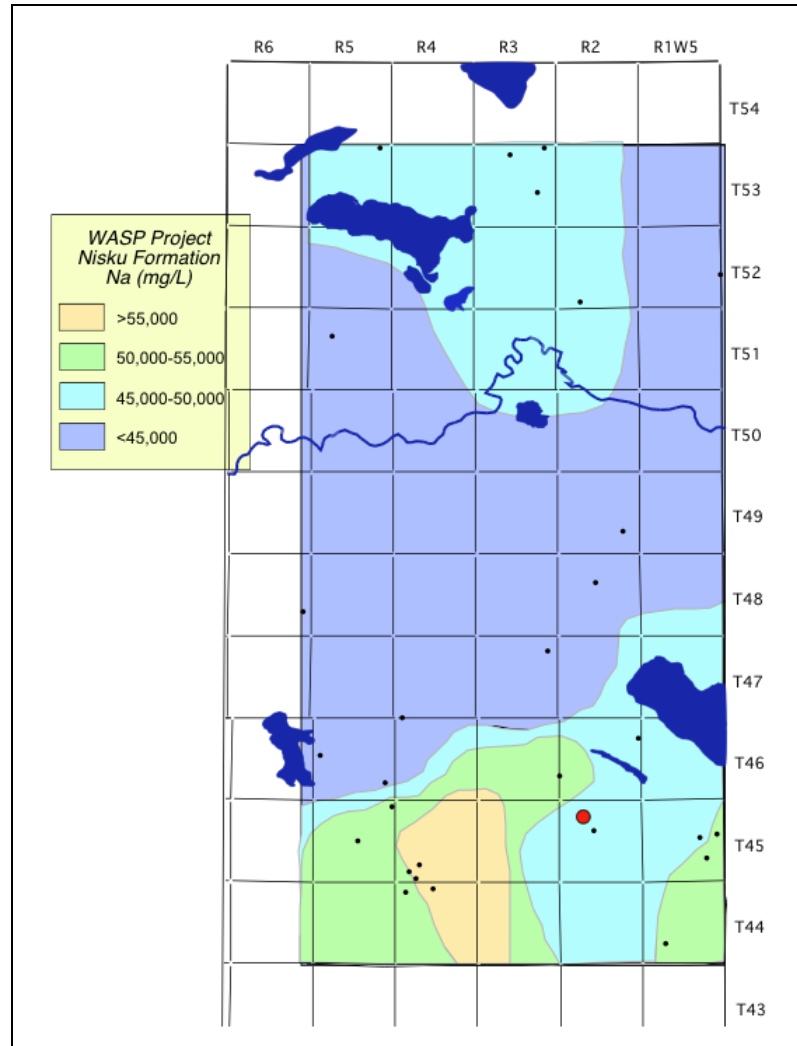


Figure 3a: WASP contour plots of sodium concentrations.

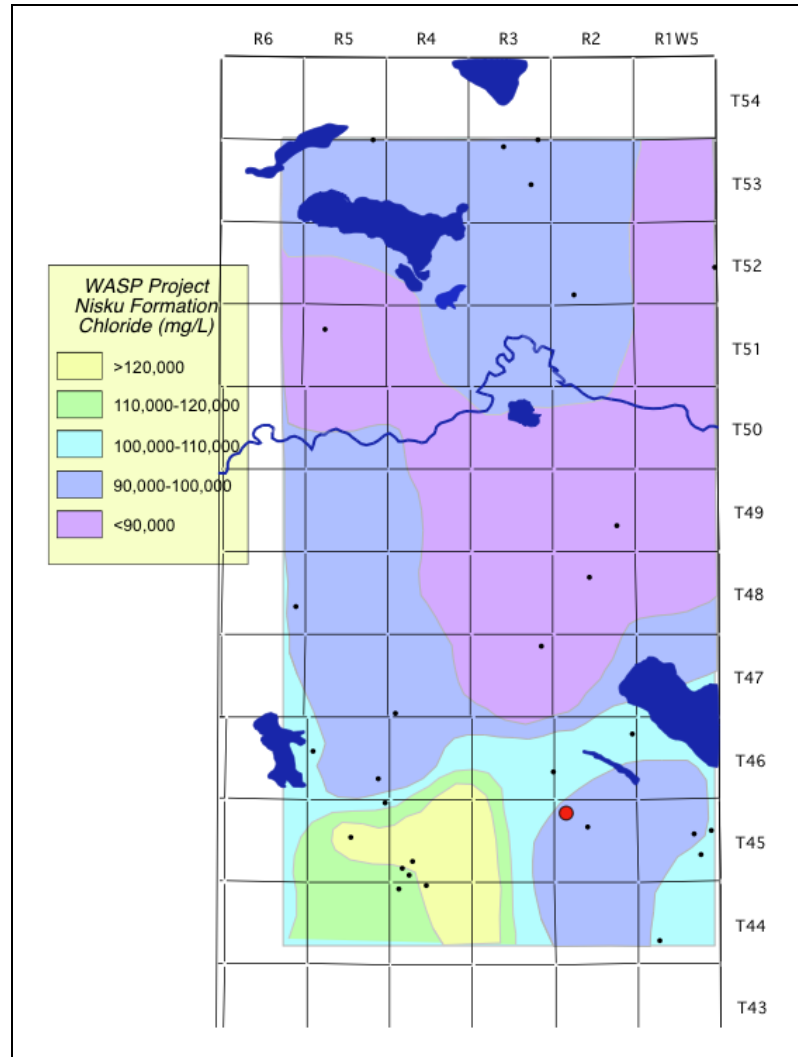


Figure 3b: WASP contour plots of chloride concentrations.

Figure 4 summarizes calcium and bicarbonate concentrations for the WASP study area. Ca concentrations vary from more than 15,000 mg/L in the SW to less than 12,500 in the central and northern part of the study area. Bicarbonate (HCO_3^-) concentrations are low throughout the study area not exceeding 1,000 mg/L. Fluids from the water source well have calcium and bicarbonate concentrations of 15,430 and 577 mg/L respectively.

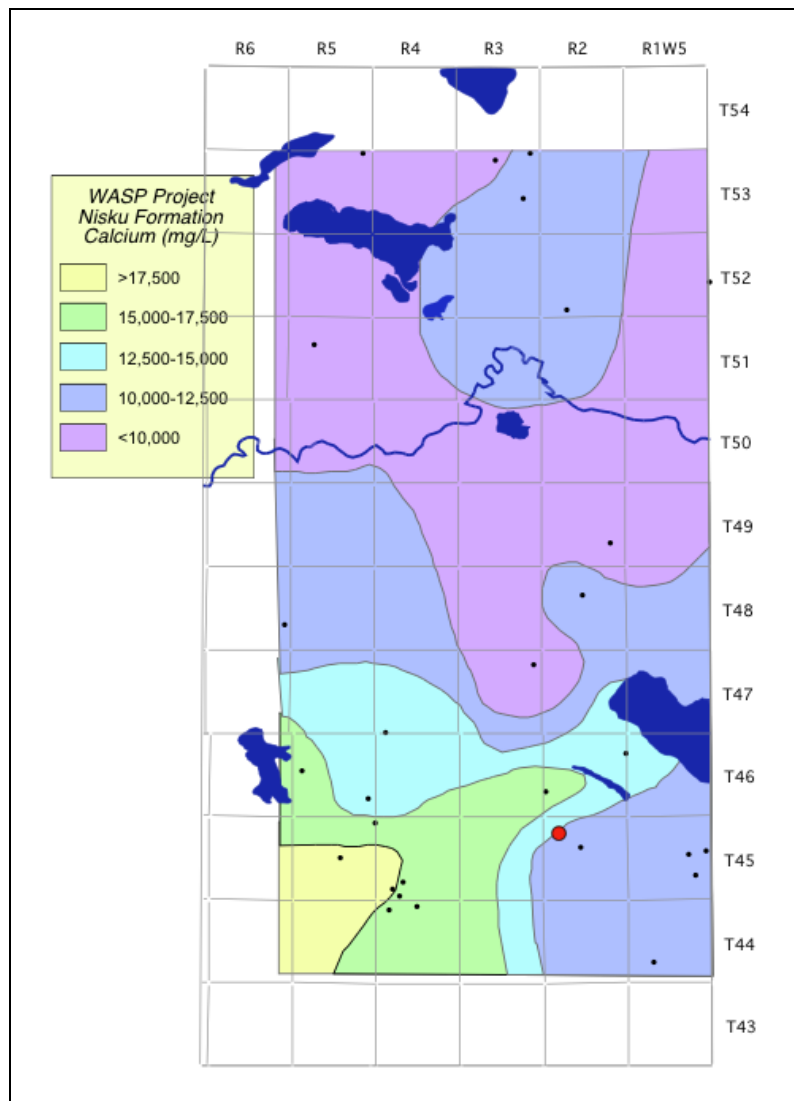


Figure 4a: WASP contour plots showing calcium concentrations.

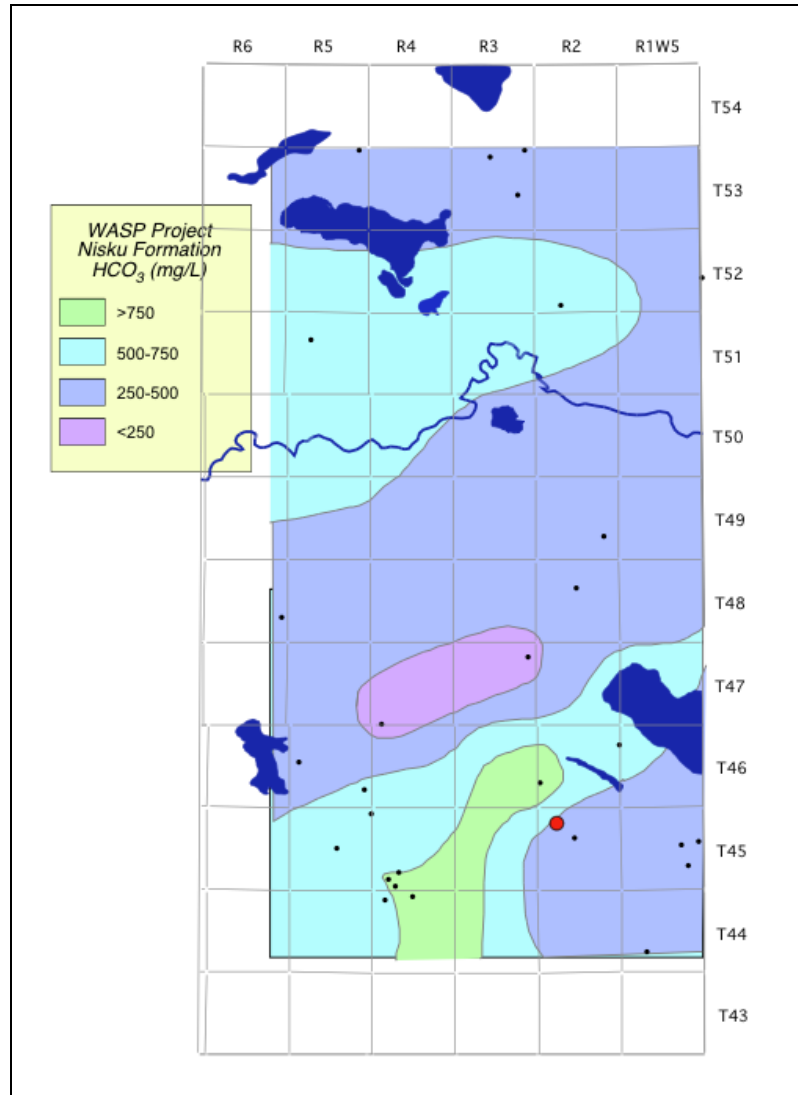


Figure 4b: WASP contour plots showing HCO_3^- concentrations.

1.2.2 Isotopic Composition

Figure 5 shows contour maps of $\delta^{13}\text{C-HCO}_3$ and $\delta^{34}\text{S-SO}_4$ values using data obtained from Simpson's Ph.D. thesis [5]. The WASP study area is outlined in red on the map and the red dot represents the only location for which isotope data are available in the study area. The $\delta^{13}\text{C-HCO}_3$ value determined for the sample from the water source well of -8.2 ‰ is within the range of carbon isotope ratios observed for dissolved inorganic carbon in the vicinity of the study area ranging from -10 to 0 ‰ (Figure 5). The $\delta^{34}\text{S-SO}_4$ value of 22.9 measured for the sample from the water source well is also consistent with sulfur isotope ratios of < 25 ‰ in the vicinity of the southern part of the study area (Figure 5). Towards the northeast, there appears to be a trend of increasing $\delta^{34}\text{S}$ values for dissolved sulfate but the rate of change shown in Figure 5 is highly speculative due to lack of data in the northern portion of the WASP study area.

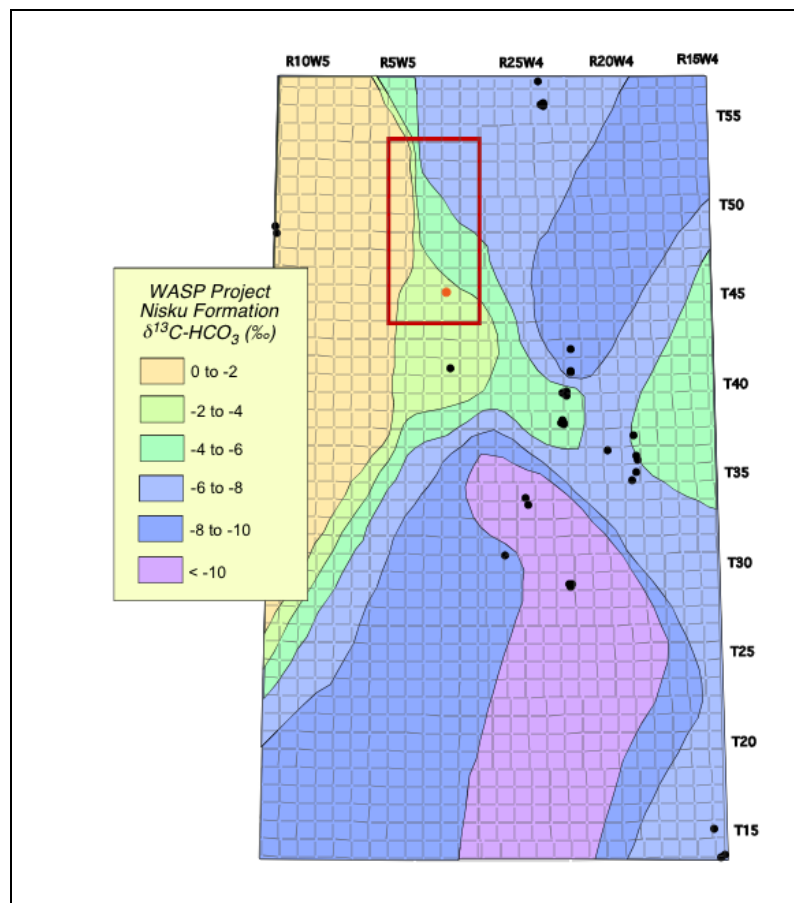


Figure 5a: Contour plots showing $\delta^{13}\text{C-HCO}_3$ values for Nisku fluids sampled in the vicinity of the WASP study area.

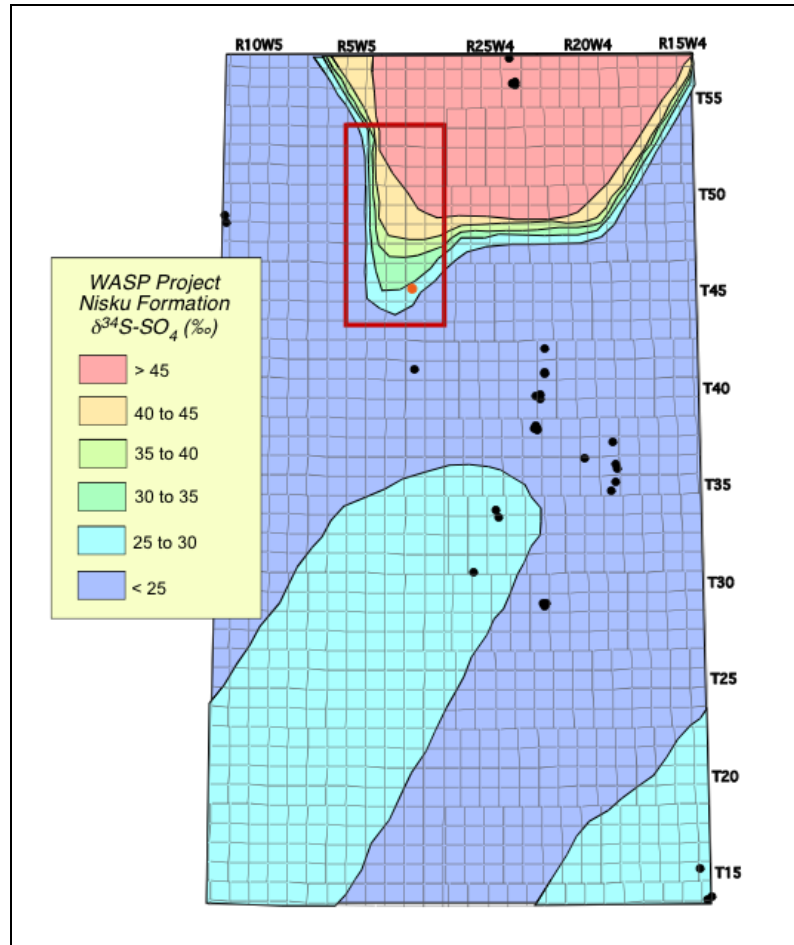


Figure 5b: Contour plots showing $\delta^{34}\text{S-SO}_4$ values for Nisku fluids sampled in the vicinity of the WASP study area.

Figure 6 shows the contour plot for $\delta^{34}\text{S}$ values of dissolved sulphide (S^{2-}) from Simpson's data set [5]. The measured $\delta^{34}\text{S}$ - S^{2-} value of 16.1 ‰ for the sample from the water source well in the study area is in excellent agreement with sulphur isotope values for dissolved sulphide in the vicinity of the WASP study area ranging from 15 to 20 ‰.

$\delta^{34}\text{S}$ values near +23 ‰ for dissolved sulphate are consistent with dissolution of Devonian anhydrite as the dominant sulphate source. The presence of significant quantities of H_2S with $\delta^{34}\text{S}$ values only 7 ‰ lower than those of dissolved sulphate indicates that thermo-chemical sulphate reduction (TSR) must have occurred [5].

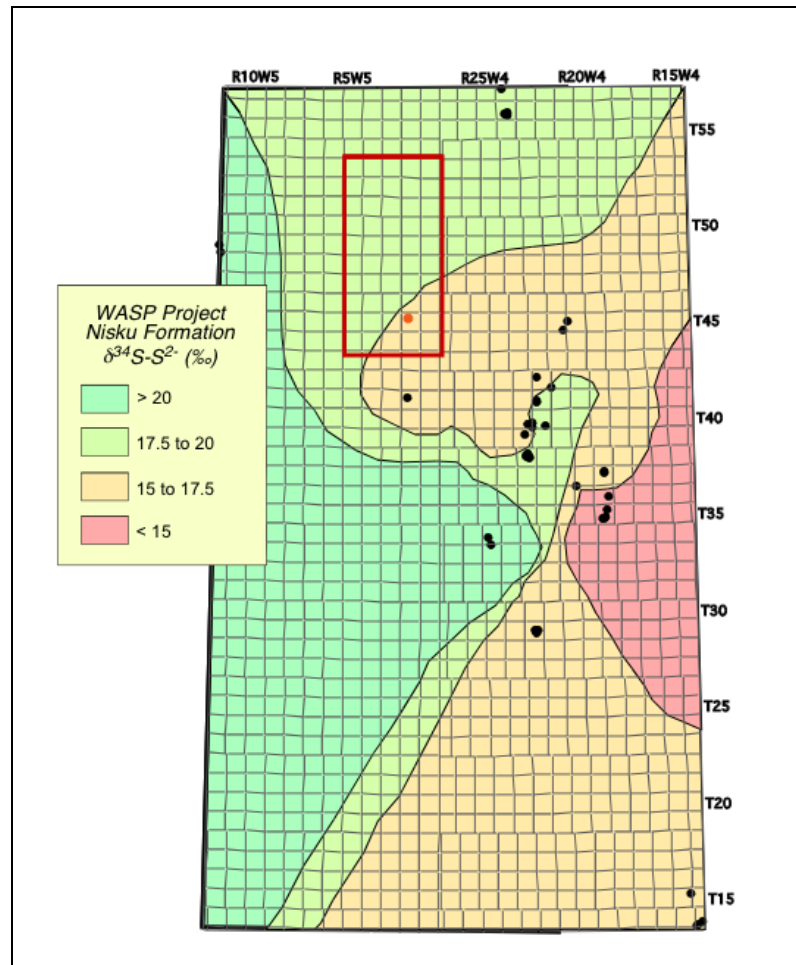


Figure 6: Contour plot of $\delta^{34}\text{S}$ - S^{2-} values obtained from [5].

1.3 Geochemistry of Fluids and Gases from the Water Source Well

Table 3 summarizes the data collected for fluids and gases obtained from well 100/11-29-045-02W5 during its initial completion in 2003 and 2004 as well as the data collected during two sampling trips in 2008. Figure 7 shows the evolution of the gas composition over this time period. Initially, the gas was predominantly composed of nitrogen (97 mole %) likely as an artifact of well construction and completion. Thereafter, methane (41-80 mole %) and H₂S (9-49 mole %) were the major constituents with CO₂ and N₂ representing less than 6 and 4 mole %, respectively. Gas production rates are not available for this well.

The results of chemical analyses conducted in 2008 are in excellent agreement with the historical data (Table 3). Total dissolved solids (TDS) remained constant around 196,000 mg/L, indicating that the concentration of the major dissolved species Na, Ca, K and Cl in the water had not changed significantly over the five-year observation period. The concentration of dissolved sulphide (H₂S_(aq)) collected at the well head varied between 177 and 660 mg/L (see section 3.2 for conversion to down-hole conditions). Sulphur isotope data suggest that H₂S is formed via thermochemical sulphate reduction (TSR) [5].

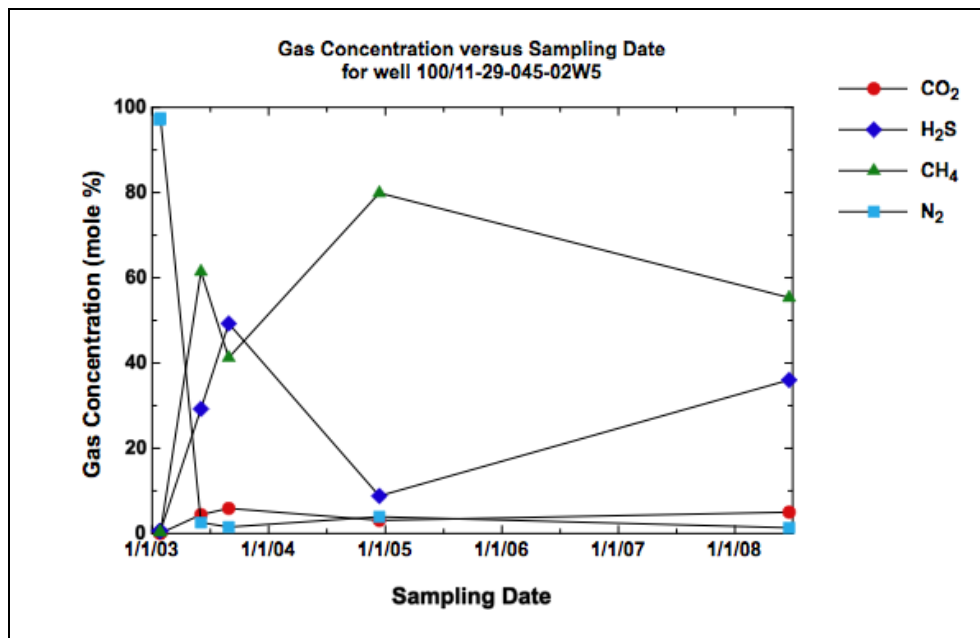


Figure 7: Gas concentration versus sampling date for four gases from well 100/11-29-045-02W5.

2. MINERALOGY

To reach the goals of this project it was important to determine the mineralogical composition of the aquifer rocks and the caprock in the WASP study area.

2.1 Sample Selection and Methods

Twelve samples were collected from archived core from both the Nisku (eight samples) and Calmar (four samples) formations. The eight samples collected from the Nisku Formation included two separate lithofacies: i.e., four samples were collected from an open marine lithofacies, and four samples were collected from a hyper-saline lithofacies.

Samples collected were subdivided at the University of Calgary, i.e., approximately one third of the sample was archived, one-third was used for thin-section preparation, and one third was ground for whole rock geochemistry. Polished thin-sections for each of the twelve samples were prepared by Calgary Rock and Material Services (Calgary, Alberta). Thin-section analysis was completed at the University of Calgary using a Nikon Optiphot polarizing microscope, and a Jeol JXA-8200 electron microprobe in energy dispersion (EDS) mode. Bulk chemical analyses, including: X-ray Fluorescence (XRF), Inductively Coupled Plasma-Atomic Emission Spectrometry (ICP-AES), X-ray Diffraction (XRD), total carbonate, and total sulfur analysis, was completed by SGS Laboratories (Lakefield, Ontario).

Quantitative mineralogy was determined using linear programming normative analysis (LPNORM [7]) at the University of Calgary in consultation with Dr. John Bloch of the University of New Mexico, Albuquerque, New Mexico, USA. Carbon isotope ratios of carbonate rocks ($^{13}\text{C}/^{12}\text{C}$) were determined in the Isotope Science Laboratory at the University of Calgary using standard techniques.

2.2 Bulk Chemical Composition

The bulk chemical composition (major constituents) of each of the twelve samples analyzed is summarized in Table 5.

Table 5: Bulk Chemical Composition of Individual Core Samples (Ni = Nisku, C = Calmar).

Sample	Formation	SiO ₂ %	Al ₂ O ₃ %	Fe ₂ O ₃ %	MgO%	CaO%	K ₂ O%	CO ₂ %	S%
W1	Ni	3.1	0.6	0.3	20.2	30.6	0.2	45.3	0.0
W2	Ni	1.9	0.8	0.3	18.5	32.8	0.3	44.8	0.0
W3	Ni	35.0	2.7	2.2	12.4	18.2	1.4	26.9	0.7
W4	Ni	1.4	0.2	0.2	10.8	36.0	0.1	23.6	11.0
W5	Ni	2.1	0.2	0.3	18.7	32.0	0.1	45.1	0.1
W6	Ni	0.6	0.1	0.1	21.4	30.9	0.1	45.9	0.2
W7	Ni	1.1	0.2	0.5	20.8	30.3	0.1	45.3	0.1
W8	Ni	0.5	0.2	0.2	21.0	30.5	0.1	45.8	0.0
W9	C	70.5	12.0	2.9	2.3	1.1	5.1	1.5	0.9
W10	C	70.3	9.8	2.2	2.8	2.5	4.6	3.6	0.8
W11	C	68.8	13.5	3.5	1.8	0.3	5.8	0.2	1.4
W12	C	72.9	11.8	2.8	1.7	0.4	5.1	0.2	1.0

The results are consistent with the known lithologies of the two formations, i.e., samples from the Calmar Formation (9-12) are shale/mudstones and composed primarily of aluminium and silicon oxides; samples from the Nisku Formation (1-8) are predominantly dolomite and composed primarily of calcium, magnesium and carbonate. Two exceptions within the Nisku group include: Sample 3, which contained a significant amount of silicon, aluminum, and potassium; and Sample 4, which contained a significant amount of sulfur and calcium relative to the rest of the group suggesting the presence of anhydrite. There were no discernable differences between the two separate lithofacies (open marine and hyper-saline) of the Nisku Formation.

The carbon isotope ratios of carbonate ($\delta^{13}\text{C}$) of the eight samples from the Nisku Formation were determined and results are summarized in Table 6. The $\delta^{13}\text{C}$ values of the Nisku samples ranged from -4.4 to -6.9 ‰ and are lower than those of Late Devonian seawater (+2.0 to +3.0 ‰; [8]).

Table 6: Carbon isotope ratios of Nisku carbonates.

Sample	$\delta^{13}\text{C}_{\text{carbonate}}$ (‰)
W1	-4.4
W2	-4.9
W3	-6.9
W4	-4.6
W5	-4.5
W6	-5.3
W7	-5.6
W8	-4.7

The obtained $\delta^{13}\text{C}$ values for samples from the hyper-saline facies (samples 3, 4, 5 and 7) are consistent with those of Whittaker et al. [9]. These authors suggested that shelf carbonates reflect a more restricted environment than open marine, and that carbon isotope ratios of carbonate may be lower than those of open marine carbonates due to carbon input via organic matter respiration. It is

possible that the lower than expected $\delta^{13}\text{C}$ values for the open marine samples (samples 1, 2, 6 and 8) are in part the result of re-crystallization of the original deposit in the presence of ^{13}C depleted meteoric water [9].

2.3 Microscopy

The presence and composition of major mineral phases was established by analysis of thin-sections using a conventional petrographic microscope and by electron microprobe.

The shales of the Calmar Formation consist of small clasts of quartz, feldspars (k-spar and albite), and micas (predominately muscovite) in a fine clay (illite) matrix (Figure 8). Finely disseminated pyrite was found in all four shale samples analyzed.

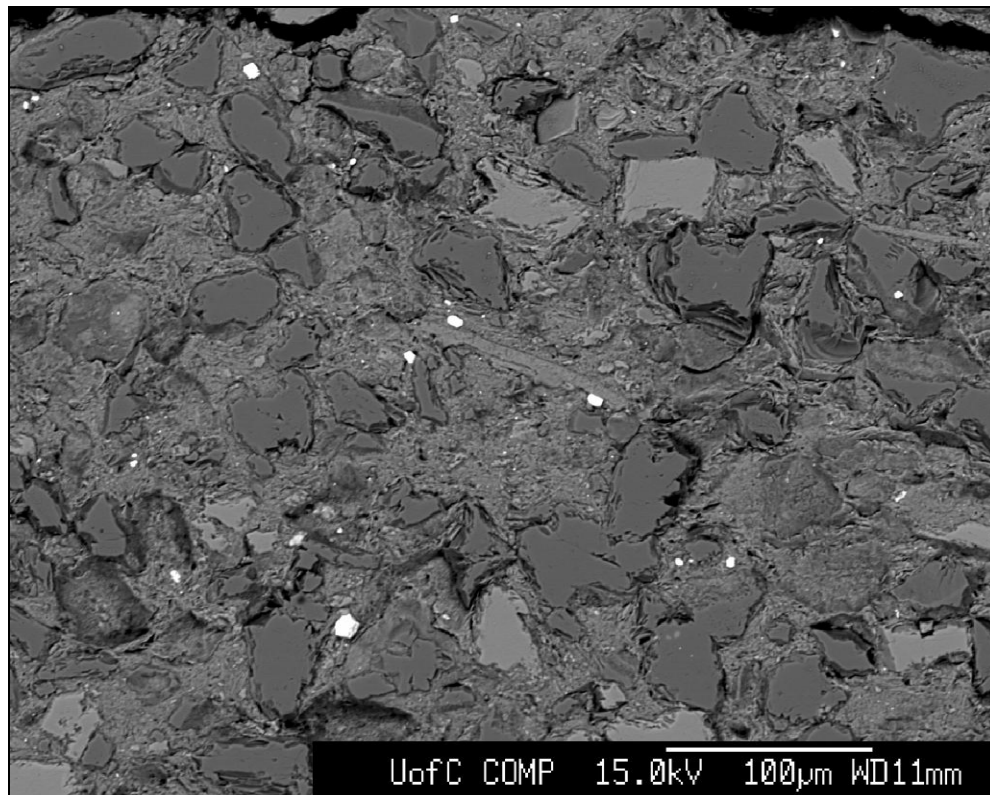


Figure 8: Photomicrograph of the Calmar Formation.

A photomicrograph of a typical Nisku carbonate is shown in Figure 9. A significant amount of replacement dolomitization of the original limestone is evident in the eight samples of Nisku core analyzed.

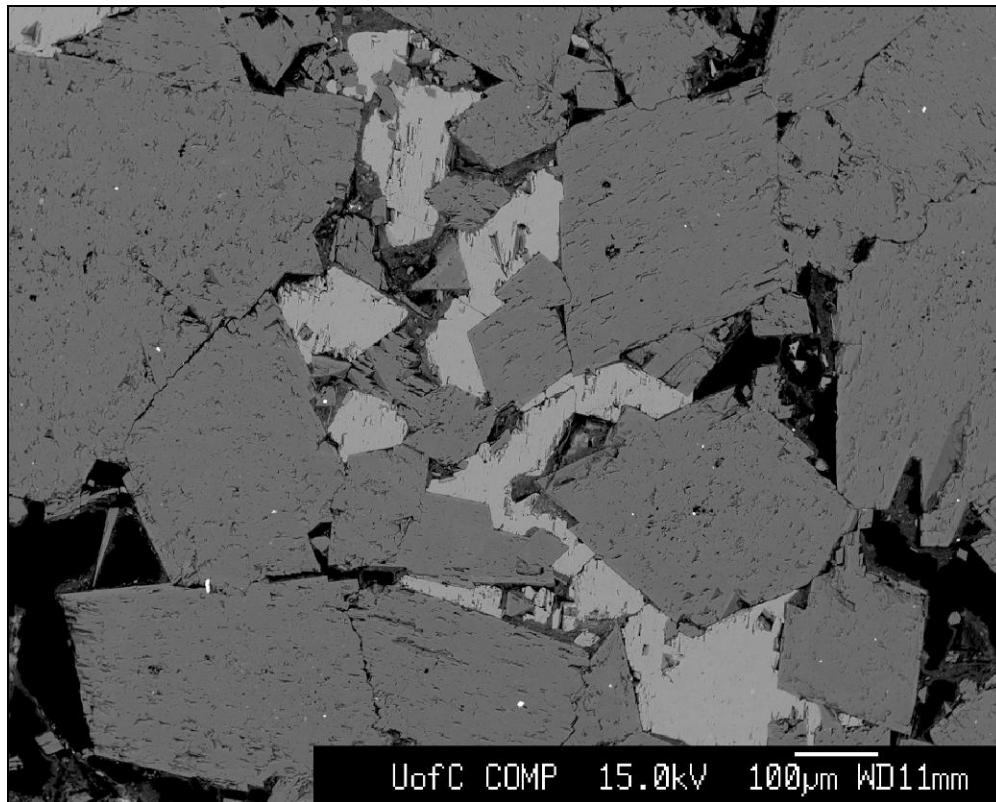


Figure 9: Photomicrograph of the Nisku Formation (Sample W12).

The residual limestone is composed of stoichiometric calcite i.e., composed largely of calcium and carbonate with very little substitution of magnesium, iron, manganese or strontium for calcium (Table 7).

Table 7: Average Composition of Nisku Formation Calcite (wt%).

CaO	MgO	FeO	MnO	SrO	CO ₂
53.8	0.5	0.3	0.3	0.2	45.0

The replacement dolomite crystals are often compositionally zoned (Figure 10) with the outer crystal being slightly more calcium-rich relative to the inner crystal.

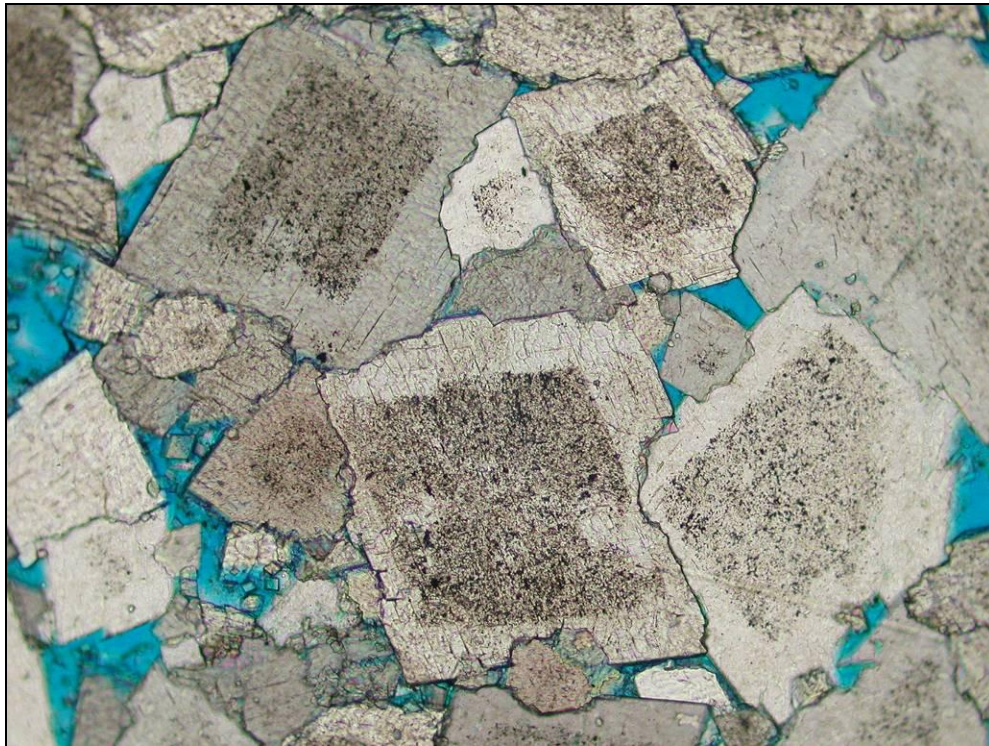


Figure 10: Photomicrograph of Zoned Dolomites (Sample W2).

The average composition of the Nisku Formation dolomite is presented in Table 8.

Table 8: Average Composition of Nisku Formation Dolomite (wt%).

CaO	MgO	FeO	MnO	SrO	CO ₂
34.9	16.9	0.3	0.1	0.1	47.7

In samples composed primarily of carbonate rock, there were no discernable differences in either appearance or chemical composition between the two separate lithofacies (open marine and hyper-saline) of the Nisku Formation (Figures 11 and 12).

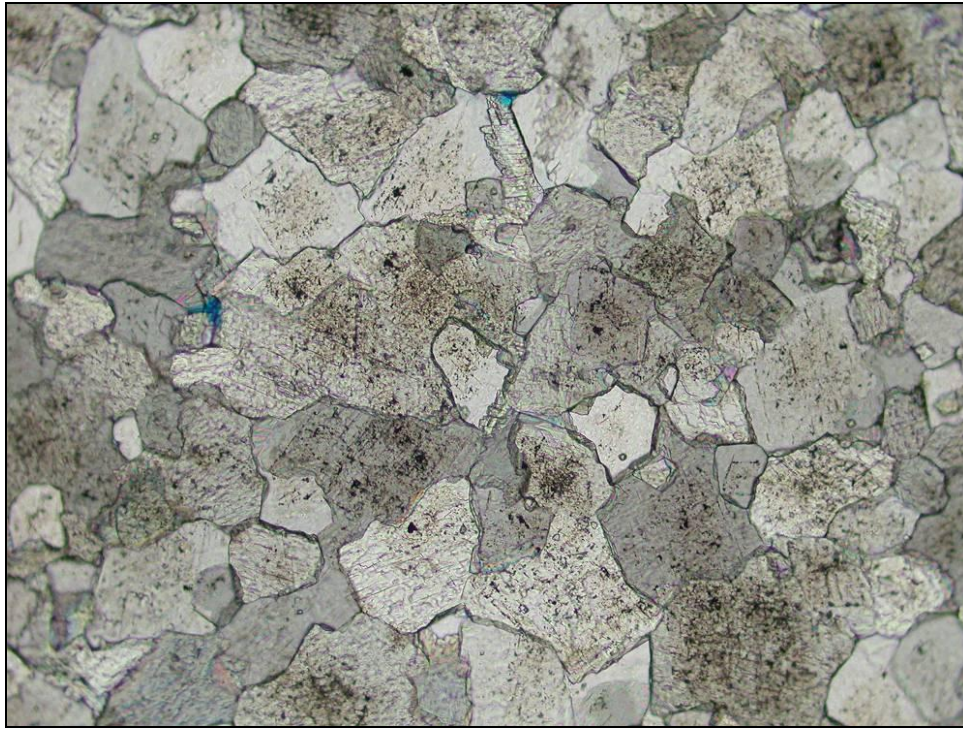


Figure 11: Photomicrograph of Nisku Open Marine Facies (Sample W6).

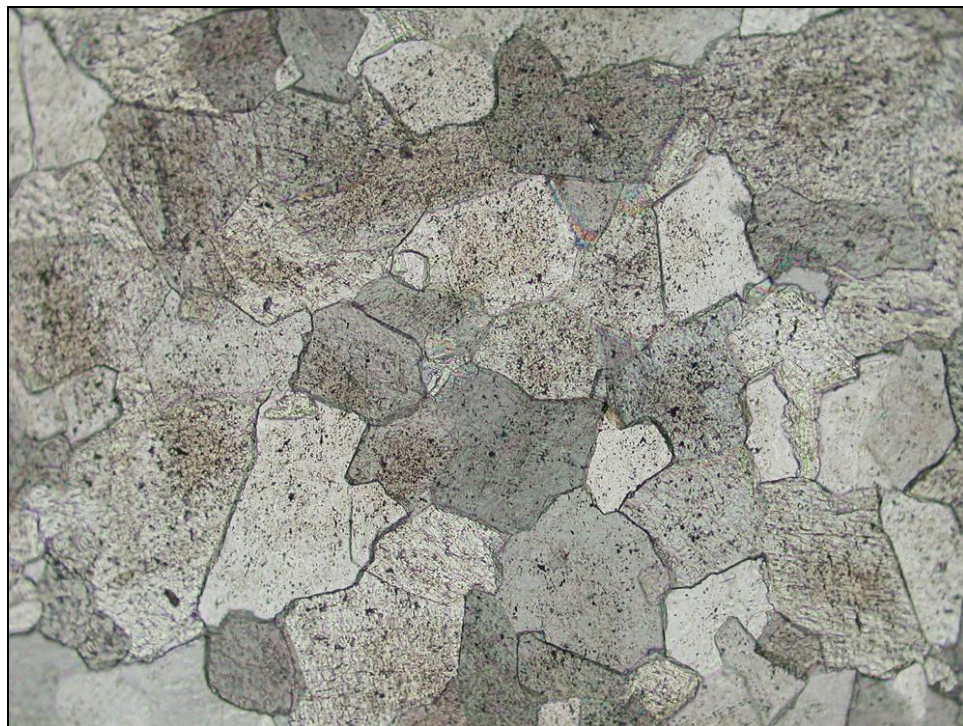


Figure 12: Photomicrograph of Nisku Hyper-Saline Facies (Sample W7).

Sample W3 (Figure 13) was found to contain a significant amount of detrital quartz, feldspar and mica (predominantly muscovite) in addition to dolomite.

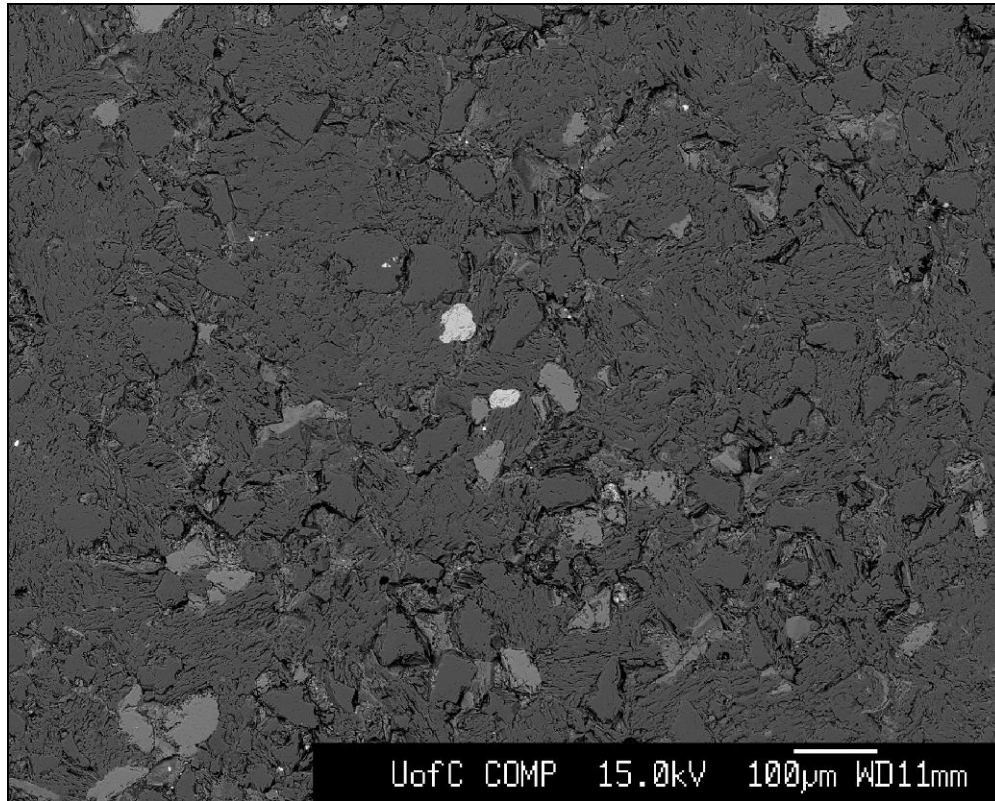


Figure 13: Photomicrograph of Nisku Sample W3.

A significant amount of anhydrite was observed in Sample W4 (Figure 14). The presence of anhydrite in the hyper-saline facies of the Nisku Formation was not unexpected. Machel [10] suggested that anhydrite is genetically related to the replacive dolomites present.

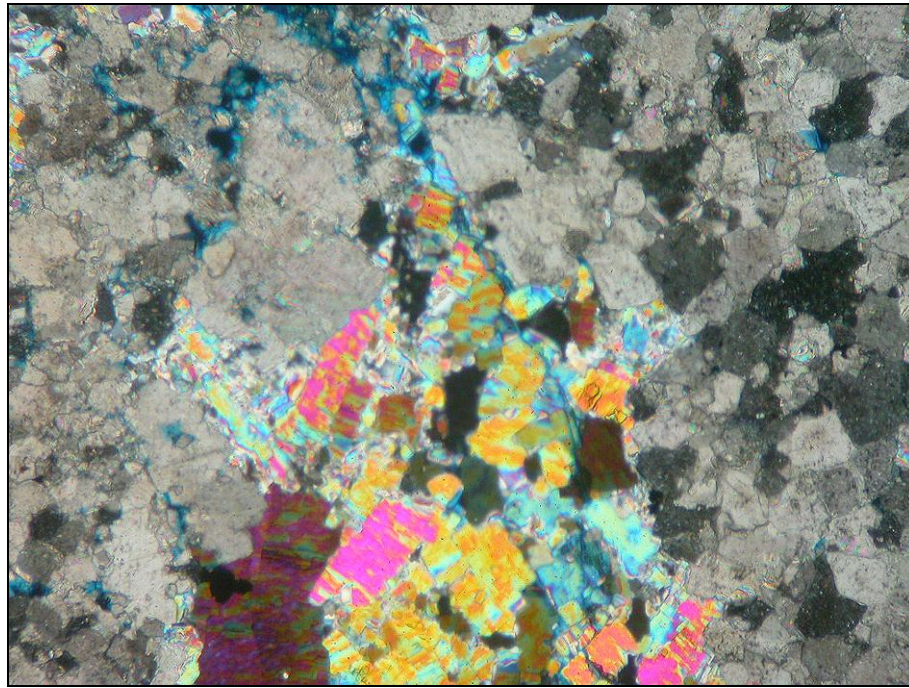


Figure 14: Photomicrograph of Nisku Anhydrite (Sample W4).

2.4 Quantitative Mineralogy

Quantitative mineralogy was determined using a linear programming normative analysis (LPNORM) program [7]. There are advantages to using LPNORM analysis over mineral point counting from thin sections, and/or XRD alone, i.e., LPNORM incorporates mineralogical information from several sources (polished thin-section examination, XRD, and electron microprobe) with whole-rock analysis (XRF, ICP, total carbonate, and total sulfur). The quantitative mineralogy of each of the twelve samples analyzed is summarized in Table 9.

Table 9: Quantitative Mineral Composition (wt%).

Sample	Calcite	Dolomite	Quartz	Albite	K-spar	Ill/Mus	Anhydrite	Pyrite
W1	6.2	89.2	2.0	0.0	0.2	2.0	0.0	0.0
W2	15.2	79.9	0.0	0.6	0.9	1.9	0.0	0.0
W3	3.8	52.9	27.6	1.7	5.1	4.4	0.0	1.3
W4	5.5	44.4	0.9	0.0	0.4	0.5	47.1	0.0
W5	11.7	83.8	1.4	0.5	0.6	0.0	0.0	0.2
W6	5.9	90.7	0.3	0.0	0.6	0.0	0.0	0.0
W7	5.1	90.2	0.4	0.5	0.3	0.0	0.0	0.2
W8	4.7	91.6	0.0	0.0	0.4	0.5	0.0	0.0
W9	0.5	2.7	43.4	2.5	14.9	29.6	0.0	1.7
W10	0.7	6.9	46.7	2.5	16.2	22.1	0.0	1.5
W11	0.0	0.4	37.8	3.4	17.6	33.5	0.1	2.6
W12	0.5	0.0	45.5	3.4	15.8	28.7	0.0	1.9

The average composition of the four Calmar Formation shales analyzed is: 43.4% quartz, 28.5% illite/muscovite, 16.1% k-spar, 3.0% albite, 2.5% dolomite, and 1.9% pyrite.

With the exception of samples 3 and 4, the Nisku samples are predominantly composed of dolomite (up to 91.6%), with smaller amounts of calcite (up to 15.2%) present. Sample 3, was found to contain 27.6% detrital quartz, and smaller amounts of detrital feldspars (6.8%), micas (4.4%), as well as dolomite (52.9%). Sample 4, contains a substantial amount of anhydrite (47.1%) as well as dolomite (44.4%).

Knowledge of the mineralogical composition of aquifer rocks and caprocks is an essential input parameter for geochemical modelling of the fate of injected CO₂ in the WASP study area.

3. GEOCHEMICAL MODELLING

3.1 SOLMINEQ88

Geochemical modelling was conducted using the sampled well water analysis summarized in Table 4 and the geochemical computer program SOLMINEQ88 [11] to determine the saturation indices of selected minerals. The saturation index (SI) measures the saturation state of a mineral phase whose chemical components are dissolved in the produced fluid. A mineral that yields SI < -0.3 is considered under-saturated and hence has the potential to dissolve. Conversely, a mineral that yields SI > 0.3 is considered over-saturated suggesting that the mineral may precipitate from the fluid. A SI value in the range of -0.3 < SI < 0.3 is generally accepted as being in equilibrium with the fluid. This range is somewhat arbitrary but is based on typical analytical accuracies and sample

variabilities, as well as the slower reaction rates of phases as they approach equilibrium. Actual mineral dissolution or precipitation is controlled by temperature-dependant kinetic reaction rates and by the reactive surface area of the mineral. The saturation index is an indication of the potential to dissolve or precipitate a mineral and does not necessarily mean that the predicted reaction is actually taking place at a significant rate.

The Nisku Formation is composed of dolostones (dolomite) and limestone (calcite). The Calmar caprock is predominantly composed of shales. The bottom rock is the Ireton, which is composed of calcareous shales and argillaceous limestone [12].

Based on the chemical data summarized in Table 4, saturation indices for calcite, dolomite, anhydrite and quartz were determined and are summarized in Table 10 for the downhole pressure (17.5 MPa) and temperature (82.5 °C) of the well. The SI for quartz fell within the equilibrium range, $-0.3 < SI < 0.3$, which is expected for an unperturbed reservoir. Anhydrite had a SI of -0.51 indicating that anhydrite has the potential to slowly dissolve. The two carbonate minerals, calcite and dolomite, have a positive SI, indicating the potential for carbonate mineral precipitation. Since CO₂ injection will result in increasing bicarbonate contents in the reservoir fluids, the potential for calcite and dolomite to precipitate will likely persist or increase.

Table 10: Saturation Indices for common minerals found in the Nisku formation, the Calmar caprock and the Ireton bottom-rock.

Mineral	Saturation Index
Calcite	0.45
Dolomite	1.09
Anhydrite	-0.51
Quartz	-0.10

3.2 H₂S Saturation Modelling

The measured concentrations of H₂S_(aq) in produced waters collected at the well head are not identical to the H₂S content at reservoir conditions since H₂S exsolves during pumping of produced fluids to the well head. Therefore the actual down-hole H₂S content was determined using geochemical models. The solution obtained from the water source well was a 2.55 M NaCl solution. According to Duan et al. [13], for a solution with a partial pressure of 16 MPa, 60°C and 2.55 M NaCl, the solubility of H₂S in water is 1.63 moles per kg of water or 63,180 mg/L. When this water is moved from depth to the surface and depressurized to 101 kPa and 25°C, the concentration of H₂S_(aq) in the water decreases to 0.0678 moles per kg or 2,640 mg/L. Measured H₂S concentrations at the well head varied between 177 and 660 mg/L (Table 3). Based on a gas/water ratio of 4:1 (personal communication), and using the equations from Duan et al. [13], the concentration of H₂S_(aq) in the reservoir at depth and pressure at the time of sampling was calculated to be 0.069 moles per kg or 2,350 mg/L, which is significantly less than the saturation value of 63,180 mg/L. Thus the Nisku waters are under saturated with respect to H₂S_(aq).

3.3 ToughReact Modelling

ToughReact [14] is a reactive transport code that uses chemically speciation and water-rock-gas interaction calculations as well as multidimensional non-isothermal multiphase flow and mass transport. It is used to simulate deep saline aquifer storage of CO₂ [15]. Here, this code has been used to simulate the geochemical processes occurring in two reservoirs where CO₂ injection is occurring, one with H₂S present and the other without.

3.3.1 Problem Setup

A single layer uniform carbonate formation with a thickness of 70 m is considered in the present model. The hydrological parameters of the formation are representative of those for a carbonate formation. The formation is assumed to be uniform throughout and extends infinitely in the horizontal direction. A non-uniform radial grid is used with spacing increasing away from the well.

This fluid flow is a very simple model, i.e., a first order model, and does not consider formation heterogeneities that would result in non-uniform sweeps or buoyancy forces that would tend to drive the CO₂ towards the top of the aquifer. Initially, injected CO₂ will tend to accumulate and spread out near the top of the permeable layer and will partially dissolve in the aqueous layer. The dissolution of the CO₂ in the aqueous layer will cause its density to increase over time and will eventually give rise to buoyancy driven convection where CO₂ enriched waters will migrate downward [16]. The dissolution process and aqueous phase convection will vertically mix the aqueous CO₂ with a mixing time scale on the order of hundreds of years or more [17] and is similar to the time scales for significant interactions of CO₂.

The hydrogeological parameters used in the simulations are summarized in Table 11. The carbonate formation was assumed to be homogeneous. Injection of carbon dioxide was simulated at 31.69 kg/s (1 MT/year) for 50 years. The initial pressure was 16 MPa at the top of the formation. In all simulations the initial reservoir pressure was set at 17.5 MPa, formation temperature of 60°C, a permeability of 30 mD and a porosity of 10%. The simulations were conducted over a 50-year injection period where the injection rate was 1MT/year of CO₂ or 31.69 kg/sec.

The initial mineral composition used in the modelling is consistent with samples from well 2 (see section 2) as summarized in Table 12. The kinetic data for orthoclase were not available and therefore a substitution of k-feldspar was made. Since H₂S is present in the reservoir, secondary minerals, such as pyrite, were chosen. Also chosen as a secondary mineral was magnesite given that significant amounts of magnesium may be released from dolomite dissolution.

The water composition used is that measured for fluids from the water source well summarized in Table 4. The water composition given in Table 4 is representative for surface conditions, i.e., after the sample degassed while moving from depth to surface. The water used in the simulation was re-equilibrated with the degassing H₂S, CH₄ and CO₂ using SOLMINEQ88 [11] as shown in Table 12. Two species shown in Table 13 were not measured, AlO₂⁻ and O_{2(aq)}. A small amount of each was added since the first would probably be present due to the presence of silicate minerals and O_{2(aq)} was necessary for redox reactions to occur.

Table 11: Hydrogeological parameters for the Nisku carbonate formation.

Parameter	
Permeability (m ²)	0.3×10^{-13}
Porosity	0.10
Temperature (°C)	60
Pore Compressibility (Pa ⁻¹)	4.5×10^{-10}
Tortuosity [21]	0.3
Compressibility (Pa ⁻¹) [21]	1×10^{-8}
Diffusivity (m ² /s) [21]	1×10^{-9}
Relative Permeability	
Liquid [18]	
$k_{rl} = \sqrt{S^* \{1 - (1 - [S^*]^{1/m})^m\}^2}$	$S^* = (S_l - S_{lr}) / (1 - S_{lr})$
S_{lr} : irreducible water saturation m: exponent	$S_{lr} = 0.3$ $m = 0.457$
Gas [19]	
$k_{rg} = (1 - \hat{S})^2 (1 - \hat{S}^2)$	$\hat{S} = (S_l - S_{lr}) / (S_l - S_{lr} - S_{gr})$
S_{gr} : irreducible gas saturation	$S_{gr} = 0.05$
Capillary Pressure	
[18]	
$P_{cap} = -P_0 ([S^*]^{-1/m} - 1)^{1-m}$	
S_{gr} : irreducible gas saturation m: exponent	$S_{lr} = 0.0$ $m = 0.457$
P_0 : strength coefficient (kPa)	$P_0 = 19.61$

Table 12: Initial mineral volume fractions and possible secondary minerals used in the ToughReact simulations.

Mineral	Chemical Formula	Volume % of Solid	Volume % of Medium
Primary			
Dolomite	$\text{CaMg}(\text{CO}_3)_2$	81.22	80.49
Calcite	CaCO_3	15.45	16.04
Illite	$\text{K}_{0.6}\text{Al}_{1.8}\text{Mg}_{0.25}(\text{Al}_{0.5}\text{Si}_{3.5}\text{O}_{10})(\text{OH})_2$	1.89	1.89
K-feldspar	KAlSi_3O_8	0.86	0.95
Low-Albite	$\text{NaAlSi}_3\text{O}_8$	0.58	0.62
Secondary			
Kaolinite	$\text{Al}_2\text{Si}_2\text{O}_5(\text{OH})_4$		
Na-smectite	$\text{Na}_{0.29}\text{Mg}_{0.26}\text{Al}_{1.77}\text{Si}_{3.97}\text{O}_{10}(\text{OH})_8$		
Ca-smectite	$\text{Ca}_{0.145}\text{Mg}_{0.26}\text{Al}_{1.77}\text{Si}_{3.97}\text{O}_{10}(\text{OH})_8$		
Dawsonite	$\text{NaAlCO}_3(\text{OH})_2$		
Aragonite	SrCO_3		
Siderite	FeCO_3		
Ankerite	$\text{CaMg}_{0.3}\text{Fe}_{0.7}(\text{CO}_3)_2$		
Magnesite	MgCO_3		
Pyrite	FeS_2		

Table 13: Initial total dissolved chemical species concentrations used in the ToughReact simulations.

Species	Concentration (mol/kg)
pH	6.10
Ca^{2+}	0.41
Mg^{2+}	9.33×10^{-2}
Na^+	2.56
K^+	0.10
Sr^{2+}	1.08×10^{-2}
Fe^{2+}	9.35×10^{-6}
$\text{SiO}_{2(\text{aq})}$	4.56×10^{-4}
HCO_3^-	2.01×10^{-2}
SO_4^{2-}	5.21×10^{-3}
Cl^-	3.44
AlO_2^-	1.36×10^{-7}
$\text{O}_{2(\text{aq})}$	4.88×10^{-70}
$\text{H}_2\text{S}_{(\text{aq})}$	3.97×10^{-2}

Two groups of simulations were performed. The first group was for an aquifer with the mineralogical composition listed in Table 12 and the water composition listed in Table 13 with no $H_2S_{(aq)}$ present. The second group was identical but included $H_2S_{(aq)}$.

Table 14 provides the parameters for the kinetics of dissolution and precipitation for the minerals used in the models [20]. Calcite was used as an equilibrium mineral in the simulations. Specific details about the kinetics used in the simulations can be found in Xu et al. [21].

Table 14: Parameters for calculating kinetic rate constants of minerals used in the simulations [20].

Mineral	A (cm^2/g)	Parameters for kinetic rate law							
		Neutral Mechanism		Acid Mechanism			Base Mechanism		
		k^{25} ($mol/m^2/s$)	E (kJ/mol)	k^{25}	E	$n(H^+)$	k^{25}	E	$n(H^+)$
Dolomite	9.1	$2.9512 \cdot 10^{-8}$	52.2	$6.4565 \cdot 10^{-04}$	36.1	0.500			
Illite	108.7	$1.6596 \cdot 10^{-13}$	35.0	$1.0471 \cdot 10^{-11}$	23.6	0.340	$3.02 \cdot 10^{-17}$	58.9	-0.400
K-feldspar	9.1	$3.8905 \cdot 10^{-13}$	38.0	$8.7096 \cdot 10^{-11}$	51.7	0.500	$6.3096 \cdot 10^{-22}$	94.1	-0.823
Low-Albite	9.1	$2.7542 \cdot 10^{-13}$	69.8	$6.9183 \cdot 10^{-11}$	65.0	0.457	$2.5119 \cdot 10^{-16}$	71.0	-0.572
Kaolinite	108.7	$6.9183 \cdot 10^{-14}$	22.2	$4.8978 \cdot 10^{-12}$	65.9	0.777	$8.9125 \cdot 10^{-18}$	17.9	-0.472
Nasmectite	108.7	$1.6596 \cdot 10^{-13}$	35.0	$1.0471 \cdot 10^{-11}$	23.6	0.340	$3.0200 \cdot 10^{-17}$	58.9	-0.400
Casmectite	108.7	$1.6596 \cdot 10^{-13}$	35.0	$1.0471 \cdot 10^{-11}$	23.6	0.340	$3.0200 \cdot 10^{-17}$	58.9	-0.400
Dawsonite	9.1	$1.2598 \cdot 10^{-09}$	62.76	$6.4565 \cdot 10^{-04}$	36.1	0.500			
Aragonite	9.1	$4.5709 \cdot 10^{-10}$	23.5	$4.1687 \cdot 10^{-07}$	14.4	1.000			
Siderite	9.1	$1.2598 \cdot 10^{-09}$	62.76	$6.4565 \cdot 10^{-04}$	36.1	0.500			
Ankerite	9.1	$1.2598 \cdot 10^{-09}$	62.76	$6.4565 \cdot 10^{-04}$	36.1	0.500			
Magnesite	9.1	$4.5709 \cdot 10^{-10}$	23.5	$4.1687 \cdot 10^{-07}$	14.4	1.000			
Pyrite	12.87	$2.8184 \cdot 10^{-05}$	56.9 $n(O_{2(aq)}) =$ 0.5	$3.2022 \cdot 10^{-08}$	56.9 $n(H^+) =$ -0.5, $n(Fe^{3+}) =$ 0.5				

- Notes:**
- (1) all rate constants are for dissolution
 - (2) A is specific area, k^{25} is kinetic rate constant at 25°C, E is activation energy, n is power term (Eq. (3), [21])
 - (3) power terms n for both acid and base mechanism are with respect to H^+
 - (4) for pyrite, the neutral mechanism has n with respect to $O_2(aq)$, the acid mechanism has two species involved: one n with respect to H^+ and another n with respect to Fe^{3+} (Eq. (3), [21])

3.3.2 Results

The output from the ToughReact simulations consists of information in three categories:

1. compositions of the aqueous phase,
2. distribution of primary and secondary minerals,
3. physical properties of the system, e.g., porosity.

Data presented in this report is for four time periods, 1 year, 10 years, 25 years and 50 years of injection over a radial distance of up to 10,000 metres.

The pH distribution along the radial distance is shown in Figure 15. For all the simulations the pH increases from a low value to 5.1 at a distance of 19.7 m after year 1, remains constant for a distance of ~500 m, and increases again to ~6.4 while remaining constant over the rest of the radial distance. This pattern was observed for both H₂S and non-H₂S aquifers. With increasing time after CO₂ injection, the distance of the initial pH increase changed from 19.7 m after year 1 to 146 m after 50 years. The second increase of pH values changed from an initial distance of ~500 m for year 1 to ~5000 m after 50 years.

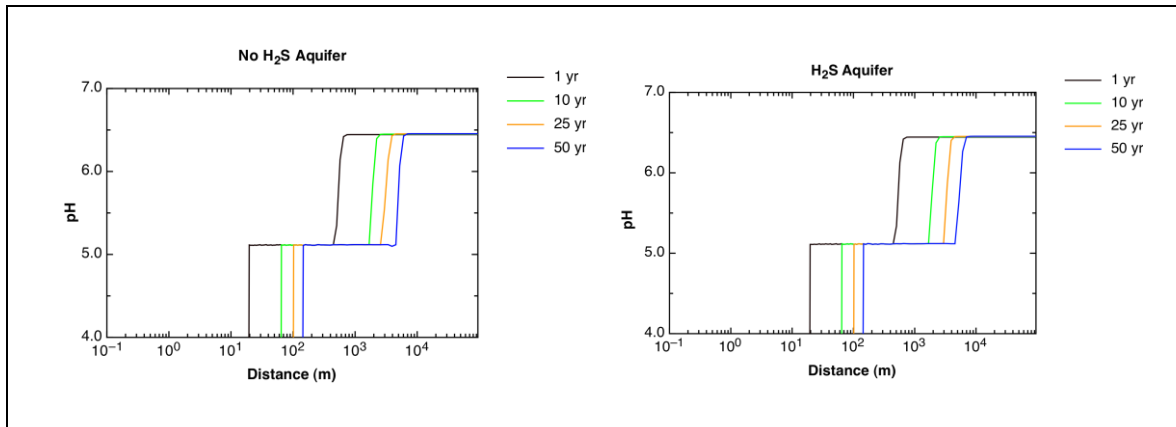


Figure 15: pH of aquifer as a function of radial distance after initiation of CO₂ injection for both non-H₂S and H₂S aquifers.

Figure 16 shows the concentration of bicarbonate (in moles/kg) as a function of distance. The initial concentration of bicarbonate in the water is 0.02 moles/kg across the entire modelling area. After one year, the concentration of bicarbonate in the water increased to ~1.25 moles/kg at a distance of 19.7 m from the injector and remained elevated to a distance of ~500 m. Thereafter bicarbonate concentrations decreased to baseline values (~0.02 moles/kg). A similar pattern of increasing and decreasing bicarbonate concentrations was observed after 10, 25 and 50 years at increasing distances from the injector.

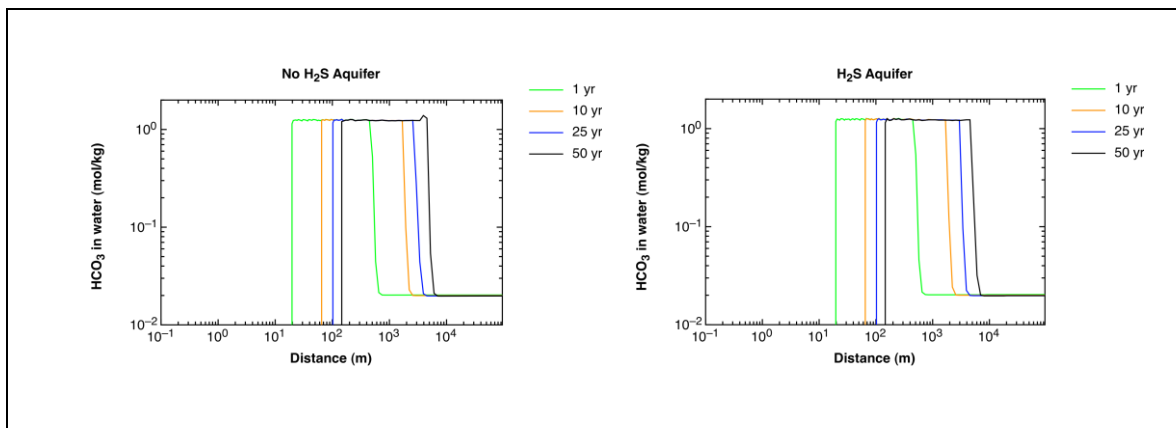


Figure 16: HCO₃ concentration as a function of radial distance after initiation of CO₂ injection for both non-H₂S and H₂S aquifers.

Figures 17 and 18 show the concentrations of calcium and magnesium respectively as a function of distance and time. For calcium the concentration decreased significantly from the initial value of 0.41 moles/kg (red dotted line in Figure 17). Magnesium, however, increased significantly from the initial value of 0.093 moles/kg (red dotted line in Figure 18). The radial trend for the Ca^{2+} and Mg^{2+} concentrations was similar to that of bicarbonate. The concentrations of both species, calcium and magnesium, were zero until 19.2 m for the first year of injection. At this distance, the concentration increased to ~ 0.02 mol/kg for calcium and ~ 0.60 mol/kg for magnesium and remained constant to a radial distance of ~ 570 m. Thereafter, the concentrations decreased and remained constant. This pattern was similar for all years at increasing distances from the injector well (Figures 17 and 18).

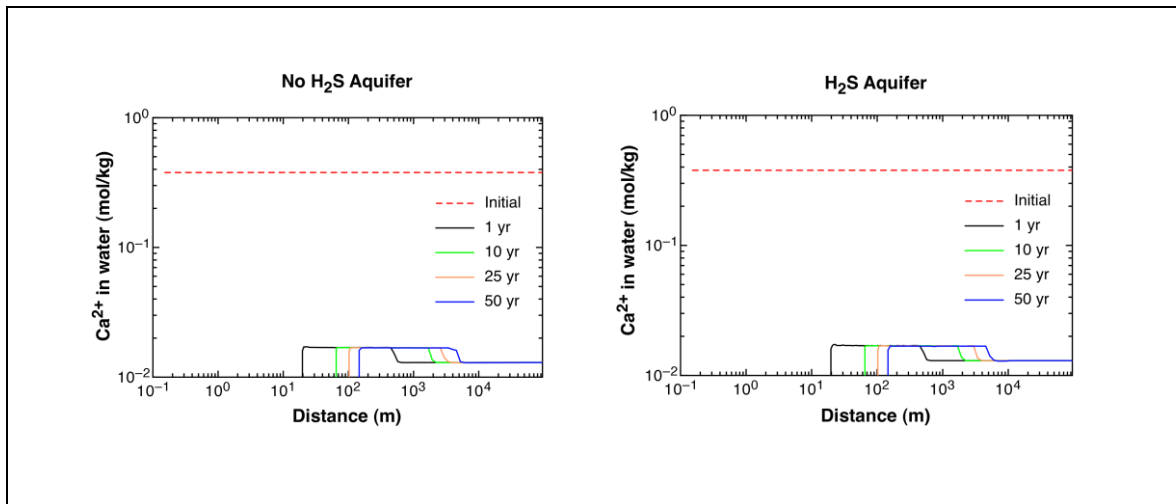


Figure 17: Ca concentration as a function of radial distance after initiation of CO_2 injection for both non- H_2S and H_2S aquifers.

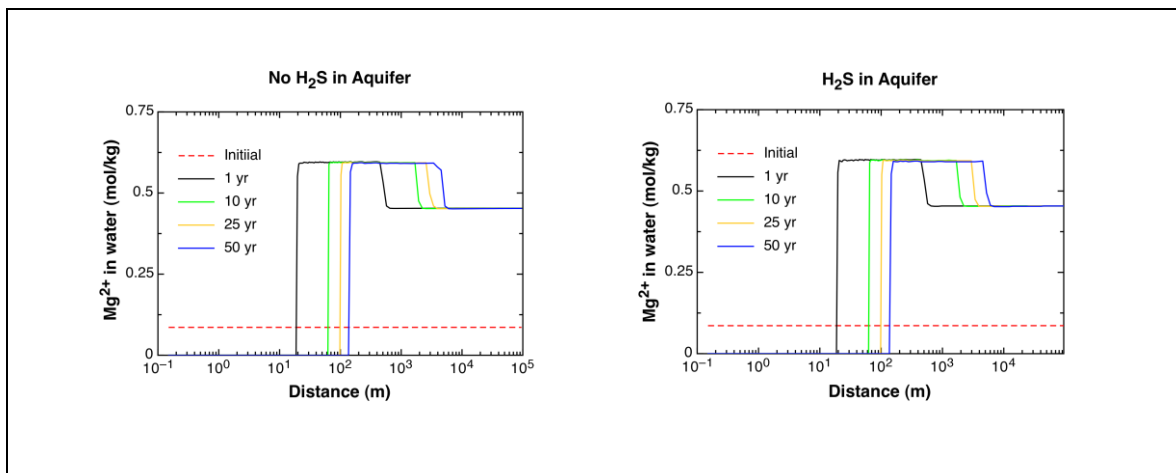


Figure 18: Mg concentration as a function of radial distance after initiation of CO_2 injection for both non- H_2S and H_2S aquifers.

Figure 19 shows the abundance of dolomite (as a volume fraction) as a function of distance. The initial volume fraction of dolomite (80.49%) decreased by circa 0.4% to a minimum value of 80.10% between 7.8 m and ~500 m. Thereafter, the volume fraction of dolomite increased to ~80.20%. The distance over which the increase in dolomite abundance occurred ranged from ~500 m after one year to ~5200 m after 50 years of injection.

The abundance of calcite as a function of distance and time is shown in Figure 20. Initially the volume fraction of calcite was 0.1604, increasing by 0.36% to 0.1640 between 7.8 and ~500 m, thereafter decreasing to 0.1635. The change in volume fraction was observed up to ~2200 m after 10 years and up to ~5000 m after 50 years.

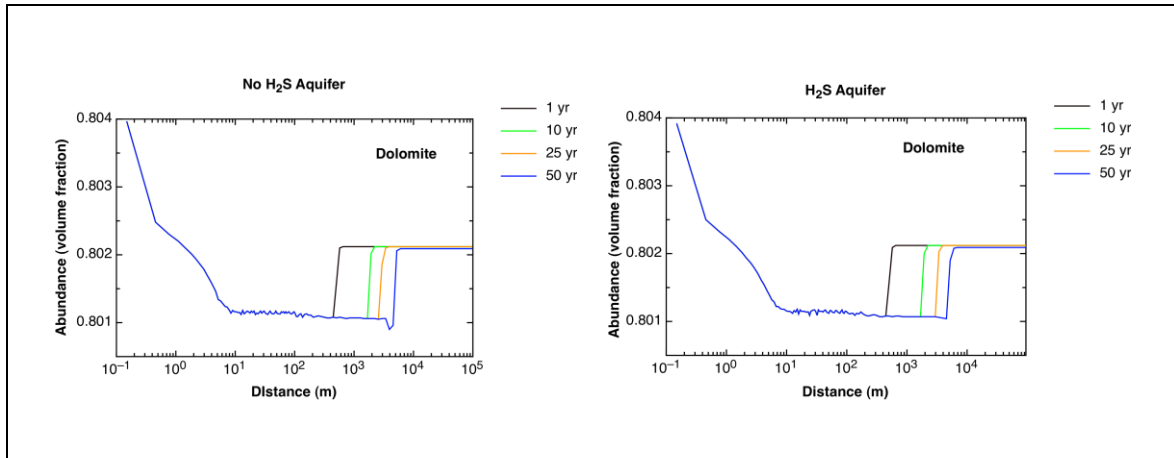


Figure 19: Dolomite mineral abundance as a function of radial distance after initiation of CO₂ injection for both non-H₂S and H₂S aquifers.

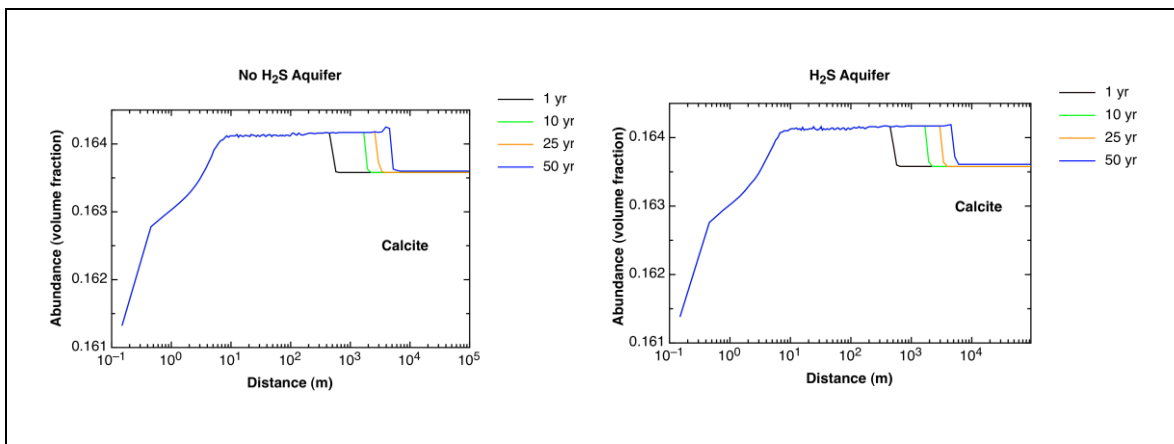


Figure 20: Calcite mineral abundance as a function of radial distance after initiation of CO₂ injection for both non-H₂S and H₂S aquifers.

Figure 21 shows the changes in the volume fraction of magnesite as a function of distance and time. Initially, there was no magnesite present. After 10 years of injection a small increase in the volume fraction of magnesite on the order of 10^{-5} was observed at a distance of ~ 1450 m. This small increase persisted throughout the next 50 years without change of the radial distance with almost identical trends for H_2S and no H_2S in the aquifer simulations.

Figure 22 shows the amount of CO_2 sequestered in the mineral phase as a function of both radial distance and time. A decrease in the amount of CO_2 sequestered in mineral form of ~ 0.36 kg/m^3 was observed at a radial distance of ~ 500 m after one year of injection indicating that carbonate (dolomite and calcite) dissolution was occurring. The radial distance where carbonate dissolution was occurring increased as injection progressed from ~ 500 m after one year to ~ 5200 m after 50 years, and the amount continued to increase slightly to ~ 0.4 kg/m^3 . Outside this dissolution zone, positive CO_2 sequestration values were observed indicating that mineral precipitation is occurring. Mineral sequestration values of ~ 0.311 kg/m^3 were observed after one year at a radial distance greater than ~ 500 m and ~ 0.334 kg/m^3 after 50 years and at a radial distance greater than ~ 5200 m.

The change in overall porosity as a function of distance and time is shown in Figure 23. After one year of injection, the porosity remained constant at $\sim 10\%$ within a radial distance of ~ 570 m. Thereafter the porosity decreased slightly by less than 0.1% to 9.96% for the remaining radial distance. This pattern was similar during the remaining injection period except that the radial distance at which the porosity decrease occurred increased from ~ 500 m after one year to ~ 1200 m after five years of injection and ~ 5200 m after 50 years of injection.

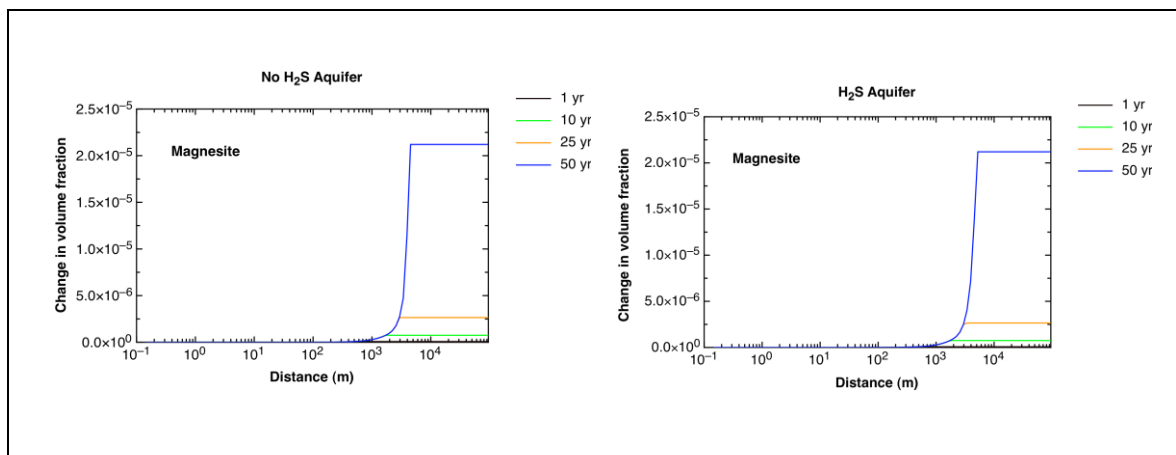


Figure 21: Change in volume fraction of magnesite as a function of radial distance after initiation of CO_2 injection for both non- H_2S and H_2S aquifers.

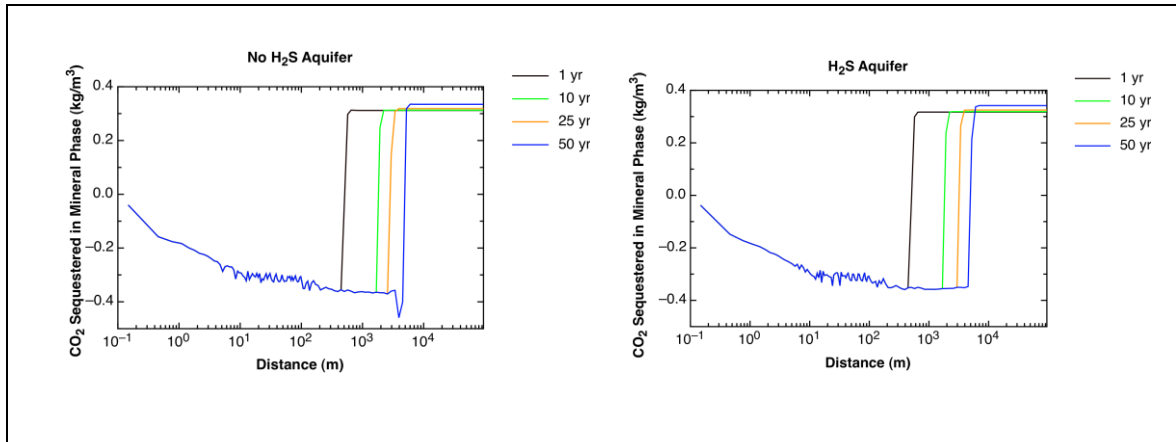


Figure 22: Amount of CO₂ sequestered in the reservoir in all mineral forms as a function of radial distance after initiation of CO₂ injection for both non-H₂S and H₂S aquifers.

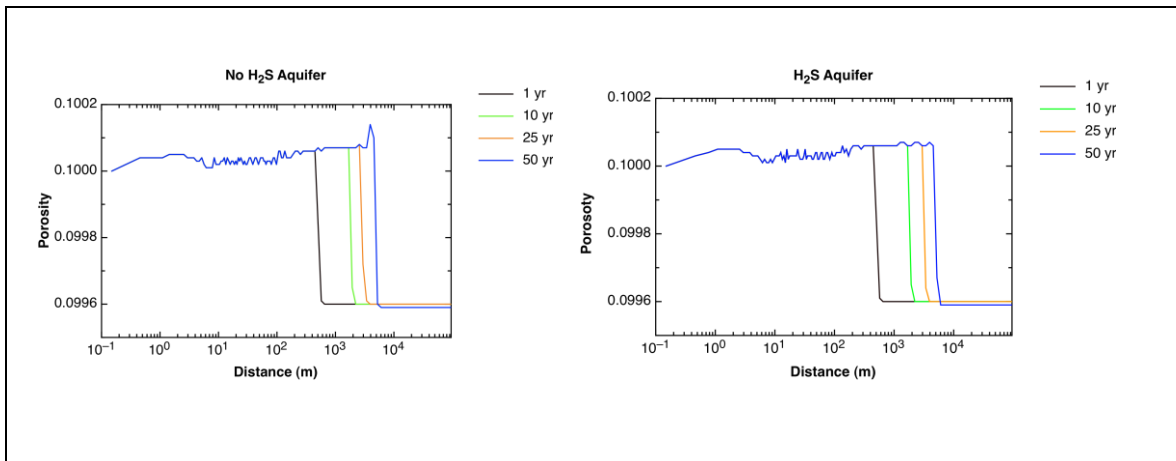


Figure 23: Changes in the porosity of the reservoir as a function of radial distance after initiation of CO₂ injection for both non-H₂S and H₂S aquifers.

3.3.3 Key Findings and Implications

Around the injection well, a region of **complete dehydration** was detected where the value of gas saturation is 1.00. Therefore, no pH values and concentrations of dissolved species are available for this region (Figures 15 to 18). This complete dehydration was probably due to the high rate of injection of dry CO₂, 1MT/yr (31.69 kg/sec). Table 15 summarizes the dehydration region as a function of time ranging from 19.7 m after one year to 136.1 m after 50 years.

Table 15: Injection time of CO₂ and radius of dehydrated region for both H₂S and non-H₂S aquifers.

Time (years)	Radius of the dehydrated region (m)
1.0	19.7
5.0	42.3
10.0	62.3
12.5	67.8
25.0	98.0
37.5	119.6
50.0	136.1

The pH of the initial fluid was 6.1. After one year of CO₂ injection, the reservoir fluid pH decreased to 5.1 within a radius of ~500 m around the injector with a pH increase to 6.4 outside of this region. The lowering of the pH value to 5.1 is caused by CO₂ injection resulting in formation of carbonic acid followed by some dissociation into bicarbonate. The latter results in a significant increase in bicarbonate concentrations in the same region from an initial value of 0.02 moles/kg to 1.25 moles/kg. A similar change in pH and bicarbonate concentrations was evident for all times but at increasing distances from the injector. The increase in bicarbonate concentrations in concert with the decrease in pH indicates that **solubility trapping** was occurring in this region. Table 16 summarizes the amount of CO₂ sequestered in the brine by solubility trapping over the 50-year injection phase. A gradual increase in sequestration of CO₂ over time from 34% to 56% was observed due to the larger fluid volumes available as the CO₂ moves progressively away from the injector into the reservoir.

Table 16: Injection time of CO₂ and amount of CO₂ stored as HCO₃⁻ in the reservoir waters for both H₂S and non-H₂S aquifers.

Time (years)	Amount of CO ₂ stored in brine as HCO ₃ ⁻ (MT)	Percentage of injected CO ₂ stored as HCO ₃ ⁻
1.0	0.28	34%
5.0	1.66	33%
10.0	3.96	39%
12.5	5.50	44%
25.0	10.8	43%
37.5	17.8	48%
50.0	27.8	56%

A decrease in the concentration of Ca^{2+} (Figure 17) and an increase in the concentration of Mg^{2+} (Figure 18) suggest that dolomite dissolution occurred while calcite precipitated. This was confirmed by dolomite abundances decreasing slightly by 0.3 % (from 80.4 to 80.1 %) due to dissolution within a ~500 m radius around the injector (Figure 19). Calcite showed the opposite trend, i.e., calcite was precipitating over the first ~500 m from an initial volume abundance of 16.1 to 16.4% (Figure 20). Net-carbonate dissolution resulted in minor amounts of ionic trapping. The amount of magnesite formed during the 50-year injection period was negligible, although it represented a new mineral forming in the rock matrix and another potential sink for the injected CO_2 over the longer term.

As CO_2 passed through the reservoir mineral dissolution initially occurred decreasing the amount of dolomite (Figure 19) resulting in more CO_2 released than sequestered. After one year, CO_2 sequestration was observed at a distance >570 m from the injector while this distance increased to ~5200 m after 50 years. The total amount of CO_2 sequestered in the mineral phase after 50 years was 0.334 kg/m^3 at a radial distance of 5200 m. This amount of mineral sequestration is low compared to the amount sequestered in the brine, ~1.25 moles/kg or 8.62 kg/m^3 . This indicates that ~26 times more CO_2 is sequestered in the brine compared to mineral trapping. Therefore, the amount of CO_2 sequestration by **mineral trapping** is negligible when compared to the amount of CO_2 sequestered due to solubility and ionic trapping.

The dissolution of dolomite and precipitation of calcite had a very minor effect on the porosity of the reservoir rock, causing a less than 0.1% decrease up to ~570 m after one year of injection and up to ~5200 m after 50 years of injection. While this change in porosity is very small, it is important to evaluate whether precipitation of calcite occurs in the pore or throat region. The latter may negatively impact permeability.

4. SUMMARY

An understanding of the baseline geochemistry of a formation is extremely important in designing a monitoring and modelling program for tracing the fate of injected CO₂ in a saline aquifer (see Lawton et al., this report). Despite the comparatively low number of wells in the Nisku Formation of the study area, a solid understanding of the chemical and isotopic compositions of fluids and gases was obtained by using data from a number of different sources (Section 1). Mineralogical information was compiled using 12 samples from various cores (Section 2). The obtained data were used for geochemical modelling (Section 3) with the goal to assess the fate of CO₂ in the saline aquifer over a 50-year injection period. The key findings of the simplified model runs are as follows:

1. CO₂ injection will likely create a dehydrated region around the injector with a radius increasing from 19.7 m after one year to 136.1 m after 50 years.
2. After one year of CO₂ injection, 34 % of the injected CO₂ will likely be sequestered in the brine as H₂CO₃ and HCO₃⁻ due to solubility trapping. After 50 years, 56% of the injected CO₂ will likely be sequestered in the brine via solubility trapping.
3. Minor amounts of dolomite are predicted to dissolve and small amounts of calcite will likely precipitate in the reservoir. The extent of ionic and mineral trapping of injected CO₂ will be, however, small compared to solubility trapping in the saline aquifer. According to the simplified model approximately 26 times more CO₂ will be sequestered in the brine via solubility trapping as compared to mineral trapping.
4. There were no significant observable differences in the chemical or mineralogical reactions between the H₂S and non-H₂S containing saline aquifers.
5. The porosity of the reservoir rocks will likely decrease in the CO₂ injection zone by less than 0.1%. It was impossible to assess the impact of the porosity change on permeability within the scope of this study.

REFERENCES

- [1] Schrag, D.P., 2007, Preparing to capture carbon. *Science*, 315. No. 5813, 812.
- [2] Raistrick, M., Mayer, B., Shevalier, M., Perez, R., Hutcheon, I., Perkins, E., and Gunter, B., 2006, Using chemical and isotopic data to quantify ionic trapping of injected carbon dioxide in oil field brines, *Environmental Science and Technology*, 40:6744-6749.
- [3] S. Emberley, S., Hutcheon, I., Shevalier, M., Durocher, K., Gunter, W.D., and E.H. Perkins, E.H. (2005), Geochemical monitoring of fluid-rock interaction and CO₂ storage at the Weyburn CO₂-injection enhanced oil recovery site, Saskatchewan, Canada. *Applied Geochemistry*, 29:1393-1401.
- [4] Gunter, W.D., and E.H. Perkins, E.H., and Hutcheon, I.E., 2000, Aquifer disposal of acid gases: modelling of water-rock reactions for trapping of acid wastes. *Applied Geochemistry*, 15:1085-1095.
- [5] Simpson, G., 1999, Sulfate reduction and fluid chemistry of the Devonian Leduc and Nisku formations in south-central Alberta. Ph.D. Thesis, University of Calgary (unpublished).
- [6] Bachu, S., Sauveplane, C.M., Lytviak, A.T., Hitchon, B., 1987, Analysis of Fluid and heat regimes in sedimentary basins: techniques for use with large data bases. *American Association of Petroleum Geology Bulletin*, 71:822-843.
- [7] de Caritat, P., Bloch, J., and Hutcheon, I., 1994. LPNORM: A linear programming normative analysis code; *Computers and Geosciences*, v. 20, p. 313-347.
- [8] Carpenter, S. J., and Lohmann, K. C. d18O and d13C variations in Late Devonian marine cements from the Golden Spike and Nevis Reefs, Alberta, Canada: *Journal of Sedimentary Petrology*, v. 59, (1989) p. 792-814.
- [9] Whittaker, S. G. and Mountjoy, E. W. Diagenesis of an Upper Devonian Carbonate-Evaporite Sequence: Birdbear Formation, Southern Interior Plains, Canada *Journal of Sedimentary Research, Section A: Sedimentary Petrology and Processes* Vol. 66 (1996) No. 5. (September), Pages 965-975
- [10] Machel, H.G. (1985) Facies and diagenesis of the Upper Devonian Nisku Formation in the subsurface of central Alberta. Ph.D. Thesis, McGill University, Montreal, 392.
- [11] Kharaka, Y. K., Gunter, W., Aggarwal, P. K., Perkins, E. H. and De Braal, J. D., 1988. SOLMINEQ88: a computer programme for geochemical modelling of water-rock reactions. *USGS Water Resources Investigation Report*, 88-4227.
- [12] Alberta Geological Survey, 2005, Test Case for Comparative Modelling of CO₂ Injection, Migration and Possible Leakage - Wabamun Lake Area, Alberta, Canada, Alberta Geological Survey Website, http://www.ags.gov.ab.ca/co2_h2s/wabamun/Wabamun_base.html
- [13] Duan, Z., Sun, R., and Zhu, C., 2007, Accurate thermodynamic model for the calculation of H₂S solubility in pure water and brines, *Energy and Fuels*, 21:2056-2065.
- [14] Xu, T., Pruess, K., and Brimhall, G., 1999, An improved equilibrium-kinetics speciation algorithm for redox reactions in variably saturated subsurface flow systems. *Computers and Geoscience*, 25:655-666.
- [15] Xu, T., Apps, J., and Pruess, K., 2004, Numerical simulation of CO₂ disposal by mineral trapping in deep aquifers. *Applied Geochemistry*, 19:917-936.

- [16] Weir, G.J., White, S.P., Kissling, W.M., 1995. Reservoir storage and containment of Greenhouse gases. In: Pruess, K. (ed.), Proceedings of the Tough Workshop '95. Lawrence Berkeley National Laboratory Report LBL-37200, pp. 223-238. Berkeley, California.
- [17] Ennis-King, J. and Patterson, L., 2003. Role of convective mixing of the long term storage of carbon dioxide in deep saline formations. Paper SPE 84344, Presented at Society of Petroleum Engineers Annual Fall Technical Conference and Exhibition, Denver CO, October 2003.
- [18] Van Genuchten, M.Th., 1980, A closed-form equation for predicting the hydraulic conductivity of unsaturated soils. *Soil Sci. Soc. Am. J.*, 44, 892–898.
- [19] Corey, A.T., 1954, The interrelation between gas and oil relative permeabilities. *Prod. Mon.* 38–41.
- [20] Palandri, J., Kharaka, Y.K., 2004, *A compilation of rate parameters of water–mineral interaction kinetics for application to geochemical modelling*. US Geol. Surv. Open File Report 2004-1068.64.
- [21] Xu, T., Apps, J., Pruess, K., Yamamoto, H., 2007, Numerical modelling of injection and mineral trapping of CO₂ with H₂S and SO₂ in a sandstone formation, *Chem. Geol.*, 242,i 319–346.

Seismic Characterizations of the Nisku Formation

Wabamun Area CO₂ Sequestration Project (WASP)

Authors

Abdullah Alshuhail

Don Lawton

Helen Isaac

Rev.	Date	Description	Prepared by
3	October 16, 2009	Final Draft	Abdullah Alshuhail, Don Lawton and Helen Isaac

Table of Contents

SUMMARY	9
1. Introduction	9
2. Data Calibration And Normalization	11
3. Regional Trend: 2d Seismic Data.....	15
4. Local Trends: 3d Seismic Data.....	19
5. Interpolation And Depth Conversion	26
6. Numerical Modelling	29
7. Seismic Attributes	34
8. Acoustic Impedance Inversion.....	40
9. Porosity Estimation	50
10. Rock Physics: Fluid Replacement Modelling	52
11. Conclusions	58
ACKNOWLEDGMENTS.....	59
REFERENCES.....	59

List of Tables

Table 1: Summary of available seismic and wireline data. HGFA refers to the WASP high-grade focus area.* Borehole data refers to both sonic log and Ireton top.	11
Table 2: Summary of some of the geological features within the multi-segment line (Figure 14).	25
Table 3: Comparison between the measured and estimated depth values using kriging algorithm (Figure 16). The difference between the two is also shown. The interpolation algorithm seems to honour the actual data, except at well 100163504701W500.	28
Table 4: Correlation coefficient (over a designed correlation window) between seismic data and synthetic seismogram from selected wells within the study area. The well locations are shown in the base map. The blue lines show the location of the 2D seismic (Figure 27) and the inline (Figure 30) invoked in the inversion.	42
Table 5: Parameters pertaining to the main constituents in the Gassmann FRM. The pressure, temperature, porosity and thickness of the Nisku Formation were 15 MPa, 50.3 Co, 9%, and 56 m respectively (Michael et al., 2008). Salinity and viscosity were adopted from Michael et al. (2008) whereas the rest of the parameters were calculated using the CREWES Fluid Property Calculator (Ursenbach, 2009) which is based on a paper by Batzle and Wang (1992) and the Peng-Robinson (1976) equation of state.	54

List of Figures

Figure 1: Base map showing the distribution of the seismic and borehole data. Cyan shapes indicate bodies of water.	10
Figure 2: Flowchart outlining the major steps followed in the seismic data calibration and normalization.	11
Figure 3: Seismic-to-well tie at the water source well (1F1-11-29-45-2W5). The location of the well and the seismic line (blue) are shown on the map. The correlation coefficient is 0.92 over the outlined zone (dashed rectangle) in the bottom image.	13
Figure 4: The 2D seismic line shown in Figure 3 with the synthetic track inserted at the well location (1F1-11-29-45-2W5). The seismic-to-well tie over the zone of interest enclosing the Nisku event (dashed rectangle) is enlarged in the bottom image.	14
Figure 5: Line 1 of the LITHOPROBE regional 2D seismic data with some of the major seismic events identified, including the Nisku. The location of Line 1 is shown by the blue line in the inset base map. The dashed arrow in the inset base map points to the location of a sudden change in the time structure (dashed rectangle), which could be associated with the Moon Lake reef boundary or simply a result of Line 1 turning into the updip direction. BH Lake is the Beaverhill Lake event.	15
Figure 6: Line 2 of the LITHOPROBE regional 2D seismic data with some of the major seismic events, identified including the Nisku. The location of Line 2 is shown by the blue line in the inset base map. The dashed arrow in the inset base map points to the location of the transition between the Nisku bank and Nisku shale basin (dashed rectangle). BH Lake is the Beaverhill Lake event.	16
Figure 7: Line 3 of the LITHOPROBE regional 2D seismic data with some of the major seismic events identified, including the Nisku. The location of Line 3 is shown by the blue line in the inset base map. The dashed arrow in the inset base map points to the location of the dashed ellipse, which marks a local anomaly interpreted to be caused by a discontinuity in the Wabamun event. BH Lake is the Beaverhill Lake event.	17
Figure 8: Line 4 of the LITHOPROBE regional 2D seismic data with some of the major seismic events identified, including the Nisku. The location of Line 4 is shown by the blue line in the inset base map. The dashed arrow in the inset base map points to the location of the dashed rectangle enclosing a local depression in the Wabamun event. BH Lake is the Beaverhill Lake event.	18
Figure 9: The time structure of the Nisku event after data calibration. The dashed black rectangle shows the extent of the zoom-in display over the study area in Figure 10.	20
Figure 10: Zoom-in display of the Nisku time structure map in Figure 9. The locations of some of the major anomalies are specified: Wabamun karsting (see Figure 14), Wabamun discontinuities, and the Nisku local time low. It should be emphasized that the karsting and discontinuity effects shown here are the footprints of those anomalies and do not indicate that the Nisku has been physically affected.	21
Figure 11: NRMS amplitude map of the Nisku event after data calibration and RMS amplitude normalization. Note the strong variations in the Nisku amplitude map compared to the time structure map. The dashed black rectangle shows the extent of the zoom-in display over the study area in Figure 12.	22

Figure 12: Zoom-in display of the Nisku NRMS amplitude map in Figure 11. Some of the major amplitude anomalies are specified: Wabamun karsting (see Figure 14), Wabamun discontinuities, and the Nisku amplitude low. It should be emphasized that the karsting and discontinuity effects shown here are the footprints of those anomalies and do not indicate that the Nisku has been physically affected..... 23

Figure 13: A multi-segment seismic section passing through some of the geological features within the reference 3D volume. The base map shows the location and orientation of the multi-segment section. The nodes are shown at their corresponding location along the horizontal axis. The right side of the colour scale in the base map represents the amplitude within the section (-3 to 3). The dashed rectangle indicates the extent of the zoom-in display in Figure 14. 24

Figure 14: A zoom-in display of the multi-segment line through the 3D volume in Figure 13. Segment 1-2 passes through the karsting (k) originating in the Wabamun event. Segments 2-3 and 3-4 cross local Wabamun discontinuities (d). Segments 4-5, 5-6, and 6-7 show an example of the Nisku amplitude changing from high (h) to low (l) to high (h) again. Note the broadening in the Nisku cycle in segment 5-6. Segment 7-8 shows some amplitude anomalies between 1150 and 1200 ms, which are interpreted to be associated with the Cretaceous strata. The change from moderate (m) to high (h) Nisku amplitude is illustrated in segment 8-9. Segment 8-9 also traverses an area of local Nisku amplitude thinning (t), which is mapped by the seismic attribute amplitude thickness of the peak (ATP). 25

Figure 15: Interpolated time structure map (Figure 9) using a kriging algorithm with a grid size of 50 × 50 m. 26

Figure 16: Interpolated depth structure map using a kriging algorithm with a grid size of 50 × 50 m. 27

Figure 17: Sequential display of the normal incidence synthetic seismogram in which the Nisku event amplitude is modelled as function of thickness and average P-wave velocity. The top of the Nisku event is identified as the peak at approximately 1130 ms (the green bracket along the time axis approximates the frequency cycle through the formation). In each blue bracket (thickness effect), there are 11 traces, each representing the seismic amplitude associated with that thickness and an average Nisku P-wave velocity increasing from 5500 m/s to 6500 m/s at an increment of 100 m/s. The modelling was undertaken using well 100-10-05-052-02W5. The actual Nisku thickness and average P-wave velocity at this well are 100 m and 6100 m/s, respectively..... 30

Figure 18: Nisku event amplitude (top) and time (bottom) as a function of thickness and average P-wave velocity. The actual Nisku thickness and average P-wave velocity are 100 m and 6100 m/s, respectively. The maps represent the Nisku amplitude and time horizons that resulted from picking the peak amplitude corresponding to the Nisku event in Figure 17. The black dashed rectangle outlines the most likely Nisku thickness and average velocity values within the study area based on well control. The results suggest that the Nisku average P-wave velocity (or impedance) effect is far more significant than the thickness effect. Thus, the highest sensitivity is along the vertical axis. 31

Figure 19: Nisku amplitude modelling result in which the difference between the thickness and average P-wave velocity effect on the Nisku event amplitude is evident. The actual Nisku thickness and average P-wave velocity are 100 m and 6100 m/s, respectively..... 32

Figure 20: Ireton event amplitude (top) and time (bottom) as a function of Nisku thickness and average P-wave velocity. The maps represent the Ireton amplitude and time horizons that resulted from picking the trough amplitude corresponding to the Ireton event in Figure 17. The black dashed rectangle outlines the most likely Nisku thickness and average P-wave velocity values within the study area based on well control. The results suggest that the effect of the Nisku average P-wave velocity (or impedance) footprint on the Ireton event is far more significant than the thickness effect. 33

Figure 21: Average NRMS Nisku amplitude over a 10 ms window (centred on the Nisku horizon pick). In addition to the patterns already defined in the NRMS Nisku amplitude map (Section 4 and Figure 12), another low amplitude pattern emerges from the map. The NRMS amplitude averaging window of 10 ms seems appropriate except within the north-eastern region of the easternmost 3D volume. The relative position to the large study area is shown by the dashed rectangle in the base map in Figure 11. 35

Figure 22: Amplitude thickness of the Nisku peak (ATP) in ms. The inset schematic illustrates the concept of ATP. Note the elongated (NE-SW) thinning pattern that is not captured by the NRMS amplitude map. See the multi-segment line in Figures 13 and 14 for a cross-sectional view of those anomalies. The relative position to the large study area is shown by the dashed rectangle in the base map in Figure 11. 36

Figure 23: Amplitude thickness of the Nisku peak (ATP in ms) of the synthetic seismogram in Figure 17. The ATP is highly sensitive to variations in the Nisku Formation thickness and average P-wave velocity over the expected range of those parameters. There is a distinct separation in the velocity effect over the expected Nisku Formation thickness (~ 40 – 80 m). The separation seems to be occurring around the tuning thickness (~ 60 m) and the corresponding average P-wave velocity (~ 6100 m/s). 37

Figure 24: Inline difference (coherency) attribute of the Nisku event in ms. The difference method shows more sensitivity toward discontinuities within the Nisku compared with other seismic attributes as can be seen, for instance, with the Wabamun karsting effect on the Nisku event. See the multi-segment line in Figures 13 and 14 for a cross-sectional view of some of the identified anomalies. The relative position to the large study area is shown by the dashed rectangle in the base map in Figure 11. 38

Figure 25: Crossline difference (coherency) attribute of the Nisku event in ms. Note the sensitivity, also, to the direction in which the difference is measured compared to the inline difference in Figure 24. The crossline difference was not as robust as the inline difference in defining geologic features within the reference 3D volume (e.g., the Wabamun karsting effect). However, it performed better in defining some of the features associated with other seismic volumes, such as the local time low (also shown in the time structure map in Figure 10). See the multi-segment line in (Figures 13 and 14) for a cross-sectional view of some of the identified anomalies. The relative position to the large study area is shown by the dashed rectangle in the base map in Figure 11. 39

Figure 26: Flowchart outlining the major steps followed in the seismic inversion to extract the acoustic impedance map of the Nisku event. 41

Figure 27: Seismic section near the water source well (Figure 3 and Table 4). The green curve at the well location is the correlated synthetic seismic trace. The correlation coefficient is 0.92. 43

Figure 28: The initial acoustic impedance model. The blue curve at the well location is the correlated synthetic seismic trace while the black curves are the actual seismic traces. 43

Figure 29: Estimated acoustic impedance along the 2D seismic line near the water source well (Figure 3) using band-limited (top) and model-based (bottom) inversion methods. The inserted blue curve at the well location represents the computed acoustic impedance from the sonic and density logs. The black curves represent the acoustic impedance from the band-limited inversion whereas in the model-based inversion they represent the misfit error..... 44

Figure 30: Inline extracted from the reference 3D seismic volume (Table 4). The green curve at the well location is the correlated synthetic seismic trace. The correlation coefficient is 0.80. 45

Figure 31: The initial acoustic impedance model corresponding to the inline in Figure 30. The blue curve at the well location is the correlated synthetic seismic trace while the black curves are the actual seismic traces..... 45

Figure 32: Estimated acoustic impedance of the inline in Figure 30 and Figure 31 using band-limited (top) and model-based (bottom) inversion methods. The inserted blue curve at the well location represents the computed acoustic impedance from the sonic and density logs. The black curves refer to the acoustic impedance from the band-limited inversion whereas in the model-based inversion they represent the misfit error..... 46

Figure 33: Estimated Acoustic impedance (I_p) map of the Nisku Formation using band-limited inversion. Due to lack of well control, the inversion was not performed on the entire dataset. The relative position to the large study area is shown by the dashed rectangle in the base map in Figure 11. 47

Figure 34: Estimated Acoustic impedance (I_p) map of the Nisku Formation using model-based inversion. Due to lack of well control, the inversion was not performed on the entire dataset. The relative position to the large study area is shown by the dashed rectangle in the base map in Figure 11. 48

Figure 35: Acoustic impedance (I_p) of the synthetic seismogram in Figure 17 using band-limited (top) and model-based (bottom) inversion methods. Similar to the seismic amplitude response, the acoustic impedance shows high sensitivity toward variations in the Nisku Formation average P-wave velocity rather than thickness. The maps illustrate the direct proportionality between average P-wave velocity and acoustic impedance. Note the similarity in the results except for the small difference in the magnitude of the acoustic impedance due to scaling issues. 49

Figure 36: Estimated bulk porosity of the Nisku event using Wylie’s time-average equation with bulk velocity derived from the band-limited acoustic impedance inversion. The relative position to the large study area is shown by the dashed rectangle in the base map in Figure 11..... 51

Figure 37: Predicted changes in the average acoustic (\bar{I}_p) and shear (\bar{I}_s) impedance of the Nisku Formation as a result of increasing the CO₂ saturation from 0 to 100%. The highest incremental change is associated with increasing the CO₂ saturation from 0 to 20%. Shortly after that, the acoustic impedance reaches a plateau. The shear impedance, on the other hand, is rather insensitive to the fluid replacement..... 55

Figure 38: Top left: Offset dependent synthetic seismogram generated using the Zoeppritz equations after NMO correction and stacking; all 11 traces are identical (in the base survey) and they represent an initial condition in which the reservoir is 100% brine saturated. Top right: the same offset dependent synthetics but in this case (monitor survey) each trace has undergone a saturation transformation between brine and CO₂ as indicated by the values along the horizontal axis (red label). Bottom: the difference between the monitor and base. Changes in reservoir properties were only applied to the zone of interest, i.e., Nisku (2238 m) to Ireton (2288 m). The highest incremental change is associated with the first 10% of CO₂ saturation (trace 2). The subtle difference between the two surveys suggests that the Nisku matrix is so stiff that the fluid replacement process is only having a small effect on the observed seismic response. The modelling was undertaken using the water source well (1F1-11-29-45-2W5). 56

Figure 39: Mosaic display of the fluid substitution effect on the time and amplitude response of the Nisku and Ireton events, respectively, between the base and monitor surveys: (a) difference in the Nisku event two-way time (ms); (b) difference in the Ireton event two-way time (ms); (c) difference in the Nisku event amplitude; (d) difference in the Ireton event amplitude. Each horizon is obtained by subtracting the corresponding horizons between the monitor and base surveys (difference = monitor - base) in Figure 38. In all the plots the highest incremental change in time and amplitude is associated with the initial increase in CO₂ saturation (i.e., from 0 to 10%). Shortly after that, the seismic response reaches a plateau and becomes virtually unresponsive to the increase in CO₂ saturation. The modelling was undertaken using the water source well (1F1-11-29-45-2W5) shown in Figure 3. 57

SUMMARY

Seismic characterization of the Nisku Formation in the Lake Wabamun area has revealed two primary groups of anomalies. The first group consists of anomalies interpreted to be footprints of geological discontinuities induced by dissolution in the overlying Wabamun Formation. Even though there is no evidence to indicate that the integrity of the Nisku Formation has been compromised, such geologic discontinuities should be taken into consideration if CO₂ were to be injected into the Nisku Formation. Regional 2D lines show no sign of faulting in the study area which might cause these observed discontinuities.

The second group of anomalies outlines contrasts in acoustic impedance caused by lateral changes in lithology and/or porosity of the Nisku Formation. This interpretation is constrained by well control and supported by seismic modelling, which suggests that changes in Nisku thickness over the range encountered in the study area has an insignificant effect on seismic amplitudes. If so, then seismic amplitude mapping may provide one approach in pursuing favourable sites for CO₂ injection in addition to acoustic impedance, which has rather limited implementation due to the scarcity of well control with appropriate log types and formation tops. In addition to the conventional time structure and amplitude maps, several seismic attributes were generated to further refine our interpretation of both geologic discontinuities and lithological variations of the Nisku Formation in the study area.

Our analysis revealed favourable low-impedance, high-porosity locations that could be potential injection sites. Finally, fluid replacement modelling was undertaken to predict the feasibility of time-lapse seismic monitoring for detecting an injected CO₂ plume. The results suggest that changes in seismic response will most likely be subtle and that the plume will probably be at the lower threshold of seismic detectability.

1. INTRODUCTION

Seismic characterization of the Nisku Formation in the Wabamun Area CO₂ Sequestration Project (WASP) high-grade focus area (HGFA) is based on analyzing and interpreting post-stack seismic datasets comprising more than two hundred 2D seismic lines and seven 3D volumes. The primary objectives were:

1. To map the Nisku Formation within the WASP high-grade focus area using available seismic data.
2. To delineate the seismic character of the Nisku Fm. (i.e., porosity/lithology indicators).
3. To identify geologic features that may compromise the Nisku Fm. caprock (e.g., anomalies and karsting).
4. To extract appropriate attributes from the seismic data for input into the static geological model.

The study area is surrounded by two major hydrocarbon resources in Alberta; the Leduc reef play (east) and the Moon Lake reef play (northwest). Thus, part of the study area was mapped using vintage surface seismic data that had been acquired as part of hydrocarbon exploration in the area. Table 1 gives an outline of the volume and approximate areal coverage of the analyzed seismic data as well as the number of wells with appropriate log curves and formation tops that were available for integration into the seismic data analysis. No new seismic data were acquired as part of Phase I of the project. The spatial distribution of the available seismic data is illustrated in Figure 1, and shows that the data coverage is not distributed uniformly. Thus characterization was constrained to

those areas with good coverage. The 2D seismic data were used primarily for identifying long-wavelength structures, whereas the high-quality 3D data were used for detailed mapping, inversion and generation of seismic attributes.

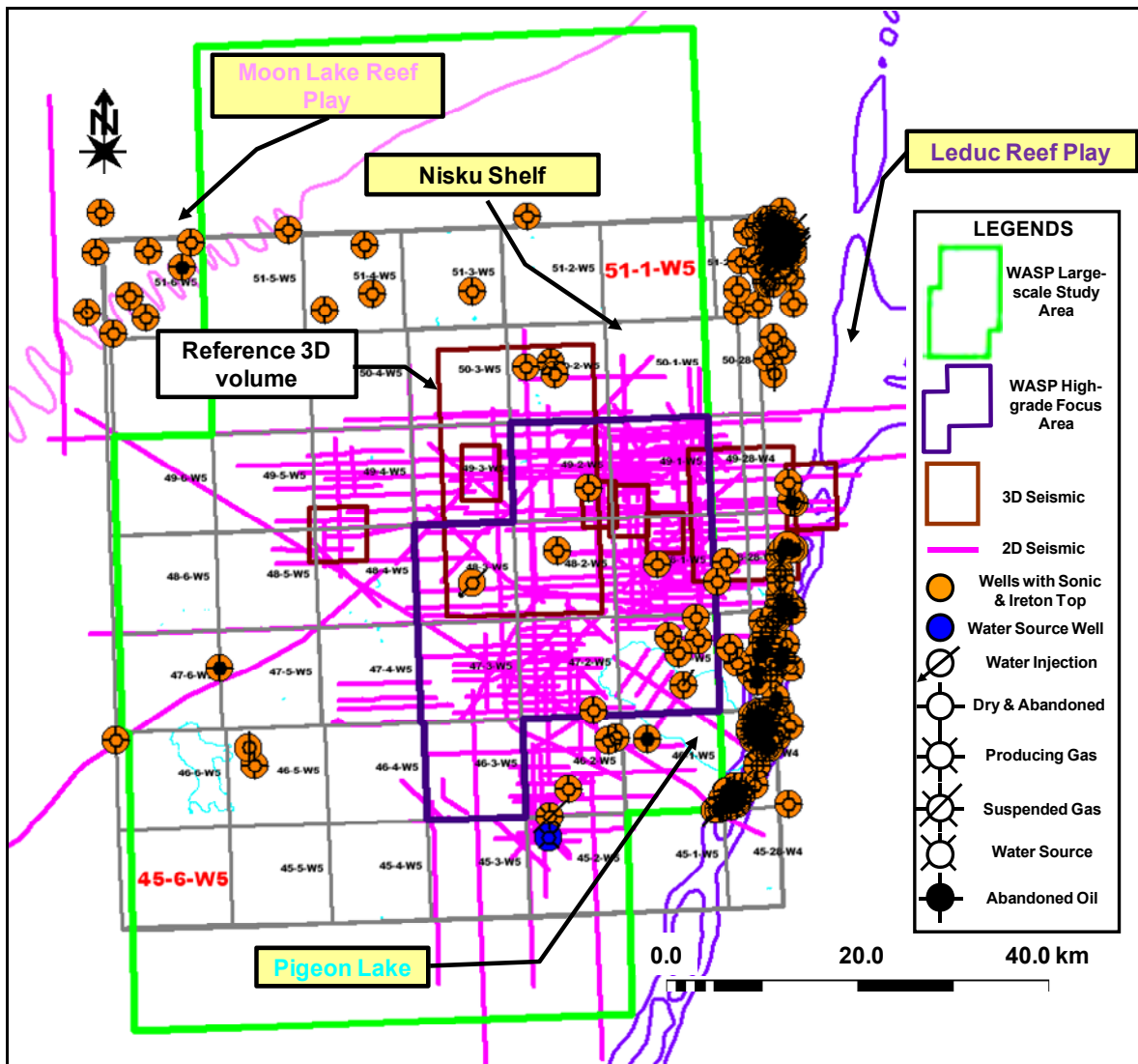


Figure 1: Base map showing the distribution of the seismic and borehole data. Cyan shapes indicate bodies of water.

Table 1: Summary of available seismic and wireline data. HGFA refers to the WASP high-grade focus area.* Borehole data refers to both sonic log and Ireton top.

Source	Data Type	Description
Seismic Data	2D	200 seismic lines, approximately 2,432 km in total length
	3D	7 seismic volumes covering an area of 419 km ²
Borehole Data*	Within HGFA	7 wells, only 2 coincide with seismic coverage
	Nearby HGFA	Over 15 wells, only 6 coincide with seismic coverage

2. DATA CALIBRATION AND NORMALIZATION

The 2D and 3D seismic datasets have different acquisition and processing specifications and were acquired over many years prior to this project being undertaken. Therefore, prior to interpretation, inversion and attribute analysis, two primary steps were undertaken: data calibration and amplitude normalization. These steps were necessary to account for the vintage and datum differences within the data. Figure 2 gives an overview of the data calibration and normalization approach.

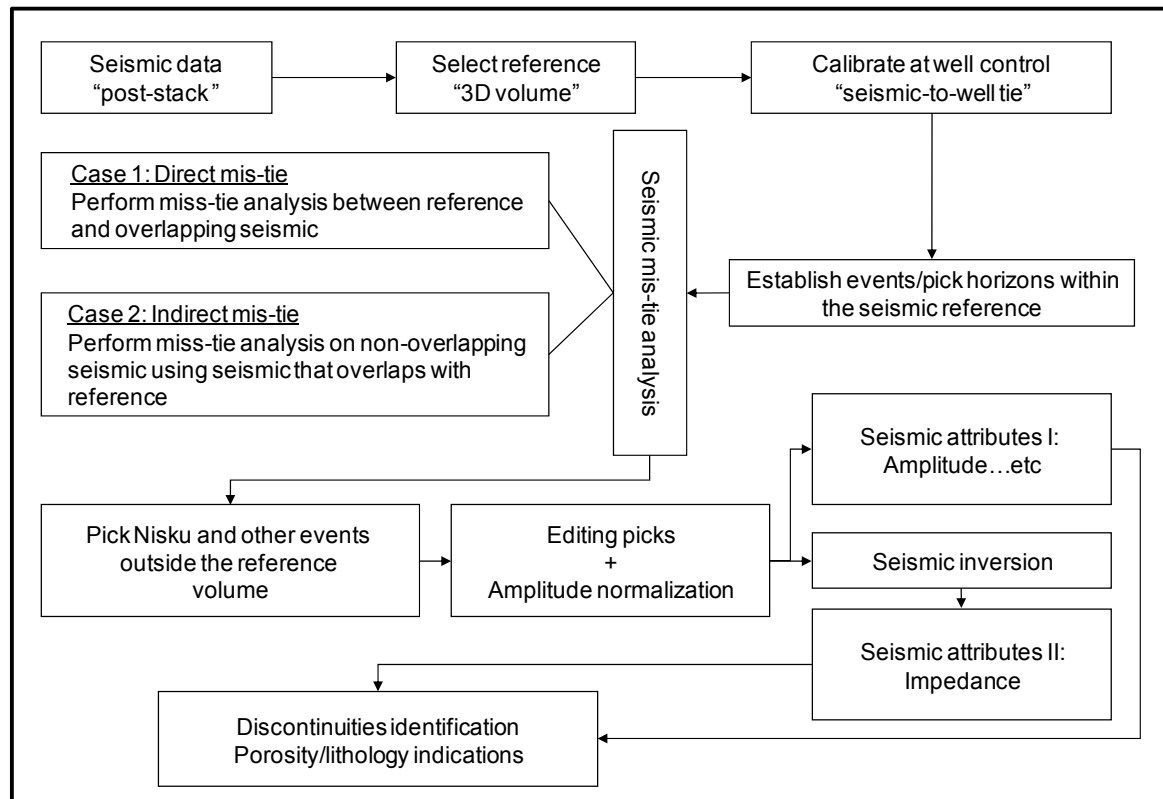


Figure 2: Flowchart outlining the major steps followed in the seismic data calibration and normalization.

Starting with the reference 3D volume, which is the largest brown rectangle in the middle of Figure 1, the majority of the seismic events were identified and picked. The seismic-to-well tie was made at various locations using available borehole data. Overall, the seismic data exhibit good ties to the synthetic seismograms, with the correlation coefficient ranging from 0.7 to 0.9. Figure 3 shows examples of the seismic-to-well tie near the water source well (1F1-11-29-45-2W5), at which a very good correlation is obtained (0.92).

Following the seismic-to-well tie and identification of seismic events within the reference 3D volume, data calibration was begun by first applying a time and phase shift and amplitude adjustments to those 2D seismic lines overlapping the reference 3D volume. The calibrated overlapping lines were then used to calibrate those that do not overlap the reference 3D volume. The process was repeated until all data were calibrated with respect to the reference 3D volume. Once the data were calibrated, their seismic amplitudes were normalized to a root-mean square (RMS) value of 1.0 using a time window designed to include the Nisku Formation.

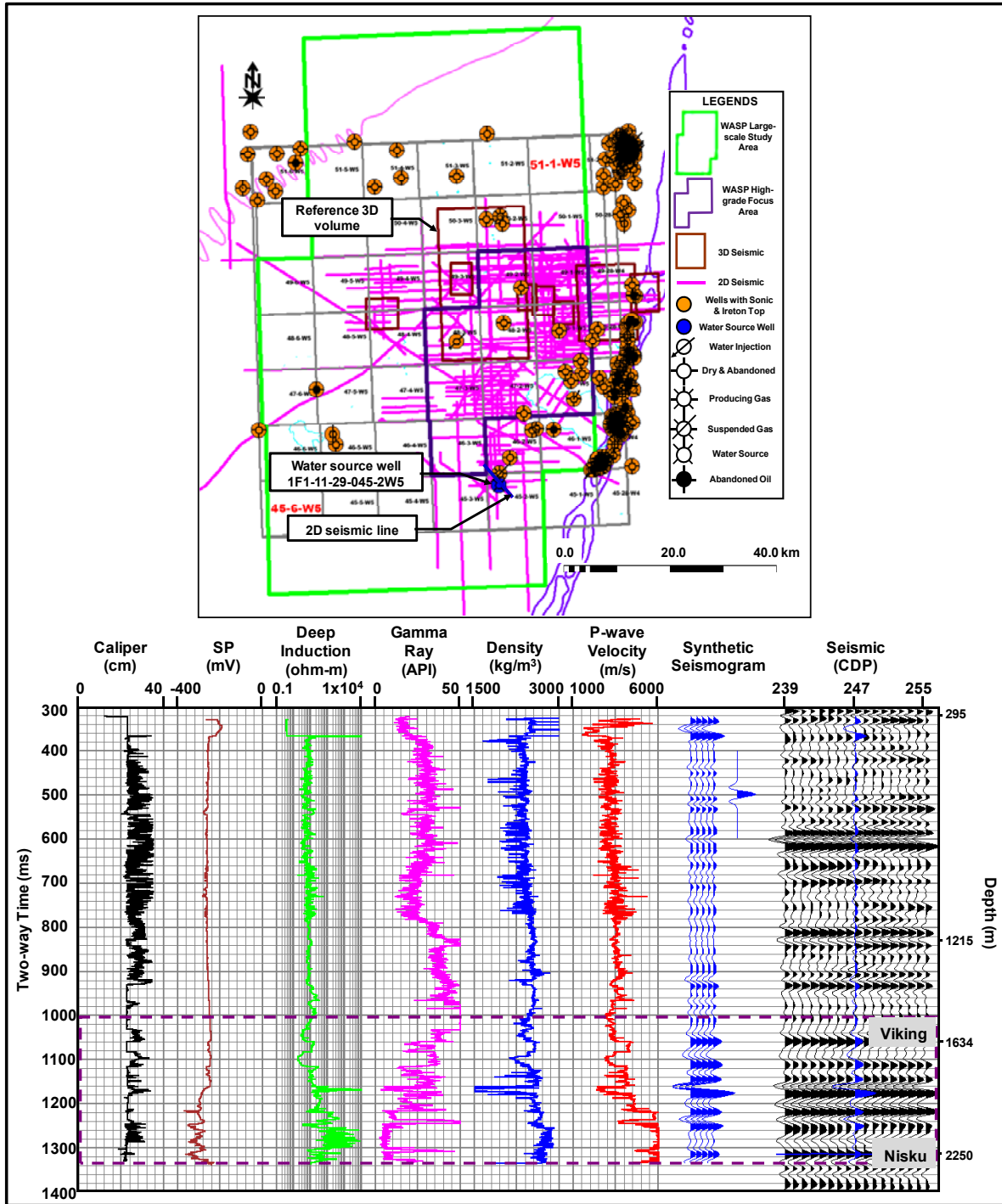


Figure 3: Seismic-to-well tie at the water source well (1F1-11-29-45-2W5). The location of the well and the seismic line (blue) are shown on the map. The correlation coefficient is 0.92 over the outlined zone (dashed rectangle) in the bottom image.

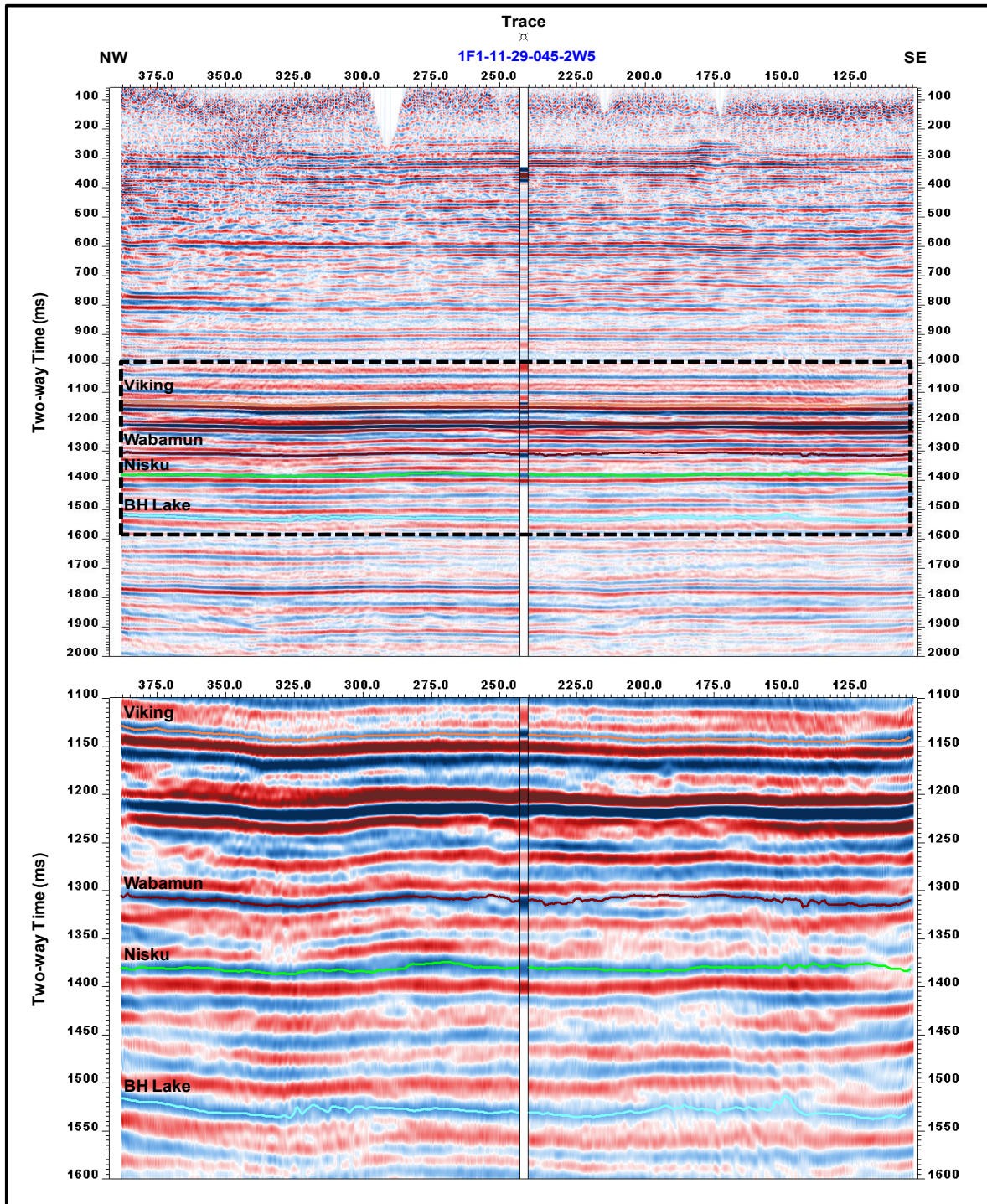


Figure 4: The 2D seismic line shown in Figure 3 with the synthetic track inserted at the well location (1F1-11-29-45-2W5). The seismic-to-well tie over the zone of interest enclosing the Nisku event (dashed rectangle) is enlarged in the bottom image.

3. REGIONAL TREND: 2D SEISMIC DATA

The regional seismic expression encountered in the study area is depicted in four of the regional LITHOPROBE 2D seismic lines (Figure 5 through 8). Several seismic events were identified throughout these regional lines, including: the Viking, the Wabamun, the Nisku, and the Beaverhill Lake events, as well as a Precambrian marker. The Viking Formation is composed of sandstone and is part of the Lower Cretaceous series. The Wabamun Formation, on the other hand, is mainly made of dolostone and it is the shallowest formation in the Upper Devonian strata that also includes the underlying dolomitized Nisku Formation. The reflection from the Beaverhill Lake Formation marks the transition between the Upper and Middle Devonian. The Precambrian marker represents the reflection from what it thought to be the Basal Sandstone Formation. In all the seismic lines the Nisku and underlying top Ireton events are represented by one period of the seismic data.

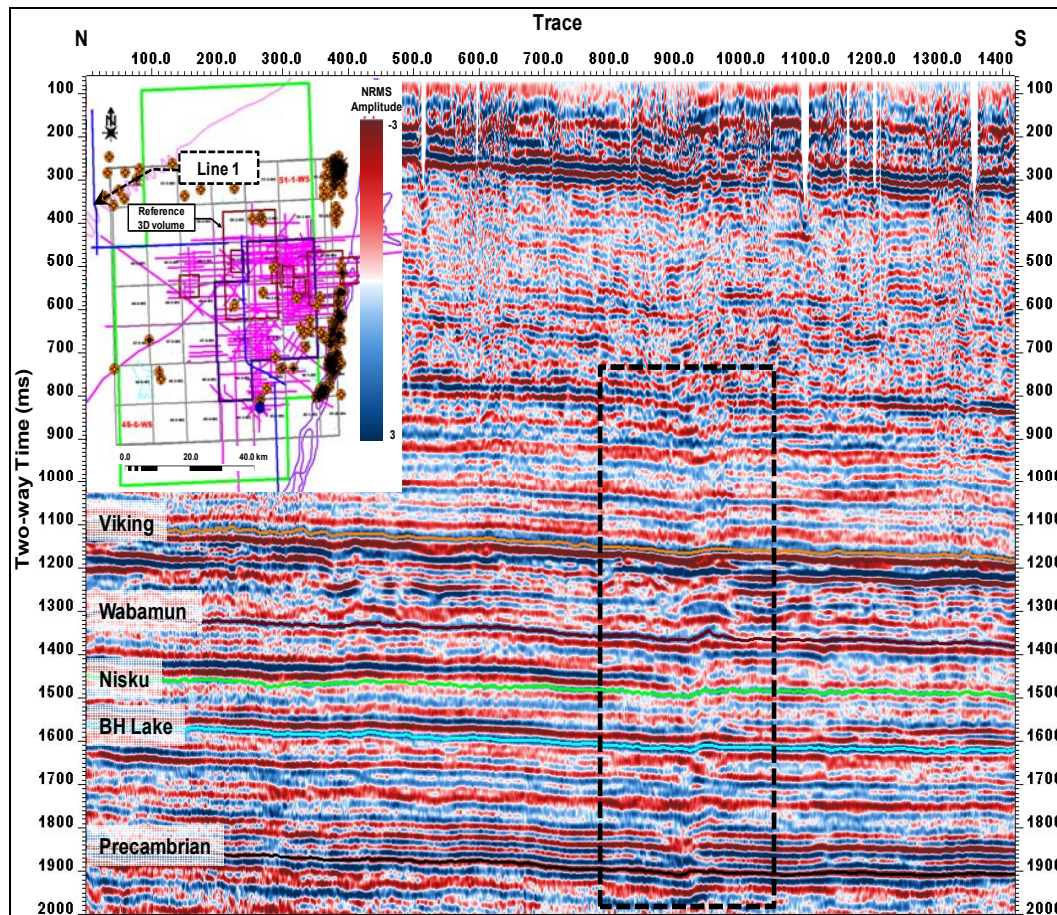


Figure 5: Line 1 of the LITHOPROBE regional 2D seismic data with some of the major seismic events identified, including the Nisku. The location of Line 1 is shown by the blue line in the inset base map. The dashed arrow in the inset base map points to the location of a sudden change in the time structure (dashed rectangle), which could be associated with the Moon Lake reef boundary or simply a result of Line 1 turning into the updip direction. BH Lake is the Beaverhill Lake event.

In Line 1 (Figure 5) there is a small change in the Nisku time structure as the line turns southward at trace 950 (within the dashed rectangle). This occurs near the Moon Lake reef boundary but it also coincides with a change in the survey orientation. A more interesting anomaly is outlined by the dashed rectangle in Line 2 (Figure 6), which marks the interpreted transition between the Nisku bank and the Nisku shale basin to the northwest. The regional dip, which is toward the southwest, is seen clearly on both Lines 1 and 2. In Line 3 (Figure 7), which traverses the WASP focus area in the north-south direction, the Nisku event is identified at approximately 1.37 s and is fairly flat. On Line 4 (Figure 8), the Nisku event is also flat and no major anomalous features can be identified in the Nisku. A sudden drop in the overlying Wabamun event is observed between traces 850 and 1100.

The variation in the Nisku event amplitude, as observed in these regional LITHOPROBE 2D sections, can be clearly seen in the NRMS amplitude map (Figure 11). The integrity of the Nisku Formation, as well as the integrity of the caprock (Calmar Formation), does not seem to be compromised in the focus area. Furthermore, none of the regional seismic lines exhibits any sign of major faulting. However, the dashed ellipse in Line 3 (Figure 7) indicates the location of a local discontinuity in the Wabamun event. This and similar anomalies are more clearly imaged by the 3D seismic data and will be discussed in the next section.

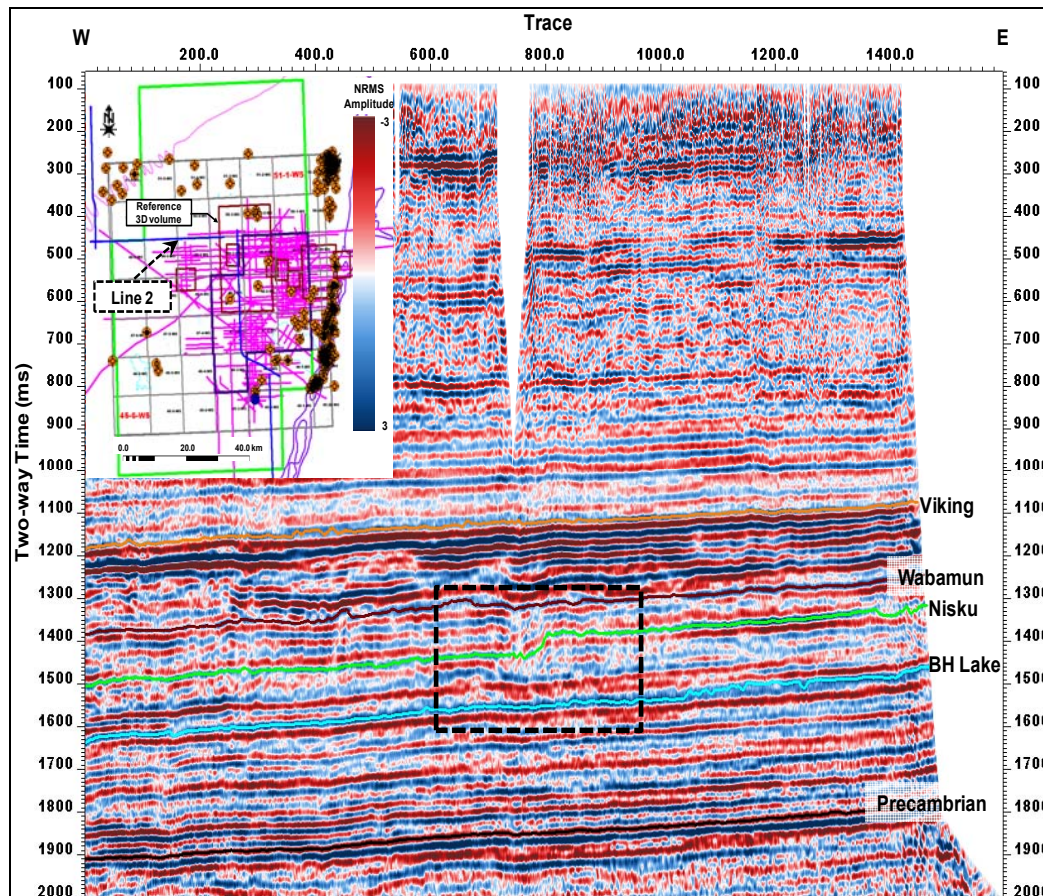


Figure 6: Line 2 of the LITHOPROBE regional 2D seismic data with some of the major seismic events, identified including the Nisku. The location of Line 2 is shown by the blue line in the inset base map. The dashed arrow in the inset base map points to the location of the transition between the Nisku bank and Nisku shale basin (dashed rectangle). BH Lake is the Beaverhill Lake event.

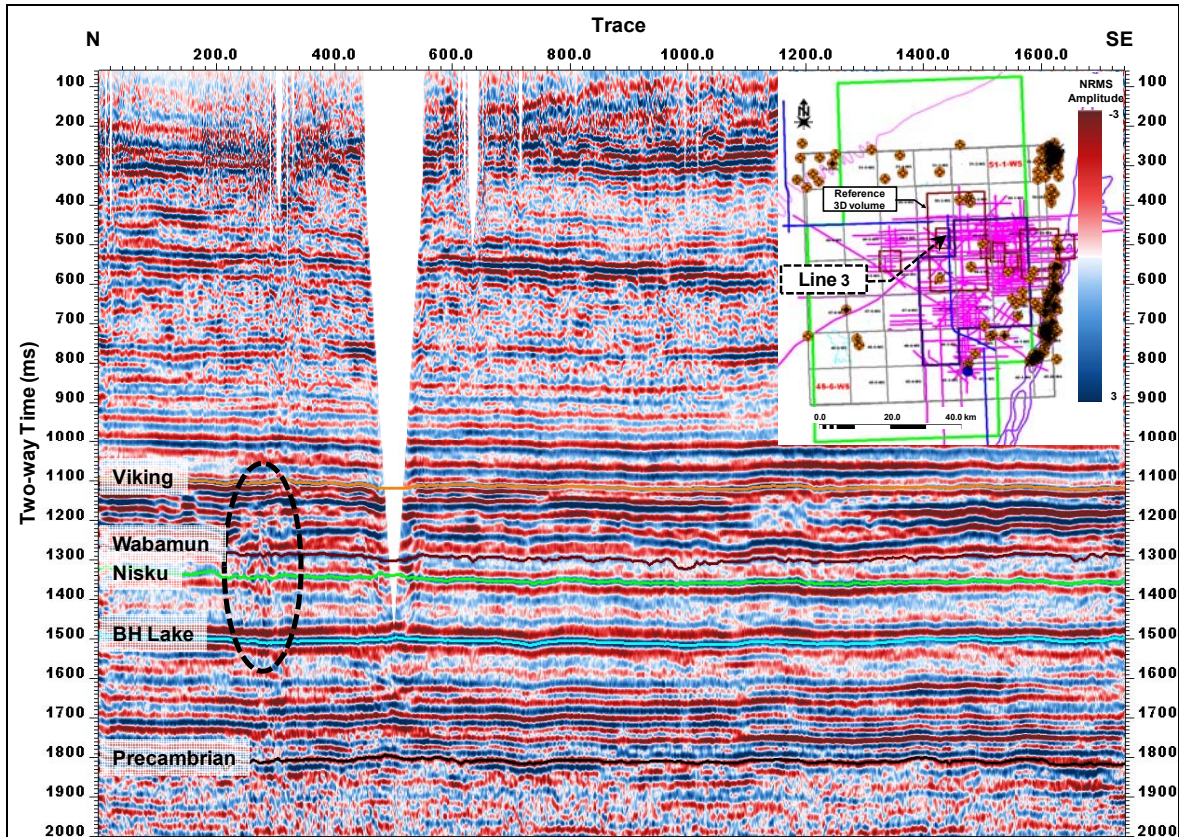


Figure 7: Line 3 of the LITHOPROBE regional 2D seismic data with some of the major seismic events identified, including the Nisku. The location of Line 3 is shown by the blue line in the inset base map. The dashed arrow in the inset base map points to the location of the dashed ellipse, which marks a local anomaly interpreted to be caused by a discontinuity in the Wabamun event. BH Lake is the Beaverhill Lake event.

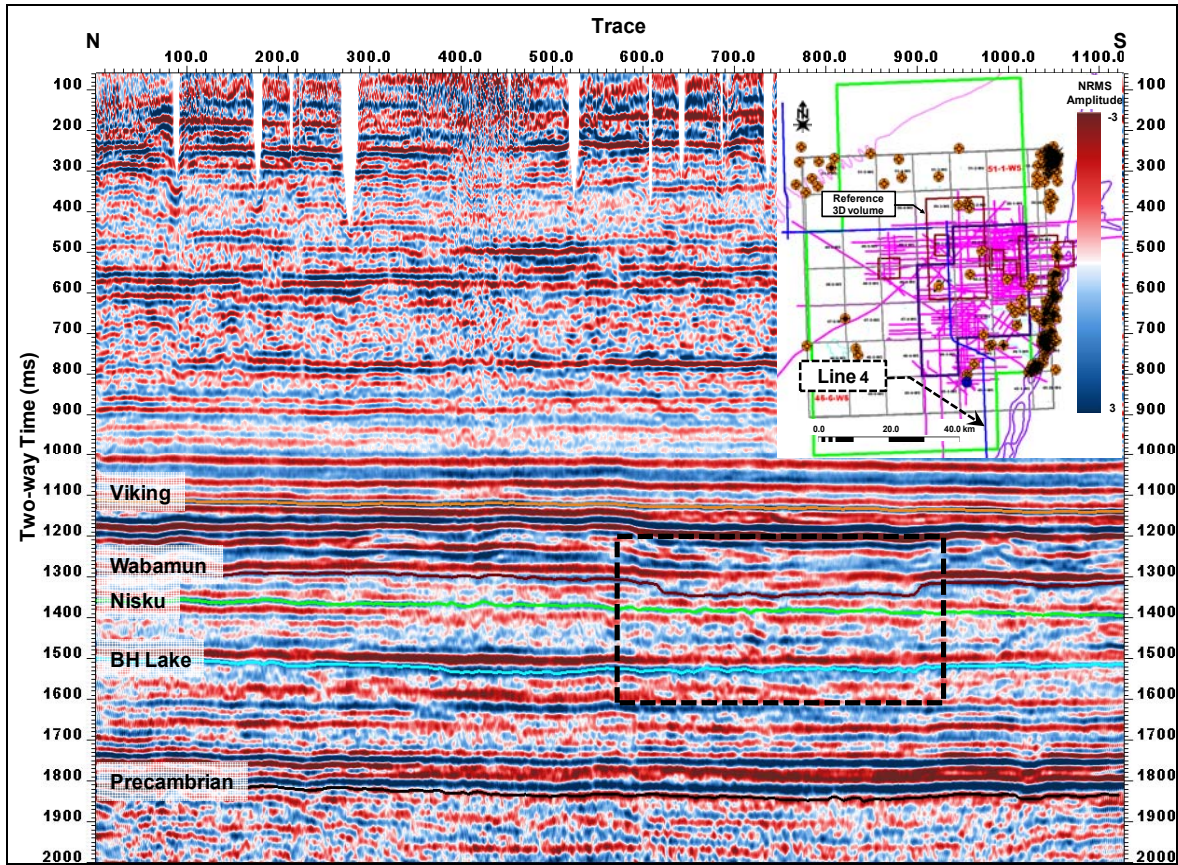


Figure 8: Line 4 of the LITHOPROBE regional 2D seismic data with some of the major seismic events identified, including the Nisku. The location of Line 4 is shown by the blue line in the inset base map. The dashed arrow in the inset base map points to the location of the dashed rectangle enclosing a local depression in the Wabamun event. BH Lake is the Beaverhill Lake event.

4. LOCAL TRENDS: 3D SEISMIC DATA

The interpretation of the Nisku Formation in the WASP focus area is fundamentally driven by the analysis of the time structure (Figure 9 and 10) and NRMS amplitude maps (Figure 11 and 12) from the 3D seismic data after calibration and amplitude normalization. In Figure 12 it is evident that only the amplitudes extracted from the 3D seismic data are reliable as the 2D seismic data are of poorer quality and do not exhibit a consistent areal pattern from which useful information could be extracted.

The time structure of the Nisku (Figure 10) is rather smooth and does not exhibit any significant variations within the WASP focus area except for following the regional dip in the northeast-southwest direction. There are local lows, such as the one associated with the discontinuity and the depression in the Nisku time structure east of the reference 3D volume (Figure 10). However, the Nisku NRMS amplitude map (Figure 12) has proven more robust in identifying several anomalies in the area. Those include karsting (k) and discontinuities (d) originating in the Wabamun, as well as low (l) and high (h) amplitude anomalies and thinning (t) of the Nisku Formation itself.

In order to delineate those anomalies in Figure 10 and 12, an arbitrary multi-segment seismic line was extracted from the reference 3D volume (Figure 13). The first and most prominent anomaly is the karsting associated with dissolution in the overlying Wabamun Formation (k in Figure 14). The seismic data indicate that the karsting covers an area of approximately 7 km² north-northwest of the WASP focus area. Other anomalies are more localized, such as the discontinuities (d in Figure 14). The data indicate that they are also originating within the Wabamun Formation. The amplitude map reveals significant variations within the Nisku Formation lithology as indicated by the undulation from low to high amplitude as well as interpreted thinning, especially within the northern and eastern regions of the reference 3D volume (l, h and t in Figure 14). Table 2 summarizes the geological features interpreted from the multi-segment line (Figure 14). Some of the anomalies will be discussed again later in this report using additional seismic attributes.

As far as the Wabamun discontinuities are concerned, it is uncertain as to what they represent and what process might have caused them, but there are two suggested explanations: the first is a mechanical process while the second is a chemical process. The mechanical process suggests that these discontinuities are actually rhombochasm, a phenomena associated with strike-slip faults in which vertical fault surface bends in the fault plane direction. However the lack of spatial (Figure 12) and temporal continuity (Figure 14) does not seem to support this explanation, as the observed discontinuities tends to be isolated and exhibit circular generally patterns. The other explanation is that chemical processes, namely dissolution, such as those responsible for producing karsting, are responsible for those discontinuities. A dissolution agent, i.e., water, would travel along conduits, such as sub-seismic fractures, and thus dissolve parts of the Wabamun even at such a small scale. However, it is suggested that dissolution in the Wabamun should display a wider areal pattern, which is not the case with these discontinuities. In any case, it is believed that those discontinuities may pose a risk and, therefore, should be taken into consideration for the location of a future CO₂ injection program.

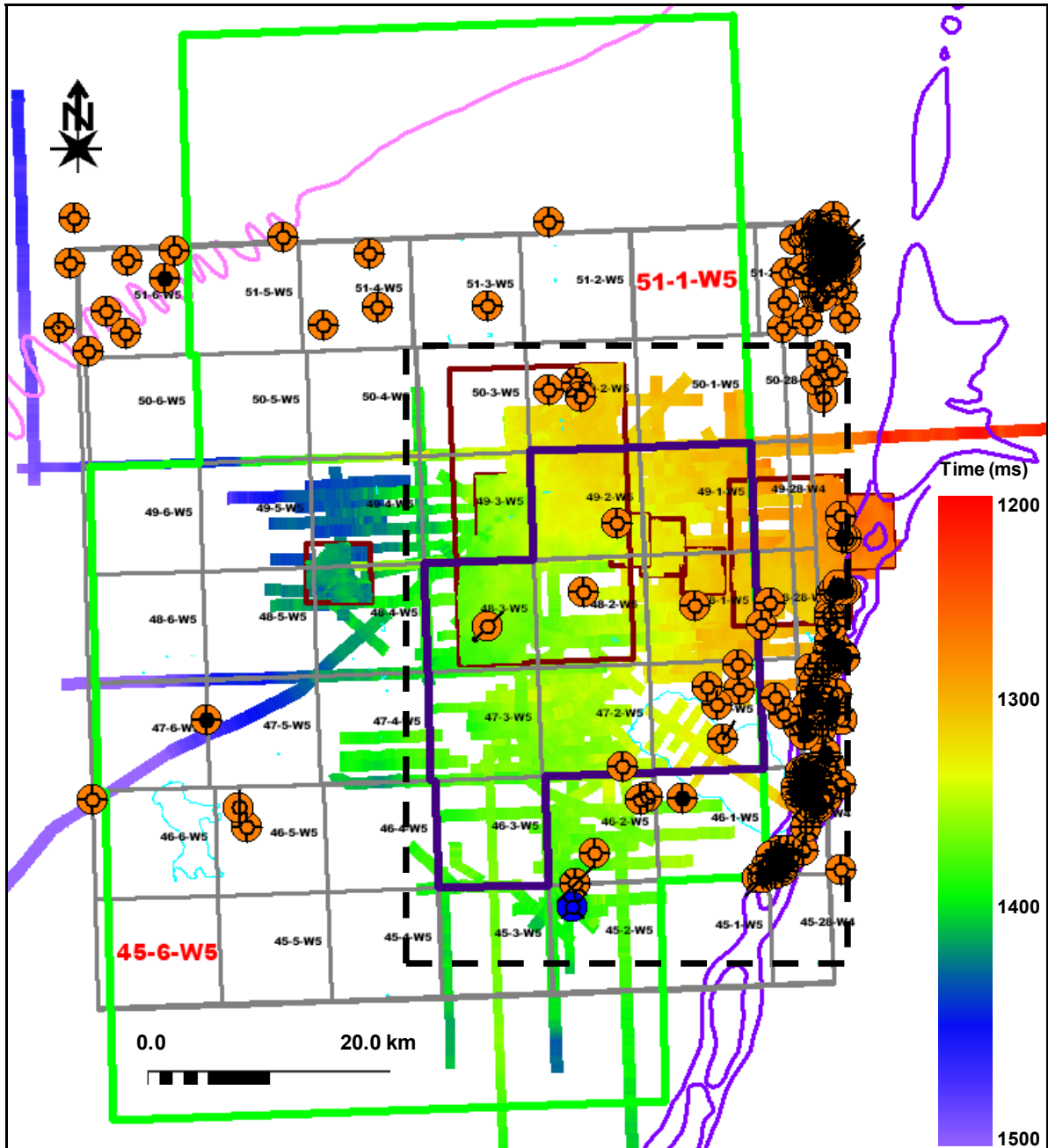


Figure 9: The time structure of the Nisku event after data calibration. The dashed black rectangle shows the extent of the zoom-in display over the study area in Figure 10.

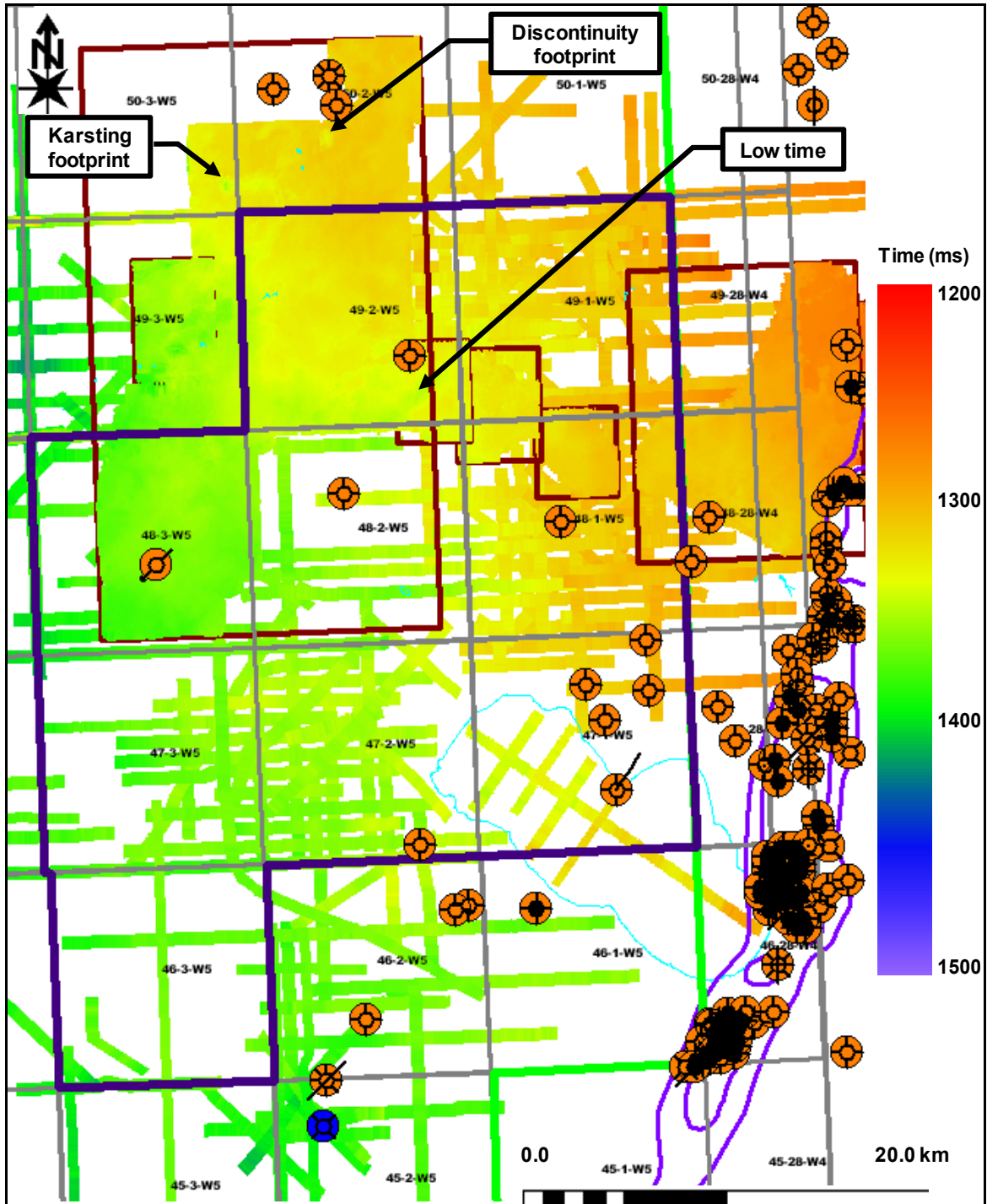


Figure 10: Zoom-in display of the Nisku time structure map in Figure 9. The locations of some of the major anomalies are specified: Wabamun karsting (see Figure 14), Wabamun discontinuities, and the Nisku local time low. It should be emphasized that the karsting and discontinuity effects shown here are the footprints of those anomalies and do not indicate that the Nisku has been physically affected.

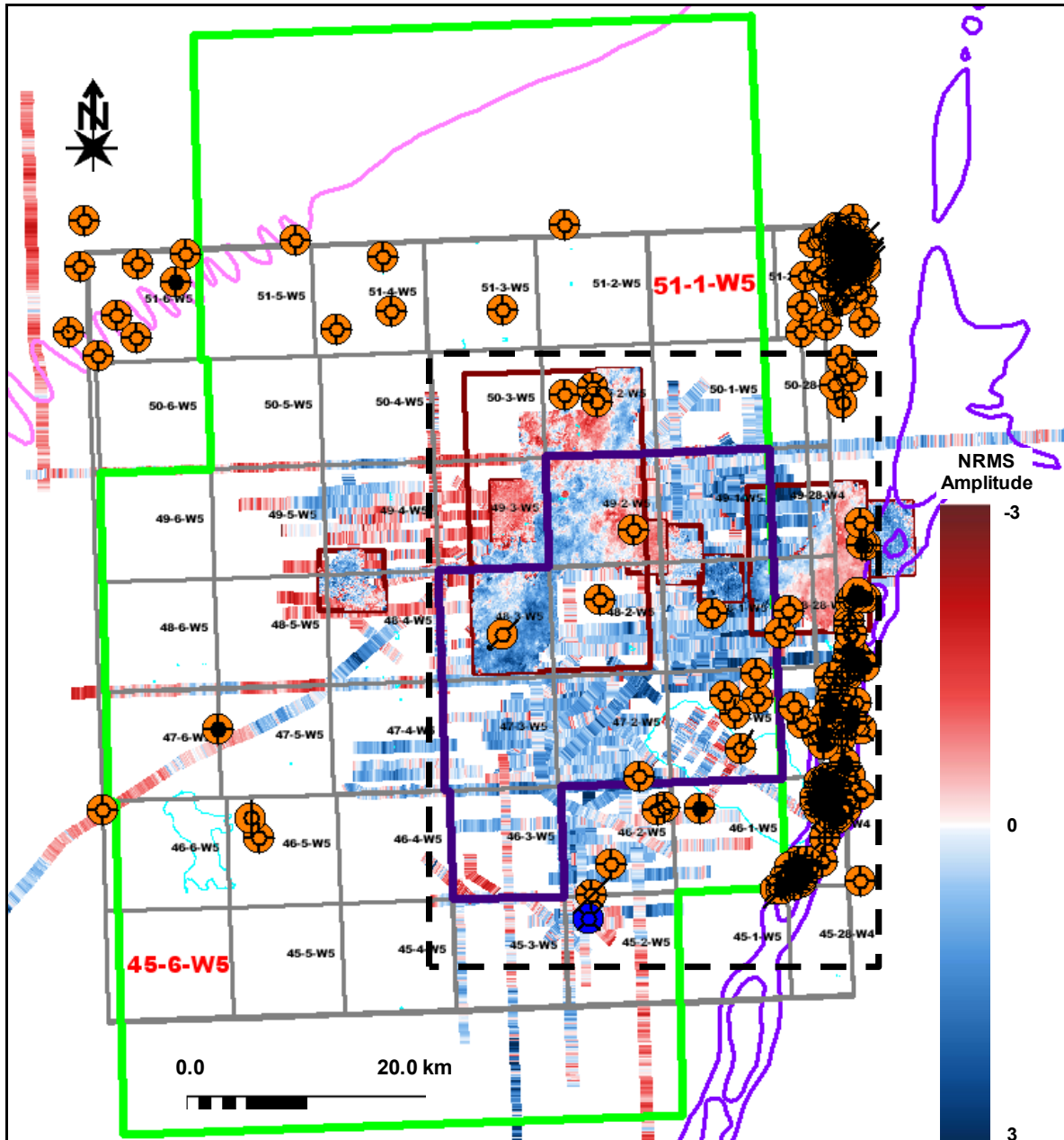


Figure 11: NRMS amplitude map of the Nisku event after data calibration and RMS amplitude normalization. Note the strong variations in the Nisku amplitude map compared to the time structure map. The dashed black rectangle shows the extent of the zoom-in display over the study area in Figure 12.

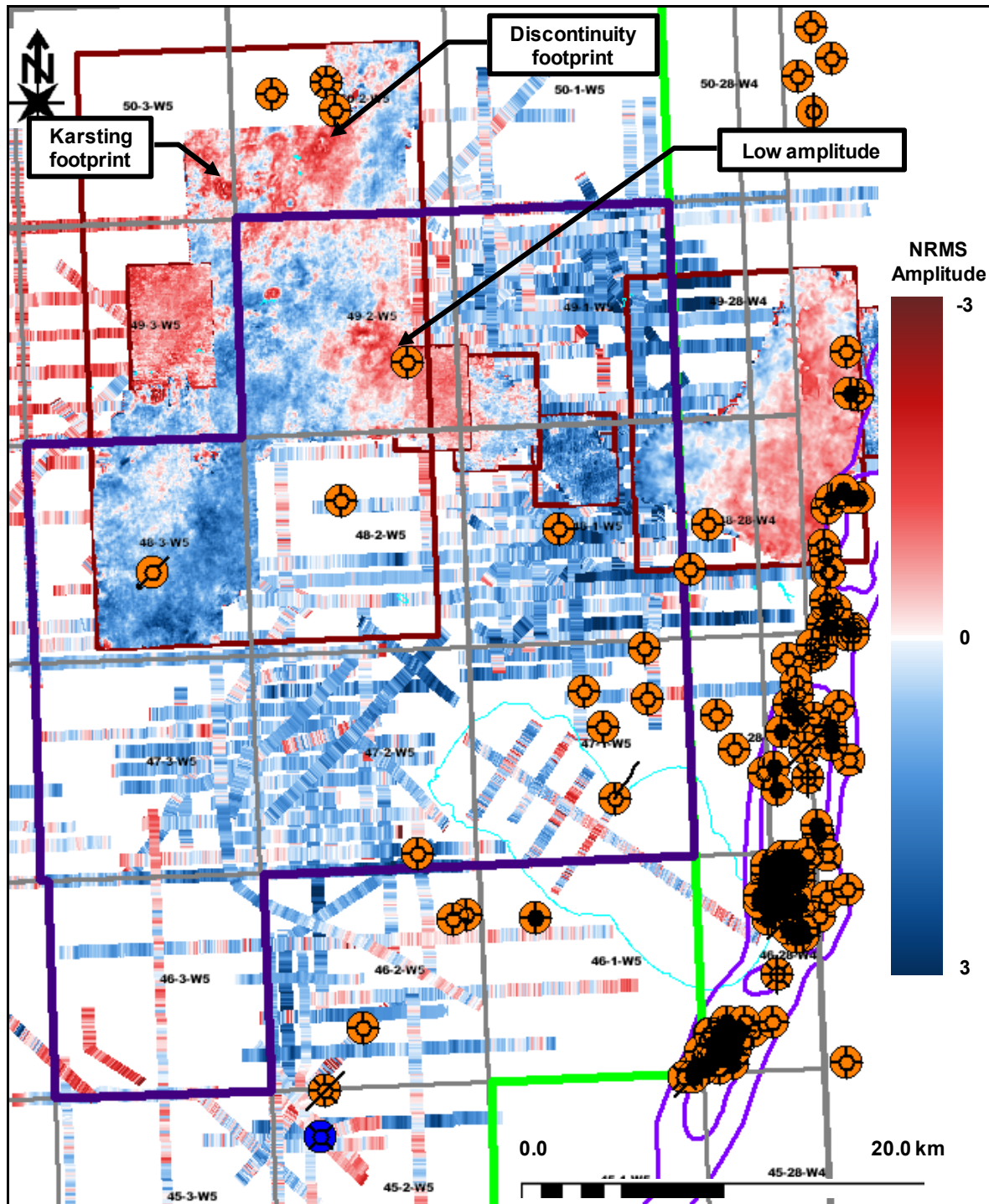


Figure 12: Zoom-in display of the Nisku NRMS amplitude map in Figure 11. Some of the major amplitude anomalies are specified: Wabamun karsting (see Figure 14), Wabamun discontinuities, and the Nisku amplitude low. It should be emphasized that the karsting and discontinuity effects shown here are the footprints of those anomalies and do not indicate that the Nisku has been physically affected.

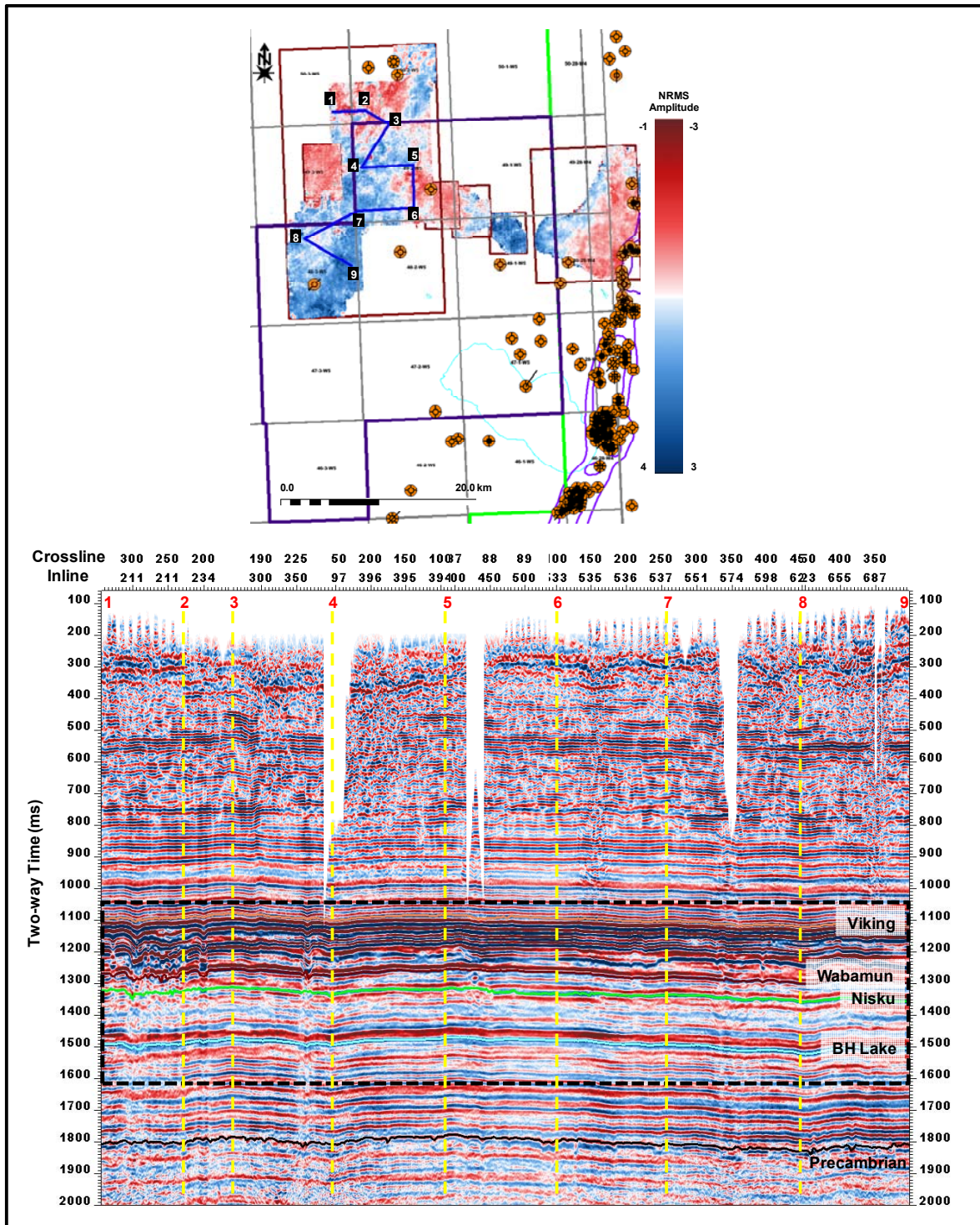


Figure 13: A multi-segment seismic section passing through some of the geological features within the reference 3D volume. The base map shows the location and orientation of the multi-segment section. The nodes are shown at their corresponding location along the horizontal axis. The right side of the colour scale in the base map represents the amplitude within the section (-3 to 3). The dashed rectangle indicates the extent of the zoom-in display in Figure 14.

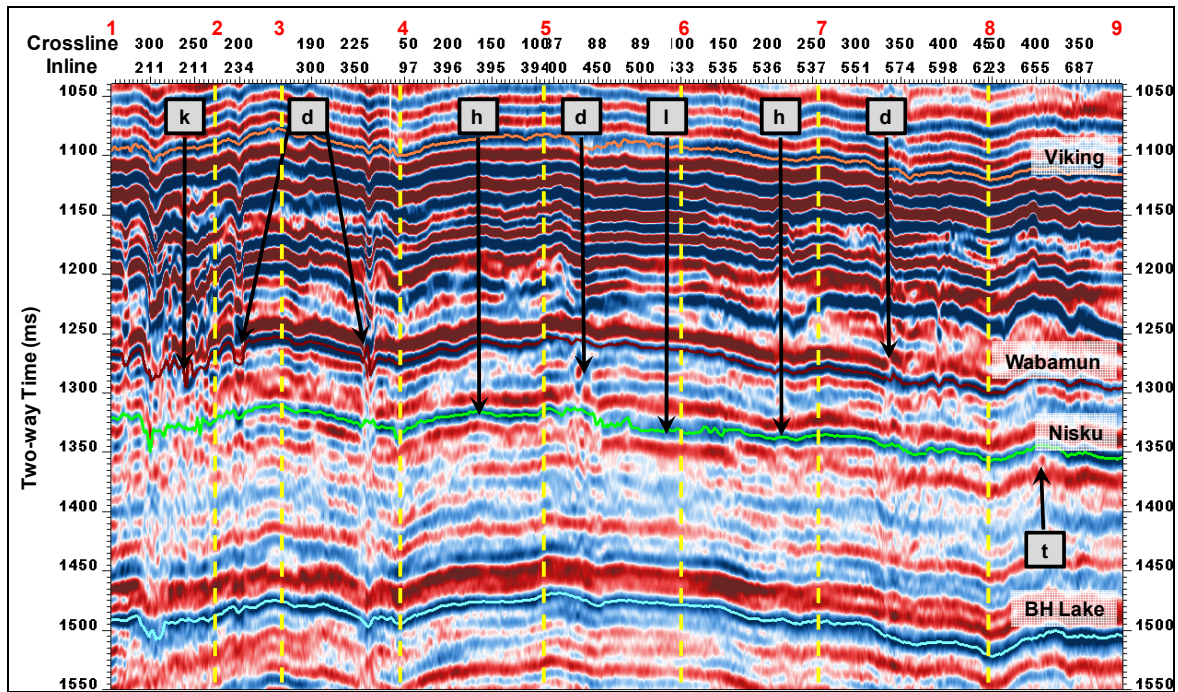


Figure 14: A zoom-in display of the multi-segment line through the 3D volume in Figure 13. Segment 1-2 passes through the karsting (k) originating in the Wabamun event. Segments 2-3 and 3-4 cross local Wabamun discontinuities (d). Segments 4-5, 5-6, and 6-7 show an example of the Nisku amplitude changing from high (h) to low (l) to high (h) again. Note the broadening in the Nisku cycle in segment 5-6. Segment 7-8 shows some amplitude anomalies between 1150 and 1200 ms, which are interpreted to be associated with the Cretaceous strata. The change from moderate (m) to high (h) Nisku amplitude is illustrated in segment 8-9. Segment 8-9 also traverses an area of local Nisku amplitude thinning (t), which is mapped by the seismic attribute amplitude thickness of the peak (ATP).

Table 2: Summary of some of the geological features within the multi-segment line (Figure 14).

Segment	Feature	Description
1-2	k: karsting	Dissolution associated feature in the Wabamun event
2-3	d: discontinuity	Local amplitude anomaly within the Wabamun event
3-4	d: discontinuity	Local amplitude anomaly within the Wabamun event
4-5	h: high amplitude	High amplitude within the Nisku event
5-6	d: discontinuity	Local amplitude anomaly within the Wabamun event
	l: low amplitude	Low amplitude within the Nisku event
6-7	h: high amplitude	High amplitude within the Nisku event
7-8	d: discontinuity	Local amplitude anomaly within the Wabamun event
8-9	t: amplitude thinning	Decreasing duration of the Nisku event

5. INTERPOLATION AND DEPTH CONVERSION

In order to undertake depth conversion and produce a continuous depth structure map, the time structure map was interpolated using a kriging algorithm (a linear least-squares interpolation method) with a grid size of 50×50 m. Both 2D and 3D Nisku horizons were used in the interpolation and the result is shown in Figure 15. Following the time structure interpolation, a simple time-to-depth conversion was executed to generate the depth structure map (Figure 16). The conversion algorithm utilized the Nisku time structure (from the horizon picks) and the Nisku depths from borehole data within the study area.

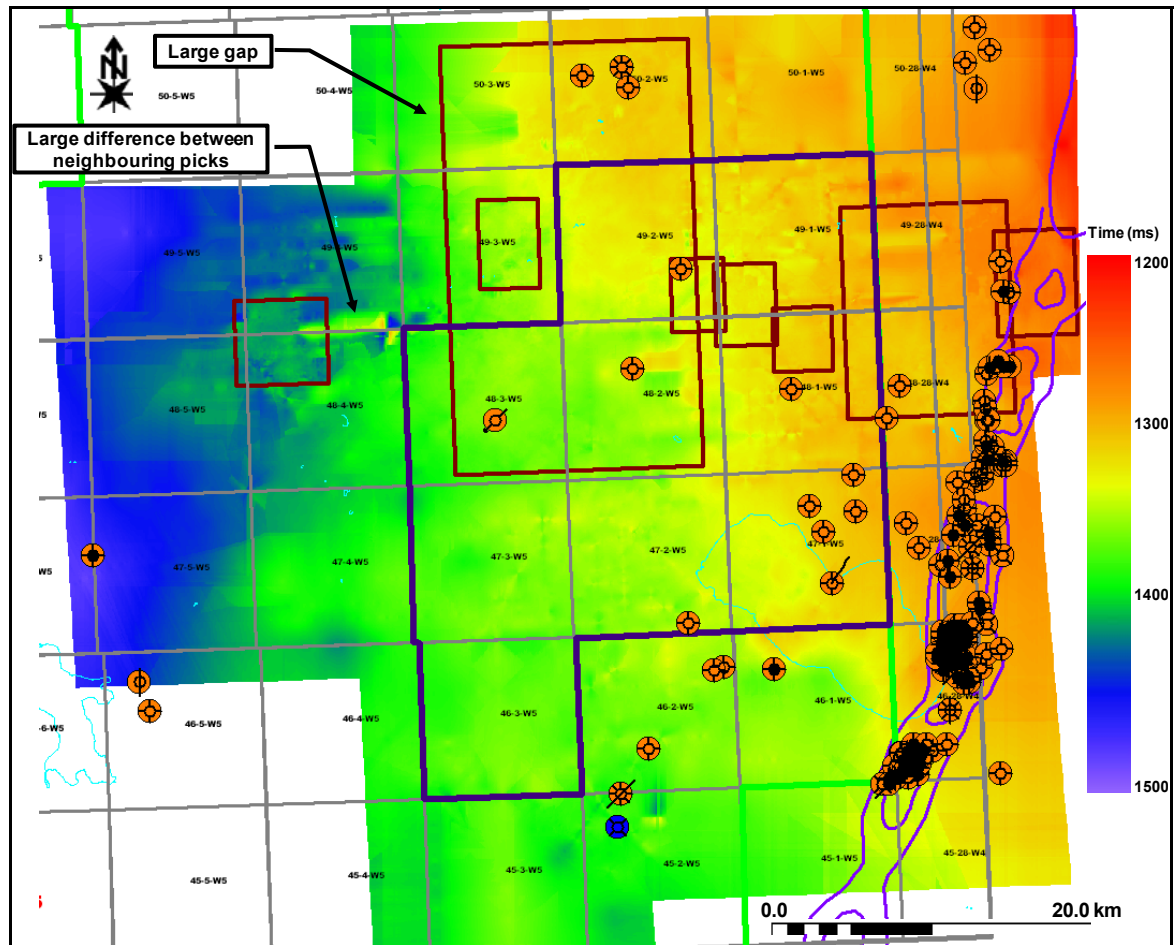


Figure 15: Interpolated time structure map (Figure 9) using a kriging algorithm with a grid size of 50×50 m.

In general, the interpolated time and depth structure maps (Figure 15 and Figure 16) honour the well data, as illustrated in Table 3, in which the well depths and the depth values estimated from the depth map are compared. However, the interpolation seems to produce inaccurate results in areas where there is a large gap in data coverage or where there is a relatively large difference between neighbouring picks (Figure 15). An additional cause of inaccuracy in the interpolated depth structure map is the absence of Nisku Formation picked depths in some of the borehole data (Figure 16). However, despite the few inaccuracies, the results suggest that the kriging interpolation algorithm has performed well within the WASP focus area. In addition to providing a more continuous perspective of the Nisku event, the interpolated time (Figure 15) and depth (Figure 16)

structure maps give an insight into the subtle depth variations in the Nisku Formation within the WASP focus area.

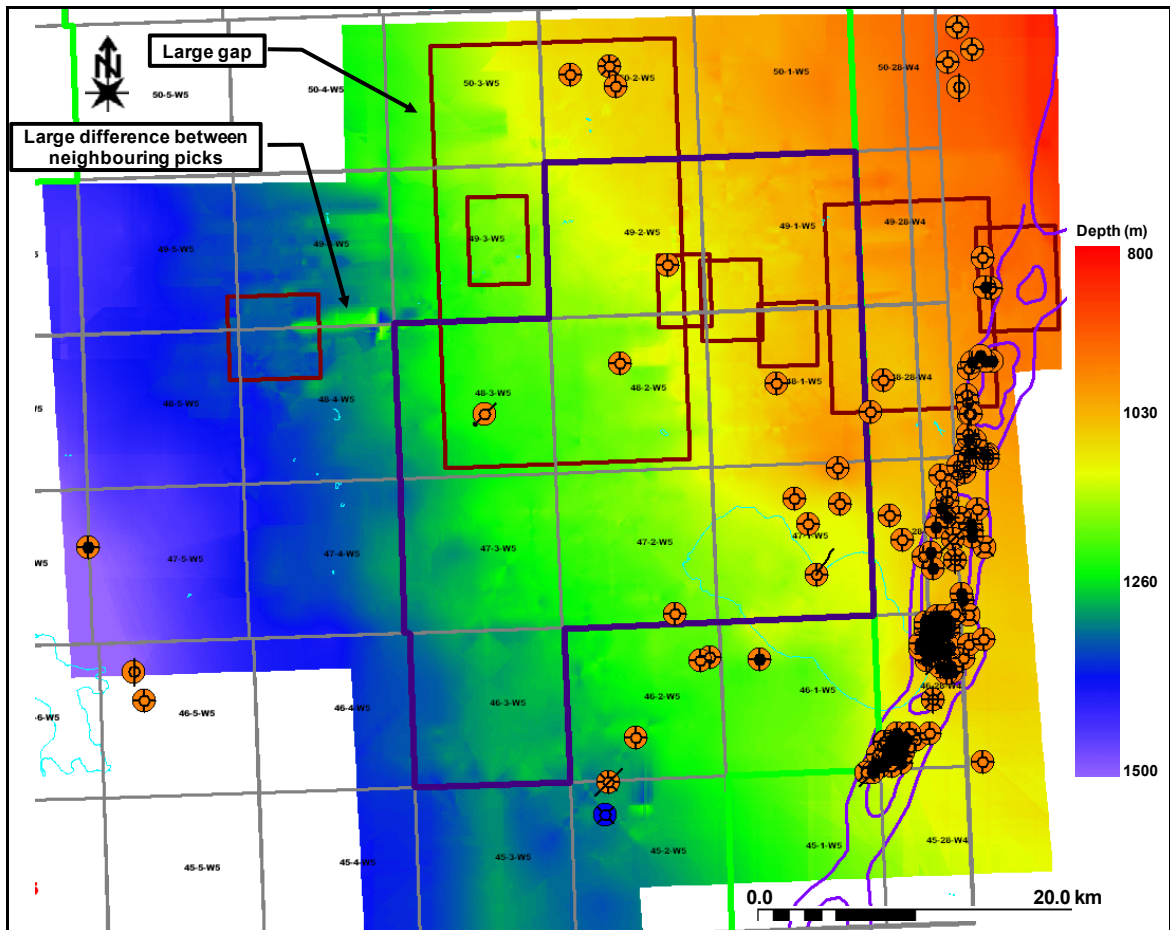


Figure 16: Interpolated depth structure map using a kriging algorithm with a grid size of 50×50 m.

Table 3: Comparison between the measured and estimated depth values using kriging algorithm (Figure 16). The difference between the two is also shown. The interpolation algorithm seems to honour the actual data, except at well 100163504701W500.

Well	Measured Depth (m)	Estimated Depth (m)	Difference (m)
100010104601W500	1111.6	1111.6	0.0
100020104601W500	1114.9	1114.9	0.0
100022104801W500	1178.6	1178.6	0.0
100022304828W400	1038.1	1038.1	0.0
100022804802W500	1148.1	1148.1	0.0
100022804802W500	1148.1	1148.1	0.0
100052005002W500	1075.1	1075.1	0.0
100060204702W500	1198.8	1198.8	0.0
100060204702W500	1198.8	1198.8	0.0
100061504803W500	1219.5	1219.5	0.0
100062904601W500	1170.6	1170.6	0.0
100082604701W500	1082	1082.7	-0.7
100090104601W500	1104.8	1106.4	-1.6
100091004701W500	1107.9	1101.1	6.8
100092404706W500	1488	1488	0.0
100100904602W500	1257.9	1257.9	0.0
100102105002W500	1063.3	1063.3	0.0
100102204701W500	1098.2	1098.2	0.0
100102504602W500	1200	1200	0.0
100122704701W500	1098.8	1099	-0.2
100131104828W400	1042	1042.4	-0.4
100131304728W400	1066.8	1066.8	0.0
100142904605W500	1502.2	1502.2	0.0
100143204502W500	1285.3	1285.3	0.0
100151104902W500	1092.1	1093	-0.9
100152304728W400	1069.8	1069.8	0.0
100161605002W500	1063.5001	1062.9	0.6
100163504701W500	1292.1	957.9	334.2
102122504602W500	1197.9	1197.9	0.0
1F1112904502W500	1297	1297	0.0

6. NUMERICAL MODELLING

Seismic amplitude plays an important role in seismic interpretation and site characterization. In this project, substantial emphasis has been placed on the Nisku event amplitude to provide one approach for favourable injection site selection. In general, the seismic amplitude response can be modelled as a function of the following parameters:

$$\text{Seismic Amplitude } \alpha, f(\text{thickness}) + f(\text{impedance}) + f(\text{wavelet}) + \text{noise} \quad 1$$

Where $f(\text{thickness})$ represents the change in the Nisku thickness, $f(\text{impedance})$ represents the change in its acoustic impedance (P-wave velocity multiplied by the density), $f(\text{wavelet})$ is the seismic wavelet, and noise is the amount of noise present in the data. Prior to undertaking the modelling, it was important to decide on the range of these parameters and their effect on the seismic amplitude. Therefore, taking into consideration the data calibration and normalization in addition to examining the well control in the study area, we observed the following:

1. The Nisku Formation thickness in the study area varies between 40 and 80 m and thus thickness should be taking into consideration as a primary element in the modelling.
2. The Nisku Formation acoustic impedance (I_p) is another critical parameter that has to be included in the modelling. However, by examining the well control, it was found that the Nisku impedance is mainly driven by variations in P-wave velocity rather than density:

$$\Delta I_p = \Delta \alpha \times \Delta \rho \approx \Delta \alpha \quad 2$$

Where α is the P-wave velocity in m/s and ρ is the density in kg/m^3 . The average P-wave velocity ($\alpha_{\text{avg.}}$) of the Nisku Formation was found to vary between 5500 m/s and 6500 m/s.

3. The wavelet is assumed to be stationary; this follows from the data calibration.
4. The noise is assumed to be random; therefore adding it contributes insignificantly to the observed amplitude.

Based on these observations and after running some sensitivity analyses, it was decided that thickness and average P-wave velocity are the primary Nisku parameters affecting the seismic Nisku event amplitude. Subsequently, zero-offset synthetic seismograms were generated using a 25 Hz Ricker wavelet and the convolutional model to further understand the effect of these two parameters on the Nisku event's amplitude and time, and effect on the underlying Ireton event. Figure 17 is a side-by-side panel display illustrating the thickness and average P-wave velocity effect on time and amplitude of the Nisku and Ireton events. In order to better discern the individual effects, the time and amplitude associated with those two events were picked using the peak at approximately 1130 ms for the Nisku event and the underlying trough (~ 1170 ms) for the Ireton event.

For the Nisku event, the modelling results (Figure 18 and 19) suggest that the amplitude variations in the study area, excluding those associated with discontinuities footprint, are most likely due to variability in the average acoustic impedance (mainly average P-wave velocity) rather than thickness. For instance, changing the average velocity (vertical axis) will cause over a 60% change in amplitude whereas changing the thickness (horizontal axis) will only cause about an 8% variation in amplitude (Figure 19). The highest amplitude effect is observed for a high average P-wave velocity. The results also suggest that there would be a time shift in the Nisku event, and it would be more prominent at relatively low Nisku thickness values and an average P-wave velocity. Figure 20 illustrates the footprint effect on the Ireton event as a result of changing the thickness and

average P-wave velocity of the Nisku Formation. As expected, the maximum time delay in the Ireton event time is associated with low average Nisku P-wave velocity whereas the highest amplitude change correlates with high average Nisku P-wave velocity. In all the modelling results (Figure 18 and 20), the conclusion is that the highest sensitivity in the seismic amplitude and travel time is associated with changes in the average P-wave velocity rather than thickness.

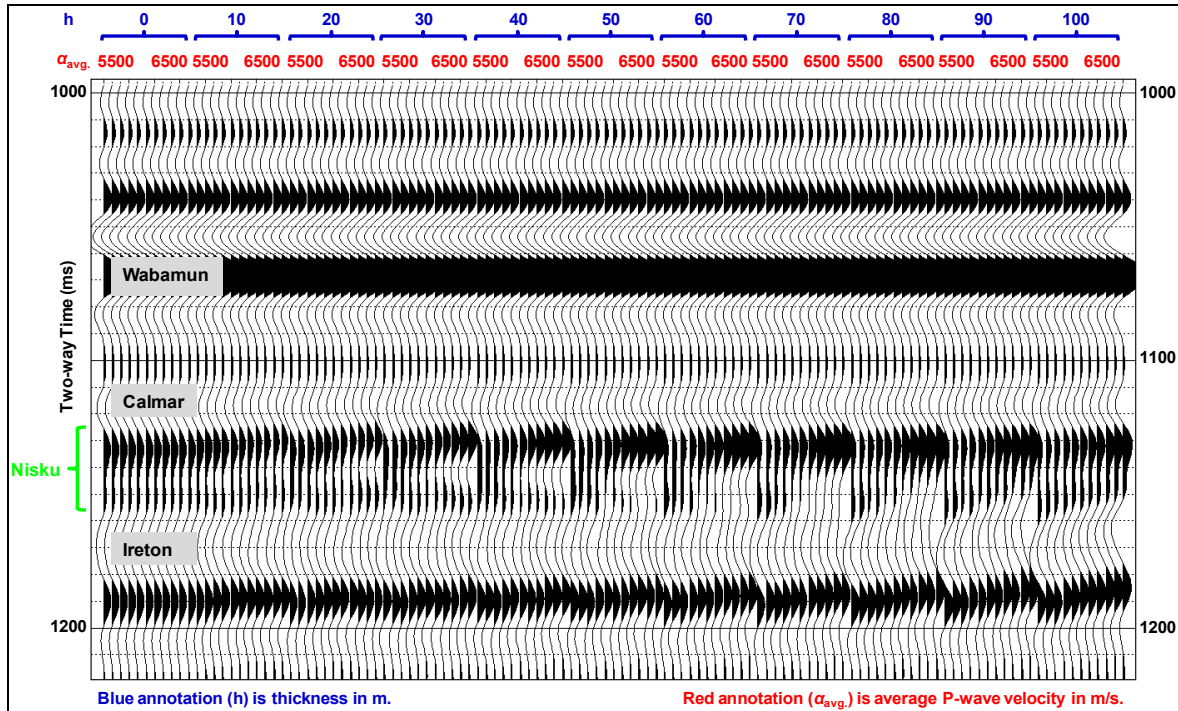


Figure 17: Sequential display of the normal incidence synthetic seismogram in which the Nisku event amplitude is modelled as function of thickness and average P-wave velocity. The top of the Nisku event is identified as the peak at approximately 1130 ms (the green bracket along the time axis approximates the frequency cycle through the formation). In each blue bracket (thickness effect), there are 11 traces, each representing the seismic amplitude associated with that thickness and an average Nisku P-wave velocity increasing from 5500 m/s to 6500 m/s at an increment of 100 m/s. The modelling was undertaken using well 100-10-05-052-02W5. The actual Nisku thickness and average P-wave velocity at this well are 100 m and 6100 m/s, respectively.

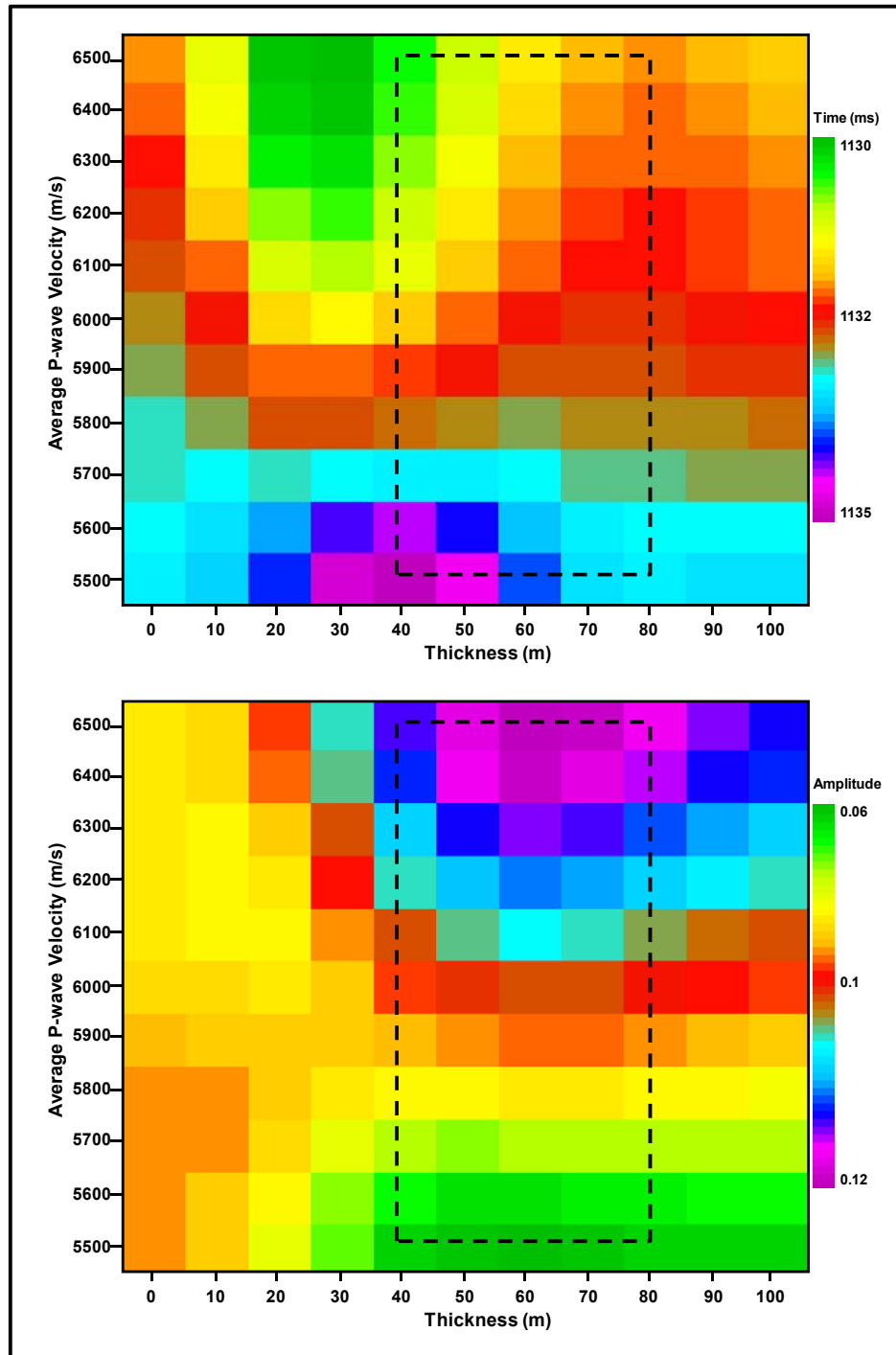


Figure 18: Nisku event amplitude (top) and time (bottom) as a function of thickness and average P-wave velocity. The actual Nisku thickness and average P-wave velocity are 100 m and 6100 m/s, respectively. The maps represent the Nisku amplitude and time horizons that resulted from picking the peak amplitude corresponding to the Nisku event in Figure 17. The black dashed rectangle outlines the most likely Nisku thickness and average velocity values within the study area based on well control. The results suggest that the Nisku average P-wave velocity (or impedance) effect is far more significant than the thickness effect. Thus, the highest sensitivity is along the vertical axis.

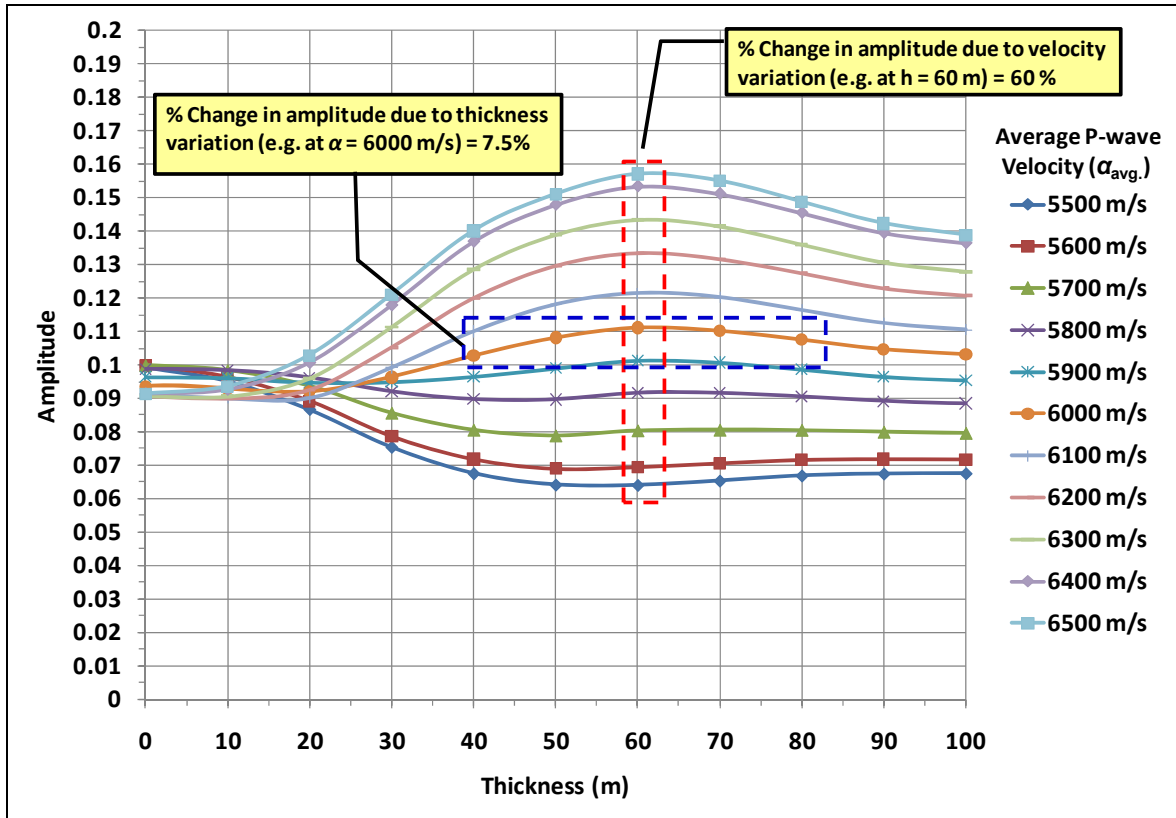


Figure 19: Nisku amplitude modelling result in which the difference between the thickness and average P-wave velocity effect on the Nisku event amplitude is evident. The actual Nisku thickness and average P-wave velocity are 100 m and 6100 m/s, respectively.

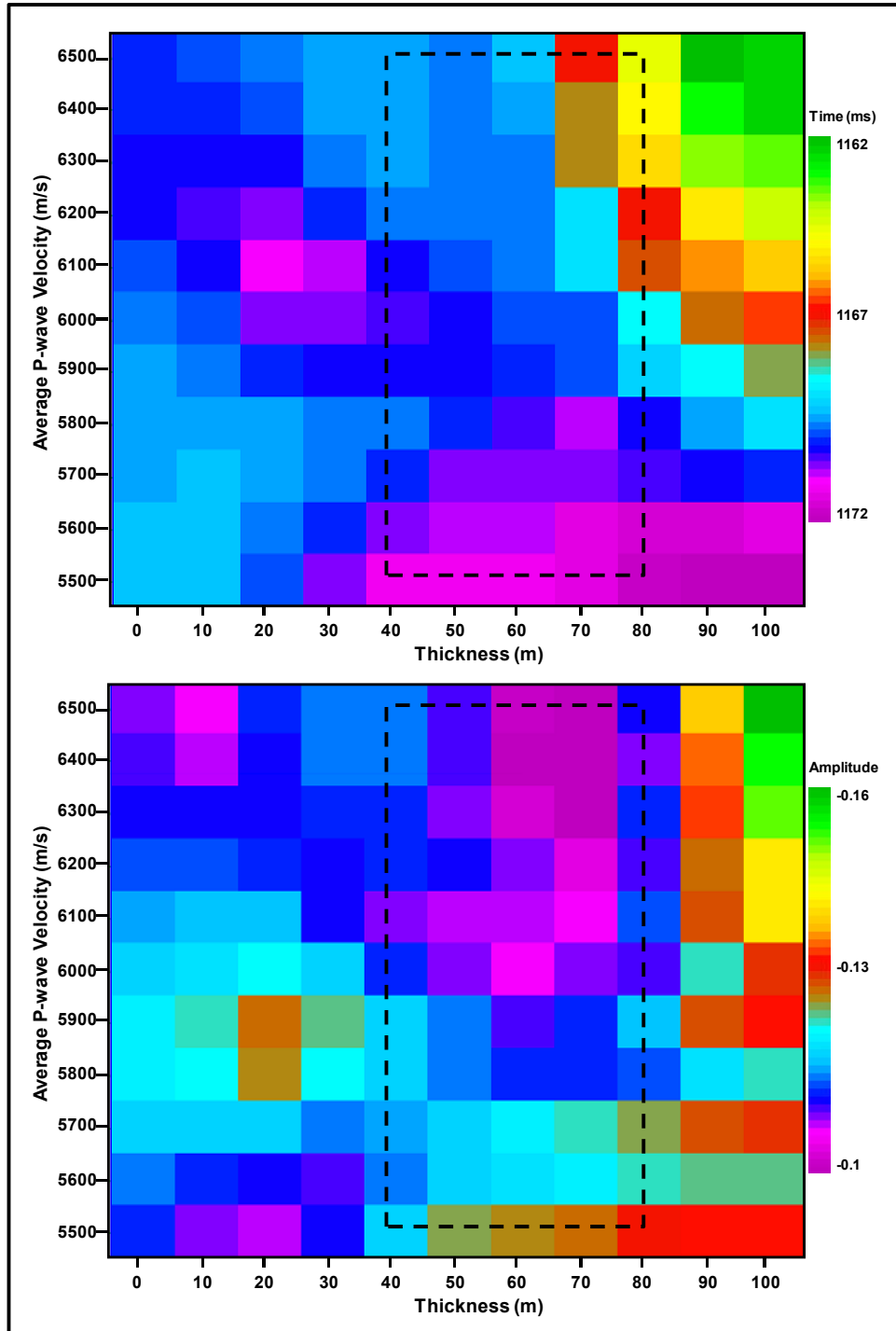


Figure 20: Ireton event amplitude (top) and time (bottom) as a function of Nisku thickness and average P-wave velocity. The maps represent the Ireton amplitude and time horizons that resulted from picking the trough amplitude corresponding to the Ireton event in Figure 17. The black dashed rectangle outlines the most likely Nisku thickness and average P-wave velocity values within the study area based on well control. The results suggest that the effect of the Nisku average P-wave velocity (or impedance) footprint on the Ireton event is far more significant than the thickness effect.

7. SEISMIC ATTRIBUTES

In addition to amplitude, several seismic attributes, such as the average NRMS amplitude (Figure 21), the amplitude thickness of the peak (ATP) of the Nisku reflection (Figure 22) and difference attributes (Figure 24 and 25), were generated to strengthen the interpretation of the lithology changes and geologic discontinuities in the study area. Unlike acoustic impedance inversion (next section), those attributes are computed directly from the Nisku time and/or amplitude. For those attributes, only 3D seismic data were exploited as such attributes require, in addition to time and amplitude, continuous and dense two-dimensional spatial sampling, both of which are absent in the 2D seismic data.

The average NRMS amplitude of the Nisku event (Figure 21) was calculated over a window of 10 ms (centred on the Nisku horizon pick). The purpose behind this averaging is to generate another representation of the Nisku event amplitude that captures the amplitude envelope around the event rather than a single value and thus minimizes errors due to picking ambiguities. The computed average NRMS amplitude map is quite similar to the original NRMS amplitude map in Figure 12, which is an indication that the representation of the amplitude variations within the Nisku Formation in Figure 11 and 12 are appropriate. The only difference is that a new pattern emerges from the average NRMS amplitude map, as indicated in Figure 21. This pattern is better captured by the attribute called amplitude thickness of the peak (ATP).

The ATP (Figure 22) calculates the duration of the Nisku peak from zero-crossing to zero-crossing in ms; the peak being defined as amplitude value larger than zero value. One of the most interesting features associated with ATP is that it accounts very well for the transition between the various seismic volumes, something that was not fully achieved with conventional amplitude maps (Figure 12 and 21). The low ATP values indicate areas where the Nisku amplitude peak thins. Such zones can also be seen in the seismic sections as indicated by the symbol “t” in the multi-segment line in Figure 14. The thinning appears to be mainly occurring at the base of the Nisku event and there are two explanations proposed for its cause. The first is that there might be an abrupt change in the thickness of the Nisku Formation. The second is that the thinning might be associated with a change in P-wave velocity resulting from either a facies change (shale content) or porosity variations within the Nisku Formation. In order to refine our interpretation, the ATP was calculated (Figure 23) using the synthetic seismogram in Figure 17. The ATP attribute is rather complicated and suffers from non-uniqueness, as depicted in Figure 23, in which two different formation thicknesses, at $\alpha_{avg} = 6500$ m/s for instance, yield the same ATP value. Unfortunately, there is insufficient well penetration through the Nisku Formation that could be used to better calibrate this attribute. Nonetheless, it is possible to reduce the non-uniqueness by integrating high ATP values with optimum values of other attributes (e.g., low impedance and high porosity), which are used as indicators for favourable site conditions in the study area.

The difference method is a member of another class of attributes, which, in contrast, is sensitive to discontinuities in seismic signal. The method is based on a simple algorithm that subtracts a given seismic trace from its neighbouring trace and divides by their sum (Luo et al., 1996). The method has proven robust in detecting various types of discontinuities encountered in the seismic data, as can be seen in Figure 24 and 25. To account for preferential direction, the difference attribute was computed in both the inline direction (Figure 24) and in the crossline (Figure 25) direction. The former was more robust in identifying geologic discontinuities within the reference 3D, such as the Wabamun karsting footprint on the Nisku event. The crossline difference, on the other hand, was more sensitive to variations associated with some of the other seismic volumes, for instance the local time low just east of the reference volume, as shown in Figure 10.

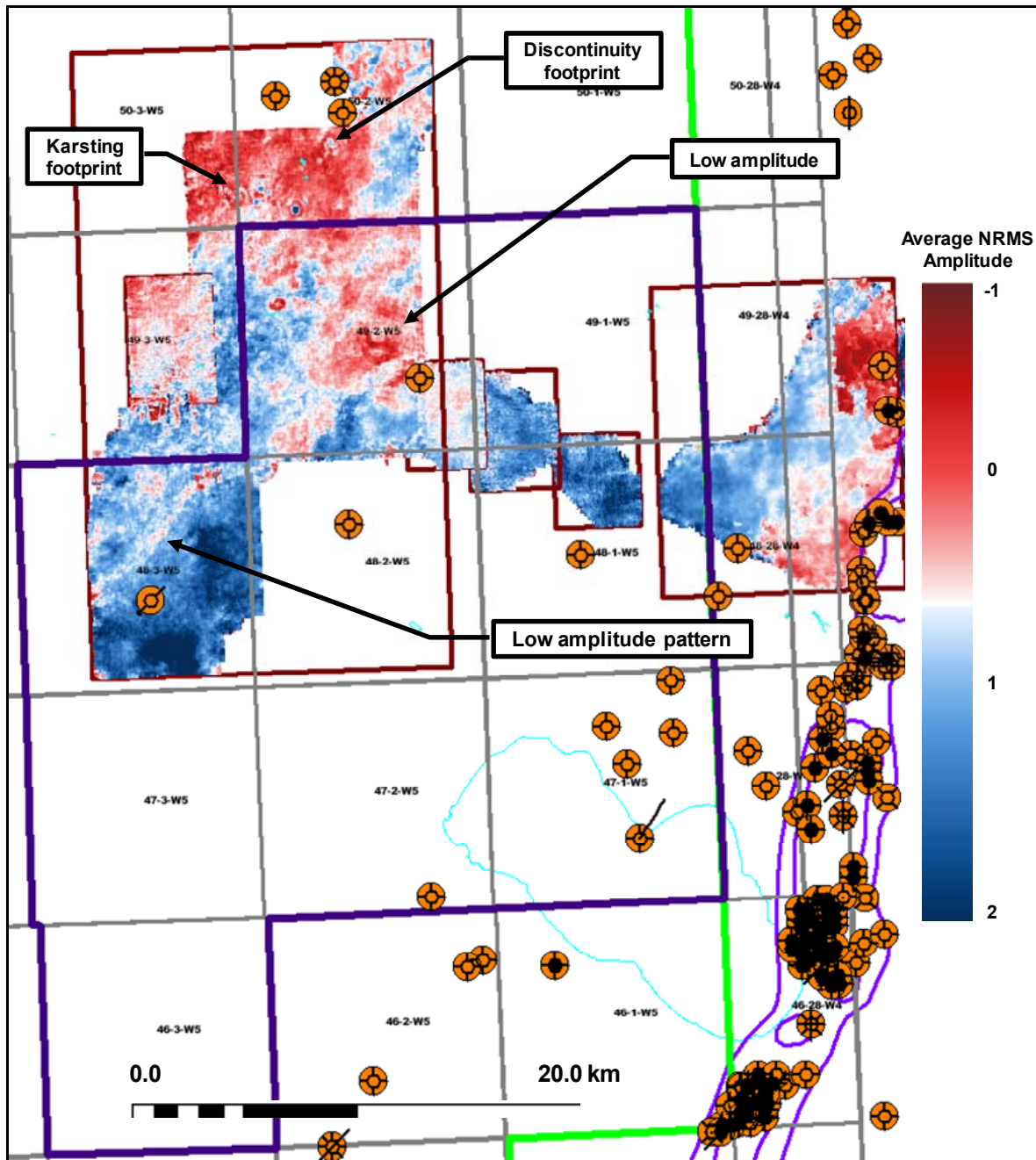


Figure 21: Average NRMS Nisku amplitude over a 10 ms window (centred on the Nisku horizon pick). In addition to the patterns already defined in the NRMS Nisku amplitude map (Section 4 and Figure 12), another low amplitude pattern emerges from the map. The NRMS amplitude averaging window of 10 ms seems appropriate except within the north-eastern region of the easternmost 3D volume. The relative position to the large study area is shown by the dashed rectangle in the base map in Figure 11.

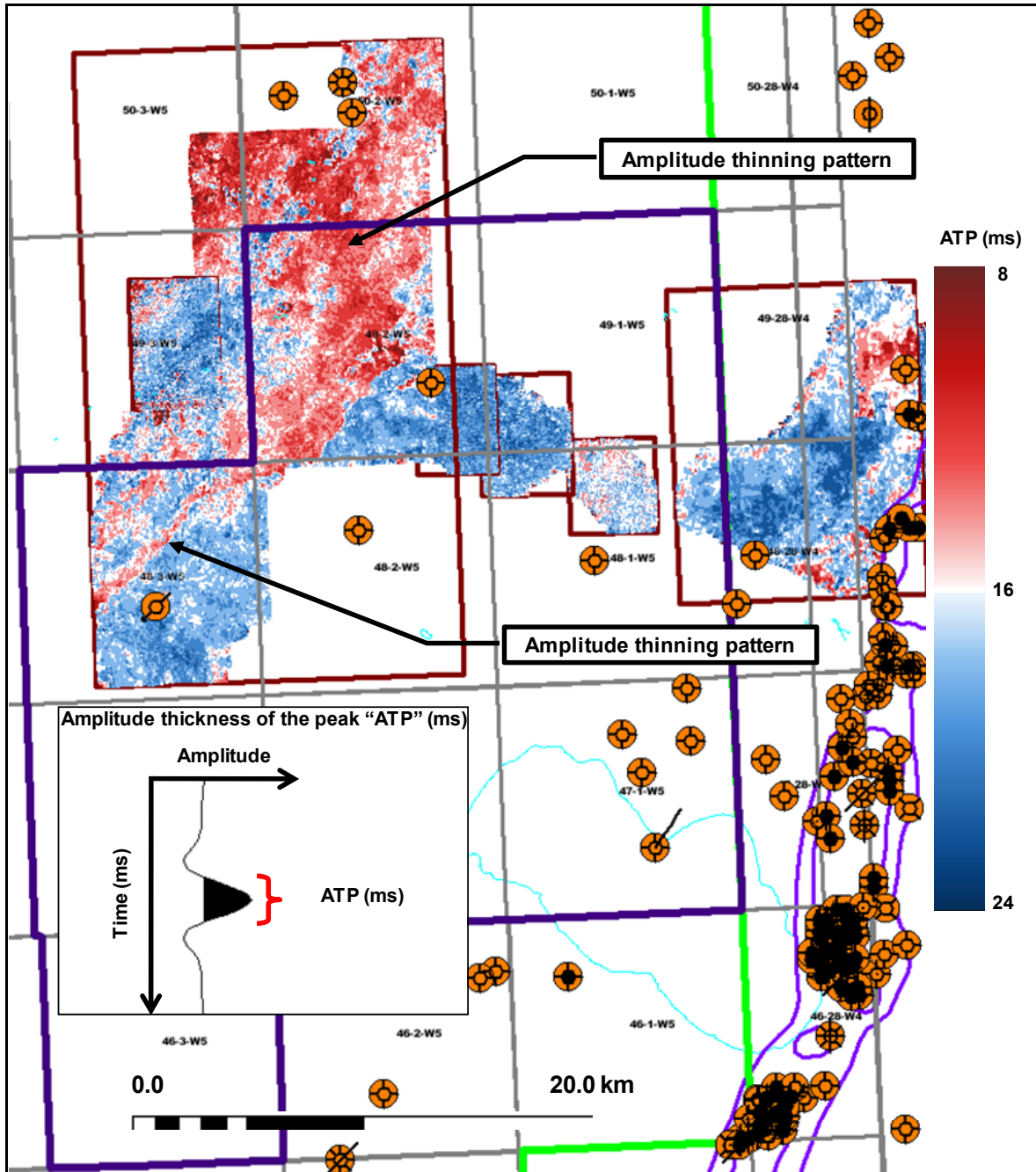


Figure 22: Amplitude thickness of the Nisku peak (ATP) in ms. The inset schematic illustrates the concept of ATP. Note the elongated (NE-SW) thinning pattern that is not captured by the NRMS amplitude map. See the multi-segment line in Figure 13 and 14 for a cross-sectional view of those anomalies. The relative position to the large study area is shown by the dashed rectangle in the base map in Figure 11.

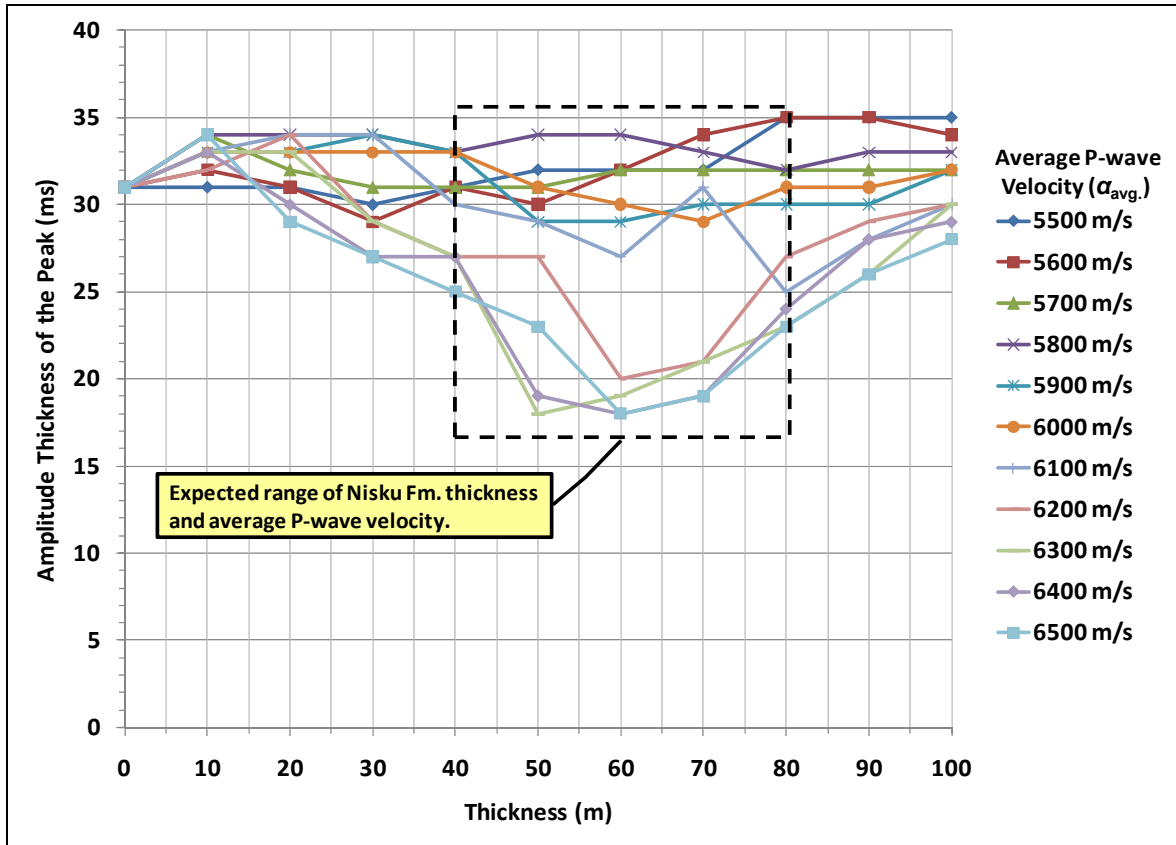


Figure 23: Amplitude thickness of the Nisku peak (ATP in ms) of the synthetic seismogram in Figure 17. The ATP is highly sensitive to variations in the Nisku Formation thickness and average P-wave velocity over the expected range of those parameters. There is a distinct separation in the velocity effect over the expected Nisku Formation thickness (~ 40 – 80 m). The separation seems to be occurring around the tuning thickness (~ 60 m) and the corresponding average P-wave velocity (~ 6100 m/s).

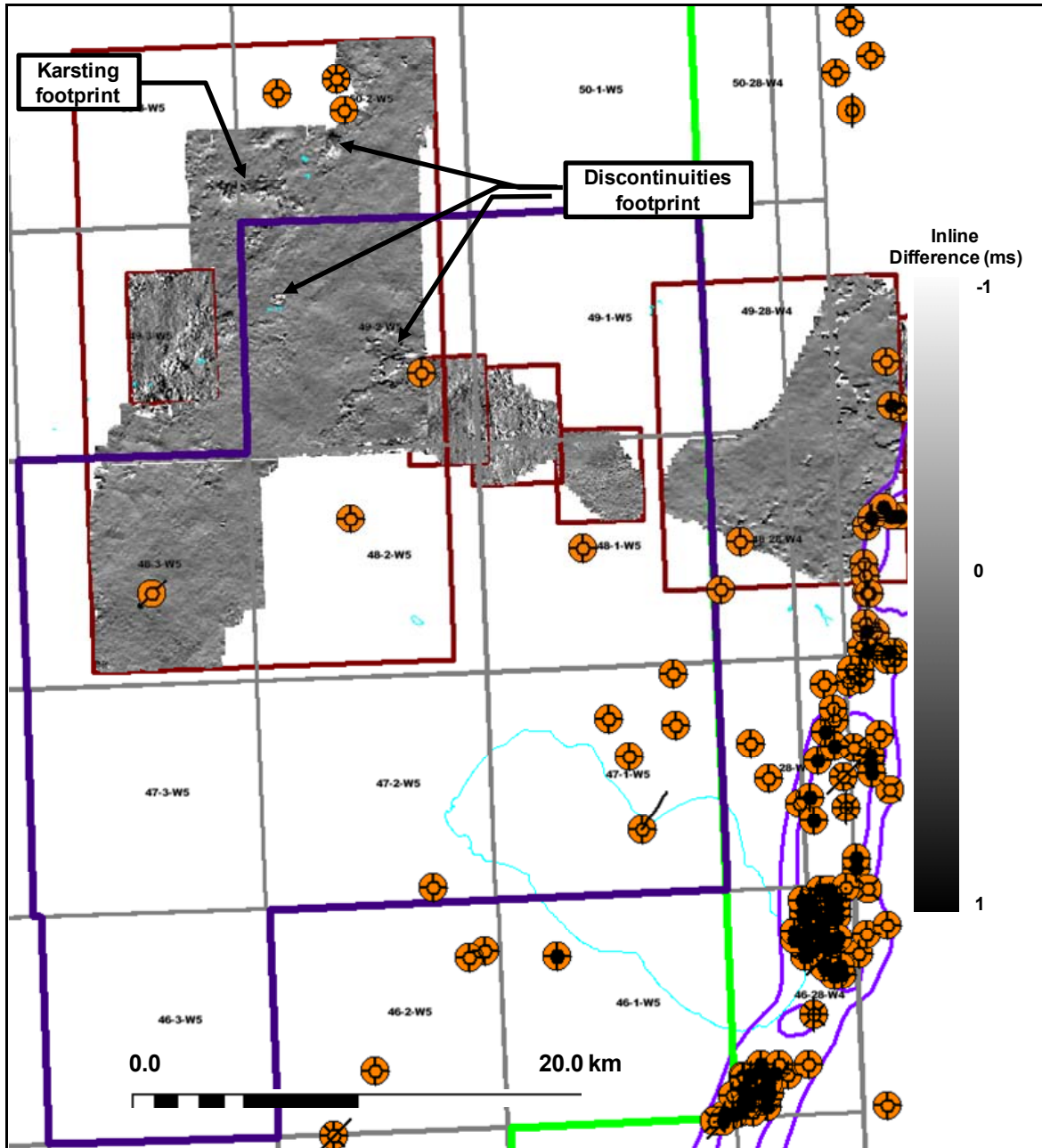


Figure 24: Inline difference (coherency) attribute of the Nisku event in ms. The difference method shows more sensitivity toward discontinuities within the Nisku compared with other seismic attributes as can be seen, for instance, with the Wabamun karsting effect on the Nisku event. See the multi-segment line in Figure 13 and 14 for a cross-sectional view of some of the identified anomalies. The relative position to the large study area is shown by the dashed rectangle in the base map in Figure 11.

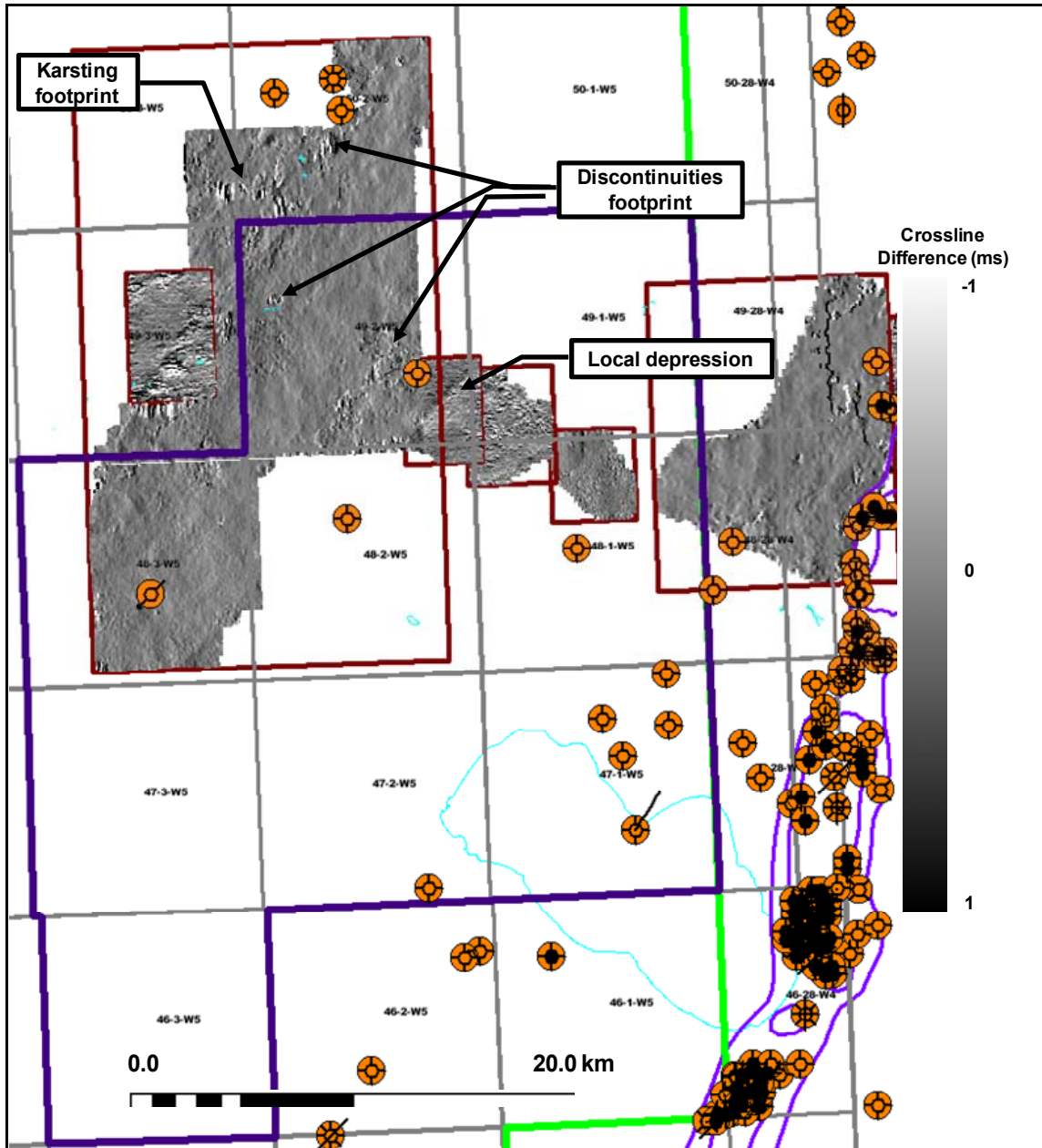


Figure 25: Crossline difference (coherency) attribute of the Nisku event in ms. Note the sensitivity, also, to the direction in which the difference is measured compared to the inline difference in Figure 24. The crossline difference was not as robust as the inline difference in defining geologic features within the reference 3D volume (e.g., the Wabamun karsting effect). However, it performed better in defining some of the features associated with other seismic volumes, such as the local time low (also shown in the time structure map in Figure 10). See the multi-segment line in (Figure 13 and 14) for a cross-sectional view of some of the identified anomalies. The relative position to the large study area is shown by the dashed rectangle in the base map in Figure 11.

8. ACOUSTIC IMPEDANCE INVERSION

Acoustic impedance is one of the most useful seismic attributes as it yields distribution of pseudo-physical properties rather than a set of observations pertaining to the physical properties distribution. However, acoustic impedance is more difficult to determine as it requires seismic inversion, which calls for good estimation of parameters as well as high quality seismic data and a good distribution of well control. Furthermore, inversion suffers from non-uniqueness.

In this project, various post-stack acoustic impedance inversion techniques were tested and only two were found to produce useful results: band-limited and model-based inversions. Band-limited inversion, also known as recursive inversion, is constrained mainly by the bandwidth of the seismic data, which typically falls between 7 and 60 Hz. The method estimates the acoustic impedance recursively by first extracting an estimate of the reflection coefficient from the seismic data and then re-arranging the normal incidence reflection coefficient relation to solve for the acoustic impedance of the $n^{\text{th}}+1$ layer (Z_{n+1}):

$$R_n = \frac{Z_{n+1} - Z_n}{Z_{n+1} + Z_n} \xrightarrow{\text{solving for } Z_{n+1}} Z_{n+1} = \frac{Z_n(1+R_n)}{1-R_n} \quad 3$$

Where R_n is the reflection coefficient of the n^{th} layer, Z_n is the acoustic impedance of the n^{th} layer ($\text{kg/m}^2 \cdot \text{s}$), and n is a positive integer. Recall that the acoustic impedance of the n^{th} layer is its P-wave velocity (m/s) multiplied by its density (kg/m^3), i.e., $Z_n = \alpha_n \times \rho_n$ (Cooke and Schneider, 1983).

Model-based inversion uses a different approach. First, the well control and the seismic data (horizons) are used to build an initial low-frequency estimated model of the acoustic impedance distribution. Using an estimate of the source wavelet, the model is then perturbed and the model response, in the form of synthetic seismogram, is measured. The model responses are then compared to the actual seismic traces, usually by means of cross correlation. The process is iterated until the model converges, i.e., the model response becomes within a predefined acceptable range from the actual observation. The misfit error between the two is quantified through various means; one of the most commonly used measures is the sum of the squared differences (Lines and Treitel, 1984).

There are many elements that could degrade the reliability of the inversion results, some of which could not be controlled, such as noise, whereas others could not be precisely calculated, such as the source wavelet. However, each method has its own advantages and disadvantages in regard to those limitations and it is suggested that by using both methods some of the ambiguities associated with the inversion results could be minimized. More information about those and other inversion methods can be found in Waters (1978), Aki and Richards (1980), Lines and Treitel (1984), Russell (1988), and the STRATA software theory manual.

Figure 26 depicts some of the major steps adopted in the acoustic impedance inversion framework. A critical factor to achieving good inversion results is the seismic-to-well tie. The correlation coefficients associated with the wells used in the inversion are shown in Table 4. Prior to showing the Nisku acoustic impedance map, two examples were selected to illustrate the performance of each of the inversion methods. The first example is from the 2D seismic line near the water source well (Figure 27) while the other is from an inline extracted from the reference 3D volume (Figure 30). Figures 28 and 31 show the initial “guessed” model for the 2D data and the extracted inline

seismic sections while the inversion results using band-limited and model-based inversion for those two sections are illustrated in Figure 29 and 32, respectively.

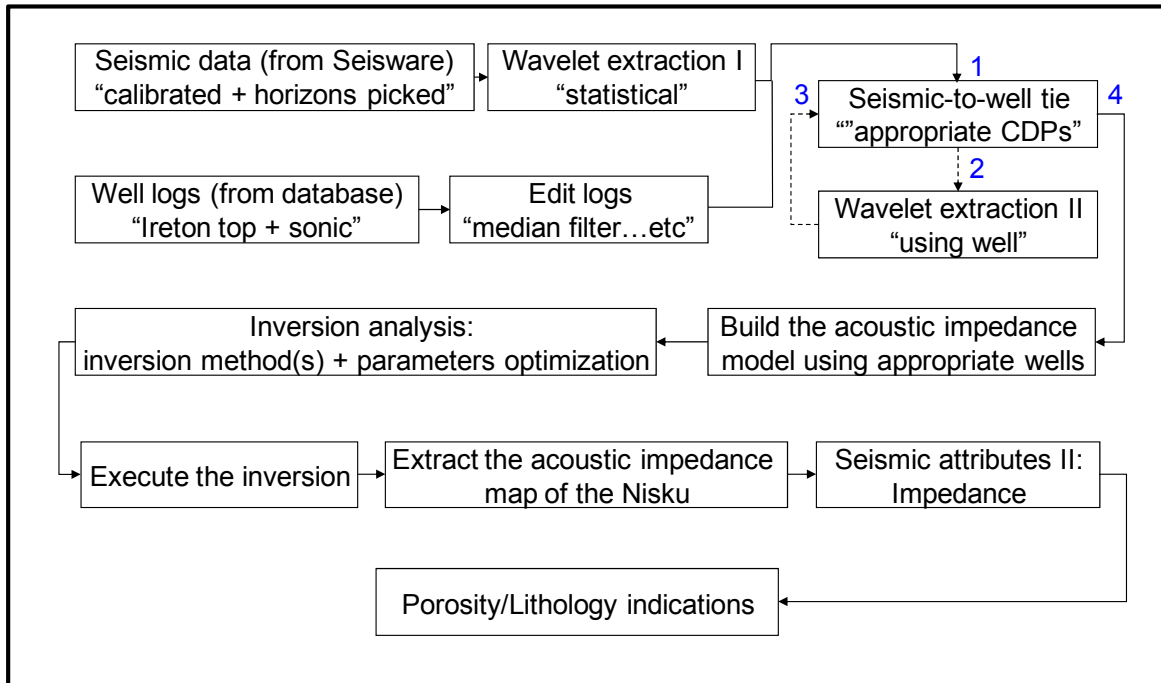


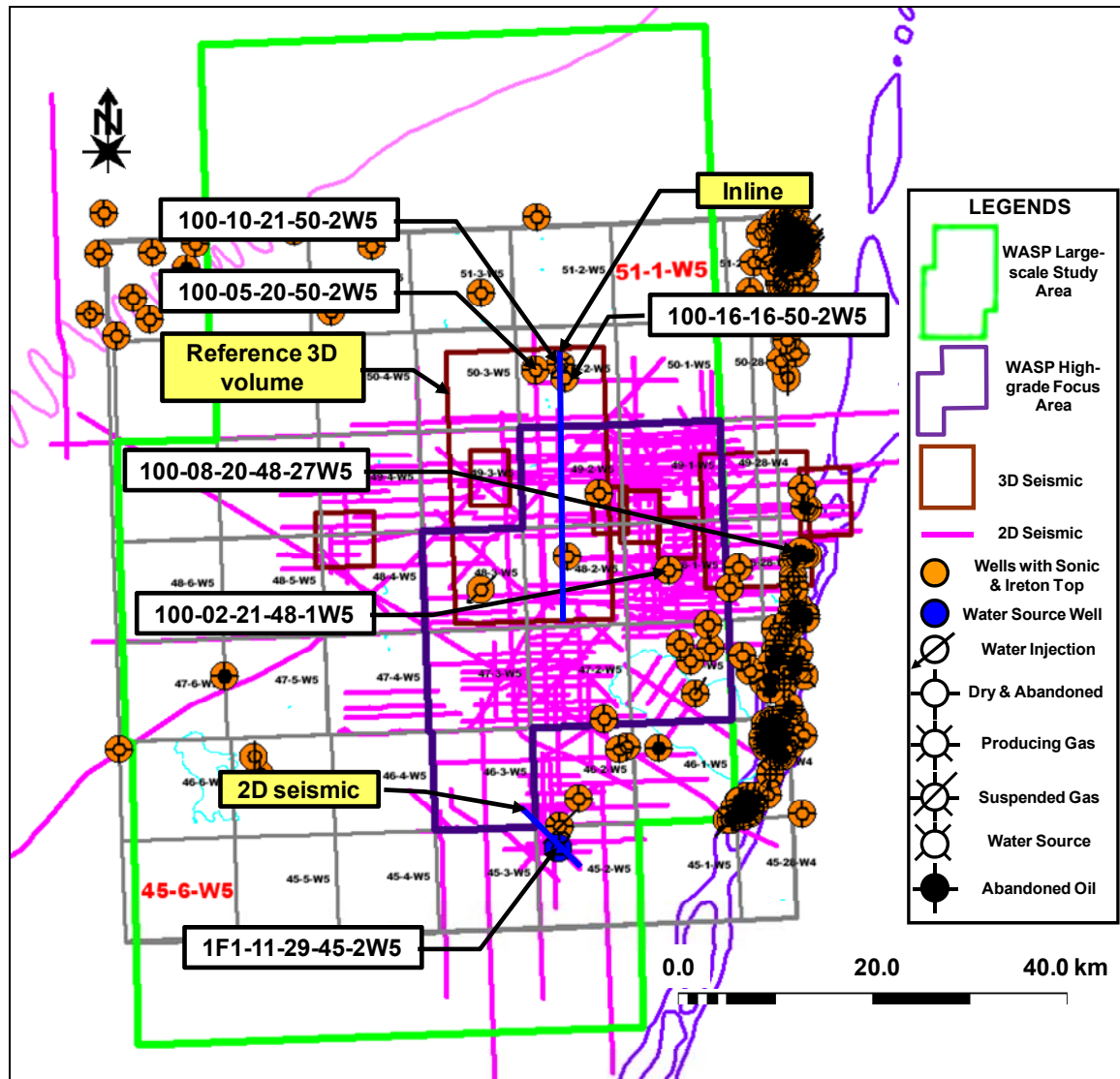
Figure 26: Flowchart outlining the major steps followed in the seismic inversion to extract the acoustic impedance map of the Nisku event.

The band-limited inversion appears to produce a more detailed acoustic impedance model than the model-based inversion. For instance, the Wabamun and the Nisku formations are clearly separated by low impedance in the band-limited inversion whereas they are hardly separated in the model-based inversion results (Figures 29 and 32). However, for the acoustic impedance of the Nisku Formation, both methods yield similar results (Figures 33 and 34), the only apparent difference being in the magnitude of the impedance. This is probably due to scaling differences. Furthermore, because there is a lack of well control, it is crucial that the impedance maps are interpreted only in terms of relative rather than absolute changes in acoustic impedance.

Several interesting low impedance zones are highlighted in Figures 33 and 34. The impedance determination from the 2D seismic line near the water source well is also shown for comparison. By examining those maps, there seems to be two categories of low impedance: one that is associated with lithological changes in the Nisku Formation and another which is associated with discontinuities in the overlying Wabamun event. A useful way to differentiate between those two classes is to use the difference attribute in Figure 24 and Figure 25. Any low acoustic impedance that cross-correlates between the impedance and the difference attributes is likely to be associated with Wabamun event discontinuities. With respect to the lithological changes, low acoustic impedance (Figures 33 and 34) appears to normally correspond to low NRMS and low average NRMS amplitude (Figure 12 and 21).

To relate variations in the acoustic impedance to the two primary physical parameters of interest, i.e., thickness and average P-wave velocity, the acoustic impedance model for the synthetic seismogram in Figure 17 was reconstructed using band-limited and model-based inversion methods (Figure 35). As with the amplitude modelling, variations in the average P-wave velocity seems to be the primary factor shaping the extracted acoustic impedance of the Nisku Formation.

Table 4: Correlation coefficient (over a designed correlation window) between seismic data and synthetic seismogram from selected wells within the study area. The well locations are shown in the base map. The blue lines show the location of the 2D seismic (Figure 27) and the inline (Figure 30) invoked in the inversion.



Well	Seismic Reference	Correlation Coefficient
1F1-11-29-45-2W5	2D	0.92
100-10-21-50-2W5	3D	0.80
100-16-16-50-2W5	3D	0.83
100-05-20-50-2W5	3D	0.72
100-02-21-48-1W5	3D	0.63
100-08-20-48-27W4	3D	0.80

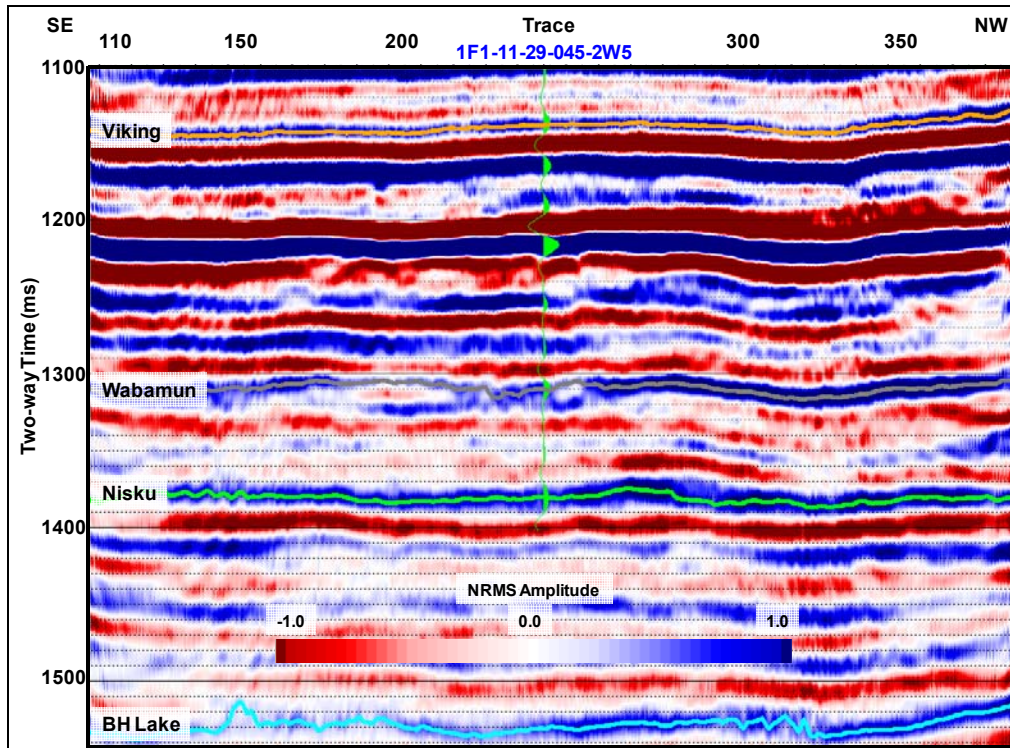


Figure 27: Seismic section near the water source well (Figure 3 and Table 4). The green curve at the well location is the correlated synthetic seismic trace. The correlation coefficient is 0.92.

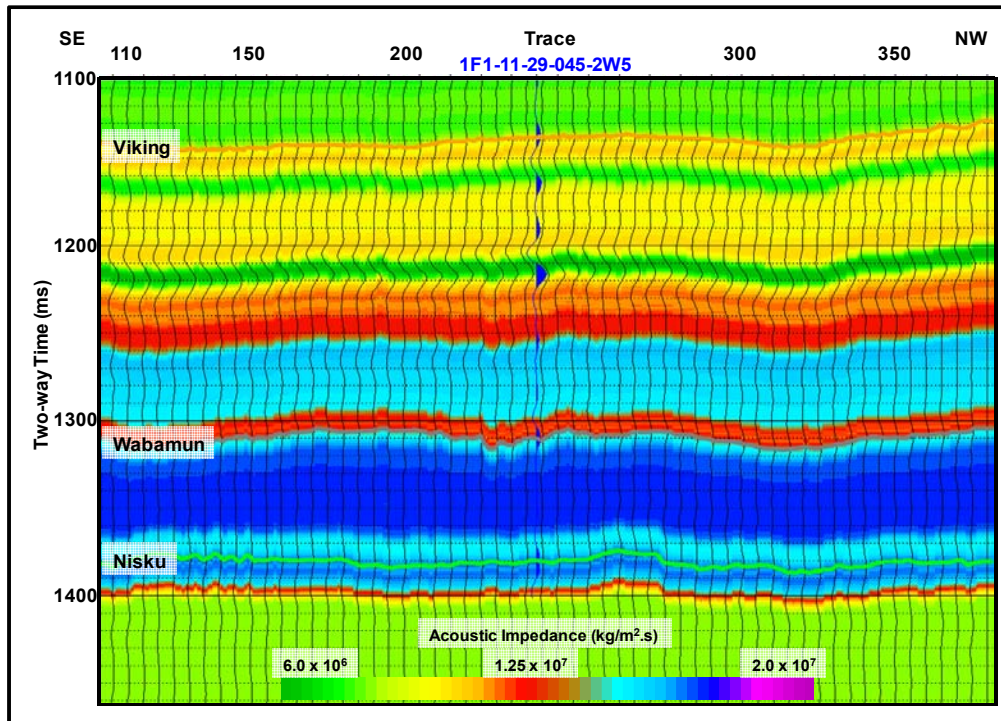


Figure 28: The initial acoustic impedance model. The blue curve at the well location is the correlated synthetic seismic trace while the black curves are the actual seismic traces.

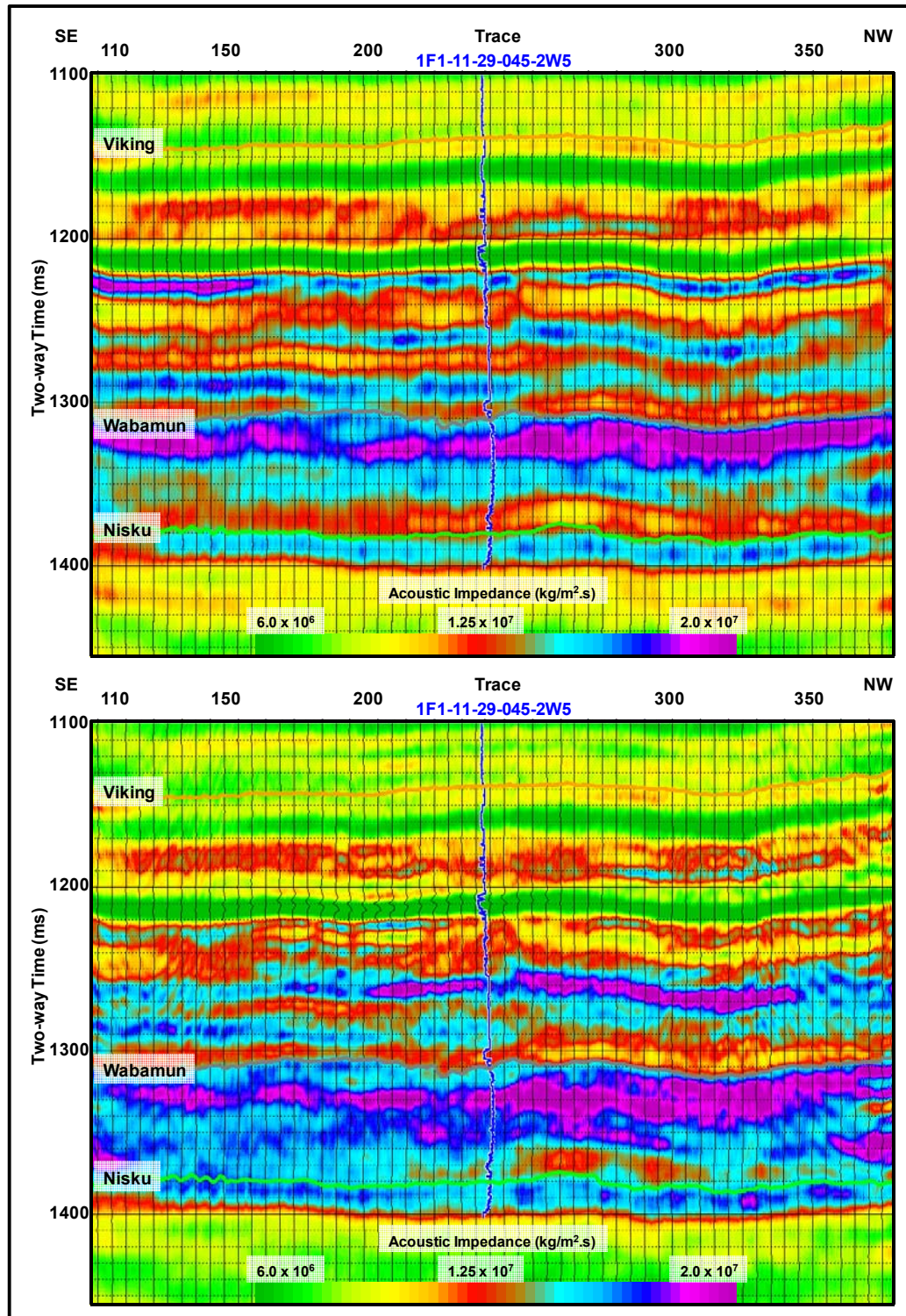


Figure 29: Estimated acoustic impedance along the 2D seismic line near the water source well (Figure 3) using band-limited (top) and model-based (bottom) inversion methods. The inserted blue curve at the well location represents the computed acoustic impedance from the sonic and density logs. The black curves represent the acoustic impedance from the band-limited inversion whereas in the model-based inversion they represent the misfit error.

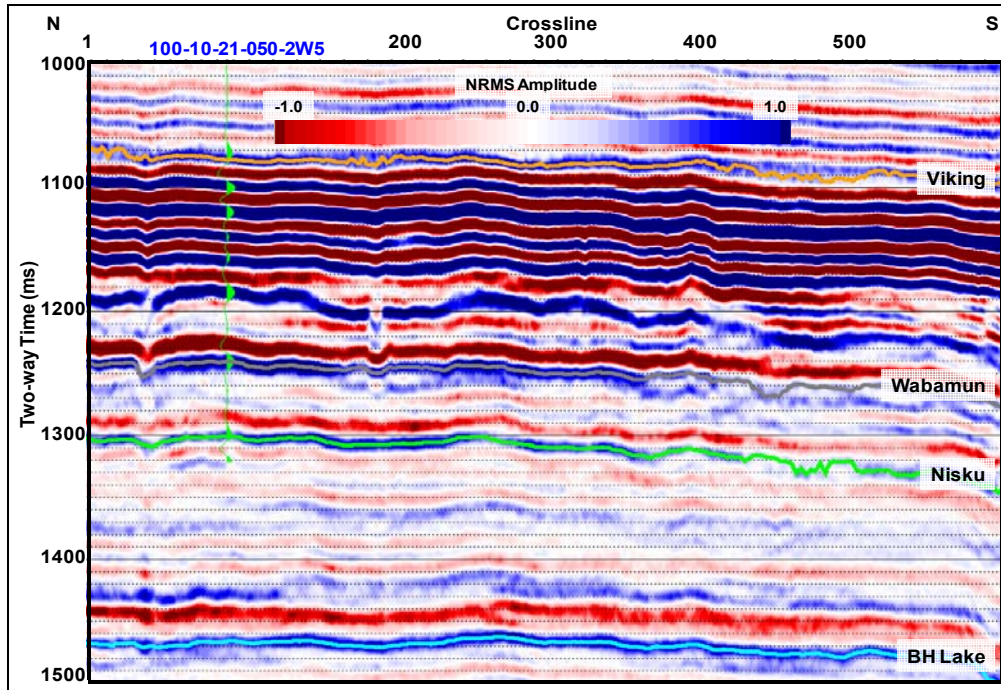


Figure 30: Inline extracted from the reference 3D seismic volume (Table 4). The green curve at the well location is the correlated synthetic seismic trace. The correlation coefficient is 0.80.

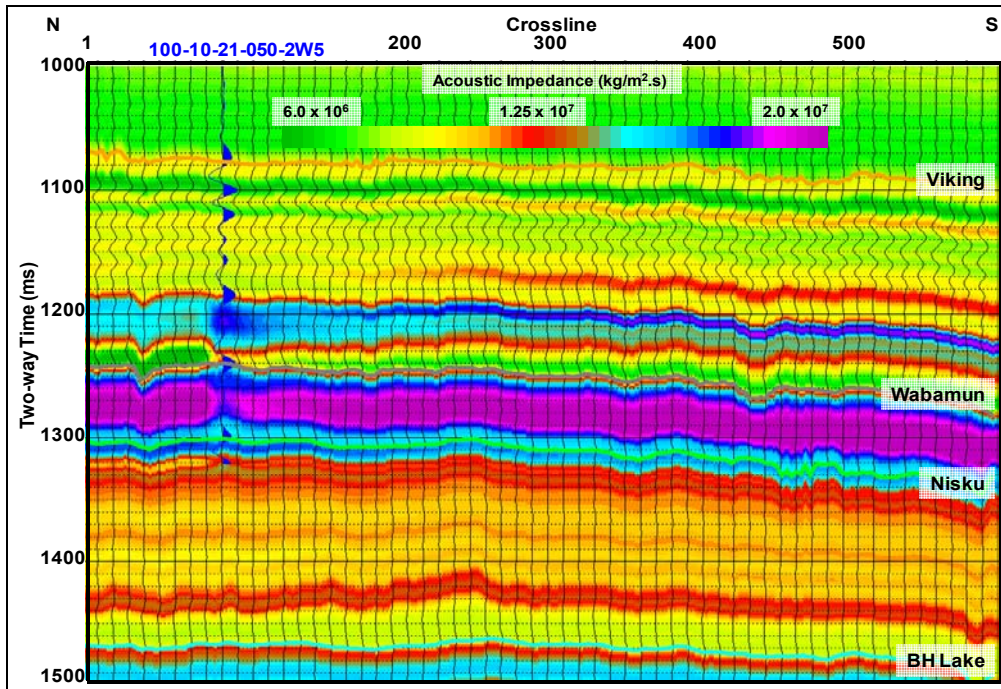


Figure 31: The initial acoustic impedance model corresponding to the inline in Figure 30. The blue curve at the well location is the correlated synthetic seismic trace while the black curves are the actual seismic traces.

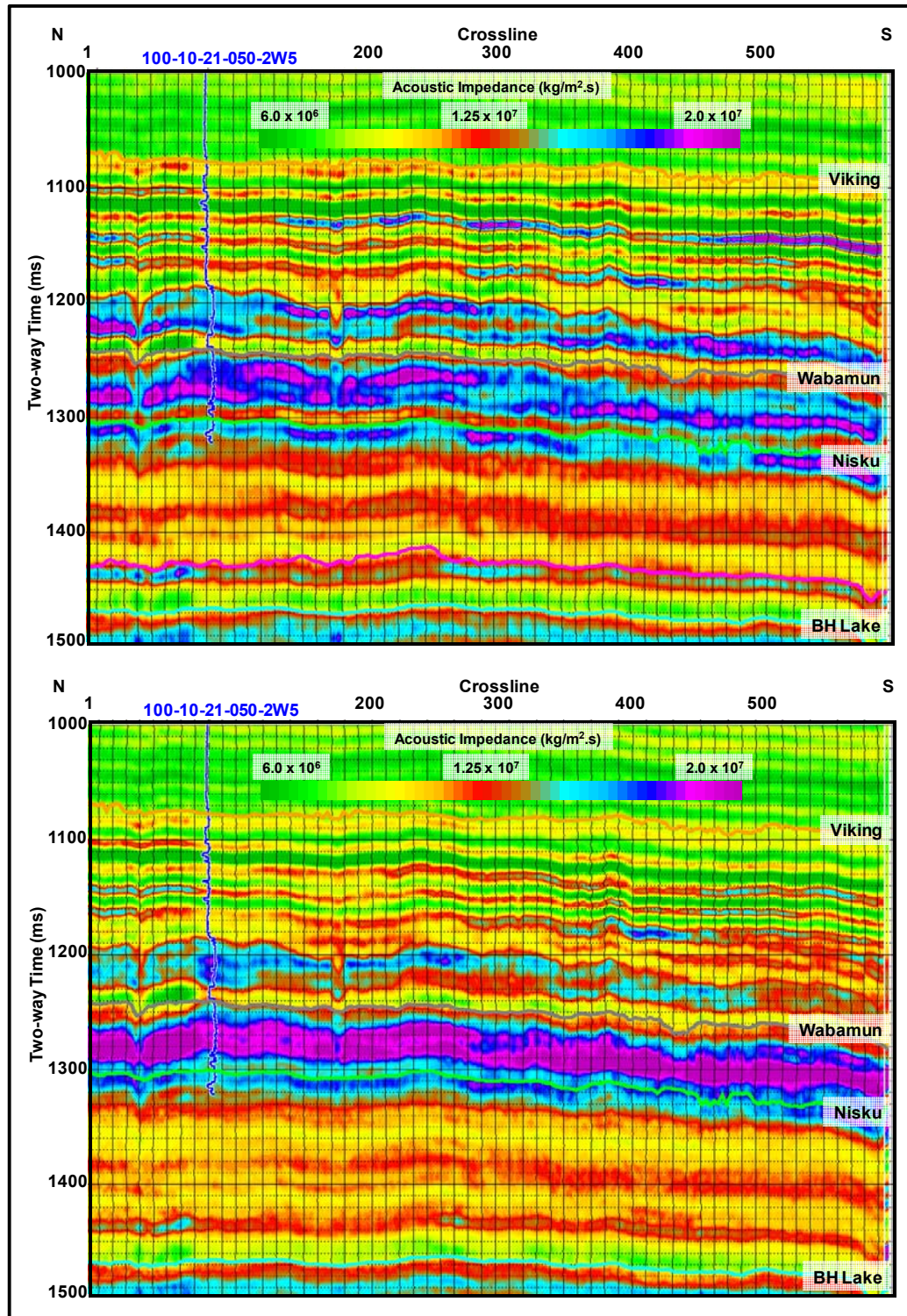


Figure 32: Estimated acoustic impedance of the inline in Figure 30 and Figure 31 using band-limited (top) and model-based (bottom) inversion methods. The inserted blue curve at the well location represents the computed acoustic impedance from the sonic and density logs. The black curves refer to the acoustic impedance from the band-limited inversion whereas in the model-based inversion they represent the misfit error.

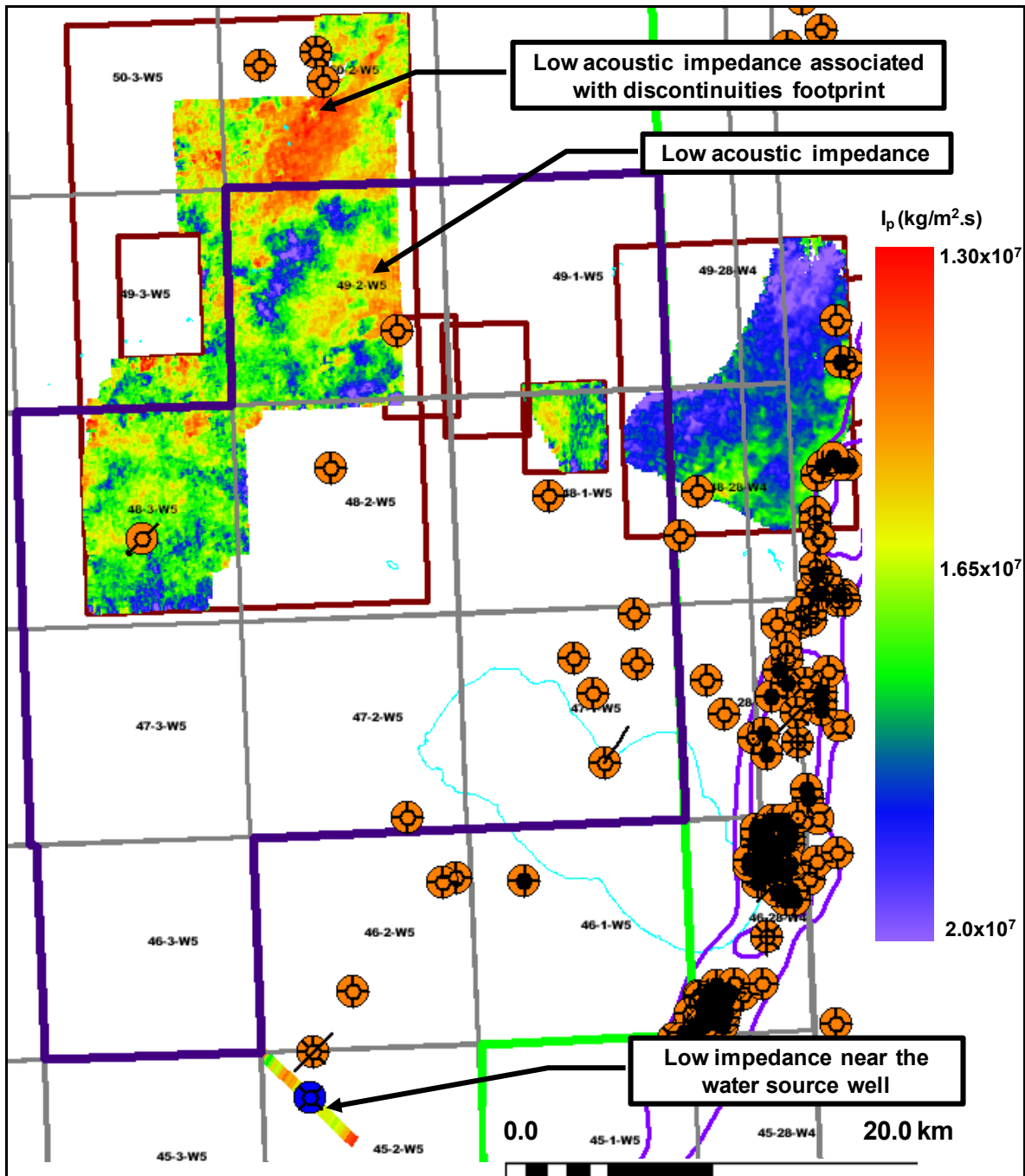


Figure 33: Estimated Acoustic impedance (I_p) map of the Nisku Formation using band-limited inversion. Due to lack of well control, the inversion was not performed on the entire dataset. The relative position to the large study area is shown by the dashed rectangle in the base map in Figure 11.

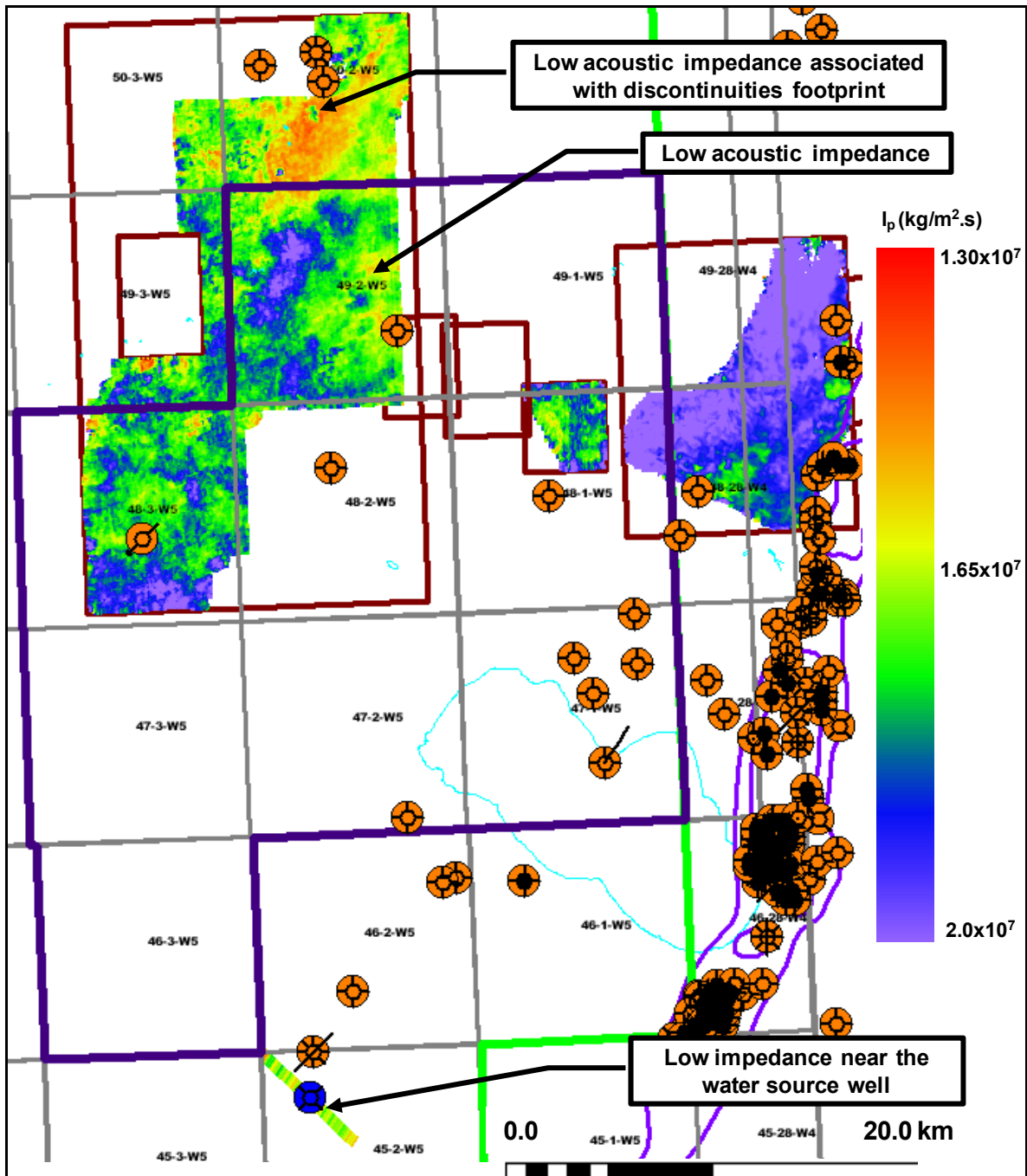


Figure 34: Estimated Acoustic impedance (I_p) map of the Nisku Formation using model-based inversion. Due to lack of well control, the inversion was not performed on the entire dataset. The relative position to the large study area is shown by the dashed rectangle in the base map in Figure 11.

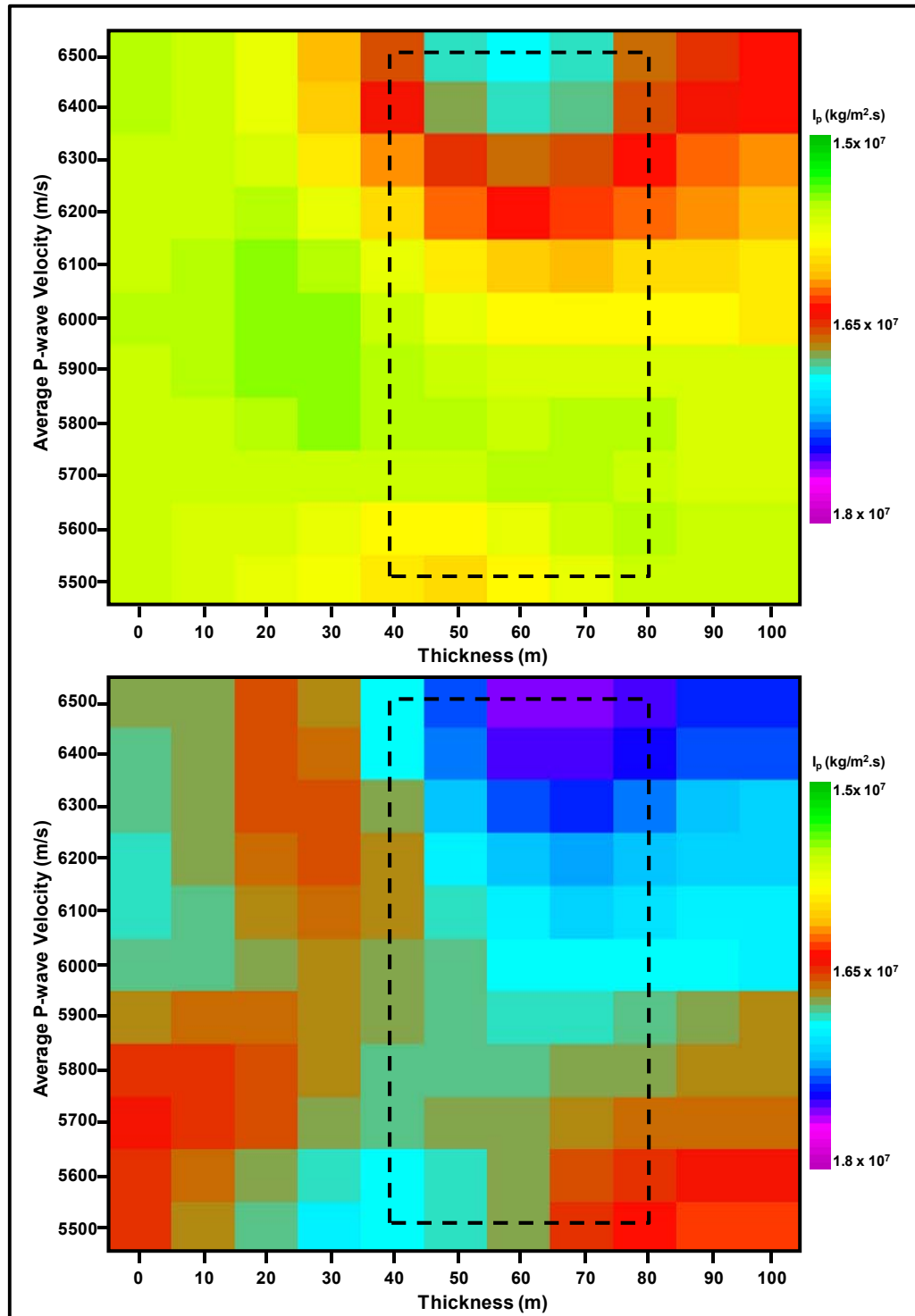


Figure 35: Acoustic impedance (I_p) of the synthetic seismogram in Figure 17 using band-limited (top) and model-based (bottom) inversion methods. Similar to the seismic amplitude response, the acoustic impedance shows high sensitivity toward variations in the Nisku Formation average P-wave velocity rather than thickness. The maps illustrate the direct proportionality between average P-wave velocity and acoustic impedance. Note the similarity in the results except for the small difference in the magnitude of the acoustic impedance due to scaling issues.

9. POROSITY ESTIMATION

Using the P-wave velocity derived from the band-limited acoustic impedance inversion, the bulk porosity of the Nisku Formation was estimated by invoking Wylie's (1956) time-average equation, which states that:

$$\frac{1}{\alpha_{bulk}} = \frac{(1 - \phi)}{\alpha_{matrix}} + \frac{\phi}{\alpha_{fluid}} \quad 4$$

where ϕ is the porosity (dimensionless), α_{matrix} is P-wave velocity of the Nisku matrix (assumed to be ≈ 6800 m/s), α_{fluid} is the P-wave velocity of the Nisku pore fluid (brine ≈ 1600 m/s), and α_{bulk} is the Nisku bulk P-wave velocity (m/s) derived from the band-limited acoustic impedance inversion. Re-arranging equation (4) and solving for porosity (ϕ):

$$\phi = \frac{\alpha_{fluid} [\alpha_{matrix} - \alpha_{bulk}]}{\alpha_{bulk} [\alpha_{matrix} - \alpha_{fluid}]} \quad 5$$

The resultant pseudo-porosity map in Figure 36 correlates fairly well with the low impedance zones in Figures 33 and 34, which is expected since the bulk velocity (α_{bulk}) used in estimating the porosity is derived from the acoustic impedance itself. Although Wylie's time-average equation assumes clean consolidated formations with uniformly distributed pores (Sherriff, 1991), the estimated porosity values seem to fall within the expected range based on wireline data (resistivity log) and core analysis.

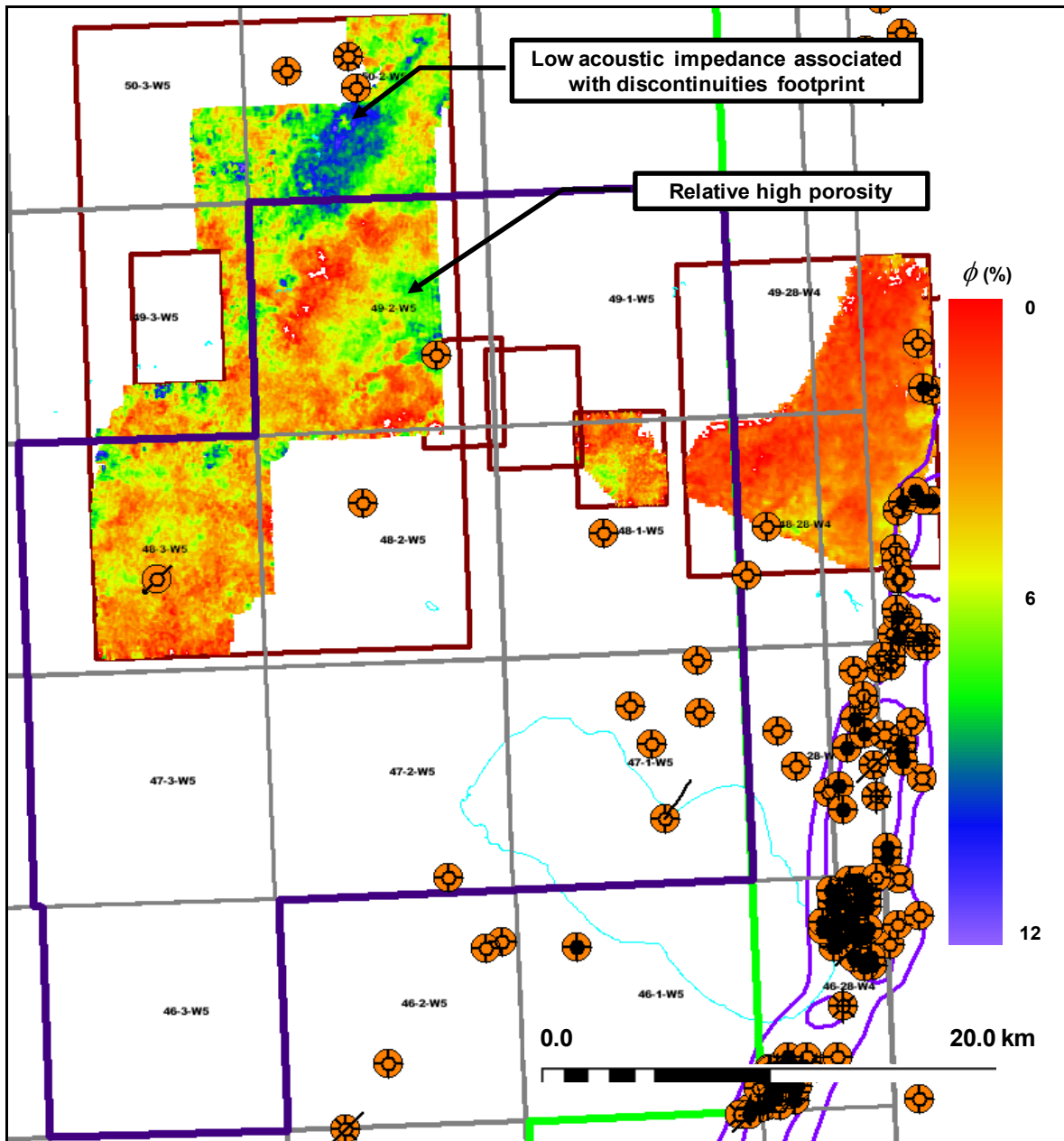


Figure 36: Estimated bulk porosity of the Nisku event using Wylie’s time-average equation with bulk velocity derived from the band-limited acoustic impedance inversion. The relative position to the large study area is shown by the dashed rectangle in the base map in Figure 11.

10. ROCK PHYSICS: FLUID REPLACEMENT MODELLING

Understanding the seismic response to fluid changes within the Nisku Formation is crucial to success of any time-lapse seismic monitoring that may be implemented as part of a measurement, monitoring and verification (MMV) program associated with carbon capture and storage in the study area. Therefore, fluid replacement modelling (FRM) was undertaken to estimate changes in the rock elastic moduli that would result if the original pore-filling fluid in the rock (i.e., brine) is replaced with another fluid (i.e., supercritical CO₂). In our modelling, we invoked the Gassmann (1951) approach. Wang (2001) and Smith et al. (2003) provide a good overview of the Gassmann method and the underlying assumptions. In a concise form, the Gassmann's equation states that:

$$K_{\text{saturated}}^{\text{fluid 1}} = K_{\phi} + \frac{\left(1 - \frac{K_{\phi}}{K_{\text{mineral}}}\right)^2}{\left(\frac{\phi}{K_{\text{fluid}}^{\text{fluid 1}}} + \frac{(1-\phi)}{K_{\text{mineral}}} - \frac{K_{\phi}}{(K_{\text{mineral}})^2}\right)}$$

6

Where:

$K_{\text{saturated}}^{\text{fluid 1}}$ is the bulk modulus of the rock (saturated with the initial fluid) in GPa.

K_{ϕ} is the bulk modulus of the porous rock frame in GPa.

K_{mineral} is the bulk modulus of the rock mineral matrix GPa.

$K_{\text{fluid}}^{\text{fluid 1}}$ is the bulk modulus of the pore-filling (initial) fluid GPa.

ϕ is the porosity (dimensionless).

The bulk modulus of the rock with the initial saturation ($K_{\text{saturated}}^{\text{fluid 1}}$) is given by:

$$K_{\text{saturated}}^{\text{fluid 1}} = \rho_{\text{saturated}}^{\text{fluid 1}} \left[\left(\alpha_{\text{saturated}}^{\text{fluid 1}}\right)^2 - \frac{3}{4} \left(\beta_{\text{saturated}}^{\text{fluid 1}}\right)^2 \right]$$

7

Where the S-wave velocity $\beta_{\text{saturated}}^{\text{fluid 1}}$ is related to the shear modulus $\mu_{\text{saturated}}^{\text{fluid 1}}$ through:

$$\mu_{\text{saturated}}^{\text{fluid 1}} = \rho_{\text{saturated}}^{\text{fluid 1}} \left(\beta_{\text{saturated}}^{\text{fluid 1}}\right)^2 \Rightarrow \beta_{\text{saturated}}^{\text{fluid 1}} = \sqrt{\frac{\mu_{\text{saturated}}^{\text{fluid 1}}}{\rho_{\text{saturated}}^{\text{fluid 1}}}}$$

8

The density $\rho_{\text{saturated}}^{\text{fluid 1}}$ is calculated through the relation:

$$\rho_{\text{saturated}}^{\text{fluid 1}} = \phi \rho_{\text{fluid}}^{\text{fluid 1}} + (1-\phi) \rho_{\text{mineral}}$$

9

Where $\rho_{\text{fluid}}^{\text{fluid 1}}$ is the density of the initial fluid (i.e., brine), and ρ_{mineral} is the density of the matrix (i.e., dolostone). The necessary parameters (P-wave velocity [$\alpha_{\text{saturated}}^{\text{fluid 1}}$], S-wave velocity [$\beta_{\text{saturated}}^{\text{fluid 1}}$], density [$\rho_{\text{saturated}}^{\text{fluid 1}}$] and porosity [ϕ]) required to solve for equation (6) are usually estimated using

wireline data (in our modelling we used the data from the water source well 1F1-11-29-45-2W5 shown in Figure 3). One of the key aspects of the Gassmann method is that K_ϕ remains unchanged regardless of the fluid with which the rock is saturated. Thus, the next major step is to re-arrange the above equation to solve for (K_ϕ):

$$K_\phi = \frac{K_{\text{saturated}}^{\text{fluid 1}} \left(\frac{\phi K_{\text{mineral}}}{K_{\text{fluid}}^{\text{fluid 1}}} + 1 - \phi \right)}{\left(\frac{\phi K_{\text{mineral}}}{K_{\text{fluid}}^{\text{fluid 1}}} + \frac{K_{\text{saturated}}^{\text{fluid 1}}}{K_{\text{mineral}}} - 1 - \phi \right)} \quad 10$$

So once it is known, then it is possible to saturate the system with a replacement fluid ($K_{\text{fluid}}^{\text{fluid 2}}$) and thus calculate the resultant bulk modulus ($K_{\text{saturated}}^{\text{fluid 2}}$):

$$K_{\text{saturated}}^{\text{fluid 2}} = K_\phi + \frac{\left(1 - \frac{K_\phi}{K_{\text{mineral}}} \right)^2}{\left(\frac{\phi}{K_{\text{fluid}}^{\text{fluid 2}}} + \frac{(1-\phi)}{K_{\text{mineral}}} - \frac{K_\phi}{(K_{\text{mineral}})^2} \right)} \quad 11$$

Where:

$K_{\text{saturated}}^{\text{fluid 2}}$ is the bulk modulus of the rock (saturated with the new fluid) in GPa.
 $K_{\text{fluid}}^{\text{fluid 2}}$ is the bulk modulus of the pore-filling (new) fluid GPa.

Finally, the bulk and shear moduli of the new system are used to calculate the new P-wave ($\alpha_{\text{saturated}}^{\text{fluid 2}}$) and S-wave ($\beta_{\text{saturated}}^{\text{fluid 2}}$) velocities, and subsequently, the acoustic impedance:

$$\alpha_{\text{saturated}}^{\text{fluid 2}} = \sqrt{\frac{\frac{4}{3} K_{\text{saturated}}^{\text{fluid 2}} + \mu_{\text{saturated}}^{\text{fluid 2}}}{\rho_{\text{saturated}}^{\text{fluid 2}}}} \quad 12$$

$$\beta_{\text{saturated}}^{\text{fluid 2}} = \sqrt{\frac{\mu_{\text{saturated}}^{\text{fluid 2}}}{\rho_{\text{saturated}}^{\text{fluid 2}}}} \quad 13$$

Note that the shear modulus is assumed to be insensitive to fluid properties and therefore:

$$\mu_{\text{saturated}}^{\text{fluid 1}} = \mu_{\text{saturated}}^{\text{fluid 2}}$$

The density of the new saturated system ($\rho_{\text{saturated}}^{\text{fluid 2}}$) is calculated through the relation:

$$\rho_{\text{saturated}}^{\text{fluid 2}} = \phi S_w \rho_{\text{fluid 1}}^{\text{fluid 1}} + \phi(1 - S_w) \rho_{\text{fluid 2}}^{\text{fluid 2}} + (1 - \phi) \rho_{\text{mineral}}$$
14

where S_w is the water saturation, and $\rho_{\text{fluid 2}}^{\text{fluid 2}}$ is the density of the new fluid (i.e., CO₂). For the FRM, the following constituents were selected for the modelling:

1. Dolostone as the single mineralogy of which the rock matrix is comprised (mineral).
2. Brine as the initial fluid with which the pore space is filled (fluid 1).
3. Supercritical carbon dioxide (CO₂) as the new fluid being introduced into the reservoir (fluid 2).

The values and ranges selected for the above constituents are given in Table 5. The results obtained using those parameters and the fluid substitution method discussed above suggest that changes in the average acoustic impedance is rather small and the change in the shear impedance is insignificant as a function of increasing CO₂ saturation (Figure 37).

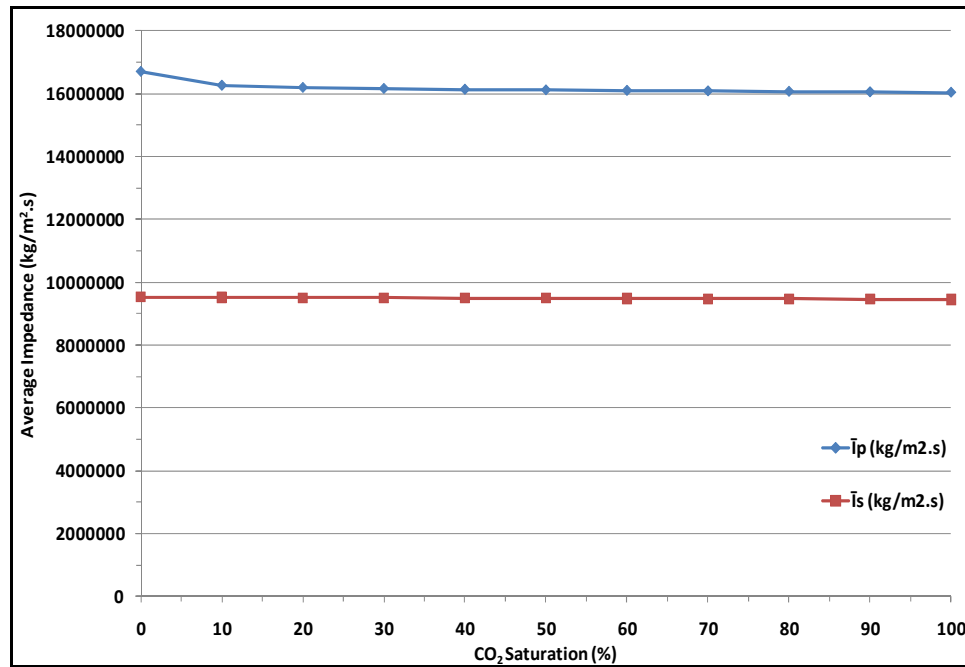
Table 5: Parameters pertaining to the main constituents in the Gassmann FRM. The pressure, temperature, porosity and thickness of the Nisku Formation were 15 MPa, 50.3 Co, 9%, and 56 m respectively (Michael et al., 2008). Salinity and viscosity were adopted from Michael et al. (2008) whereas the rest of the parameters were calculated using the CREWES Fluid Property Calculator (Ursenbach, 2009) which is based on a paper by Batzle and Wang (1992) and the Peng-Robinson (1976) equation of state.

	Brine (Fluid 1)	Dolomite (Mineral)	CO₂ (Fluid 2)
Bulk Modulus	3.3 GPa	94.9 GPa	0.081 GPa
Shear Modulus	-	45 GPa	-
Density	1112 kg/m ³	2840 kg/m ³	659 kg/m ³
Salinity	170 g/l	-	-
Viscosity	0.75 Pa.s	-	0.062 Pa.s
Initial Saturation	100%	-	0%
Final Saturation	0%	-	100%

For the seismic component of the modelling, the Zoeppritz equations (Zoeppritz, 1919; Aki and Richards, 1980) were chosen to model the offset-dependent seismogram response to the changes in the reservoir fluid properties. Synthetic seismograms were generated at 100 m increments with the maximum offset being 1500 m. The synthetic traces were normal move out (NMO) corrected and stacked to mimic the response of a post-stack seismic section. The difference between the base and monitor synthetic seismograms associated with increasing the CO₂ saturation from 0% to 100% is very subtle (Figure 38), which suggests that identifying the CO₂ plume in the Nisku Fm. will be challenging for any prospective time-lapse seismic monitoring program. The greatest change in the seismic response correlates with increasing the CO₂ saturation from 0% to 20% (Figure 39). For instance, the Ireton event shows only about a 1 ms increase in the two-way travel time (Figure 39b), most of which (~ 90%) occurs within the first 20% of CO₂ saturation in the Nisku Formation. Interesting also is the observed delay in the Nisku event travel time between the base and monitor surveys (Figure 39a). Furthermore, the Nisku event also experiences some amplitude dimming (Figure 39c); a phenomenon typically associated with class 1 and 2 amplitude variation with offset

(AVO) anomalies (Castagna, 1993). Nonetheless, the overall subtlety of the seismic response suggests that the Nisku Formation matrix is stiff and is therefore rather insensitive to fluid changes.

It is important to understand that the assumptions underlying Gassmann’s equation are not always appropriate for CO₂ fluid replacement modelling. For example, the method assumes that no interaction takes place between the fluid and the rock matrix. However, this assumption is likely to be violated due to the acidity of the CO₂, which will react with carbonate rocks. Nonetheless, the results presented here should provide an estimate of the effect of fluid replacement on the time-lapse seismic response.



CO ₂ Saturation (%)	\bar{I}_p (kg/m ² .s)	$\Delta \bar{I}_p$ (kg/m ² .s)	% Change \bar{I}_p	\bar{I}_s (kg/m ² .s)	$\Delta \bar{I}_s$ (kg/m ² .s)	% Change \bar{I}_p
0	16690486.0	0.0	0.0	9526013.3	0.0	0.0
10	16250069.4	-440416.6	-2.6	9518701.3	-7312.0	-0.1
20	16182492.3	-507993.7	-3.0	9511383.7	-14629.7	-0.2
30	16148989.8	-541496.2	-3.2	9504416.2	-21597.1	-0.2
40	16124977.4	-565508.6	-3.4	9497087.5	-28925.8	-0.3
50	16105336.2	-585149.8	-3.5	9489753.2	-36260.1	-0.4
60	16087978.5	-602507.5	-3.6	9482413.2	-43600.1	-0.5
70	16072566.9	-617919.1	-3.7	9475424.1	-50589.3	-0.5
80	16057404.0	-633082.0	-3.8	9468072.8	-57940.5	-0.6
90	16042815.7	-647670.3	-3.9	9460716.5	-65296.8	-0.7
100	16028630.8	-661855.2	-4.0	9453353.9	-72659.5	-0.8

Figure 37: Predicted changes in the average acoustic (\bar{I}_p) and shear (\bar{I}_s) impedance of the Nisku Formation as a result of increasing the CO₂ saturation from 0 to 100%. The highest incremental change is associated with increasing the CO₂ saturation from 0 to 20%. Shortly after that, the acoustic impedance reaches a plateau. The shear impedance, on the other hand, is rather insensitive to the fluid replacement.

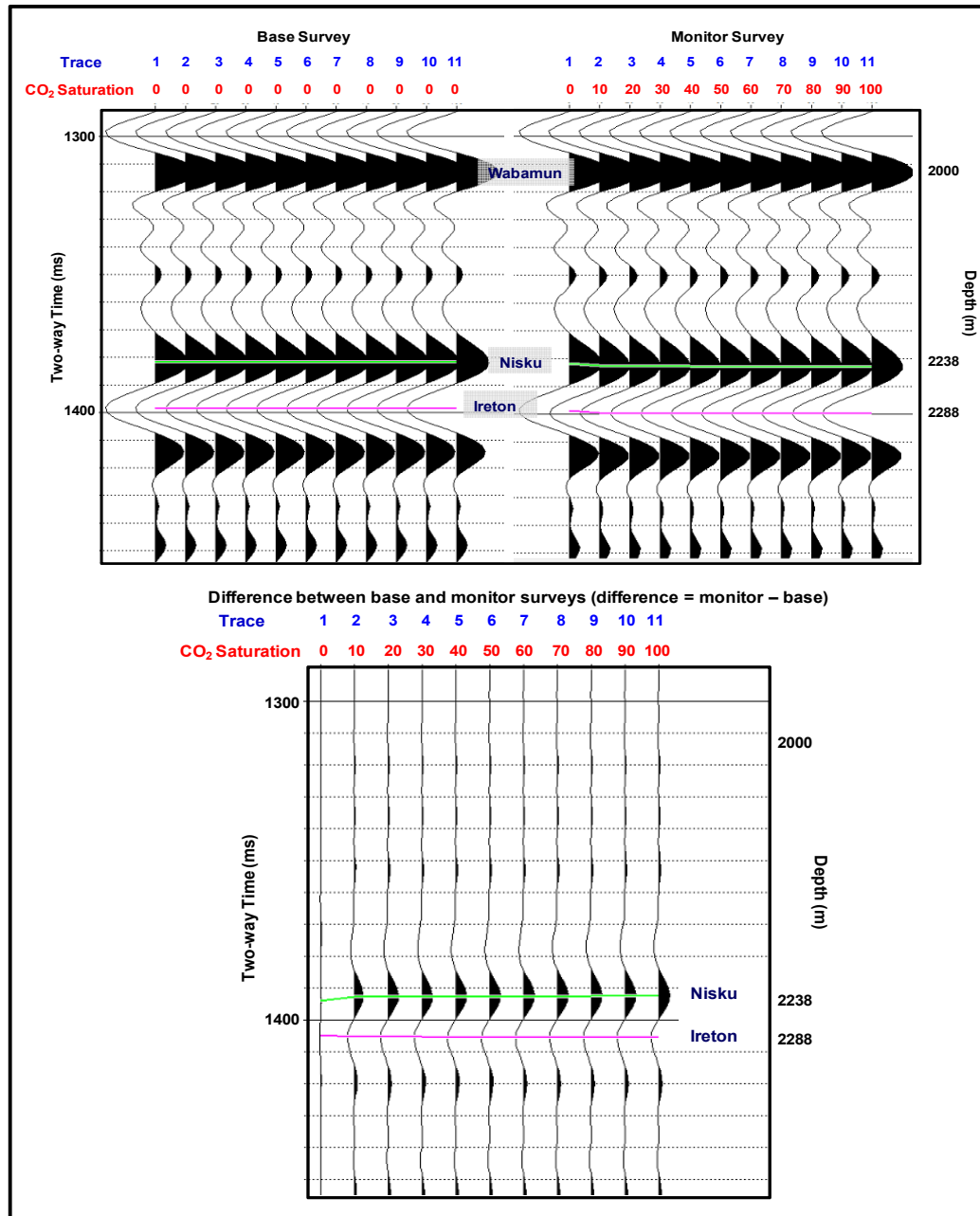


Figure 38: Top left: Offset dependent synthetic seismogram generated using the Zoeppritz equations after NMO correction and stacking; all 11 traces are identical (in the base survey) and they represent an initial condition in which the reservoir is 100% brine saturated. Top right: the same offset dependent synthetics but in this case (monitor survey) each trace has undergone a saturation transformation between brine and CO₂ as indicated by the values along the horizontal axis (red label). Bottom: the difference between the monitor and base. Changes in reservoir properties were only applied to the zone of interest, i.e., Nisku (2238 m) to Ireton (2288 m). The highest incremental change is associated with the first 10% of CO₂ saturation (trace 2). The subtle difference between the two surveys suggests that the Nisku matrix is so stiff that the fluid replacement process is only having a small effect on the observed seismic response. The modelling was undertaken using the water source well (1F1-11-29-45-2W5).

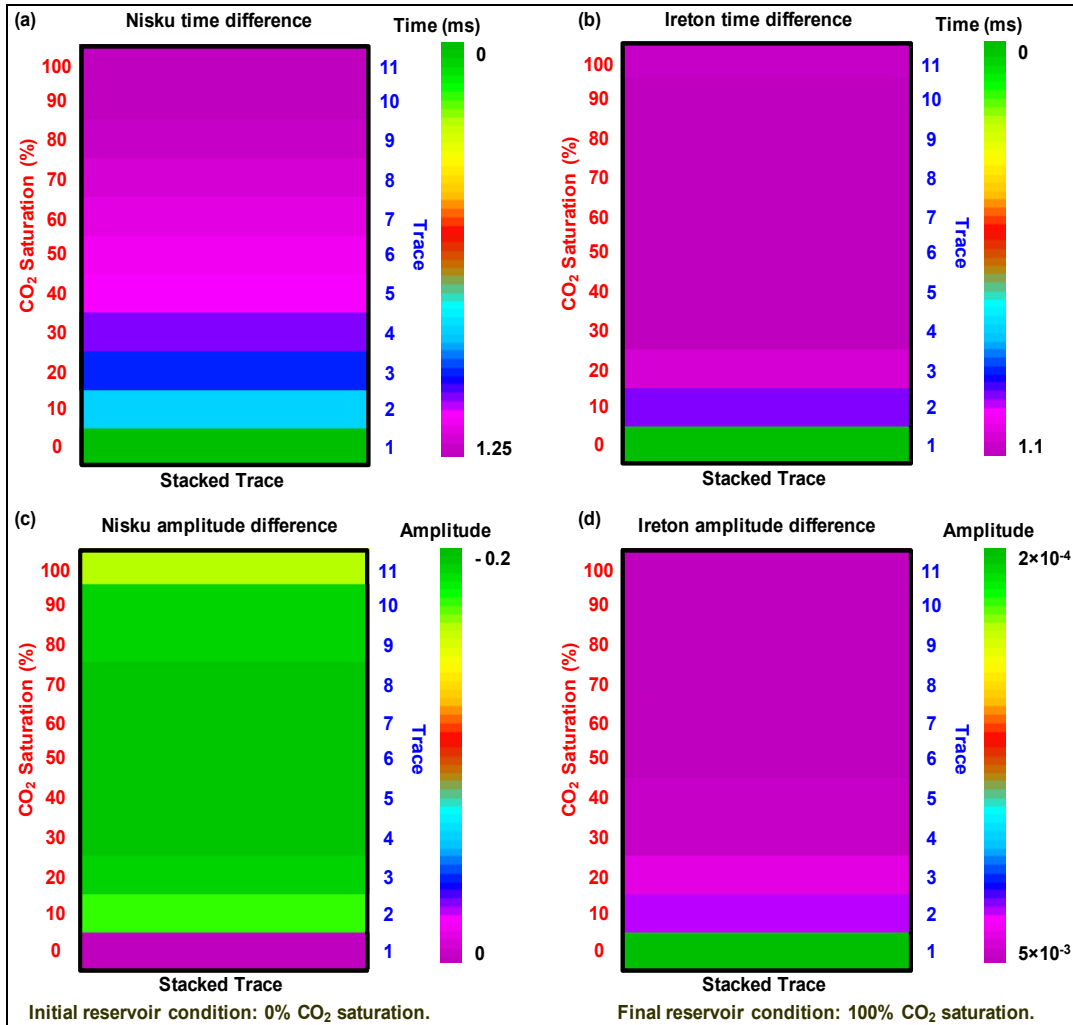


Figure 39: Mosaic display of the fluid substitution effect on the time and amplitude response of the Nisku and Ireton events, respectively, between the base and monitor surveys: (a) difference in the Nisku event two-way time (ms); (b) difference in the Ireton event two-way time (ms); (c) difference in the Nisku event amplitude; (d) difference in the Ireton event amplitude. Each horizon is obtained by subtracting the corresponding horizons between the monitor and base surveys (difference = monitor - base) in Figure 38. In all the plots the highest incremental change in time and amplitude is associated with the initial increase in CO₂ saturation (i.e., from 0 to 10%). Shortly after that, the seismic response reaches a plateau and becomes virtually unresponsive to the increase in CO₂ saturation. The modelling was undertaken using the water source well (1F1-11-29-45-2W5) shown in Figure 3.

11. CONCLUSIONS

The seismic characterization of the Nisku Formation in WASP study area has revealed two major groups of anomalies: one is associated with geological discontinuities, primarily in the overlying Wabamun Formation, while the other is interpreted to be a result of lithological/thickness changes within the Nisku Formation. In addition, regional 2D seismic lines (Figure 5, Figure 6, Figure 7, and Figure 8) were used to interpret long-wavelength geological features, the results of which indicate that there is no sign of major faulting in the study area. In comparison, detailed mapping, attribute analysis and acoustic impedance inversion were achieved using high quality 3D seismic in the northern part of the study area.

The interpreted time structure map of the Nisku Fm. (Figure 10) is rather smooth and consistent with the regional NE-SW dip orientation. The normalized root-mean squares (NRMS) amplitude map (Figure 12) shows stronger variations across the study area. Those anomalies are most likely associated with lithological variations and geological discontinuities. In order to differentiate between the two types of anomalies, seismic attributes and acoustic impedance inversion were exploited, in addition to NRMS amplitude, to delineate anomalies caused by lithological variations in contrast to those induced by geological discontinuities. Seismic amplitude modelling was undertaken to establish the principal factor affecting seismic amplitude. The modelling results (Figure 18) imply that amplitude variations in the Nisku event are caused by variations in the average P-wave velocity of the Nisku Formation driven by lithology and porosity variations. The hypothesis that lithology and porosity variations rather than thickness changes are responsible for the amplitude variations was tested against a good quality brine-bearing zone of the Nisku Formation near the southern corner of the study area. The seismic data around this water source well show significant variations in the NRMS amplitude but data from neighbouring wells suggest only a small variation in the Nisku thickness.

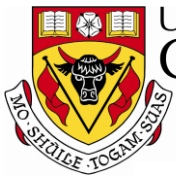
Seismic attributes, such as the amplitude thickness of the peak (ATP) revealed an interesting Nisku pattern that is not captured by the NRMS amplitude map. Unfortunately, there are no wells that penetrate the Nisku within that feature but, in general, by using this attribute in conjunction with the estimated bulk porosity map, we arrived at one way of identifying favourable sites. Coherency-sensitive seismic attributes, such as the difference method (Figure 24 and Figure 25), reveal numerous geologic discontinuities in the Nisku event amplitude. Even though those are interpreted to be induced by dissolution in the overlying Wabamun Formation and do not necessarily reflect physical discontinuities within the Nisku Fm. itself, they should be taken into consideration in any future CO₂ sequestration program in the area. Several favourable zones of low acoustic impedance (Figure 33) and high bulk porosity (Figure 36) are identified in the study area. However, differentiation between acoustic impedance changes caused by enhanced porosity and those associated with a possible increase in shale content remains tenuous. Finally, the fluid replacement modelling results (Figure 37 and 38) and the fact that the Nisku-Ireton is represented by one cycle in the seismic data suggest that the success of any time-lapse surface seismic program to track the CO₂ plume in the Nisku Fm will be difficult.

ACKNOWLEDGMENTS

We would like to thank the WASP sponsors and the Natural Sciences and Engineering Research Council of Canada (NSERC) for funding the project and the WASP technical team for valuable discussions, ENCANA for kindly providing access to the seismic data, and Jimmy Haszard (ENCANA), Jay LeBlanc (ENCANA), and Ian Reglar (formerly ENCANA) for providing valuable technical support. Hampson-Russell, Seismic-Micro Technology and Zokero are thanked for providing seismic interpretation software.

REFERENCES

- Aki, K., Richards, P.G., 1980. *Quantitative Seismology*, Freeman and Co., New York.
- Batzle, M. and Wang, Z., 1992, Seismic properties of pore fluids: *Geophysics*, 57, 1396–1408.
- Cooke, D. A., and Schneider, W. A., 1983, Generalized linear inversion of reflection seismic data: *Geophysics*, 48, 665–676.
- Gassmann, F., 1951, *Über die elastizität poroser medien: Verteljahrss-chrift der Naturforschenden Gesellschaft in Zurich*, 96, 1–23. Translated to English in the 16th issue of *Geophysics*: Gassmann, F., 1951, Elastic waves through a packing of spheres: *Geophysics*, 16, 673–23.
- Castagna, J., 1993, Petrophysical imaging using AVO: *The Leading Edge*, 12, 172.
- Ursenbach, Charles, 2009, CREWES Fluid Property Calculator Applet: <<http://www.crewes.org/ResearchLinks/ExplorerPrograms/FIProp/FluidProp.htm>>.
- Lines, L. R., and Treitel, S., 1984, A review of least-squares inversion and its application to geophysical problems: *Geophysical Prospecting*, 32, 159–186.
- Luo, Y., Higgs, W.G., and Kowalik, W.S., 1996, Edge detection and stratigraphic analysis using 3D seismic data: 66th Ann. Internat. Mtg., Soc. Expl. Geophys., Expanded Abstracts, 324–331.
- Michael, K., S. Bachu¹, B. Buschkuehle¹, K. Haug, and S. Talman, 2008, Comprehensive Characterization of a Potential Site for CO₂ Geological Storage in Central Alberta, Canada: AAPG Manuscript, 40 p.
- Peng, D.-Y. and Robinson, D. B., 1976, A New Two-Constant Equation of State: *Ind. Eng. Chem., Fundam.*, 15, 59–64.
- Russell, B.H., 1988, *Introduction to seismic inversion methods: Society of Exploration Geophysicists, Course Notes Series, No. 2*, S. N. Domenico, Series Editor.
- Sherriff, R. E., 1991. *Encyclopedic Dictionary of Exploration Geophysics: Society of Exploration Geophysicists, 4th edition*, Tulsa, Oklahoma.
- Smith, T. M., Sondergeld, C. H., and S. R Chandra, 2003, Gassmann fluid substitutions: A tutorial: *Geophysics*, 68, 430–440.
- Wang, Z., 2001, Fundamentals of seismic rock physics: *Geophysics*, 66, 398–412.
- Waters, K. H., 1978, *Reflection seismology: John Wiley and Sons*.
- Wylie, M. R., Gregory, A. R., and Gardner, L. W., 1956, Elastic wave velocities in heterogeneous and porous media: *Geophysics*, 21, 41–70.
- Zoeppritz, R., 1919, On the reflection and propagation of seismic waves: *Erdbebenwellen VIII B; Göttinger Nachrichten*, I, 66–84.



Aquifer Material Balance

WABAMUN AREA CO₂ SEQUESTRATION PROJECT (WASP)

Author

Rob Lavoie

Rev.	Date	Description	Prepared by
1	August 3, 2009	Nisku Oil Pool Aquifer Material Balance Analysis	Rob Lavoie
2	December 21, 2009	Nisku Oil Pool Aquifer Material Balance Analysis	Rob Lavoie

Table of Contents

INTRODUCTION.....	5
BACKGROUND	5
DISCUSSION	6
1. Study Approach.....	6
2. Paleogeography Of The WASP Study Area	7
3. Reservoir Data	9
4. Material Balance Results	10
4.1 Acheson D2-A and D2-B Pools.....	10
4.2 Golden Spike D2A.....	13
4.3 Golden Spike D2B.....	16
4.4 Leduc Woodbend D2A and D2B Pools.....	18
CONCLUSIONS	23
REFERENCES.....	24
APPENDIX 1	25

List of Tables

Table 1: Data summary for Acheson D2-A pool.	11
Table 2: Data summary for Golden Spike D2-A pool.....	13
Table 3: Data summary for Golden Spike D2-B pool.....	16
Table 4: Data summary for Leduc Woodbend D2-A pool.	18
Table 5: Data summary for Leduc Woodbend D2-B pool.	19

List of Figures

Figure 1: WASP study area.....	5
Figure 2: Water disposal well study area.	6
Figure 3: WASP study area.....	8
Figure 4: Cross section of the Nisku aquifer and adjacent stratigraphy (Reference 3).	9
Figure 5: Location of Acheson D2-A Pool.....	10
Figure 6: Acheson D2-A pool production, injection, and pressure versus time history.	12
Figure 7: Acheson D2-A pool pressure versus time history.....	12
Figure 8: Location of Golden Spike D2-A.	13
Figure 9: Golden Spike D2-A pressure, production, and injection history.	14
Figure 10: Golden Spike D2-A material balance history match.	14
Figure 11: Golden Spike D2-A mapping of aquifer shape and size.....	15
Figure 12: Golden Spike D2-B pressure, production, and injection history.	16
Figure 13: Golden Spike D2-B pressure, production, and injection history.	17
Figure 14: Golden Spike D2-B pressure, production, and injection history.	17
Figure 15: Leduc Woodbend D2-A pressure history.....	19
Figure 16: Leduc Woodbend D2-A production history (post 1961).....	20
Figure 17: Leduc Woodbend D2-A injection history (post 1961).	21
Figure 18: Leduc Woodbend D2-B pressure history.....	21
Figure 19: Leduc Woodbend D2-B production history (post 1961).....	22
Figure 20: Leduc Woodbend D2-B injection history (post 1961).	23

INTRODUCTION

BACKGROUND

One of the most useful methods of characterizing the quality of a reservoir for its deliverability or injectivity on a regional scale is to make use of analogues from similar or adjacent areas to the area of study. Furthermore, material balance analysis on analogue pools or wells can be conducted to characterize the aquifer that is providing pressure support for them. Moreover, material balance analysis is capable of characterising a very large area of investigation, if an oil or gas pool has been on depletion drive for an extended period of time. The Wabamun Area CO₂ Sequestration Project (WASP) study area is an entire 53 township of land area over top of a large portion of the Nisku aquifer in central Alberta, Figure 1. This study area was chosen intentionally to avoid existing hydrocarbon production. As such, there are no depleted pools or mature oil fields producing from the Nisku horizon in the entire study area.

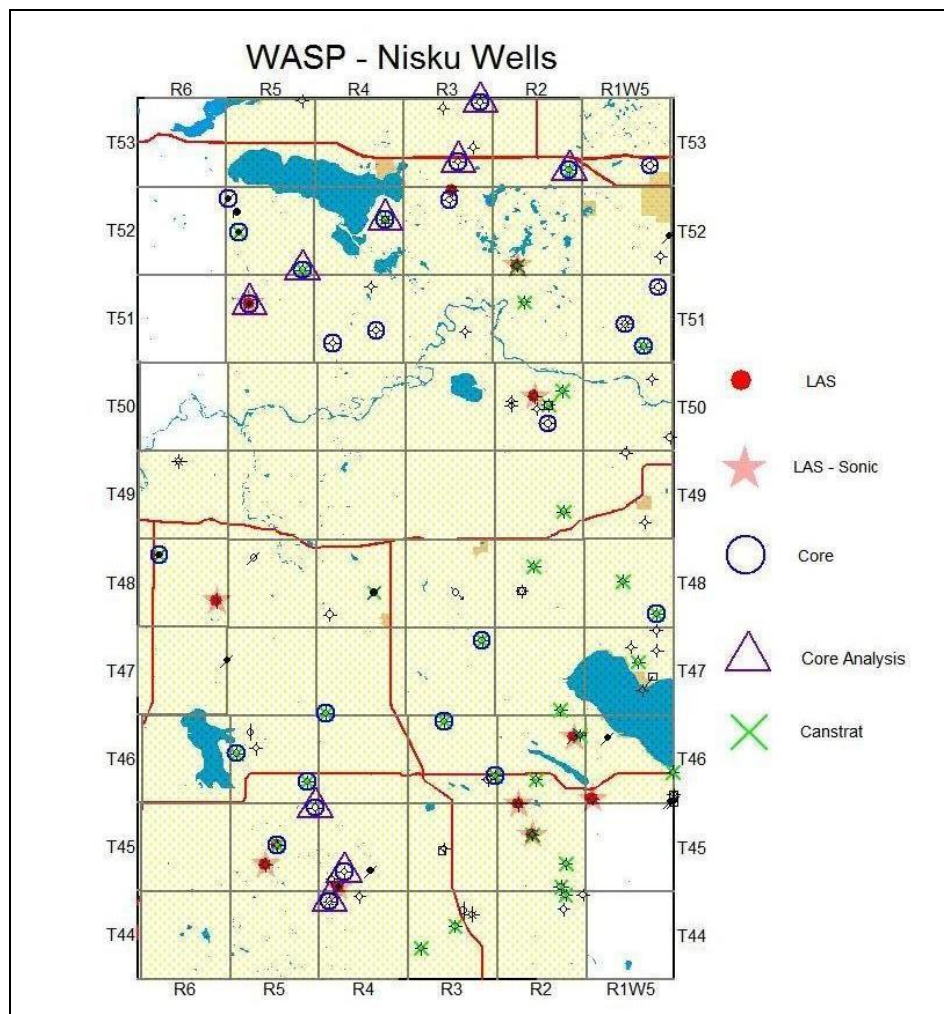


Figure 1: WASP study area.

In an attempt to find additional confirmation of good reservoir quality conditions for the Nisku aquifer, a review of mature oil pools in a study area consisting of 30 townships immediately to the east of the WASP study area was performed. Figure 2 highlights this area along with the locations of six major Nisku oil pools.

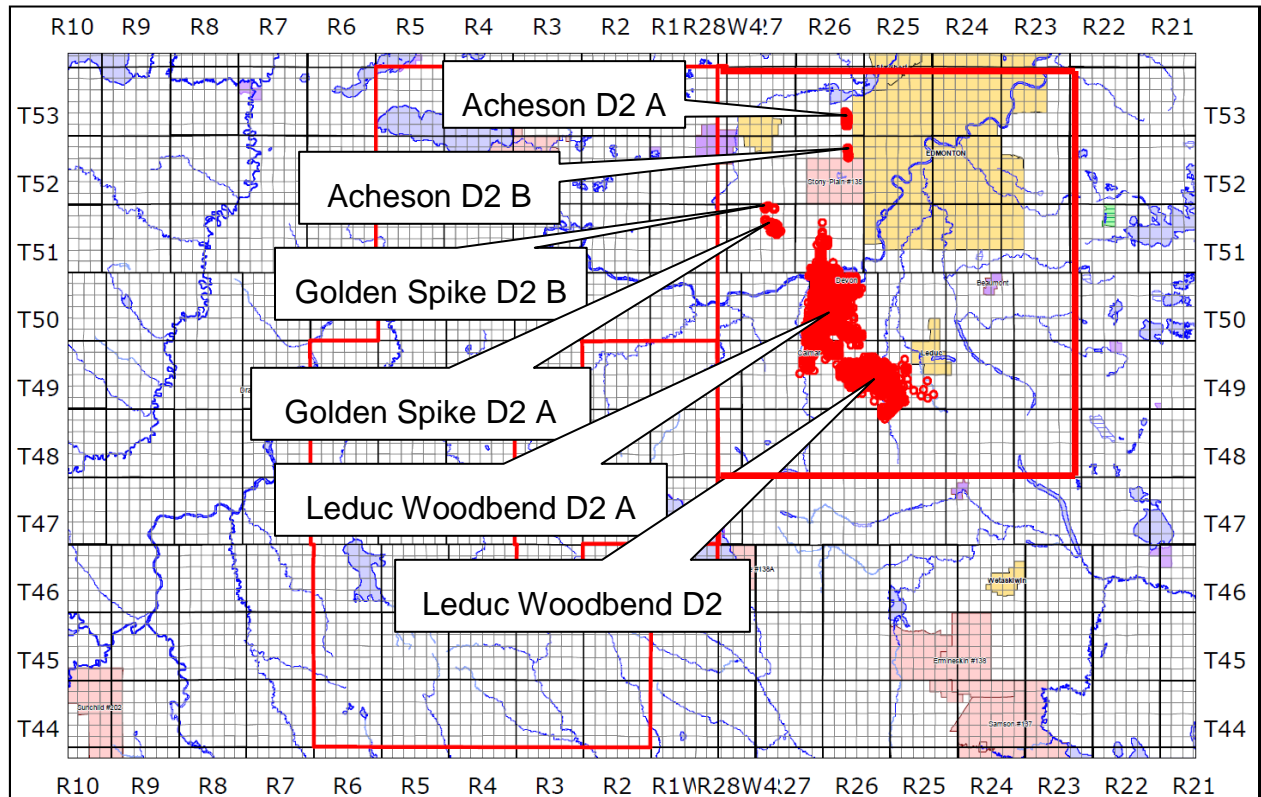


Figure 2: Water disposal well study area.

The discussion that follows provides a summary of attempts to conduct material balance characterizations of the Nisku aquifer for the mature oil pools located in this study area.

DISCUSSION

1. STUDY APPROACH

The rich set of mature oil pools located immediately to the east of the WASP study area compelled one to make the best use of public domain data to characterise the Nisku aquifer from historic production and injection data available at the Energy Resource Conservation Board (ERCB).

The study began with a fact finding mission. Literature reviews were conducted to learn as much as possible about the Nisku reservoirs from existing published engineering papers. The literature search resulted in only minor references to aquifer characterization work or geological information pertaining to the Nisku aquifer.

Given the lack of published results on Nisku aquifer properties, the next best approach is to collect production and injection histories for the oil pools connected to the Nisku aquifer and conduct analytical material balance studies on as many pools as possible. This required a search for reservoir fluid properties—Reservoir Fluid Studies, and production, injection, and pressure

histories on these pools, as well as basic volumetric reserves information for each pool. All of this was available in the ERCB archives.

The reservoir fluid study information, along with production, injection, and pressure histories were entered into Petroleum Expert's MBAL™ application (Reference 1). This application has a rich set of analytical aquifers that can be used to history match the aquifer response to pressure depletion in an oil or gas pool.

Although not all of the pools were easily history matched for a number of reasons discussed in this report, there was an adequate amount of public domain data and results were conclusive enough to make some useful conclusions on aquifer strength, as discussed in the conclusions section of this report.

2. PALEOGEOGRAPHY OF THE WASP STUDY AREA

The red outline in Figure 3 defines the location of the WASP study area. It is located between the Moon Lake Build-ups on the west side and the inboard margin of the Nisku aquifer on the east side. A series of Nisku oil pools extends down the eastern edge of the Nisku aquifer. In fact these oil accumulations are Nisku carbonate reefs that are draping over top of the underlying Leduc D3 reefs. As can be seen in Figure 3 the Nisku pools of interest range from the Big Lake pool in the extreme north down to the Bonnie Glen Pool to the south. Also observable on this diagram is the fact that the inboard margin intersects this trend of Nisku pools at about the level of the Leduc Woodbend pools. This means that pools to the south of Leduc Woodbend D2-A and D2-B will be less well connected to the Nisku aquifer and are less analogous to the type of Nisku reservoir of interest for the WASP study.

Figure 4 provides a cross section of the stratigraphy above and below the Nisku formation. From this diagram it is evident that the Nisku aquifer is located both underneath as bottom water and laterally as edge water to the Nisku oil accumulations. This should provide some indication to the type of analytical aquifer that might best be used to achieve a history match of pressure depletion for oil pools connected to the Nisku aquifer.

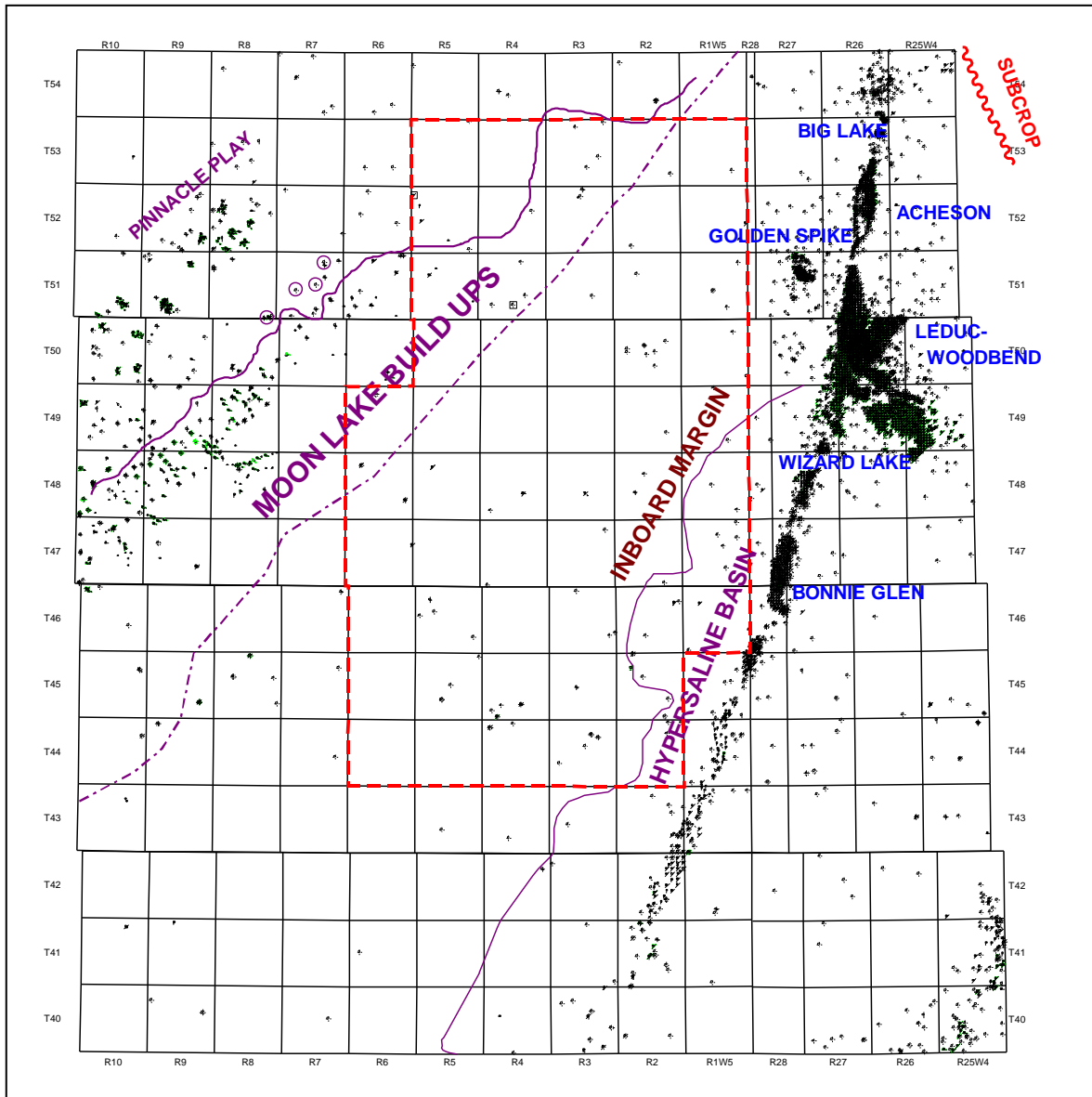


Figure 3: WASP study area.

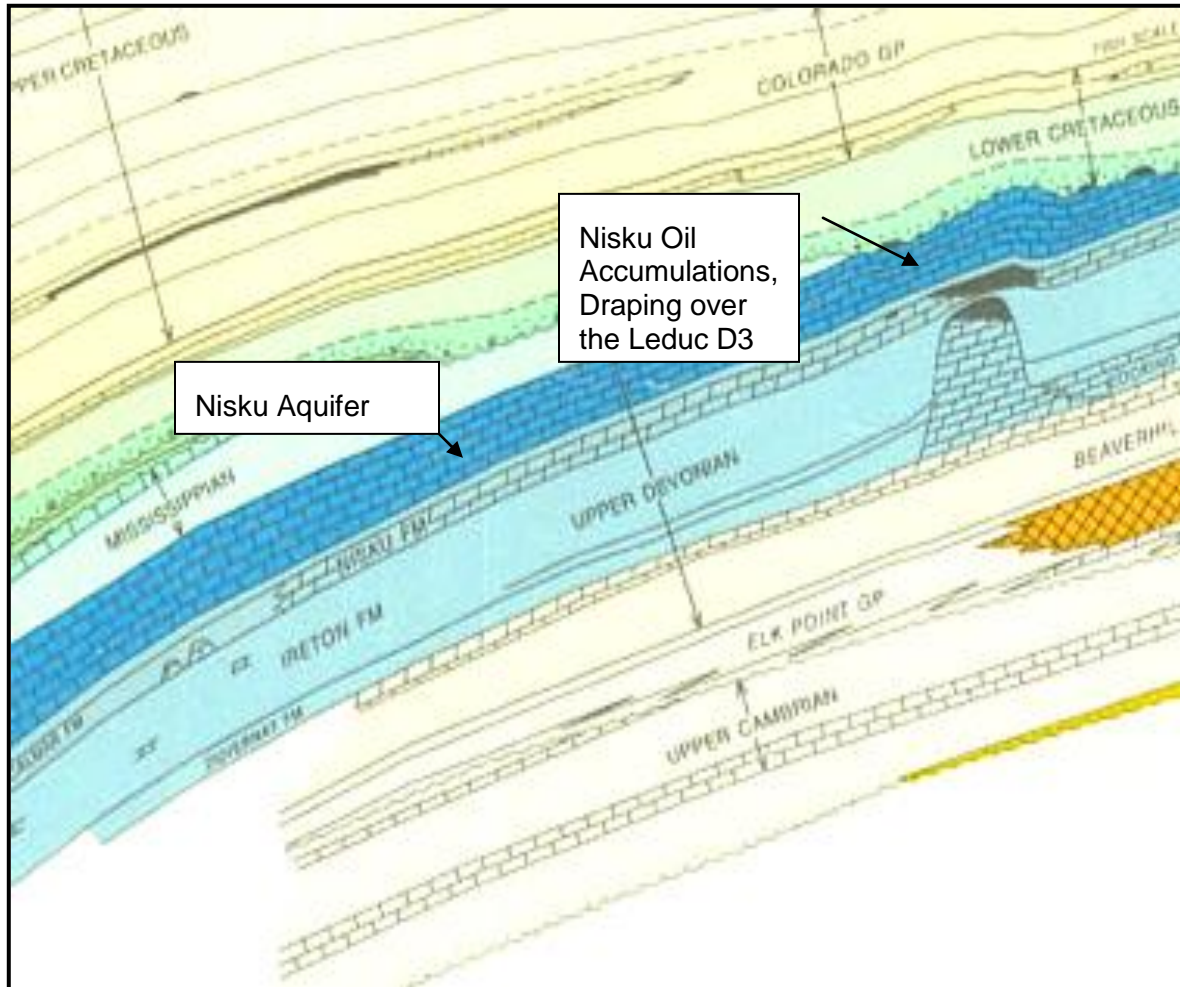


Figure 4: Cross section of the Nisku aquifer and adjacent stratigraphy (Reference 3).

3. RESERVOIR DATA

The following public-domain data are available for the Nisku oil pools:

- a. Reservoir Parameters
- b. Reserves
- c. Production
- d. Injection
- e. Fluid Studies—i.e., PVT Reports

Tables containing pool reserves data and fluid properties for each of the studied pools are included in Appendix 1.

4. MATERIAL BALANCE RESULTS

The following discussion is a pool by pool account of the results in an attempt to match production and pressure histories with an analytical aquifer model that best simulates the observed pool response. The discussions are more or less complete, depending on availability of data from the ERCB and other difficulties described for each pool.

4.1 Acheson D2-A and D2-B Pools

Figure 5 shows the location of the Acheson D2-A Pool.

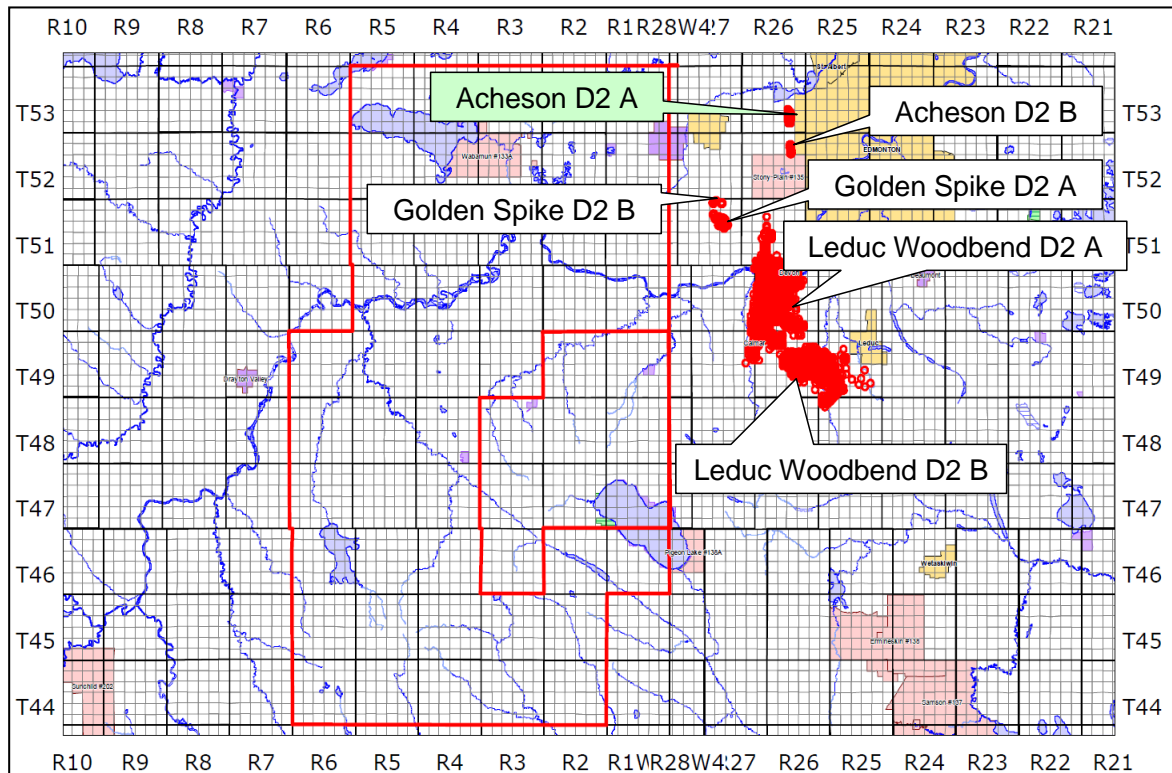


Figure 5: Location of Acheson D2-A Pool.

The Acheson D2-A Pool was first produced in 1952. It consists of twelve (12) producers and one (1) injector, see Table 1. The pool has original oil in place (OOIP) based on ERCB information of $775 \text{ e}3 \text{ m}^3$ (4,877 e3 bbl). This is a small pool with a small waterflood implemented in it. The pool reserves data sheet and reservoir fluid behaviour parameter information sheets are included in Appendix 1 for this pool.

Table 1: Data summary for Acheson D2-A pool.

Description	Pool Characteristics
Depth	1395.1 m
Area	486 ha (1201 acres)
Number of Producers	12
Number of Brine Injectors	1
Net Pay	8.17 m
Porosity	3.4%
API Gravity	38 deg API
Initial Pressure	10,994 kPa (1,595 psi)
Temperature	57 deg C
OOIP	775 e3 m ³ (4,877 e3 bbl)
Initial OOIP Recovered	60.5%

A plot of the production, water injection, and average pressure versus time history for the pool is provided in Figure 6. More detailed pressure data for individual wells in the pool is provided in Figure 7. As can be seen in both of these plots, although substantial production of both water and oil took place from this pool beginning in the early 1950s and extending until the early 1990s, the pressure decline was minimal.

As a result of the minimal pressure decline experienced in this pool, it was not possible to perform a material balance history match since this pressure response leads to the calculation of an infinite sized aquifer providing pressure support. There are two possible reasons for this kind of outcome:

- Scenario 1 Pool size is small relative to the size of the attached aquifer. In this scenario, the aquifer associated with the Acheson D2-A Pool is large compared with the pool itself. With an OOIP of less than 5 million barrels, this pool is not large compared to other Alberta oil pools and this could very much be the reason for such a small pressure decline. The total off-take from this pool may not have been large enough to have produced a significant pressure decline in the larger aquifer.
- Scenario 2 The aquifer attached to this pool is very large. It may be true that the Nisku aquifer is very large and that the minimal pressure decline is truly the result of an “infinite” aquifer response. In this case, the accuracy of the material balance approach is limited in terms of being able to accurately determine just how large the aquifer is relative to the size of the producing entity.

For the reasons described above, it was not possible to place a definitive size on the aquifer attached to the Acheson D2-A pool. The only conclusion that can be made is that the aquifer is very much larger than the oil pool.

The Acheson D2-B pool is even smaller than the D2-A pool at 49 e3 m³ (308 e3 bbl). The pressure decline is also minimal and similar material balance history matching difficulties were encountered. The only conclusion relative to aquifer size attached to the D2-B pool is similar to that for the D2-A pool, the aquifer is large relative to the size of these oil accumulations.

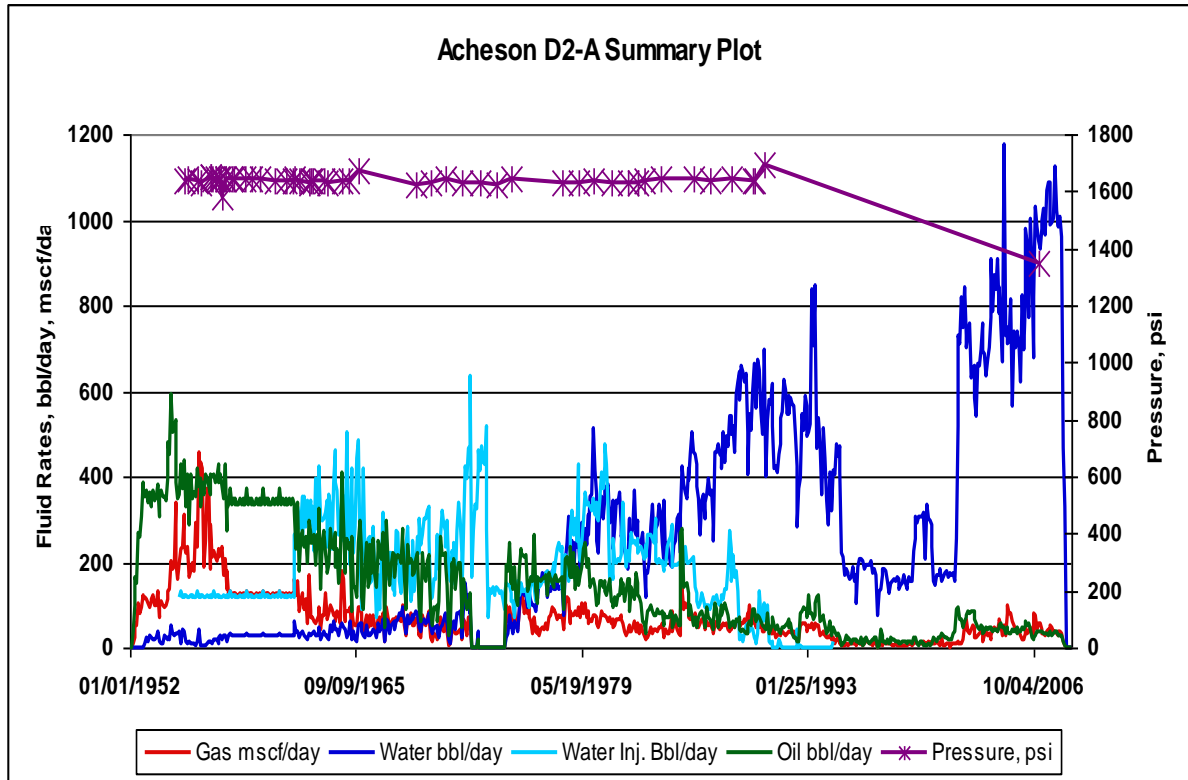


Figure 6: Acheson D2-A pool production, injection, and pressure versus time history.

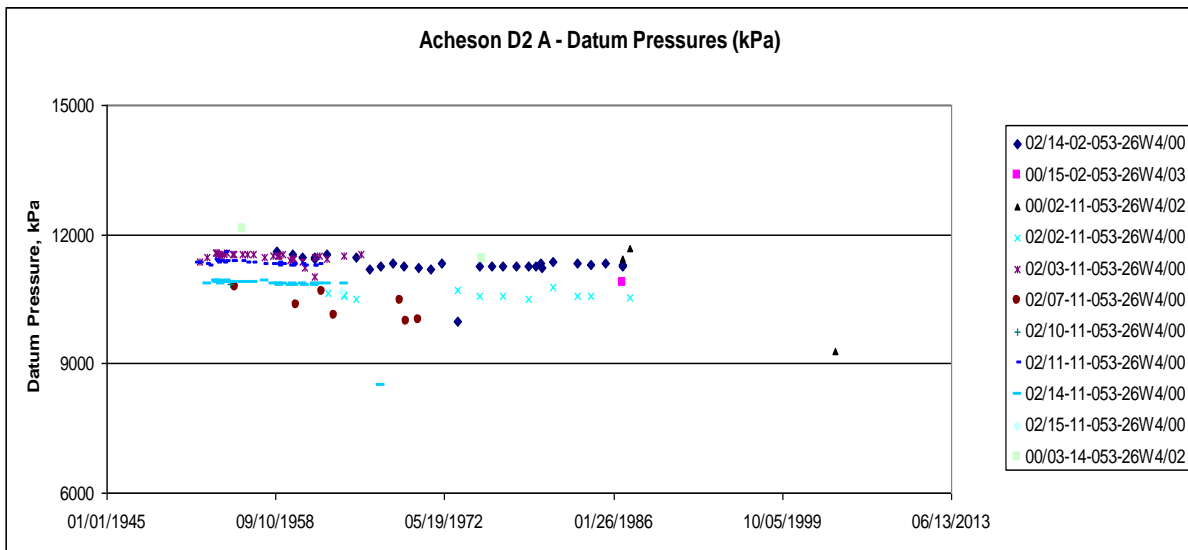


Figure 7: Acheson D2-A pool pressure versus time history.

4.2 Golden Spike D2A

The Golden Spike D2-A pool is located directly south west of the Acheson pools as seen in Figure 8. A summary of pool parameters for Golden Spike D2-A is provided below. This is a much larger pool than the Acheson pools.

Table 2: Data summary for Golden Spike D2-A pool.

Description	Pool Characteristics
Depth	1543.7 m
Area	769 ha (1900 acres)
Number of Producers	16
Number of Brine Injectors	4
Net Pay	13 m
Porosity	5.7%
API Gravity	37 deg API
Initial Pressure	12,422 kPa (1,802 psi)
Temperature	61 deg C
OOIP	2804 e3 m ³ (17,645 e3 bbl)
Initial OOIP Recovered	14.5%

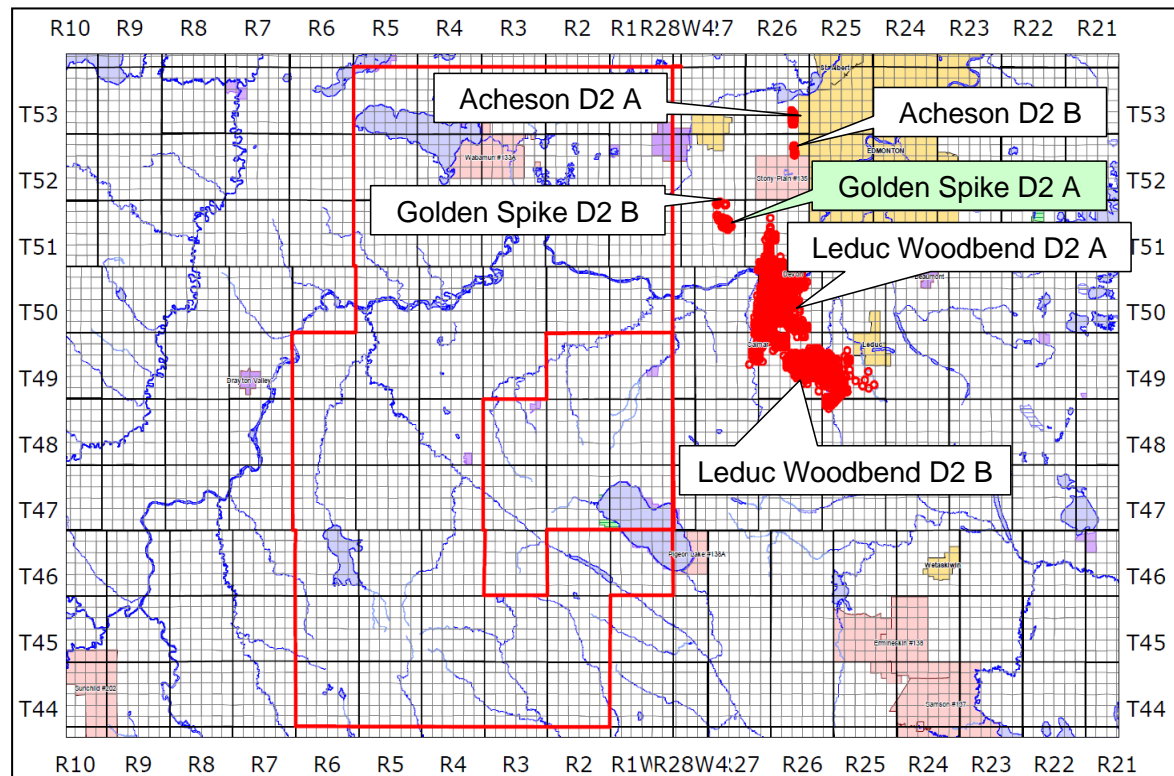


Figure 8: Location of Golden Spike D2-A.

The pressure and production history for the Golden Spike D2-A Pool is provided in Figure 9. This figure illustrates a very pronounced pressure decline followed by a repressurization shortly after the initiation of a waterflood scheme in 1965.

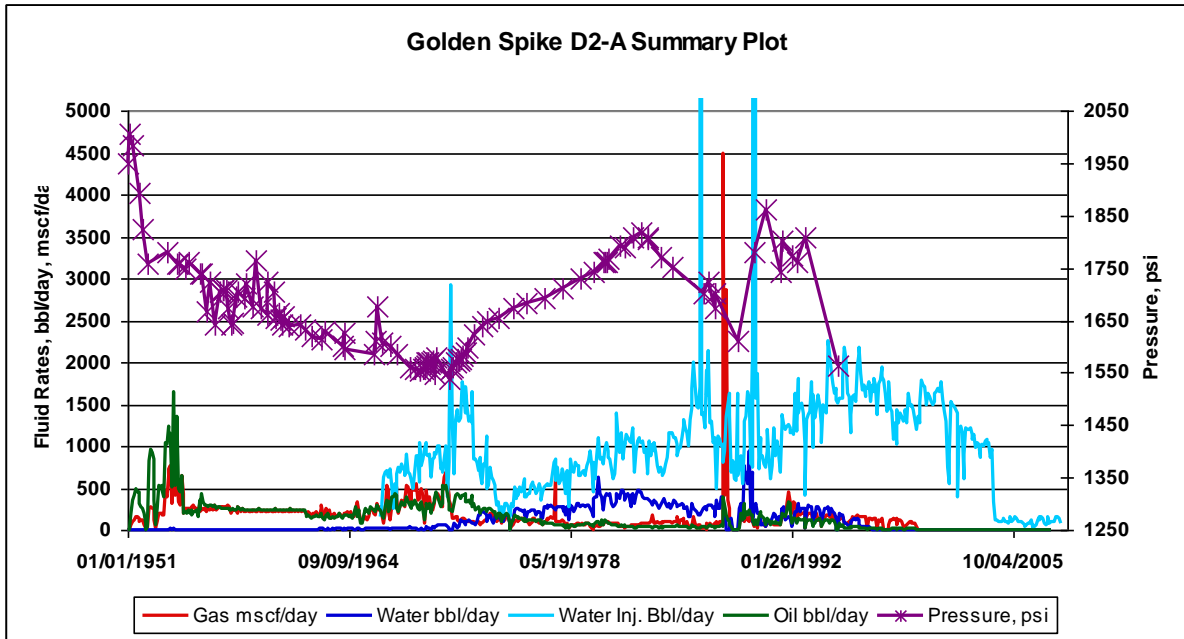


Figure 9: Golden Spike D2-A pressure, production, and injection history.

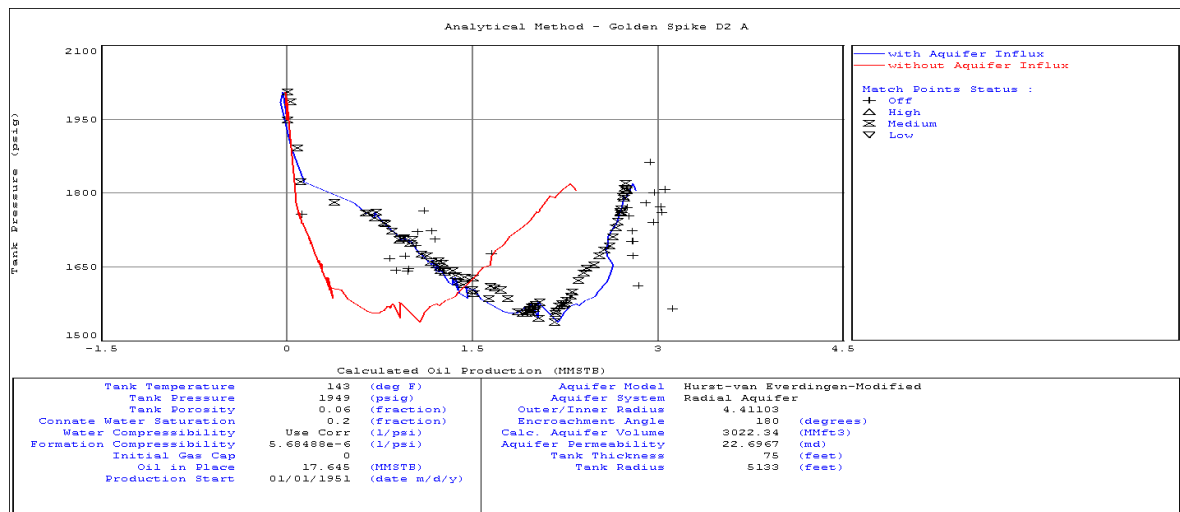


Figure 10: Golden Spike D2-A material balance history match.

The significant pressure decline observed in the early years of producing this pool enables a very accurate pressure match using a radial aquifer with an outer to inner dimension ratio of 4.4. The Hurst-van Everdingen-Modified aquifer model was used to achieve this match. As can be seen in Figure 10, the simulated pressure response without aquifer support (the red line) would have been much different than that observed (the black symbols). From the quality of this match (the blue line) we can state with a high degree of accuracy that the selected aquifer model is a good approximation of the type and size of aquifer associated with the Golden Spike D2-A Pool.

The reservoir pore volume calculated by the simulator is $4.66 \text{ e}6 \text{ m}^3$ ($29.3 \text{ e}6 \text{ bbl}$), while the aquifer volume is $85.5 \text{ e}6 \text{ m}^3$ ($538 \text{ e}6 \text{ bbl}$). This is a reservoir to aquifer ratio of 18.4. The oil reservoir radius is about 1,564 m (5,133 ft.). Assuming the aquifer exposure angle is 180 degrees and assuming an aquifer tank thickness of 22.8 m (75 ft.) and permeability of 23 md, it is possible to calculate the radius of the aquifer connected to this pool to be about 7,010 m (23,000 ft.). Figure 11 illustrates this shape relative to the Golden Spike D2-A Pool. This calculated aquifer geometry indicates how much of the Nisku aquifer the Golden Spike D2-A Pool is exposed to. It does not conclusively demonstrate the extent of the larger aquifer itself.

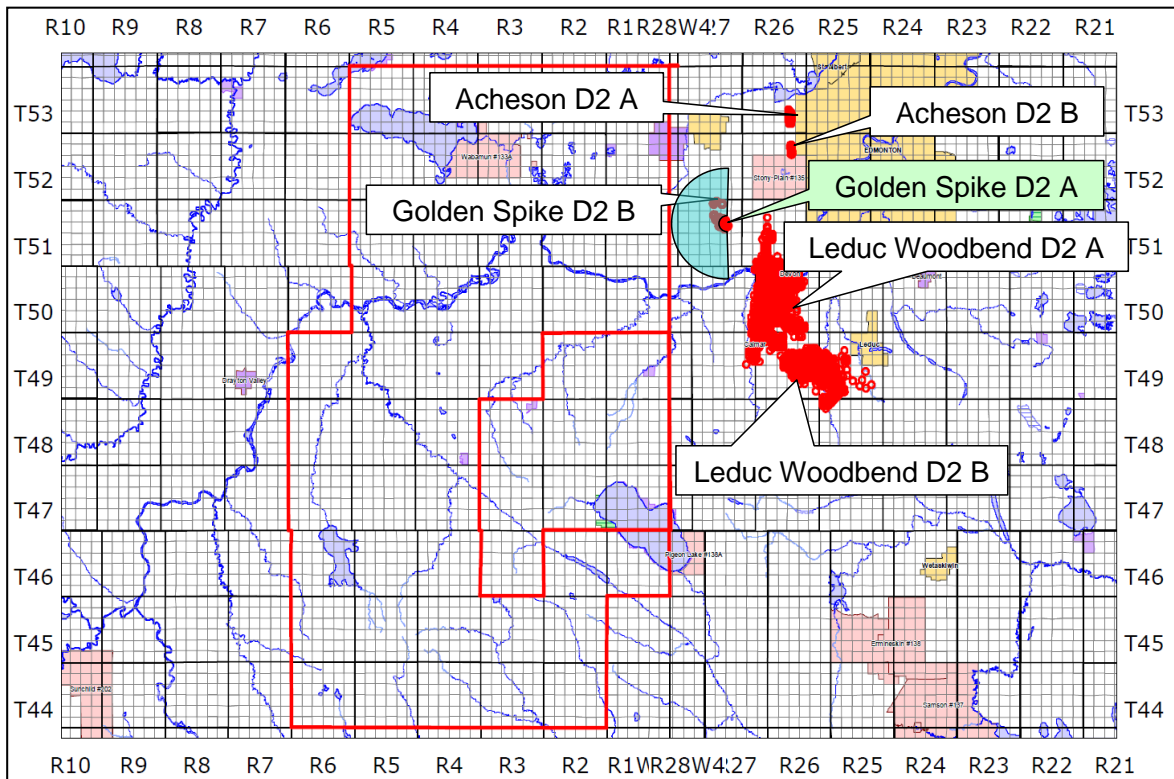


Figure 11: Golden Spike D2-A mapping of aquifer shape and size.

4.3 Golden Spike D2B

The Golden Spice D2-B Pool is considerably smaller than the Golden Spike D2-A Pool. Table 3 provides the basic pool data for this pool. The OOIP value of 356 e3 m³ or 2.2 million bbls suggests that this pool is in the size category of the Acheson pools.

Table 3: Data summary for Golden Spike D2-B pool.

Description	Pool Characteristics
Depth	1556.2 m
Area	173 ha (427 acres)
Number of Producers	4
Number of Brine Injectors	1
Net Pay	4 m
Porosity	7.8%
API Gravity	37 deg API
Initial Pressure	12,395 kPa (1,798 psi)
Temperature	61 deg C
OOIP	356 e3 m ³ (2,240 e3 bbl)
Initial OOIP Recovered	15%

Pressure data recorded for the Golden Spike D2-B pool is less complete than for the D2-A pool but since early time pressures were available, it was possible to perform a material balance analysis. Figure 12 provides the pressure, production and injection history for this pool.

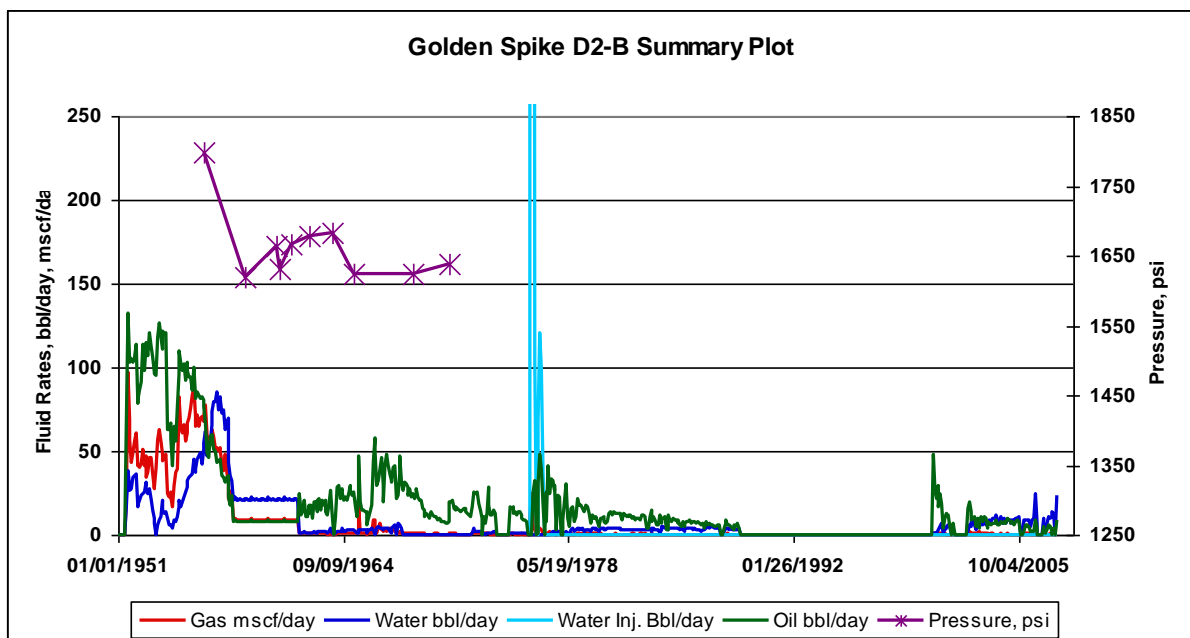


Figure 12: Golden Spike D2-B pressure, production, and injection history.

A material balance history match was obtained using the same analytical radial model as was used for the D2-A pool. This time the dimensionless outer to inner radius value was 23.2 (Figure 13).

However the oil pool radius is slightly smaller at 741 m (2,433 ft.). This yields an aquifer radius of 17,068 m or 17 km (56,000 ft. or 10 miles). Figure 14 illustrates this aquifer model on the same map as before. An aquifer permeability of 38 md was assumed to achieve this match.

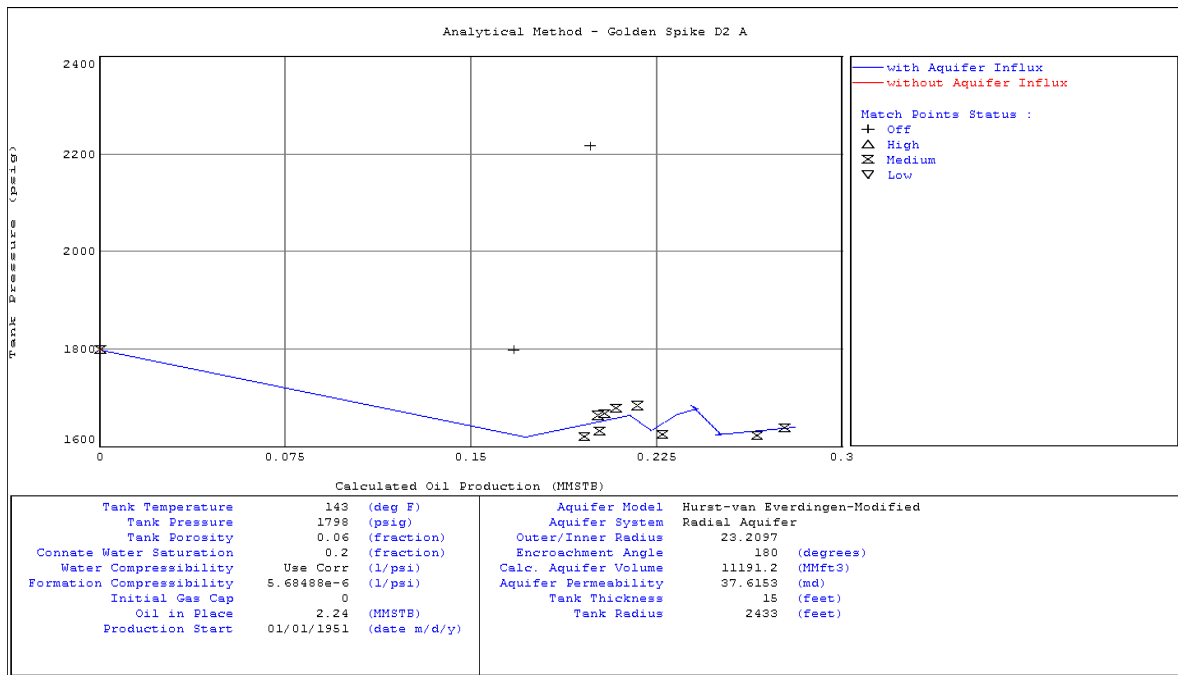


Figure 13: Golden Spike D2-B pressure, production, and injection history.

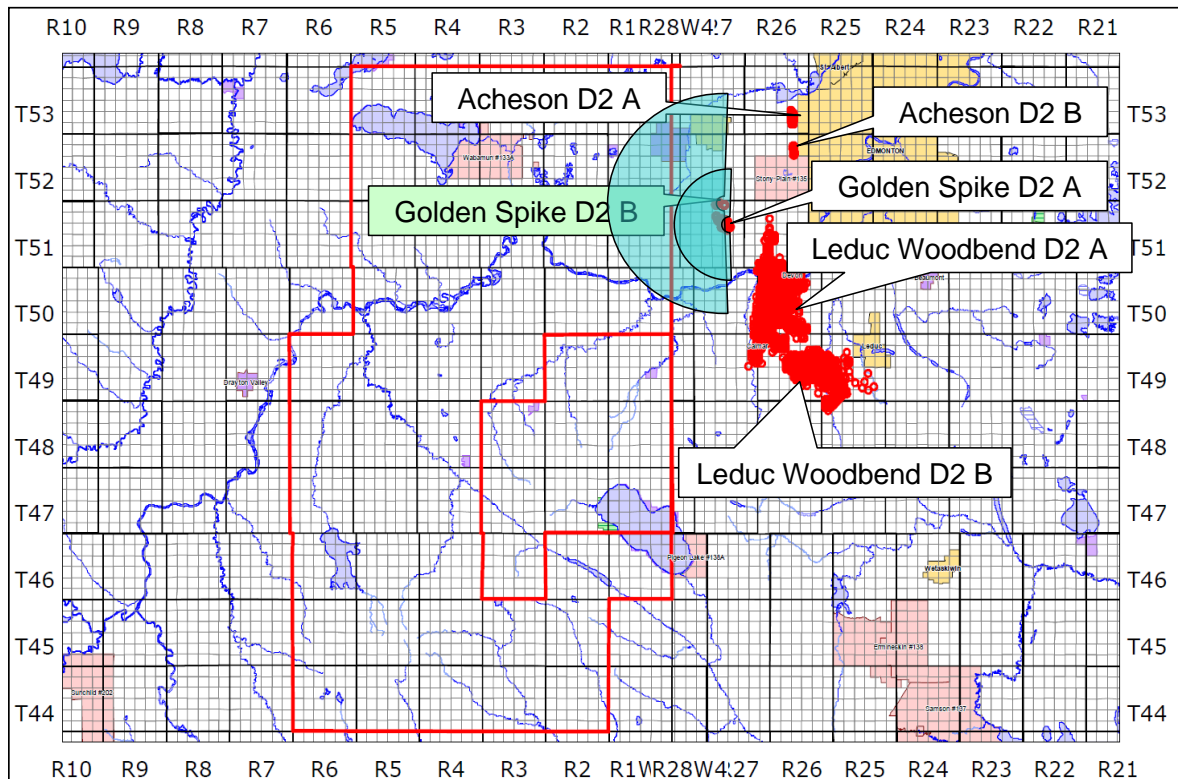


Figure 14: Golden Spike D2-B pressure, production, and injection history.

As can be seen from Figure 14, the Golden Spike D2-B aquifer solution suggests a larger radius aquifer than for the D2-A pool. This outcome must be tempered by the fact that the D2-B pool is significantly smaller than the D2-A pool and as such it does not enable as highly accurate a results for material balance matching purposes as was possible for the D2-A pool.

4.4 Leduc Woodbend D2A and D2B Pools

The Leduc Woodbend D2-A and D2-B Pools are by far the largest Nisku reef oil accumulations in the province and the largest considered for this study. Tables 4 and 5 provide reservoir parameters for both of these pools. As can be seen from these tables, large OOIP values 33 million cubic metres and 25 million cubic metres respectively for the D2-A and D2-B pools are recorded in the ERCB databases. Unfortunately, what is not recorded in the ERCB electronic database is the early years of production from these pools. The ERCB holds only production from 1962 forward. All of the previous years of data are stored in paper or micro fiche databases. This was true for the Acheson and Golden Spike pools as well, but there are so few wells associated with these pools, that it wasn't difficult to pull the prior history from paper reports to establish the full production history for material balance purposes. Since this effort would have taken an extreme amount of time for the Leduc Woodbend D2-A and D2-B pools, it was not practical to have it done.

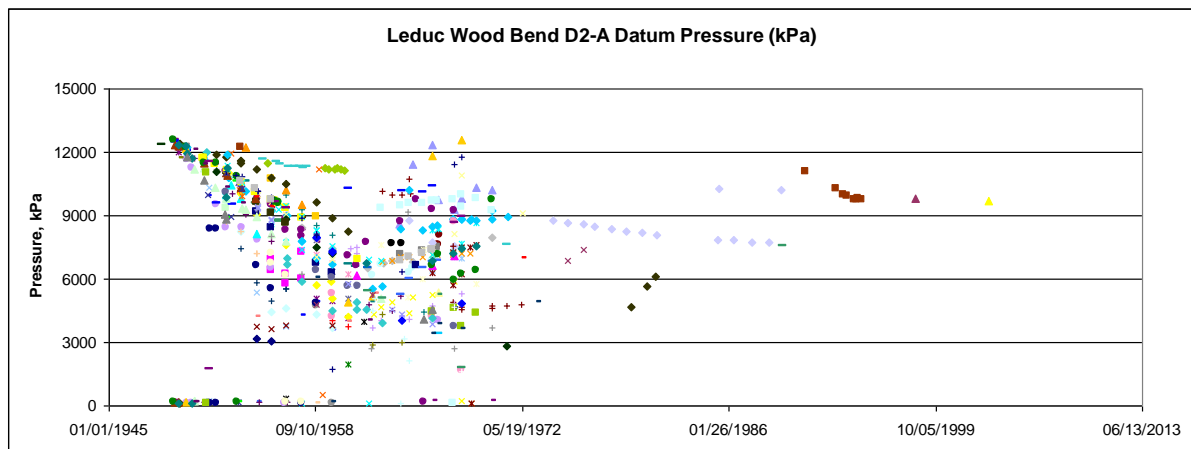
Table 4: Data summary for Leduc Woodbend D2-A pool.

Description	Pool Characteristics
Depth	1570.2 m
Area	9217 ha (22,776 acres)
Number of Producers	502
Number of Brine Injectors	52
Net Pay	30 m
Porosity	7%
API Gravity	38 deg API
Initial Pressure	12,581 kPa (1,825 psi)
Temperature	63 deg C
OOIP	32,830 e3 m ³ (206,595 e3 bbl)
Initial OOIP Recovered	43.9%

Table 5: Data summary for Leduc Woodbend D2-B pool.

Description	Pool Characteristics
Depth	1601.3 m
Area	7106 ha (17,559 acres)
Number of Producers	250
Number of Brine Injectors	35
Net Pay	14.3 m
Porosity	5%
API Gravity	38 deg API
Initial Pressure	12,834 kPa (1,861 psi)
Temperature	60 deg C
OOIP	24,606 e3 m ³ (151,406 e3 bbl)
Initial OOIP Recovered	13.8%

Since practical material balance analysis for the Leduc Woodbend pools was not possible, due to missing data, only a review of the production and pressure response data was possible. By inference, a review of the pressure histories in Figure 15 and 18 along with the production and injection data (post 1961) in Figures 16,17 and 19, 20 for the D2-A and D2-B pools, respectively, suggests that the aquifer strength associated with the Leduc Woodbend pools is similar to that observed for the Golden Spike Pools.


Figure 15: Leduc Woodbend D2-A pressure history.

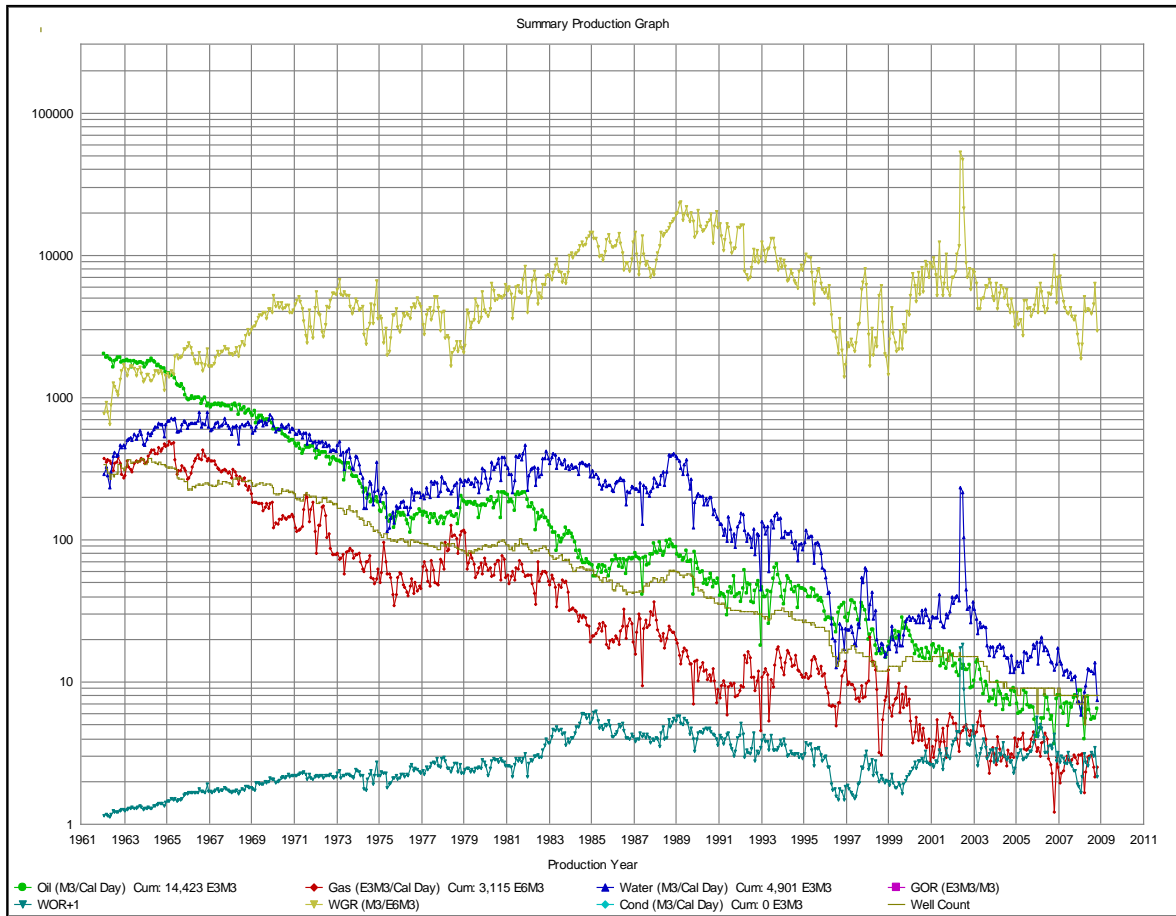


Figure 16: Leduc Woodbend D2-A production history (post 1961).

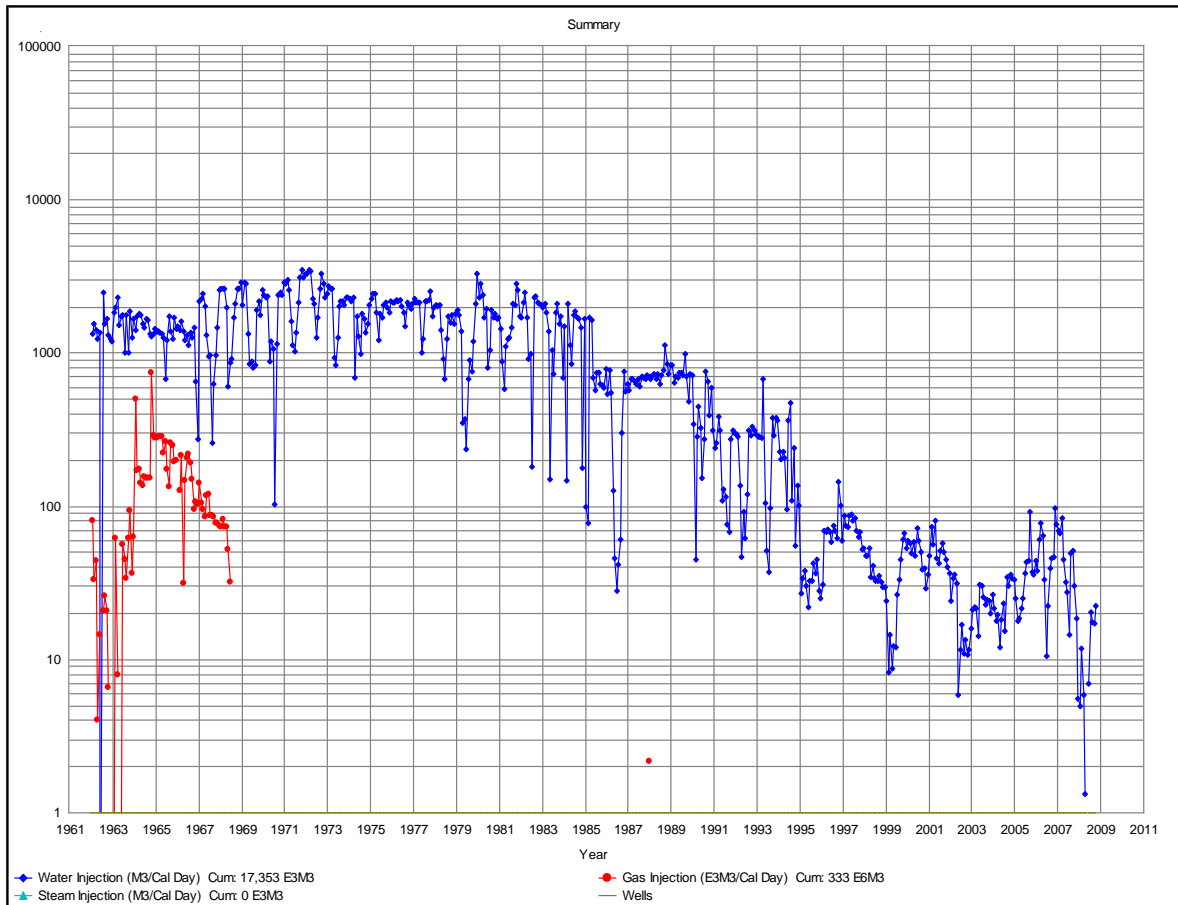


Figure 17: Leduc Woodbend D2-A injection history (post 1961).

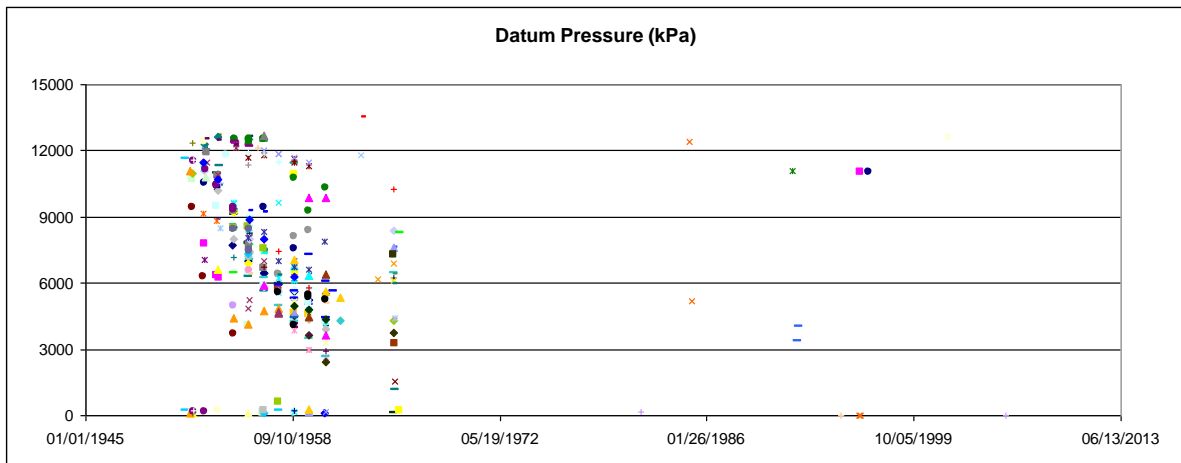


Figure 18: Leduc Woodbend D2-B pressure history.

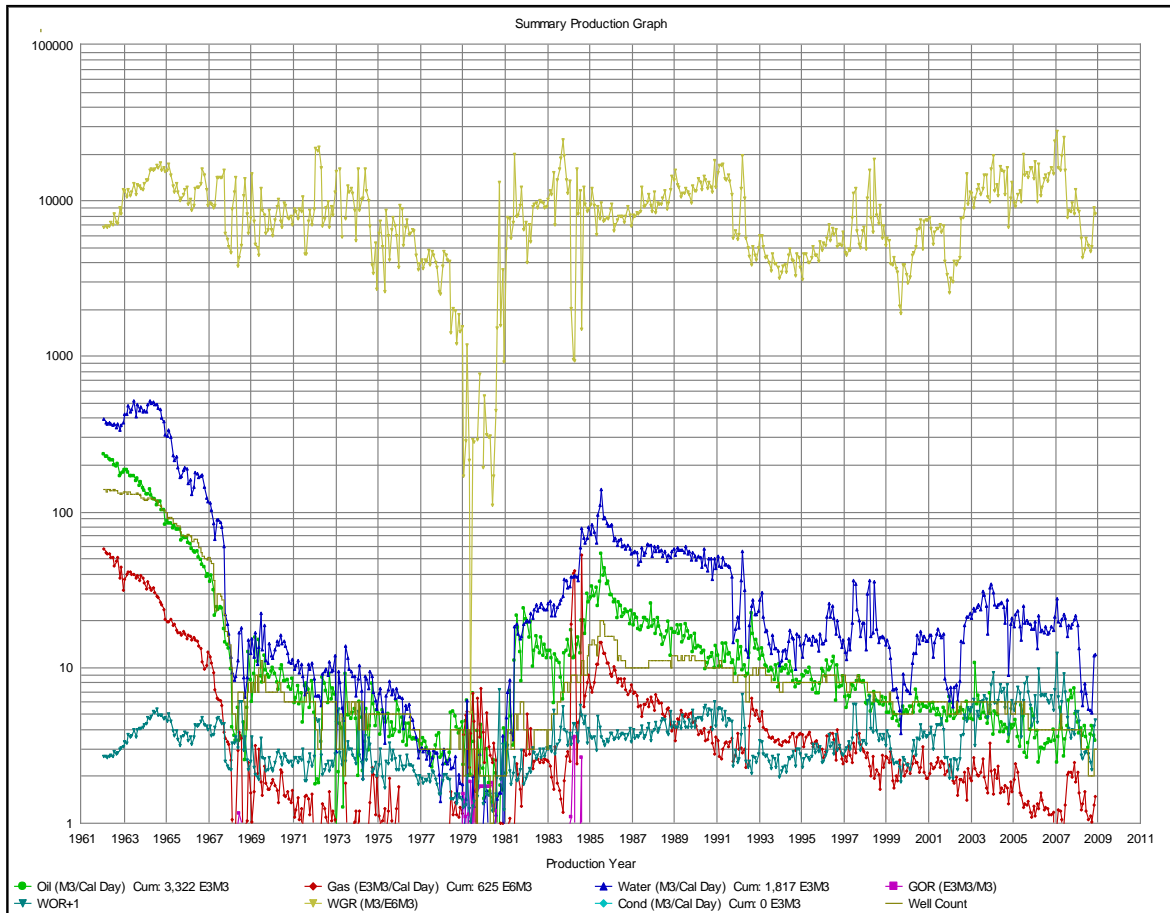


Figure 19: Leduc Woodbend D2-B production history (post 1961).

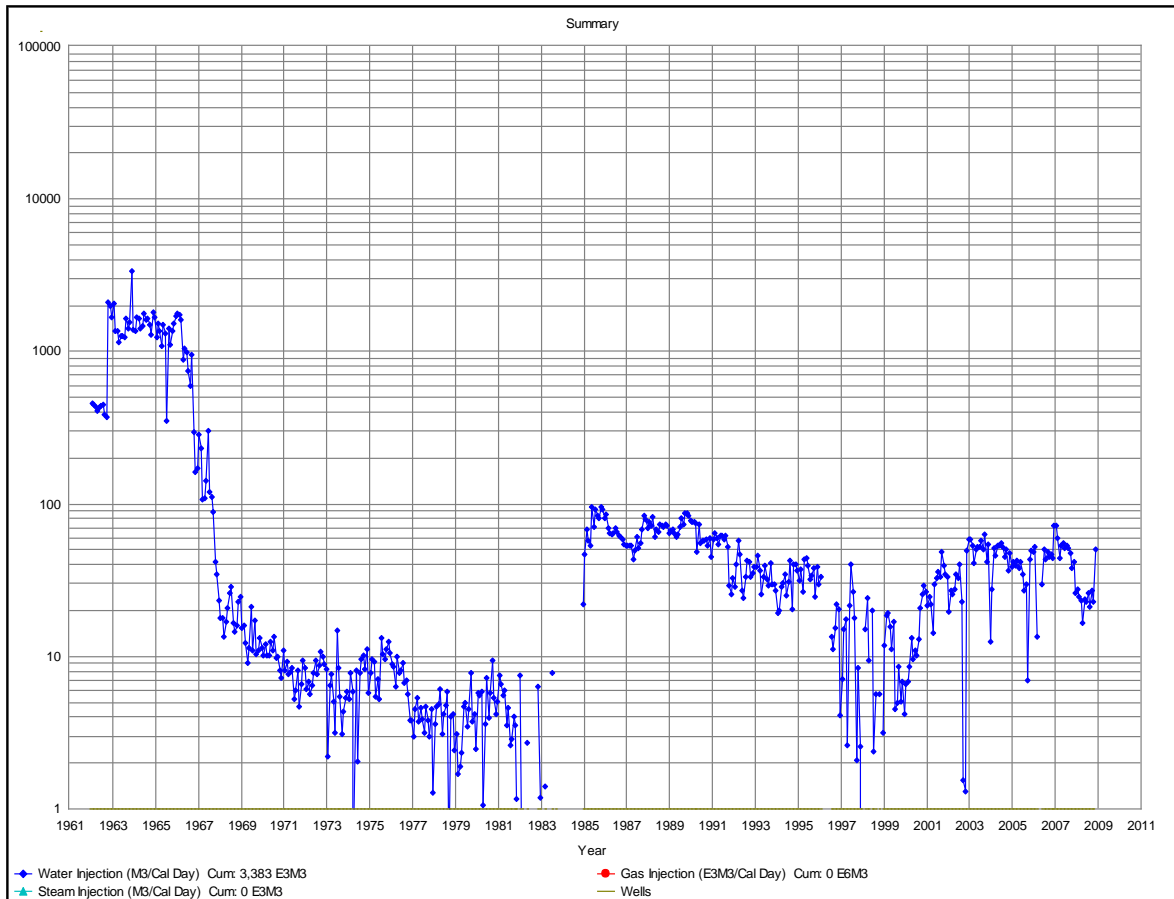


Figure 20: Leduc Woodbend D2-B injection history (post 1961).

CONCLUSIONS

Conclusions relative to aquifer strength, permeability, and size (radius), for the Nisku oil fields directly to the east of the WASP study are as follows:

- The Nisku aquifer can generally be classified as a “strong aquifer” with some variability in connectivity depending on location.
- Strong connections exist for distances ranging from a few kilometres to tens of kilometres.
- Weak connections may exist but this is, as yet, inconclusive.
- Average permeability is in the order of 10 to 40 md.

REFERENCES

1. Bob Michenson, Public Knowledge, “Oil and Gas Reserves Database”, Version 2008 1.01.
2. Petroleum Experts Ltd. “MBAL Reservoir Analytical Simulation”, Version 8.
3. Geological Survey of Canada, 1981.

APPENDIX 1

Table Number	Table Name
1	Acheson D2-A Reserve Report
2	Acheson D2-B Reserve Report
3	Golden Spike D2-A Reserve Report
4	Golden Spike D2-B Reserve Report
5	Leduc Woodbend D2-A Reserve Report
6	Leduc Woodbend D2-B Reserve Report
7	Acheson Flash Corrected PVT Data
8	Golden Spike Flash Corrected PVT Data

OIL RESERVES Detailed Report

Database Date:

Dec. 31, 2007

Field Code : 9 Pool Code : 696001
Field Name : ACHESON Pool Name : D-2 A
Field Location : 053-26W4 Pool Type : Primary
Discovery Year : 1952 Pool Class : Light-Medium Oil

	<i>Metric</i>	<i>Imperial</i>
KB (reference elevation):	705.9 m	2316 ft
Mean Formation Depth:	1395.1 m	4577 ft
Datum Elevation:	-689.2 m	-2261 ft
Area:	486 ha	1201 acres
Net Pay:	8.17 m	26.8 ft
Volume:	3971 e4 m3	32190 acre ft
Porosity:	0.034	3.4 %
Water Saturation:	0.3	30.0 %
Shrinkage:	0.82	82.0 %
Oil Density:	834.3 kg/m3	52.1 lbs/SCF
API Gravity:	38.10 deg API	38.10 deg API
Solution Gas Oil Ratio:	64 m3/m3	361 SCF/Bbl
Initial Pressure	10,994 kPa	1,595 psi
Temperature:	57 deg C	135 deg F
Initial OIP Volume:	775 e3 m3	4877 e3 bbl
Primary Recovery Factor:	0.615	61.5 %
Enhanced Recovery Factor:	0.000	0.0 %
Primary Initial Reserves:	477.0 e3 m3	3002 e3 bbl
Enhanced Initial Reserves:	0.0 e3 m3	0 e3 bbl
Total Initial Reserves:	477.0 e3 m3	3002 e3 bbl
Cumulative Production:	468.7 e3 m3	2949 e3 bbl
Remaining Reserves:	8.3 e3 m3	52 e3 bbl
Initial OIP Recovered:	0.605	60.5 %

Remarks: 2007-10 GPP

OIL RESERVES Detailed Report

Database Date:

Dec. 31, 2007

Field Code :	9	Pool Code :	696002
Field Name :	ACHESON	Pool Name :	D-2 B
Field Location :	053-26W4	Pool Type :	Primary
Discovery Year :	1952	Pool Class :	Light-Medium Oil

	<i>Metric</i>	<i>Imperial</i>
KB (reference elevation):	714.7 m	2345 ft
Mean Formation Depth:	1420.4 m	4660 ft
Datum Elevation:	-705.7 m	-2315 ft
Area:	64 ha	158 acres
Net Pay:	6.01 m	19.7 ft
Volume:	385 e4 m3	3118 acre ft
Porosity:	0.024	2.4 %
Water Saturation:	0.36	36.0 %
Shrinkage:	0.83	83.0 %
Oil Density:	834.3 kg/m3	52.1 lbs/SCF
API Gravity:	38.10 deg API	38.10 deg API
Solution Gas Oil Ratio:	64 m3/m3	361 SCF/Bbl
Initial Pressure	11,093 kPa	1,609 psi
Temperature:	56 deg C	133 deg F
Initial OIP Volume:	49 e3 m3	308 e3 bbl
Primary Recovery Factor:	0.600	60.0 %
Enhanced Recovery Factor:	0.000	0.0 %
Primary Initial Reserves:	29.4 e3 m3	185 e3 bbl
Enhanced Initial Reserves:	0.0 e3 m3	0 e3 bbl
Total Initial Reserves:	29.4 e3 m3	185 e3 bbl
Cumulative Production:	29.4 e3 m3	185 e3 bbl
Remaining Reserves:	0.0 e3 m3	0 e3 bbl
Initial OIP Recovered:	0.600	60.0 %

Remarks: 2006-12 GPP

OIL RESERVES Detailed Report

Database Date:

Dec. 31, 2007

Field Code : 421 **Pool Code :** 696001
Field Name : GOLDEN SPIKE **Pool Name :** D-2 A TOTAL
Field Location : 051-27W4 **Pool Type :** Primary
Discovery Year : 1952 **Pool Class :** Light-Medium Oil

	<i>Metric</i>	<i>Imperial</i>
KB (reference elevation):	712.0 m	2336 ft
Mean Formation Depth:	1543.7 m	5065 ft
Datum Elevation:	-831.7 m	-2729 ft
Area:	769 ha	1900 acres
Net Pay:	0 m	0.0 ft
Volume:	0 e4 m3	0 acre ft
Porosity:	0	0.0 %
Water Saturation:	0	0.0 %
Shrinkage:	0	0.0 %
Oil Density:	839.3 kg/m3	52.4 lbs/SCF
API Gravity:	37.09 deg API	37.09 deg API
Solution Gas Oil Ratio:	87 m3/m3	491 SCF/Bbl
Initial Pressure	12,422 kPa	1,802 psi
Temperature:	61 deg C	142 deg F
Initial OIP Volume:	2804 e3 m3	17645 e3 bbl
Primary Recovery Factor:	0.000	0.0 %
Enhanced Recovery Factor:	0.000	0.0 %
Primary Initial Reserves:	275.0 e3 m3	1731 e3 bbl
Enhanced Initial Reserves:	131.0 e3 m3	824 e3 bbl
Total Initial Reserves:	406.0 e3 m3	2555 e3 bbl
Cumulative Production:	405.9 e3 m3	2554 e3 bbl
Remaining Reserves:	0.1 e3 m3	1 e3 bbl
Initial OIP Recovered:	0.145	14.5 %

Remarks: 2001-12 GPP

OIL RESERVES Detailed Report

Database Date:

Dec. 31, 2007

Field Code :	421	Pool Code :	696002
Field Name :	GOLDEN SPIKE	Pool Name :	D-2 B
Field Location :	051-27W4	Pool Type :	Primary
Discovery Year :	1951	Pool Class :	Light-Medium Oil

	<i>Metric</i>	<i>Imperial</i>
KB (reference elevation):	708.7 m	2325 ft
Mean Formation Depth:	1556.2 m	5106 ft
Datum Elevation:	-847.5 m	-2781 ft
Area:	173 ha	427 acres
Net Pay:	3.93 m	12.9 ft
Volume:	680 e4 m3	5512 acre ft
Porosity:	0.078	7.8 %
Water Saturation:	0.14	14.0 %
Shrinkage:	0.78	78.0 %
Oil Density:	839.3 kg/m3	52.4 lbs/SCF
API Gravity:	37.09 deg API	37.09 deg API
Solution Gas Oil Ratio:	87 m3/m3	491 SCF/Bbl
Initial Pressure	12,395 kPa	1,798 psi
Temperature:	61 deg C	142 deg F
Initial OIP Volume:	356 e3 m3	2240 e3 bbl
Primary Recovery Factor:	0.150	15.0 %
Enhanced Recovery Factor:	0.000	0.0 %
Primary Initial Reserves:	53.4 e3 m3	336 e3 bbl
Enhanced Initial Reserves:	0.0 e3 m3	0 e3 bbl
Total Initial Reserves:	53.4 e3 m3	336 e3 bbl
Cumulative Production:	53.1 e3 m3	334 e3 bbl
Remaining Reserves:	0.3 e3 m3	2 e3 bbl
Initial OIP Recovered:	0.149	14.9 %

Remarks: 2000-11 GPP

OIL RESERVES Detailed Report

Database Date:

Dec. 31, 2007

Field Code : 551 **Pool Code :** 696001
Field Name : LEDUC-WOODBEND **Pool Name :** D-2 A TOTAL
Field Location : 050-26W4 **Pool Type :** Primary
Discovery Year : 1947 **Pool Class :** Light-Medium Oil

	<i>Metric</i>	<i>Imperial</i>
KB (reference elevation):	718.9 m	2359 ft
Mean Formation Depth:	1570.2 m	5152 ft
Datum Elevation:	-851.3 m	-2793 ft
Area:	9217 ha	22776 acres
Net Pay:	0 m	0.0 ft
Volume:	0 e4 m3	0 acre ft
Porosity:	0	0.0 %
Water Saturation:	0	0.0 %
Shrinkage:	0	0.0 %
Oil Density:	834 kg/m3	52.1 lbs/SCF
API Gravity:	38.16 deg API	38.16 deg API
Solution Gas Oil Ratio:	115 m3/m3	649 SCF/Bbl
Initial Pressure	12,581 kPa	1,825 psi
Temperature:	63 deg C	145 deg F
Initial OIP Volume:	32830 e3 m3	206595 e3 bbl
Primary Recovery Factor:	0.000	0.0 %
Enhanced Recovery Factor:	0.000	0.0 %
Primary Initial Reserves:	11160.0 e3 m3	70228 e3 bbl
Enhanced Initial Reserves:	3270.0 e3 m3	20578 e3 bbl
Total Initial Reserves:	14430.0 e3 m3	90806 e3 bbl
Cumulative Production:	14421.2 e3 m3	90751 e3 bbl
Remaining Reserves:	8.8 e3 m3	55 e3 bbl
Initial OIP Recovered:	0.439	43.9 %

Remarks: 2007-12 GPP

OIL RESERVES Detailed Report

Database Date:

Dec. 31, 2007

Field Code :	551	Pool Code :	696002
Field Name :	LEDUC-WOODBEND	Pool Name :	D-2 B
Field Location :	050-26W4	Pool Type :	Primary
Discovery Year :	1950	Pool Class :	Light-Medium Oil

	<i>Metric</i>	<i>Imperial</i>
KB (reference elevation):	734.7 m	2410 ft
Mean Formation Depth:	1601.3 m	5254 ft
Datum Elevation:	-866.6 m	-2843 ft
Area:	7106 ha	17559 acres
Net Pay:	14.33 m	47.0 ft
Volume:	101829 e4 m3	825541 acre ft
Porosity:	0.05	5.0 %
Water Saturation:	0.37	37.0 %
Shrinkage:	0.75	75.0 %
Oil Density:	834.3 kg/m3	52.1 lbs/SCF
API Gravity:	38.10 deg API	38.10 deg API
Solution Gas Oil Ratio:	98 m3/m3	553 SCF/Bbl
Initial Pressure	12,834 kPa	1,861 psi
Temperature:	60 deg C	140 deg F
Initial OIP Volume:	24060 e3 m3	151406 e3 bbl
Primary Recovery Factor:	0.139	13.9 %
Enhanced Recovery Factor:	0.000	0.0 %
Primary Initial Reserves:	3344.0 e3 m3	21043 e3 bbl
Enhanced Initial Reserves:	0.0 e3 m3	0 e3 bbl
Total Initial Reserves:	3344.0 e3 m3	21043 e3 bbl
Cumulative Production:	3320.3 e3 m3	20894 e3 bbl
Remaining Reserves:	23.7 e3 m3	149 e3 bbl
Initial OIP Recovered:	0.138	13.8 %

Remarks: 2007-12 GPP

Flash Corrected PVT Data

Reservoir Fluid Study for		Calstan Acheson 11-11 Mu 53-26						
Well		02/11-11-53-26W4						
Location		Acheson D-2 A						
California Research Corp.		Project 8036 File 568.22						
Date of Cover Letter		19158						
Date of Sample		19086						
Flash Corrected PVT								
						GOR		
Adjusted PVT data Separator Flash Conditions		psig		psig		scf/bbl		
First Stage Flash	from	1305	to	70	at	286		
Second Stage Flash at	from	70		0	at	77		
Total Flash GOR		363	scf/bbl			363		
Flash FVF		1.221	rvol/svol					
	Tres	Pressure	Bubble Pt.	Soln GOR	Oil FVF	Visc	Oil Density	
	(deg F)	(psig)	(psig)	(scf/bbl)	(rvol/svol)	(cp)	gm/cc	
	134	3000	1305	363.0	1.2006			
	134	2800	1305	363.0	1.2031	0.98		
	134	2600	1305	363.0	1.2054	0.96		
	134	2400	1305	363.0	1.2078	0.94		
	134	2200	1305	363.0	1.2103	0.92		
	134	2000	1305	363.0	1.2127	0.91		
	134	1800	1305	363.0	1.2150	0.89		
	134	1600	1305	363.0	1.2175	0.88		
	134	1400	1305	363.0	1.2198	0.86		
	134	1305	1305	363.0	1.2210	0.85	Bubble Point	
	134	1200	1305			0.88		
	134	1118	1305	332.0				
	134	1000	1305			0.93	Rem GOR	
	134	973	1305	302.9			EUB Database 276.02	
	134	846	1305	276.7				
	134	800	1305			0.99	Material Bal. 276.02	
	134	603	1305	218.5	1.1430			
	134	600	1305			1.07		
	134	458	1305	180.6	1.1225			
	134	400	1305			1.17		
	134	299	1305	132.1	1.0962			
	134	201	1305	103.0	1.0825			
	134	200	1305			1.34		
	134	104	1305	57.4	1.0609			
	134	51	1305	17.7	1.0056			
	134	14.7	1305		0.9700	1.86		



Water Disposal Well Analysis

Wabamun Area CO₂ Sequestration Project (WASP)

Author

Rob Lavoie

Rev.	Date	Description	Prepared by
1	August 3, 2009	First Draft Report	Rob Lavoie
2	December 21, 2009	Second Draft Report	Rob Lavoie

Table of Contents

Introduction.....	5
Background	5
Discussion	7
1. Estimated Per Well CO ₂ Injection Volumes.....	7
2. Study Area Water Disposal Wells into the Nisku Aquifer	8
3. Water Disposal Well Injectivities	11
4. Pressure History for Disposal Wells	14
5. Conclusion	16
References.....	16

List of Tables

Table 1: Nisku aquifer characteristics and CO₂ volume at aquifer conditions. 7

List of Figures

Figure 1: WASP study area	5
Figure 2: Water disposal well study area	6
Figure 3: List of water disposal wells in study area.	8
Figure 4: Location of top 19 water disposal wells in study area.	9
Figure 5: Plot of cumulative volumes for top 19 disposal wells.	10
Figure 6: Top six water disposal wells—daily injection rates (m ³ /day).	11
Figure 7: Location of Well #6 from Figure 6.	12
Figure 8: Typical injection performance history for Nisku water disposal well located in Nisku oil and gas accumulations adjacent to WASP study area.	13
Figure 9: Pressure time history for a typical water disposal well in the south western set of disposal wells.	14
Figure 10: Pressure time history for typical water disposal wells in south west set of disposal wells.	15

INTRODUCTION

BACKGROUND

One of the most useful methods of characterizing the quality of a reservoir for its deliverability or injectivity is to make use of analogues from similar or adjacent areas to the area of study. The production and injection history in the analogue pool or wells can be assessed for possible similarities to the study area formation. The Wabamun Area CO₂ Sequestration Project (WASP) study area is an entire 53 township of land area over top of a large portion of the Nisku aquifer in central Alberta, Figure 1. This study area was chosen intentionally to avoid existing hydrocarbon production. As such, there are no depleted pools or mature oil fields producing from the Nisku horizon in the entire study area. Nor are there any water disposal wells into the Nisku formation in the study area.

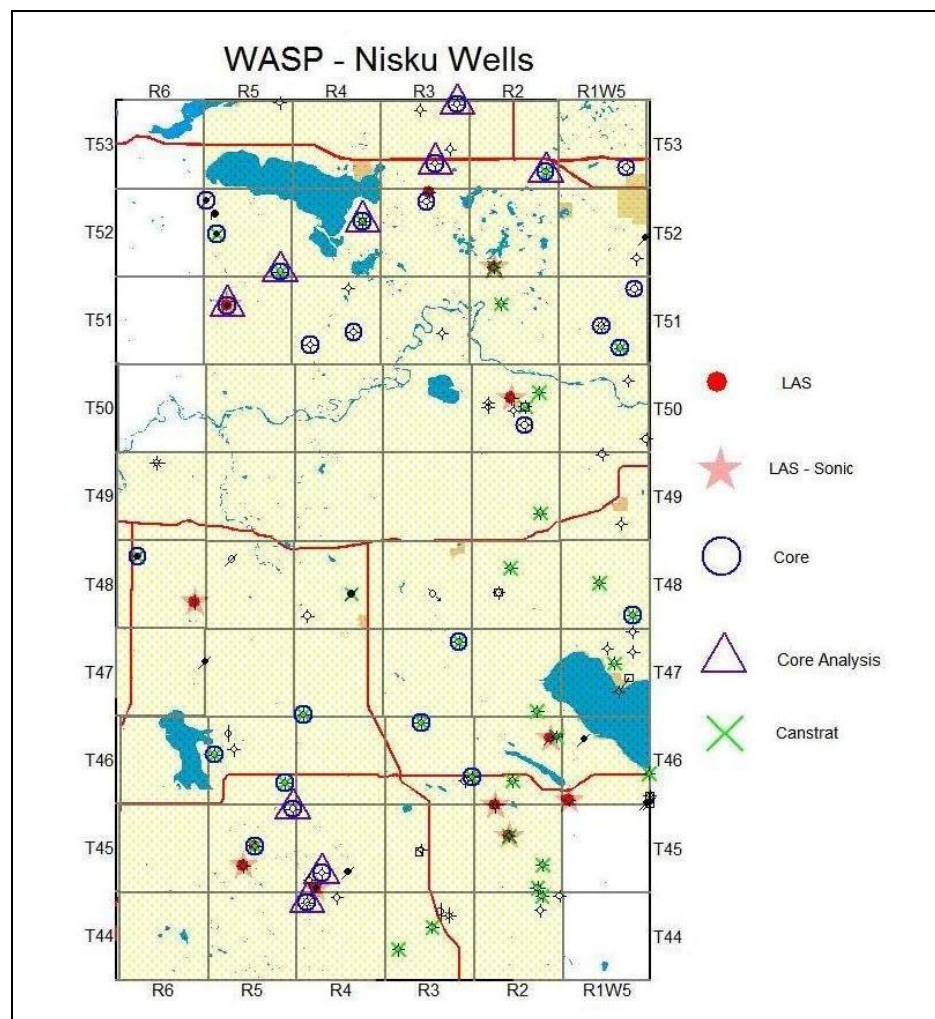


Figure 1: WASP study area

The WASP study team was able to find one water source well in the study area, as is discussed in other section of the WASP documentation. However, this source well is operated with an electrical submersible pump and there are no bottom hole pressure instruments to determine the production drawdown associated with brine production. This results in an inability to assess the deliverability parameters for this well. The operators of the well gave assurances that the drawdown is minimal and an independent assessment of this location performed by WASP indicates that a very high deliverability exists for this one well.

In an attempt to find additional confirmation of good reservoir quality conditions for the Nisku aquifer, a review of water disposal wells in a study area consisting of 30 townships immediately to the east of the WASP study area was performed. Figure 2 highlights this area along with the locations of six major Nisku oil and gas pools.

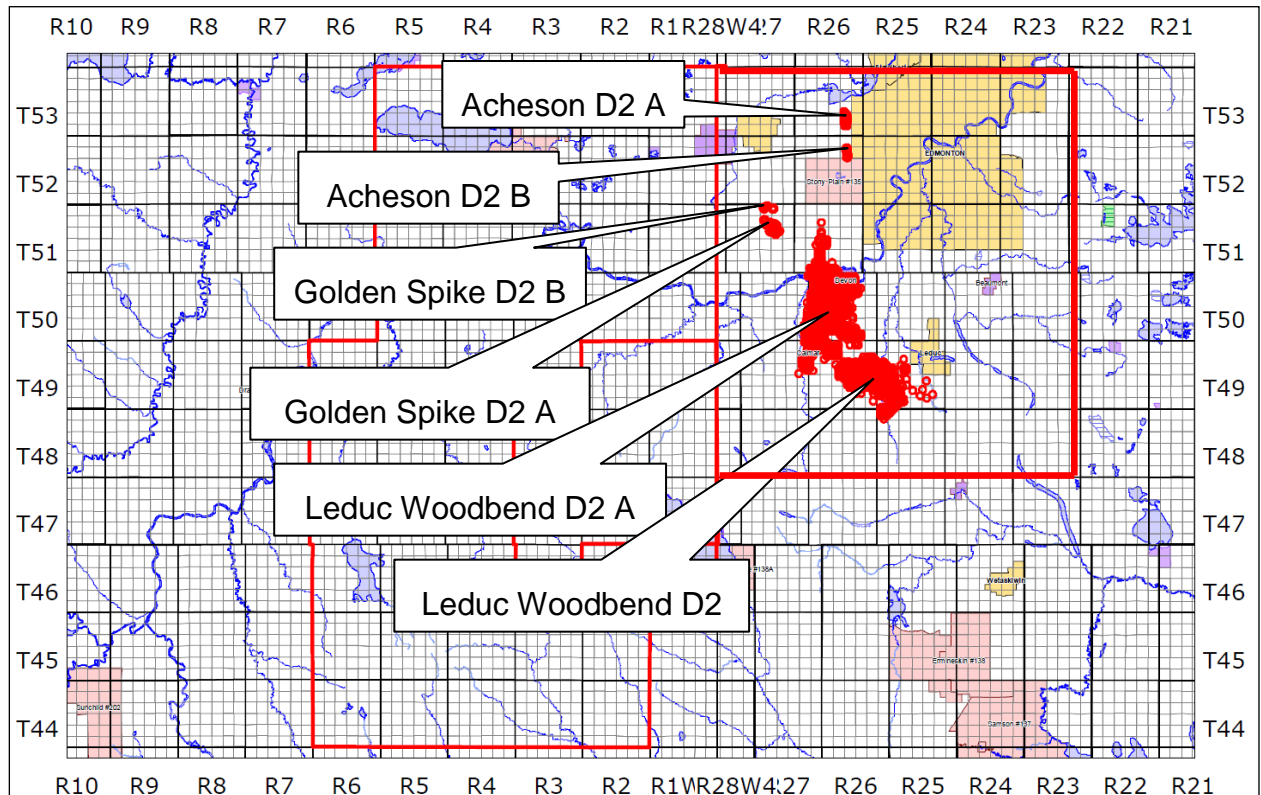


Figure 2: Water disposal well study area

The discussion that follows provides a summary of the water disposal well operating rates for wells located in this study area.

DISCUSSION

1. ESTIMATED PER WELL CO₂ INJECTION VOLUMES

A benchmark for estimated injectivity requirements for future commercial CO₂ sequestration projects would be helpful for comparison to water disposal volumes. Table 1 provides a listing of Nisku Aquifer conditions and an estimate of the injection volume requirements at reservoir conditions to dispose of 1 Mt of CO₂ per year:

Table 1: Nisku aquifer characteristics and CO₂ volume at aquifer conditions.

Description	Value	Unit of Measure
Reservoir Temperature	60	Deg. C
Reservoir Pressure	16,000	kPa
CO ₂ Density @ Res. Cond.*	595	Kg/m ³
1 Mega Tonne/Yr	2,740	Tonnes/day
Injection Rate	4,605	m ³ /day at res. cond.
Total injection over 50 years	84 million	m ³ at reservoir conditions
* Based on the Peng-Robinson equation of state at stated conditions using the web application published at http://esdtools.lbl.gov/cgi-bin/webgaseos.cgi		

The reservoir volume of CO₂ to be sequestered on a per well basis is in the order of 84 million m³ at reservoir conditions of 16 kPa and 60 deg. C. The volume injected on a daily basis would be 4,605 m³. These volumes are large in comparison to historic injection rates observed for Nisku disposal wells—as reported below.

2. STUDY AREA WATER DISPOSAL WELLS INTO THE NISKU AQUIFER

A total of 98 water disposal wells were found for the subject study area. Figure 3 provides a comparison of the cumulative injection volumes associated with each of these wells.

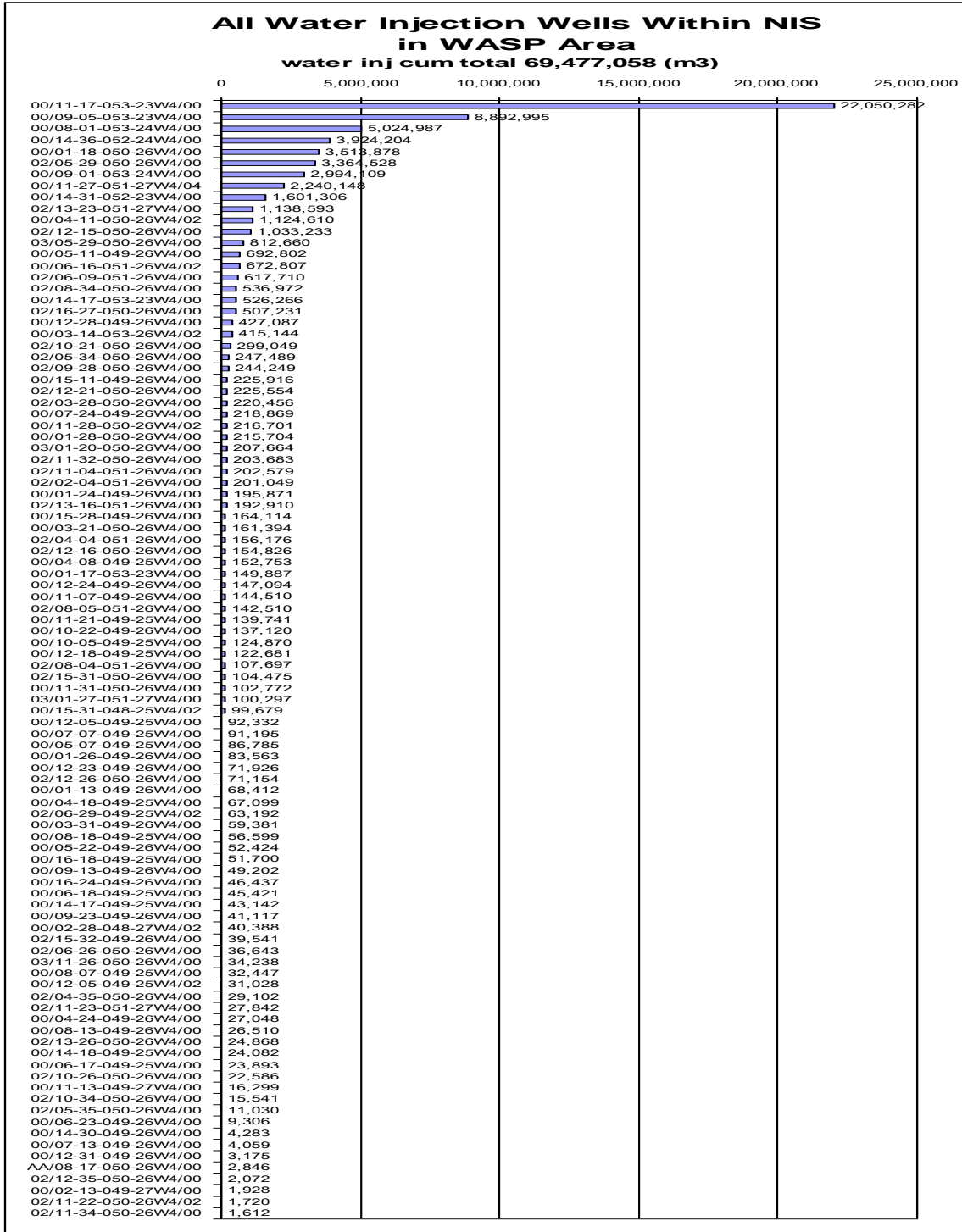


Figure 3: List of water disposal wells in study area.

Figure 4 provides a map of the locations of the top 19 wells in this list.

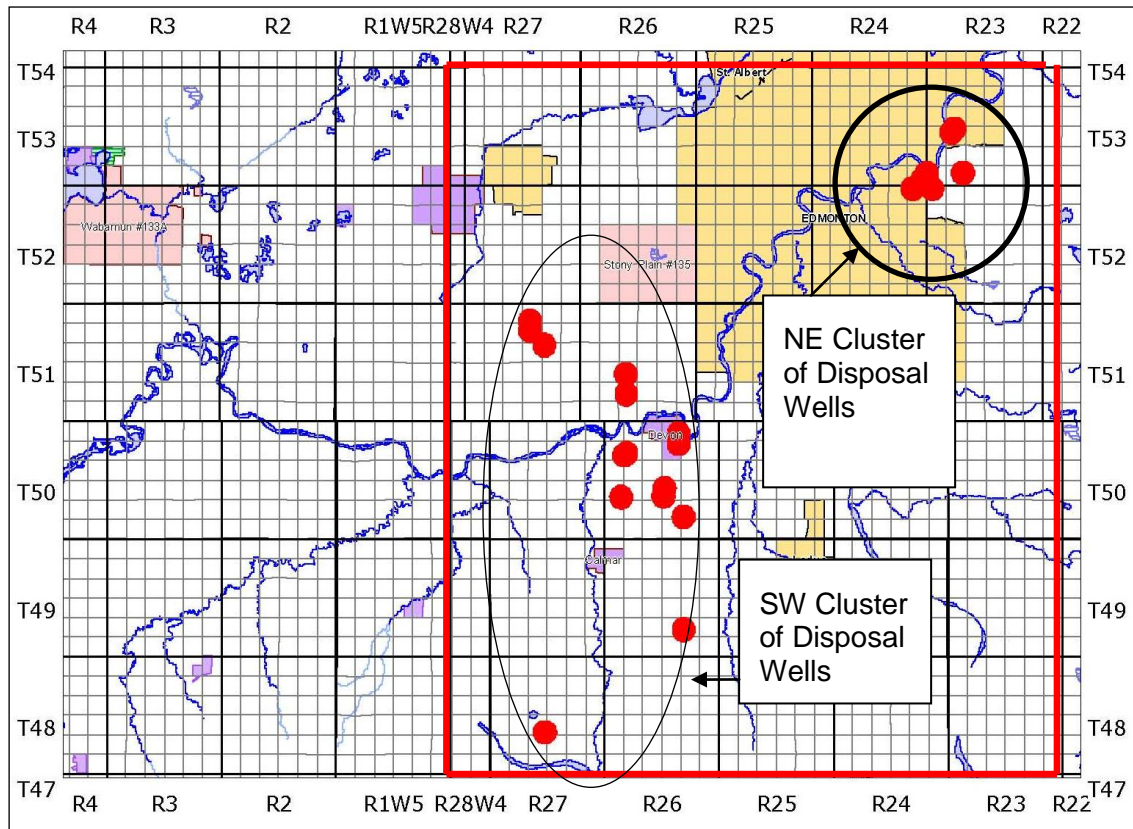


Figure 4: Location of top 19 water disposal wells in study area.

As can be seen on this map, two clusters of wells are evident. The NE cluster is located near the industrial parks of northeastern Edmonton. The SW cluster is located in the Nisku oil and gas pools SW of Edmonton.

Figure 5 provides a closer look at the cumulative volumes injected for the top 19 disposal wells. As can be seen from this diagram, the largest disposal well is located in the cluster to the north east of Edmonton. In fact, disposal wells located in this region generally have higher cumulative volumes relative to those located in the Nisku oil and gas fields to the south west of Edmonton. It is not possible to assess rigorously the injectivity parameters for these wells, but by inference only, it seems likely that the north east cluster wells have higher total injectivity. This is consistent with a geological interpretation of the Nisku aquifer that suggests there are better reservoir parameters in the vicinity of the north east cluster (Reference 1).

For the purpose of our search for analogue injectivities, the south west cluster of wells is deemed to be more representative of the reservoir characteristics associated with the WASP study area. The largest cumulative volume injected in the south west well cluster is in the order of 3.5 million m³. This is significantly lower than the 84 million m³ that would be required for a single CO₂ sequestration well with an injectivity of 1 mega tonne per yr.

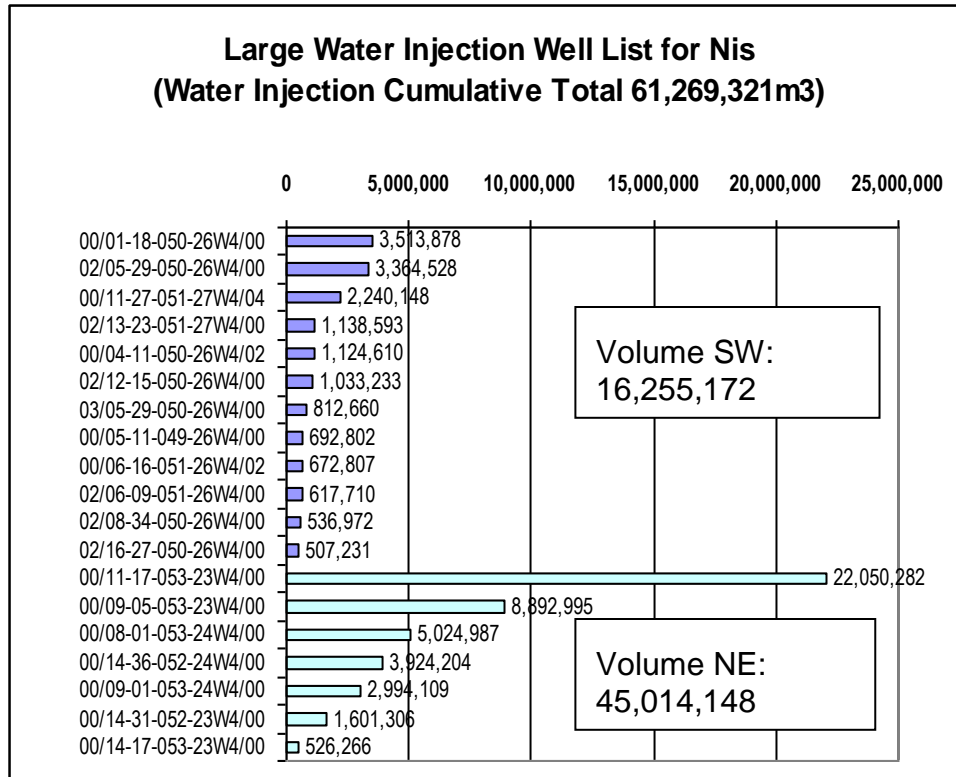


Figure 5: Plot of cumulative volumes for top 19 disposal wells.

3. WATER DISPOSAL WELL INJECTIVIES

A review of the maximum and average injection rates associated with the water disposal wells is provided in Figure 6.

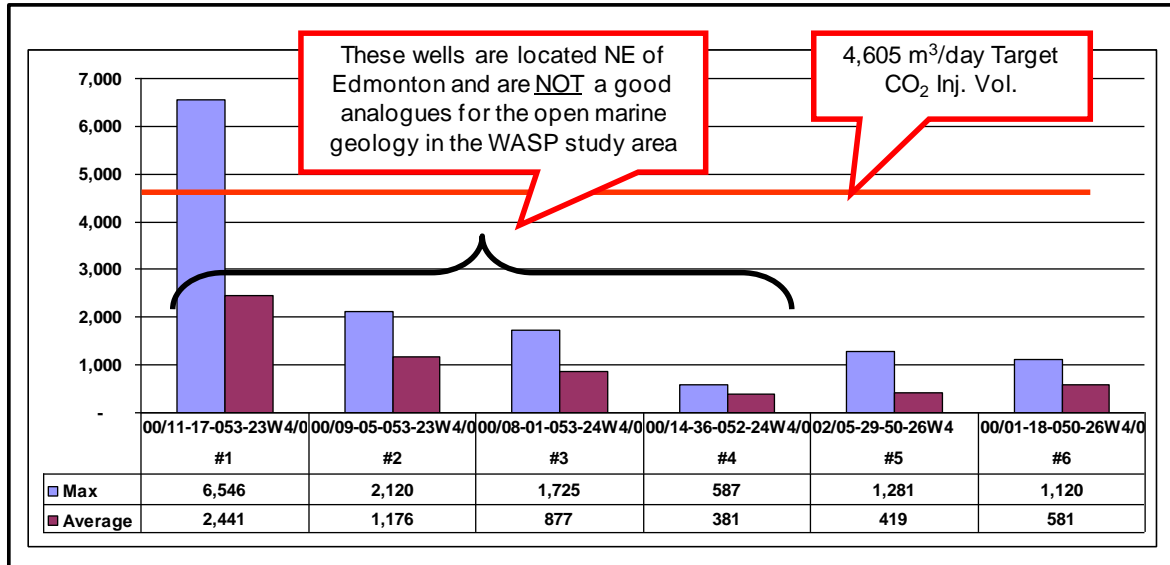


Figure 6: Top six water disposal wells—daily injection rates (m³/day).

As can be seen from Figure 6, daily injection rates of Nisku disposal wells located in the south west cluster of disposal wells are well below the reservoir volumes anticipated for a one mega tonne per year CO₂ disposal well. Once again, these results are qualitative only. It is not possible to determine the injection parameters associated with these rates from public domain data alone.

Figure 7 illustrates the location of well #6 (01-18-050-26W4) located in the south west cluster of injectors. Figure 8 provides the injection rate history plot for this well. As can be seen from the plot, injection rates were typically in the range of 1000 m³ per day. This is about 20% of the anticipated requirement for a CO₂ disposal well, as illustrated in Figure 8.

It is not possible to conclude that these injection rates were at a maximum operating condition for the wells studied. However, given that numerous water injectors were developed for each oil pool, one could speculate that this is based on water injection capacity limitations and that these wells (or most of them) are at their capacity limitation. Further information would need to be acquired from oil company files to verify this assumption.

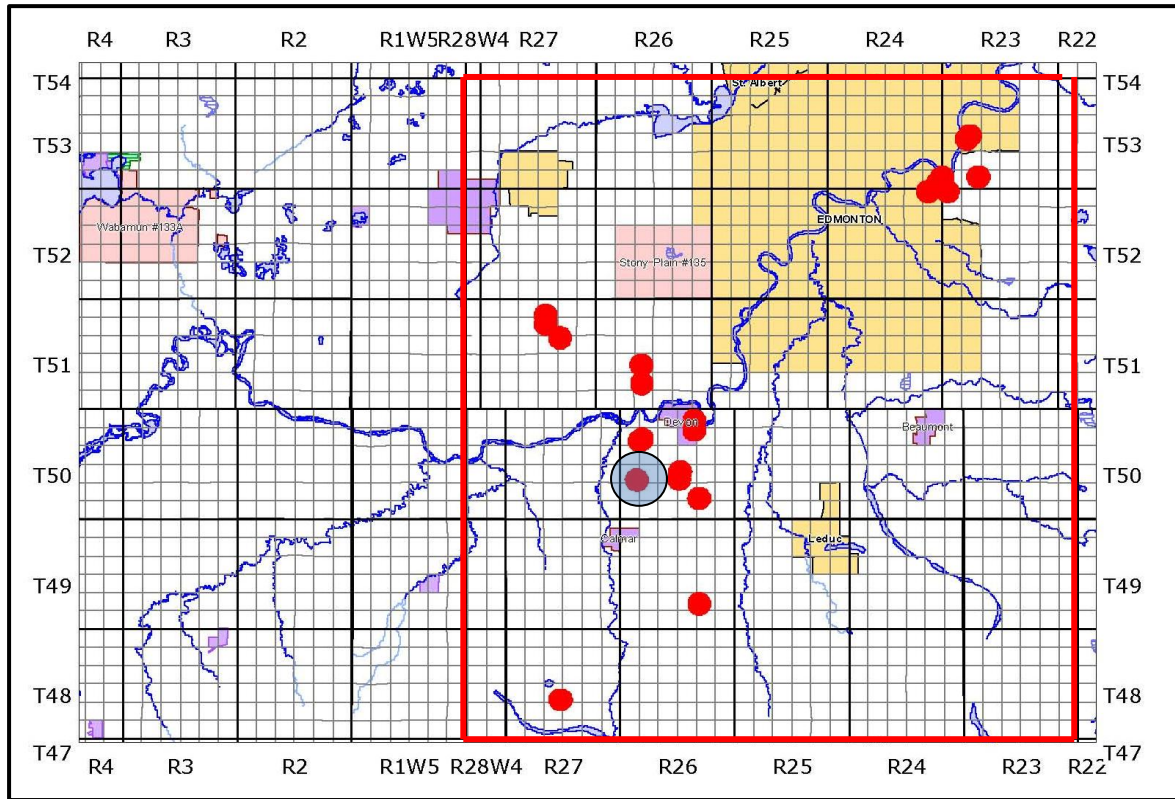


Figure 7: Location of Well #6 from Figure 6.

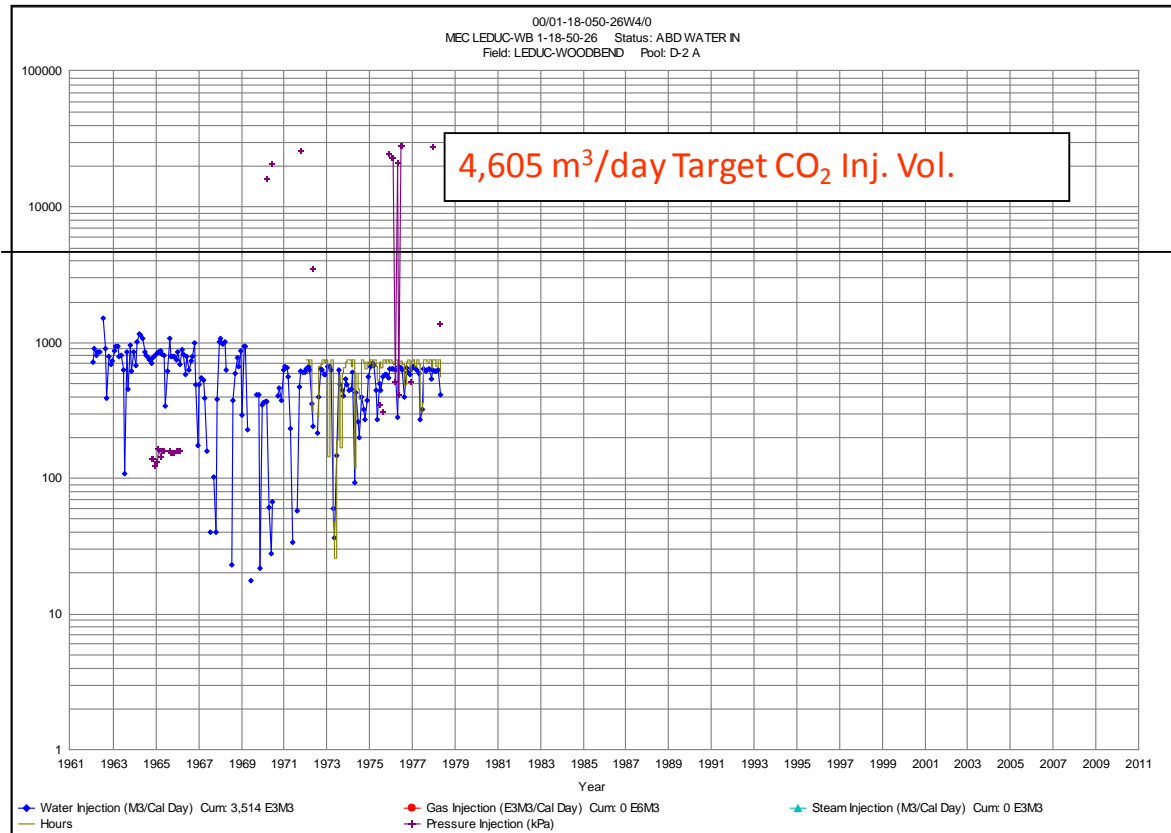


Figure 8: Typical injection performance history for Nisku water disposal well located in Nisku oil and gas accumulations adjacent to WASP study area.

4. PRESSURE HISTORY FOR DISPOSAL WELLS

Injection rates only tell part of the story, it is also important to understand the reservoir pressure these wells are injecting against. Figure 9 provides a typical pressure time history for the wells associated with this injectivity study.

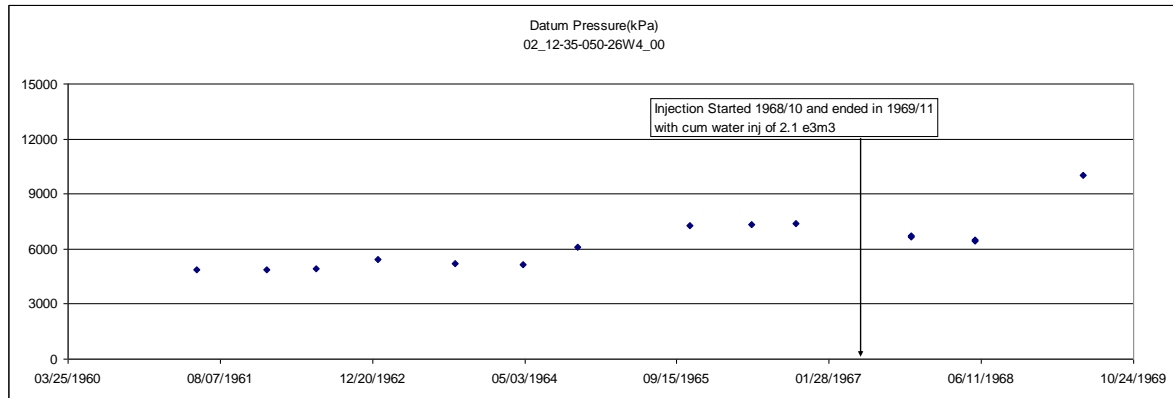


Figure 9: Pressure time history for a typical water disposal well in the south western set of disposal wells.

Figure 9 demonstrates the increase in pressure observed after a few years of injection into the water disposal wells located in the south west region of the disposal well study area. This was typical of all disposal well histories where adequate pressure history was collected. The pressure history for all wells in the Nisku oil and gas pools adjacent to the WASP study area is provided in Figure 10.

Figure 10 provides the pressure time history for all oil and gas wells located in the Nisku pools adjacent to the WASP study area. These pressure trends illustrate that some pools experienced a pressure decline during depletion of the pool but that pressure maintenance schemes in the later life of these pools successfully increase the reservoir pressure to near the original discovery pressures. Some of the Nisku oil and gas pools recorded very little pressure depletion. This is indicative of a very strong aquifer underlying these oil pools. This is discussed further in the material balance report accompanying the WASP documentation.

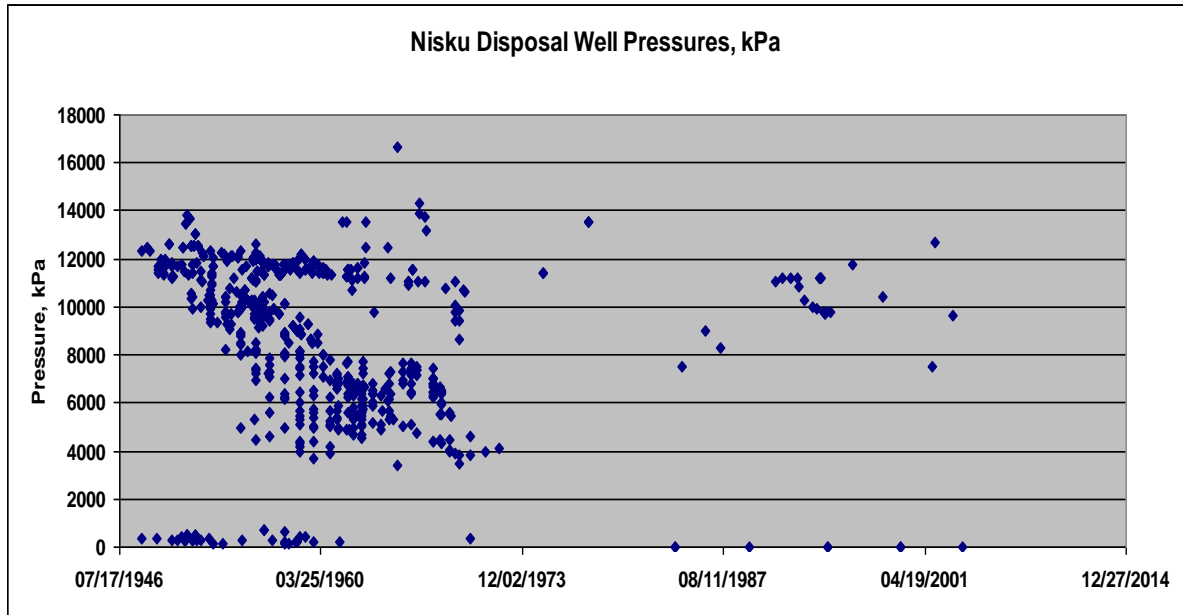


Figure 10: Pressure time history for typical water disposal wells in south west set of disposal wells.

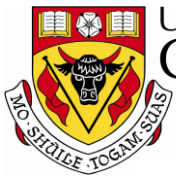
5. CONCLUSION

Only generalized conclusions are possible from this analysis. They are:

1. Injection rates of disposal fluids into the Nisku aquifer in the analogous region to the south west of Edmonton and east of the WASP study area are only about 20% of the injection rate needed for a single commercial CO₂ injection well to store 1 Mt CO₂/year. Whether or not these are the limitations of the wells investigated or simply the limitations of available disposal rates is not clear from the work done to date.
2. Reservoir pressures were depleted at the time disposal volumes were initially injected. In some oil pools that had experienced significant depletion, reservoir pressures were restored to near original conditions. Other oil pools that have shown strong aquifer support also demonstrated that disposal volumes were not large enough to impact reservoir pressures.
3. Injection volumes to the north east of Edmonton (the Edmonton industrial areas) are substantially higher than those observed in the analogous area closer to the WASP study area.

REFERENCES

1. Personal conversation with Frank Stoakes of Stoakes Consulting Group.



Lost Circulation Wells

WABAMUN AREA CO₂ SEQUESTRATION PROJECT (WASP)

Author

Rob Lavoie

Rev.	Date	Description	Prepared by
1	August 3, 2009	Lost Circulation Wells	Rob Lavoie
2	December 21, 2009	Lost Circulation Wells	Rob Lavoie

Table of Contents

INTRODUCTION.....	5
BACKGROUND	5
DISCUSSION	5
1. Methodology	5
2. Conclusion	8
REFERENCES.....	9

List of Tables

Table 1: List of wells overlaying the Nisku formation in the WASP study area.	5
Table 2: Drilling fluid and pressure data for wells with four occurrences in WASP study area.	7

List of Figures

Figure 1: Numbered wells (corresponding to Table 1) with events recorded in tour reports.....	6
Figure 2: Hydrostatic pressure for wells with tour occurrences.	8

INTRODUCTION

BACKGROUND

As part of the reservoir characterization effort undertaken for the WASP study, any data that could lead to a determination, qualitative or quantitative, of the permeability associated with the Nisku aquifer are important. A number of wells on the eastern edge of the WASP study area had experienced lost circulation conditions while drilling through the Nisku aquifer. This led to the speculation that potentially there was a link between these wells and a possible higher permeability trend along the inboard margin of the Nisku aquifer. To confirm or dispute this inference, a closer study of the lost circulation conditions associated with these wells was conducted.

Lost circulation is the loss of returned mud from the annulus of a conventionally circulated well. From a hydraulic standpoint, it means that the mud column hydrostatic pressure exceeds the ability of the formation to resist injection. There are many reasons for this. Some of these are, naturally fractured formations or vugular porosity in which the formation pore pressure is the only resistance to mud loss, high-porosity/high-permeability formations, leaks to upper intervals of various kinds, induced fractures and other types of induced inter-well communications (Reference 1).

DISCUSSION

1. METHODOLOGY

A database search of the wells in the WASP study area was conducted to determine which wells in the area had experienced lost circulation or other problems during drilling. Wells that experienced problems during drilling through the Nisku formation are listed in Table 1 and located on Figure 1.

Table 1: List of wells overlaying the Nisku formation in the WASP study area.

No.	Well I.D.	Event Recorded in the Tour Report	Date of Event
1.	100/02-21-048-01W5/00	Lost circulation	February 5, 1962
2.	100/10-22-047-01W5/00	Lost circulation	September 10, 1964
3.	100/10-25-046-02W5/00	Lost circulation	July 17, 1966
4.	100/10-14-053-03W5/00	Lost circulation	January 13, 1976
5.	100/04-14-051-03W5/00	Lost circulation	July 21, 1963
6.	100/06-10-045-04W5/00	Kick	January 7, 1986
7.	100/02-29-051-05W5/00	Lost circulation	March 22, 1994
8.	100/14-21-045-02W5/00	Lost circulation	August 20, 1960
9.	100/15-35-044-02W5/00	Lost circulation	January 19, 1988

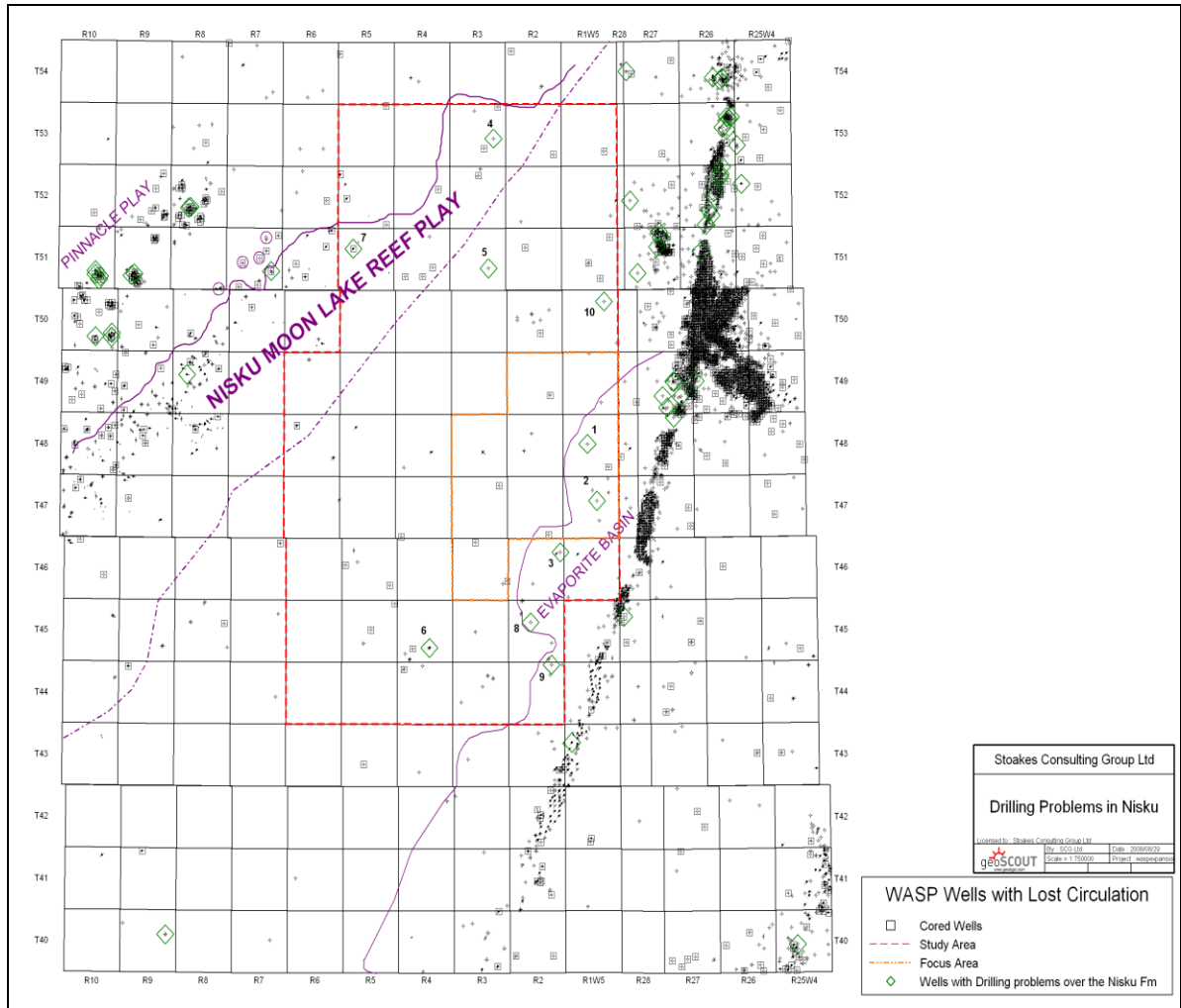


Figure 1: Numbered wells (corresponding to Table 1) with events recorded in tour reports.

Well tickets for each of these wells were printed and the tour occurrence dates noted. Additionally, the drilling rig tower sheets were obtained for each of these wells and the dates of the tour occurrences obtained from the well tickets were checked on the tower sheets. In this way drilling depths and mud densities could be used to estimate the hydrostatic pressure of the drilling fluid at the lost circulation depth. Table 2 lists the mud densities, formation depths, and column pressures for each well that had a tour occurrence while drilling in the Nisku formation.

Table 2: Drilling fluid and pressure data for wells with tour occurrences in WASP study area.

No.	Well I.D.	Mud Weight		Depth of Event Recorded in the Tour Report		Nisku Top		Pressure	
		gm/cc	ppg	m	ft.	m	ft.	kPa	psi
1.	100/02-21-048-01W5/00	1.078	9.0	1896	6221	1876	6155	20074	2911
2.	100/10-22-047-01W5/00	1.174	9.8	1995	6546	1676	5500	23000	3336
3.	100/10-25-046-02W5/00	1.102	9.2	2128	6981	2118	6950	23027	3340
4.	100/10-14-053-03W5/00	1.066	8.9	1786	5858	1781	5844	18692	2711
5.	100/04-14-051-03W5/00	1.174	9.8	1838	6030	1789	5870	21187	3073
6.	100/06-10-045-04W5/00	1.054	8.8	2510	8235	2488	8161	25863	3751
7.	100/02-29-051-05W5/00	1.018	8.5	2048	6719	2043	6703	20505	2974
8.	100/14-21-045-02W5/00	1.174	9.8	2248	7376	2204	7230	25916	3759
9.	100/15-35-044-02W5/00	1.090	9.1	2222	7290	2192	7190	23774	3448

Figure 2 shows the area wide distribution of the pressures at which tour occurrences occurred. For each well the hydrostatic pressure was calculated using the following equation:

$$\text{Pressure} = \text{MW} \times \text{Depth} \times 0.052$$

Where MW is the drilling fluid density in pounds per gallon, Depth is the true vertical depth in feet, and 0.052 is the unit conversion factor such that pressure results in units of pounds per square inch.

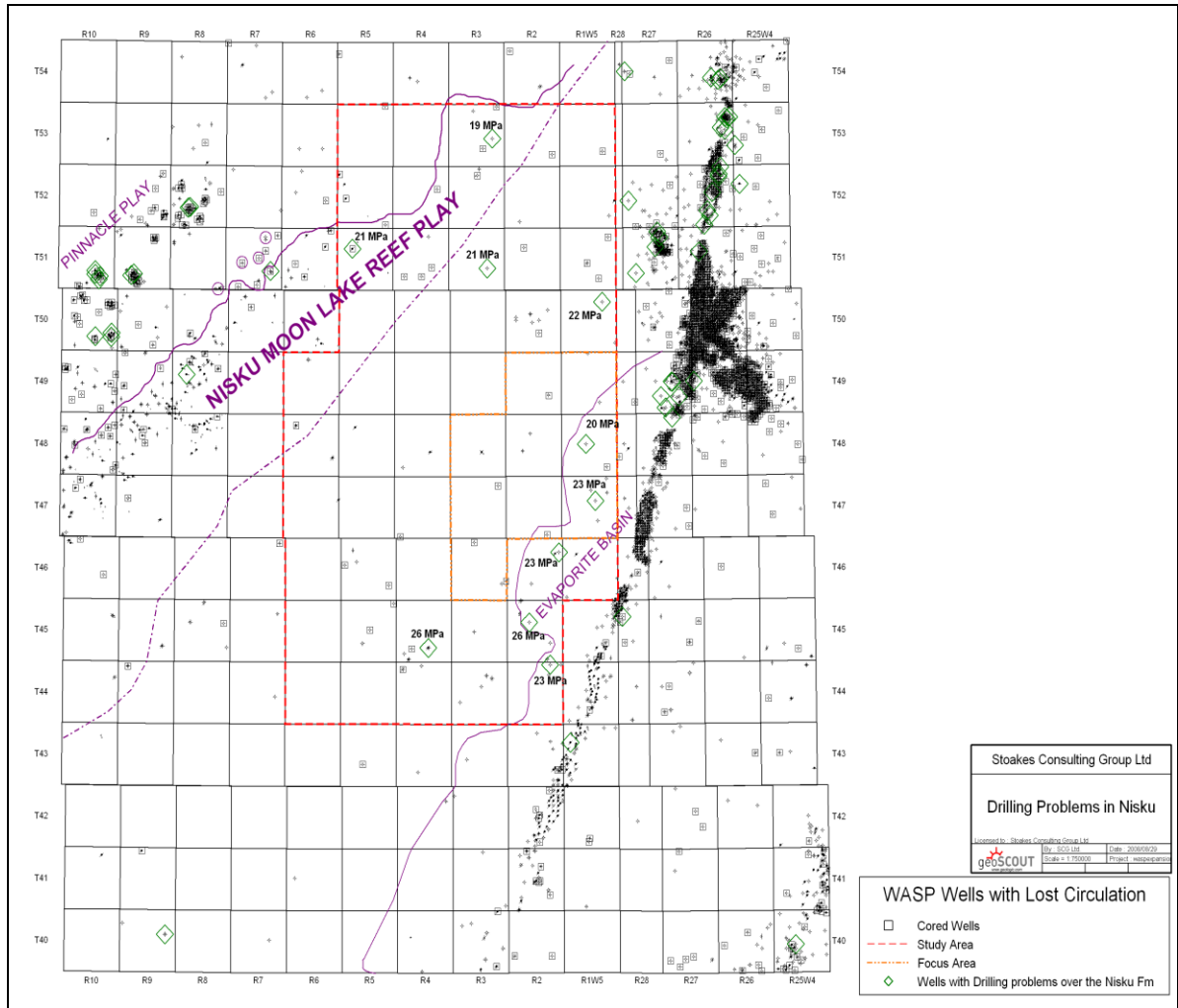


Figure 2: Hydrostatic pressure for wells with four occurrences.

2. CONCLUSION

The Nisku reservoir’s original reservoir pressure is in the order of 16 to 18 MPa. Table 2 indicates that only two of the nine (9) wells had hydrostatic mud weights greater than 24 MPa at the time they were being drilled through the Nisku aquifer. These mud weight may have been high enough to have resulted in a lost circulation condition. Five (5) of the nine (9) wells had mud weights greater than or equal to 23 MPa. These wells may also have been overpressured to the point of losing circulation.

Based on these results it is difficult to draw conclusions about a possible trend towards higher permeabilities on the eastern edge of the Nisku aquifer in the WASP study area even though it is compelling to do so for other reasons. Other wells, such as the water source well discussed elsewhere in this set of WASP reports, suggest that there might be a high permeability trend along the inboard margin of the Nisku aquifer. Our investigation of lost circulation wells neither supports nor refutes this hypothesis.

REFERENCES

1. Les Skinner, Lost Circulation, World Oil, August 2006.



Reservoir Modelling

Wabamun Area CO₂ Sequestration Project (WASP)

Authors

Seyyed Ghaderi

Yuri Leonenko

Rev.	Date	Description	Prepared by
1	August 14, 2009	First draft	Yuri Seyyed
2	August 19, 2009	Revision	Yuri Seyyed

Table of Contents

INTRODUCTION.....	5
DISCUSSION.....	5
1. NUMERICAL RESERVOIR MODELLING.....	5
1.1. Preliminary Conceptual Model.....	5
1.2. Detailed Model with Full Aquifer (Nisku) Extent.....	9
2. LONG-TERM FATE OF CO ₂	17
2.1. Pressure Field Evolution During and After Injection Until Initial Reservoir Pressure Reached.....	17
2.2. Effect of Aquifer Dip on Plume Movement and Size.....	18
2.3. Estimation of Timescale for Free-Phase CO ₂ after Injection (onset and dissolution time for natural convection scenario).....	18
3. INVESTIGATION OF THE PHASE BEHAVIOR OF H ₂ S SATURATED BRINE IN CO ₂ SEQUESTRATION PROCESS.....	19
3.1. Fluid Representation of CO ₂ -Brine and CO ₂ -H ₂ S-Brine Systems.....	19
3.2. Description of the Simulation Model.....	20
3.3. General Simulation Results.....	20
3.4. Base Case Simulation Results and Observations.....	22
3.5. Sensitivity Analysis.....	23
SUMMARY.....	26
ACKNOWLEDGMENTS.....	26
REFERENCES.....	27

List of Tables

Table 1: Reservoir properties.....	6
------------------------------------	---

List of Figures

Figure 1: Nisku relative permeability curves.	6
Figure 2: Configuration of injection wells and element of symmetry (salmon area).	7
Figure 3: Effect of different parameters on storage capacity: a) effect of distance between wells, b) effect of compressibility, c) effect of permeability, d) effect of aquifer thickness.	8
Figure 4: Top view of the Nisku formation in the Wabamun Lake area (left), study area is outlined in red and base formation/properties used are shown on the right.	10
Figure 5: Plume extension (top row) and pressure radius of investigation (bottom row) after 50 years of injection for different wells in the Nisku study area (within the red area in Figure 4).....	10
Figure 6: Pressure evolution: left, one well; right, 10 wells.....	11
Figure 7: Variation of Nisku capacity with respect to number of wells and formation properties (red curve represents base properties).	12
Figure 8: Pressure at the end of injection.	12
Figure 9: Comparison of the effect of different well orientations and stimulation on the storage capacity of the model.	13
Figure 10: Five geo-statistical realizations for porosity and permeability.	14
Figure 11: Object-based realization of porosity.	14
Figure 12: Saturation (left) and pressure (right) fields for stochastic modelling after 50 years of injection.	15
Figure 13: Injection capacity for five realizations.	15
Figure 14: Injection capacity for different fracture pressures.....	15
Figure 15: Saturation (left) and pressure (right) fields for object-based modelling after 50 years of injection.	16
Figure 16: Injection capacity for object-based modelling.....	16
Figure 17: Pressure evolution (each well injects 0.5 Mt/year for 50 years).	17
Figure 19: Saturation field for a single injector: a) base properties; b) permeability is increased to 150 mD.....	18
Figure 20: Short-term (a) and long-term (b) processes involved in geological storage.	19
Figure 21: Water-gas relative permeability curves.	20
Figure 22: Variation of gas saturation around the injection well after 200 days.	21

INTRODUCTION

Although it is recognized that deep aquifers offer the potential for very large storage capacities for CO₂ sequestration, it is not clear what the best method is to fill these aquifers with large volumes of CO₂ in a relatively short period of time within localized injection areas. The typical benchmark for the rate of CO₂ injection is 1 Mt/year when studying storage performance. This rate is very low when compared to the scale needed for storage technology to play a significant role in managing global emissions. In this report we study the feasibility of injecting large volumes of CO₂ into the Nisku aquifer, which is located in the Wabamun Lake area in Alberta, Canada [1]. In this area, large CO₂ emitters include four coal-fired power plants with emissions that range between 3 and 6 Mt/year each, which together emit ~ 20 Mt/y or ~ 1 Gt over 50 years. This number, 1 Gt, is considered the target capacity for WASP. The Nisku aquifer is believed to be a suitable choice for future sequestration projects. The main objectives of the WASP study are as follows.

- i) *Estimate storage capacity.* Traditionally, storage capacity is determined by available pore space. For this study a more practical aspect was used—the maximum amount that can be injected within a short period of time (~ 50 years) within a localized injection area (~ 30 km × 90 km). The capacity of individual reservoirs to accommodate large injection volumes should be evaluated by assessing the ability to inject CO₂ without exceeding formation fracture pressures. A number of options were also considered to increase storage capacity.
- ii) *Determine CO₂ plume movement and pressure distribution.* These factors were determined for the period during and after injection. The shape and dip of the aquifer, the number of wells and their placement (among other parameters) would be considered.
- iii) *Estimate long-term fate of injected CO₂.* Estimate the timescale for the long-term fate of the injected CO₂ associated with free-phase CO₂, aquifer pressurization, and the effect of dip on plume shape and its migration.
- iv) *Investigate phase behaviour.* Investigate the phase behaviour of H₂S initially saturated in brine in the CO₂ sequestration process.

DISCUSSION

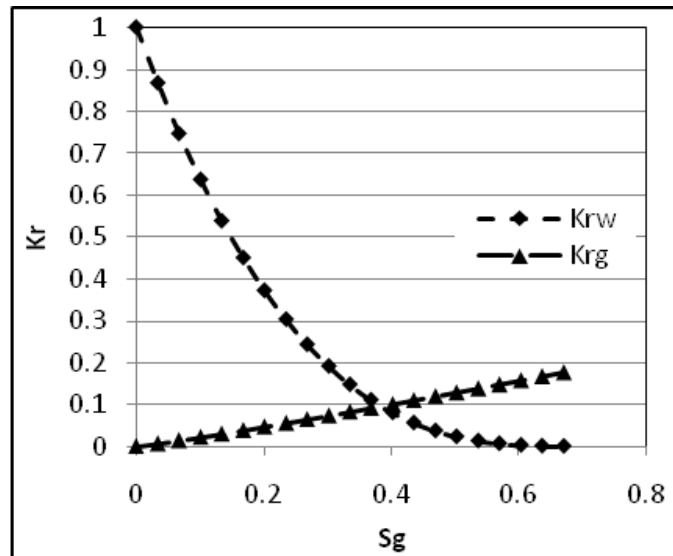
1. NUMERICAL RESERVOIR MODELLING

1.1. Preliminary Conceptual Model

To develop a benchmark at the beginning of the project, a simplified conceptual model was developed based on homogeneous properties and an infinite acting aquifer. The properties for the simulations were taken from Hitchon, 1996 [1] (Table 1). The table data was then revised using WASP preliminary analysis data: permeability was changed to 30 md, porosity to 10%, aquifer thickness to 70 m and PVT table for density and viscosity were generated based on Hassanzadek et al, 2008 [2]. The relative permeability curves (Figure 1) were taken from literature (Bennion and Bachu, 2005 [3]).

Table 1: Reservoir properties.

Description	Result
Depth (m)	1860
Thickness (m)	70
Pressure at aquifer top (MPa)	16
Temperature (°C)	60
Permeability (md)	6.2 – 400
Vertical anisotropy	0.27
Porosity (%)	6 – 12
Salinity of formation water (mg/l)	190000
Density of formation water (kg/m ³)	1155.5
Viscosity of formation water (mPa.s)	0.840


Figure 1: Nisku relative permeability curves.

For this model, a square (200 km × 200 km) simulation domain was chosen to represent an aquifer (the results were not sensitive to an increase in model size to 250 km × 250 km). By setting the model to these dimensions, the aquifer behaves as though it is infinite acting for the injection of the target volume of CO₂.

Figure 2 shows the model configuration for the different numbers of vertical injector wells, starting with 1 and ending with 25. All wells are perforated from the top to the bottom of the aquifer. The number of wells (n) was chosen to allow the use of an element of symmetry and hence reduce the total number of grid cells by a factor of four. The distance between the wells in both the x and y directions are the same and equal to λ . The total cumulative amounts of injected CO₂ (Q1, Q4, Q9, Q16 and Q25) increase with the number of wells, and these amounts are split equally between injectors in each case. For example in the case of 16 wells, the flow rate per well is Q16/(16 wells × 50 years).

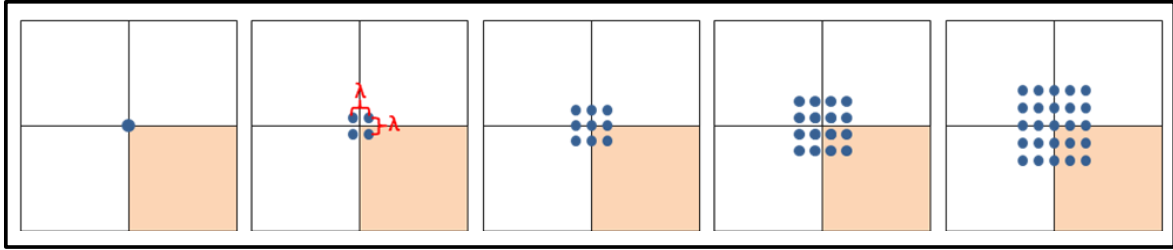


Figure 2: Configuration of injection wells and element of symmetry (salmon area).

Single Injector (capacity and plume size)

The saturation and pressure fields for a single well, as well as for multiple injection scenarios, will be shown in the following section (Section 1.2, Detailed Model with Full Aquifer Extent), since the results are very similar. A brief summary for a single injector:

- plume radius after 100 years of simulation is ~ 4.6 km; and
- capacity of one vertical well is ~ 1 Mt/y (based on $P_f = 40$ MPa), horizontal well improves capacity with a maximum rate of ~ 1.5 Mt/y. (The value for the fracture pressure will be discussed later in this report.)

Multiple Injectors

For multiple ($n > 1$) injection scenarios, CO₂ saturation plumes have no interference and n individual plumes have a radius of 4 to 5 km for each injector.

The pressure field behaves totally different than the saturation field. By the fiftieth (50th) year of CO₂ injection, there are no individual pressure plumes. Instead, most of the pressure plumes have merged into a single large (scale of hundred km) pressure disturbance. Injection capacity increases with the number of wells, but there is limited benefit to adding incremental wells after 15 to 20. These phenomena will be discussed in detail in Section 1.2 when more advanced modelling for the Nisku aquifer is considered.

Sensitivity of Injectivity to Different Reservoir Properties (permeability, rock compressibility, aquifer depth) and Well Placement (generic study)

The sensitivity study in this section was performed using generic variables. The properties of the reservoir were chosen similarly to those used in the Berkeley Laboratory inter-comparison study [4]. This study and its properties are well known, so they could be used as a benchmark for representative aquifers for generic studies. The aquifer is considered to be homogenous, isotropic, and isothermal with a thickness of 100 m and permeability of 1.0×10^{-13} m² (100 mD), porosity is 12%, rock compressibility of 4.5×10^{-10} 1/Pa, and fracture pressure equal to 30,000 kPa. In all runs, the initial conditions include a temperature of 45°C, pressure of 12000 kPa, salinity of 15% of NaCl by weight, brine saturation of 1, and gas saturation of zero. All simulation runs involve continuous injection for 50 years. Bottom hole injection pressure is monitored and constrained to less than 27 MPa over the entire injection period. These parameters define a maximum CO₂ storage capacity over a period of 50 years.

Figure 3-a shows the storage capacity considering the number of vertical wells and the distance between them. As this figure indicates, the required number of wells to achieve the target volume (1 Gt of total injection) is 25 situated 8 km apart. For practical reasons it may be better to use a smaller or larger number of wells covering a larger or smaller area. Extrapolating the green and red curves, we can roughly estimate the number of wells required. For example, 18 wells that are 10 km

apart or 28 wells that are 6 km apart will achieve the same target (although in these cases the placement will not be symmetrical and new simulations will have to be performed). With respect to the area of injection, there would be no preference between these three choices (6 km, 8 km or 10 km well separation). For sensitivity analysis, the blue curve in Figure 3-a corresponds to 25 wells that are 8 km apart. This will be used as the base case for the sensitivity study, and all other data will be compared to it. The case covers an area of 1024 km² (32 km × 32 km), which is a considerably large area. As the number of wells increase, the injection rate of each well decreases to compensate for the excess pressure build-up associated with new wells that affect the pressure response of the central wells. Hence, the initial steep slope of the graphs (from 1 to 4 wells) quickly approaches a constant slope.

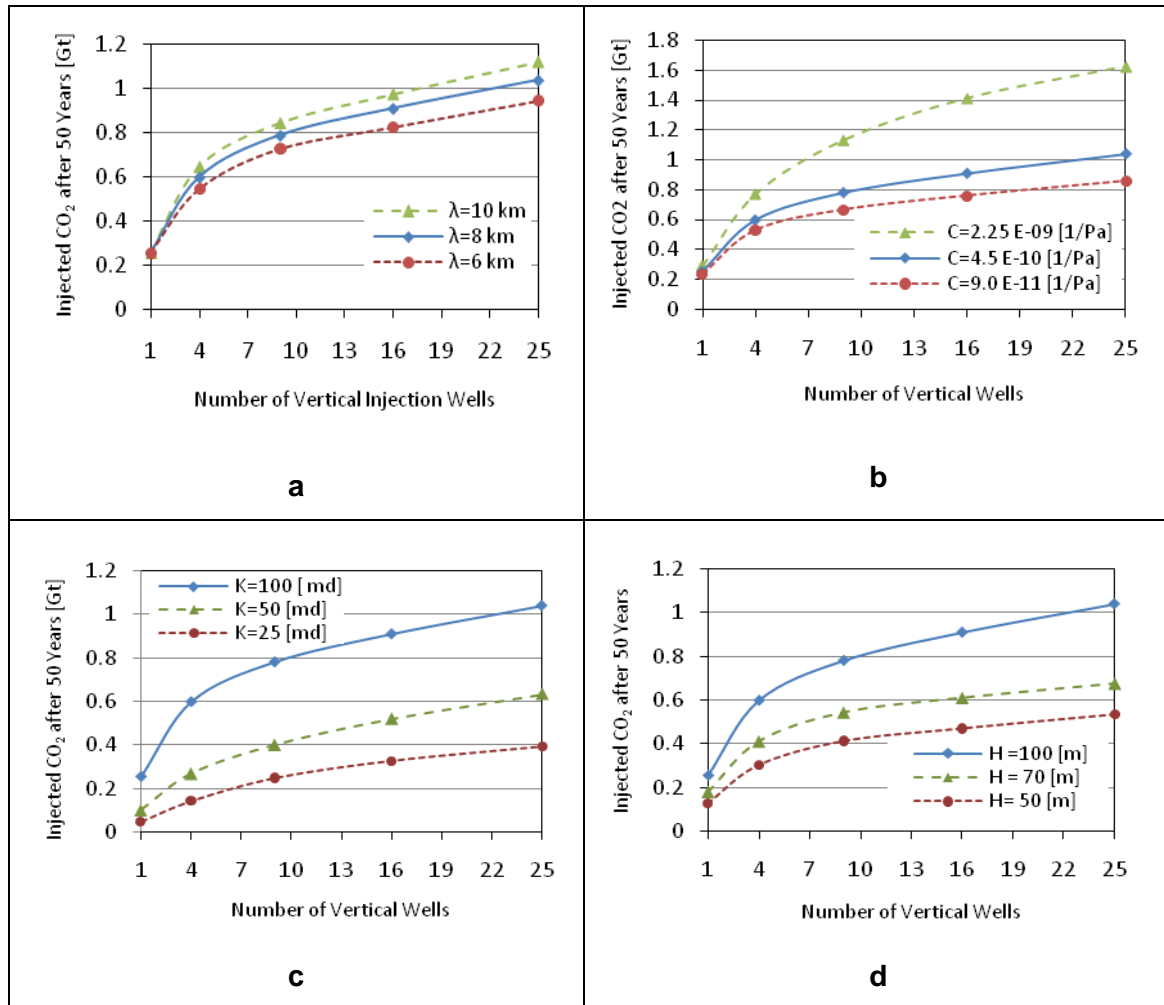


Figure 3: Effect of different parameters on storage capacity: a) effect of distance between wells, b) effect of compressibility, c) effect of permeability, d) effect of aquifer thickness.

Additional simulations were conducted to investigate the effect of some aquifer properties, such as rock compressibility, absolute permeability and thickness (Figures 3-b, 3-c and 3-d), on the amount of injected and stored CO₂ after 50 years. Since for the base case properties it was possible to inject the desired value of 1 Gt CO₂ over 50 years, the values for the parameters for the other scenarios were chosen closer to the expected aquifer properties. In all cases, the rates of CO₂ injection were

adjusted such that at the end of injection period, the maximum bottom-hole pressure reached the highest sustainable pressure.

Depending on the rock composition of the formations, the compressibility of the reservoirs varies widely. Hence for sensitivity study, the value of compressibility was varied within one order of magnitude by multiplying and dividing the base case value by five, respectively. Figure 3-b shows the outcome. Higher values of compressibility cause significant differences on the results, especially when the number of well increases.

The permeability of the formation controls both the pressure distribution over the system volume and the propagation velocity of the pressure pulse away from the injection site. According to the diffusivity equation, pressure will diffuse faster in formations with higher permeability or lower compressibility. Although it is quite possible to find localized regions with high absolute permeability within an aquifer (which are usually allocated to injection sites), generally the average permeability of the formation may be low. Figure 3-c depicts the results of simulations for different values of permeability. As the permeability is reduced by half, the amount of stored CO₂ nearly decreases by half. By reducing the permeability, the initial steep slope of the previous curves decreases. This illustrates that increasing the number of wells does not contribute significantly to capacity in low permeable formations.

The last parameter considered was the thickness of the formation. Reducing the thickness by 50% of the initial value has almost the same effect as reducing the absolute permeability by half (as would be anticipated). Figure 3-d indicates that for thinner reservoirs, more wells should be placed in the injection zone or other methods for increasing injectivity should be considered.

1.2. Detailed Model with Full Aquifer (Nisku) Extent

In the following section, the simulation results for CO₂ injection in the Nisku formation will be presented. First, a homogenous model is used to investigate the performance of a semi-infinite formation on injectivity. Then a heterogeneous model is populated with realistic permeability and porosity fields in order to demonstrate the effect of heterogeneity and reservoir dip angle on the evolution of a CO₂ plume and the associated impact on reservoir pressure.

Development of Full Aquifer Extent Geometry

Figure 4 shows the top view of the Nisku aquifer. The region covers an area of about 450 km × 640 km, while the bounded area by the red line shows the focus injection area. The majority of core and log data are related to available wells in this area and the injection site will be confined within this boundary. The area of this focus region is approximately 1500 km². The thickness of the numerical model is 70 m. Thirty layers with variable thickness are used to create the 3D model. The base properties used are the same as for the conceptual model.

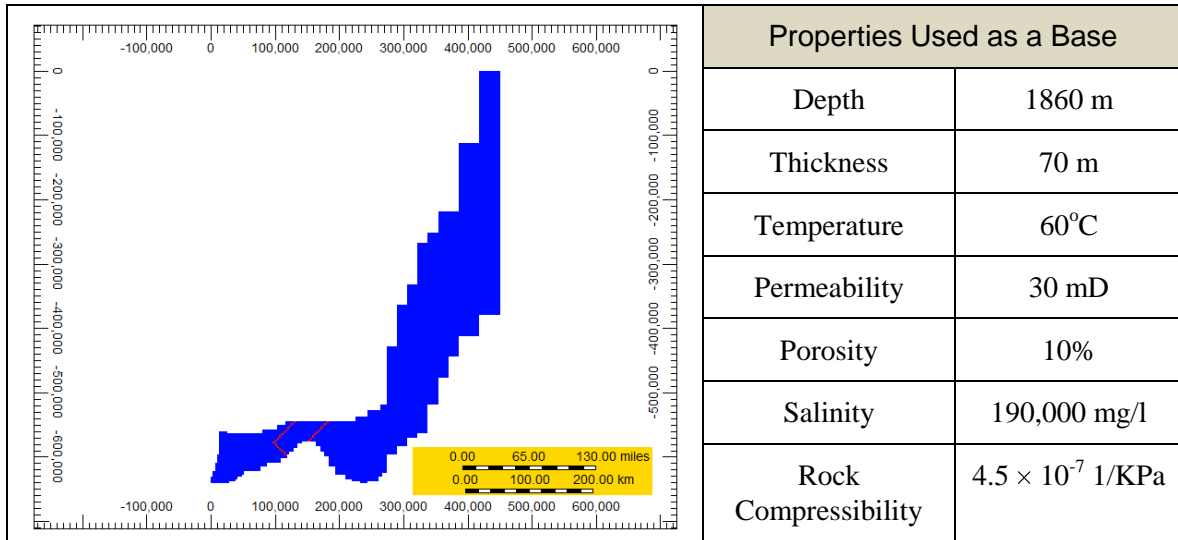


Figure 4: Top view of the Nisku formation in the Wabamun Lake area (left), study area is outlined in red and base formation/properties used are shown on the right.

Plume Size and Pressure Field Depending on Number of Injectors

Figure 5 presents the plume extension and pressure distribution after 50 years of injection using the base case properties. For the case with one well, the plume radius at the top layer is about 4.6 km, which is consistent with the conceptual model as well as the analytical solution radius [5]. It is noticeable that the size of the “*pressure plume*” is much larger at about 65 km, even for one well. In the cases of n number of injectors, one can see n individual plumes for CO₂ saturation. As the number of wells increase, the individual injector flow rate decreases (fracture pressure constraint) and consequently the plume radius decreases. However for pressure, one can see a very strong interference between injectors that pressurizes the total area of injection. The pressure build-ups and soon merges, and thereafter a cumulative pressure disturbance dissipates radially away from a central position, which is the well position for one well model and is near the centre of the focus area for the models.

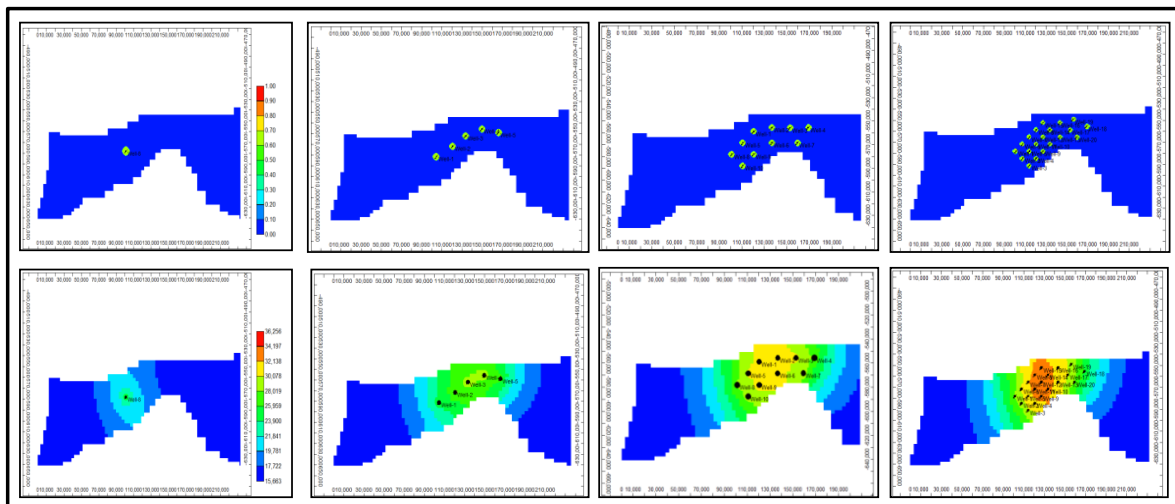


Figure 5: Plume extension (top row) and pressure radius of investigation (bottom row) after 50 years of injection for different wells in the Nisku study area (within the red area in Figure 4)

It is very important to mention that the dynamics of the pressure field is very different for one injection well, Figure 6 left, than for multiple injection wells, Figure 6 right.

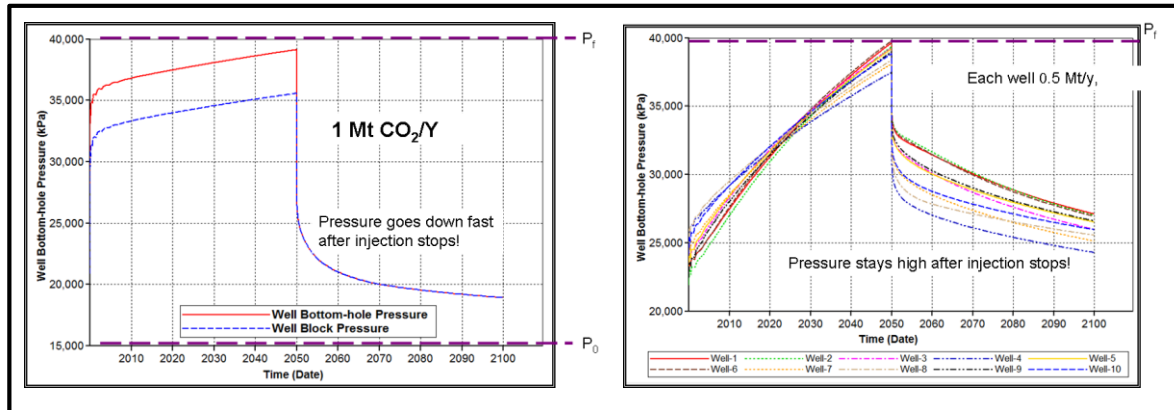


Figure 6: Pressure evolution: left, one well; right, 10 wells.

One can see that the pressure fall-off after ending CO₂ injection is much quicker for a single well. The pressure fall-off for multiple wells is delayed because of the larger pressure influence area.

Injection Capacity (versus number of wells and its sensitivity to different properties)

Starting with one well, the maximum achievable rate was determined to be as high as 1.1 Mt CO₂/year (matching the results of the conceptual model), which is equivalent to 0.055 Gt after 50 years. This flow rate causes the bottomhole pressure to reach 40 MPa at the end of the injection period. This value was assumed by the WASP team at the beginning of the project based on some literature data for Alberta reservoirs. Midway through the project, the Geomechanical Simulation Group estimated this value to be around 35 to 37 MPa. Since our original assumption was very close to the new calculated value (which is not based on real field data), we decided to keep 40 MPa in our reservoir model. The sensitivity of capacity to different fracture pressure (within the range 30 to 40 MPa) is presented later in this section. Also there is discussion (in the Geomechanical Simulation Group Report) of the impact of pressure difference on fracture pressure during injection.

When the next five wells are placed in the zone, the corresponding flow rate for each well is reduced to 0.625 Mt/year per well with cumulative injection of 0.15 Gt. Increasing the number of wells to 10 brings the flow rate to 0.418 Mt/year per well with total injected CO₂ of 0.209 Gt. Finally, the values for 20 wells are equal to 0.238 Mt/year and 0.238 Gt, respectively. These results are shown in Figure 7, red curve. We also determined what reservoir properties we would need to achieve the target of 1 Gt. The green curve on Figure 7 presents the injection capacity of the focus area with the following aquifer properties: porosity 20% and horizontal permeability 90.0 (mD). Although these values caused a significant difference in the outcome, the limitation in injectivity improvement for more than 10 wells still existed. It could not be claimed that these values are the maximum injectivity and storage of the formation because no optimization with respect to well positioning and flow rate was performed.

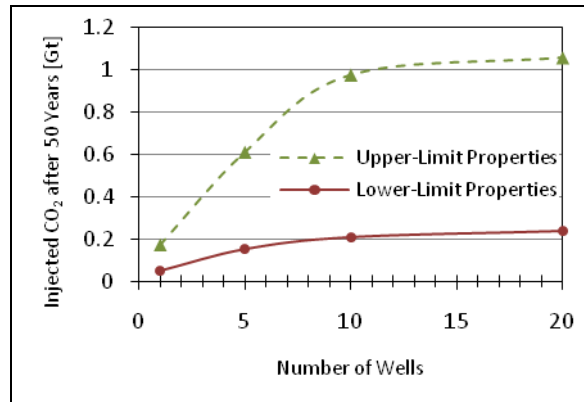


Figure 7: Variation of Nisku capacity with respect to number of wells and formation properties (red curve represents base properties).

Some Options to Increase Capacity (horizontal injection, fracturing)

In the storage process the term “capacity” could have two meanings. The apparent capacity is the available and accessible pore volume of the aquifer, and the injection capacity is the amount of CO₂ that can be realistically injected into the formation and is a function of the number of wells and the fracture pressure of the formation and the confining caprock [6]. As discussed earlier, for a restricted injection area such as in the Nisku study, increasing the number wells beyond a certain limit (which is controlled by formation properties and injection site area) has a minor effect on the injection capacity. The focus of this section is to investigate methods that lead to an increase in injection capacity in the aquifer.

The first method is to use horizontal wells instead of vertical wells. For vertical wells, it is preferable to use fully penetrated wells over the entire thickness of the aquifer. To find the minimum length for a horizontal well, the effective radius of pressure disturbance around the vertical injection well, which is again a function of formation properties, should be determined. For vertical wells, as the injection begins the pressure around the wellbore increases rapidly and causes the development of locally narrow width pressure peaks in the vicinity of the well, Figure 8.

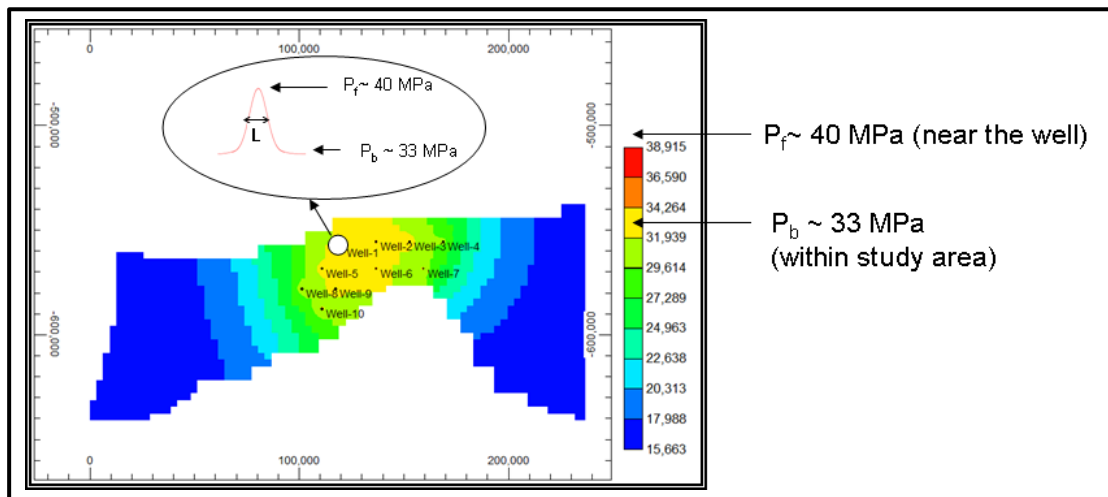


Figure 8: Pressure at the end of injection.

Using horizontal wells with total length greater than the scale of the vertical injection well's pressure peak “*L*” (for the Nisku formation this minimum required well was estimated to be equal to 3000 m) will diminish these peaks and increase injectivity, Figure 9 (H-Well Bar). The V-Well Bar corresponds to vertical injectors.

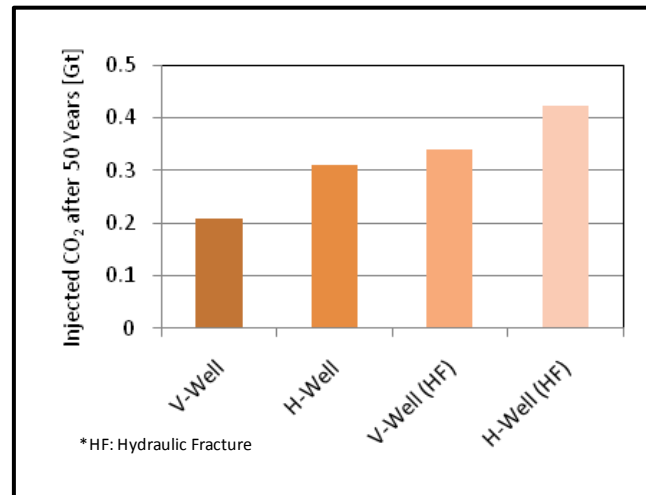


Figure 9: Comparison of the effect of different well orientations and stimulation on the storage capacity of the model.

The application of stimulation techniques, such as hydraulic fracturing, can improve injectivity as long as the caprock is not fractured. The technical feasibility of implementing these techniques requires careful geomechanical characterization of the formation. Vertical wells with hydraulic fractures were modelled by constructing thin grid blocks 400 m (fracture half length) from the well grid toward the east and west. A porosity of 0.15 and permeability of 1500 mD were assigned to these grid blocks to approximate a 400 m half-length fracture and associated damage zone. These properties were also used to construct four 100 m half lengths of four staggered hydraulic fractures for the horizontal wells. The V-Well (HF) and H-Well (HF) bars in Figure 9 shows the simulation results for 10-wells cases (located as in Figure 8) in the Nisku aquifer (V = vertical wells, H = horizontal). Another promising method of increasing CO₂ capacity would be to produce the brine [7] from the formation to prevent the reservoir pressure from building up excessively near the injection wells. This method involves transporting produced brine through surface pipelines to a location where the brine can be injected into another compatible formation or into a lower pressure region of the Nisku aquifer itself.

Heterogeneity Sensitivity Study

Two kinds of heterogeneity were considered in this study: stochastic and object-based models. The stochastic model was based on existing quantitative data (i.e., wireline log, acoustic impedance) and geostatistical tools. It relies on resistivity-derived porosities and permeabilities from nearly 60 wells. For this study, five equiprobable realizations of properties (porosity, %: max-28.6, min-1.3, mean-4.9) and (permeability, mD: min-3.1; max-393; mean-22.37) were generated, see Figure 10. All sets of realizations for this section (heterogeneity sensitivity study) were developed by the geostatistics group and the detailed description of these realizations and the methodology is presented in the Geomodelling Section of this report, which was written by Chris Eisinger and Jerry Jensen.

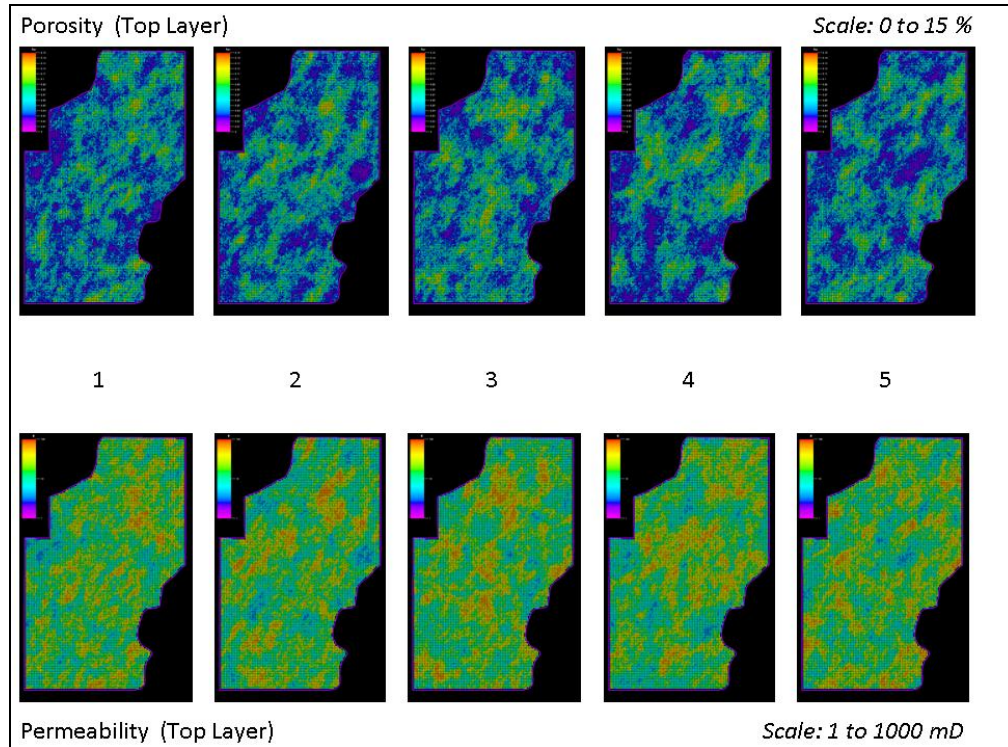


Figure 10: Five geo-statistical realizations for porosity and permeability.

Object-based models define “objects” (same sizes) as higher porosity and permeability zones, the geometry and distribution which are constrained by dimensions of existing modern carbonate analogs, conceptual understanding of Nisku carbonate in the Wabamun area, wireline log data and seismic data.

Two kinds of objects: i) dark blue (Minor width-500 m, Major/Minor ratio -5 and Thickness -5 m) and ii) light blue (Minor width-300 m, Major/Minor ratio -5 and Thickness -2 m) all oriented along the dip were distributed in each zone (upper, middle, and lower, see Figure 11 left) of the Nisku open marine. Figure 11 right (Upper third has 13 layers with average vertical grid size $z = 1.72$ m; Middle third has 5 layers with $z = 4.46$ m and Lower third has 12 layers with average $z = 1.86$ m).

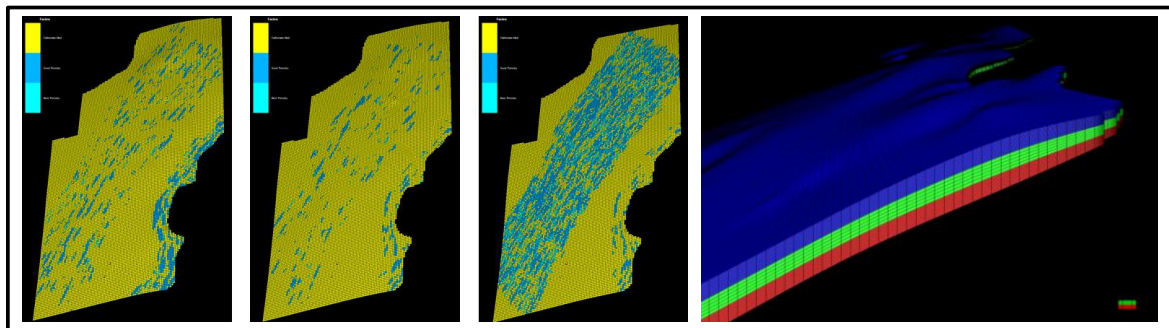


Figure 11: Object-based realization of porosity.

For the stochastic modelling examples (realizations 4 and 5), the saturation and pressure fields are shown in Figure 12.

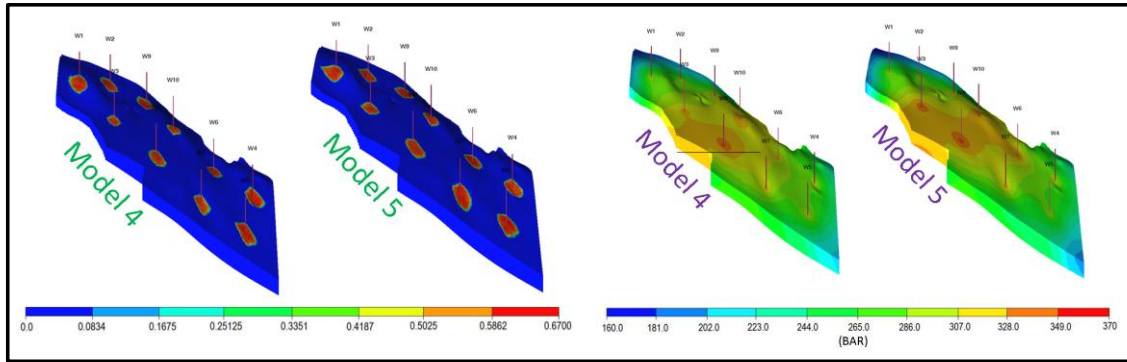


Figure 12: Saturation (left) and pressure (right) fields for stochastic modelling after 50 years of injection.

Although one can see some differences on a small scale for both fields, the injection capacities for all cases are almost identical (Figure 13), and very close to being homogeneous (Figure 7 for 10-well injection).

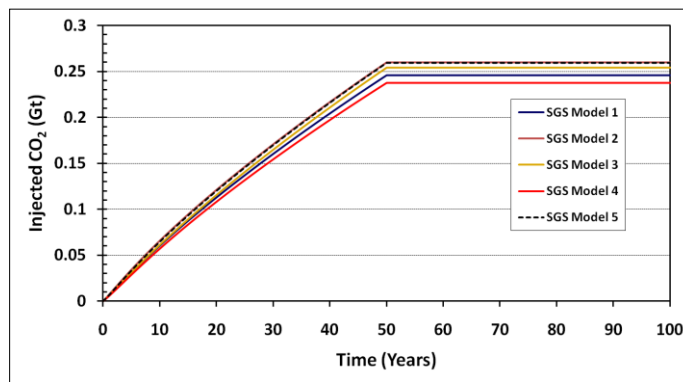


Figure 13: Injection capacity for five realizations.

The above results represent the storage capacity when the fracture pressure was set to 40 MPa. Sensitivity of capacity to fracture pressure is shown in Figure 14.

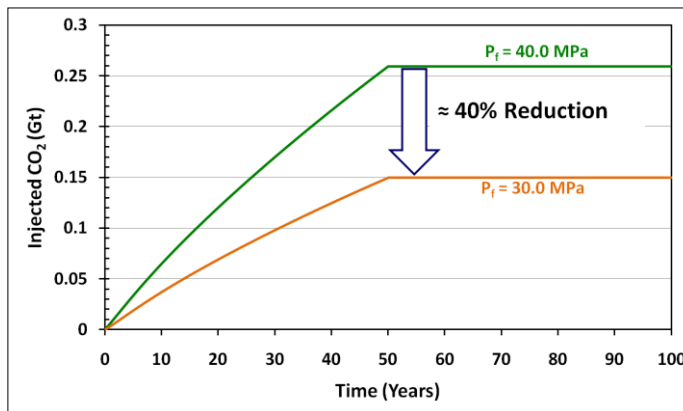


Figure 14: Injection capacity for different fracture pressures.

For object-based modelling, the saturation and pressure fields are shown in Figure 15.

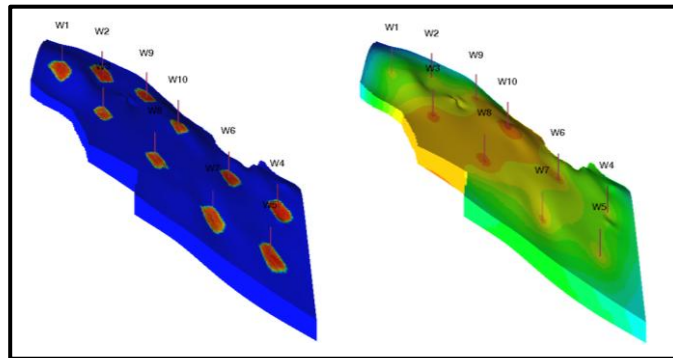


Figure 15: Saturation (left) and pressure (right) fields for object-based modelling after 50 years of injection.

Injection capacity, as in the case of stochastic modelling, is very close to the homogeneous model, see Figure 16.

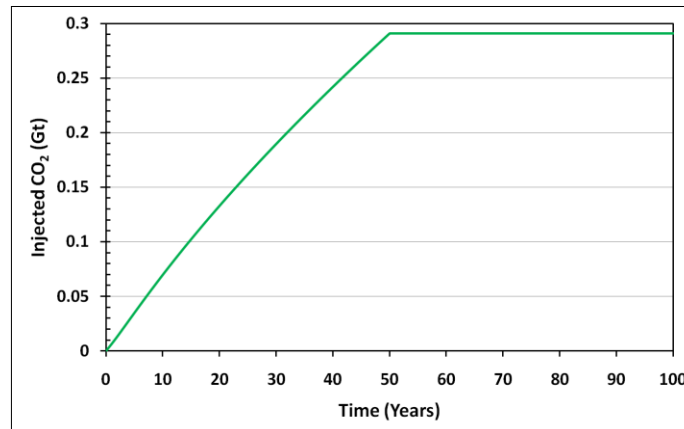


Figure 16: Injection capacity for object-based modelling.

Based on this limited number of realizations, it is possible to suggest that the small (compared to plume size) scale heterogeneity considered in this study does not play a strong role for pressure and saturation fields and for overall capacity of the injection site. For layered systems and for objects comparable to plume size it will be significant, especially by selective placement of injectors. Such a study would require more detailed knowledge of the distribution properties within the aquifer.

2. LONG-TERM FATE OF CO₂

In this section, we discuss the long-term fate associated with the following phenomenon:

- Increased aquifer pressure during and after injection.
- Migration of CO₂ beyond injection area due to dip.
- Buoyant phase of CO₂ over long periods of time.

2.1. Pressure Field Evolution During and After Injection Until Initial Reservoir Pressure Reached

As discussed in previous sections, the pressure in the aquifer (within and around the injection area) will increase during the injection period and then gradually decrease to the initial pressure distribution, due to the very large volume in the Nisku aquifer. It is important to know how long it will take for a substantial pressure disturbance to dissipate. The simulation results of a 10-well scenario are presented in Figure 17.

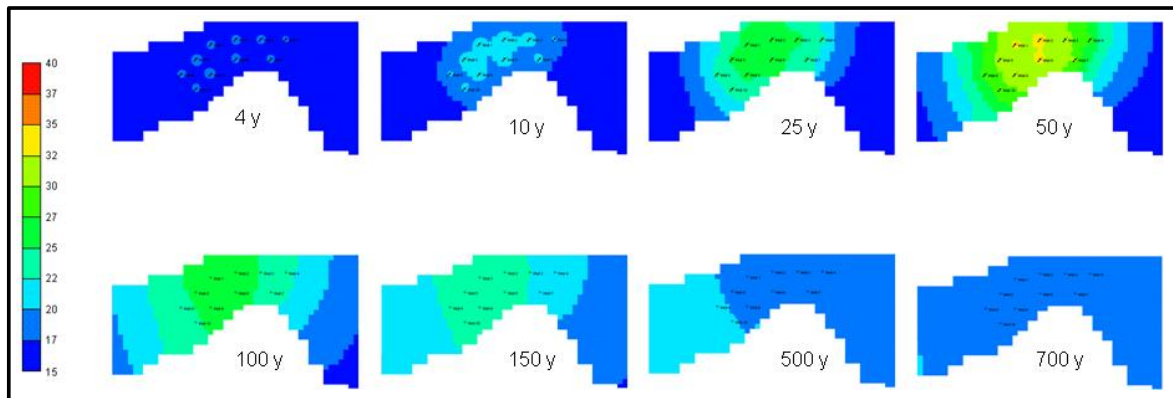


Figure 17: Pressure evolution (each well injects 0.5 Mt/year for 50 years).

One can see that the pressure does not reach initial reservoir pressure ($P_i = 16$ MPa) even 650 years after injection stops, although the difference in ΔP is small compared to the maximum difference ($\Delta P_{\max} = 24$ MPa = $P_f - P_i$ at the end of injection). The graph of ΔP versus time is presented in Figure 18, which allows for estimating the timescale of pressure decay.

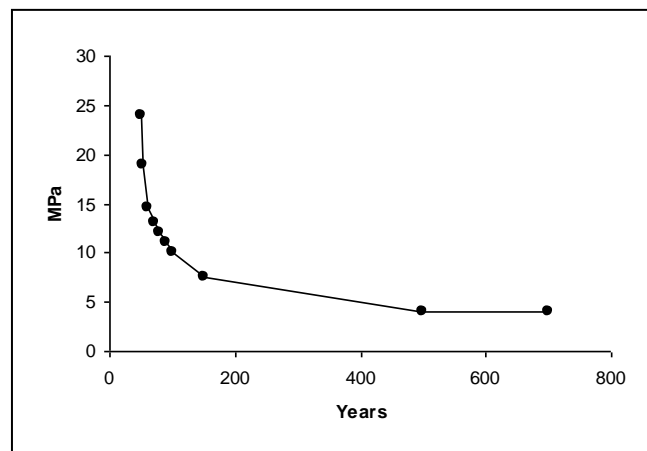


Figure 18: ΔP versus time.

From this graph (assuming exponential behavior), ΔP falls e (~ 2.7) times at ~ 120 years, thereby providing the timescale of high pressure fate for injection design.

2.2. Effect of Aquifer Dip on Plume Movement and Size

The effect of aquifer dip was evaluated by simulations using the base Nisku properties (Figure 4) for single-well injection at a rate of 1 Mt/year for 50 years. Simulations run up to 1000 years after injection started and two cases were considered for comparison: i) dip = 0 and ii) dip = 0.5°. The results of CO₂ saturation at the top layer versus time are shown in Figure 19. One can see that at base conditions the effect of dip on the plume movement is marginal (Figure 19-a), although when permeability was increased (while all other parameters remained the same) noticeable plume migration along the dip was observed (Figure 19-b).

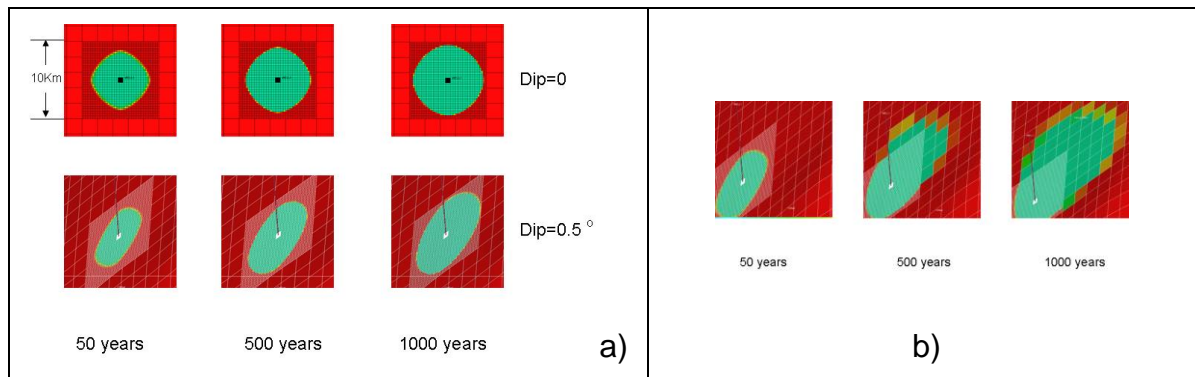


Figure 19: Saturation field for a single injector: a) base properties; b) permeability is increased to 150 mD.

What this means is if the plume reaches regions with higher permeability, it will migrate upwards and this should be taken into consideration.

2.3. Estimation of Timescale for Free-Phase CO₂ after Injection (onset and dissolution time for natural convection scenario)

The CO₂ injected into a deep aquifer is typically 10 to 40% less dense than the resident brine. Driven by density contrasts, CO₂ will first flow vertically and then horizontally spread under the caprock. If there are breaches in the caprock, leakage could occur through these high permeability zones or through artificial penetrations, such as abandoned wells. It is very important to know how long free-phase CO₂ remains in the reservoir and how long complete dissolution of CO₂ into the brine takes because this determines the time that free-phase CO₂ has to leak from the formation. After injection, free-phase CO₂ (gas or supercritical fluid) will be partially trapped as residual saturation and the remainder will slowly dissolve in the brine [8]. Depending on reservoir properties, different mechanisms may be responsible for dissolution. In this section we estimated the dissolution mechanisms for the Nisku conditions and associated timescale of dissolution. The analysis is based on Hassanzadeh et al, 2007 [9]. In the short term (Figure 20 a), during and after injection, some amount of CO₂ is residually trapped and the remainder may be dissolved by natural convection (Figure 20 b). First, we found convective mechanisms in the Nisku aquifer or at Nisku conditions, then we estimated the onset of natural convection and the corresponding timescale.

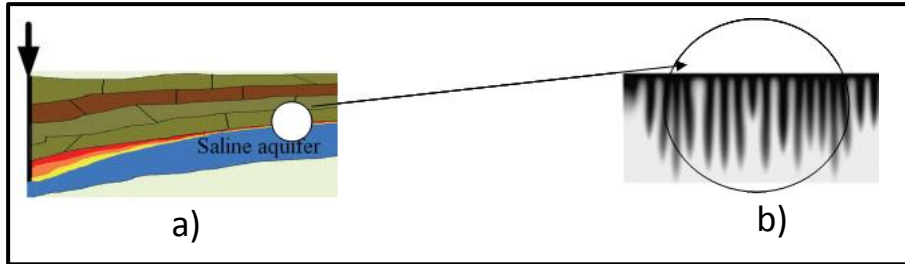


Figure 20: Short-term (a) and long-term (b) processes involved in geological storage.

The important parameter to describe the stability of such a system is the porous medium Rayleigh number. It is defined by

$$Ra = \frac{k g \Delta \rho H}{\mu \phi D}$$

where

k is permeability,

ϕ is porosity,

g is acceleration due to gravity,

H is aquifer thickness,

μ is viscosity,

$\Delta \rho$ is the density difference (CO_2 saturated and fresh brine), and

D is the molecular diffusion coefficient.

If $Ra > 49$ — natural convection occurs, Hassanzadeh et al, 2007 [9]. For the Nisku conditions, Ra is ~ 400 from which we estimated the onset of convection at these conditions ($t_{\text{onset}} \sim 80$ years) and timescale of convective dissolution ($T_{\text{dis}} \sim 3000$ years). Estimations are made based on Hassanzadeh et al, 2007 [9].

3. INVESTIGATION OF THE PHASE BEHAVIOR OF H_2S SATURATED BRINE IN CO_2 SEQUESTRATION PROCESS

It was found (see the Geochemistry section of this report) that the Nisku brine includes dissolved H_2S . The following section investigates the behavior of H_2S during the CO_2 sequestration process.

3.1. Fluid Representation of CO_2 -Brine and CO_2 - H_2S -Brine Systems

The solubility of gaseous components in the aqueous phase in CMG-GEM [10] is modelled by employing Henry's law. The fugacity of components is calculated using the Peng-Robinson Equation-of-State. GEM version 2008.12 uses accurate models for the Henry's constants of CO_2 and H_2S taking into account pressure, temperature and salinity (salting-out coefficient) by Harvey semi-empirical correlation [11]. At initial condition of the Nisku formation (pressure = 16 MPa, temperature = 60°C, and salinity = 190,000 mg/litre), the CMG calculates the concentration of dissolved H_2S in a saturated brine equal to 0.023 by mole fraction in the aqueous phase, which

aligns with the value reported in the literature, Duan et al, 2007 [12]. For calculating the viscosity and density of the aqueous phase, Kestin's [13] and Rowe's [14] correlation were used respectively.

3.2. Description of the Simulation Model

Since the focus of this study was to investigate the fate of existing H₂S in the Nisku formation during CO₂ injection, the simulation was limited to a single well located at the centre of a bounded radial model with a production well at the boundary to mimic a constant pressure boundary condition. Therefore, simulations were performed in a one-dimensional radial ($r \times z = 1$) model with the total extend: radius of 500 m and a net aquifer thickness of 5 m. The absolute permeability and porosity of the model were equal to 2000 md and 0.3, respectively to allow proper propagation of CO₂ plume after a few days. With respect to initial concentration of dissolved H₂S, two cases were considered. In the first case the initial mole fraction of dissolved H₂S was taken as 0.02; and in the second case as 0.005 (the balance being water).

Limited information about the relative permeability curves encouraged us to use the Corey correlation [15] with exponents of 2.0 and 1.5 for the gas and water relative permeability curves. Figure 21 shows the relative permeability data for gas and brine. The residual brine saturation was set equal to 0.1 and two different end points show relative permeability values for the gas phase as 0.4 and 1.0. These were considered for the base case and one for sensitivity analysis respectively. Pure CO₂ at supercritical conditions was injected for 200 days at a rate equal to 5000 SM³/day.

The effect of discretization on solution accuracy was investigated by conducting simulations with 500 × 1, 1000 × 1, 2000 × 1 grid block systems. The simulation model with a 500 × 1 resolution was not sufficiently accurate. But the comparison of results indicated that the 1000 × 1 produced results within 5% of the 2000 × 1 resolution, indicating that discretization errors become negligible at or above the 1000 × 1 resolution.

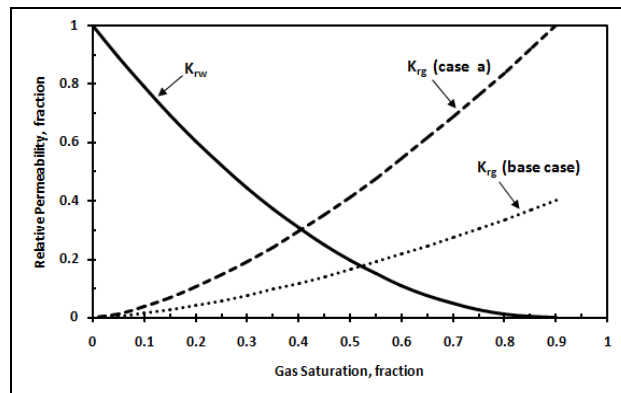


Figure 21: Water-gas relative permeability curves.

3.3. General Simulation Results

The preliminary simulation results presented below indicate that injection of pure CO₂ into a saline aquifer that contains measurable concentrations of dissolved H₂S causes the vaporization and release of dissolved H₂S into the expanding CO₂ plume. Moreover, the expanding CO₂ plume progressively delivers all of the vaporized H₂S towards the leading edge of the plume. Figure 22 shows the gas saturation variation within the aquifer after 200 days.

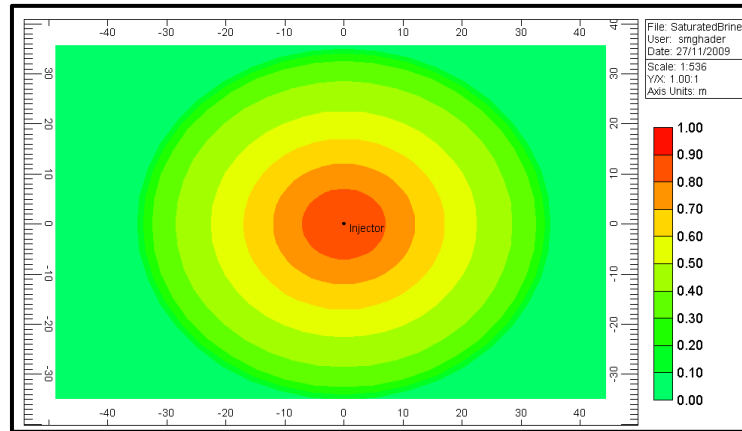


Figure 22: Variation of gas saturation around the injection well after 200 days.

As shown in Figure 23, the mole fraction of CO_2 within this plume changes from 1.0 at the point of injection and gradually decreases toward zero close to the outer boundary of the plume.

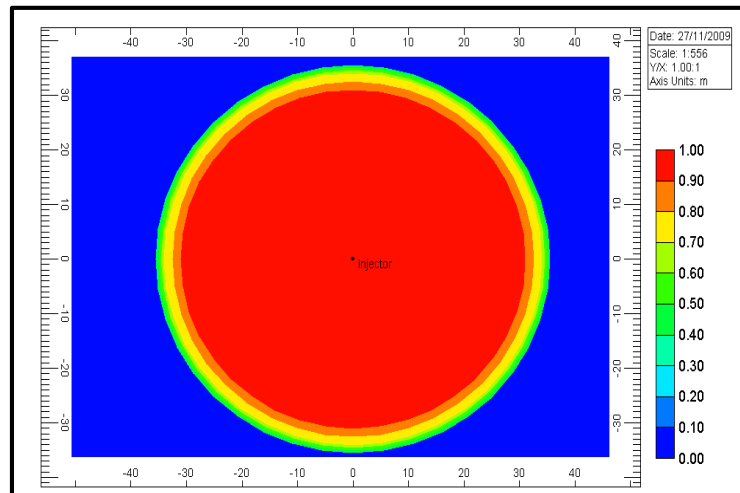


Figure 23: Variation of CO_2 mole fraction ($y_{\text{CO}_2}^v$) in the gas phase after 200 days of CO_2 injection. Note that the mole fraction of H_2S ($y_{\text{H}_2\text{S}}^v$) at any location is equal to $1.0 - y_{\text{CO}_2}^v$.

Figure 24 illustrates the variation in the composition of the plume after 200 days as a side view.

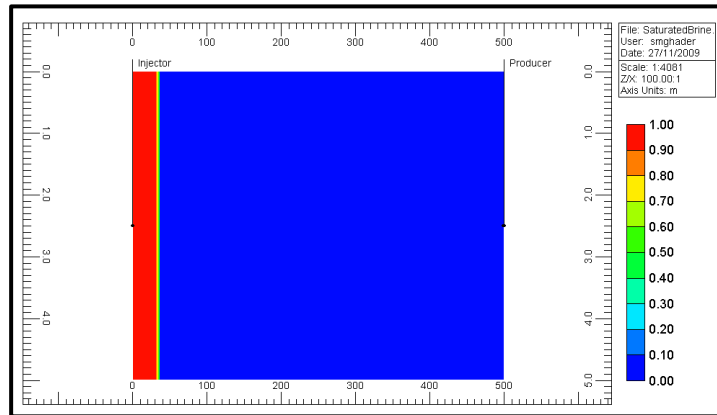


Figure 24: Side view of the variation of CO₂ mole fraction in the gas phase after 200 days. This figure also shows the position of the production well.

Since the plume expansion is symmetrical in the radial models, it is reasonable to use 2D graphs to better illustrate the development of gas saturation and H₂S evolution as the vaporizing gas drive progresses.

3.4. Base Case Simulation Results and Observations

As suggested by the above grid sensitivity results, a discretization of 1000×1 ($r \times z$) was chosen as the base case and explored to investigate the consequences of injecting CO₂ into a brine saturated with (dissolved) H₂S at initial conditions. For the base case scenario, pure CO₂ is injected at a rate of 5000 RSM³/day for 200 days into a vertical well located at the centre of the domain. As previously described, when the injected CO₂ comes into contact with the brine, H₂S progressively vaporizes out of the aqueous phase into the gas phase of the advancing CO₂ plume. The CO₂ plume pushes the mobile portion of the brine, as well as the vaporized H₂S, toward the outer boundary of the domain while the CO₂ continuously dissolves into the residual brine.

Therefore after the start of CO₂ injection, the region swept by the plume consists of two sub-regions. An inner radial sub-region extending from the injection well is characterized by the absence of H₂S in the aqueous phase. In fact, the dissolved H₂S in this inner sub-region is nearly completely removed from the brine via this vaporizing gas process. The second sub-region extends from the outer edge of the inner sub-region to the leading edge of the plume. In this outer sub-region, the concentration of H₂S in the CO₂ plume gradually increases toward an upper boundary and sometimes reaches a significantly high concentration at the leading edge of the plume. From Figure 25, it is inferred that for the base case scenario and after 200 days, the plume radius will be approximately 35.5 m, of which 27 m belong to first sub-region and the remaining 8.5 m is considered to be the second sub-region.

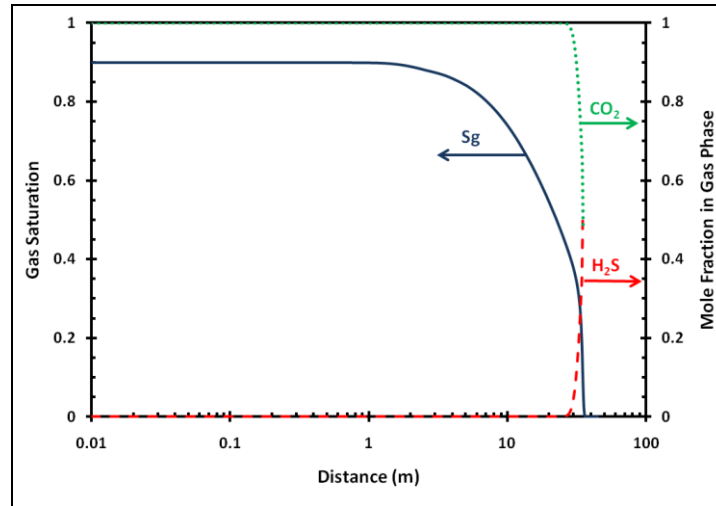


Figure 25: Distribution of different phases and components within the aquifer after 200 days. Midnight blue solid curve: variation of gas saturation versus distance around the injection well, residual brine saturation is equal to 0.1. Green dotted curve: variation of CO₂ mole fraction in the gas phase. Red dashed curve: variation of H₂S mole fraction in the gas phase.

Figure 26 clearly shows that the CO₂ has been dissolved into the immobile portion of the brine, while H₂S has been vaporized and released into the gas phase.

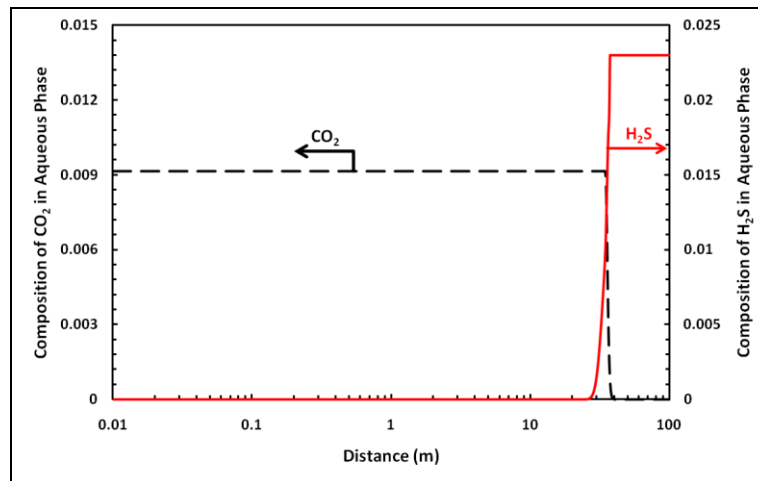


Figure 26: Composition of the aqueous phase in the region swept by the plume after 200 days. Note that the position at which the CO₂ mole fraction reaches zero coincides with the outer edge of the plume, after which the water (brine) saturation is equal to one.

3.5. Sensitivity Analysis

Simulations were conducted to investigate the effect that flow conditions have on the distribution of different phases and components, and specifically the evolution of H₂S at the leading edge of the plume. For simplicity, the results after 200 days of injection are presented. Flow conditions are affected by gas solubility, gas mobility, and initial H₂S saturation in the brine with respect to the aqueous phase. The results are illustrated in Figure 27.

(a) *Effect of Gas Solubility*

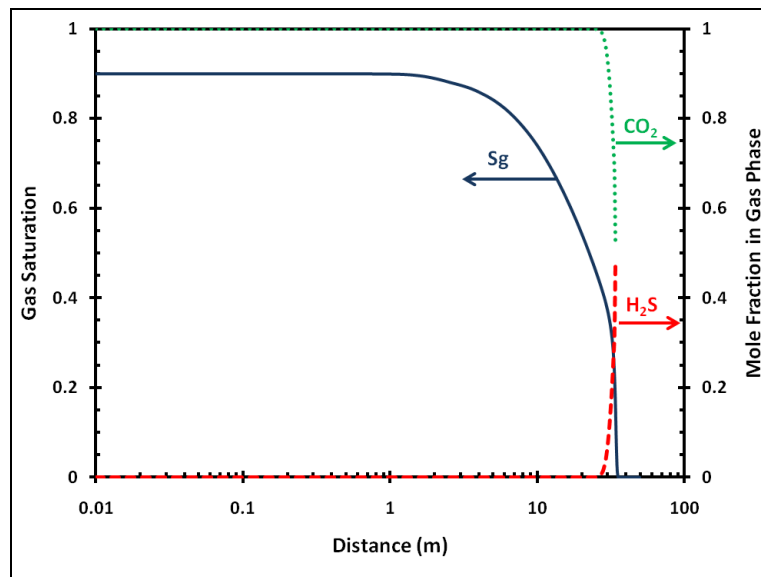
The effect of solubility was examined by considering pure water instead of brine. It was assumed that the initial concentration of H_2S was equal to the saturated brine base case. The higher solubility of the non-hydrocarbon components into the pure water relative to the brine case causes the ultimate radius of the CO_2 plume to shrink, from 35.5 to 34.5 m in the base case. This indicates less H_2S was released from the (sour) pure water case (see Figure 27-a).

(b) *Effect of Gas Mobility*

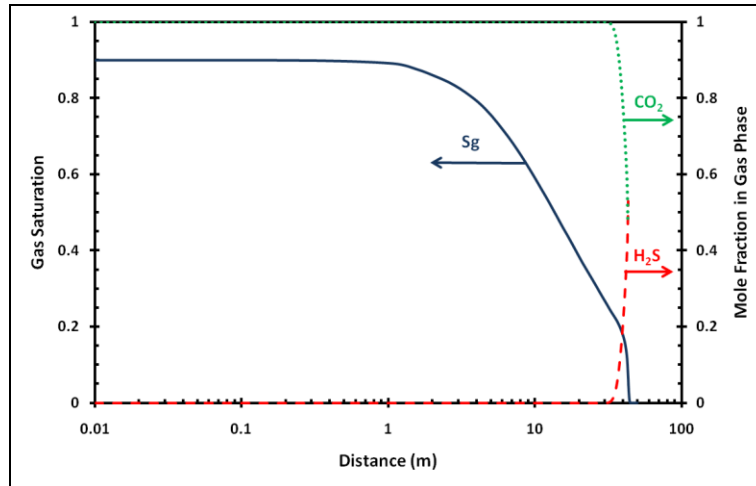
The effect of gas mobility was examined by changing the gas relative permeability and increasing the end point of gas permeability from 0.4 to 1.0 (Figure 1, K_{rg} [case a]). In the case of a more adverse mobility ratio (higher gas mobility), the gas spread over a larger contact area with the aqueous phase (larger radius of plume equalled 42 m), thereby more effectively stripping H_2S away from the brine when in contact with the advancing gas front (see Figure 27-b).

(c) *Effect of Initial Concentration of Dissolved H_2S in Brine*

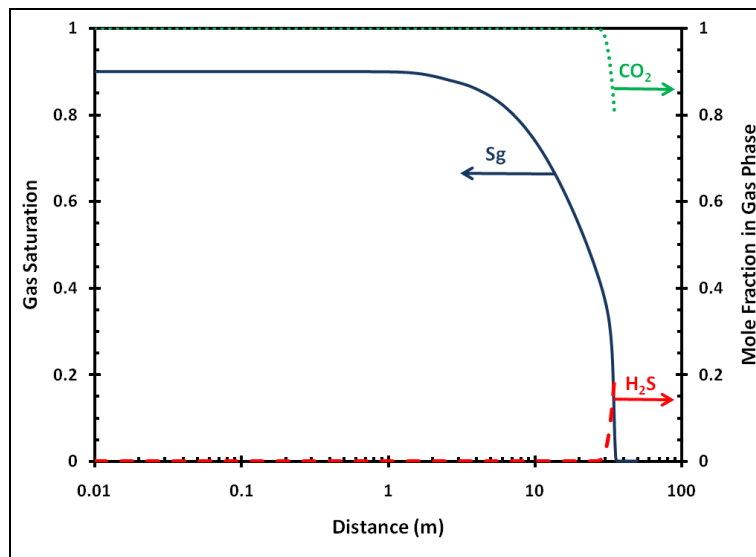
Simulations were run for another case where the initial concentration of the dissolved H_2S in the brine was decreased by 25%. Hence, in this case the initial mole fraction of H_2S in the brine was equal to 0.005. The simulation results in Figures 27-c revealed that although the cumulative mass of released H_2S (determined by calculating the area under the graph of H_2S concentration versus distance) is reduced by decreasing the initial concentration of the dissolved H_2S in brine, the mole fraction of released H_2S in the gas phase is still high. These results also illustrate the fact that the initial concentration of H_2S has a second-order effect on the evolution of H_2S during CO_2 sequestration.



(a)



(b)



(c)

Figure 27: Effect of different parameters on the distribution of different phases and components beneath the caprock after 200 days: (a) increased gas solubility, (b) increased gas mobility, (c) decreased initial mole fraction of dissolved H_2S in the brine by 25%.

SUMMARY

In this study, we performed numerical modelling of injecting large volumes of CO₂ (1 Gt target over 50 years) into the Nisku Formation. Injection was performed within localized injection areas of 30 km × 60 km. The main objectives of the study were to:

- estimate the injection capacity and CO₂ plume movement and pressure distribution during and after injection;
- estimate the timescales of the long-term fate of injection associated with free-phase CO₂, aquifer pressurization, and the effect of dip on plume shape and migration; and
- assess possible H₂S concentration (mole fraction) in the CO₂ plume over time and space.

It was shown that the capacity of injection is limited not by available pore space, but by the ability to inject without exceeding the fracture pressure of the formation. Although capacity increases with the number of injectors, increasing the number of wells has a limit. Very strong interference between pressure plumes was observed with no substantial benefit beyond 20 wells. Horizontal injection wells and aquifer fracturing may be considered as options to increase capacity. Sensitivity of capacity to reservoir permeability, rock compressibility and well placement was investigated.

The saturation and pressure field simulations show that for multiple injection scenarios (n wells), CO₂ saturation plumes have no interference; we see n individual plumes with a radius of 4 to 5 km for each injector. The pressure field behaves completely different than the saturation field. There are no individual pressure plumes, but a single large (scale of hundred km) pressure disturbance.

It was shown that the dip in the Nisku formation does not affect the results (i.e., no substantial plume movement), although free-phase CO₂ may migrate along the dip if it reaches a zone with higher permeability (above 100 mD). We estimated that at the Nisku conditions, the timescale for pressure decay is 120 years and the timescale for free-phase CO₂ dissolution is ~ 3000 years where the mechanism of dissolution is natural convection.

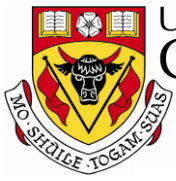
An assessment of the possible H₂S concentrations in the CO₂ plume over time and space was performed. It showed that H₂S dissolved in aquifer brine will be released into the CO₂ plume during injection and will reach a high mole fraction at the outer edge of the CO₂ plume.

ACKNOWLEDGMENTS

Financial support for this work was provided by NSERC Strategic Grant and AERI, with additional funding from industry partners through the Wabamun Area CO₂ Sequestration Project (WASP) led by the University of Calgary. Simulation software (GEM) was donated by the Computer Modelling Group. This support is gratefully acknowledged. We also wish to thank Long Neighem and Vijay Shrivastava for their help with the new version of GEM and for the useful discussions of its applications to this study.

REFERENCES

- [1] B. Hitchon, Aquifer Disposal of Carbon Dioxide, Hydrodynamic and Mineral Trapping – Proof of Concept, 1996, Geoscience Publishing Ltd., Sherwood Park, Alberta, Canada.
- [2] H. Hassanzadeh, M. Pooladi-Darvish, A. M. Elsharkawy, D. W. Keith, Y. Leonenko, Predicting PVT data for CO₂-brine mixtures for black-oil simulation of CO₂ geological storage. *Int. J. Greenhouse Gas Control*, 2008, 2, p. 65–77.
- [3] B. Bennion, S. Bachu, Relative permeability characteristics for supercritical CO₂ displacing water in a variety of potential sequestration zones in the western Canada sedimentary basin, Paper SPE 95547 at SPE Annual Technical Conference and Exhibition, Dallas, TX, p. 9–12 October, 2005.
- [4] K. Pruess, J. Garcia, T. Kavscek, C. Oldenburg, J. Rutqvist, C. Steefel, T. F. Xu, Code intercomparison builds confidence in numerical simulation models for geologic disposal of CO₂, *Energy*, 2004, 29, p. 1431–1444.
- [5] J. M. Nordbotten, M. A. Celia, and S. Bachu, Injection and storage of CO₂ in deep saline aquifers: Analytical solution for CO₂ plume evolution during injection. *Transport in Porous Media* 2005, 58(3), p. 339–360.
- [6] A. Lucier and M. Zoback, Assessing the economic feasibility of regional deep saline aquifer CO₂ injection and storage: A geomechanics-based workflow applied to the Rose Run sandstone in Eastern Ohio, USA. *Int. J. Greenhouse Gas Control*, 2008, 2, p. 230–247.
- [7] Y. Leonenko and D. W. Keith, Reservoir engineering to accelerate the dissolution of CO₂ stored in aquifers, *Environmental Science and Technology*, 2008, 42(8), p. 2742–2747.
- [8] Hassanzadeh, H.; Pooladi-Darvish, M.; Keith, D. W. Stability of a fluid in a horizontal saturated porous layer: effect of non-linear concentration profile, initial, and boundary conditions. *Transport in Porous Media*, 2006, 65, p. 193–211.
- [9] Hassan Hassanzadeh, Mehran Pooladi-Darvish, and David W. Keith, Scaling Behavior of Convective Mixing, with Application to Geological Storage of CO₂, *AIChE*, 2007, Vol. 53, No. 5, p. 1121–1131.
- [10] Nghiem, L.; Sammon, P.; Grabenstetter, J.; Ohkuma, H. Modelling CO₂ Storage in Aquifers with a Fully-Coupled Geochemical EOS Compositional Simulator, SPE Paper No. 89474, 2004.
- [11] Harvey, A.H. 1996. Semiempirical correlation for Henry's constants over large temperature ranges, *AIChE J*, Vol. 42, No. 5, p. 1491–1494.
- [12] Duan, Z., Sun, R. Liu, R. and Zhu, C., 2007. Accurate thermodynamic model for the calculation of H₂S solubility in pure water and brine. *Energy and Fuels*, 21, p. 2056–2065.
- [13] Kestin, J., Khalifa, H.E., Correia, R.J., 1981. Tables of the dynamic and kinematic viscosity of aqueous NaCl solutions in the temperature range 20–150°C and pressure range 0.1–35 MPa. *J. Phys. Chem. Ref. Data*, Vol. 10, p. 71–87.
- [14] Rowe, A.M., Chou, J.C.S., 1970. Pressure-volume-temperature-concentration relation of aqueous NaCl solutions. *J. Chem. Eng. Data*, Vol. 15, 1970, p. 61–66.
- [15] Corey, A.T., 1954. The interrelation between gas and oil relative permeabilities. *Producers Monthly*, November, p. 38–41.



UNIVERSITY OF
CALGARY

Energy &
Environmental
Systems

EES

iseee



Energy and Environmental Systems Group

Institute for Sustainable Energy, Environment and Economy (ISEEE)

Well Design and Well Integrity

WABAMUN AREA CO₂ SEQUESTRATION PROJECT (WASP)

Author

Runar Nygaard

Rev.	Date	Description	Prepared by
1	January 4, 2010	Well Design and Well Integrity	Runar Nygaard

Table of Contents

INTRODUCTION.....	5
BACKGROUND	5
DISCUSSION	5
1. WELL DESIGN AND POTENTIAL LEAKAGE PATHS	5
2. EFFECT OF CO ₂ INJECTION ON WELL CONSTRUCTION MATERIALS	7
2.1 Cement.....	7
2.2 Oil Well Cements	8
2.3 CO ₂ Effect on Portland Cements	11
2.4 CO ₂ Corrosion on Tubulars and Steel Components	17
2.5 Mechanical Effects on Wellbore.....	18
3. WELL INJECTION DESIGN.....	19
3.1 Geological Description of Well Location	19
3.2 Casing Design.....	21
3.3 Cementing Design.....	22
3.4 Completion Design.....	23
4. INJECTION WELL COST ESTIMATE	24
5. ABANDONMENT OF WELLS	27
6. EVALUATION OF EXISTING WELLS IN NISKU.....	29
7. CONCLUSIONS.....	35
8. REFERENCES.....	36
Appendix A.....	38

List of Tables

Table 1: Regular Portland cement briefly described the different classes as specified in API Specification 10A and ASTM Specification C150.	9
Table 2: Brief description of special cements (Meyer, 2008; Schlumberger, 2009; Halliburton, 2009).	10
Table 3: Materials of construction (MOC) for CO ₂ injection wells based on US experience (Meyer, 2008).	18
Table 4: Well cost model WASP project injection well.	24
Table 5: Well cost results WASP project injection well.	25
Table 6: Tubular and cementing costs for a vertical well.	26
Table 7: Drilled and abandoned wells in focus area.	33
Table 8: Drilled, cased and abandoned wells.	34

List of Figures

Figure 1: Example of possible leakage paths for CO ₂ in a cased wellbore (Celia et al, 2004).	6
Figure 2: Well design and abandonment of wells in the Wabamun Lake area (ERCB, 2007; Watson and Bachu, 2007).	7
Figure 3: Illustration of the chemical reactions zones in cement casing. First Zone Ca(OH) ₂ dissolves and CaCO ₃ forms. Second Zone CaCO ₃ dissolves when Ca(OH) ₂ is spent (Kutchko et al, 2007).	12
Figure 4: Rate of carbonation for Portland cement from laboratory tests, Barlet-Gouédard et al (2006).	13
Figure 5: Carbonation depth (mm) versus time (days) at 50 °C (Kutchko et al, 2008).	14
Figure 6: Test of Class H Portland cement in CO ₂ saturated fluid (Kutchko et al, 2008).	15
Figure 7: Validation of CO ₂ durability of different cement systems (Barlet-Gouedard et al, 2008).	16
Figure 8: Photograph of samples recovered from the 49-6 well in Texas. It shows the casing (left), gray cement with a dark ring adjacent to the casing, 5 cm core of gray cement, gray cement with an orange alteration zone in contact with a zone of fragmented shale, and the shale country rock (Carey et al, 2007).	16
Figure 9: Well design for vertical injection well.	20
Figure 10: Vertical and least horizontal stress and pore pressure gradients (Michael et al, 2008).	21
Figure 11: Carbonation depth estimated from laboratory tests after 100 year.	23
Figure 12: Drilling time for vertical well estimated based on three reference wells in the area.	25
Figure 13: Schematic of using metal alloy plug to seal and abandon production zone (Canitron, 2008).	28
Figure 14: Suggested abandonment method for CO ₂ injection wells.	29
Figure 15: Age distribution of wells drilled through Nisku in the study area. Gray wells are drilled and abandoned, white wells are drilled and cased wells.	30
Figure 16: Flow chart for identifying wells which are candidates for re-entering and conduct workover operations to improve leakage integrity.	31
Figure 17: Outline of the study area where horizontal lines are Ranges West of 5 and Vertical squares are Townships. The highlighted area is the focus area where all 27 wells were studied in detailed. Twelve additional wells were randomly selected (indicated in green).	32
Figure 18: Spatial distribution of all wells penetrating Nisku in the study area.	34

INTRODUCTION

BACKGROUND

To successfully inject CO₂ into the subsurface to mitigate green house gases in the atmosphere, the CO₂ must be trapped in the subsurface and not be allowed to leak to the surface or to potable water sources above the injection horizon. Potential leakage can occur through several different mechanisms, including natural occurrences or along wells. To avoid leakage from injection wells, the integrity of the wells must be maintained during the injection period and for as long as free CO₂ exists in the injection horizon. In addition to injection wells, monitoring wells will most likely be required to observe the plume movement and possible leakage. The Environmental Protection Agency (EPA) in the United States has stated that its goal is to be able to account for 99% of the CO₂ injected (NETL, 2009).

The experience from more than 100 CO₂ enhanced oil recovery (EOR) projects over the last 30 years has shown that CO₂ can be successfully transported and injected into a reservoir in the subsurface (Moritis, G. 2008). CO₂ EOR projects, along with wells drilled in H₂S-rich environments and high-temperature geothermal projects, have delivered developments for improved well designs and materials, such as improved tubing and types of cement.

However for CO₂ sequestration, the time aspect is very different than for typical EOR projects. The CO₂ should be safely stored and prevented from rising to the surface or to formations higher up in the geological succession in the foreseeable future. That has been translated loosely into the 1000 year well integrity problem.

In addition to the new injection and monitoring wells, saline aquifers are seen as attractive storage sites for CO₂, but are often located in areas where oil production and a large number of wells exist. In the province of Alberta alone, there already exists more than 350,000 wells and around 15,000 are drilled each year (ERCB, 2009). The integrity of existing wells that penetrate the capping formation also needs to be addressed to avoid CO₂ leakage.

The study's first objective was to identify a wellbore design that will effectively secure long-term well integrity for new CO₂ injection and monitoring wells. The second objective was to evaluate the leakage risk of existing wells within the Wabamun CO₂ storage project area.

DISCUSSION

1. WELL DESIGN AND POTENTIAL LEAKAGE PATHS

After CO₂ is injected into the subsurface, the CO₂ plume may move upwards or sideways because of pressure difference and buoyancy. Wells are an obvious pathway for CO₂ to escape the reservoir formation. There are several possible pathways (see Figure 1). CO₂ can leak along the interfaces between the different materials, such as the steel casing cement interface (Figure 1a), cement plug steel casing (Figure 1b), or rock cement interface (Figure 1f). Leakage can also occur through cement (Figure 1c) or fractures in the cement (Figure 1d and 1e). In addition to these smaller scale features, leakage can occur when wells are only cemented over a short interval or the cement sheet is not uniformly covering the entire circumference of the well. Casing corrosion can also lead to casing failure and large leakage pathways.

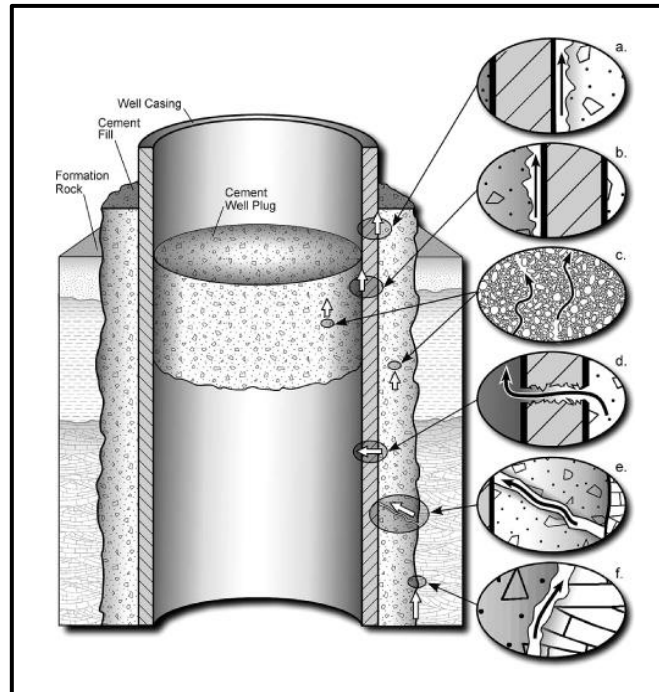


Figure 1: Example of possible leakage paths for CO₂ in a cased wellbore (Celia et al, 2004).

Different types of wells and the status of a well gives rise to different leakage scenarios. For instance, in the case of an exploration well the main section of the hole is drilled but not cased. After drilling, the well is abandoned with cement plugs set across the porous formations (Figure 2). The main leakage path is caused by problems that occurred while the cement plugs were set, or the plugs are missing. Cement plugs are quite thick and therefore a properly set plug provides a thick barrier for the CO₂ to penetrate. A cased well has cement in an annulus between the formation and the steel casing, which protects the outside of the casing. The cement sheet for cased wells is thin compared to abandonment plugs, since the thickness of the cement is limited to the annular space between the casing and the rock formation. Cased wells may also have casing exposed directly to the formation because the casing is not always cemented to the surface. When cased wells are abandoned (i.e., production or injection wells), a cement plug is set over the producing interval or a bridge plug is used with or without a cement plug over top. The cased well with a short cement interval inside the casing represents another possible leakage path (Figure 2).

Several recent studies have investigated the integrity of wells around the world. They have identified that out of 316,000 wells analyzed in Alberta—4.6% have leaks. Gas migration occurred in 0.6% of the wells and surface casing vent flow (SCVF) in 3.9% (Watson and Bachu, 2007). In a subset of 20,500 wells, 15% leaked with drilled and abandoned wells making up 0.5% and cased wells 14.5%. The reported leakage occurred mainly from formations shallower than those suitable for CO₂ injection and related to thermal operations. In the Norwegian sector of the North Sea, between 13 and 19% of the production wells experienced leakage, while 37 to 41% of the injectors experienced leakage (Randhol and Carlsen, 2008; NPA, 2008). Further, estimates from the Gulf of Mexico indicate that a significant portion of wells have sustained casing pressure, which is believed to be caused by gas flow through cement matrix (Crow, 2006). In a study of the K-12B gas field in the Dutch sector of the North Sea where CO₂ is injected, 5% of tubulars were degraded because of pitting corrosion (Mulders, 2006).

The main observation from these studies is that cased wells are more prone to leakage than drilled and abandoned wells, and injection wells are more prone to leakage than producing wells.

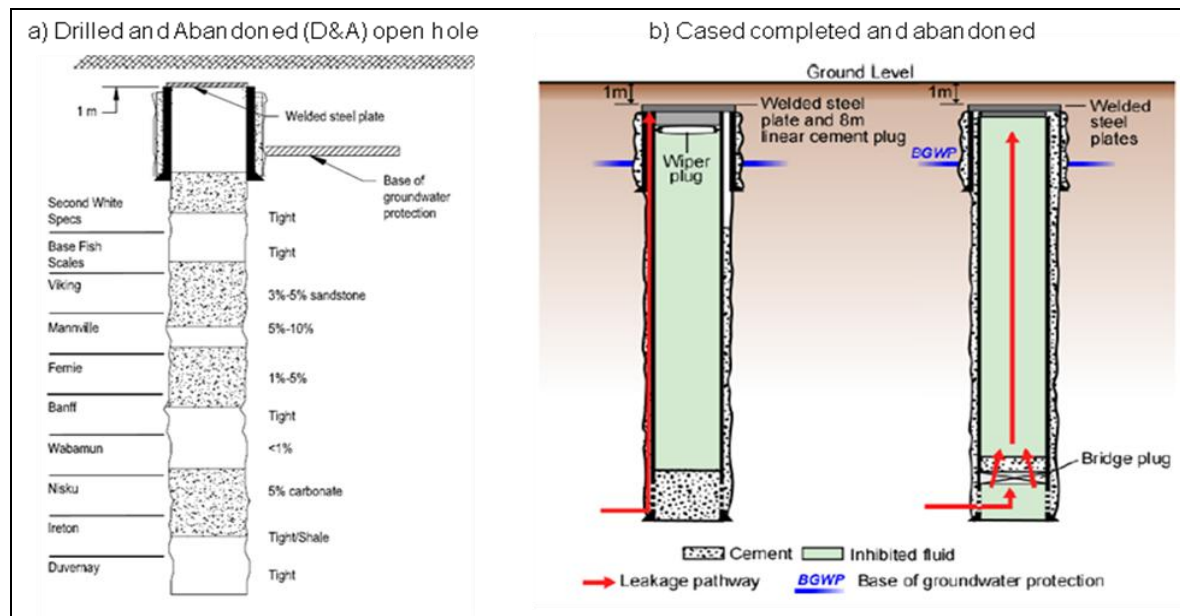


Figure 2: Well design and abandonment of wells in the Wabamun Lake area (ERCB, 2007; Watson and Bachu, 2007).

2. EFFECT OF CO₂ INJECTION ON WELL CONSTRUCTION MATERIALS

CO₂ can react with the different materials used to construct a well. When it reacts with cement, the cement's strength is reduced and its permeability increased. CO₂ can also corrode steel. This chapter summarizes the effect CO₂ has on the various materials used in well construction and how these problems can be mitigated.

2.1 Cement

Cementing can be divided into two broad categories, primary and remedial. Primary cementing is used during regular drilling operations to support the casing and stop fluid movement outside the casing (zonal isolation). Cement also protects the casing from corrosion and loads in deeper zones, prevents blow outs and seals off thief and lost circulation zones. The cement sheath is the first barrier around a wellbore that the CO₂ will encounter.

The well construction process only allows one chance to design and install a primary cementing system. A less than optimal cement sheath can significantly reduce an injection well's value by not preventing CO₂ from leaking into shallower formations. To solve the problem, the injection process must be interrupted to perform costly remedial cementing treatments. In a worst case scenario, failure of the cement sheath can result in the total loss of a well.

During the drilling phase of a well, the cement sheath must withstand the continuous impact of the drill string, particularly with directional wells. During well completion when the drilling fluid is replaced by a relatively lightweight completion fluid, the negative pressure differential can cause de-bonding at the casing cement and/or cement formation interfaces. The cement sheath must

withstand the stresses caused by the perforating operation and resist cracking from the extreme pressure created by the hydraulic fracturing operation.

The key to good cementing is good operational practices. The two most important factors to good cementing is to centralize the casing by frequently mounting centralizers on the casing and to reciprocate and/or rotate the casing during the cementing operation. It is important to run the casing at a speed that will not fracture the formation. After the casing is in place, common cement failures occur in one of two ways: poor primary cementing or cement failure after setting. Poor primary cementing occurs because a thick mud filter cake lines the hole and prevents good formation bonding. Proper displacement techniques, such as pre-flush, spacers and cement plugs, may not be sufficient because the conventional cement is not the best displacement fluid. Secondly, gas can invade the cement while it sets. During gelling and prior to complete hydration, conventional cement slurry actually loses its ability to transmit hydrostatic pressure to the formation and fluids from the formation migrate freely into the cement. This forms channels that can create future gas leaks. Cement failure after setting occur from mechanical shock from pipe tripping, expansion of the casing and compression of the cement during pressure testing, or expansion and contraction of the pipe due to cycles in injection pressure and temperature.

2.2 Oil Well Cements

Oil well cement consists of clinker material containing various calcium silicates and iron and aluminum compounds. Regular cement used in the petroleum industry is Portland cement, which contains at least two-thirds calcium silicates. The clinker is made from a blend of burned (calcined) limestone and clay. The clinker is ground to a powder and a small amount of gypsum ($\text{CaSO}_4 \cdot \text{H}_2\text{O}$) is often added to increase strength and slow setting time. The American Petroleum Institute (API) has classified different cement types (denoted from A to H) for different temperature and pressure (depth) ranges. Today, Types H and G are the most common. The different cement types are briefly described in Table 1. Some of these types have variations for increased sulfate resistance. In addition to the regular Portland cement, oil well cement slurry contains different additives that change the density, viscosity, filtration properties and setting time of the cement.

Additives are used with API Portland cements to modify the properties of the cement slurry. They fall into five main categories.

- 1) Density reduction materials: reduces cement density and prevents fracturing of the formation. Examples are Bentonite and other clay minerals, such as Pozzolans and nitrogen (used in foam cement).
- 2) Weight materials: increases the slurry's density. Examples are Barite, Hematite and sand.
- 3) Viscosifiers: reduces the viscosity of the cement slurry and prevent fracturing while the cement slurry is pumped. Examples are sodium chloride and calcium lignosulfonate (lignosulfonate works also as retarder).
- 4) Filtration control: prevents leakage of the cement slurry into porous and permeable formations by using caustic soda or calcium hydroxide.
- 5) Accelerators and retarders: modifies the time it takes to harden the cement (setting time). Accelerators reduce the setting time (i.e., the time before the cement develops strength and seals off fluids). Examples of accelerators are calcium chloride, sodium chloride and potassium chloride. Retarders increase the setting time and are mainly based on organic compounds, such as calcium lignosulfonate or cellulose.

Table 1: Regular Portland cement briefly described the different classes as specified in API Specification 10A and ASTM Specification C150.

API Class (ASTM type)	Description
Class A (Type I)	Portland cement for situation where no special properties are required. Class A cement is available only in ordinary (O) grade. Applicable for depth from surface down to 6000 ft. (1830 m) depth.
Class B (Type II)	Portland cement with sulfate-resistant properties to prevent deterioration of the cement from sulfate attack in the formation water. Processing additions may be used in the manufacture of the cement, provided the additives meet the requirements of ASTM C465. Available in both moderate sulfate-resistant (MSR) and high sulfate-resistant (HSR) grades. Applicable for depth from surface to 6000 ft. (1830 m) depth.
Class C (Type III)	Class C cement is used when high early strength and/or sulfate resistance is required. Processing additions may be used in the manufacture of the cement, provided the additives meet the requirements of ASTM C465. This product is intended for use when conditions require early high strength. Available in ordinary (O), moderate sulfate-resistant (MSR), and high sulfate-resistant (HSR) grades. The depth range is 6000 to 10,000 ft. (1830 to 3050 m).
Class G	No additions other than calcium sulfate or water, or both. Shall be blended with the clinker during manufacture of Class G cement. Class G is a basic well-cement and available in moderate sulfate-resistant (MSR) and high sulfate-resistant (HSR) grades. Depth range is 10,000 to 14,000 ft. (3050 to 4270 m). Class G is ground to a finer particle size than Class H.
Class H	No additions other than calcium sulfate or water, or both. Shall be blended with the clinker during manufacture of Class H cement. This product is for use as basic well cement and is available in moderate sulfate-resistant (MSR) and high sulfate-resistant (HSR) grades. Surface to 8,000 ft. (2440 m).

In addition to the API or ASTM classified cement, various special types of cement materials can be used for cementing wells (see Table 2). Many of these special cements are developed for specific applications. Some are a dry blend of API cements with a few additives, while others are cements containing other chemical characteristics. The composition of these cements is controlled and often kept confidential by the supplier.

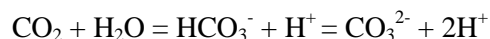
Table 2: Brief description of special cements (Meyer, 2008; Schlumberger, 2009; Halliburton, 2009).

Name	Description
Pozzolan-Portland Cement	Pozzolan materials are often dry blended with Portland cements to produce lightweight (low density) slurries for well cementing applications. Pozzolan materials includes any natural or industrial siliceous or silica-aluminous material, which in combination with lime and water, produces strength-developing insoluble compounds similar to those formed from hydration of Portland cement. The most common sources of natural pozzolan materials are volcanic materials and diatomaceous earths (from silica fossils). Artificial pozzolan materials are usually obtained as an industrial byproduct, or natural materials such as clays, shales and certain siliceous rocks. Adding pozzolan materials to API or ASTM cements reduces permeability and minimizes chemical attack from some types of corrosive formation waters.
Gypsum Cement	Gypsum cement is blended cement composed of API Class A, C, G or H cement and the hemi-hydrate form of gypsum ($\text{CaSO}_4 \cdot 0.5\text{H}_2\text{O}$). In practice, the term “gypsum cements” normally indicates blends containing 20% or more gypsum. Gypsum cements are commonly used in low temperature applications because gypsum cement set rapidly, has early high strength, and has positive expansion (approximately 2.0%). Cement with high gypsum content has increased ductility and acid solubility, and because of these characteristics, is not considered appropriate for CO_2 service.
Microfine Cement	Microfine cements are composed of very finely ground cements of either sulfate-resisting Portland cements, Portland cement blends with ground granulated blast furnace slag, or alkali-activated ground granulated blast furnace slag. Microfine cements have an average size of 4 to 6 microns, and a maximum particle size of 15 microns, which make them harden fast and penetrate small fractures. An important application is to repair casing leaks in squeeze operations, particularly tight leaks that are inaccessible by conventional cement slurries because of penetrability.
Expanding Cements	Expansive cements are available primarily for improving the bond of cement to pipe and formation. Expansion can also be used to compensate for shrinkage in neat Portland cement.
Calcium Aluminate Cement	High-alumina cement (HAC) or calcium aluminate cements (CAC) are used for very low and very high temperature ranges. Several high alumina cements have been developed with alumina contents of 35 to 90%. The setting time for calcium aluminate cement is controlled by the composition and no materials are added during grinding. These cements can be accelerated or retarded to fit individual well conditions, however, the retardation characteristics differ from those of Portland cements. The addition of Portland cement to this cement causes very rapid hardening; therefore, they must be stored separately. Calcium aluminate phosphate cement blended with a few additives produce cements that are highly resistant to the corrosive conditions found in wells exposed to naturally occurring wet CO_2 gas or CO_2 injection wells.

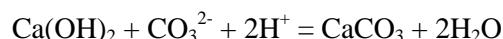
Name	Description
ThermaLock™	ThermaLock cement is specially formulated calcium phosphate cement that is both CO ₂ and acid resistant. This cement is well suited for high temperature geothermal wells. ThermaLock has been laboratory tested and proven at temperatures as low as 60°C and as high as 371°C.
Latex Cement	Latex cement is a blend of API Class A, G or H with polymer (latex) added. A well distributed latex film may protect the cement from chemical attack in some corrosive conditions, such as formation waters containing carbonic acid. Latex also makes the hardened cement elasticity and improves the bonding strength and filtration control of the cement slurry.
Resin or Plastic Cements	Resin and plastic cements are specialty materials used for selectively plugging open holes, squeezing perforations, and the primary cement for waste disposal wells, especially in highly aggressive acidic environments. A unique property of these cements is their capability to be squeezed under applied pressure into permeable zones to form a seal within the formation.
Sorel Cement	Sorel cement is magnesium oxychloride cement used as a temporary plugging material for well cementing. The cement is made by mixing powdered magnesium oxide with a concentrated solution of magnesium chloride. Sorel cements have been used to cement wells at very high temperatures (up to 750°C).
EverCRETE™ CO ₂	EverCRETE CO ₂ is marketed as CO ₂ -resistant cement that can be applied for carbon capture and storage, as well as CO ₂ enhanced oil recovery projects. EverCRETE cement has proven highly resistant to CO ₂ attack during laboratory tests, including wet supercritical CO ₂ and water saturated with CO ₂ environments under downhole conditions. It can be used both for standard primary cementing operations, as well as plugging and abandoning existing wells.

2.3 CO₂ Effect on Portland Cements

Since the cement sheath in a wellbore will be the first material exposed to the injected CO₂ in the subsurface, the stability of the cement in a CO₂ rich environment has drawn a lot of attention. When CO₂ is in contact with regular Portland cement, the latter is not chemically stable. CO₂ gas in water will reach equilibrium with the water through the following reaction:



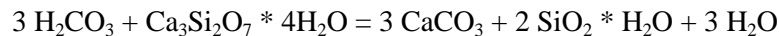
Regular Portland-based cements contain Ca(OH)₂, which reacts with CO₂ when water is present to form solid calcium carbonate through the following chemical reaction:



This process is named cement carbonation. Even if this process alters the composition of the cement, it leads to lower porosity in the cement because calcium carbonate has a higher molar volume (36.9 cm³) than Ca(OH)₂ (33.6 cm³) (Shen and Pye, 1989). For cement sheath integrity, this reaction actually improves the cement's properties and the carbonation is therefore a self healing

mechanism in the carbonate. Bachu and Bennion (2008) performed two sets of flow experiments for 90 days at 60°C on a Class G cemented annulus. First set of experiments used CO₂ saturated brines and the second set used ethane instead of CO₂. The CO₂ flushed sample had the lowest permeability, which was probably caused by the carbonation.

In a CO₂ sequestration project, the supply of CO₂ around the wellbore will continue the carbonation process as long as Ca(OH)₂ is present in the cement. The calcium carbonate is also soluble with the CO₂, even though it is more stable than Ca(OH)₂. Experiments by Kutchko et al (2007) showed that when all Ca(OH)₂ has reacted in the carbonation process, the pH will drop significantly (Zone 1 on Figure 3). When the pH drops, more of the CO₂ will react with water and form HCO₃⁻ (Zone 2 on Figure 3). The abundance of HCO₃⁻ will react with the calcium carbonate to form calcium (II) carbonate, which is soluble in water and can move out of the cement matrix through diffusion (Kutchko et al, 2007). The final reaction that occurs in Zone 3 (close to the cement surface) is calcium silicate hydrate reacting with H₂CO₃ to form calcium carbonate (CaCO₃) according to the following chemical reaction:



The volume of calcium silicate hydrate is larger than the calcium carbonate and this reaction will increase the porosity of the cement in Zone 3, which is the closest to the reservoir formation containing the CO₂.

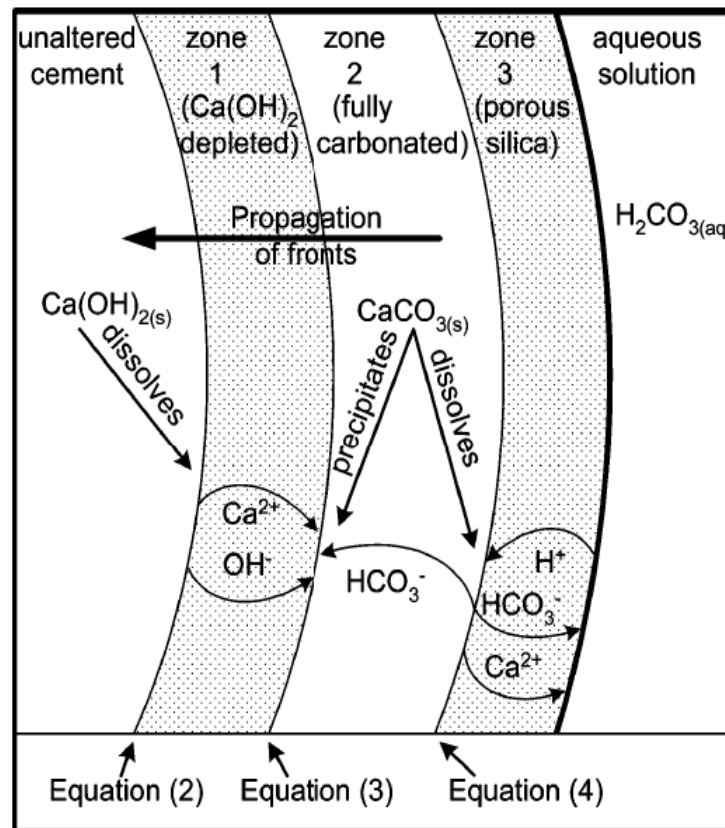


Figure 3: Illustration of the chemical reactions zones in cement casing. First Zone Ca(OH)₂ dissolves and CaCO₃ forms. Second Zone CaCO₃ dissolves when Ca(OH)₂ is spent (Kutchko et al, 2007).

The effect of CO₂ alterations on Portland cement containing calcium silicate hydrates and calcium hydroxide was studied in both laboratory experiments and field tests. Barlet-Gouedard et al (2006) tested a Portland cement API Class G in both CO₂ saturated water and supercritical CO₂ at 90°C. The rate that carbonation occurred is shown in Figure 4. For wet supercritical CO₂ conditions, the rate of the alteration front can be calculated based on:

$$\text{Depth of CO}_2 \text{ alteration front (mm)} = 0.26 \times (\text{time in hours})^{1/2}$$

For example, the carbonation process will have penetrated 10 mm into the sample after 60 days or 100 mm after 17 years. Kutchko et al (2008) performed similar experiments on a Class H Portland cement slurry at 50°C with a CO₂ saturated brine (Figure 5 and 6). The results for CO₂ supercritical brine at 50°C showed a slower alteration front within the cement. The curve fit estimating alteration depth based on Kutchko et al (2008) results for supercritical CO₂, which is shown as:

$$\text{Depth of CO}_2 \text{ alteration front (mm)} = 0.016 \times (\text{time in days})^{1/2}$$

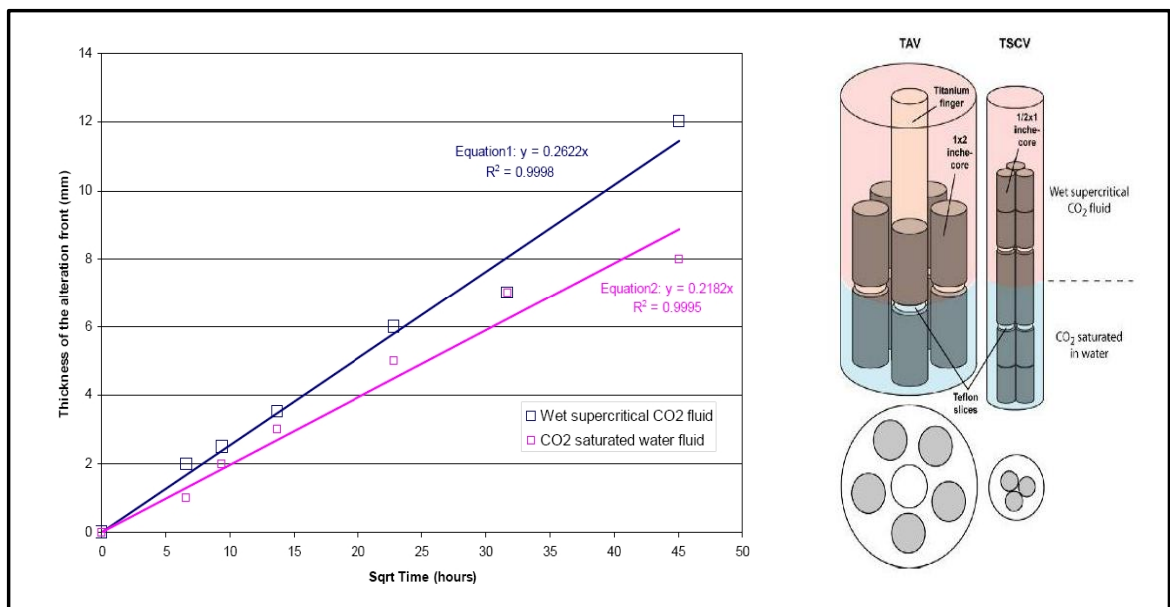


Figure 4: Rate of carbonation for Portland cement from laboratory tests, Barlet-Gouédard et al (2006).

In this example, the carbonation process will have penetrated 10 mm after 1000 years and 100 mm after 100,000 years. The main difference between these experimental procedures, excluding the cement type and temperature, is that Barlet-Gouedard et al (2006) used de-ionized water while Kutchko et al (2008) used 0.17 molar NaCl brine. Barlet-Gouedard et al (2008) performed additional experiments with a 4 molar NaCl brine to simulate downhole formation water conditions. It was observed that the carbonation rate was a tenth of the carbonation rate found in the 2006 experiments and the results were more in agreement with Kutchko et al (2008) and field experiments. The experiments clearly documented that increased salinity reduces the carbonation rate. Another difference between these experiments is that Kutchko et al (2008) used neat cement (API Class H), while Barlet-Gouedard et al (2006, 2008) used cement blends. Kutchko et al (2008) tested cement samples with bentonite additives. This sample showed a much higher degree of

carbonation, similar to Barlet-Gouedard et al (2006). Another interesting observation is that any fracture or weakness in the cemented sample showed a higher degree of carbonation.

Milestone et al (1986) showed that increasing the content of silicate in the cement and a reduction of $\text{Ca}(\text{OH})_2$ content resulted in a deeper carbonation front in the tested cement specimen, and increased the porosity in the cement at a faster rate. However, a 20% silica content is often needed in the cement mixture to get below the API recommended 0.01 mD permeability threshold. Silica also increases the compressive strength of the cement. High-strength silicate-rich cements samples that were exposed to CO_2 for 10 months lost 60% of their volume, while the samples without silicate lost 35% (Milestone et al, 1990). Even though a reduction in silica enhances the CO_2 resistance of the cement, it is difficult to obtain for Portland-based cement mixtures. The carbonation for cement attacked by supercritical CO_2 was also increased by an increase in the partial pressure of the CO_2 and an elevated temperature (Onan, 1984).

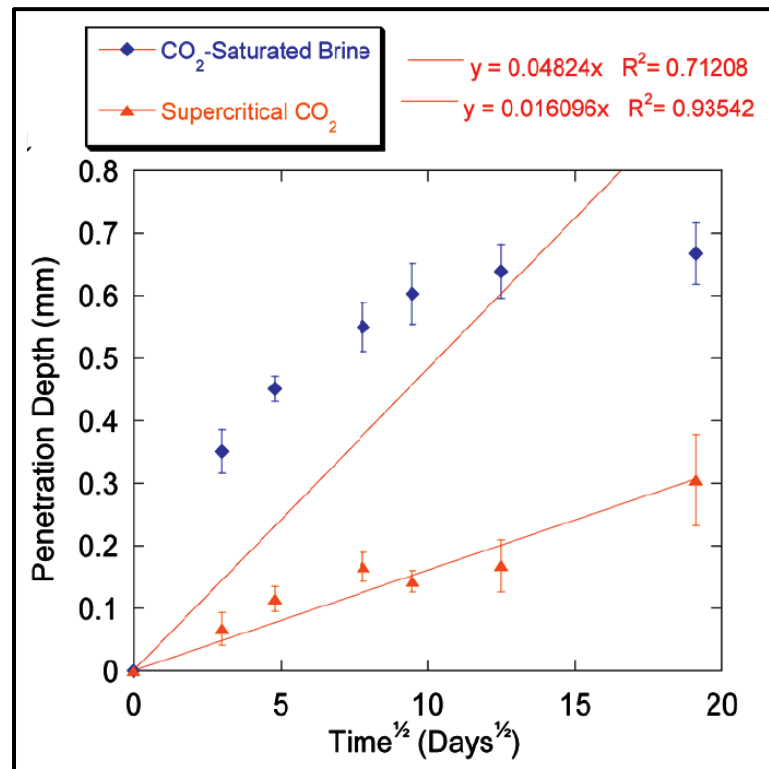


Figure 5: Carbonation depth (mm) versus time (days) at 50°C (Kutchko et al, 2008).

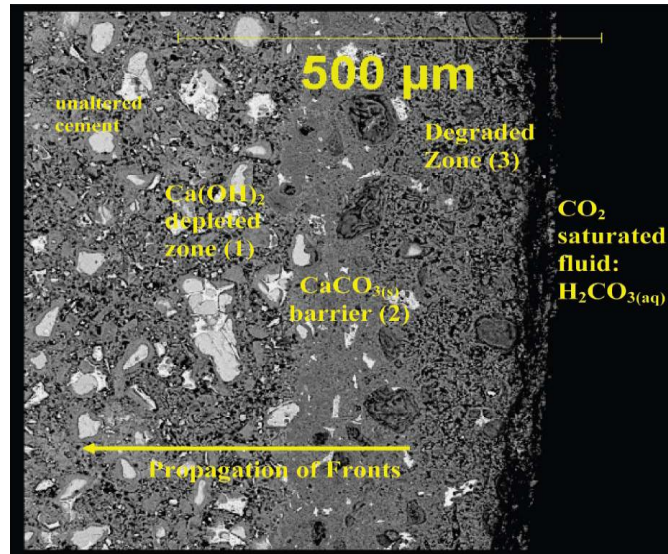


Figure 6: Test of Class H Portland cement in CO₂ saturated fluid (Kutchko et al, 2008).

Barlet-Gouedard et al (2008) summarized their CO₂ durability experiments for different cement mixtures (see Figure 7). The results indicate that only the Schlumberger proprietary EverCrete™ is stable towards long-term CO₂ attack. The Thermalock™ from Halliburton was not part of the study.

In the SACROC unit in West Texas, a 240 m thick limestone reservoir at 2000 m deep with a temperature of 54°C and a pressure of 18 MPa has been flooded with CO₂ (Carey et al, 2007). The 49-6 well was drilled in 1950 and cemented with a Type A Portland cement without additives. The well went on production and experienced CO₂ breakthrough in 1975. It continued to be a producer for the next 10 years and was converted to an injection well for the next 7 years. During its active years, a total of 110,000 tonnes of CO₂ passed through the well. Samples of the casing, cement and adjacent caprock were taken from about 4 to 6 m above the caprock reservoir contact (Figure 8). The cement was found to be partly carbonated. The cement that was in contact with the shale rock was heavily carbonated. The cement close to the casing had pure carbonate like a vein filling. No obvious proof of direct CO₂ interaction with the shale was found. The permeability of the cement was found to be higher than pristine Portland cement. SEM imaging showed that CaCO₃ had precipitated in the void spaces.

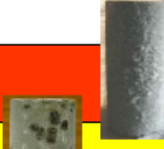
Durability validation at 90deg.C- 280 bars - CO ₂ + water					
System	1 week	3 weeks	1months	3 months	6 months
Magnesium Potassium Phosphate	Not tested			Not tested	Not tested
Calcium Aluminate Phosphate	Not tested			Not tested	Not tested
Portland cement					
Portland/Fly ash type F	Not tested		Not tested		
Portland/Fly ash type C	Not Tested		Not Tested		
CO ₂ Resistant cement					

Figure 7: Validation of CO₂ durability of different cement systems (Barlet-Gouedard et al, 2008).

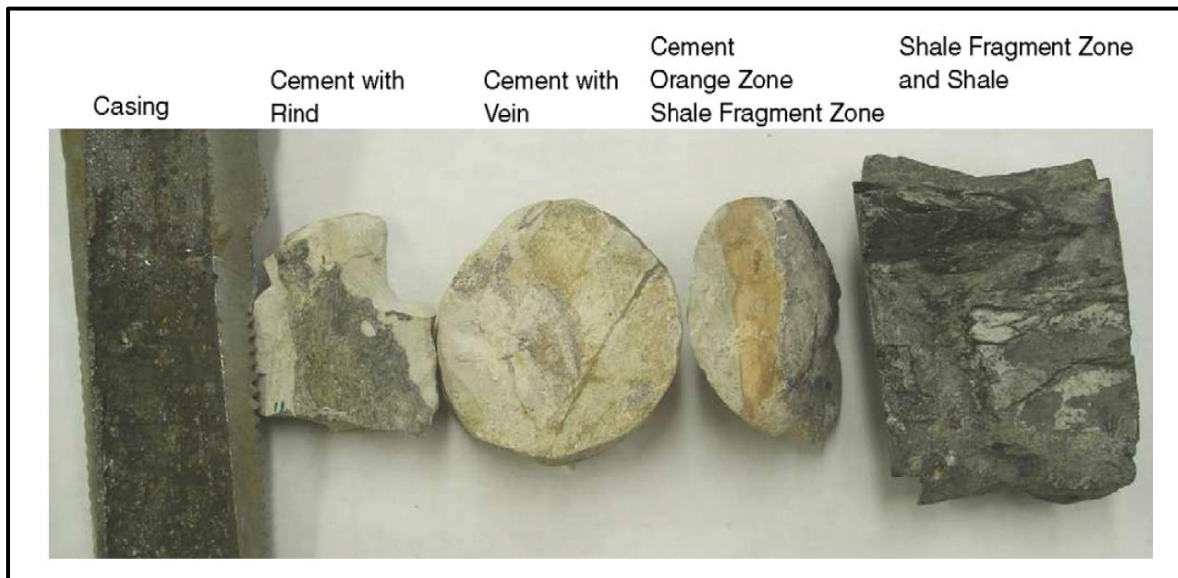


Figure 8: Photograph of samples recovered from the 49-6 well in Texas. It shows the casing (left), gray cement with a dark ring adjacent to the casing, 5 cm core of gray cement, gray cement with an orange alteration zone in contact with a zone of fragmented shale, and the shale country rock (Carey et al, 2007).

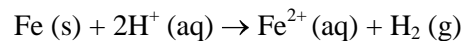
It was generally concluded that the structural integrity of the Portland cement was adequate to prevent a significant transport of fluids. However, it is believed that CO₂ had migrated along the cement casing and cement shale interfaces for some time.

Shen and Pye (1989) examined geothermal wells and the carbonation by CO₂ of Class G cement. To stabilize Portland cement at high temperatures, silica flour was added. In geothermal well cements there is little or no Ca(OH)₂, so the C-S-H phases can be attacked directly by the CO₂. The CO₂ content for the wells were 12,200 ppm CO₂ (0.20 mol/kg), while the temperatures were in the range of ~ 200 to 300°C. They found that the carbonation was dependant on temperature, CO₂ concentration and location. Both carbonated and uncarbonated cement had fractures and fissures, which was probably caused by the thermal cycles in the well. Shen and Pye (1989) found that the number of shutdowns correlated with the increase in permeability. This fits with the observed fractures, where sharp changes in temperature led to the deformation in the cement and likely caused the fracturing of the cement. There was no correlation evident between the extent of the carbonation and porosity. However, temperature and the amount of calcium carbonate formed in the cement due to CO₂ showed a clear relationship.

Krilov et al (2000) studied wells exposed to 180°C and 22% CO₂. After 15 years of service, the performance of the wells dropped. Debris was found downhole in the wells. Krilov et al (2000) found CO₂ to be the main reason of the degradation. They performed tests at simulated downhole conditions and concluded that the loss of compressive strength and cement integrity was caused by high temperature and CO₂ concentration.

2.4 CO₂ Corrosion on Tubulars and Steel Components

Steel products in wellheads, casing and completion strings are subjected to corrosion in an acidic environment. The main corrosion reaction in carbon steel is:



where the solid iron dissolves into iron ions in solution to create a corroded surface on the steel. The basic requirement for this reaction to occur is water. When CO₂ is used for enhanced oil recovery, most likely water alternated with CO₂ gas (WAG) or recycled CO₂ is injected. In capture and sequestration projects, dry CO₂ (with CO₂ purity above 95%) will be injected and therefore, corrosion problems are not expected to be any more severe for CO₂ storage as compared to regular CO₂ EOR operations.

For the last 35 years, wellhead and completion tubing materials for CO₂ enhanced oil recovery projects has been developed in the US based on industry practice. The materials used for the different components are summarized in Table 3 (Meyer, 2008). In the United States, the oil and gas industry operates over 13,000 CO₂ EOR wells, has over 3500 miles of high-pressure CO₂ pipelines, injects over 600 million tons of CO₂ (11 trillion standard cubic feet) and produces about 245,000 barrels of oil per day from CO₂ EOR projects. Meyer (2008) summarizes the technological advancement as follows:

- Corrosion resistant materials, such as stainless and alloy steels (e.g., 316 SS, nickel, Monel, CRA), for piping and metal component trim. Use of corrosion protection of the casing strings via impressed and passive currents and chemically inhibited (e.g., oxygen, biocide, corrosion inhibitor) fluid in the casing tubing annulus.
- Use of special procedures for handling and installing production tubing to provide tight seals between adjacent tubing joints and eliminate coating or liner damage.

- Use of tubing and casing leak detection methods and repair techniques, using both resin and cement squeeze technologies. Also the insertion of fiberglass and steel liners.
- Formulation and implementation of criteria unique to well sites in or near populated areas, incorporating fencing, monitoring and atmospheric dispersion monitoring elements to protect public safety. Current industry experience shows that when these technologies and practices are used, EOR operators can expect wellbore integrity at levels equivalent to those seen for conventional oil and gas wells.

Table 3: Materials of construction (MOC) for CO₂ injection wells based on US experience (Meyer, 2008).

<u>Component</u>	<u>MOC</u>
Upstream Metering & Piping Runs	316 SS, Fiberglass
Christmas Tree (Trim)	316 SS, Nickel, Monel
Valve Packing and Seals	Teflon, Nylon
Wellhead (Trim)	316 SS, Nickel, Monel
Tubing Hanger	316 SS, Incoloy,
Tubing	GRE lined carbon steel, IPC carbon steel, CRA
Tubing Joint Seals	Seal ring (GRE), Coated threads and collars (IPC)
ON/OFF Tool, Profile Nipple	Nickel plated wetted parts, 316 SS
Packers	Internally coated hardened rubber of 80-90 durometer strength (Buna-N), Nickel plated wetted parts

2.5 Mechanical Effects on Wellbore

Randhol and Cerasi (2009) provide a recent review of mechanical factors that can influence the integrity of the wellbore cement sheath. They pointed out that fractures in the cement sheath can occur from de-bonding of cement and fracturing at the rock formation interface, which is generally caused by water activity in the shale and cement. If the filter cake or mud is not properly removed, channeling of the cement can occur. Normal cement tends to shrink if no additives are used to prevent it. This creates poor bonding between the cement and the casing or formation, as well as fractures within the cement itself.

During injection, changes in temperature and pressure will lead to stress exposure in the injection wells, which conventional Class G cement is not suited for (Pedersen et al, 2006). Potential deformation caused by uplift of the reservoir during injection may rise to deformation loads on casing and cement and possible fractures (Orlic et al, 2008). Adding elastomeric and fibre materials to the cement can improve the amount of deformation that cements can tolerate (Randhol and Cerasi, 2009).

3. WELL INJECTION DESIGN

3.1 Geological Description of Well Location

The well design in this report is based on injecting CO₂ into the dolomitic Nisku formation. Currently there has been no decision made as to a specific location, so the information described below is for a generic well within the study area. The top of the Nisku formation is assumed to be 1890 m deep. The depth to the top of the Nisku formation in the Wabamun Lake area ranges from less than 1600 m in the northeast to deeper than 2200 m in the southwest. The formation is on average 72 m thick, typically ranging from approximately 60 to 100 m, but thinning to less than 40 m in the northwest. It is capped by the Calmar formation shale ranging in thickness from 5 to 15 m. The caprock is overlain by the upper Devonian-Lower Cretaceous aquifers (Figure 9). Ultimately, the thickness of the Colorado and Lea Park aquitards above these aquifers will act as a final barrier to any vertically migrating CO₂ (Figure 9). However, the Devonian Lower Cretaceous aquifer system contains several oil and gas fields in the area. Therefore, to prevent CO₂ migrating towards existing production, it is important to determine if the Calmar may be breached during or after injection.

The reported Sv gradient in the area is 23 kPa/m and the average fracture gradient in the Wabamun Lake study area is 20 kPa/m (Figure 10). This translates to a maximum allowable injection pressure of 33.4 MPa at 1890 m, which is 90% of the fracturing pressure at that depth and is lower than the area average of 37 MPa for well depths from 1850 to 1900 m (ERCB Directive 051, 1994).

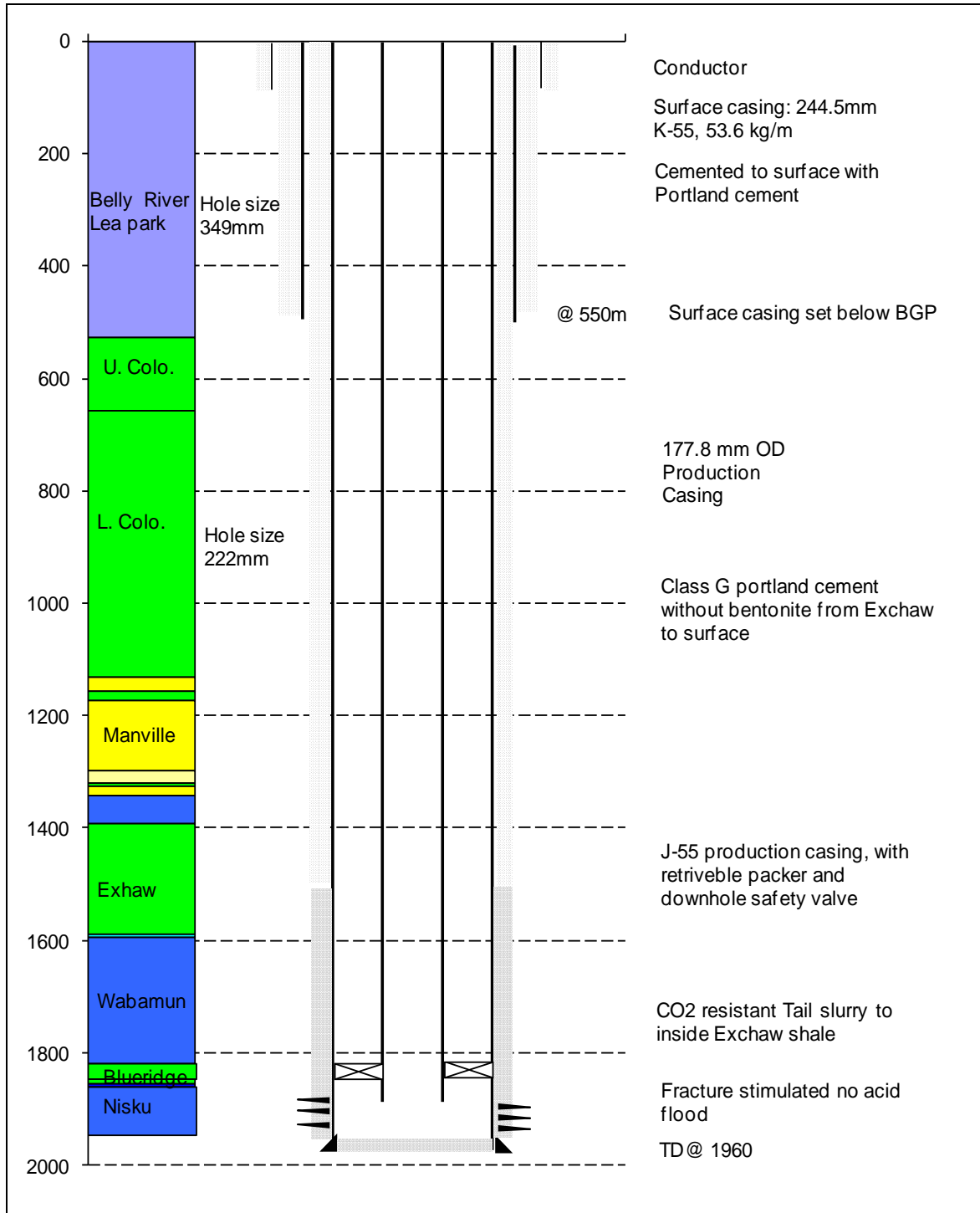


Figure 9: Well design for vertical injection well.

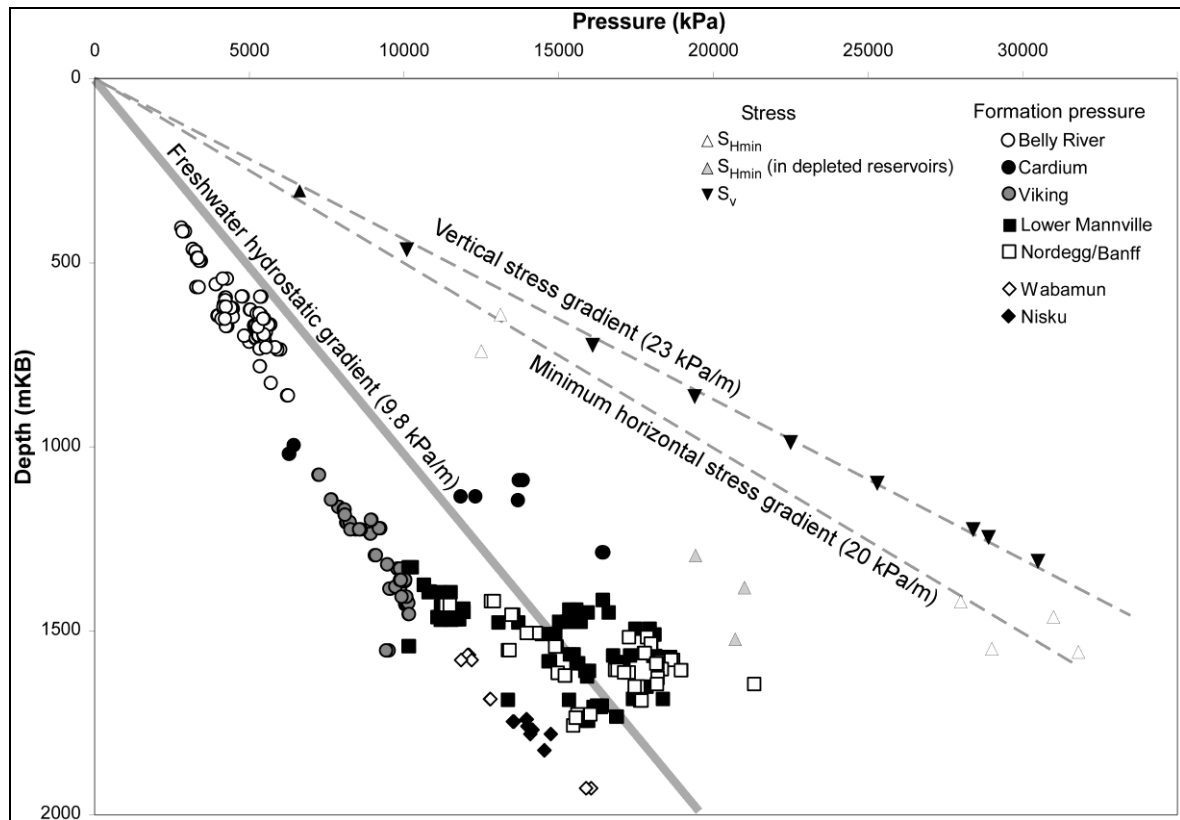


Figure 10: Vertical and least horizontal stress and pore pressure gradients (Michael et al, 2008).

3.2 Casing Design

A CO₂ injection well in Alberta is classified as a Class III well. Class III wells are used for the injection of hydrocarbons, inert gases, CO₂ and acid gases for the purpose of storage or enhancing oil recovery from a reservoir matrix (ERCB directive 051, 1994). A Class III well is required to have cement across usable ground water, but there is no requirement to have surface casing below base ground water protection. The base ground water protection is below 450 m for the area, so if the surface casing is set below the water protection zone a conductor is required. The Nisku formation has below normal hydrostatic gradient, but some of the formation higher up is pressurized in the area (Figure 10). The maximum pressure recorded in the Nordegg/Banff is 19,000 KPa (when disregarding the one outlying point in Figure 10). For a fluid pressure gradient of 11.8 KPa/m, the surface casing depth has to be 400 m for a 1960 m deep well to satisfy ERCB directive #8. With surface casing, the well can be drilled to TD with a mud gradient between 11 and 18 KPa/m. However, exact mud weight cannot be determined before the final well location is set.

In the selected casing design, the surface casing is set below the ground water protection area. The rationale for setting the surface casing is to get a second leakage barrier from the wellbore through both casing strings. Setting the surface casing this deep requires a conductor to be set (Figure 9). The production casing will be cemented and perforated down to TD.

The casing material selection strategy is to avoid having the casing come in contact with wet CO₂. To prevent CO₂ from coming in contact with the casing, completion tubulars, chemical inhibitors in the completion fluid used to fill the annular space, and cement outside the casing will be used as

barriers. This approach prevents the casing from being in direct contact with the injected CO₂, except in the perforated Nisku interval, where regular carbon steel will be sufficient.

3.3 Cementing Design

For the current well design, there are two or three possible cementing operations. First, the conductor may be cemented in place, then the surface casing is cemented from a depth of around 550 m to the surface. The production casing is cemented from the injection horizon to the surface. Cementing operations should have verified returns. To reduce to possibility of escape paths, all annular spaces between the casing strings and the hole annulus should be cemented.

It is unlikely that the surface casing will come in contact with carbon acid (H₂CO₃) from the deeper part of the injection formation, since there are several porous formations where the CO₂ will escape (e.g., Wabamun Group), therefore specialty cement is not required. The carbonation reaction is temperature dependant and also reduces the carbonation rate at surface casing depths. Cement slurry consisting of API Class G cement may include an accelerator for reducing the setting time for the low temperature of the surface casing. Typically 2% calcium chloride is added to the cement slurry as an accelerator. Good cementing practices are most important for getting good leak-free cement. Therefore operational practices should include a pre-flush with water, add scratchers or wipers on the casing, add centralizers for each stand (three joints) of casing and rotate the casing string during the injection of cement. And lastly, the cement should return to the surface.

During the injection phase, cement will only encounter dry CO₂. However after the injection phase and all the free CO₂ around the wellbore is dissolved in the brine, the wellbore will be attacked by carbonic acid (H₂CO₃). The carbonic acid will only attack the reservoir portion of the production casing, therefore special consideration of CO₂ cement needs only to be considered for the reservoir, primary seal and a safety zone above the reservoir. If the pressured CO₂ escapes along the cement and through the caprock, it will bleed off into the permeable and low-pressured Wabamun Group. Therefore as mentioned above, special CO₂ cement should not be necessary for anything shallower than the Wabamun Group.

The laboratory studies of cement discussed in Section 4 shows that Portland cement is subjected to carbonation when H₂CO₃ is present. Even though the carbonation itself is not a process that is inherently bad for well cement since it reduces its permeability, a continuing source of H₂CO₃ will increase porosity and permeability of the cement (Section 4). Two of the carbonation rate results presented in Section 4 are plotted in Figure 11. As indicated on the figure, the carbonation depth will be 1 mm or 200 mm after 100 years dependant on the salt concentration of the brine. With only a 22 mm thick cement sheet outside the casing in the well, a CO₂-resistant cement slurry should be selected. The more expensive CO₂-resistant cement is suggested as tail slurry with a cement top in the Exshaw shale above the normal pressured and permeable Wabamun Group. Regular cement should be sufficient over the CO₂-resistant cement. However since two different cement slurries will be used, a CO₂-resistant cement that is compatible with regular Portland cement has to be used to prevent flash setting (Section 4).

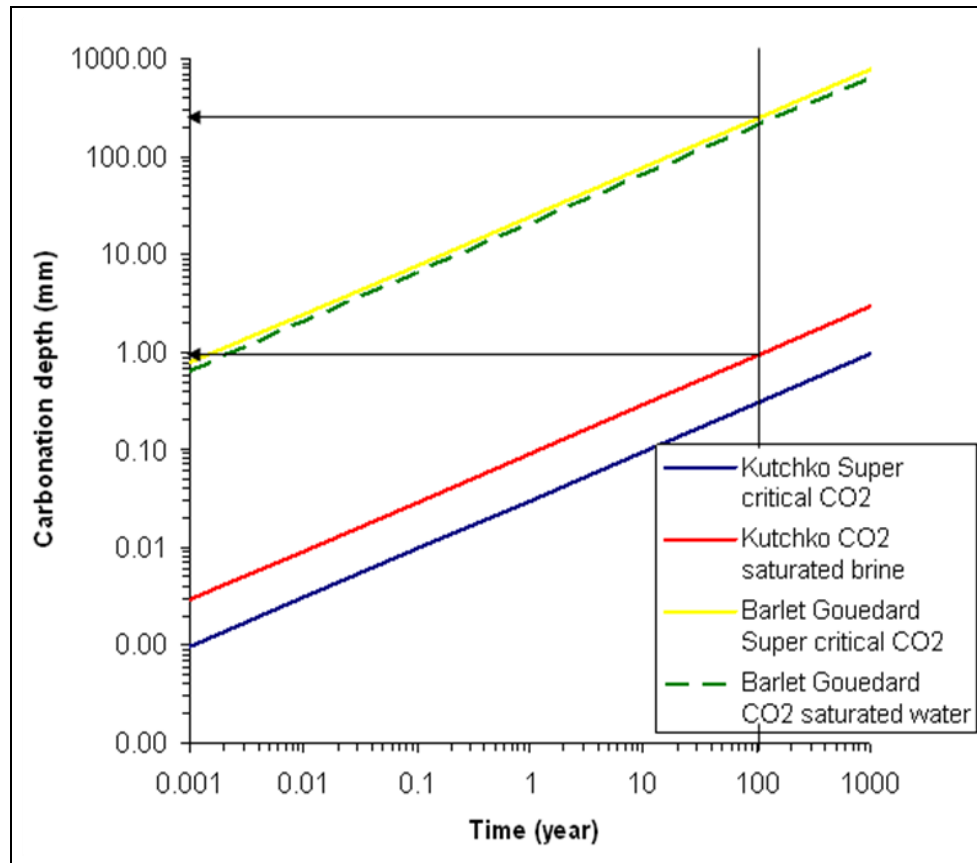


Figure 11: Carbonation depth estimated from laboratory tests after 100 year.

3.4 Completion Design

Corrosion problems have been minimal with dry CO₂ (Meyer 2008; Hadlow, 1992). Since the injected CO₂ will most likely have been transported through carbon steel pipelines, it should not be necessary to change completion materials for the injection wells. The cost estimate is based on a Christmas tree wellhead combination with J55 60.3 mm production tubing. The combined wellhead has casing annulus valves to access all annular spaces to measure the pressure between the casing strings and between the casing and production tubular. Above the Christmas tree is mounted a CO₂ injection valve and an access valve for running wirelines from the top. The production tubing is set on a retrievable packer above the injection horizon to ease the changing of the tubing if pitting is identified during regular inspections, and to seal off the annular space between injection tubular and casing. A safety valve/profile nipple can be used to isolate the wellbore from the formation to allow the tubing string to be replaced. Injection will be conducted through the perforated casing. In the base case there is no stimulation method used, but hydro fracturing may be an option. Using acids to improve injectivity is not recommended because of the possible damage to the cement sheath and casing.

4. INJECTION WELL COST ESTIMATE

This chapter provides a cost estimate for drilling and completing an injection well in the Nisku formation based on the given injection well design. The well assumes a Nisku formation top at 1890 m TVD and a total depth of 1960 m TVD. This well is used as the reference well for estimating well costs for vertical and horizontal wells for various depth ranges. Table 4 outlines the different items of the cost model. In the well cost, it is assumed that the drilling will be conducted during the summer and thereby the PTAC well cost report for summer 2008 was extensively used to identify the costs for the different line items (PTAC 2008). In the basic well design, a 5-day injection test was included but no stimulation fracturing. The time depth curves for three recently drilled wells were used to establish rate of penetration times for the different formations (Figure 12). Average casing running and cementing times were taken from the reference wells. Based on the thickness of the formations at our given location, a drilling time depth curve for our well was constructed (Figure 12). The well will be drilled in 14.9 days (12.7 days without coring the Calmar and Nisku formations).

Table 4: Well cost model WASP project injection well.

Well Cost Model WASP Project Injection Well	
<i>Drilling Cost</i>	
Well fixed costs	Survey, Surface rights, Well design, Site preparation and restoration, Rig move and mobilization
Depth-based well cost	Casing, cementing, mud, logging, and coring
Time-based drilling costs	Loaded rig rate, including rig, fuel, personnel, and equipment rentals
Fixed drilling cost	Total bit costs
<i>Completion Cost</i>	
Completion fixed costs	Wellhead, packer, valves, perforation and wireline runs
Depth-based completion costs	Tubulars and completion fluids
Time-based completion costs	Total rig rate for service rig including, boiler, personnel, engineering services and laboratory analysis
Five-day injection test	Cost associated with five-day injection test

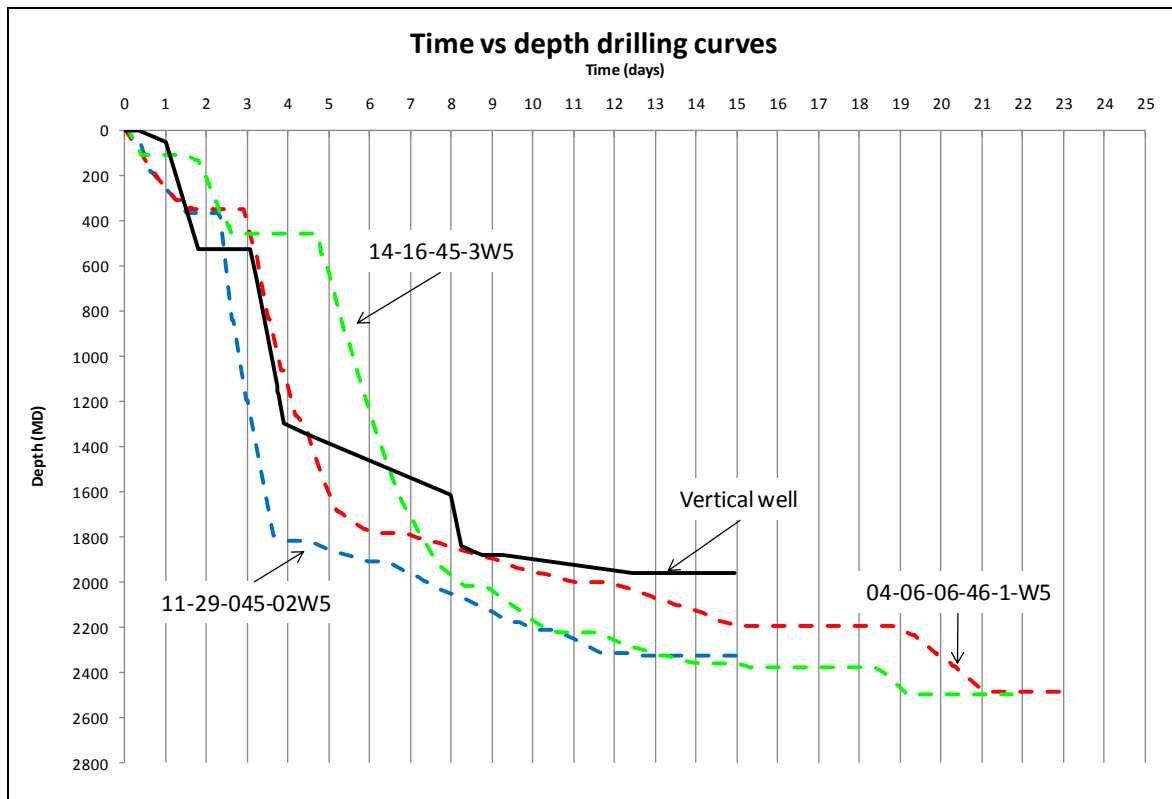


Figure 12: Drilling time for vertical well estimated based on three reference wells in the area.

The estimated cost for drilling the injection well is \$1.32 million, with drilling cost \$0.93 million and completion cost \$0.33 million including 5% contingency costs (Table 5). Table 6 shows the cost for tubulars and cementing. The detailed line-by-line cost including its source is shown in Appendix A.

Table 5: Well cost results WASP project injection well.

Single Vertical Well Cost	Item Cost
Drilling Cost	\$ 932,993
Well fixed costs	168,920
Depth based well costs	400,708
Time based drilling cost per day	330,365
Fixed drilling cost	33,000
Completion Cost	\$ 325,633
Completion fixed costs	38,000
Depth based completion costs	83,793
Time based completion costs	138,840
5 day Injection test	65,000
Total Well Cost	1,258,626
Total Well Cost Plus 5% Contingency	\$ 1,321,557

Table 6: Tubular and cementing costs for a vertical well.

Casing, Tubular and Cementing Costs for a Vertical Well					
Type		Conductor	Surface Casing	Production Casing	Production Tubing
Casing depth	m	50	550	1,960	1890
Cost	\$/m	92	92	72	36
Scratchers, centralizers float and guiding shoe	\$/m	2.6	2.6	2.6	
Crew	\$/m	6	6	3	
Cement cost and rentals	\$/m	62	62	19	
Cement costs	\$/m			18	
CO ₂ resistant cement	\$/m			27	
Total cost casing	\$	8,130	89,430	190,076	68,040

5. ABANDONMENT OF WELLS

When a well is drilled and if it is a dry exploration well, it will be immediately abandoned. Current abandonment practices are to cement all porous zones with a cement plug (Figure 4 left). The cement plug has to be minimum of 30 m (or 60 m for plugs deeper than 1500 m) and extend a minimum of 15 m above and below the porous zone being covered (ERCB Directive 20, 2007). Unacceptable plugs, which are located too low (less than 8 m coverage into non-porous formations) or too high or misplaced (i.e., does not cover the intended porous zone), have to be circulated/drilled out and a new cement plug set. To protect groundwater, a plug must be set from 15 m below the groundwater base to 15 m above the surface casing shoe. If a casing string is covering the base of groundwater protection zone, remedial cementing and or cement plugs have to cover the zone.

For a well that has production casing, the abandonment procedure is more customized. All non-saline water sources have to be protected and hydraulic isolation must exist between porous zones. This rigorous requirement has been in place since 2003. There are five different options to abandon cased wells using plugs, packers or cement plugs. The three main types are 1) bridge plug set above the perforations with cement over top the plug, 2) squeeze cement in the perforations, and 3) cement plug across perforations. All methods have one common requirement, and that is to have at least 8 m of cement inside the casing that has been pressure tested to 7000 kPa.

At the surface, casing strings are cut 1 to 2 m below the surface and a steel plate is welded to prevent access to the casing strings. This is done after the well is tested for gas migration and surface casing vent flow.

Squeezing cement into openings in casing as remedial cement is often not successful because of the cement's high viscosity. Metal alloy that expand (~ 1%) upon solidification has recently been suggested for remediate cementing and cement plugs (Canitron, 2008). The alloy is placed in the wellbore and a heating tool melts it. The alloy flows to fit the openings of the casing and the volume inside the casing. The expansion helps to avoid micro-fissures that cement can experience because of its shrinkage. Alloy is also claimed to not go through a weak transitional phase during solidification like cement does, and it bonds stronger against clean steel than pure Portland cement. Molten alloy has low surface tension and viscosity and is claimed to fill small fissures and perforations efficiently (Figure 13). Alloys should be CO₂ resistant.

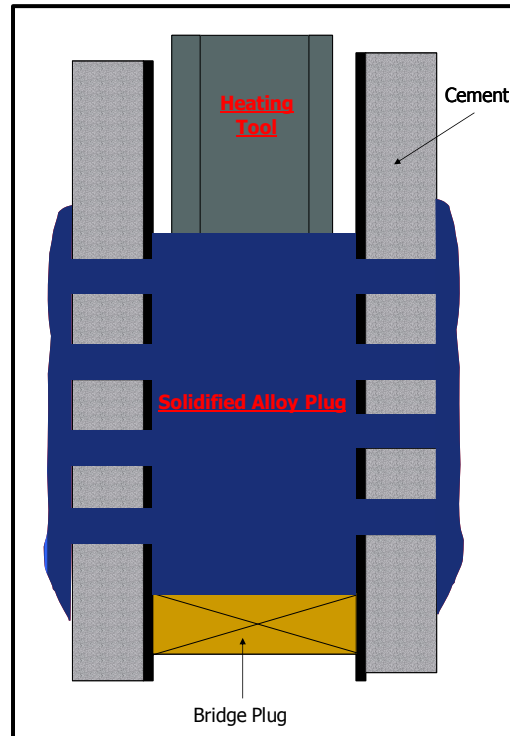


Figure 13: Schematic of using metal alloy plug to seal and abandon production zone (Canitron, 2008).

Removing the casing in certain areas is another method to mitigate leakage caused by poor bond or de-bonding between casing and cement. If wells are plugged and abandoned permanently, both Gray et al, 2007 and Carlsen and Abdollahi, 2007 (Figure 9) suggest the casing steel be removed before installing the final cement plugs. This will remove the most-likely leakage path along the casing. Besides, CO₂ can attack both steel and cement and create leakage paths. In the West Texas field case, it has been seen that reactions have occurred at the casing cement interface and the cement formation interface. Before the final cement squeeze and plug is set, a CO₂-resistant polymer may be injected in the near well bore region to prevent CO₂ from coming in contact with the cement after injection. Cements that are resistant to CO₂ are recommended to seal the reservoir as the cement will be exposed to CO₂ in the future. An open hole completion will reduce the need for milling the casing and may be a simplified solution where appropriate.

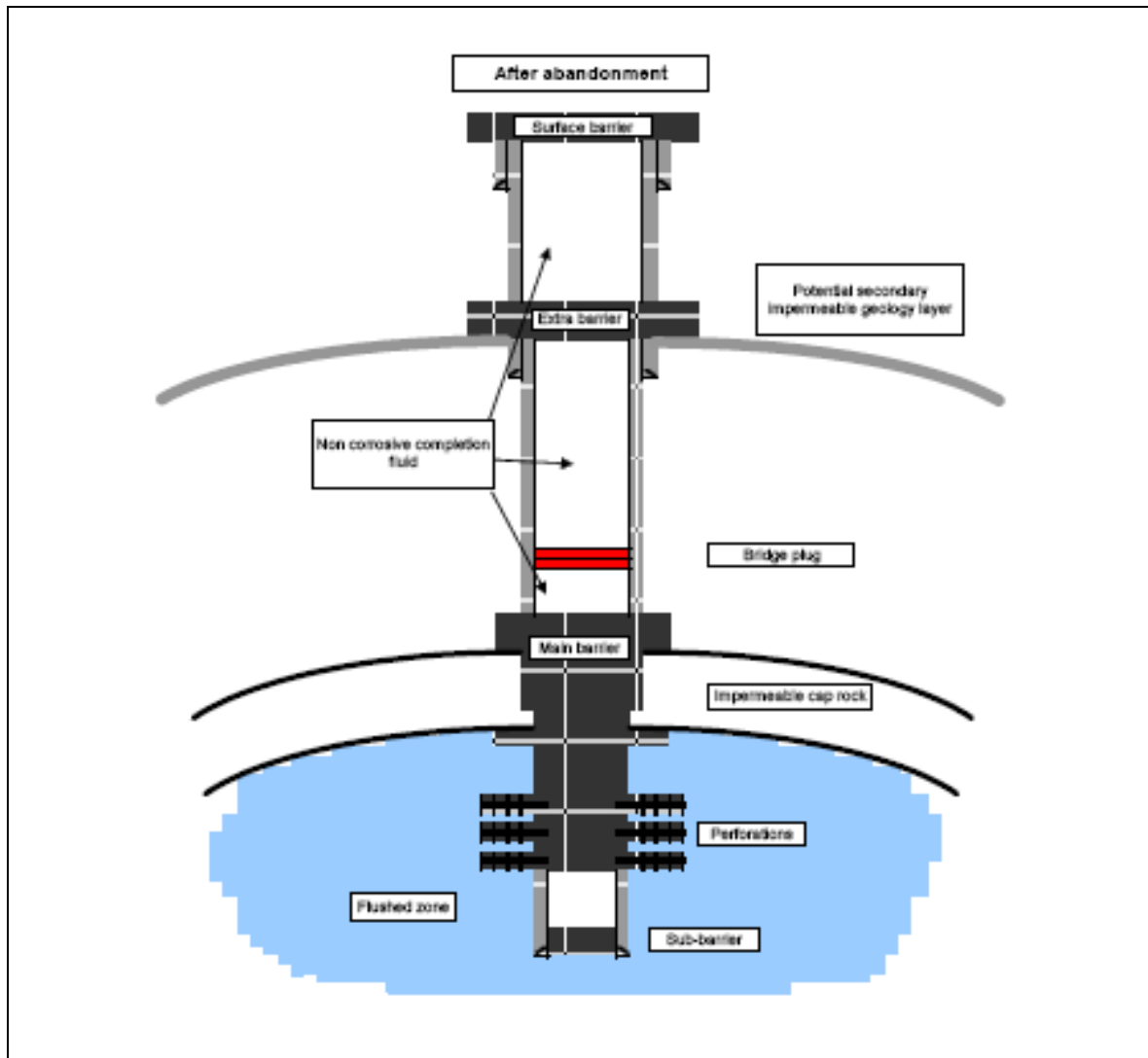


Figure 14: Suggested abandonment method for CO₂ injection wells.

6. EVALUATION OF EXISTING WELLS IN NISKU

A second objective for this study was to evaluate the leakage risk of existing wells within the Wabamun CO₂ storage project area. To identify the number of wells to include in the study, it was assumed that the Calmar seal will hold and only the wells penetrating the Calmar and Nisku formations are at risk. In the area there are 95 wells that penetrate the Nisku formation. Figure 15 presents the age distribution of when these wells were drilled. The wells is classified as either D&A—drilled and abandoned (grey colour) or DC—drilled and cased (white colour). The earliest well was drilled in 1948 and the newest in 2005.

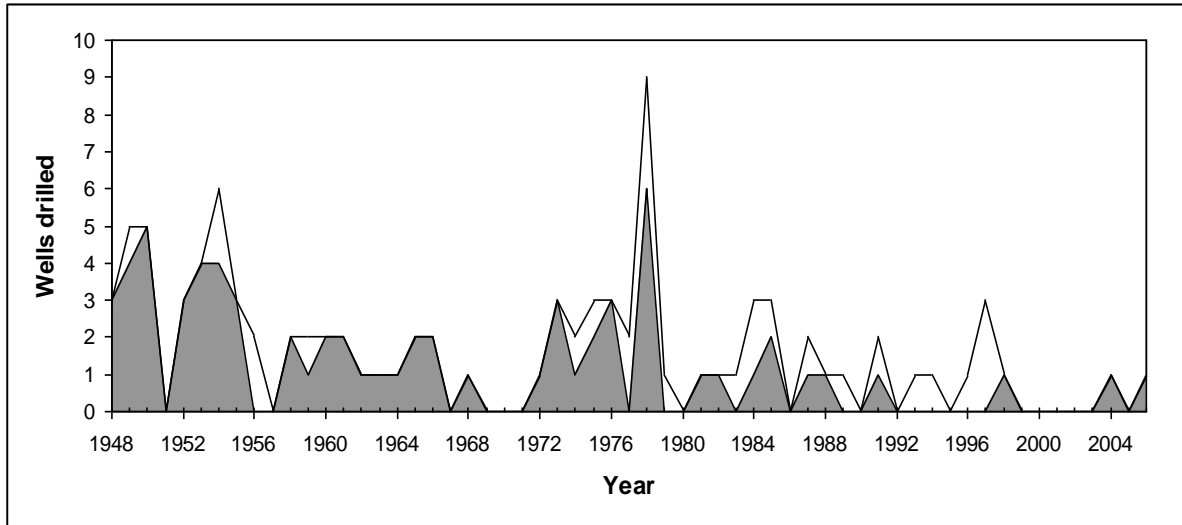


Figure 15: Age distribution of wells drilled through Nisku in the study area. Gray wells are drilled and abandoned, white wells are drilled and cased wells.

The approach taken was to determine if the wells were in an unacceptable condition and a re-abandonment or workover was required. A flow chart was developed to determine which wells were within the pressurized plume area and were candidates for workovers (Figure 16). The first decision in the flow chart is if the wells are drilled after 2003. For these wells, the stricter requirements for zonal isolation were in place and the wells should have little likelihood of leakage. Active wells with cement through Calmar are considered safe, since these wells have their production regularly monitored. Any CO₂ breakthrough would be identified at the wellhead for these wells.

Non-active wells are either suspended or abandoned. Suspended wells in the pressure plume area should be abandoned, or if they currently have a cement sheath through the Calmar seal, should be monitored. The rationale is that older suspended wells may not have the necessary protection around ground water resources. Since cement was not required, carbon steel in casing is not long-term CO₂ resistant and may create a leakage path. Wells abandoned after 1995 are tested for surface casing vent flow and gas migration and is expected to have sufficient integrity.

For earlier abandoned wells, they are either cased and abandoned or plugged or abandoned. Cement in open hole cement plugs in abandoned wells are pure cement or contain a low amount of additives (2% CaCl, 2% bentonite). If open hole plugs exist through caprock wells, the wells should have sufficient seal with a carbonation rate of less than 1mm/10 year. Wells with production casing tend to have higher additive content (2% CaCl, up to 50% bentonite) and thickness of 26 to 57 mm. Higher carbonation rates (e.g., 1mm/year) will expose casing to CO₂ corrosion in a matter of years when wet CO₂ is present. Produced sections with perforations and stimulation through hydraulic fracturing and/or acidizing creates fractures that may have caused increased permeability of the cement sheath. Further bridge plugs with capped cement has shown to be prone to leakage inside the casing. Produced zones can be expected to have low cement integrity for CO₂ brine exposure. If CO₂ enters inside the casing, it can reach the surface. Therefore cased and abandoned wells need further action if cement types and length both inside and outside the casing cannot be verified.

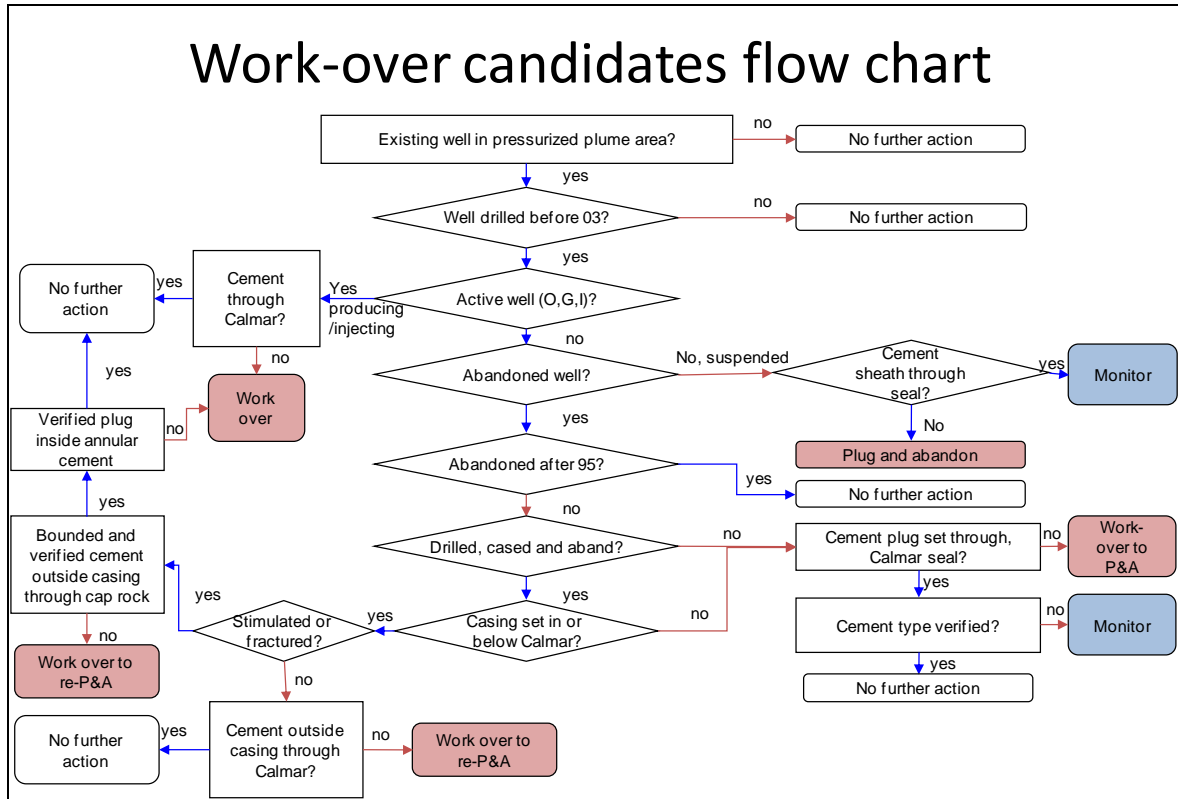


Figure 16: Flow chart for identifying wells which are candidates for re-entering and conduct workover operations to improve leakage integrity.

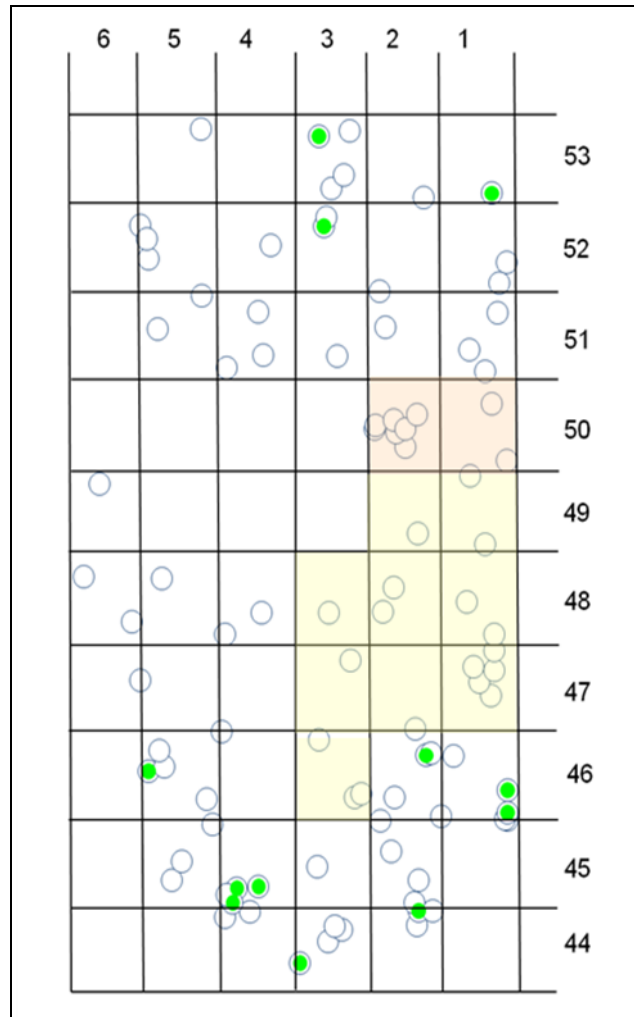


Figure 17: Outline of the study area where horizontal lines are Ranges West of 5 and Vertical squares are Townships. The highlighted area is the focus area where all 27 wells where studied in detailed. Twelve additional wells where randomly selected (indicated in green).

The flow chart was applied to 27 wells inside an 11 township area (the high-graded focus area) (Figure 17). Based on the analysis of 2 out of 17 drilled and abandoned wells, they did not have a verified cement plug through the Calmar and need to be re-abandoned with a new cement plug set (Table 7). For the cased and abandoned wells, 2 out of 8 did not have verified cement inside and outside the casing and therefore require re-abandonment (Table 8). For most of the drilled and cased wells, the production casing was set above the Calmar formation and therefore the well had a verified pure cement plug through the Calmar seal. A small random sample of 12 wells was analyzed for the area to get within a 25% uncertainty range. For those 12 wells, none required workovers. Figure 18 gives the current situation for all wells in the whole WASP study area.

Table 7: Drilled and abandoned wells in focus area.

Well ID	Year Abandoned	Workover Needed?	Plug Length in Nisku (m)	Plug Length Above Nisku (m)
100/11-12-046-03W5/00	1953	no	16.76	51.80
100/16-12-046-03W5/00	1948	yes	0.00	0.00
100/11-33-046-03W5/00	1953	no	66.16	11.60
100/10-22-047-01W5/00	1964	no	16.44	15.00
100/08-26-047-01W5/00	1973	no	13.76	39.00
100/16-35-047-01W5/00	1973	no	14.94	41.40
100/04-36-047-03W5/00	1949	yes	0.00	0.00
100/16-02-048-01W5/00	1952	no	13.12	24.10
100/08-17-048-02W5/00	1984	no	58.90	191.10
100/04-11-049-01W5/00	1950	no	20.46	27.70
100/16-33-049-01W5/00	1954	no	20.14	13.40
100/15-11-049-02W5/00	1950	no	51.08	6.10
100/16-01-050-01W5/00	1952	no	13.50	26.80
100/15-26-050-01W5/00	1949	no	76.20	15.20
100/15-10-050-02W5/00	1948	no	0.00	45.70
100/16-16-050-02W5/00	1960	no	32.30	68.30
100/02-26-050-02W5/00	1954	no	73.80	32.90

For the existing wells that require workovers, the shallow cement plugs will have to be drilled out so that the existing wellbores can be re-entered. New cement plugs will be set through the Nisku and Calmar formations. This workover operation should be conducted safely since the expected downhole pressures are known from the original drilling operation. However, if the wells are within the pressurized plume created by CO₂ injection, wellheads and old casing strings may not have the integrity to handle the elevated pressure. The existing wells will not be CO₂ compliant and the complexity and cost required to abandon these wells will be higher because of the higher pressures and the presence of CO₂. Therefore it is recommended that these wells be re-abandoned before CO₂ injection commences.

Table 8: Drilled, cased and abandoned wells.

Well ID	Year Abandoned	Workover Needed?	Cased in Nisku	Plug Length in Nisku (m)	Plug Length Above Nisku (m)
100/09-10-047-01W5/00	1987	yes	yes	Outside cement to Inside Manville (1592 TVD)	Plug @ 950 m md)
100/12-27-047-01W5/00	1965	No	no	15.3	45.7
100/06-02-047-02W5/00	1961	No	no	0.0	12.8
100/02-21-048-01W5/00	1962	No	no	16.8	16.7
100/02-28-048-02W5/00	1955	No	no	8.3	24.7
100/04-20-050-02W5/00	1958	no	no	84.4	16.8
100/05-20-050-02W5/00	1965	no	no	44.8	11.6
100/02-22-050-02W5/00	1955	yes	no	0.0	0.0

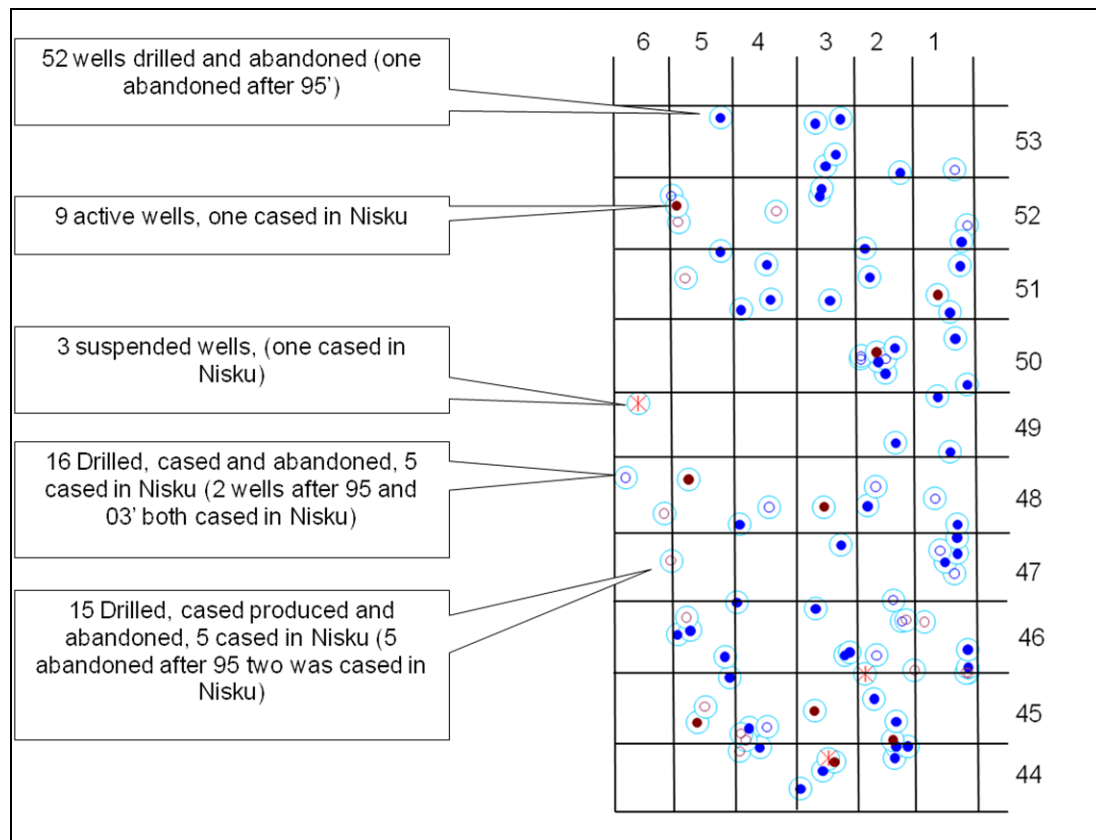


Figure 18: Spatial distribution of all wells penetrating Nisku in the study area.

7. CONCLUSIONS

The well design does not require fundamental changes for a CO₂ injector when compared to regular well designs, since dry CO₂ is expected to be injected into the study areas formation. The cost of one vertical injection well is estimated to be around \$1.3 million CAD.

When analyzing the existing well population, only 4 out of 27 wells are workover candidates. This result makes well leakage from existing wells less of a problem than first anticipated. For the existing wells, only a few have production casing through the Nisku, which is more prone to leakage. The other wells have cement plugs through the caprock with a cement type that will prevent leakage from the Calmar. For existing wells that requires workovers, they need to be performed before pressurizing the reservoir area. The cost and complexity to abandon these wells will increase when the pressures are higher and when CO₂ is present.

The literature survey identified that current well design and abandonment methods should be sufficient to prevent leakage from injection wells. However, there are still some unanswered question relating to the effect thermal and pressure cycles will have on cement sheath integrity in CO₂ injection wells.

8. REFERENCES

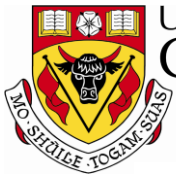
- Bachu, S and Bennion, B, 2008. Experimental assessment of brine and/or CO₂ leakage through well cements at reservoir conditions, *International Journal of Greenhouse Gas Control*. Volume 3, Issue 4, July 2009, p. 494–501.
- Barlet-Gouédard V, Rimmelé G, Goffe, B and Porcherie, O., 2006. Mitigation strategies for the risk of CO₂ migration through wellbores. SPE paper 98924. Proceedings of the 2006 IADC/SPE Drilling Conference, Miami Florida, 21–23 February 2006.
- Barlet-Gouédard V, Ayache B, Rimmelé G, 2008. Cementitious Material Behaviour under CO₂ environment. A laboratory comparison. 4th Meeting of the Well Bore Integrity Network, Paris, France, 18–19 March 2008.
- Carey J., Wigand M., Chipera S., Wolde G., Pawar R, Lichtner P., Wehner S, Raines M., and Guthrie G., 2007. Analysis and performance of oil well cement with 30 years of CO₂ exposure from the SACROC Unit, West Texas, USA, *International Journal of Greenhouse Gas Control*, p. 75–85.
- Carlsen M. and Abdollahi, J., 2007. Permanent, abandonment of CO₂ storage wells, Sintef report 54523200.
- Celia, M. A., S. Bachu, J. M. Nordbotten, S. Gasda, H. K. Dahle, 2004. Quantitative estimation of CO₂ leakage from geological storage: Analytical models, numerical models, and data needs, In, E.S. Rubin, D.W. Keith and C.F. Gilboy (Eds.), *Proceedings of 7th International Conference on Greenhouse Gas Control Technologies*. Volume 1: Peer-Reviewed Papers and Plenary Presentations, IEA Greenhouse Gas Programme, Cheltenham, UK.
- Canitron, 2008. Alloy Squeeze technology, A New Method for Casing Repair and Vent Gas Flow Shut Off, Industry presentation given 17 March 2008, Calgary, AB.
- Crow, W. 2006. Studies on wellbore integrity. Proceedings of the 2nd Wellbore Integrity network Meeting, Princeton, New Jersey, 28–29 March 2006.
- ERCB, Directive 51, 1994, Injection and Disposal Wells-Well Classifications, Completions, Logging and Testing Requirements, March 1994.
- ERCB Directive 20, 2007, Well abandonment guide, December 2007.
- ERCB, 2009. www.ercb.ca.
- Gray, K., Podnos, E. and Becker E., 2007. Finite Element Studies of Near-Wellbore Region During Cementing Operations: Part I. Production and Operations Symposium, 31 March–April 2007, Oklahoma City, Oklahoma, U.S.A. SPE-106998.
- Hadlow, R.E., 1992. Update of Industry Experience with CO₂ Injection, 67th SPE Annual Technical Conference and Exhibition, 4–7 October 1992, Washington, D.C., SPE-24928.
- Halliburton, 2009. www.halliburton.com.
- Krilov Z, Loncaric B and Miksa Z, 2000. Investigation of a Long-Term Cement Deterioration under a High-Temperature, Sour Gas Downhole Environment, SPE 58771.
- Kutchko BG, Strazisar BR, Dzombak DA Lowry GV, and Thaulow N, 2007. Degradation of wellbore cement by CO₂ under geologic sequestration conditions, *Environ Sci. Technol.* 41, p. 4787–4792.

- Kutchko BG., Strazisar BR, Lowry GV, Dzombak DA, and Thaulow N, 2008. Rate of CO₂ Attack on Hydrated Class H Well Cement under Geologic Sequestration Conditions, *Environ. Sci. Technol.*, 42, p. 6237–6242.
- Meyer, 2008. API special reports, Summary of Carbon Dioxide Enhanced Oil Recovery (CO₂ EOR) Injection Well Technology, 62 p.
- Milestone, N. and Aldridge L., 1990. Corrosion of Cement Grouts in Aggressive Geothermal Fluids, *Geothermal Resources Council Transactions*, 14, p. 423–429.
- Milestone N., Sugama T, Kukacka LE, and Carciello N, 1986. Carbonation of Geothermal Grouts – Part 1: CO₂ Attack at 150°C, *Cement and Concrete Research*, 16, p 941–950.
- Moritis, G., 2008, SWP advances CO₂ sequestration, ECBM, EOR demos: *Oil & Gas Journal*, v. 106.37, p. 60–63.
- Mulders F., 2006. Studies on Wellbore Integrity, Proc. 2nd Wellbore Integrity Network Meeting, Princeton, New Jersey, 28–29 March 2006.
- NETL, 2009, Project solicitation innovative and advanced technologies and protocols for monitoring/verification/accounting (MVA), simulation, and risk assessment of carbon dioxide (CO₂) sequestration in geologic formations, U.S. Department of Energy (DOE) DE-FOA0000023-01.
- Onan D. D, 1984. Effect of Supercritical CO₂ on well cement, SPE paper 12593, p. 161–172
- Orlic B and Benedictus T, 2008. Some geomechanical aspects of well integrity, 4th Meeting of the Well Bore Integrity Network, Paris, France, 18–19 March.
- Pedersen RO, Scheie A, Johnson C, Hoyos JC, Therond E and Khatri DK, 2006. Cementing of an offshore disposal well using a novel sealant that withstands pressure and temperature cycles, SPE 98891. IADC/SPE Drilling Conference, Miami, Florida, USA, 21–23 February 2006.
- PTAC, 2008.
- Randhol, P. and Carlsen, I.M. 2008. Assessment of Sustained Well Integrity on the Norwegian Continental shelf. Fourth meeting of the IEA-GHG Wellbore Integrity Network, 18–19 March 2008, Paris, France.
- Randhol, P. Cerasi, P. 2009. CO₂ Injection Well Integrity. Sintef report. 31.6953.00/01/08.
- NPA, 2008. Norwegian Petroleum Safety Authority, 2008. Well integrity survey phase 1. www.ptil.no.
- Schlumberger, 2009. www.slb.com
- Shen, J and Pye. D., 1989, Effects of CO₂ attacks on Cement in High Temperature Applications, SPE/IADC 18618, presented at SPE/IADC drilling conference, New Orleans, LA, 28 February–3 March 1989.
- Watson, T.L. and Bachu, S. 2007. Evaluation of the Potential for Gas and CO₂ Leakage along Wellbores. SPE 106817. E&P Environmental and Safety Conference, 5–7 March 2007, Galveston, Texas, U.S.A.

APPENDIX A

Appendix A: Vertical well cost model WASP project injection well					
Line cost	Item description	Cost	# Units based on well design	Cost per Unit	Units Source
Well fixed costs		168,920			
	Survey, Surface rights, Well design	16,500 \$			
	Surface lease	2,500 \$	1	2500 \$	PTAC 2008 well study average
				/hectar	hectar cost
	Surveying	3,500 \$	1	3500 \$/day	PTAC 2008 well study
	License and application fee	500 \$	1	500 \$/licen	PTAC 2008 well study
				se	
	Detailed engineering	10,000 \$	80	125 \$/hour	PTAC 2008 well study for hourly rate
	Site preparation and restoration	104,000 \$			
	Road	20,000 \$	2	10,000 \$/km	PTAC 2008 well study, typical road length evaluated based on existing road density in Wabamun area
	Site preparation	40,000	4	10,000 \$/day	PTAC 2008 well study
	Restoration	40,000	4	10,000 \$/day	PTAC 2008 well study
	Special construction	0			
	Company man supervision	4,000	4	1000 \$/day	PTAC 2008 Well study
	Rig move and mobilization	48,420 \$			
	Rig move	38,400	20	1920 \$/load	Cost per load assuming 8 hour per 100km, 80 km from Edmonton to Wellsite
	Rig permit	500 \$	1	500	PTAC 2008 Well study
	Rig mobilization	9,520 \$	1	9,520 \$/day	PTAC 2008 Well study
Appendix A page 2					
Depth based well cost		400,609 \$			
	Conductor	8,130			Details in report
	Surface casing and cementing	89,430 \$			Details in report
	Intermediate surface casing and cementing	0			
	Production casing and cementing	190,076 \$			Details in report
	Production liner	0			
	Mud	30,589			
	Surface mud and chemicals	4,187 \$	84	\$50 \$	PTAC 2008 Well study
	Main mud and chemicals	18,112 \$	121	\$150 m3	PTAC 2008 Well study
	Mud removal	6,037 \$	121	\$50	PTAC 2008 Well study
	Waste management	2,253 \$		\$2,253	PTAC 2008 Well study
	Logging	25,480 \$			
		25,480 \$	1,960	\$13.00 \$/m	PTAC 2008 Well study
	Coring	56,903 \$			
	Time Based drilling costs	330,365 \$	12.70	Days	From ROP evaluation
	Time based drilling cost per day	26,013			
	Loaded rig rate	21,338 \$/day			
	Rig rate	11,900 \$/day		11675	PTAC 2008 Well study
	Rig insurance	100 \$/day	1	100	PTAC 2008 Well study
	Fuel	1,500 \$/day		1500	PTAC 2008 Well study
	Personell				
	Drilling supervisor	1,250 \$/day	1	1250	PTAC 2008 Well study
	Well site geologist	- \$/day	0	1000	PTAC 2008 Well study
	Driller	1,008 \$/day	2	\$42	CAODC May 2009
	Assistant Driller	888 \$/day	2	\$37	CAODC May 2009
	Derrickhand	864 \$/day	2	\$36	CAODC May 2009
	Motorhand	756 \$/day	2	\$32	CAODC May 2009
	Floorhand	720 \$/day	2	\$30	CAODC May 2009
	Leasehand	672 \$/day	2	\$28	CAODC May 2009
	Accommodation cost	1,680 \$/day	12	\$140	CAODC May 2009
	Crew transportation	180 \$/day	12	\$15	Assumed
	Mud logging	775 \$/day	1	\$775	Fully loaded cost (PTAC 2008)
	Wac truck	1,600 \$/day	1	\$1,600	PTAC 2008 Well study

Appendix A Page 3					
Rentals					
Well site trailer	4,675	\$/day			
Solid equipment	450	\$/day	2	225	PTAC 2008 Well study
Sump pumps	175	\$/day	1	175	PTAC 2008 Well study
Tank rental	800	\$/day	1	800	PTAC 2008 Well study
Down hole tool rental	1,000	\$/day	1	1000	PTAC 2008 Well study
water and trucking	1,300	\$/day	50	26	PTAC 2008 Well study
	950	\$/day	1	950	PTAC 2008 Well study
Fixed drilling cost	\$ 33,000				
Total bit costs	\$ 33,000				
Conductor	-	\$			
Surface hole	5,000	\$	1	5000	PTAC 2008 Well study
Intermediate hole	-	\$			
Production hole	28,000	\$	2	14000	PTAC 2008 Well study
Production liner					
Total drilling costs	932,893.61				
Completion fixed costs	38,000	\$			
Well head	14,000	\$	1	14000 \$	PTAC 2008 Well study
Packer	12,000	\$	1	12000 \$	PTAC 2008 Well study
Safety valve	12,000	\$	1	12000 \$	PTAC 2008 Well study
Perforating	8,000	\$	1	8000 \$	PTAC 2008 Well study
Wireline	10,000	\$	5	2000 \$	PTAC 2008 Well study
Depth based completion costs	83,793	\$			
Tubular	68,040	\$			PTAC 2008 Well study
Completion fluids	15,753	\$	14.3	1100 \$/m3	PTAC 2008 Well study
Time based completion costs	138,840	\$			
Rig rate fully loaded	17,355		8		PTAC 2008 Well study
Service rig	7,500				PTAC 2008 Well study
Boiler	1,950				PTAC 2008 Well study
CSA	800				PTAC 2008 Well study
Crew transport	780				PTAC 2008 Well study
Hauling and trucking	1,500				PTAC 2008 Well study
Vacuum truck	1,450				PTAC 2008 Well study
Vater and trucking	1,000				PTAC 2008 Well study
Completion supervision	1,500				PTAC 2008 Well study
Fluid analysis	500				PTAC 2008 Well study
Engineering services	375				PTAC 2008 Well study
Appendix A Page 4					
5 day Injection test	65,000	\$	5	5500	Estimate for additional injection testing equipment, crew and analysis
Total Completion costs	325,632.76				
Total well cost, 5% contingency	1,321,453				



UNIVERSITY OF
CALGARY

Energy &
Environmental
Systems

EES

iseee



Energy and Environmental Systems Group

Institute for Sustainable Energy, Environment and Economy (ISEEE)

Geomechanical Analysis

Wabamun Area CO₂ Sequestration Project (WASP)

Author

Runar Nygaard

Rev.	Date	Description	Prepared by
1	January 8, 2010	Geomechanical Analysis	Runar Nygaard

Table of Contents

INTRODUCTION.....	5
1. DOWN HOLE GEOLOGICAL MODEL.....	5
2. IN-SITU STRESS	7
2.1 In-situ Stress Methodology.....	7
2.2 WASP In-Situ Stress Field	7
3. GEOMECHANICAL ROCK PROPERTIES	8
3.1 Methodology for Establishing Geomechanical Rock Properties	8
3.2 Table of Geomechanical Properties	11
4. IN-SITU STABILITY OF NISKU INJECTION HORIZON.....	12
5. CONCLUSIONS	14
REFERENCES.....	14

List of Tables

Table 1: WASP area stress gradients and stress orientations.	8
Table 2: Lithological dependant regression constants for UCS determination based on the sonic log correlation in Equation 5.	10
Table 3: Geomechanical properties for each Geomechanical Unit (GMU).	12

List of Figures

Figure 1: Downhole model shows the stratigraphic succession for the Wabamun Lake study area, from the Upper Devonian to the surface (from Haug et al, 2008).....	6
Figure 2: Vertical and least horizontal stress and pore pressure gradients (Michael et al, 2008).....	8
Figure 3: Correlations between unconfined compressive rock strength (UCS) and p-wave sonic travel time from wireline logs (Hareland and Hareland, 2007).....	11
Figure 4: Mohr Diagram of existing in-situ effective stress level in the Nisku formation and the corresponding failure envelope for the reservoir and caprock.....	13

INTRODUCTION

To minimize the potential for CO₂ leakage during and after injection, a geomechanical assessment must be performed to determine the potential for fracturing and faulting caused by the injection process. Potential CO₂ leakage paths can be controlled using geomechanical parameters, such as in-situ stress, rock stiffness and rock strength. It can also be controlled by sealing the top of the formation. When selecting a storage site, major existing faults and fractures should be avoided and proper injection procedures should be followed to reduce the likelihood of CO₂ leakage.

The first phase of the geomechanical assessment was to establish the properties of the formation, including rock stiffness and rock strength, as well as determining the in-situ conditions. The second phase of the assessment was to perform numerical analyses using the findings from the first phase. Those findings have been provided in the Geomechanical Modelling section of this report.

The purpose for studying the geomechanical properties of the injection site is to ensure seal integrity during and after CO₂ injection. To conduct a geomechanical characterization, we need to obtain stress and pressure information and geomechanical information, such as strength and deformation properties of the injection horizon and caprock.

In this project, no new wells were drilled and therefore no recently captured and undisturbed cores were available for geomechanical testing. It was therefore decided to base the geomechanical characterization on data obtained from downhole logging tools. This approach is a well established method used in the oil and gas industry. The characterization of rock properties for this area was recently studied by Haug et al (2008), and this report is an expansion of that work. In-situ stress has also been extensively studied for the area, so no new significant data was available for the project. Therefore, the in-situ stress analysis is based on previously published material for the area.

1. DOWN HOLE GEOLOGICAL MODEL

The geological study of the Nisku formation defined the site as a likely injection horizon for CO₂ and as a result, the geomechanical work concentrated on establishing the properties of the Nisku aquifer formation and identified aquitards (non-flowing) formations higher in the subsurface. Figure 1 shows the stratigraphy in the Wabamun Lake area above the Nisku formation. The sedimentary succession is divided by the thick Colorado Group shale aquitard and two main hydrostratigraphic groups—the Upper Devonian-Lower Cretaceous and the post-Colorado. Each major group contains several aquifers and intervening aquitards. The Nisku Formation is part of the Upper Devonian-Lower Cretaceous hydrostratigraphic group and is capped by the overlying Calmar formation aquitard.

The Nisku formation is on average 72 metres thick and typically ranges from approximately 60 to 98 metres, but thins to less than 40 metres in the northwest. It is capped by the Calmar Formation shale ranging in thickness from 5 to 15 metres. The caprock is overlain by the upper Devonian-Lower Cretaceous aquifers (> 500 metres). Ultimately, the thickness of the Colorado and Lea Park aquitards (> 500 metres) above them would act as a final barrier to any vertically migrating CO₂. The Devonian-Lower Cretaceous aquifer system, however, contains several oil and gas field in the area. To prevent CO₂ from migrating towards existing petroleum production, it is important to determine if the Calmar may be breached during or after injection.

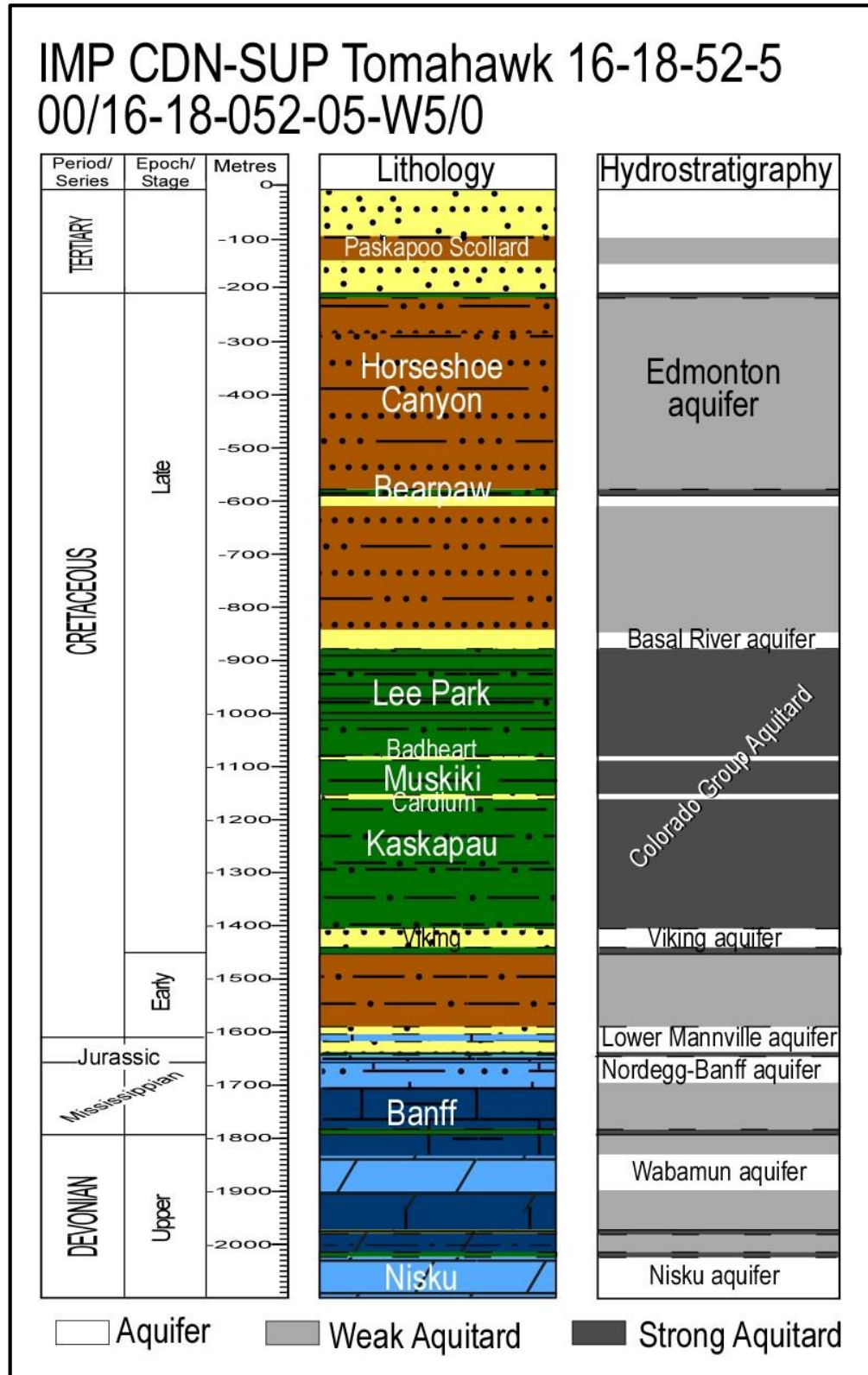


Figure 1: Downhole model shows the stratigraphic succession for the Wabamun Lake study area, from the Upper Devonian to the surface (from Haug et al, 2008).

2. IN-SITU STRESS

2.1 In-situ Stress Methodology

In the subsurface, the underground formation has to carry the weight of the overlying rock. The vertical stress (S_v) at any point in the underground is equivalent to the weight of the overburden. Integration of a bulk density log conducted while the well was logged after it was drilled provides the vertical stress at depth (D), with the stress derived from the formula:

$$S_v = \int \rho_b(z)gz \quad [1]$$

where $\rho_b(z)$ is the bulk density of the fluid-saturated rock, which changes with the depth according to the density logs. The gravity constant is g . In most wells there is an upper interval that is unlogged, and an average density for the rock in this unlogged interval has been assumed. Since the rock is porous, it will be filled with fluids. The fluid pressure can be calculated similar to the equation for vertical stress, but instead integrating fluid density.

The z -axis in the equation above is vertical with $z = 0$, which corresponds to the earth's surface. Since there is no shear stress acting at the surface, the vertical stress is one of the principal stresses (when the earth surface is completely flat). The stress in the underground consists of three mutually orthogonal principal stresses with two horizontal and oriented 90° apart. The two horizontal stresses often deviate in magnitude from each other with the largest horizontal stress denoted as SH_{max} and the least horizontal stress SH_{min} . Due to geological events, such as tectonic activity and push from mountains, the SH_{max} (as well as SH_{min}) can be larger than the vertical stress.

The minimum horizontal stress magnitude can be evaluated using a variety of tests. The most accurate method for determining SH_{min} is through micro-fracture testing, where a wellbore is carefully fractured by injecting fluids into a small portion of the open hole. Mini-fracturing, leak-off tests and fracture breakdown pressures can also be used to estimate the horizontal stress (Bell, 2003; Bell and Bachu, 2003). Estimating the minimum horizontal stress (SH_{min}) in a well provides the lower limit of the fracturing pressure and puts a limit on the allowable injection pressure in a well.

The SH_{min} orientation can be determined from borehole breakouts, which are spalled cavities that occur on opposite walls of a borehole in the SH_{min} orientation, or from tensile fractures with orientation parallel to the SH_{max} (Bell, 2003).

2.2 WASP In-Situ Stress Field

The reported S_v gradient in the area is 23 kPa/m (see Figure 2). The average gradient SH_{min} in the Wabamun Lake study area is 20 kPa/m (Michael et al, 2008). These two stress gradients (S_v and SH_{min}) provide loose lower and upper bounds for the fracturing pressure gradient, which was generally found to be ~ 19 kPa/m for the entire Alberta basin (Bachu et al, 2005).

The direction of SH_{min} was approximately 145° in a general southeast-northwest direction. This means that fractures will form and propagate in a vertical plane in a southwest-northeast direction ($\sim 55^\circ$), essentially perpendicular to the Rocky Mountain deformation front. Regional scale studies of the stress regime indicate that in south and central Alberta, vertical stress (S_v) is the largest principal stress and is greater than the maximum horizontal stress (SH_{max}) (Bell and Bachu, 2003).

Since the reported breakouts have a distinct orientation, $S_{H_{max}}$ will be higher than the horizontal stress. These two data points constrain $S_{H_{max}}$ at a value higher than 20, but lower than 23 kPa/m, which roughly corresponds to a value of around 21 to 22 kPa/m.

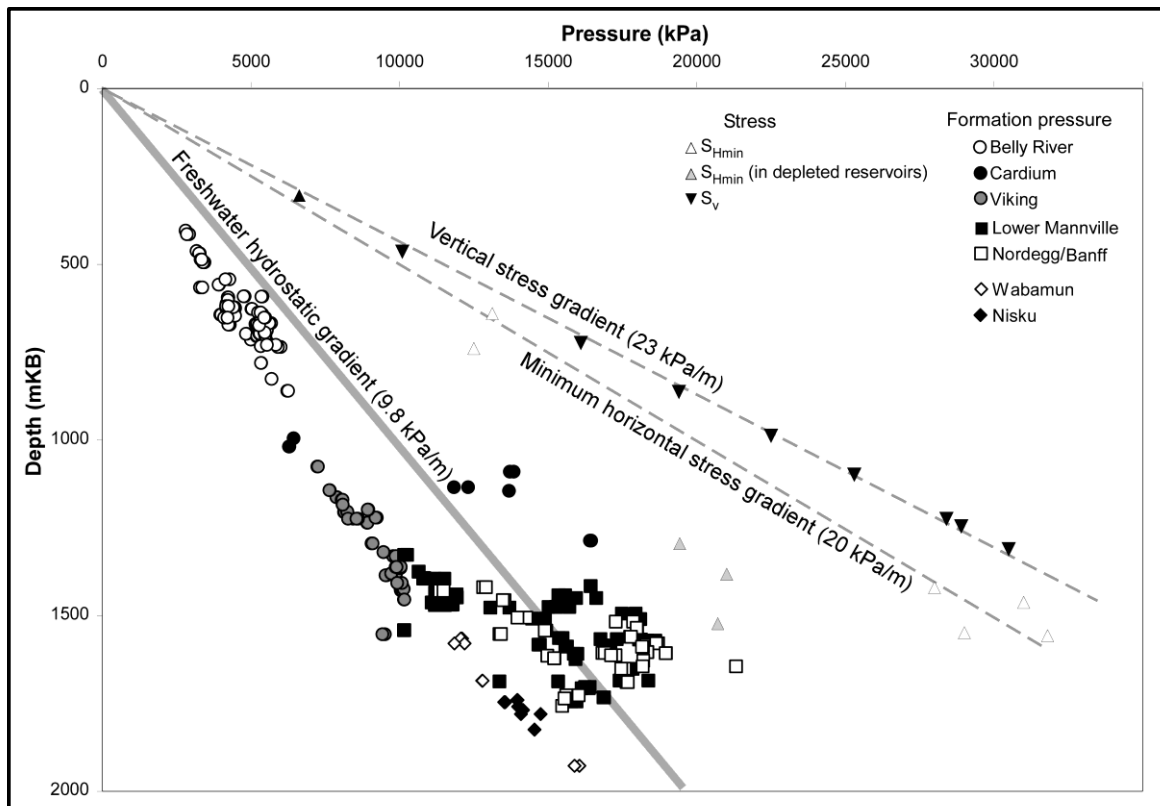


Figure 2: Vertical and least horizontal stress and pore pressure gradients (Michael et al, 2008).

Table 1: WASP area stress gradients and stress orientations.

	Vertical Stress (MPa/km)	Largest Horizontal Stress (MPa/km)	Least Horizontal Stress
Magnitude	23	~ 22 (20–23)	20
Orientation	Vertical	55° (NE)	145° (SE)

3. GEOMECHANICAL ROCK PROPERTIES

3.1 Methodology for Establishing Geomechanical Rock Properties

In this project there were no new wells drilled, and therefore no recently captured and preserved core samples to evaluate. As a result, the geomechanical characterization study was based on data obtained from downhole logging tools. The geomechanical characterization of rock properties in this area was recently studied by Haug et al (2008). This report expands on this previous work.

The most comprehensive and accurate method for establishing geomechanical information on the strength and deformation of a material is by conducting rock mechanical laboratory tests of the preserved core material. Core material is hard to find for most overburden formations and water-

filled reservoirs. This is especially true in the early phases of a storage project, where localization has not been finalized and detailed engineering work not yet started. However if laboratory tests are performed, they only represent a single point in a formation without taking into account spatial variations in geomechanical parameters. This means that indirect measurements of these properties will have to be used to obtain rock strength and deformation properties. This approach is a well-established method used in the oil and gas industry for similar types of analyses, such as caprock integrity, wellbore stability and sand production.

With a lack of laboratory measurements for deformation properties, the properties will have to be obtained from well logs. Dynamic elastic properties, such as Poisson's ratio and Young's modulus, can be calculated using wireline logs. The Poisson's ratio and Young's modulus are determined from P- and S-wave velocity (sonic) and density logs. The dynamic Poisson's ratio (ν_d) is calculated from the relationship between the P-wave velocity (V_p) and S-wave velocity (V_s) as:

$$\nu_d = \frac{V_p^2 - 2V_s^2}{2(V_p^2 - V_s^2)} \quad [2]$$

The Elastic Young's modulus can be calculated from velocity and rock density logs based on:

$$E_d = 2\rho * V_s^2 (1 - \nu_d) \quad [3]$$

where E_d is dynamic Young's modulus (GPa), ρ is rock density (g/cm^3), V_s is shear velocity and ν_d is dynamic Poisson's ratio calculated based on Equation 2. Dynamic Poisson's ratio is a good approximation to the static dynamic modulus. However in a velocity measurement, the strain rate varies from about 10^{-2} to 10^{-4} s^{-1} and has a maximum strain of 10^{-6} while rock mechanical tests, which measure static deformation properties, are conducted at a strain rate of 10^{-2} s^{-1} and a maximum strain of 10^{-2} . The variation in strain and strain rate causes the moduli calculated using dynamic measurements to be higher than moduli calculated based on static measurements conducted in a laboratory. Based on the following correlation from Haug et al (2008) between unconfined compressive strength (UCS) and static Young's module:

$$E_s = 111 * UCS^{1.2} \quad [4]$$

where E_s is static Young's module (in GPa) and UCS (in MPa) is the ratio between dynamic and static Young's module. The ratio was determined to be 2.7:1, and the conversion factor was used for all formations to convert dynamic to static Young's module values. The bulk modulus, which is a function of Poisson's ratio and Young's module, is reported as well.

Two distinctly different modes can cause rock to fail. One is when the stress on the rock reaches the critical limit in tension and the rock is pulled apart (e.g., during hydraulic fracturing of a wellbore), and the second is when shear stress is above a critical level and a shear plane is created. The critical limit for tensile failure is tensile strength, and the critical limit for shear strength is the cohesive strength or unconfined compressive strength. The unconfined compressive strength is the force required to break the rock when compressed without any side support.

The use of sonic velocity logs to determine unconfined compressive rock strength is well established. There exists several correlations between rock strength and sonic travel time or a combination of different logs (e.g., Kasi et al, 1983; Onyia, 1988; Hareland and Nygaard 2007; Andrews et al, 2007). Onyia (1988) conducted laboratory tri-axial compressive tests from different

lithologies to develop a continuous log-based rock strength based on wireline compressional sonic travel. The experimental relationship for calculating unconfined compressive strength that Onyia established is given in Equation 5:

$$UCS = \left(\frac{1.00}{k_1 (\Delta t_c - k_2)^{k_3}} \right) + k_4 \quad [5]$$

where Δt_c is travel time in $\mu\text{s}/\text{ft}$, UCS is sonic-based unconfined compressive, and k_1 , k_2 , k_3 and k_4 are lithology dependant constants (see Table 2). In this study we used correlations on limestone and dolomites from Onyia's work. For shales and sandstones, the unconfined compressive strength laboratory results and sonic log data from Hareland and Nygaard (2007) were used to derive the lithology dependant constants used in Equation 5. In addition to the shale and sandstone correlations, a combined (combo) shale and sandstone correlation was derived from the same dataset to be used for shaly sandstones and sand-rich shales. Gamma ray log readings were used to distinguish between the clastic lithologies, and the sandstone correlation was used for all gamma ray readings below 40 API units, shale correlation were used for all gamma ray readings above 110 API units, and the combined correlation was used for all readings in between.

Figure 3 shows the correlations between UCS and sonic travel time from wireline log data for the different lithologies. The correlations are derived based on rock mechanical tests with reported UCS values in the range of 8 to 120 MPa.

Table 2: Lithological dependant regression constants for UCS determination based on the sonic log correlation in Equation 5.

Lithology	Limestone	Dolomite	Sandstone	Shale	Combo
k1	8.07E-06	1.65E-04	2.48E-06	1.83E-05	1.34E-05
k2	23.87	0	23.87	23.87	23.87
k3	2	1	2.35	1.80	1.92
k4	0.014	20.99	0	0	0

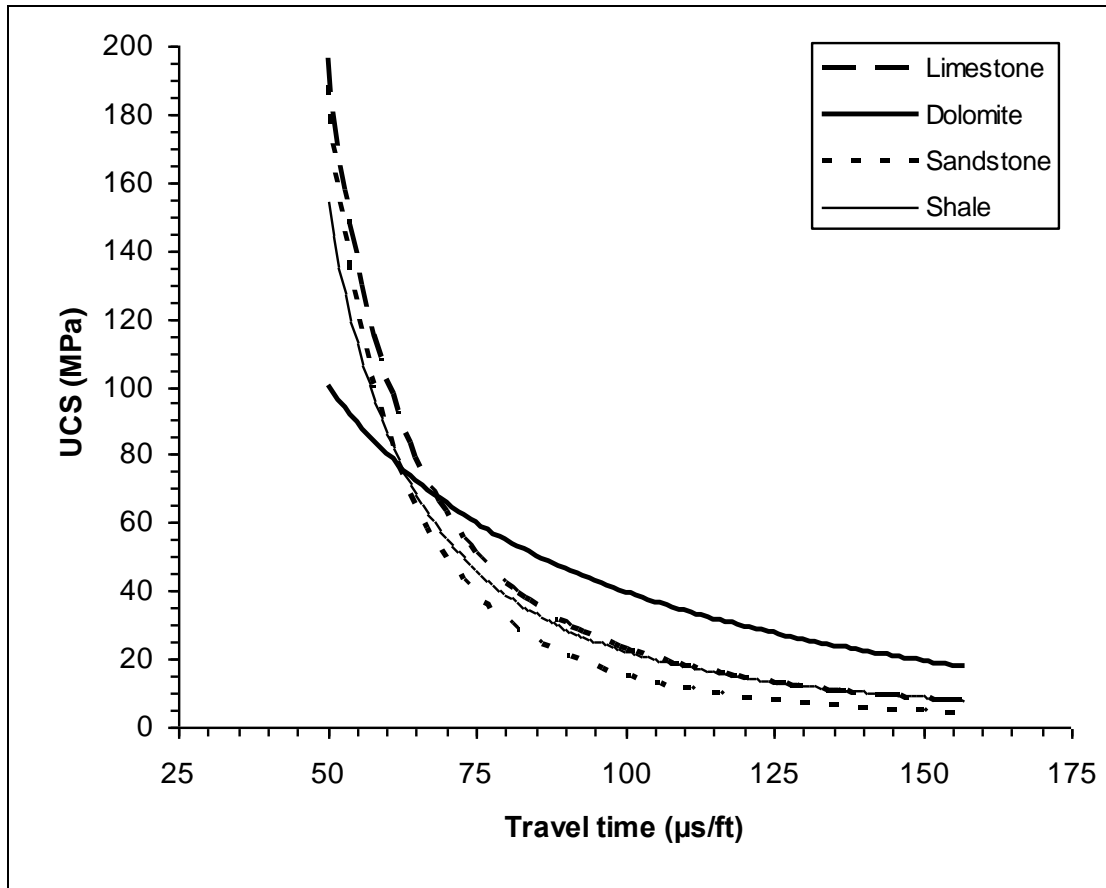


Figure 3: Correlations between unconfined compressive rock strength (UCS) and p-wave sonic travel time from wireline logs (Hareland and Hareland, 2007).

In the subsurface the rock has side support from horizontal stress, which makes the rock appear stronger in the subsurface due to the horizontal stress support. To determine the confined strength, tests can be conducted at different confining stress points with the test results plotted as a function of confining stress. From this a failure line can be drawn. The angle of this line is the failure angle. Another method is to report the failure data in Mohr-Coulomb failure criteria in shear stress and mean stress space where the failure line is determined by cohesion and friction angle. Both sets of values are reported.

3.2 Table of Geomechanical Properties

When characterizing the geomechanical properties of geological formations, the formations are combined into similar geomechanical units (GMU). This is done to reduce the amount of data that needs to be distributed into a geomechanical simulation at a later stage. It also helps reduce the complexity of the geomechanical model and computational time. The geological formations were combined when the lithology and geomechanical properties were of similar values. However the vertical resolution of each GMU was kept high enough so that the geomechanical properties were fairly constant with respect to depth within each GMU. The average value of the rock mechanical properties for each GMU is given in Table 3.

In Table 3 both dynamic and static Young's modulus and bulk modulus are reported, and the value of static moduli is significantly lower than the dynamic moduli. The reason for this difference is

because of the very different strain and strain rate the rock experiences in a tri-axial compressional test when compared to sonic log measurement. Similar behaviour may be expected for the dynamically measured Poisson’s ratio. However the effect is less for Poisson’s ratio, since the same difference will be observed for both vertical and horizontal strain measurements and will be negated when calculating Poisson’s ratio. However, the results show that relying on dynamic properties alone will under predict the deformation that will occur in the formations when they are subjected to changes in stress.

Table 3: Geomechanical properties for each Geomechanical Unit (GMU).

GMU	Dominant Lithology	Depth	Thickness	Young's Module STATIC	Young's Module Dynamic	Poisson's Dynamic	Bulk Module Static	Bulk Module Dynamic	UCS	Failure Angle	Tensile Strength	Cohesion	Friction
				GPa	GPa		GPa	Gpa	MPa	°	MPa		°
Upper Colorado	Sh	1209.7	129.4	6.7	18	0.33	6.5	17.6	26	61	2.2	6.7	17
Lower Colo.	Sh	1339.1	474.5	8.1	22	0.32	7.5	20.4	32	63	2.7	8.3	19
Viking	SS	1813.6	23.9	12.2	33	0.25	8.1	22.0	39	77	3.3	10.1	39
Joli Fou	SH	1837.5	17.0	8.5	23	0.30	7.1	19.2	33	64	2.8	8.5	20
Manville	SS	1854.5	124.2	10.7	29	0.30	9.0	24.2	39	77	3.3	10.1	39
Glauc. ss	SS	1978.7	22.3	15.2	41	0.29	12.1	32.5	65	65	5.4	16.8	21
Ostracod zone	SH	2001.0	4.5	16.3	44	0.29	12.9	34.9	69	71	5.8	17.9	29
Ellerslie	SS	2005.5	16.7	13.3	36	0.22	7.9	21.4	41	77	3.4	10.6	40
Nordegg	SH	2022.2	50.6	20.7	56	0.23	12.8	34.6	106	81	8.8	27.4	47
Banff	SH	2072.8	196.5	21.5	58	0.25	14.3	38.7	87	80	7.3	22.5	45
Exhaw	SH	2269.3	4.5	15.6	42	0.21	8.9	24.1	56	69	4.7	14.5	26
Wabamun	Ca	2273.8	225.0	27.4	74	0.28	20.8	56.1	103	81	8.6	26.7	47
Blueridge	Sh	2498.8	29.4	29.3	79.0	0.29	23.2	62.7	107	75	8.9	27.7	36
Calmar – Shale	Sh	2528.2	8.0	24.8	67.0	0.27	18.0	48.6	100	75	8.3	25.9	35
Calmar Dolo-shale	Sh	2536.0	5.0	24.8	67.0	0.27	18.0	48.6	160	79	13.3	41.4	43
Nisku tight	Ca	2541.3	85.9	28.9	78.0	0.29	22.9	61.9	200	84	16.7	51.8	53
Nisku high perm	CA.			16.7	45.0	0.29	13.2	35.7	80	80	6.7	20.7	45

4. IN-SITU STABILITY OF NISKU INJECTION HORIZON

The current in-situ effective stresses for the Nisku formation is plotted as a Mohr circle in Figure 4. The effective vertical stress is approximately 26 MPa and the effective horizontal stress is approximately 20 MPa. The corresponding shear stress is low at around 3 MPa (the peak value at the Mohr circle), and the corresponding effective normal stress is 23 Mpa. Shear failure will occur when the Mohr circle intersects the failure line. Any Mohr circle below the failure line indicates a stable condition. From the graph we can also see the porous portion of the Nisku formation has a

lower failure strength than the Calmar caprock. That will help in arresting any shear fractures occurring in the porous parts from propagating through the harder Nisku and Calmar caprock.

When injection starts, the effective stresses will be reduced and the in-situ stress Mohr circle will move to the left. It is very unlikely that shear fracturing will occur during injection. The most likely scenario will be the creation of tensile hydraulic fractures, but as long as the injection pressure is kept below the lowest horizontal stress, it is unlikely that tensile fractures will occur. Since the geological model indicates that the lower portion of the Nisku is the most porous and the upper more competent parts have a higher tensile strength, any fractures will unlikely be able to migrate upwards. Since the Calmar formation is more competent than porous, it is unlikely that fractures will extend into the harder Calmar formation. This may cause hydraulic fracturing to be an attractive option to increase injectivity in the Nisku formation. However this does not consider the effect of thermal contraction in the rock caused by the injected CO₂ when its temperature is lower than the reservoir temperature. The cooling effect will reduce the least horizontal stress gradient in the cooled area, which will reduce the fracture gradient and increase the likelihood for vertical fractures to occur. Creating new shear fractures is still unlikely, since even at zero effective horizontal stress the Mohr circle in Figure 4 will not intersect any of the shear failure lines. The likelihood of fracturing the caprock due to thermal stresses is addressed in the Geomechanical Modelling and Analysis section.

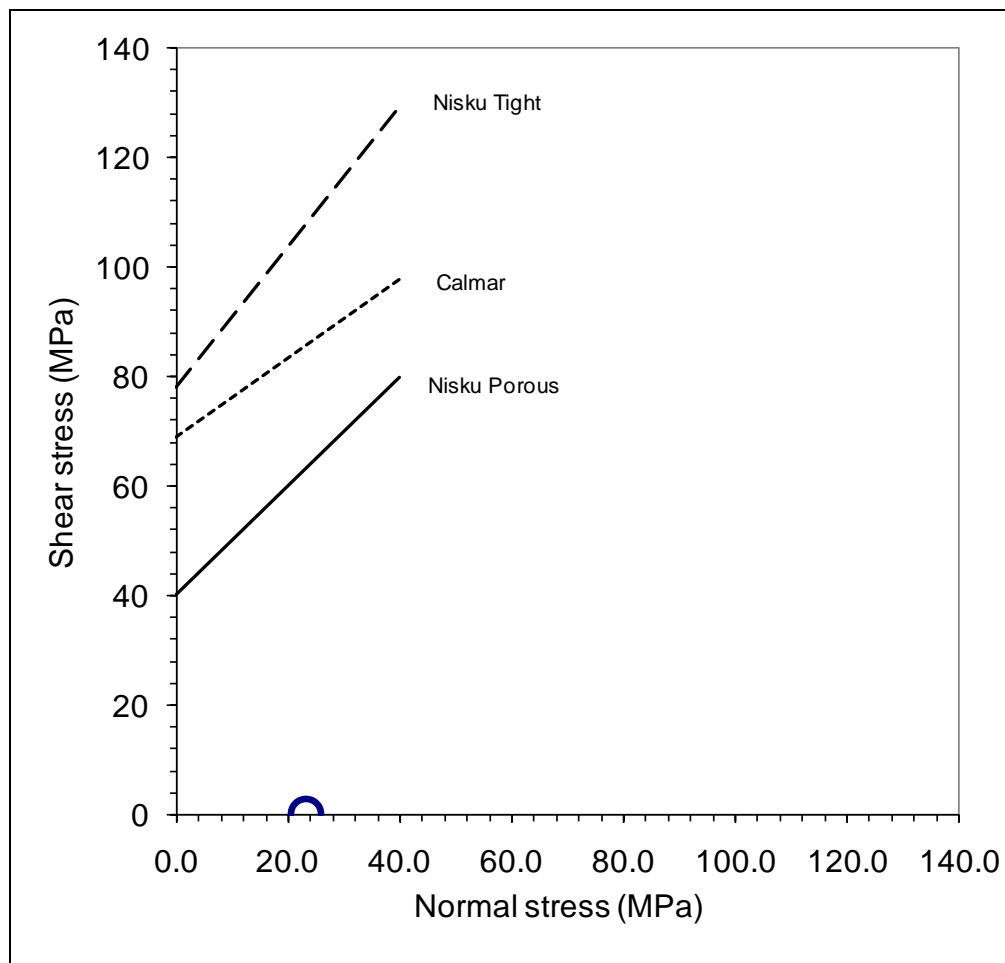


Figure 4: Mohr Diagram of existing in-situ effective stress level in the Nisku formation and the corresponding failure envelope for the reservoir and caprock.

5. CONCLUSIONS

In-situ stress characteristics for the subsurface of the Wabamun CO₂ storage area were established using existing analyses to provide guidance for maximum injection pressure, and to act as boundary conditions for further geomechanical modelling efforts.

A table of geomechanical properties for the subsurface of the Wabamun CO₂ storage area was established. Well logs were used to establish dynamic deformation properties (Young's modulus, Poisson's ratio, and bulk modulus) and correlations were used to determine static deformation properties. The unconfined compressive strength (UCS) was established for each lithology based on correlations with log properties. The database that was created was used as input for the geomechanical modelling.

The lower sedimentary succession with the Nisku aquifer and Calmar caprock is very competent and stiff rock.

A few laboratory tri-axial tests are recommended in the future to confirm the accuracy of the UCS correlations for this specific site and to adjust the dynamic-to-static conversion factors.

REFERENCES

- Andrews, R., Hareland, Nygård, R., G., Engler, T. & Virginillo, B. Method of using logs to quantify drillability, Presented at; SPE Rocky Mountain Oil and Gas Technology Symposium, 16–18 April 2007, Denver, Colorado USA.
- Bell, J. S., 2003, Practical methods for estimating in-situ stresses for borehole stability applications in sedimentary basins: *Journal of Petroleum Science and Engineering*, v. 38, no. 3-4, p.111–119.
- Bell, S.J. and S. Bachu 2003, In-situ stress magnitude and orientation estimates for Cretaceous coal-bearing strata beneath the plains area of central and southern Alberta: *Bulletin of Canadian Petroleum Geology*, v. 51, p. 1–28.
- Hareland, G., Nygård, R. 2007, Calculating unconfined rock strength from drilling data, Accepted in; 1st Canada-U.S. Rock Mechanics Symposium, 27–31 May 2007, Vancouver, British Columbia, Canada.
- Kasi, A. Zekai, S. & Bahsa-Eldin, H., 1983. Relationship between Sonic Pulse Velocity and Uniaxial Compressive Strengths of Rocks. *Proc. Of the 24th U.S. Symp. On Rock. Mech. Texas A&M University*, 20–23 June 1983, TX, US: 409–419.
- Michael, K., Bachu, S., Buschkuehle, M., Haug, K., and S. Talman. in press. *Comprehensive Characterization of a Potential Site for CO₂ Geological Storage in Central Alberta, Canada*, AAGP Special Publication on Carbon Dioxide Sequestration.
- Onyia, E.C., 1988. Relationships Between Formation Strength, Drilling Strength, and Electric Log Properties. 63rd Ann. Tech. Conf. Houston, 2–5 October 1988, TX, USA. SPE 18166.



UNIVERSITY OF
CALGARY

Energy &
Environmental
Systems

EES

iseee



Energy and Environmental Systems Group
Institute for Sustainable Energy, Environment and Economy (ISEEE)

Geomechanical Modelling and Analysis

Wabamun Area CO₂ Sequestration Project (WASP)

Authors

Somayeh Goodarzi

Dr. Antonin (Tony) Settari

Rev.	Date	Description	Prepared by
1	September, 2009	Geomechanical Modelling and Analysis	Somayeh Goodarzi Dr. Antonin (Tony) Settari

Table of Contents

BACKGROUND	5
1. INTRODUCTION	5
2. OBJECTIVES	6
3. THE WASP MODEL	6
3.1. Model Geometry.....	6
3.2. The Flow Model.....	8
3.3. Geomechanical Properties	10
4. RESULTS—ISOTHERMAL INJECTION WITHOUT CONSIDERATION OF FRACTURING	12
4.1. Stress Changes and Displacement Pattern	13
4.2. Stress variation with pore pressure changes	14
4.3. Shear Failure.....	16
4.4. Sensitivity Analysis.....	19
5. RESULTS—ISOTHERMAL INJECTION CONSIDERING FORMATION FRACTURING	20
5.1. Modelling Fracture Propagation	20
5.1.1 Transmissibility multipliers	21
5.1.2 Porosity Multiplier	23
5.2. Results of Injection at 2 Mton/yr Allowing Fracture Propagation	23
6. THERMAL EFFECTS	25
6.1. Thermal Effects for Injection Below Fracturing Pressure.....	26
6.2. Thermal Effects on Dynamic Fracturing.....	27
7. CONCLUSIONS	29
8. RECOMMENDATIONS	30
9. REFERENCES	31

List of Tables

Table 1: Input rock mechanical properties.	11
Table 2: Cohesion and friction angle for geomechanical model.	18
Table 3: Thermal properties of fluid and rock.	25

List of Figures

Figure 1: Plan-view of the pressure (kPa) distribution at the middle of Nisku aquifer after 50 years of injection.	7
Figure 2: Brine-CO ₂ relative permeability curves for Nisku carbonate aquifer (from Bennion and Bachu, 2005).	8
Figure 3: Solution Gas (CO ₂) Water Ratio for Nisku carbonate aquifer.	9
Figure 4: CO ₂ saturated Water Formation Volume Factor for Nisku carbonate aquifer.	9
Figure 5: CO ₂ Formation Volume Factor.	10
Figure 6: Stress profile from Alberta Geological Survey database.	11
Figure 7: Lithology and principal stress directions in Wabamun area. The yellow dotted boundary line shown on this diagram illustrates the edges of the porous and permeable regions of the Nisku Aquifer. The red box is the WASP project region (Mossop and Shetsen).	12
Figure 8: Vertical Displacement (metre) at ground surface after 50 years of injection at 1Mton/yr below fracture pressure.	13
Figure 9: X-Direction Displacement (metre) at Reservoir's top layer after 50 years of injection at 1Mton/yr below fracture pressure (see Figure 7 for orientations of the x and y directions).	13
Figure 10: Y-Direction Displacement (metre) at Reservoir's top layer after 50 years of injection at 1Mton/yr below fracture pressure.	14
Figure 11: Variation of horizontal stresses versus pressure. x and y in the regression equations represents the pressure and horizontal stresses respectively.	15
Figure 12: Mohr Coulomb Diagram.	16
Figure 13: Stress level at Nisku's middle layer after 50 years of injection of 1Mton/yr below fracture pressure. Stress level which shows the closeness of the formation rock to shear failure, varies between 0 and 1.	18
Figure 14: Mohr Coloumb Criteria for Nisku aquifer layer.	19
Figure 15: Sensitivity analysis for rock cohesion value—stress level at the wellbore as a function of rock cohesion.	20
Figure 16: Induced fracture plane.	21
Figure 17: x-Direction permeability multiplier as a function of net pressure.	22
Figure 18: Vertical permeability multiplier as a function of pressure.	22
Figure 19: Incorporated porosity multiplier function.	23
Figure 20: Vertical surface displacement (metre) after 50 years of isothermal CO ₂ injection of 2Mton/yr allowing fracture initiation and propagation in the Nisku aquifer.	23
Figure 21: Gas saturation after 50 years of isothermal CO ₂ injection at 2Mton/yr allowing fracture initiation and propagation.	24
Figure 22: Magnified picture of gas saturation after 50 years of isothermal CO ₂ injection of 2Mton/yr allowing fracture initiation and propagation.	25
Figure 23: Minimum stress and pressure history for thermal and isothermal model, in the case of injection of 1Mton/yr below fracture pressure.	26
Figure 24: Surface displacement for thermal and isothermal model, for the case of injection of 1Mton/yr below fracture pressure.	27
Figure 25: Gas saturation at well block cross section for thermal model.	28
Figure 26: Comparison of fracture propagation pressure for isothermal and thermal model.	29

BACKGROUND

Large stationary CO₂ emitters are located in central Alberta with cumulative annual emissions in the order of 30 Mt CO₂. This includes four coal-fired power plants in the Wabamun Lake area, southwest of Edmonton with emissions between 3 and 6 Mt/year. Although significant CO₂ storage capacity exists in depleted oil and gas reservoirs in this area, these may not be available in the near future because most of these reservoirs in the Wabamun lake area are still producing. Moreover, the large Pembina Cardium oil fields, located just south of the Wabamun Lake area, now producing as mature waterfloods, are in the initial stages of investigating possible use of CO₂ as a miscible flooding agent to further enhance oil recovery. Commercial scale use of CO₂ for this purpose is still a few years away and until then these pools will require only pilot scale volumes of CO₂ for EOR reservoir characterization and test purposes. As a result, CO₂ storage in deep saline aquifers is the most likely near future scenario for large scale CO₂ sequestration. While it is certainly possible to move CO₂ from the Wabamun area to distant storage locations, it is of considerable interest to public policy makers to determine if very large scale storage is feasible in the immediate vicinity of the power plants.

The study will perform a comprehensive characterization of large-scale CO₂ storage opportunities in the Wabamun Lake area and to analyze any potential risks. As a benchmark, the project will examine the feasibility of storing 20 Mt-CO₂/year for 50 years within a study area of 60 km by 90 km in the Wabamun area. This Gigaton-scale storage project is one to two orders of magnitude larger than the commercial projects now under study. It will fill a gap between the province-wide capacity estimates (which do not involve site specific studies of flow and geomechanics, etc.) and the detailed commercial studies of small CO₂ storage projects currently underway. Unlike the commercial projects, this study has been conducted as a public non-confidential project lead by the University of Calgary (Keith *and Lavoie*, 2008).

1. INTRODUCTION

Based on current sequestration pilot projects and enhanced oil recovery efforts, evidence suggests that geologic sequestration is a technically viable means to significantly reduce anthropogenic emissions of CO₂. One of the most important concerns with respect to the long term CO₂ storage is that stress changes caused by injection could lead to the formation or reactivation of fracture networks and fault movements which could potentially provide pathways for CO₂ migration through previously impermeable rocks (Quintessa et al., 2007). A portion of injected CO₂ can escape the storage domain if the integrity of the seal rock is violated by geomechanical mechanisms such as fault reactivation, propagation of induced fractures or rock shear failure. In order to determine whether the stress state compromises the ability of the formation to act as an effective storage unit, a geomechanical assessment of the formation integrity must be carried out, by the means of coupled flow and geomechanical modelling. In recent decades there has been significant effort towards developing simulation techniques to model the aforementioned mechanisms for petroleum industry applications. The goal of this study is to further develop this simulation technology and modelling tools to model and understand the mechanisms and physics of the geomechanical effects occurring during or after CO₂ injection.

2. OBJECTIVES

The purpose of this report is to study the geomechanical effects of CO₂ injection in the Nisku aquifer located in Wabamun Lake area. The study utilized GEOSIM, a fully coupled reservoir flow and geomechanical model. GEOSIM is a commercial code of TAURUS Reservoir Solutions Ltd., which is available for research at University of Calgary under academic license.

The following major objectives are addressed in this report.

1. Study the stress variation and displacement pattern.
2. Examine the possibility of shear failure in reservoir and caprock layer.
3. Investigate the possibility of increasing well injectivity by injection at fracturing pressure, study fracture propagation and evaluate the risk of fracturing the caprock.
4. Incorporate thermal effects in the geomechanical model and determine the effects of cooling due to injection on stresses, displacements and fracture propagation.
5. Investigate the benefit of using production wells to crossflow to other zones in order to reduce average pressure increase.

The results can be then used, in conjunction with other work done in the WASP feasibility study, to define the optimum injection scenario in terms of technical and economical feasibility of the WASP project. In particular, the injection at fracturing conditions (i.e., propagating dynamic fracture during injection) and the use of production wells are novel ideas for increasing the efficiency of CCS.

3. THE WASP MODEL

3.1. Model Geometry

The model geometry and reservoir characterization was derived from the flow model built in reservoir simulation sub-task of the WASP study. Figure 1 shows the pressure distribution after 50 years of injection in the Nisku aquifer. Since the pressure plume is not extended to the north side of the aquifer and because the geomechanical effects strongly depend on pressure variation, the north side of the aquifer is not included in this study. The geomechanical model, which only included the area inside the red dashed rectangle (Figure 1), was superimposed on the updated flow model. The areal extent of the flow and geomechanical models is the same but the geo-model is extended in the vertical direction to model the caprock and the shallow layers up to the surface. The areal size of both models is $338,100 \times 119,340$ (m) and the vertical thickness of the flow and geo-model are 70 (m) and 1930 (m) respectively. The flow and geomechanical models consist of $97 \times 62 \times 4 = 24,056$ and $97 \times 62 \times 9 = 54,126$ grid blocks, respectively. The reservoir is represented by 4 layers, with the smallest layer at the top, in order to capture the CO₂ plume override. A detailed CO₂ placement study carried out in the reservoir simulation subtask of the WASP study shows that even more layers are required for high accuracy, but finer models were not possible at this stage due to very large computer requirements of the coupled model.

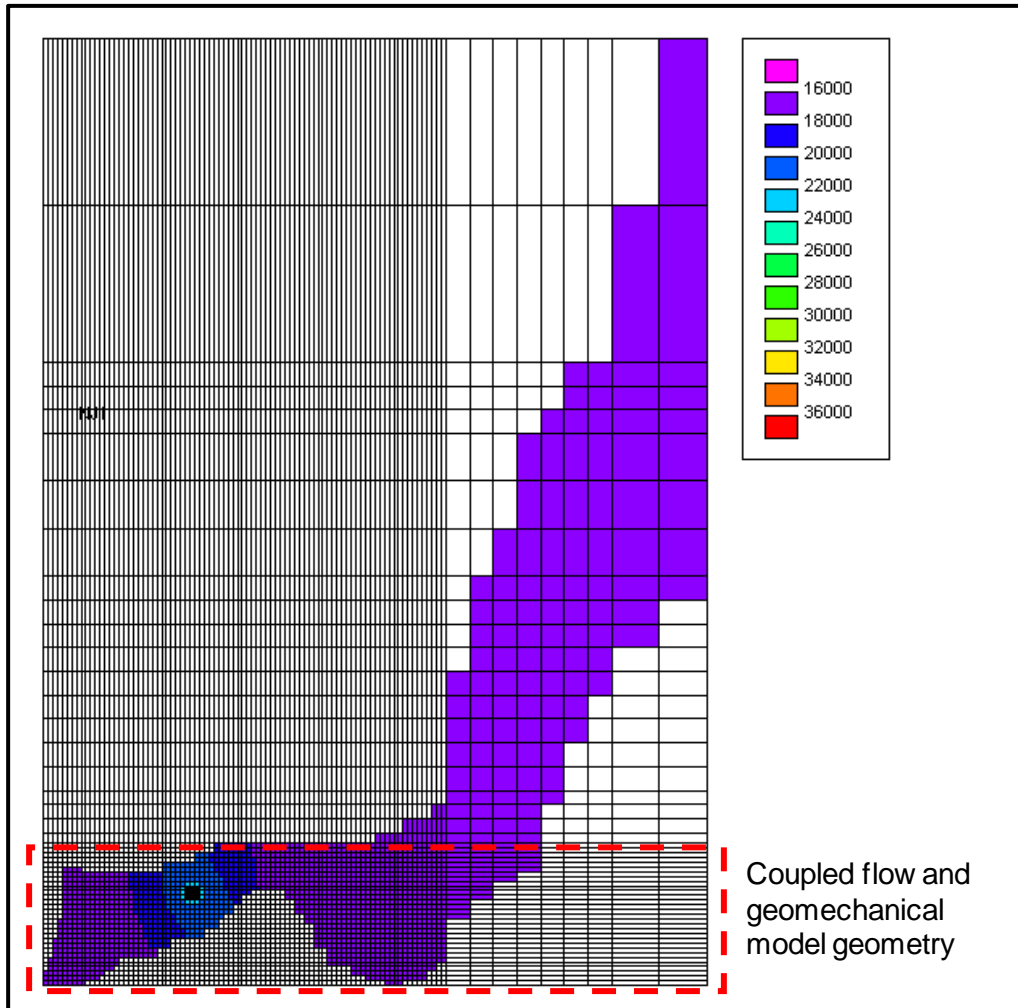


Figure 1: Plan-view of the pressure (kPa) distribution at the middle of Nisku aquifer after 50 years of injection.

3.2. The Flow Model

The water-gas relative permeability functions for the Nisku carbonate aquifer are derived from the experimental data published by Bennion and Bachu (2005) and are shown in Figure 2.

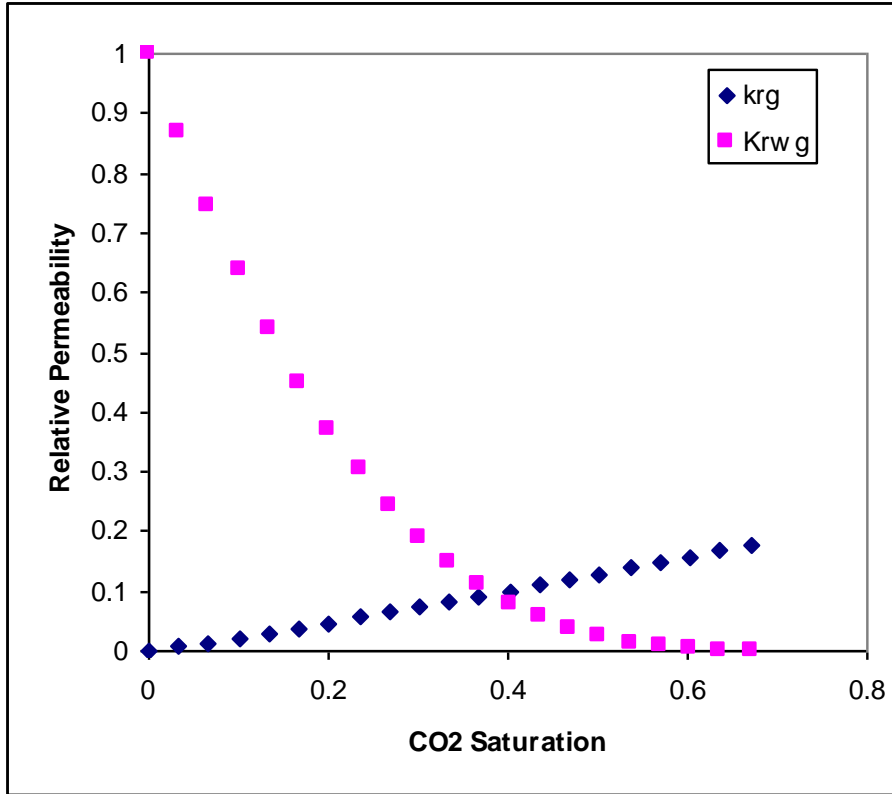


Figure 2: Brine-CO₂ relative permeability curves for Nisku carbonate aquifer (from Bennion and Bachu, 2005).

The PVT model is generated using the method developed by Hassanzadeh et al. (2007), which creates 2-component black oil PVT data for densities, solubility of CO₂ and viscosities. To generate the Nisku PVT data, formation temperature and water salinity level are estimated at 60 C and 190,000 ppm respectively (Hitchon, 1996). The PVT input data for the GEOSIM model is shown in Figures 3, 4 and 5.

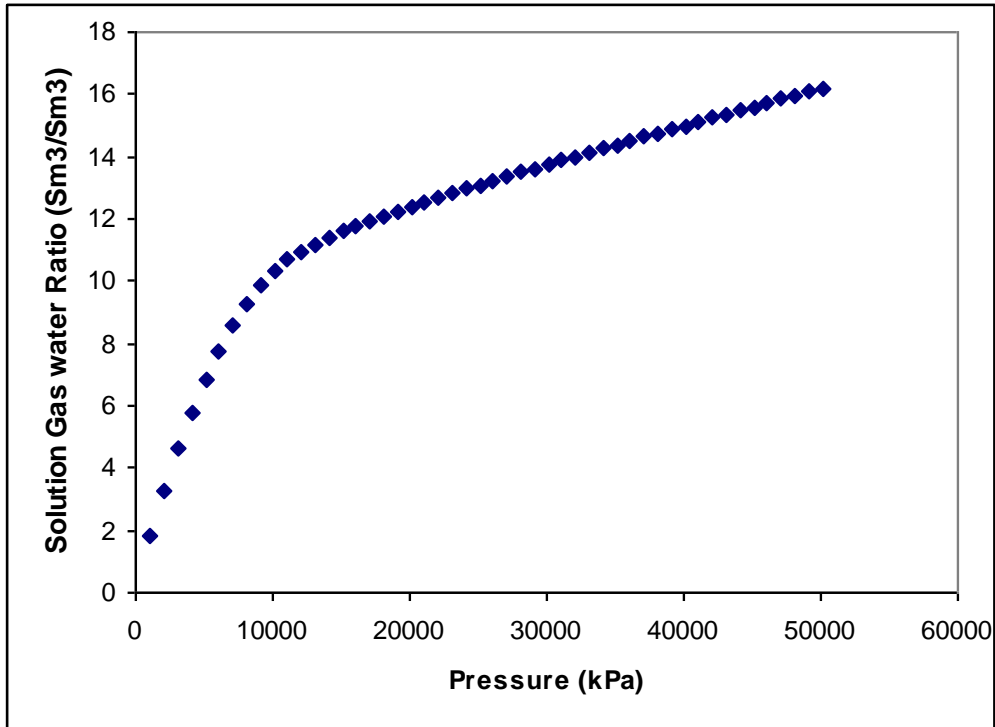


Figure 3: Solution Gas (CO₂) Water Ratio for Nisku carbonate aquifer.

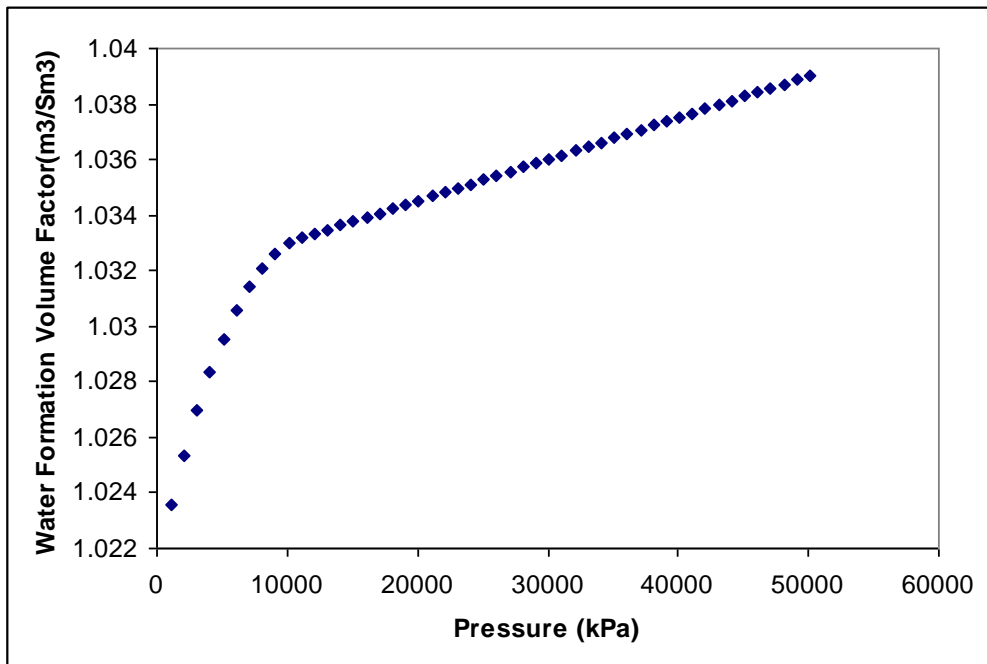


Figure 4: CO₂ saturated Water Formation Volume Factor for Nisku carbonate aquifer.

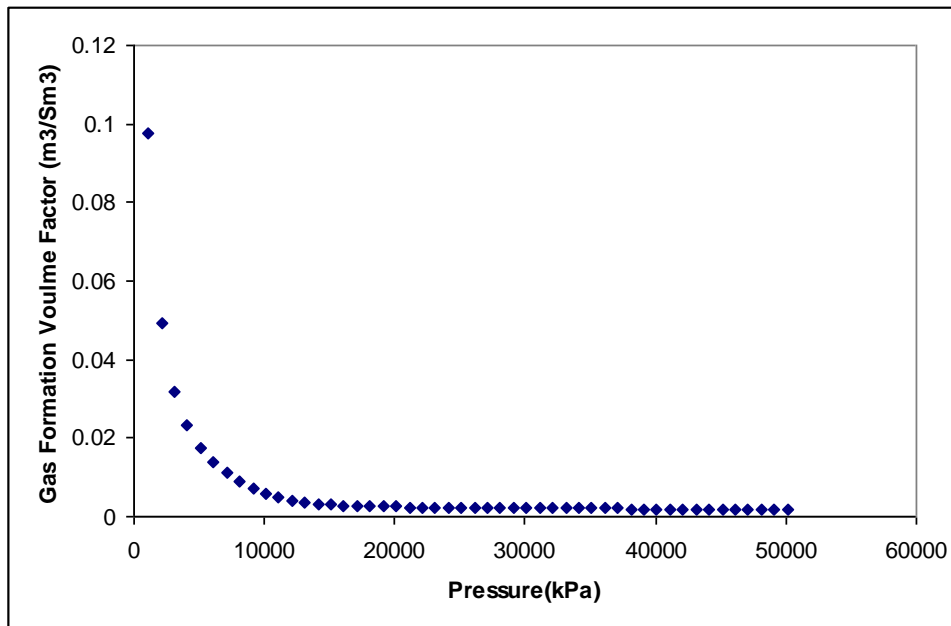


Figure 5: CO₂ Formation Volume Factor.

3.3. Geomechanical Properties

Geomechanical properties were available for the Nisku aquifer and the overlying geological layers up to 1200 m depth. Since the geomechanical input data were not provided for shallow layers with less than 1200 m depth, the remaining overburden was modelled as one layer. Its properties were obtained by extending the given properties of the topmost layer. Table 1 lists the input rock mechanical properties used for the target zone and the layers above it.

The initial distribution of stresses was assumed to have constant gradients for the S_{Hmax} (maximum horizontal stress), S_{Hmin} (minimum horizontal stress) and S_v (vertical stress) and is shown in Figure 6 (Michael et. al., 2008). The pore pressure gradient was considered equal to fresh water hydrostatic gradient. The maximum stress gradient was approximated to be in the range of 20-23 kPa/m. Due to normal faulting regime in Wabamun lake area, the maximum stress was assumed to be equal to the vertical stress. The direction of S_{Hmin} was approximately 145°, in a general southeast-northwest direction (Bell and Bachu). The stress directions are shown in Figure 7. Because of the lack of more detailed stress-strain data, linear elasticity was assumed in the simulation, with the parameters from Table 1.

The data in Table 1 have been provided by the Geomechanical Characterization group of the WASP team. The corresponding derivation method can be found in section 3 of this team's report. The mechanical properties were kept constant for each geological layer and layers with similar geological and geomechanical properties were lumped together. Therefore more spatial refinement is required in order to accurately represent the local rock properties and stress profile at particular well locations.

Table 1: Input rock mechanical properties.

Layers	Thickness (m)	Young's Modulus (kPa)	Poisson's Ratio	Thermal Expansion Coefficient (1/oC)	Grain Modulus (kPa)	Bulk Density (Kg/m ³)
Shale, surface-Joli Fou	1173.3	2.16E+07	0.32	1.51E-05	6.00E+07	2500
Sandstone, Ellerslie-Manville	167.7	3.17E+07	0.29	1.79E-05	7.00E+07	2500
Carbonate, Wabamun-Nordegg	476.6	6.52E+07	0.26	1.50E-05	8.00E+07	2500
Shale, Calmar	42.4	7.53E+07	0.28	1.76E-05	6.00E+07	2500
Carbonate, Nisku	70	6.15E+07	0.29	1.50E-05	8.00E+07	2500

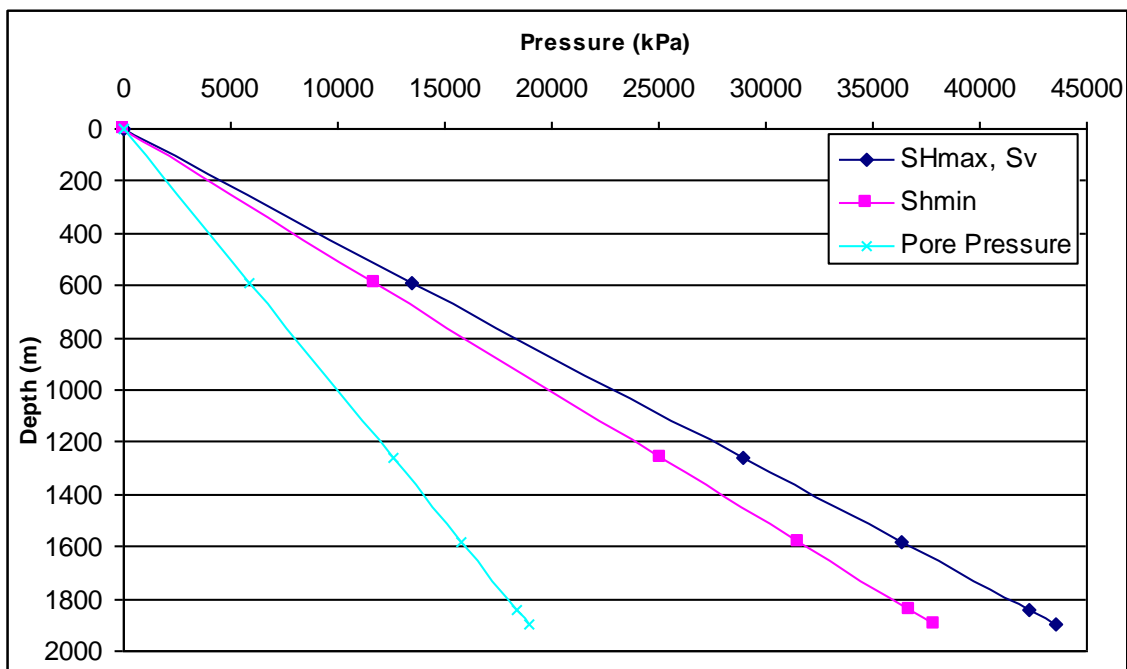


Figure 6: Stress profile from Alberta Geological Survey database.

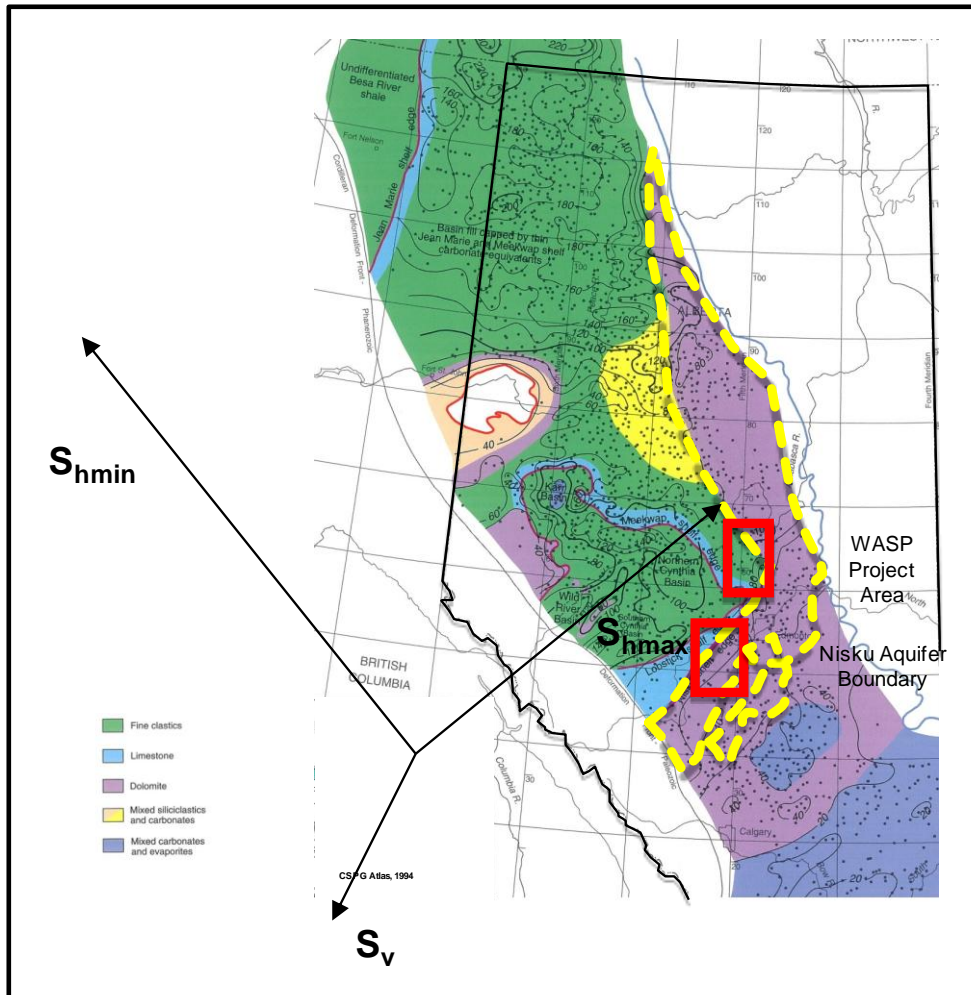


Figure 7: Lithology and principal stress directions in Wabamun area. The yellow dotted boundary line shown on this diagram illustrates the edges of the porous and permeable regions of the Nisku Aquifer. The red box is the WASP project region (Mossop and Shetsen).

4. RESULTS—ISOTHERMAL INJECTION WITHOUT CONSIDERATION OF FRACTURING

The first set of results presented is for the case when the injection pressure is limited by assumed fracturing pressure of 40 MPa and fracture propagation is not considered. The well in those models was injecting at a rate of 1 Mton/yr (=51,362 MScf/day). The limiting pressure was the same as in the work of the WASP group doing uncoupled flow modelling, to provide consistency between the results, and the reasoning for the choice of this value is presented elsewhere.

All the results in this Section are obtained using isothermal modelling (i.e., the injected CO₂ temperature equal to reservoir temperature). In Section 6 we will examine the effect of injecting cooler CO₂ which will dramatically affect the fracturing pressure.

4.1. Stress Changes and Displacement Pattern

As expected, after CO₂ has been injected in the Nisku aquifer, the formation will undergo deformations in all directions in order to place the injected volume. In this section the displacements in three different directions are presented.

At the end of injection, the maximum vertical displacement will reach ~4 mm at reservoir's topmost layer. As one travels from reservoir's topmost layer to the surface the value of the vertical displacement will decrease to ~2 mm. The extent of this decay in deformation depends on the mechanical properties of the overburden. The vertical displacement at the surface after 50 years of injection is shown in Figure 8. The magnitudes of displacements after this long-time injection are small and on the order of 1 millimetre.

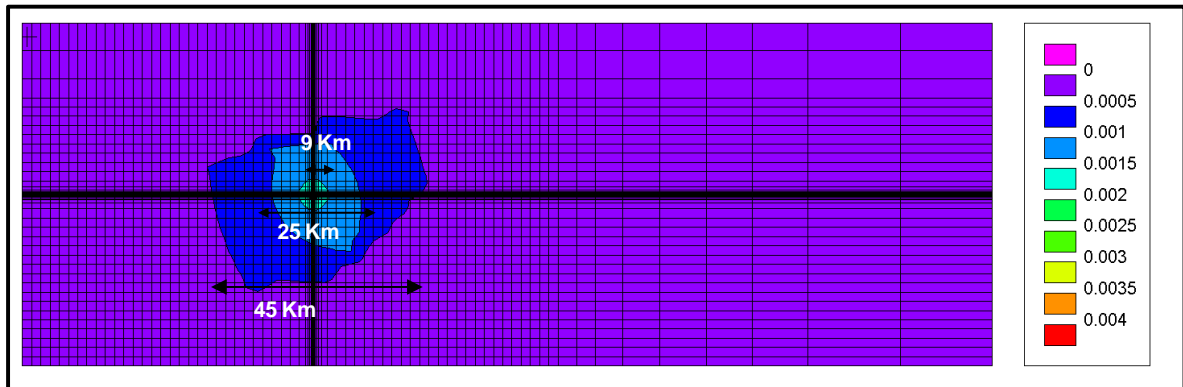


Figure 8: Vertical Displacement (metre) at ground surface after 50 years of injection at 1Mton/yr below fracture pressure.

The horizontal displacements of the reservoir layer are shown in Figures 9 and 10. Since the model is not symmetric around the wellbore in the x-direction, the horizontal displacement in this direction is not symmetric. However in y direction since the two boundaries has roughly the same distance to the wellbore, a symmetric pattern is observed.

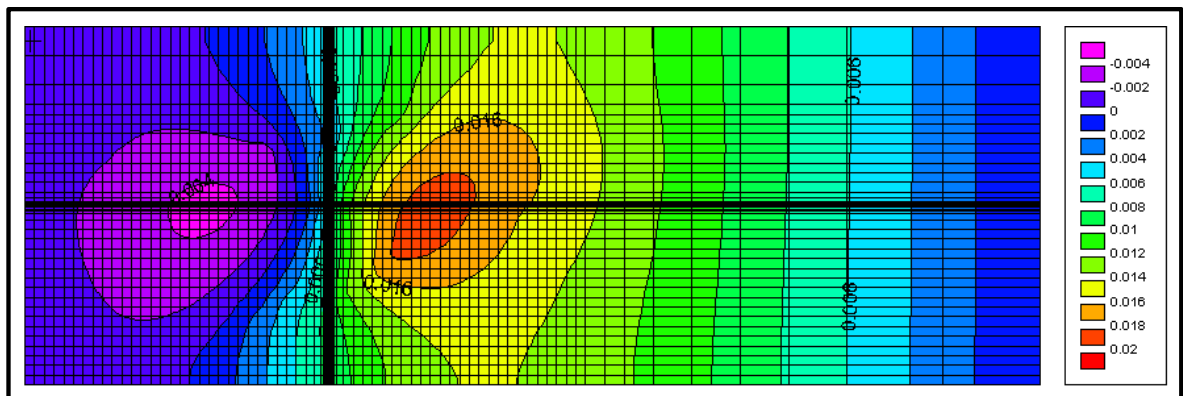


Figure 9: X-Direction Displacement (metre) at Reservoir's top layer after 50 years of injection at 1Mton/yr below fracture pressure (see Figure 7 for orientations of the x and y directions).

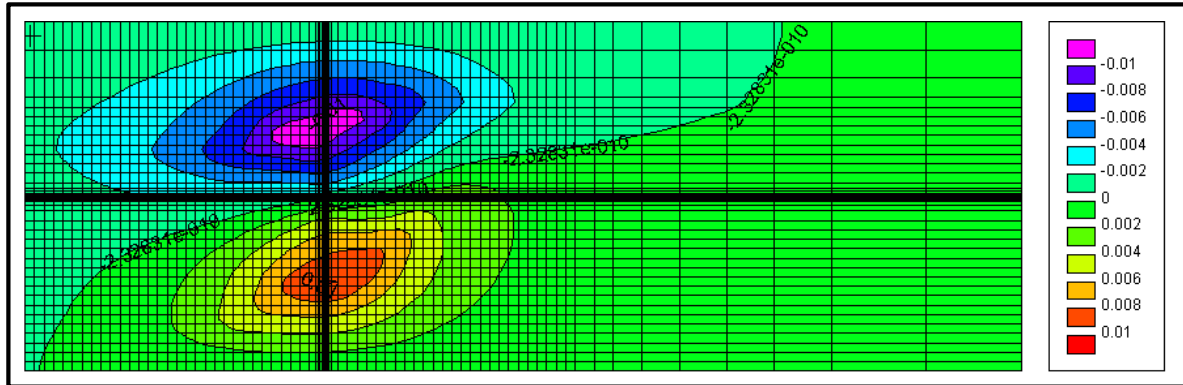


Figure 10: Y-Direction Displacement (metre) at Reservoir's top layer after 50 years of injection at 1Mton/yr below fracture pressure.

The results presented are preliminary and are based on the input mechanical properties and stresses as discussed in Section 3. The displacements are an important result of the simulation because they can be matched to the uplift, tiltmeter and other data and also be used for planning the location of instrumentation and improving the quality of input rock mechanical properties.

Also since the downhole tiltmeter measurements can identify where the pressure plume is, surface displacement measurements could be utilized to validate the flow model and determine the extent of pressure plume.

The measured magnitude of the deformations (vertical uplift) can be used to confirm system compressibility in the injection zone (important for injectivity) and possibly mechanical properties of the overburden.

4.2. Stress variation with pore pressure changes

The area around the well will gradually pressure up during the injection period. In order to study the effect of increased pore pressure on total stresses and to confirm the 1-D consolidation theory, the well block in Nisku's middle layer is considered for analysis. Figure 11 shows the horizontal stress variation with pressure for the well grid block in Nisku.

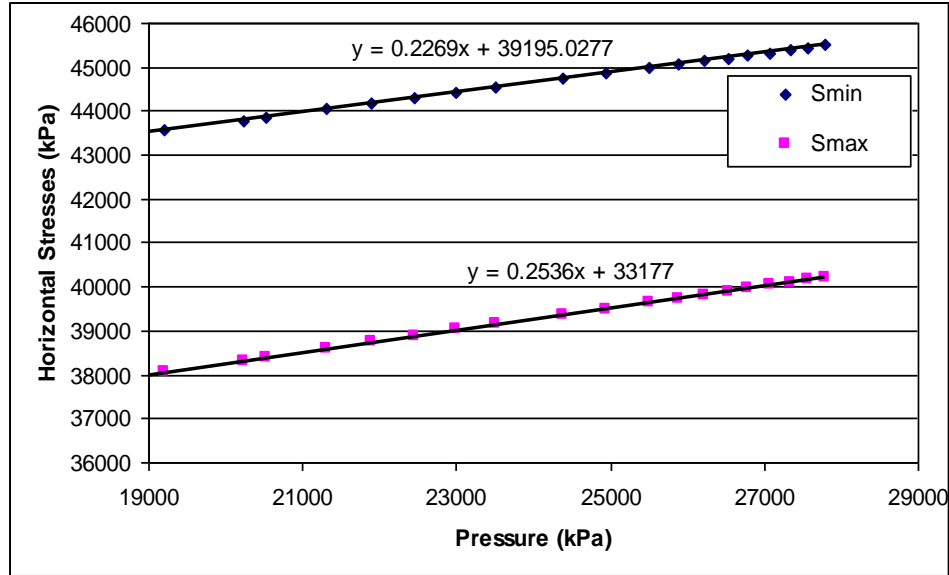


Figure 11: Variation of horizontal stresses versus pressure. x and y in the regression equations represents the pressure and horizontal stresses respectively.

As pore pressure is increasing, small variations in all stresses are observed. If it is assumed that the behavior of the rock is following the 1-D consolidation theory, then the horizontal stresses will change with the average reservoir pressure P according to the following equation:

$$S_h = S_v \frac{\nu}{1-\nu} + \alpha P \frac{1-2\nu}{1-\nu} = S_{hi} + \eta P$$

$$\alpha = 1 - \frac{C_s}{C_b} = 1 - \frac{K_b}{K_s}$$

Where,

- S_h is the horizontal stress.
- S_v is the vertical stress.
- ν is the Poisson ratio.
- α is the Biot's constant.
- C_s is the grain compressibility.
- C_b is the bulk compressibility.
- K_b is the rock's bulk modulus.
- K_s is the rock's grain modulus .
- P is the pressure.

The Biot's constant for Nisku was calculated from the input geomechanical properties as 0.39 and then η was determined from the following equation.

$$\eta = \alpha \frac{1-2\nu}{1-\nu} = 0.2307$$

Then the slope of S_h versus P in Figure 10 should be equal to η . For our data, $\eta = 0.2307$ which agrees with the simulation data. This means that the deformation around the injector is close to uniaxial.

4.3. Shear Failure

As it is well known, it is possible for a formation to reach shear failure even before exceeding fracture pressure. Figure 12 shows the concept of the Mohr Coulomb criteria for shear failure. When the magnitude of shear stress exceeds the shear strength of the rock, the state of stress will exceed the failure envelope of the Mohr Coulomb diagram and shear failure will happen.

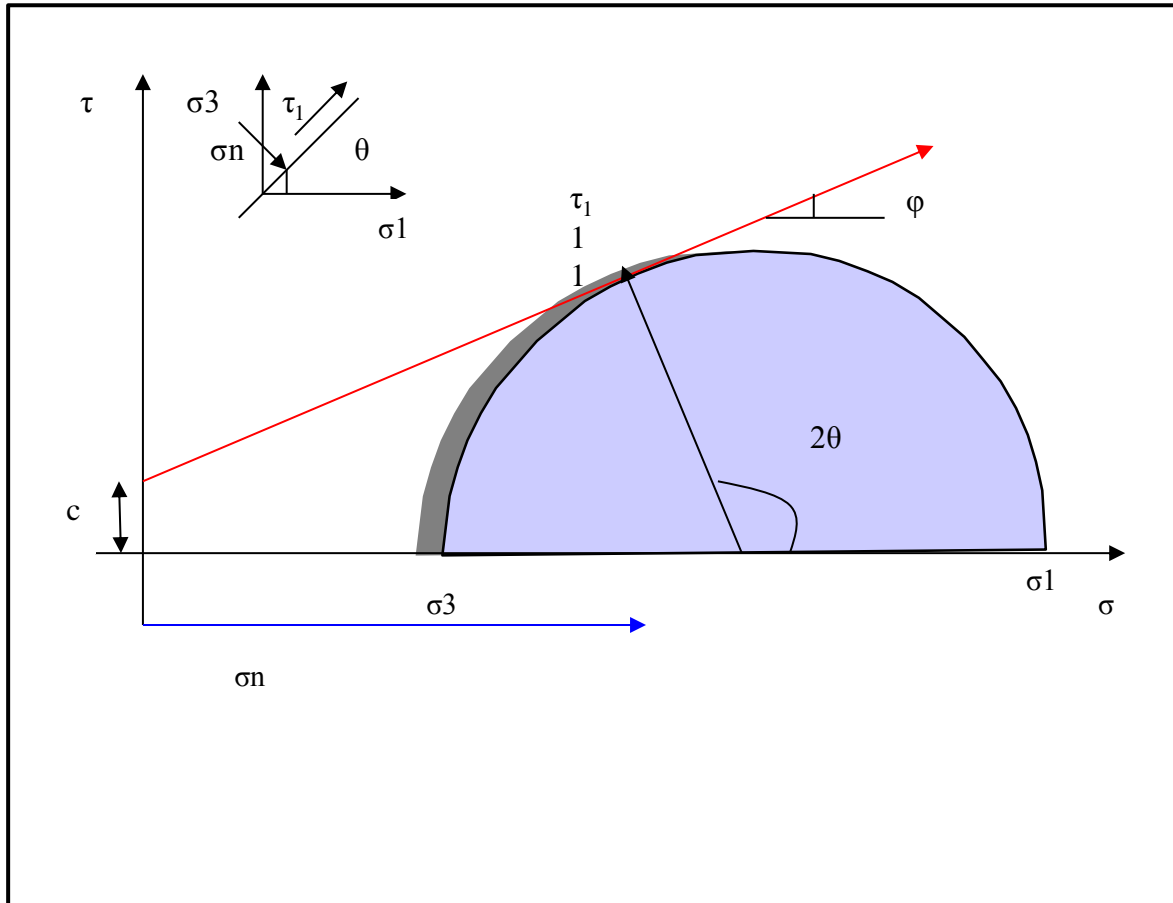


Figure 12: Mohr Coulomb Diagram.

The failure envelope of Mohr-Coulomb is defined by the following formula.

$$\tau = c + \tan(\varphi)\sigma$$

Where,

- τ is the shear stress.
- c is Cohesion.
- φ is friction angle.
- σ is normal stress.

In order to determine how close this formation is to shear failure, the concept of stress level is introduced here. Stress level is defined as the ratio of deviatoric stress at the current condition to the deviatoric stress at failure condition and is presented by the following equation:

$$l_{\sigma} = \frac{\sigma'_{dev}}{(\sigma'_{dev})_f} \leq 1 \quad \sigma'_{dev} = \sigma'_{max} - \sigma'_{min}$$

Where,

l_{σ} is the stress level.

σ'_{dev} is the deviatoric stress at the current condition.

$(\sigma'_{dev})_f$ is the deviatoric stress at failure.

σ'_{max} is the maximum principal stress.

σ'_{min} is the minimum principal stress.

The deviatoric stress at failure is a function of cohesion c and friction angle ϕ according to:

$$(\sigma'_{dev})_f = \frac{2c \cos\phi + 2\sigma'_3 \sin\phi}{(1 - \sin\phi)}$$

When the stress level is less than 1, the shear stress has not exceeded the shear strength of the rock and when it exceeds 1, the shear strength of the rock has been reached in a plane which is aligned in the direction found from the Mohr Coulomb circle. The cohesion and friction angle used in this study are listed in Table 2. The friction angle is assumed to be constant and equal to 30 for all layers since it has been suggested that it is a good rough estimate for this value (Zoback, 2007). Cohesion was calculated from the following correlation given the friction angle and provided unconfined compressive strength.

$$UCS = 2c \frac{\cos\phi}{1 - \sin\phi}$$

Where,

UCS is unconfined compressive strength.

c is cohesion.

ϕ is friction angle.

Figure 13 shows stress level values in the formation after 50 years of injection. These values are all significantly less than one which implies that this formation is not in danger of shear failure under this scenario.

Table 2: Cohesion and friction angle for geomechanical model.

Layers	Thickness(m)	Cohesion(MPa)	Friction angle (Deg)
Shale, surface-Joli Fou	1173.3	8.97	30
Sandstone, Ellerslie-Manville	167.7	12.55	30
Carbonate, Wabamun-Nordeg	476.6	27.79	30
Shale, Calmar	42.4	32.31	30
Carbonate, Nisku	70	40.41	30

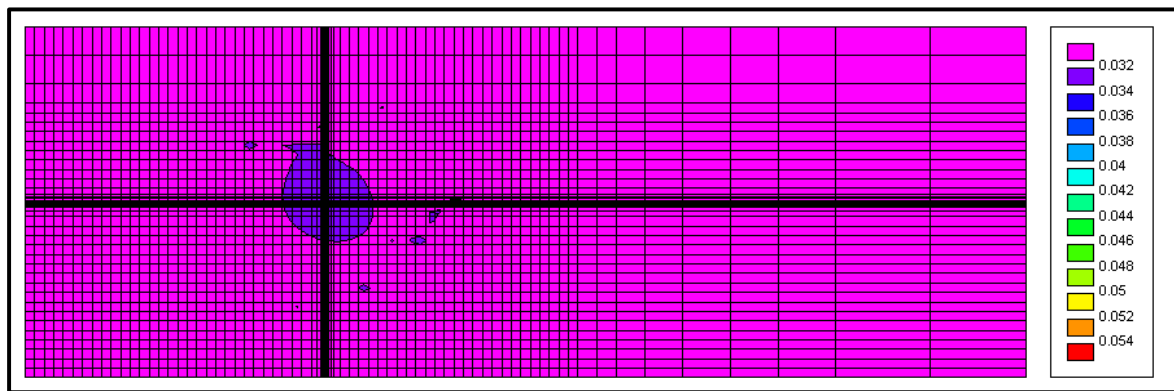


Figure 13: Stress level at Nisku’s middle layer after 50 years of injection of 1Mton/yr below fracture pressure. Stress level which shows the closeness of the formation rock to shear failure, varies between 0 and 1.

Figure 14 shows the stress state of Nisku layer inside the Mohr Coulomb at the beginning of injection and after 50 years. Once the pressure increases in the reservoir, which helps reduce the effective stress, the Mohr Coulomb circle moves to the left. If the circle touches the Mohr criterion which is shown by the red line in Figure 14, the rock fails in shear. As it is observed, the Nisku aquifer is not likely to experience shear failure. This is due to the large value of cohesion used (40 Mpa) and relatively small differences in the initial principal stresses.

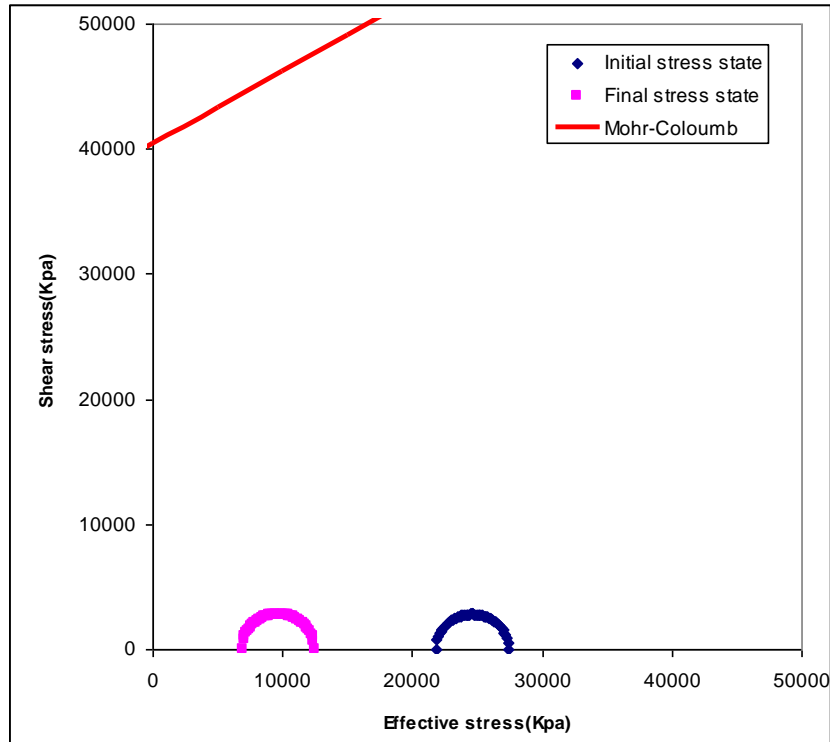


Figure 14: Mohr Coloumb Criteria for Nisku aquifer layer.

4.4. Sensitivity Analysis

Since the friction angle of the rock mass can be assumed to be constant at 30 Deg (Zoback, 2007), a sensitivity analysis has been carried out on the cohesion value. Cohesion of the intact carbonate rock is high, but the effective value can be much lower due to the presence of natural fractures and other heterogeneities. As expected when the cohesion value of the rock decreases, the likelihood of shear failure grows. This is illustrated in Figure 15, where the same simulation was run with different cohesion values. As c decreases, the stress level in the well block increases significantly. However shear failure is not reached even at zero cohesion (i.e., stress level=1), due to small difference between the maximum and minimum stress. Given the uncertainty of other data, there could be some failure if the effective cohesion is very low.

Another consideration is the friction angle of the interface between the Nisku and the shale (if such interface exists). For example, thin clay layers can have much lower cohesion, as well as friction angle. Failure would then happen along the interface, and this mechanism would stop fracture vertical growth.

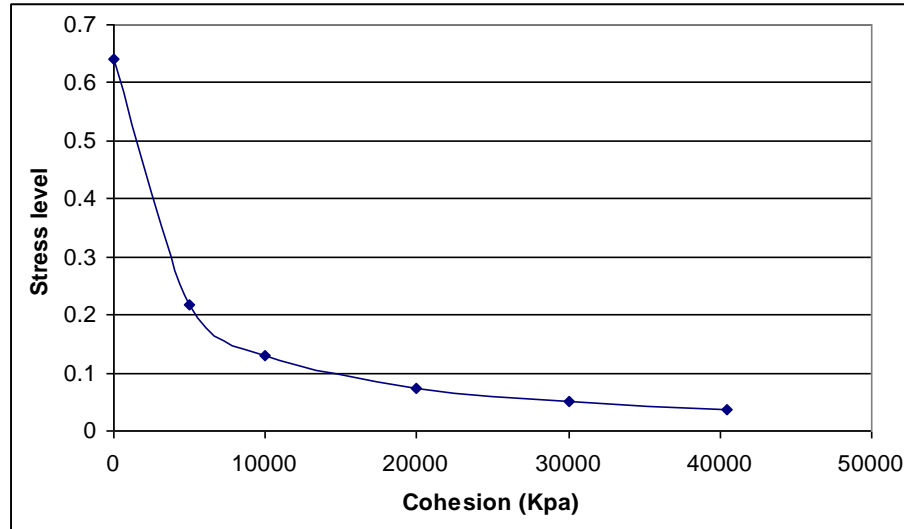


Figure 15: Sensitivity analysis for rock cohesion value—stress level at the wellbore as a function of rock cohesion.

5. RESULTS—ISOTHERMAL INJECTION CONSIDERING FORMATION FRACTURING

Allowing dynamic fracturing (by removing the BHIP restriction) has the potential for increasing the well injectivity. However it is important to model (and monitor in the actual operation) the fracture growth for several reasons:

- To make sure fracture would not propagate through the caprock to the extent that it would create a loss of containment (i.e., connect to other permeable zone)
- To use the information on fracture length to design correctly the well pattern
- To be able to control the injection rates to avoid excessive fracture lengths

The results presented here are the first preliminary work in this area, which demonstrates the concepts of the modelling and feasibility of the process. More detailed work would be required to arrive at reliable fracture growth predictions that could be used to design the injection scheme. Such work should be supported by field pilot data and lab geomechanical data.

5.1. Modelling Fracture Propagation

It is important to model the fracture growth both laterally and vertically to make sure it would not propagate through the caprock and reach other potential loss zones. To do that, the caprock layers were included in the flow model to track the possible fracture growth through them. A small porosity of 0.01, horizontal and vertical permeability of 3×10^{-5} md and 3×10^{-7} md were assigned to the caprock layers. Then the fracture was allowed to propagate both in the Nisku zone and in the layers above, using the numerical techniques described below. Since the minimum stress is in the y direction, the induced fracture plan would be perpendicular to this direction. Figure 16 shows the stress direction along with the induced fracture plane. This figure shows a section which is cut from the full geomechanical model and the well is located at the front corner of this element. Blue and yellow layers in this picture show the reservoir and shale layers respectively.

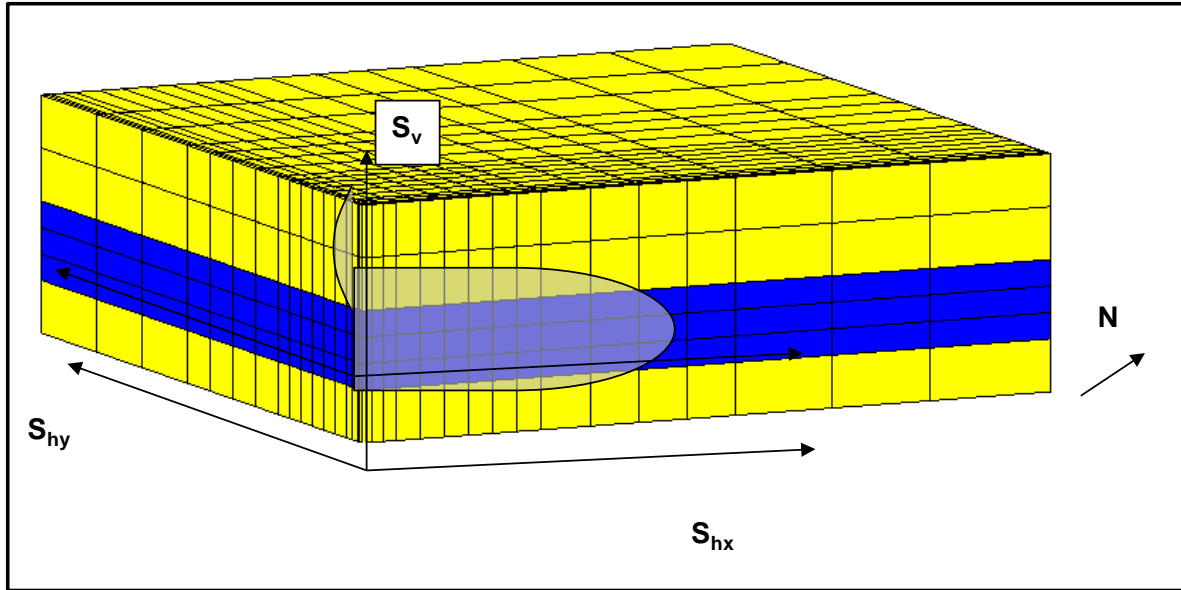


Figure 16: Induced fracture plane.

5.1.1 Transmissibility multipliers

In order to model the dynamic fracture propagation, a transmissibility multiplier table is incorporated in the model. All entries are calculated based on the estimation of fracture opening of Griffith fracture model as follows:

$$TMULT = \frac{K_m A_m + K_f A_f}{K_m A_m} = 1 + \frac{w_f^3}{12K_m w}$$

$$w_f = \frac{\Delta PL}{E} = \frac{\Delta PL * 4(1 - \nu^2)}{E}$$

Where,

TMULT is the transmissibility multiplier.

K is permeability.

A is the cross section area for fluid flow.

W_f is the fracture spacing.

W is the fracture thickness.

ΔP is a representative value of net pressure or effective stress on the rock.

L is the fracture half-height (based on the 2-D Perkins-Kern geometry assumption of vertical fracture with smooth closure at the top and bottom) (Perkins and Kern, 1961)

E is the Young's Modulus of the formation rock.

ν is the Poisson's ratio of the formation rock.

Subscript m refers to matrix property

Subscript f refers to fracture property

The Transmissibility Multiplier table can be incorporated in the model both as a function of pressure or effective minimum stress. In order to calculate the multiplier, a fracture half height of

35 m (equal to half-height of the Nisku aquifer) is considered and the rest of the data are taken from the mechanical properties of the injection zone. Figure 17 and 18 show the incorporated permeability multiplier in the X and Z directions. If the fracture height exceeds the value used, the actual multipliers would be higher, but this representation is still valid.

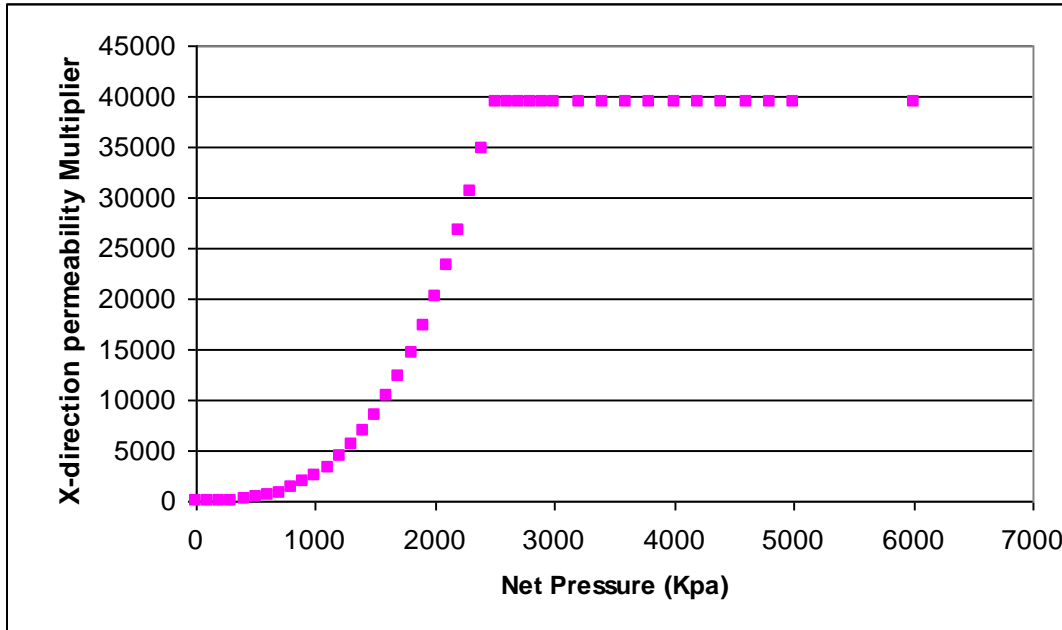


Figure 17: x-Direction permeability multiplier as a function of net pressure.

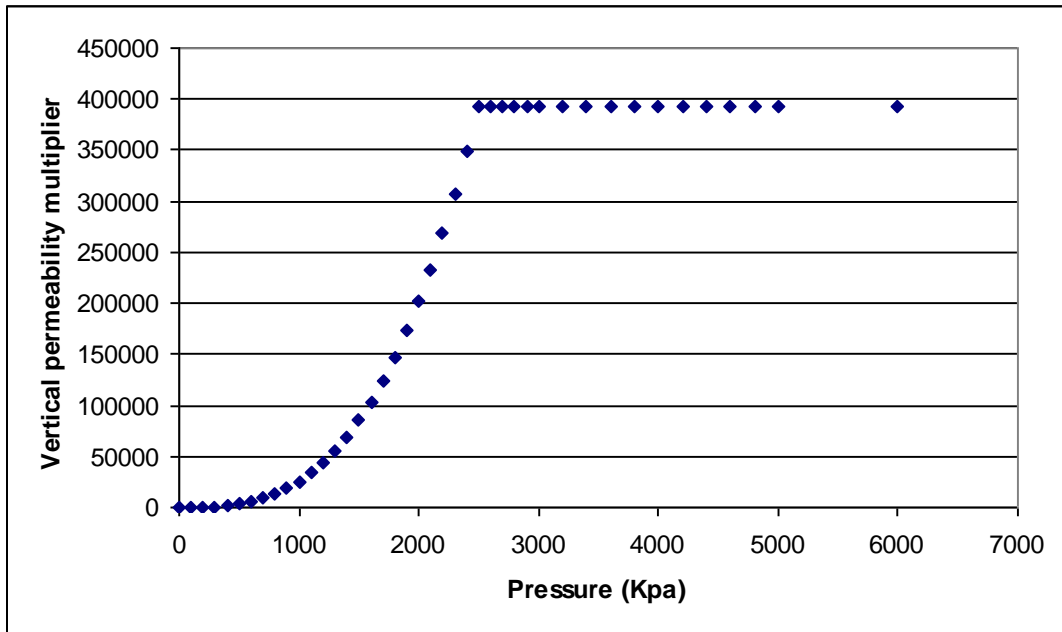


Figure 18: Vertical permeability multiplier as a function of pressure.

5.1.2 Porosity Multiplier

Once the fracture initiates in the formation and starts to propagate, the volume of the fracture will contribute to the porosity of the computational block. This can be accounted for by changing the porosity of the formation rock as a function of pressure in a fashion analogous to the transmissibilities. As a result, the compressibility in the fractured blocks will also change. This effect can be important for the calculation of the maximum volume of CO₂ which can be injected in the reservoir. Therefore a porosity multiplier as a function of net fracture pressure is introduced in the model to account for the added compressibility. The porosity function based on the same fracture parameters is shown in Figure 19.

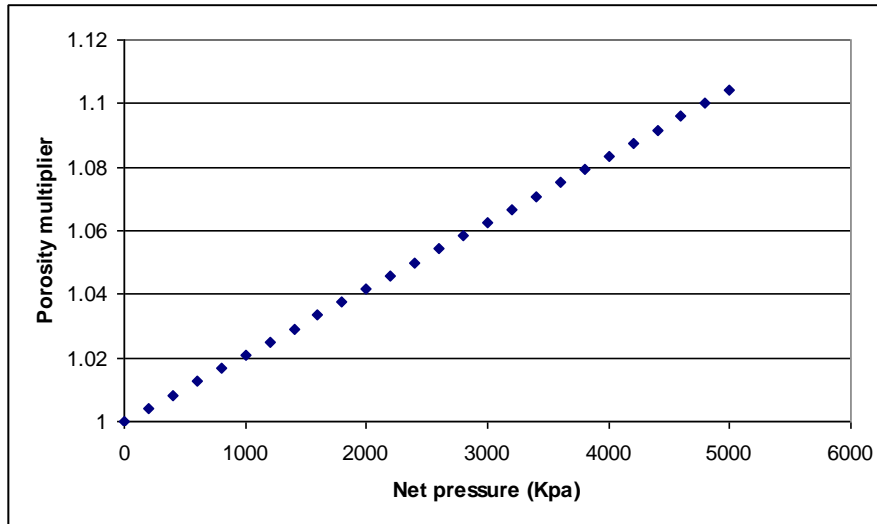


Figure 19: Incorporated porosity multiplier function.

5.2. Results of Injection at 2 Mton/yr Allowing Fracture Propagation

After 50 years of CO₂ injection above the fracture pressure of 2 Mt/yr, a total volume of 100 Mt would be injected into Nisku in 50 years. Figure 20 shows the vertical displacement at surface at the end of injection. Since the injection rate is higher than in the non-fractured case, the displacements are also bigger in the fractured case.

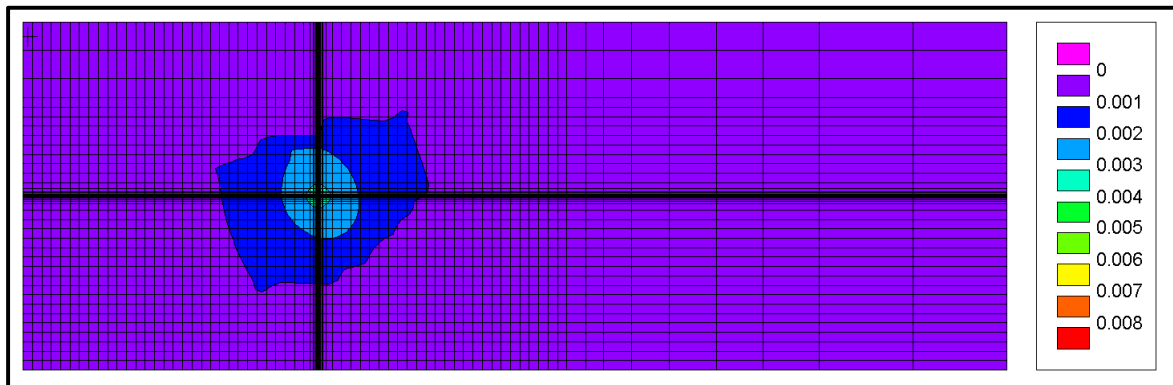


Figure 20: Vertical surface displacement (metre) after 50 years of isothermal CO₂ injection of 2Mton/yr allowing fracture initiation and propagation in the Nisku aquifer.

Figure 21 shows the gas saturation at well block cross section after 50 years of injection. Since there is no stress barrier in the caprock, once the pressure develops in the caprock layer resulting in a negative minimum effective stress, fracture propagation starts in that layer. Figure 22 illustrates a magnified picture of gas saturation for the fractured case after 50 years of injection at the same cross section as in Figure 21.

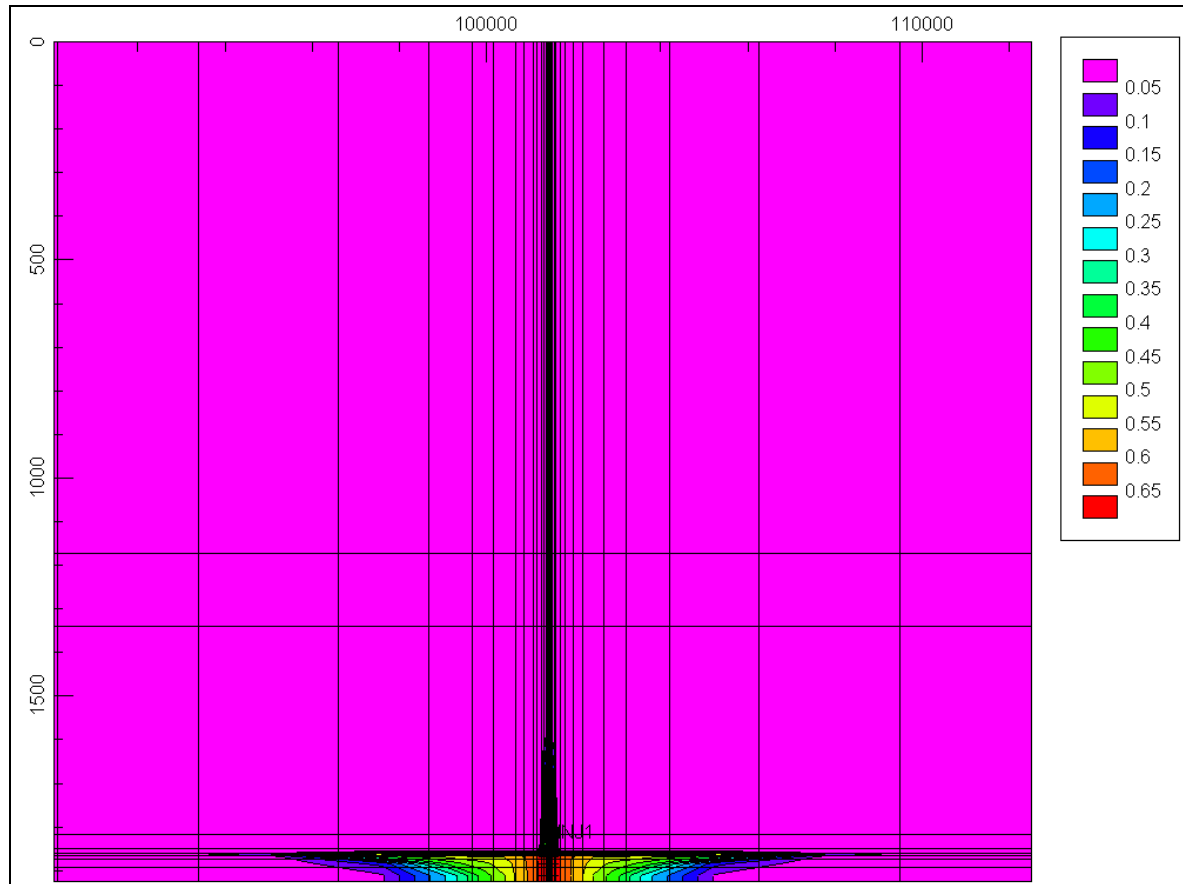


Figure 21: Gas saturation after 50 years of isothermal CO₂ injection at 2Mton/yr allowing fracture initiation and propagation.

The fracture half-length and full height for the isothermal model after 20 years of injection is 27 m and 80 m, and after 50 years of injection reaches approximately 140 m and 112 m, respectively. The fracture growth increases in the late stages due to overall pressurization of the Nisku aquifer, but the CO₂ plume extends well beyond the fracture. It should be noted that due to large computing requirements of the coupled model (runs taking several days), it was not possible to have enough refinement in the 3rd caprock layer, and, as a result, the fracture vertical growth in this layer is over estimated. In addition, the model did not include underburden layers below the Nisku aquifer. More resolution is needed to estimate the fracture height growth accurately. It is important to realize that there are other fracture mechanisms which are not considered in this study and might change the fracture propagation through caprock (Sneddon et al., 1969, Economides and Nolte, 2000, Settari, 1988).

The vertical fracture growth in the isothermal case is sensitive to caprock permeability. We observed that when the caprock permeability is increased, the vertical fracture grows higher into the

caprock. However since the realistic model will include thermal effects (presented in section 6), the effect of caprock permeability is not discussed here but is considered in thermal models.

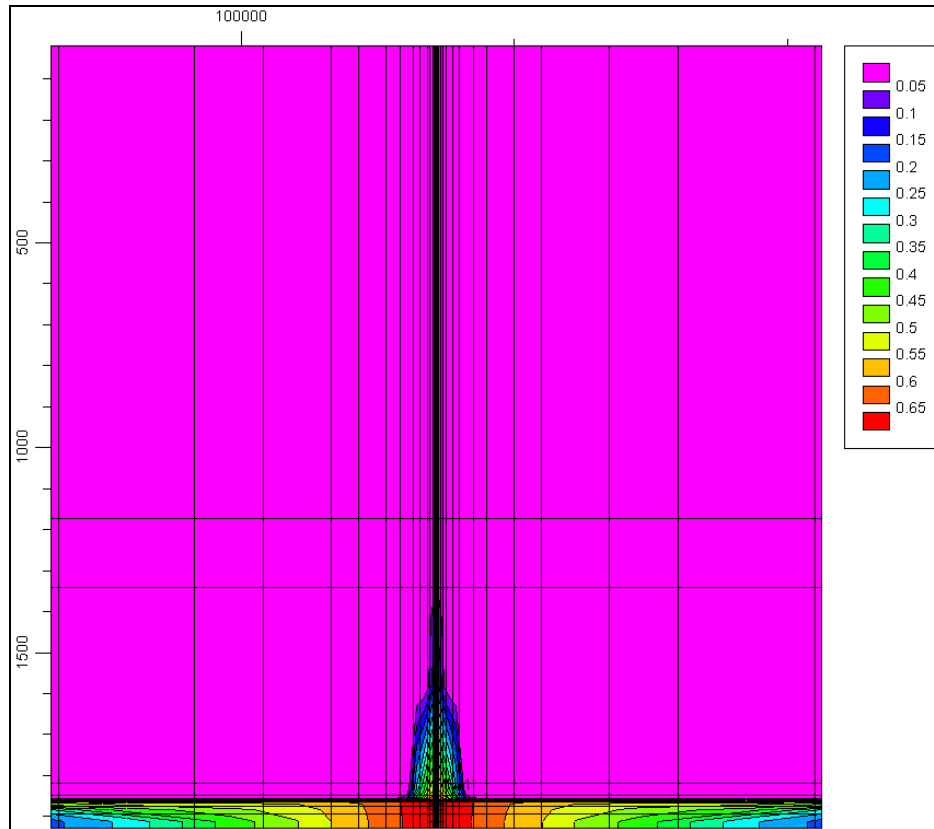


Figure 22: Magnified picture of gas saturation after 50 years of isothermal CO₂ injection of 2Mton/yr allowing fracture initiation and propagation.

6. THERMAL EFFECTS

Since cold CO₂ (at approximately 30 deg C) will likely be injected into the relatively hot Nisku formation (at 60 deg C), thermal effects of injection should be included in the model. Cooling of the formation reduces the total stresses and therefore lowers the fracture propagation pressure. This reduces the pressure differential available for injection, and therefore injectivity. In the case of injection at fracturing conditions, the fracture propagation pressure will decrease and, if the same injection rate is used, this will accelerate fracture propagation.

The isothermal model was extended to include thermal effects of injection. The thermal data used are listed in table 3.(Clauser and Huenges., 1995; Côté and Konrad., 2005)

Table 3: Thermal properties of fluid and rock.

	Rock	Water	CO ₂
Thermal Expansion Coefficient (1/K)	1.5E-5	2.6E-4	-
Heat Capacity(Kj/Kg K)	1.2	4.187	0.84
Thermal Conductivity(Kj/m C Day)	165	-	-

6.1. Thermal Effects for Injection Below Fracturing Pressure

We first consider the case of injection below fracturing pressure, described previously. Figure 23 shows the stress and pressure history of both the thermal and isothermal model.

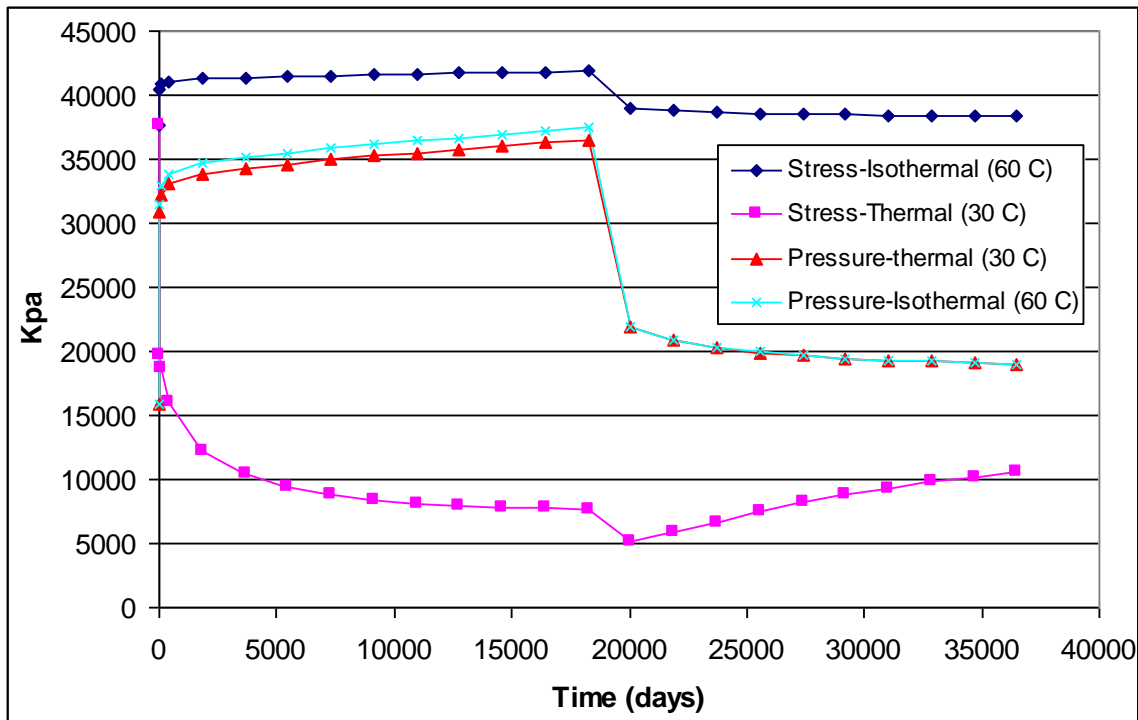


Figure 23: Minimum stress and pressure history for thermal and isothermal model, in the case of injection of 1Mton/yr below fracture pressure.

The reason for this pressure difference is that in the thermal model the injection is modelled at 30 Deg C as opposed to 60 Deg C in the isothermal model. Since the total injected mass of CO₂ is the same for both models and because CO₂ will occupy less volume at 30 Deg C, the pressure will be slightly smaller in the thermal model.

The reduction of stresses in the thermal model is related to the inclusion of temperature effects in the calculation of stresses. After injection stops and temperature rises, stresses will increase again. It should be noted that in the thermal model, the minimum horizontal stress falls below injection pressure at early injection time and creates negative effective stress and therefore would initiate fracture in the formation. It is important to realize that the stress magnitudes after fracturing are not valid in this figure because fracture propagation is not allowed in this model.

Figure 24 shows the surface displacement for thermal and isothermal model. Once the thermal effects in Nisku have influenced a relatively large area around the wellbore, the reduction in Nisku's stress will be transferred to the surface and the surface displacement for the thermal model will fall below that of the isothermal model.

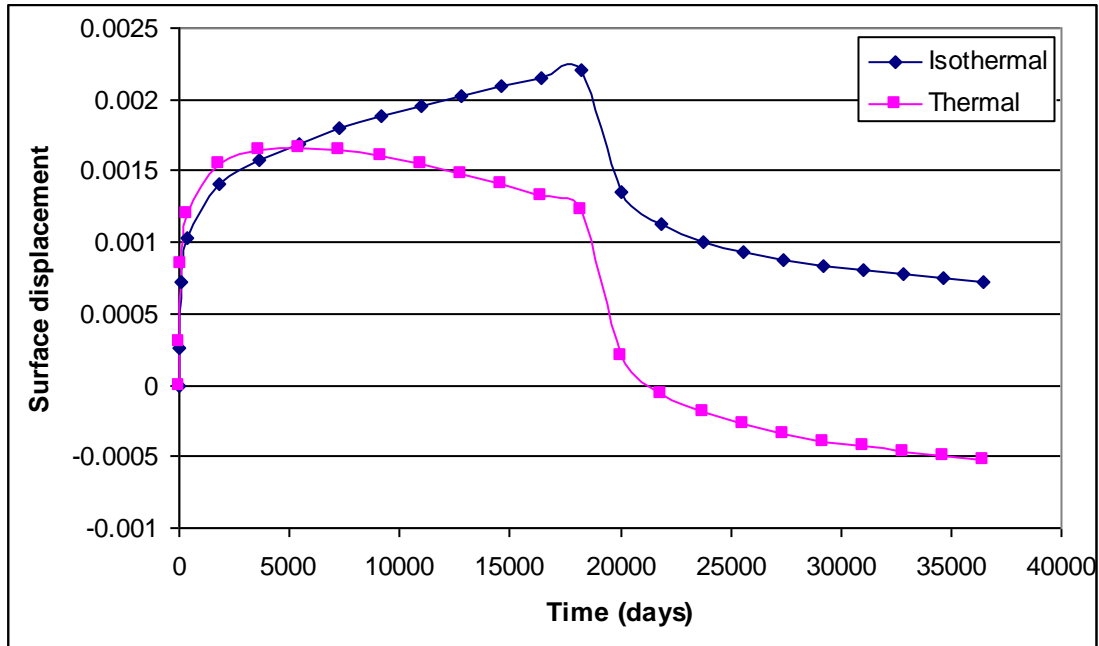


Figure 24: Surface displacement for thermal and isothermal model, for the case of injection of 1Mton/yr below fracture pressure.

6.2. Thermal Effects on Dynamic Fracturing

Including the thermal effects in the dynamic fracture model, there are two important aspects to study:

- Thermal effects on fracture length and vertical growth
- Thermal effects on fracture propagation pressure

In order to study the thermal effects on fracture length and height, the previously described fracture model (Section 5.1) was extended to include the thermal effects of injection. Figure 25 shows the gas saturation at wellbore cross section. This Figure has the same scale as Figure 21.

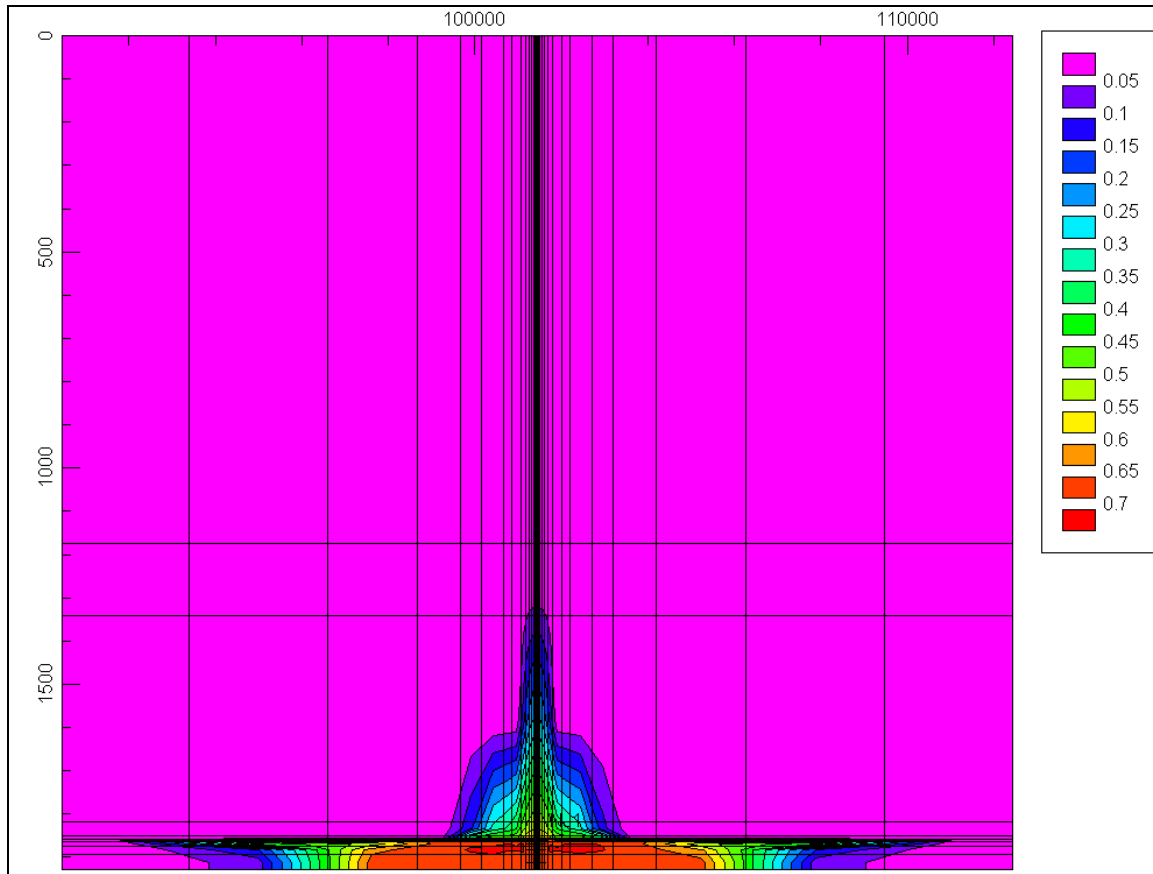


Figure 25: Gas saturation at well block cross section for thermal model.

The dynamics of the fracture propagation is complex as it depends on both poroelastic and thermal effects on stresses. In particular, the vertical growth in the thermal case is different compared to the isothermal one. At early times, since the fracture grows faster in the reservoir layer for the thermal model (due to reduction in temperature), there would be a larger volume of fluid flow into the caprock and the pressurization of the caprock will be higher for the thermal model (fracture permeability effect). However once the temperature change in the caprock starts to help reduce the effective stress to negative values and initiate fracture in the caprock, there would be less pressure drop between the caprock and the aquifer layer (compared to the isothermal case) and, therefore, there would be less fluid flow to the caprock (pressure drop effect), resulting in smaller vertical propagation. We note that limited fracture growth into the caprock is not necessarily harmful. Only if the fracture would grow completely through the caprock, then it would serve as a fluid source for the overlying geological layers.

The thermal effects will help reduce the minimum effective stress and therefore the fracturing pressure. This will result in a smaller pressure drop between the fracture pressure and far-field reservoir pressure for the thermal case compared to the isothermal case. The fracture half-length and height in the thermal case at 20 years are 2700 m and 80 m, respectively, which is larger compared to the isothermal case. After 50 years of injection, the half-length remains constant but the fracture height reaches approximately 112 m. As shown in Figure 25, the gas saturation zone is also larger in comparison to the isothermal case shown in Figure 21a. Due to the dominance of thermal effects, the fracture dimensions are relatively independent of caprock permeability.

Figure 26 shows the fracture propagation pressure for the thermal and isothermal model. As expected since the thermal effects help reduce the effective stress, the fracture propagates at much lower pressure in the presence of thermal effects. This is an important result, because the injection temperature of CO₂ can be controlled at the surface and it can be therefore one of the optimization variables.

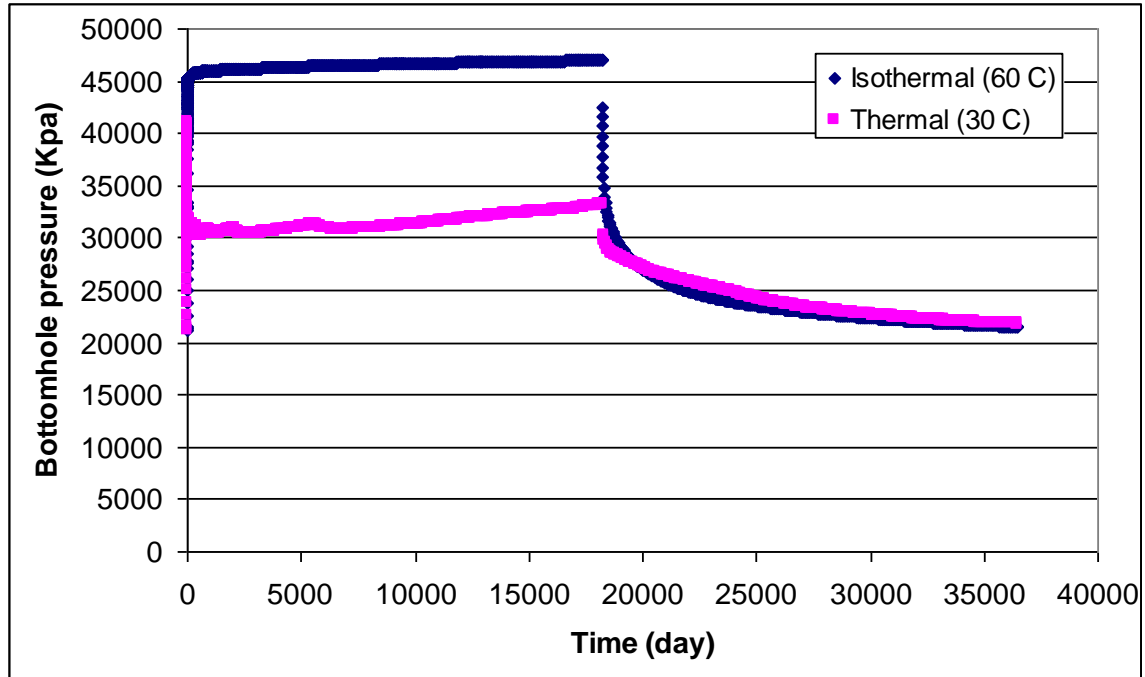


Figure 26: Comparison of fracture propagation pressure for isothermal and thermal model.

7. CONCLUSIONS

1. Injection in the Nisku aquifer (below or at fracture pressure) is not likely to cause any significant surface heave and is not likely to have any environmental impact associated with surface deformations. Surface deformation data can be used in conjunction with seismic measurements to solve an inverse problem for mechanical properties of Nisku and overlying layers. It also can help to plan for the location of the instrumentation and surface monitoring.
2. Injection above the fracture pressure will have the potential to increase the well injectivity but also the possibility of fracturing the caprock. The degree of vertical propagation will strongly depend on the caprock stress state and mechanical properties.
3. Thermal effects of cold CO₂ injection will reduce the fracture pressure and enhance the horizontal fracture propagation through caprock. However, the results of simulation of vertical propagation have been obtained under the most unfavourable assumption of constant minimum stress gradient and are only preliminary (and likely pessimistic).

8. RECOMMENDATIONS

1. One of the main concerns in building a geomechanical model is to avoid the effects of boundaries on the solution. The geomechanical model developed in this study did not include any geomechanical layers below the flow model at its bottom end due to the already large size of the model. It is recommended to extend the geomechanical model to include added layers at the bottom end of the model to eliminate this boundary effect.
2. As mentioned in the Conclusions, the fracture propagation strongly depends on caprock's stress condition. A small stress barrier (i.e., higher stresses in caprock compared to reservoir layer) can prevent fracture from propagating through the caprock layers. Since caprocks commonly act as stress barriers due to their higher Poisson's ratio, it is recommended to study the fracture propagation in the presence of higher stresses in the caprock.
3. After 50 years of CO₂ injection above the fracture pressure in Nisku aquifer, the reservoir pressure will rise from the original value of 16 Mpa and fracture length and height will constantly increase. However if it would be possible to connect the Nisku aquifer and the overlying Wabamun Group, water will start to flow to the latter and the pressure rise in the Nisku aquifer would be smaller and therefore it would be likely that this pressure maintenance scenario would prevent fracture from propagating through the Calmar caprock.
4. Drilling a pilot well and well testing can provide a data source for model validation and to measure flow properties. The following well test plan is proposed for this purpose:
 - A) Start the well with a small injection rate and perform a fall off test and measure the Nisku rock properties
 - B) Increase the injection rate and perform a step rate test to measure the value of minimum horizontal stress
 - C) Inject with higher injection rate to initiate a fracture and use micro-seismic to measure the extent of the fracture.
5. Thermal effects of injection will enhance the fracture propagation. The CO₂ injection stream which comes from the power plant has already been cooled and compressed for increasing injection efficiency. Due to the large extent of thermal effects, it is recommended to control the injection temperature and use the saved compression energy of the power plant to inject lower density CO₂ in order to avoid fracture propagation through the caprock.
6. Experimental results on compressibility and thermal expansion coefficient of rock were received at the time when the geomechanical simulation was already completed. The reported values for these two properties are 1-2 orders of magnitude different from what was used before in geomechanical models. This difference could make a noticeable difference in injectivity and thermal effects of injection. It is recommended to update the flow and geomechanical models based on the new reported properties.

9. REFERENCES

- Bennion, B., Bachu, S., (2005), "Relative Permeability Characteristics for Supercritical CO₂ Displacing Water in a Variety of Potential Sequestration Zones in the Western Canada Sedimentary Basin", SPE 95547.
- Clauser, C., Huenges, E., (1995), "Thermal Conductivity of Rocks and Minerals", American Geophysical Union.
- Côté, J., Konrad, J.-M., (2005), "Thermal conductivity of base-course materials", Canadian Geotechnical Journal 42: 61–78.
- Economides, M.J. and Nolte, K.G. (editors) (2000). *Reservoir Stimulation*, John Wiley and Sons, 2000.
- Hassanzadeh, H., Pooladi-Darvish, M., Elsharkawy, A.M., Keith, D.W. and Leonenko, Y., (2007), "Predicting PVT data for CO₂-brine mixtures for black-oil simulation of CO₂ geological storage", International Journal of Greenhouse Gas Control.
- Hitchon, B., (1996), "Aquifer Disposal of Carbon Dioxide, Hydrodynamic and Mineral Trapping - Proof of Concept". Sherwood Park, Geoscience Publishing Ltd.:P. 58.
- Keith, D., Lavoie, R., (2008), "Wabamun Area CO₂ Sequestration Project (WASP)", Project Overview.
- Michael, K., Bachu, S., Buschkuehle, M., Haug, K., and S. Talman. in press. Comprehensive Characterization of a Potential Site for CO₂ Geological Storage in Central Alberta, Canada, AAGP Special Publication on Carbon Dioxide Sequestration.
- Bell, S.J. and Bachu, S., (2003), "In-situ stress magnitude and orientation estimates for Cretaceous coal-bearing strata beneath the plains area of central and southern Alberta: Bulletin of Canadian Petroleum Geology", v. 51, p. 1–28.
- Mossop, G., Shetsen, I., "Geological Atlas of the Western Canadian Sedimentary Basin", Chapter 12, P. 191, Devonian Woodbend-Winterburn Strata, Copyright 1994, Canadian Society of Petroleum Geologists, Alberta Research Counsel, ISBN: 0-920230-53-9.
- Quintessa, National Institute of Advanced Industrial Science and Technology of Japan, Quintessa Japan, JGC Corporation, Mizuho Information and Research Institute, (2007), "Building Confidence in Geological Storage of Carbon Dioxide" Ministry of Economy, Trade and Industry (METI), IEA Greenhouse Gas R&D Programme (IEA GHG).
- Settari, A., (1988), "Quantitative Analysis of Factors Influencing Vertical and Lateral Fracture Growth", SPE Prod. Eng. (Aug. 1988), pp. 310-322.
- Sneddon, I. N. and Lowengrub, M. (1969). *Crack Problems in the Classical Theory of Elasticity*, John Wiley & Sons Inc., New York, 1969.
- Zoback, M.D., (2007), Reservoir Geomechanics, Cambridge University Press, Cambridge, 449 p.
- Perkins, T.K. and Kern, L.R., "Widths of hydraulic fractures", Journal of Petroleum Technology, Sept. 1961, Vol, 13, No.9, 937–949.



January 2010

Wabamun Area Sequestration Project: Risk-based Leakage Model

Submitted to:
Rob Lavoie
Project Manager
Wabamun Area Sequestration Project
University of Calgary
Energy & Environmental Systems

REPORT



A world of
capabilities
delivered locally

Project Number: 08-1334-0082

Distribution:

Golder Associates
University of Calgary
Wabamun Area Sequestration Project





Table of Contents

1.0 INTRODUCTION	1
2.0 CONCEPTUAL MODEL DESCRIPTION	2
2.1 Transient Pressure in an Injection Reservoir	4
2.2 Radial Extent of the CO ₂ Plume	5
2.3 CO ₂ Leakage to Surface from an Abandoned Nisku Well	8
2.4 CO ₂ Leakage to Surface from an Abandoned Banff Well.....	9
3.0 SIMULATOR DEVELOPMENT	13
3.1 User Interface	13
4.0 BENCHMARKING.....	24
4.1 CO ₂ Leakage – Abandoned Nisku Well	24
4.2 CO ₂ Leakage – Abandoned Banff Well.....	24
4.3 Plume Migration – Nisku Formation	25
5.0 WASP SPECIFIC DATA	26
5.1 Probabilistic Inputs.....	26
6.0 SENSITIVITY ANALYSIS.....	29
6.1 Leakage in Nisku Abandoned Well	29
6.2 Leakage in Banff Abandoned Well.....	31
6.3 CO ₂ Plume Migration in the Nisku.....	33
7.0 SUMMARY AND RECOMMENDATIONS	35
8.0 REFERENCES	36

TABLES

Table 1: Time to Reach 5 km Distance from Injection vs. S_{res}	7
Table 2: Parameters and Distribution Types for the Nisku Formation Model Inputs	16
Table 3: Parameters and Distribution Types for the Banff Formation Model Inputs.....	17
Table 4: Parameters and Distribution Types for the Nisku Abandoned Well	18
Table 5: Parameters and Distribution Types for the Banff Abandoned Well.....	20
Table 6: Description of Model Outputs	23



WASP RISK-BASED LEAKAGE MODEL

Table 7: Probabilistic Inputs for Nisku and Banff Formation Properties26

Table 8: Probabilistic Inputs for Abandoned Wells Parameters28

FIGURES

Figure 1: Conceptual Model of Leakage from Injection Formation through Single Well in the Nisku Formation2

Figure 2: Conceptual Model of Cross-Formational Leakage through Multiple Wells3

Figure 3: Transient Pressure at Distances of 1 to 20 km from the Injection Location5

Figure 4: Maximum Radial Extent of Plume in Reservoir Formation for $S_{res}=0.384$7

Figure 5: CO₂ Leakage Rate for Single Abandoned Well Model with $r=1$ km, $k_{1s}=10^{-15}m^2$, $D_{1s}=10m$ and $r_{1s}=0.1m$ 8

Figure 6: CO₂ Leakage Rate as a Percent of Cumulative Annual Injected Rate for a Single Abandoned Well Model with $r=1$ km, $k_{1s}=10^{-15} m^2$, $D_{1s}=20$ m and $r_{1s}=0.1$ m9

Figure 7: Leakage Rate Curve for $r_1=5$ km, $r_2=1$ km, $k_{12}=10^{-11} m^2$, $k_{2s}=10^{-15} m^2$ $r_{w1}=0.1$ m and $D_{w1}=10$ m.....10

Figure 8: Plume Arrival Curve for $r_1=5$ km, $r_2=1$ km, $k_{12}=10^{-10} m^2$, $k_{w1}=k_{w2}=10^{-15} m^2$ $r_w=0.1$ m and $D_w=10$ m.....12

Figure 9: Simulation Model Main Dashboard.....13

Figure 10: Input for CO₂ Injection Rate.....14

Figure 11: Nisku Formation Properties Dashboard.....16

Figure 12: Banff Formation Properties Dashboard17

Figure 13: Nisku Abandoned Well Properties Dashboard18

Figure 14: Banff Abandoned Well Properties Dashboard20

Figure 15: Check Box for Well Leakage Scenario Selection21

Figure 16: Dialog Box for Simulation Duration and Number of Time Steps.....22

Figure 17: Dialog Box for Setting Number of Monte Carlo Realizations22

Figure 18: Results Dashboard23

Figure 19: Transient Leakage Flux Curve in m³/s for Abandoned Well in Nisku24

Figure 20: Transient Leakage Flux Curve as a % of Injection Rate for Abandoned Well in Banff25

Figure 21: Maximum CO₂ Plume Radius for the Nisku for $S_{res}=0.3$ 25

Figure 22: Tornado Plot of the Sensitivity Analysis Results for Leakage Through Abandoned Nisku Well30

Figure 23: X-Y Function Chart of Sensitivity Results for Leakage through Abandoned Nisku Well31

Figure 24: Tornado Plot of the Sensitivity Analysis Results for Leakage Through Abandoned Banff Well32

Figure 25: X-Y Function Chart of Sensitivity Results for Leakage through Abandoned Banff Well.....32

Figure 26: Tornado Plot of the Sensitivity Analysis Results for Plume Migration in the Nisku33

Figure 27: X-Y Function Chart of Sensitivity Results for Leakage Plume Migration in the Nisku.....34



WASP RISK-BASED LEAKAGE MODEL

APPENDICES

APPENDIX A

Conversion from Hydraulic Head to Pressure

APPENDIX B

Nordbotten et al. Equations for Multiple Wells and Multiple Layers

APPENDIX C

Leakage Flux for One Injection Well and One Abandoned Well with One Aquifer Penetration

APPENDIX D

Leakage Flux for One Injection Well and Two Abandoned Wells with Two Aquifer Penetrations



1.0 INTRODUCTION

The Wabamun Area Sequestration Project (WASP) is a desktop study led by the University of Calgary that is investigating the feasibility of geologically storing one gigatonne of carbon dioxide (CO₂) in the Wabamun Lake area of Alberta where four coal-fired power plants collectively emit over 30 MT of CO₂ each year. The primary WASP study area contains substantial oil and gas activity and includes the presence of thousands of producing and abandoned wells dating back to the 1950s. The success of a geological storage program will depend in part on the ability to choose storage formations from which only minimal amounts of CO₂ will leak back to the surface (NKCB, 2009). Wells, in particular those that are long abandoned and completed to uncertain standards, are generally considered to be one of the major potential pathways for release of CO₂ from a storage reservoir.

Within the High Grade Study Area, the Devonian Nisku formation was selected as the prime target for CO₂ storage by the WASP investigators. There are 18 abandoned wells penetrating the Nisku within a few kilometers of a potential CO₂ injection location. In the same area there are over 100 well penetrations in the overlying Banff formation, separated from the Nisku by the Calmar Aquiclude. While the potential leakage of CO₂ through the abandoned wells in the Nisku formation is of obvious importance, leakage through the more prevalent wells in the overlying Banff formation via indirect pathways must also be evaluated.

As a participant in WASP, Golder Associates was tasked to develop a probabilistic analytical simulator capable of evaluating alternative leakage scenarios associated with legacy wells in multiple formations. The scope of the initial simulation tool included the simplest scenario of leakage to the surface via a single abandoned well in the Nisku formation and was extended to leakage through a combination of wells in the Nisku and Banff formations. The simulator that was developed is based to a large extent on the analytical solutions developed by Nordbotten, Celia and Bachu (Nordbotten et al., 2004 and Nordbotten et al., 2005). The use of analytical expressions in the simulator allows the uncertainty in the input parameters to be explicitly represented and propagated in the model calculations using the Monte Carlo simulation method. The probabilistic method facilitates sensitivity analysis for prioritizing the site characterization data needs for reducing the overall uncertainty in system performance. The simulator is scalable and can be expanded to represent CO₂ release through additional leakage pathways such as faults, fracture networks and spill points.

The simulator includes an intuitive, user interface for defining the input parameters and describing different release scenarios (i.e., 'what if' analysis) that are fundamental in CO₂ sequestration risk analysis and useful for developing a diagnostic understanding of the different leakage scenarios. The user interface provides a number of predefined model outputs including time histories of formation pressure, CO₂ plume migration within the injection formation, and CO₂ flux rates from breached wells. The default input parameters in the simulator that describe the potential leakage characteristics of the abandoned wells in the Wabamun region were developed by members of the WASP research team.

This report describes the conceptual model of the geologic sequestration system represented in the simulator and the analytical expressions used to approximate the movement of CO₂ through an injection formation and its potential release through one or more abandoned wells. The mathematical implantation of the analytical solutions in the simulator is summarized and the input parameters identified. Initial estimates for the input parameter for the model developed by the WASP team are defined. The user interface for the simulator is then described and example outputs are presented.



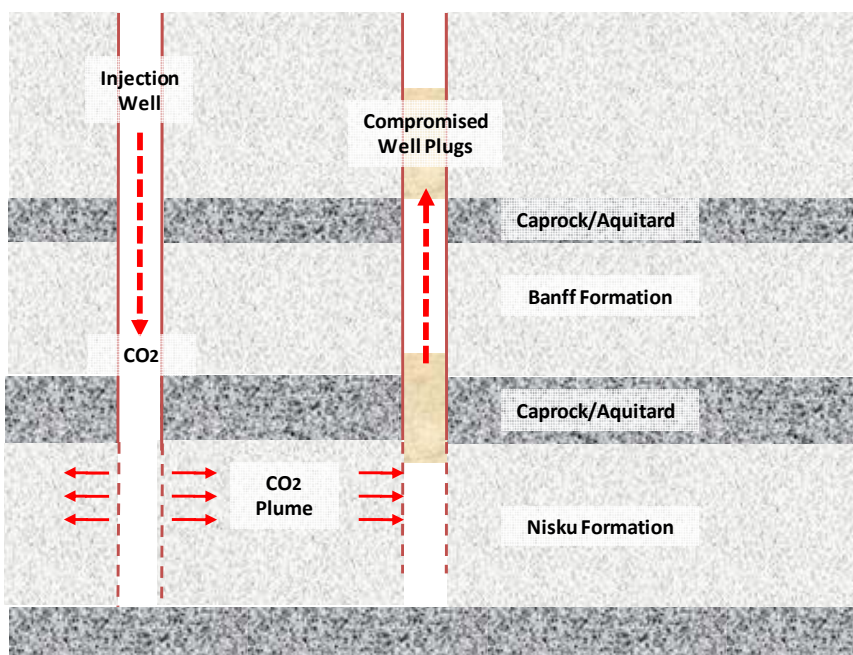
2.0 CONCEPTUAL MODEL DESCRIPTION

The Wabamun Lake area of Alberta has supported substantial oil and gas activity dating back to the 1950s involving thousands of producing and abandoned wells drilled to intersect multiple formations in the area. Within what is referred to as the High Grade Study Area, there are a total of 95 wells, 56 of which have been abandoned. The wells, in particular those long abandoned and completed to uncertain standards, represent potential pathways for release of CO₂ if one or more of the reservoir formations in this area are used for geologic sequestration.

The WASP study team has identified the Devonian Nisku formation as a prime candidate for potential CO₂ sequestration in the Wabamun Lake area. Out of the 52 abandoned wells in the High Grade Study Area, 32 were completed in formations above the Nisku and twelve were completed below. Well integrity in the High Grade Study Area has been studied by Nygaard (2009) who concluded that approximately 50% of the cement plugs in the abandoned wells were likely to be fractured. Of the five wells that were studied in detail, one well was an open hole (i.e., was not plugged). These preliminary results demonstrate the uncertainty associated with the abandoned wells as potential leakage mechanisms if the area is eventually used for CO₂ sequestration. While the potential leakage of CO₂ through the abandoned wells in the Nisku formation is of obvious importance, leakage through the more prevalent wells in the overlying Banff formation via indirect pathways must also be evaluated.

As a member of the WASP Team, Golder Associates was tasked to develop a probabilistic simulator based on the methodology and equations developed in Nordbotten et al. [2004, 2005a, 2005b and 2009]. The scope of the initial phase of the simulator consists of two scenarios: 1) the leakage of CO₂ from the injection formation (i.e., the Nisku) to the surface via a single abandoned well assumed to intersect the Nisku (Figure 1), and 2) the leakage rate for a cross-formational flow through two wells, from the injection formation into an overlying aquifer and then to the surface (Figure 2). The Monte Carlo method is used to explicitly represent the uncertainty in the analytical expressions based on the existing site information or expert opinion where little to no data exists.

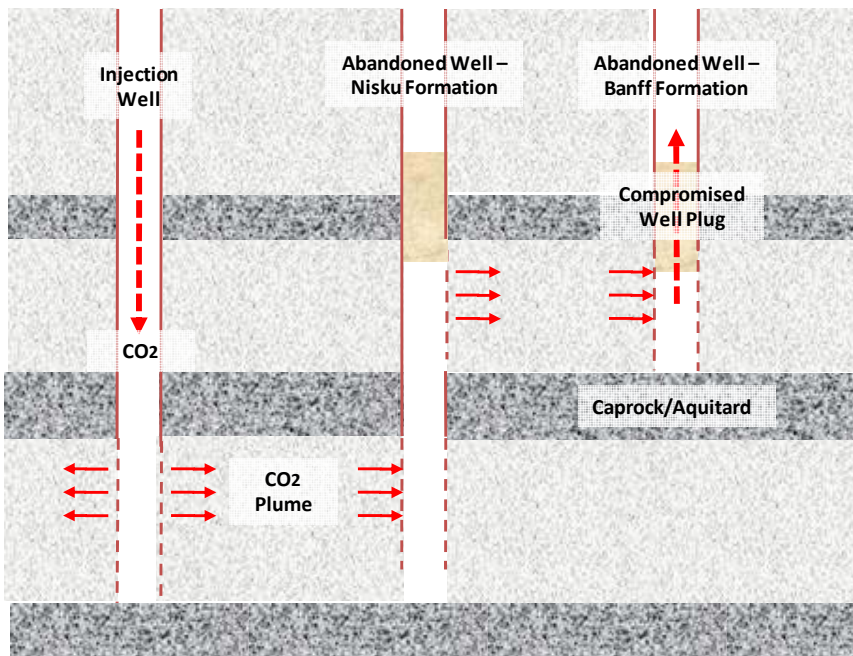
Figure 1: Conceptual Model of Leakage from Injection Formation through Single Well in the Nisku Formation





WASP RISK-BASED LEAKAGE MODEL

Figure 2: Conceptual Model of Cross-Formational Leakage through Multiple Wells



The simulator was developed in the following steps:

- Define the mathematical models – The analytical expressions and algorithms for plume migration and well leakage from Nordbotten et al. were reviewed and modified to represent single and two-well scenarios in Figures 1 and 2.
- Implement the mathematical models in a simulation software package – The analytical expressions and algorithms were implemented using the GoldSim simulation software code. This step included the development of a user interface to facilitate use by other WASP Team members.
- Verify and benchmark the simulator – Benchmark component calculations in the simulator against independent calculations developed in Excel.
- Coordinate a preliminary data set for the simulator - Gather input data including probability distributions for uncertain input parameters in the simulator.
- Sensitivity analysis – Perform sensitivity analyses for the major performance metrics (e.g., formation pressure, plume migration, CO₂ flux) in the simulator to determine the input parameters that have the greatest influence on projected performance.

The simulator, based on a set of assumed conditions and properties, can be used to evaluate the following performance metrics:

- arrival times for the CO₂ plume reaching abandoned wells in the Nisku or Banff formations (i.e., cross-formational flow through scenario);



WASP RISK-BASED LEAKAGE MODEL

- transient formation pressure at the base of the abandoned wells;
- leakage rates from abandoned wells in the Nisku and Banff formations; and
- sensitivity of the plume and leakage rate projections to variations in the input parameters in the simulator.

These performance metrics are important considerations for planning purposes for both geological sequestration and enhanced oil recovery. The performance metrics are calculated based on the following input parameters to the model:

- injection rate;
- injection duration;
- distance between the injection and abandoned wells;
- well radius;
- length, permeability and radius of the wellbore plug in the abandoned wells;
- formation hydrogeologic properties; and
- CO₂ properties.

2.1 Transient Pressure in an Injection Reservoir

The starting point for developing the simulator was estimating the transient pressure in the reservoir formation during CO₂ injection. The change in the formation pressure as CO₂ is injected into a reservoir is approximated using the standard Theis well pumping equation (Nordbotten et al., 2004):

$$p(r, t) = p_{init} + \frac{\mu Q_0}{4\pi k_1 b_1} W(u) \quad (1)$$

where $W(u)$ is the familiar well function from hydrogeology (Freeze and Cherry, 1979) which is an exponential integral function of the first order $E_1(u)$. For evaluation of the exponential integral see (Gautsch and Cahill, 1964). The argument u of the well function is given by

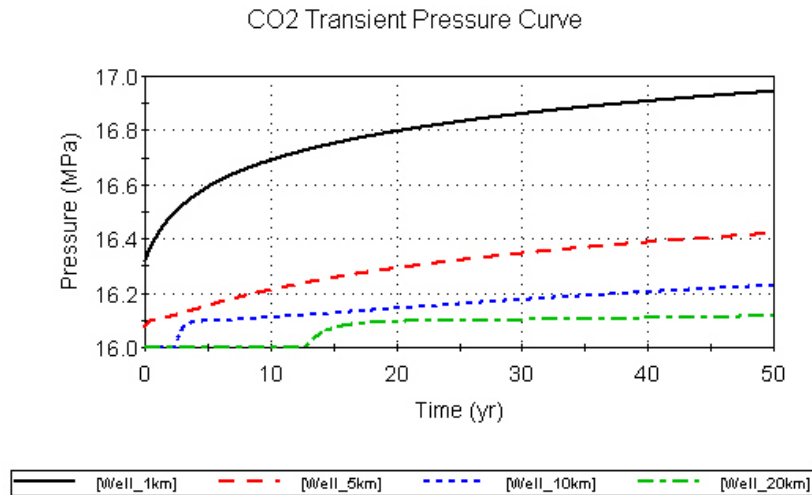
$$u = u(r, t) = \frac{c\mu r^2}{4k_1 b_1 t} \quad (2)$$

Where c is the compressibility of the CO₂-rock system, μ is CO₂ viscosity, r is the radial horizontal distance from the injection site, k_1 is the permeability of the reservoir formation, b_1 is the thickness of the reservoir formation and t is time.

Figure 3 shows the transient pressure curves in the CO₂ reservoir at variable distances from the injection location for an injection period of 50 years.



Figure 3: Transient Pressure at Distances of 1 to 20 km from the Injection Location



Note that the transient pressure curves follow a “smoothed” step function in time which decreases in overall magnitude with distance for a given injection period.

2.2 Radial Extent of the CO₂ Plume

The radial extent of the CO₂ plume from an injection well is calculated using a 2-phase radial flow analytical solution developed by Nordbotten et al. (2005). Assuming the CO₂ injection rate (Q_0) is constant, the radial extent of the CO₂ plume r_{max} is given by

$$r_{max} = \sqrt{\frac{\lambda_c V(t)}{\pi \phi \lambda_w b_1}} \tag{3}$$

Where λ_c is mobility of CO₂, λ_w is the mobility of water, $V(t)$ is the cumulative CO₂ volume injected at time t , ϕ is porosity of the reservoir and b_1 is the thickness of the reservoir. The mobility values are related to the viscosities μ_α and relative permeability values k_α by

$$\lambda_\alpha = \frac{k_\alpha}{\mu_\alpha} \tag{4}$$

Where $\alpha = c$ or w . The two relative permeability values are a function of the CO₂ saturation fraction S_{res} and have been measured and tabulated for the Wabamun formation by Benion and Bachu (2005).

In the case where $S_{res}=0.384$, the relative permeability values for the two phase are equal and then

$$\frac{\lambda_c}{\lambda_w} = \frac{\mu_w}{\mu_c} \tag{5}$$



WASP RISK-BASED LEAKAGE MODEL

Note that for constant injection rate, $V(t)$ can be replaced by Q_0t . Figure 4 shows the radial extent of the plume as a function of time. Plume arrival times at a distance 5 km from an injection well are tabulated for different

values of S_{res} in Table 1. The arrival times are based on the expected value for all the model parameters.



WASP RISK-BASED LEAKAGE MODEL

Figure 4: Maximum Radial Extent of Plume in Reservoir Formation for $S_{res}=0.384$

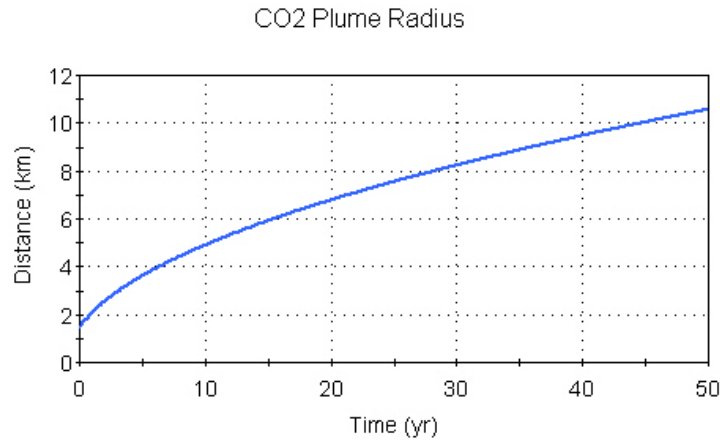


Table 1: Time to Reach 5 km Distance from Injection vs. S_{res}

Saturation Fraction S_{res}	Time to Reach 5 km (yr)
0.36	7.4
0.37	6.6
0.38	5.9
0.384 (Default)	5.6
0.4	4.6
0.41	4.0

Equation (4) can also be used to calculate the radial extent of a CO₂ plume in a shallower formation (Banff) under the cross-formational scenario. The volume injected is replaced by the volume leaked from the injection reservoir formation to the shallower formation through the Nisku abandoned well (Figure 2). The resulting equation is

$$r_{\max(\text{Banff})} = \sqrt{\frac{\lambda_c V_{12}(t)}{\pi \phi \lambda_w b_2}} \quad (6)$$

Where $V_{12}(t)$ is the volume of CO₂ entering the Banff formation through the abandoned well and b_2 is the thickness of the Banff formation. $V_{12}(t)$ is given by

$$V_{12}(t) = \int_0^t Q_{12}(t') dt'$$

Where from Appendix D

$$Q_{12}(t) = \frac{k_{12} \pi r_w^2}{\mu D_{12}} \left[\frac{(a_1 + b_1)d_2 - (a_2 + b_2)d_1}{(a_1 b_2 - a_2 b_1)} \right] \quad (7)$$



and the coefficients a_1 through d_3 are in turn functions of 4 time-dependent well functions.

Equation 3 is based on the following assumptions:

- a vertically averaged pressure within the formation;
- radial propagation of pressure (Darcy flow) in the formation;
- isotropy in the reservoir permeability tensor; and
- the injection formation is confined.

2.3 CO₂ Leakage to Surface from an Abandoned Nisku Well

The leakage component is modelled as a one-dimensional Darcy process through an abandoned well. Leakage from the injection reservoir to the surface is driven by the pressure difference between transient pressure at the base of the well in the reservoir formation and atmospheric (surface) pressure. Several well leakage paths were identified in Chapter 5 of the IPCC report (IPCC, 2005), in papers by Bachu and coworkers, such as (Gasda et al., 2004).

Starting from the analytical solutions developed by Nordbotten et al. (2004) as detailed in Appendix B and Appendix C, the pressure $p(r_1, t)$ at the foot of the abandoned well, located at distance r_1 from the injection well can be estimated. This is then substituted into the one dimensional Darcy equation in the vertical direction to give the following expression for surface leakage flux through the plug in the first abandoned well.

$$Q_{1s}(t) = \frac{\pi r_{w1}^2 k_{1s}}{h D_{1s}} \left[p_{init} + \frac{h Q_0 W(u_1(r_1, t))}{4\pi k_1 b_1} + \frac{k_{1s} r_{w1}^2 p_s W(u_1(r_{w1}, t))}{4 k_1 b_1 D_{1s}} \right] \left(1 + \left(\frac{k_{1s} r_{w1}^2 W(u_1(r_{w1}, t))}{4 k_1 b_1 D_{1s}} \right) \right)$$

Here k_{1s} is the permeability of the abandoned well plug between the reservoir and the surface, r_{w1} is the abandoned well radius, p_s is atmospheric pressure, $\gamma = 0.92$ is the constant from the Nordbotten et al. theory, and D_{1s} is the length of the cement plug.

Figure 5 shows the transient surface leakage during the injection period through a single abandoned well penetrating the Nisku located 1 km from the injection site. The well leakage parameters pertain to those for a fractured cement plug. Note the leakage profile is similar to the pressure profile smoothed step function shape of the transient leakage profile. Also note that the model predicts that leakage already exists prior to injection because of the pre-existing pressure difference between the atmosphere and the Nisku formation. The onset of leakage of actual CO₂ must be estimated using the two-phase plume migration model as described in Section 2.2. The time of arrival of the CO₂ plume arrival is estimated using equation (3).

Figure 5: CO₂ Leakage Rate for Single Abandoned Well Model with $r=1$ km, $k_{1s}=10-15m^2$, $D_{1s}=10m$ and $r_{1s}=0.1m$

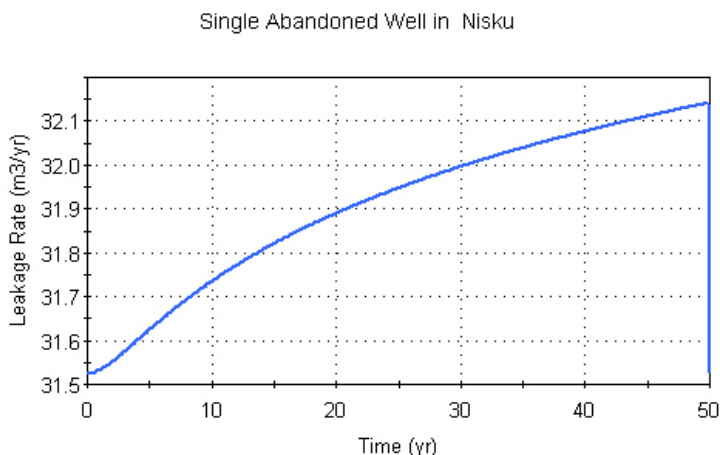
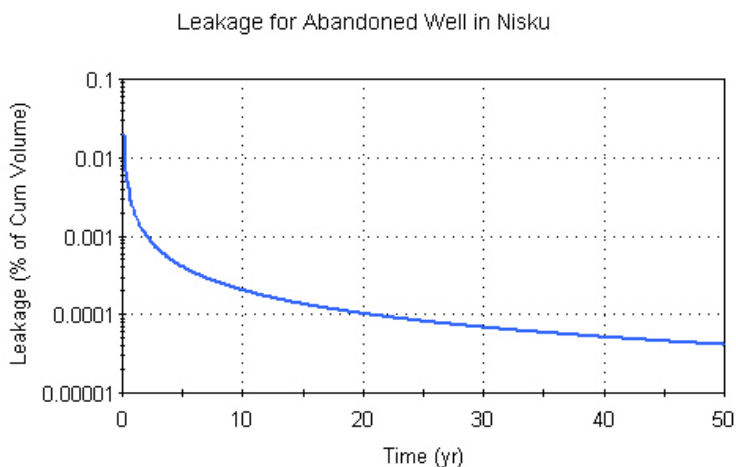


Figure 6 shows the same CO₂ leakage rate expressed as a percent of the cumulative storage volume.

Figure 6: CO₂ Leakage Rate as a Percent of Cumulative Annual Injected Rate for a Single Abandoned Well Model with $r=1$ km, $k_{1s}=10^{-15}$ m², $D_{1s}=20$ m and $r_{1s}=0.1$ m



2.4 CO₂ Leakage to Surface from an Abandoned Banff Well

The conceptual model for cross-formational flow from an abandoned well in the Nisku to an abandoned well in the Banff formation is shown in Figure 2. As in the previous section, the conceptual model is based on Nordbotten et al., (2004). The model makes the following assumptions:

- a vertically averaged pressure within the injection (Nisku) and overlying (Banff) formations;
- radial propagation of pressure (Darcy flow) in both formations;
- isotropy in the Nisku and Banff formation permeability tensors;
- no leakage through the underlying aquiclude and overlying (Calmar) and higher aquicludes (cap rocks);



WASP RISK-BASED LEAKAGE MODEL

- one dimensional Darcy flow from the Nisku formation to the Banff Formation through the first abandoned well cement plug;
- one dimensional Darcy flow from the Banff formation to the surface through the second abandoned well cement plug; and
- no leakage from the Nisku to the surface through the abandoned well.

Similar to the single abandoned well solution, the formation pressure is calculated as a function of the radial distance from the injection location within the reservoir formation. This is done by using the well pumping function (exponential integral) for single phase flow in a porous medium. The leakage component is modelled as a vertical one-dimensional Darcy process through the abandoned well which permits leakage between the Nisku and Banff formations. This process is driven by the pressure difference between CO₂ pressures in the two formations. Darcy flow is assumed in the Banff formation with the leakage flux acting as the system driver in the same way that the injection flux was the driver for radial flow in the Nisku formation. This radial flow causes a pressure increase at the bottom of abandoned wells penetrating the Banff formation which in turn causes leakage to the surface, modelled as vertical one-dimensional Darcy flow.

The next step in the modelling process is to evaluate the CO₂ pressure at the location of the abandoned well in the two formations. The pressure at the foot of the well penetrating the Banff formation is used in the one dimensional vertical Darcy equation to compute the CO₂ leakage rate through the abandoned well to the surface from the Banff formation.

The resulting equation for leakage from the Banff formation to the surface is given by the expression

$$Q_{2s}(D) = \frac{k_{2s} \pi r_w^2}{\mu D_{2s}} \left[p_s - \frac{(a_2 b_3 - a_3 b_2) d_1 + (b_1 a_3 - a_1 b_3) d_2 + (a_1 b_2 - a_2 b_1) d_3}{[(a_1 b_2 - a_2 b_1) c_3]} \right] \quad (9)$$

Where k_{2s} is the permeability of the (2nd) abandoned well plug between the Banff formation and the surface, r_{w2} is the radius of the 2nd abandoned well, p_s is atmospheric pressure, and D_{2s} is the length of the cement plug for the 2nd abandoned well. The set of coefficients a_1 through d_3 are defined in Appendix D. Some are dependent on the two well pumping functions which govern horizontal radial CO₂ flow from the injection well to the 1st abandoned well, and the CO₂ flow from the 1st abandoned well to the 2nd abandoned well (penetrating the Banff). Others depend on the well functions associated with vertical leakage flow from the Nisku to the Banff layers and also from the Banff to the surface.

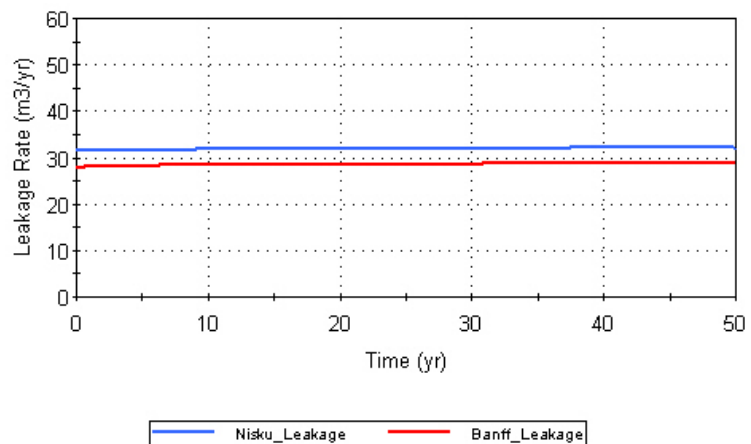
Figure 7 shows an example of the leakage flux through an abandoned well penetrating the Banff to the surface for $r_1=5$ km, $r_2=1$ km, $k_{2s}=10^{-15}$ m², $k_{12}=10^{-11}$ m², $r_w=0.1$ m and $D_w=10$ m, where $w=1s, 2s, 12$. The horizontal distance between the injection well and the 1st abandoned well is r_1 and the horizontal distance between the 1st and 2nd abandoned wells is r_2 . The permeability of the 1st abandoned well pathway allowing leakage from the Nisku to the Banff is that of a compromised well plug ($k_{12}=10^{-11}$ m²). Because of the relatively high permeability, the leakage rate from the well penetrating the Banff is almost equal to that from the Nisku well.

Figure 7: Leakage Rate Curve for $r_1=5$ km, $r_2=1$ km, $k_{12}=10^{-11}$ m², $k_{2s}=10^{-15}$ m², $r_{w1}=0.1$ m and $D_{w1}=10$ m



WASP RISK-BASED LEAKAGE MODEL

Well Leakage

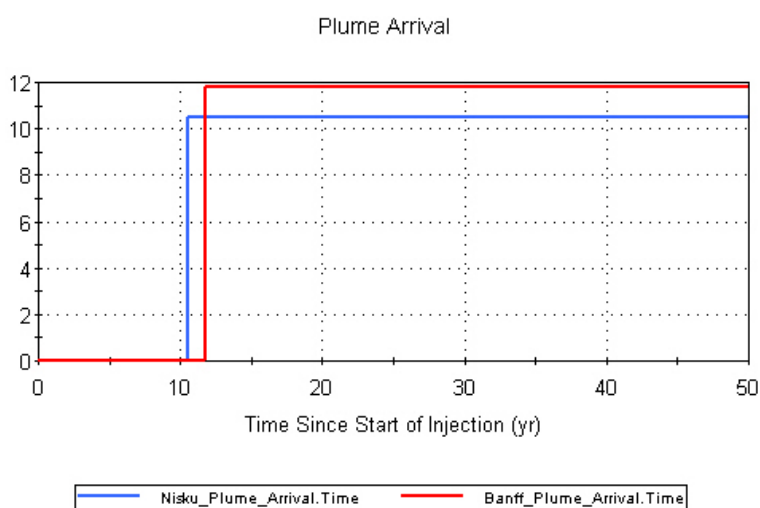




WASP RISK-BASED LEAKAGE MODEL

Although the leakage from the Banff formation is relatively large for the above parameters, the onset of the CO₂ leakage is delayed until the arrival of the CO₂ plume. Figure 8 shows the arrival time of the CO₂ plume at theoretical wells in the Nisku and Banff formations 5 km and 6 km respectively from the injection well. The arrival time of the plume at the abandoned well in the Nisku is the time since the onset of injection whereas the arrival time of the CO₂ plume at the abandoned well in the Banff is the time from the onset of arrival of the plume at the well in the Nisku formation (i.e., the total time for the plume to reach the well in the Banff is given by the sum of the two times which is approximately 22 years).

Figure 8: Plume Arrival Curve for $r_1=5$ km, $r_2=1$ km, $k_{12}=10^{-10}$ m², $k_{w1}=k_{w2}=10^{-15}$ m² $r_w=0.1$ m and $D_w=10$ m





3.0 SIMULATOR DEVELOPMENT

The analytical solutions presented in Section 2 were implemented using the GoldSim software package, a publically available, dynamic probabilistic simulation software platform. It is used to develop simulation platforms in a wide range of market sectors from mining to aerospace. The software uses an object-oriented programming language to develop a mathematical model that calculates changes in the specified system as a function of time. The simulation duration and time steps between calculations is specified by the user. Input parameters can be represented as deterministic or probabilistic values and the software uses the Monte Carlo method to propagate the uncertainties throughout the model calculations. The software has a library of distribution types (e.g., normal, log-normal, uniform, Weibull) that can be used to represent the probability distribution functions for uncertain inputs. Inputs and outputs can be controlled using a series of dashboards that serve as the user interface for the simulator.

The software programming language allows for the mathematical expressions of the different components in the system (e.g., reservoir pressure, plume migration, well bore flux rate) to be developed in a modular fashion. The components are linked through the parameters and functions they have in common. This hierarchical architecture facilitates revisions and additions to the model as the complexity of the system representation is increased or the conceptual model evolves. Additional components in the model architecture are used to store the input parameters, model outputs and user interface instructions for the simulator.

3.1 User Interface

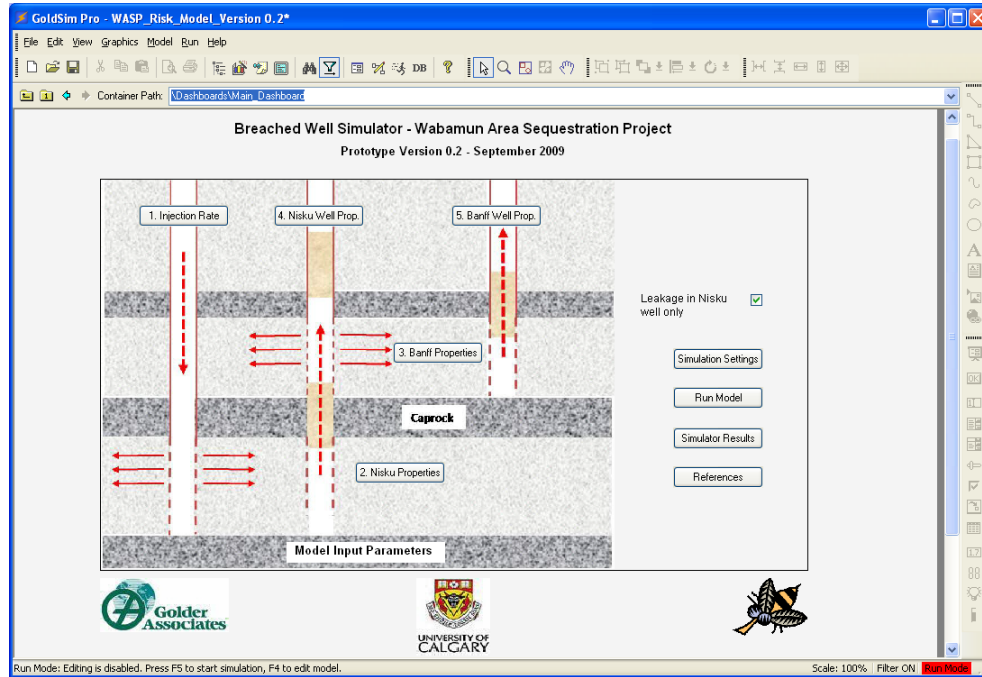
The user interface for the simulator consists of a series of dashboards to define the input parameters and assumptions in the simulation and display the results in various graphical and tabular formats. The Main dashboard is shown in Figure 9. The Main dashboard contains links to other dashboards for entering the input parameters for the simulation, selecting different abandoned well scenarios to run (i.e., single vs. multiple wells), and generating graphical and tabular outputs of the simulation results.

The graphic of the conceptual model in the Main dashboard contains a series of five links for setting the input parameter values to be used in a simulation. The input parameter dashboards are accessed by clicking on the “buttons” shown in Figure 9.

Figure 9: Simulation Model Main Dashboard



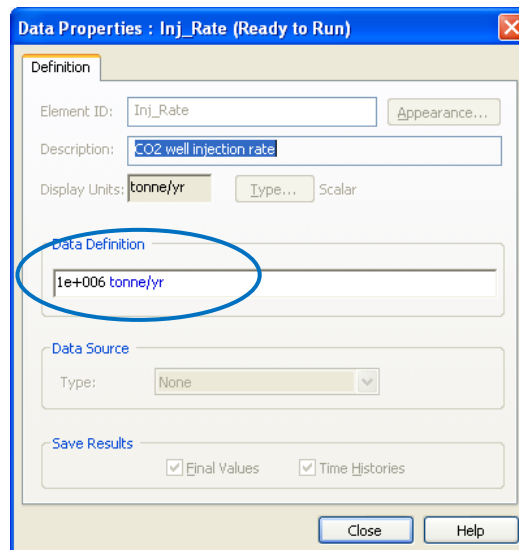
WASP RISK-BASED LEAKAGE MODEL



Injection Rate

The analytical expressions for calculating the formation pressure and CO₂ plume migration assume a constant CO₂ injection rate over the simulation period. The rate is set by clicking on the button labeled “Injection Rate” in the Main dashboard which produces the text box shown in Figure 10. The injection rate units are metric tonnes per year.

Figure 10: Input for CO₂ Injection Rate





Nisku Properties

The input parameters to define the properties of the Nisku formation are contained in a separate dashboard that is accessed by clicking on the “Nisku Properties” button on the Main dashboard. The Nisku formation properties dashboard is shown in Figure 11. Table 2 shows the parameters and the associated probability distribution types assumed in the model. Changes to the model are made by entering the distribution parameters in the dashboard (e.g., mean and standard deviation for a normal distribution). The probability distribution functions for the Nisku formation porosity and permeability are discrete distributions based on empirical data developed by the WASP team (Eisenger, 2009). The discrete data for these distributions is fixed, i.e., it cannot be changed by the user. Return to the Main dashboard by clicking on the button at the bottom of the screen.



WASP RISK-BASED LEAKAGE MODEL

Figure 11: Nisku Formation Properties Dashboard

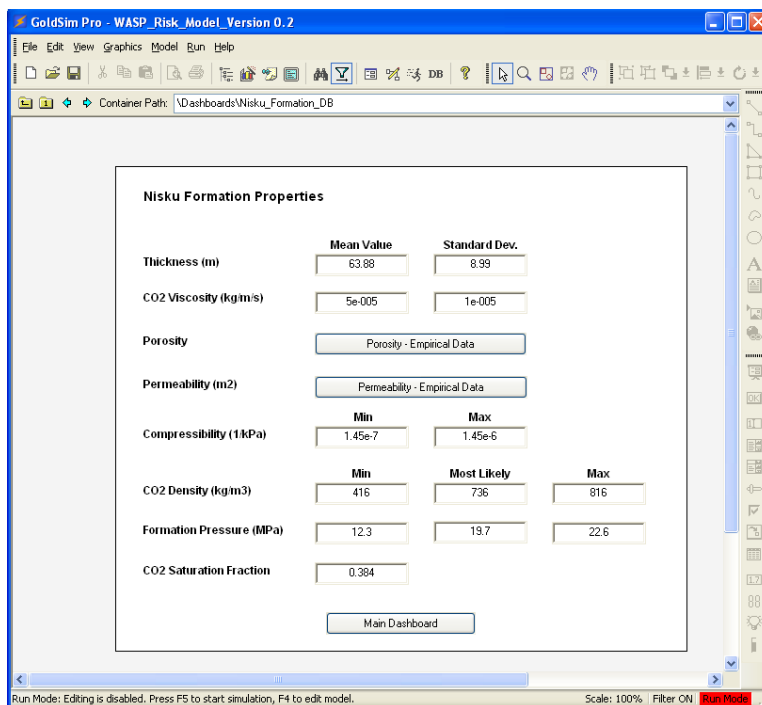


Table 2: Parameters and Distribution Types for the Nisku Formation Model Inputs

Input Parameter	Probability Distribution Function
Formation thickness	Log-normal
CO ₂ viscosity	Normal
Porosity	Discrete PMF
Permeability	Discrete PDF
Formation compressibility	Uniform
CO ₂ density	Triangular
Initial formation pressure	Triangular
CO ₂ saturation fraction	Uniform

Banff Properties

The input parameters to define the properties of the Banff formation are contained in a separate dashboard that is accessed by clicking on the “Banff Properties” button on the Main dashboard. The Banff formation properties dashboard is shown in Figure 12. Table 3 shows the parameters and the associated probability distribution types assumed in the model. Changes to the model are made by entering the distribution parameters in the dashboard (e.g., mean and standard deviation for a normal distribution). The probability distribution functions for the Banff formation porosity is a discrete distribution based on the empirical data from the Nisku formation



WASP RISK-BASED LEAKAGE MODEL

(Eisenger, 2009). The discrete data is fixed, i.e., it cannot be changed by the user. The user returns to the Main dashboard by clicking on the button at the bottom of the screen.

Figure 12: Banff Formation Properties Dashboard

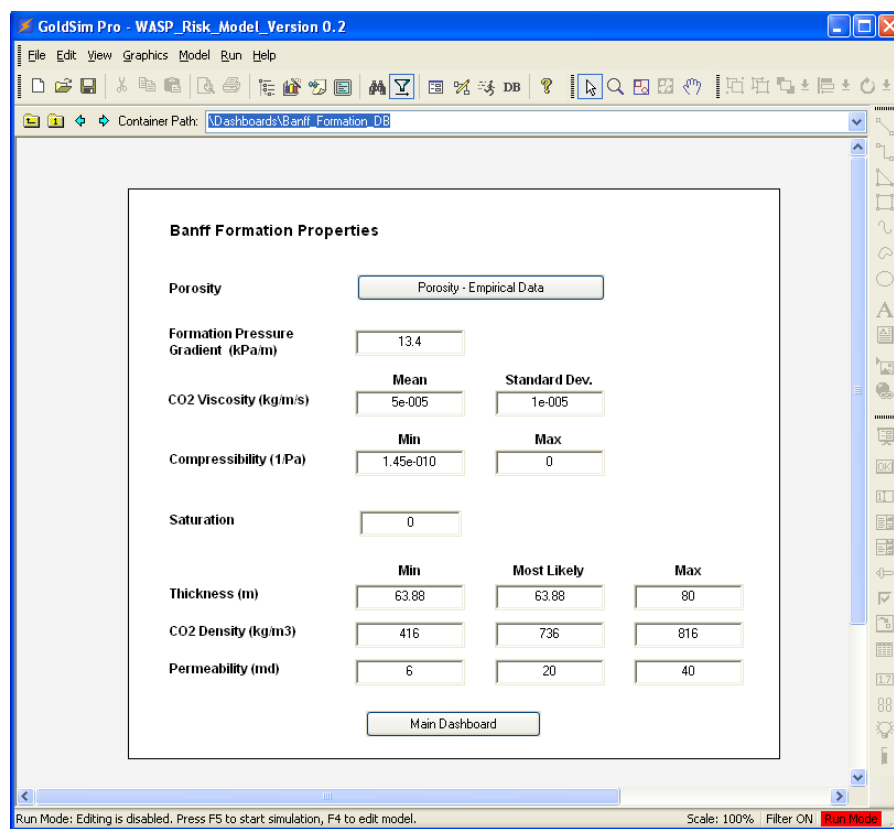


Table 3: Parameters and Distribution Types for the Banff Formation Model Inputs

Input Parameter	Probability Distribution Function
Formation thickness	Log-normal
CO ₂ viscosity	Normal
Porosity	Discrete PMF
Permeability	Discrete PDF
Formation compressibility	Uniform
CO ₂ density	Triangular
Initial formation pressure	Triangular
CO ₂ saturation fraction	Uniform



Nisku Abandoned Well Properties

The input parameters to define the properties of the abandoned well in the Nisku formation are contained in a separate dashboard that is accessed by clicking on the “Nisku Well Prop,” button on the Main dashboard. The abandoned well properties dashboard is shown in Figure 13. Table 4 contains a list of the parameters and the associated probability distribution functions.

Figure 13: Nisku Abandoned Well Properties Dashboard

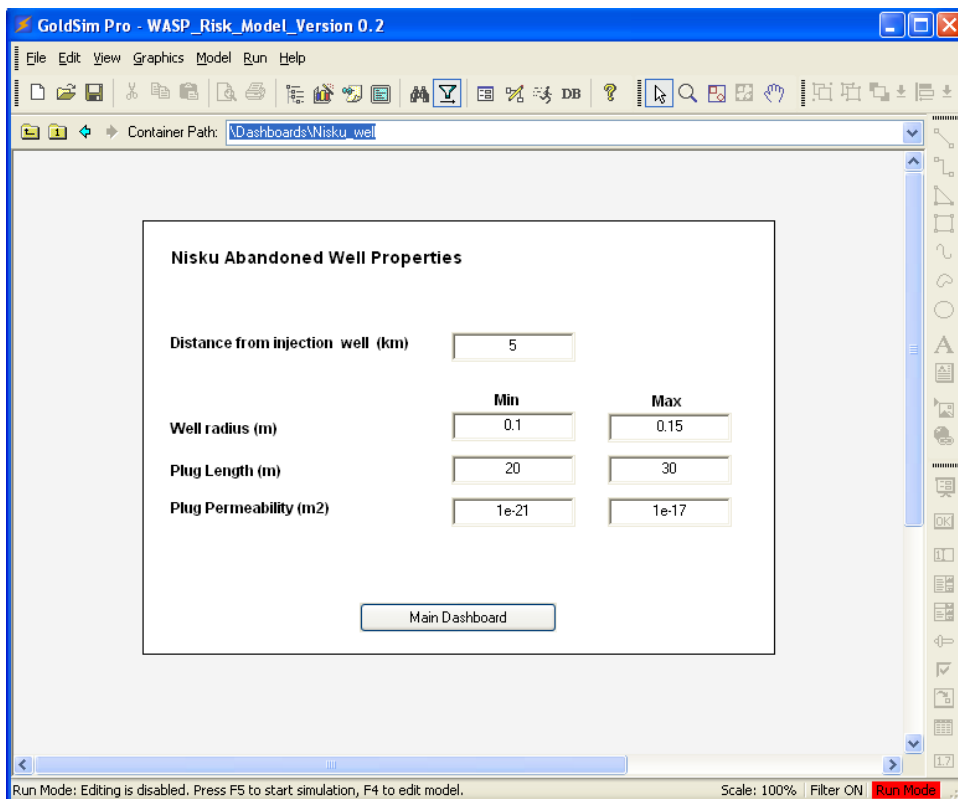


Table 4: Parameters and Distribution Types for the Nisku Abandoned Well

Input Parameter	Probability Distribution Function
Distance from injection well	Deterministic
Well radius	Uniform
Plug length	Uniform
Plug permeability	Uniform

Banff Abandoned Well Properties

The input parameters to define the properties of the abandoned well in the Banff formation are contained in a separate dashboard that is accessed by clicking on the “Banff Well Prop,” button on the Main dashboard. The



WASP RISK-BASED LEAKAGE MODEL

Banff abandoned well properties dashboard is shown in Figure 14. Table 5 contains a list of the parameters and the associated probability distribution functions.



WASP RISK-BASED LEAKAGE MODEL

Figure 14: Banff Abandoned Well Properties Dashboard

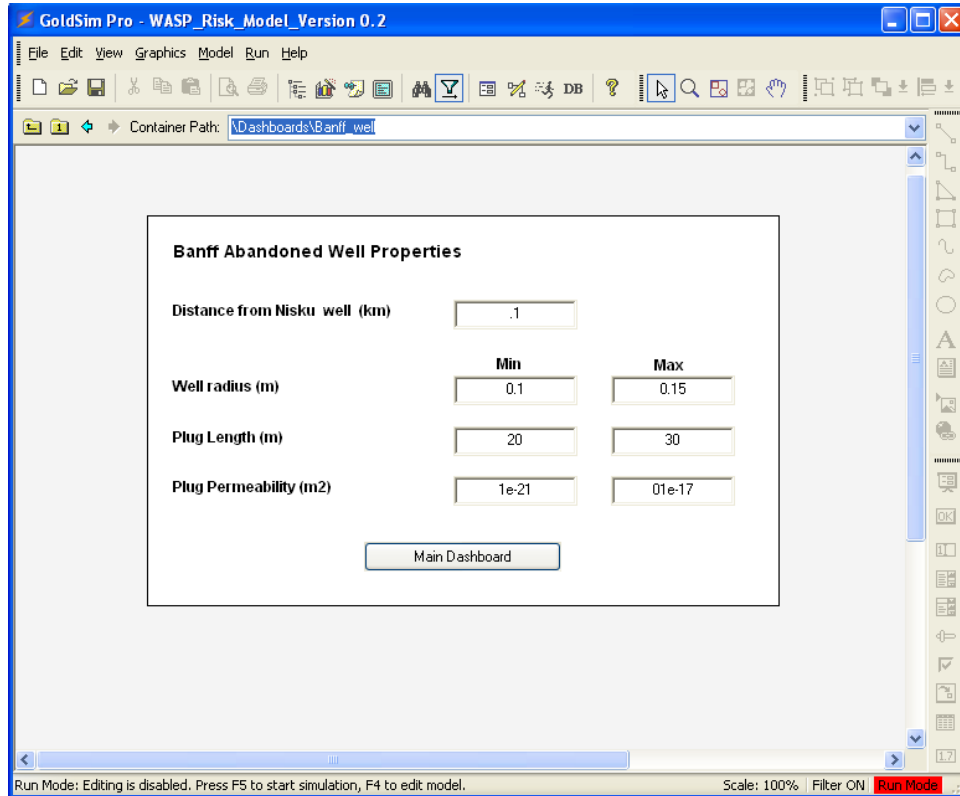


Table 5: Parameters and Distribution Types for the Banff Abandoned Well

Input Parameter	Probability Distribution Function
Distance from Nisku well	Deterministic
Well radius	Uniform
Plug length	Uniform
Plug permeability	Uniform

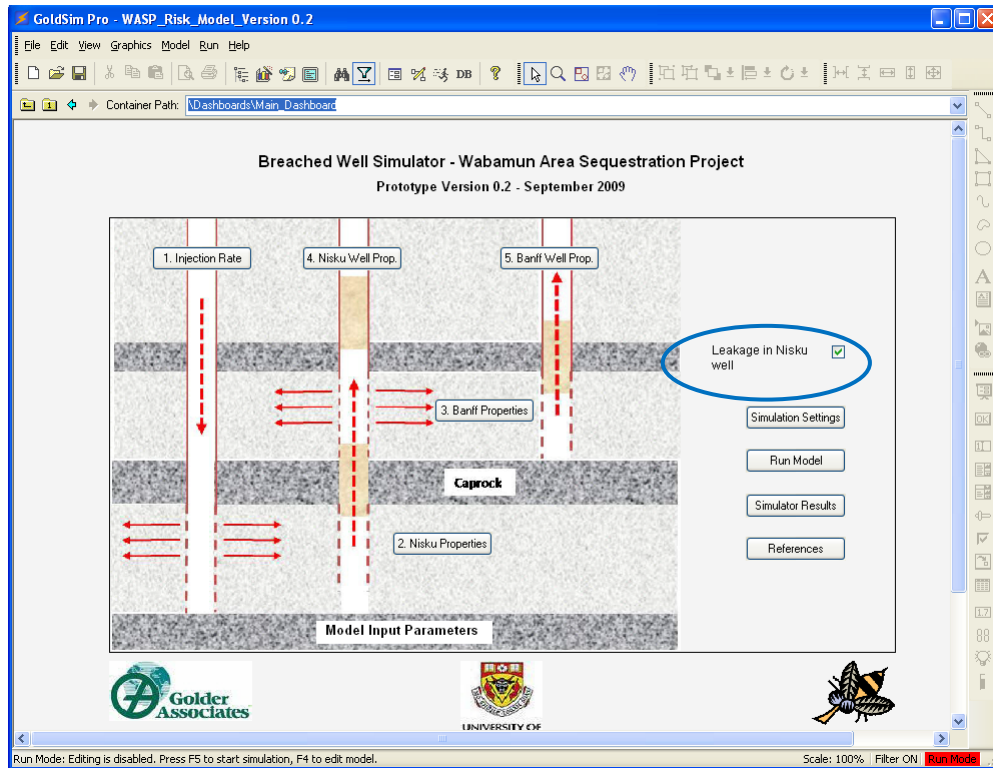
Abandoned Well Scenario Selection

The simulator includes two abandoned well scenarios as described in Section 2. The leakage scenario shown in Figure 1 through a single well in the Nisku formation is selected by placing a check mark in the check box to the right in the Main dashboard (Figure 15). The leakage scenario shown in Figure 2 from the Nisku, through the Nisku abandoned well into the Banff formation and then through the Banff abandoned well is selected by clearing the check box.



WASP RISK-BASED LEAKAGE MODEL

Figure 15: Check Box for Well Leakage Scenario Selection



Simulation Settings

The Simulation Settings button on the Main dashboard is used to set the duration of the simulation, the number of time-steps (and, therefore, the time step length), and the number of Monte Carlo realizations to run. The dialog box for the simulation settings is shown in Figure 16 (note: “Time” tab at top of box must be selected). CO₂ injection is assumed to take place over the entire duration of the simulation. Therefore the total injected mass of CO₂ is equal to the duration entered and the injection rate entered in a separate dashboard in the model. The timestep interval is determined by the number of time steps entered in the lower section of the dialog box. For example, a value of 50 time steps and a duration of 50 years results in a one-year time step intervals in the simulation. A value of 600 would result in a one-month time step.

Clicking on the “Monte Carlo” tab at the top of the dialog box produces the dialog box shown in Figure 17. The number of iterations or individual model simulations that are performed for a Monte Carlo analysis is selected using the input field at the top of the dialog box. A deterministic run (a single realization) can be selected by clicking on the radio button in the lower field of the dialog box (Figure 17).



WASP RISK-BASED LEAKAGE MODEL

Figure 16: Dialog Box for Simulation Duration and Number of Time Steps

Simulation Settings...

Time Monte Carlo Globals Information

Specify model start time and duration, and define global time steps for model calculations and result plotting.

Basic Time Settings

Time Display Units: yr

Duration: 50 yr

Start-time: 1/21/2009 12:00:00 AM

End-time: 1/21/2059 12:00:00 PM

Time Phase Settings

Time Range [Yr]	#Steps	Length [Yr]	Plot Every	FV
0 - 50	50	1	1	<input checked="" type="checkbox"/>

Add... Remove Advanced...

OK Cancel Help

Figure 17: Dialog Box for Setting Number of Monte Carlo Realizations

Simulation Settings...

Time Monte Carlo Globals Information

Define Monte Carlo options to carry out a probabilistic simulation, and specify the sampling method for Stochastic variables.

Probabilistic Simulation

Realizations: 1000 # Histories to save: 1000

Run the following Realization only: Realization: 1

Use Latin Hypercube Sampling

Repeat Sampling Sequences Random Seed: 1

Deterministic Simulation

Simulation deterministically using:

Element Deterministic Values

Element Mean Values

Specified Quantile: 0.5

OK Cancel Help



WASP RISK-BASED LEAKAGE MODEL

Simulation Results

Simulation results can be viewed by clicking on the Simulation Results button on the Main dashboard. The Results dashboard is shown in Figure 18. Table 6 contains a description of each of the model outputs that can be accessed from the dashboard.

Figure 18: Results Dashboard

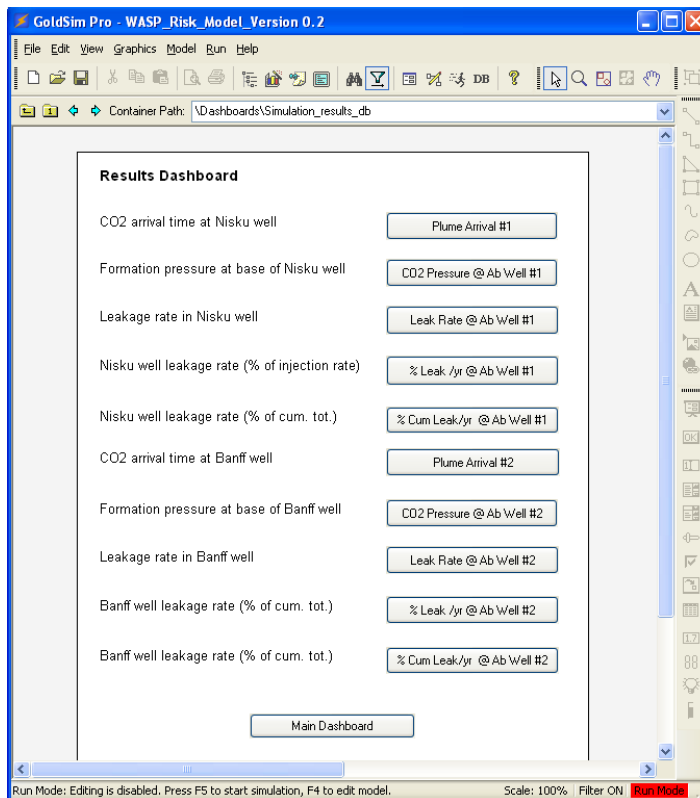


Table 6: Description of Model Outputs

Model Output	Description
Plume Arrival #1	PDF of CO ₂ plume arrival at base of Nisku abandoned well
CO ₂ Pressure @ Ab Well #1	PDF of formation pressure at base of Nisku abandoned well in MPa
Leak Rate @ Ab Well #1	PDF of leakage rate from Nisku abandoned well to surface in m ³ /yr
% Leak/yr @ Ab Well #1	PDF of leakage rate from Nisku abandoned well to surface as a percentage of annual CO ₂ volume injected
% Cum Leak/yr @ Ab Well #1	PDF of leakage rate from Nisku abandoned well to surface as a percentage of total volume injected to date
Plume Arrival #2	PDF of CO ₂ plume arrival at base of Banff abandoned well in years
CO ₂ Pressure @ Ab Well #2	PDF of formation pressure at base of Banff abandoned well in MPa
Leak Rate @ Ab Well #2	Leakage rate of CO ₂ from the Banff abandoned well to the surface in units of m ³ /yr
% Leak/yr @ Ab Well #2	Leakage rate of CO ₂ from the Banff abandoned well to the surface as a percentage of the injection rate
% Cum Leak/yr @ Ab Well #2	Leakage rate of CO ₂ from the Banff abandoned well to the surface as a percentage of total CO ₂ volume stored



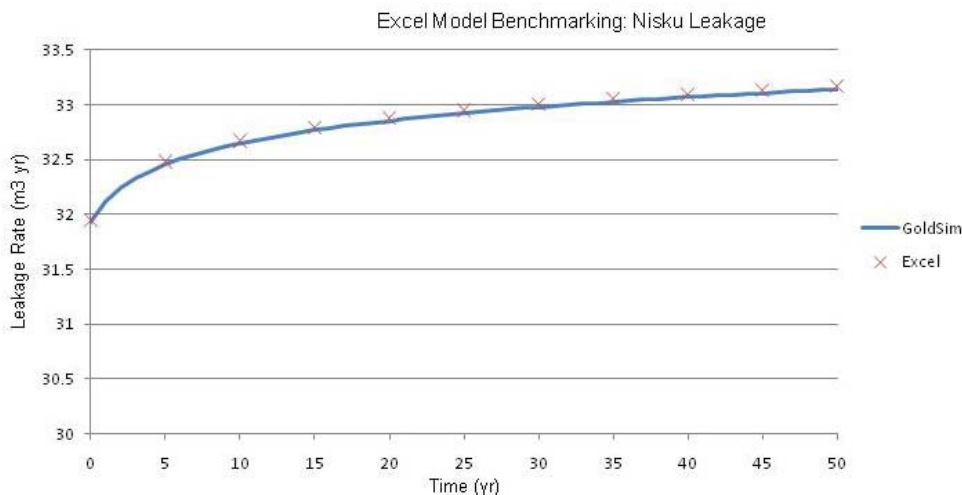
4.0 BENCHMARKING

The WASP leakage simulator was benchmarked against independent calculations that were performed by repeating the main analytical calculations in an Excel spreadsheet developed by Golder and also a spreadsheet developed by Lavoie (2009) for the plume migration calculations. A more rigorous benchmarking of the leakage model against a numerical simulator such as TOUGH2 (2009) is required to test the validity of the assumptions and the accuracy of the mathematical development. This is one of the major follow on tasks recommended in the Section 7.

4.1 CO₂ Leakage – Abandoned Nisku Well

Figure 19 shows leakage rate outputs from the Simulator and Excel models for the abandoned well in the Nisku in m^3/yr . The input parameters for the two different methods are the expected values in Table 2 with the two well plug permeabilities equal to $10^{-15} m^2$. Close agreement is observed for the two different models.

Figure 19: Transient Leakage Flux Curve in m^3/s for Abandoned Well in Nisku

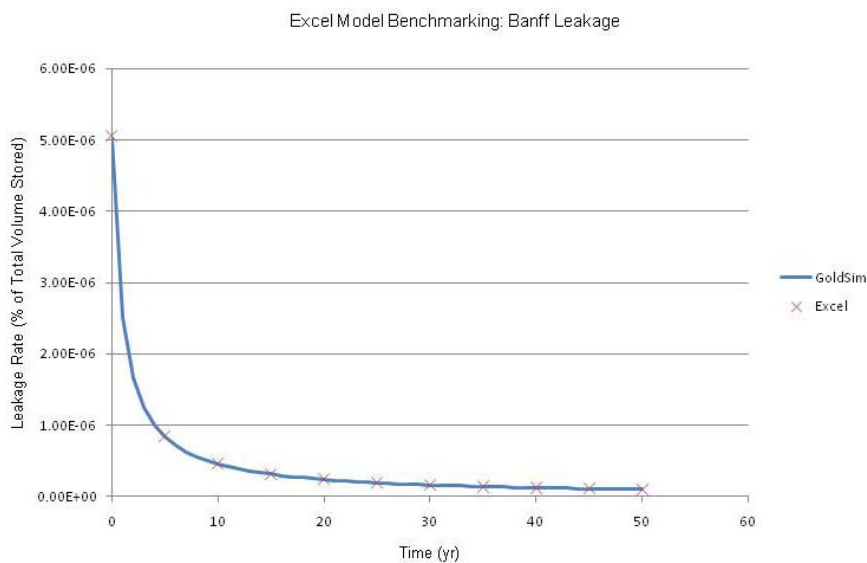


4.2 CO₂ Leakage – Abandoned Banff Well

Figure 20 shows leakage rate outputs from the GoldSim model and Excel model for the abandoned well in the Banff as a percentage of total volume stored. The input parameters are the deterministic parameters from Table 2 with the two well plug permeabilities equal to $10^{-15} m^2$. The results from the two different models are essentially the same.



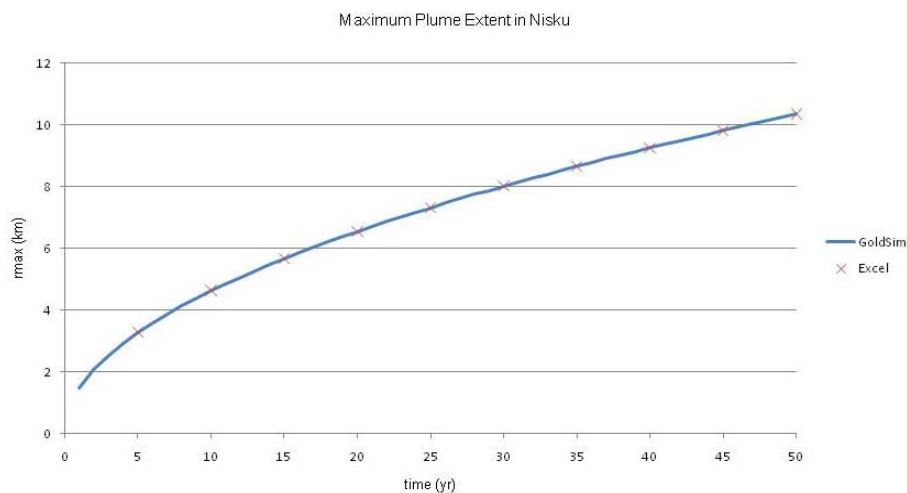
Figure 20: Transient Leakage Flux Curve as a % of Injection Rate for Abandoned Well in Banff



4.3 Plume Migration – Nisku Formation

Figure 21 shows the maximum extent of the plume for the GoldSim model and Excel model for $S_{res}=0.384$. The input parameters are the deterministic parameters from Table 2. The results from the two different models are almost identical.

Figure 21: Maximum CO₂ Plume Radius for the Nisku for $S_{res}=0.3$





5.0 WASP SPECIFIC DATA

This section summarizes the site specific input data for the WASP High Grade Study Area. Deterministic values were used for all input parameters during model development and testing. Probabilistic values were implemented in the simulator for the sensitivity analyses discussed in Section 6.

5.1 Probabilistic Inputs

Many of the input parameters in the model are uncertain due to limited site data, natural variability and the difficulty in characterizing hydrogeological systems. These uncertain quantities are represented in the model by probability distribution functions and are propagated in the calculations of leakage flux through the abandoned wells and plume radii using the Monte Carlo method. Parameters describing the formation characteristics were supplied by the WASP team (Eisinger, 2009) and are summarized in Table 7.

The uncertainty in the permeability and porosity of the Nisku formation are represented by discrete distributions based on the WASP Static Model (2008). Permeability is represented by a discrete cumulative distribution function (CDF) which was input directly into the simulator while the formation porosity is represented by a discrete probability mass function (PMF). The permeability, porosity and thickness distributions for the Banff formation were assumed to be the same as the Nisku.

The uncertainty in the initial pressure in the Nisku formation is represented by a triangular distribution (Lavoie, 2008). The spread of the distribution is approximately $\pm 25\%$ of the mean value. The initial pressure in the Banff is based on the same distribution that is reduced based on an assumed linear relationship between formation pressure and depth (AAPG, 1996).

The uncertainty distribution for the formation compressibility is represented by a uniform distribution. The data on the thickness of the Nisku formation (Eisinger, 2009) was fit to a log normal distribution using an Anderson-Darling fit .

The leaky well parameters for the abandoned well plugs are represented by uniform distributions based on the ranges suggested by Nygaard (2009) for intact and fractured cements and an open hole.

Table 7: Probabilistic Inputs for Nisku and Banff Formation Properties

Name	Symbol	Value	Expected Value	Reference	
Permeability of Nisku formation	k_1	CDF: Discrete		$1.59 \times 10^5 \text{ md}$	Eisinger, 2009
		$P(k_1)$	$k_1(\text{md})$		
		0	0		
		0.05	0.01		
		0.19	0.1		
		0.3	1		
		0.3	1		
		0.59	10		
		0.81	100		
0.975	1,000				
Compressibility of CO ₂ rock system in Nisku	c_1	PDF: Uniform Distribution $c \sim U(1.45 \times 10^{-10} - 1.45 \times 10^{-9}) (\text{Pa})^{-1}$	$7.975 \times 10^{-10} (\text{Pa})^{-1}$	Eisinger, 2009	
Compressibility of CO ₂ rock system in Banff	c_2	Assumed to be the same as Nisku	$7.975 \times 10^{-10} (\text{Pa})^{-1}$		



WASP RISK-BASED LEAKAGE MODEL

Table 7: Probabilistic Inputs for Nisku and Banff Formation Properties (continued)

Name	Symbol	Value	Expected Value	Reference																																																								
Thickness of Nisku formation	b_1	PDF: Lognormal: $b_1 \sim LN(63.88, 8.99) m$	63.88 m	Eisinger, 2009																																																								
Porosity of Nisku Formation	\square_1	PMF: Discrete <table border="1"> <thead> <tr> <th>$p(\square)$</th> <th>$\square(\%)$</th> <th>$p(\square)$</th> <th>$\square(\%)$</th> </tr> </thead> <tbody> <tr><td>0.014</td><td>1e-006</td><td>0.004</td><td>0.13</td></tr> <tr><td>0.146</td><td>0.01</td><td>0.003</td><td>0.14</td></tr> <tr><td>0.274</td><td>0.02</td><td>0.002</td><td>0.15</td></tr> <tr><td>0.22</td><td>0.03</td><td>0.002</td><td>0.16</td></tr> <tr><td>0.114</td><td>0.04</td><td>0.002</td><td>0.17</td></tr> <tr><td>0.07</td><td>0.05</td><td>0.002</td><td>0.18</td></tr> <tr><td>0.04</td><td>0.06</td><td>0.002</td><td>0.19</td></tr> <tr><td>0.038</td><td>0.07</td><td>0.002</td><td>0.2</td></tr> <tr><td>0.018</td><td>0.08</td><td>0.002</td><td>0.21</td></tr> <tr><td>0.014</td><td>0.09</td><td>0.002</td><td>0.22</td></tr> <tr><td>0.011</td><td>0.1</td><td>0.002</td><td>0.23</td></tr> <tr><td>0.009</td><td>0.11</td><td>0.001</td><td>0.24</td></tr> <tr><td>0.006</td><td>0.12</td><td></td><td></td></tr> </tbody> </table>	$p(\square)$	$\square(\%)$	$p(\square)$	$\square(\%)$	0.014	1e-006	0.004	0.13	0.146	0.01	0.003	0.14	0.274	0.02	0.002	0.15	0.22	0.03	0.002	0.16	0.114	0.04	0.002	0.17	0.07	0.05	0.002	0.18	0.04	0.06	0.002	0.19	0.038	0.07	0.002	0.2	0.018	0.08	0.002	0.21	0.014	0.09	0.002	0.22	0.011	0.1	0.002	0.23	0.009	0.11	0.001	0.24	0.006	0.12			0.04	Eisinger, 2009
$p(\square)$	$\square(\%)$	$p(\square)$	$\square(\%)$																																																									
0.014	1e-006	0.004	0.13																																																									
0.146	0.01	0.003	0.14																																																									
0.274	0.02	0.002	0.15																																																									
0.22	0.03	0.002	0.16																																																									
0.114	0.04	0.002	0.17																																																									
0.07	0.05	0.002	0.18																																																									
0.04	0.06	0.002	0.19																																																									
0.038	0.07	0.002	0.2																																																									
0.018	0.08	0.002	0.21																																																									
0.014	0.09	0.002	0.22																																																									
0.011	0.1	0.002	0.23																																																									
0.009	0.11	0.001	0.24																																																									
0.006	0.12																																																											
Porosity of Banff Formation	\square_2	Assume same as Nisku	0.04																																																									
Initial pressure in Nisku	p_1^{init}	$p_1^{init} \sim tri(12.3, 19.7, 22.6) MPa$	18.2 MPa	Eisinger, 2009																																																								
Initial pressure in Banff	p_2^{init}	$p_2^{init} \sim p_1^{init} - 4.08 MPa \sim tri(10, 13, 16) MPa$ Use same as Nisku, except correct for pressure change with decreased depth	15.2	(Lavoie, 2008) and (AAPG, 1996)																																																								
Permeability of Banff formation	k_2	~Assumed same as Nisku.	18.7 md																																																									
Thickness of Nisku formation	h_2	~Assumed same as Nisku	63.88 m																																																									
CO ₂ viscosity in Nisku formation	c_1	Kolmogorov-Smirnov fit to WASP measured data $\square \sim N(5 \times 10^{-5}, 1 \times 10^{-5}) Pa \cdot s$	$5 \times 10^5 Pa \cdot s$	Data: (Eisinger, 2009)																																																								
CO ₂ density in Nisku formation	\square_1	Kolmogorov-Smirnov fit to WASP measured data $\square \sim tri(416, 736, 816) kg$	$565 kg/m^3$	Data: (Eisinger, 2009)																																																								
CO ₂ viscosity in Banff formation	\square_2	Assume same as Nisku	$5 \times 10^5 Pa \cdot s$	Data: (Eisinger, 2009)																																																								
CO ₂ density in Banff formation	\square_2	Assume same as Nisku	$5 \times 10^5 Pa \cdot s$	Data: (Eisinger, 2009)																																																								



WASP RISK-BASED LEAKAGE MODEL

Table 8: Probabilistic Inputs for Abandoned Wells Parameters

Name	Symbol	Value	Expected Value	Reference
Permeability of well plug in 1 st abandoned well between Nisku and surface	k_{1s}	These will depend on well completion state. The following distributions will be used: $k_w \sim U(10^{-21}, 10^{-17}) m^2$: Open Hole	$5 \times 10^{-18} m^2$	Data from Nygaard, 2009
Permeability of well plug in 2 nd abandoned well between Banff and surface	k_{2s}	$k_w \sim U(10^{-16}, 10^{-14}) m^2$: Fractured cement $k_w \sim U(10^{-12}, 10^{-10}) m^2$: Intact cement	$5 \times 10^{-18} m^2$	
Permeability of well plug in 1 st abandoned well between Nisku and Banff	k_{12}		$5 \times 10^{-18} m^2$	
Length of well plug in 1 st abandoned well between Nisku and surface	D_{1s}	These will depend on well completion state. The following distributions will be used:		
Length of well plug in 2 nd abandoned well between Banff and surface	D_{2s}	$D_w \sim U(0.1-10) m$: Open Hole $D_w \sim U(10-20) m$: Fractured cement $D_w \sim U(20, 30) m$: Intact cement	25 m	
Length of well plug in 1 st abandoned well between Nisku and Banff	D_{12}		25 m	
Radius of 1 st abandoned well between Nisku and surface	r_{1s}	These will depend on well completion state. The following distributions will be used:		
Radius of 1 st abandoned well between Banff and surface	r_{2s}	$r_w \sim U(0.19-0.22) m$: Open Hole $r_w \sim U(0.15-0.2) m$: Fractured cement $r_w \sim U(0.1-0.15) m$: Intact cement	0.125 m	
Radius of 1 st abandoned well between Nisku and Banff	r_{12}		0.125 m	



6.0 SENSITIVITY ANALYSIS

Sensitivity analysis is used to identify the input parameters which most strongly influence a specific output from the model. The model outputs used to evaluate the simulator sensitivity are the two leakage rates for the abandoned wells penetrating the Nisku and Banff formations and the maximum extent of the CO₂ plume migration. Each sensitivity analysis is a series of simulations in which selected independent variables are varied, one variable at a time, through a range of values while the other values are assigned their expected value. A lower bound, central, and upper bound value are assigned to each independent variable. Simulations are run at the three different values for the first dependent variable while the other independent variables are assigned their central value. The process is repeated for each independent variable. The central, lower and upper bound values in the sensitivity analysis are based on the 50th, 5th and 95th percentile values respectively from the probability distribution functions in Tables 2 and 3 in Section 5.

The results of a sensitivity analysis can be illustrated using a Tornado diagram, a graphical representation of the degree to which a model output is sensitive to the specified independent variables. The x-axis of a Tornado chart represents the values of the result for different values of the independent variables. Each bar represents the range of result values produced when each independent variable is set to lower bound, central, and upper bound values (with the other variables being held constant). A light blue bar indicates that the value was produced by the lower bound value (Low), and a dark blue bar indicates that the value was produced by the upper bound value (High). The variables are organized from top to bottom according to the total range of results produced. That is, the variable that produces the largest range of the result between the lower and upper bound values is at the top of the chart. Hence, bars become smaller toward the bottom of the chart, and the overall effect is to take on the appearance of a “tornado”. The solid vertical line represents the value of the result when the central values are used for all independent variables. Figure 25 in the next section is an example of a Tornado chart.

The X-Y function chart is another type of sensitivity analysis that provides a graphical representation of the degree to which the result is sensitive to the specified independent variables. Similar to the method used for the Tornado plots, a series of deterministic simulations are performed, varying one independent variable at a time through its range of values. In addition to the lower bound, central and upper bound values, simulations are performed at other intermediate values. The charts in the figures include 11 points or values. There is one line for each variable. Each line illustrates how the result changes when that independent variable is varied from its lower bound to its upper bound (with the other variables being held constant). Because the variables sometimes have different units and a different range, the x-axis does not represent actual values; rather it represents normalized values (and hence they all range from 0 to 1). Figure 22 in Section 6.1 is an example of an X-Y function chart.

The results from the sensitivity analyses for the four outputs are described below.

6.1 Leakage in Nisku Abandoned Well

The parameters identified as potentially having a strong influence on the leakage in the Nisku abandoned well are:

- plug permeability in the abandoned well;
- plug length;
- abandoned well radius;
- density of CO₂ in the Nisku formation;

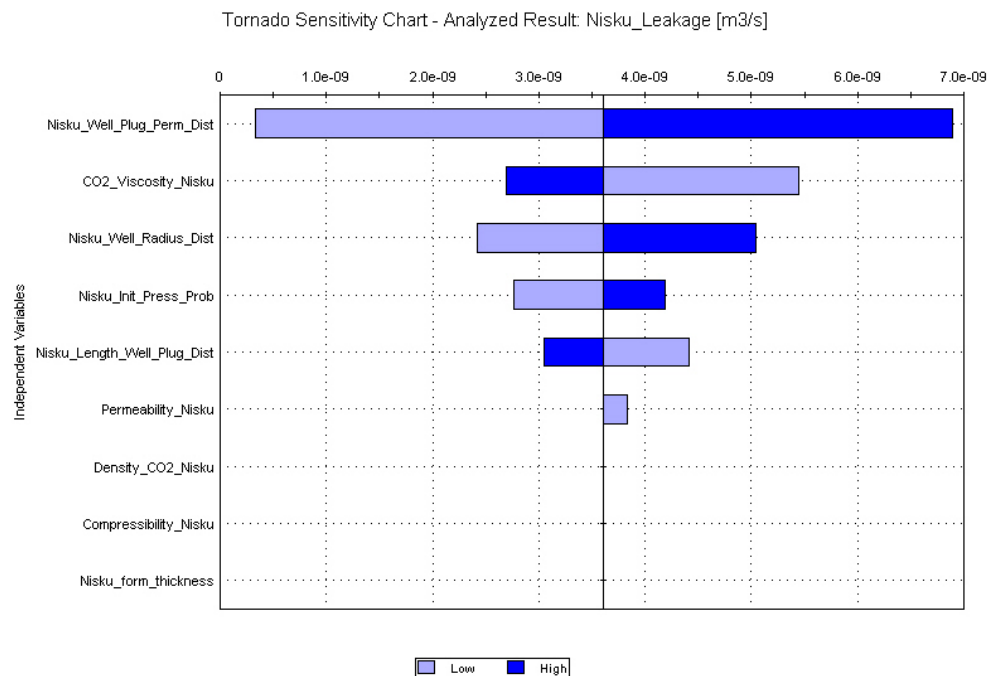


WASP RISK-BASED LEAKAGE MODEL

- CO₂ viscosity in the Nisku;
- permeability of the Nisku formation;
- initial pressure in the Nisku; and
- Nisku thickness.

The results of the sensitivity analyses for the leakage through an abandoned well in the Nisku formation are shown in Figures 22 and 23. The parameter with the strongest influence on well leakage is plug permeability with a linear relationship between permeability and the leakage rate. The CO₂ viscosity and abandoned well radius are the next to parameters with the greatest influence on the leakage rate. The CO₂ viscosity relationship is nonlinear at the lower range of the distribution included in the sensitivity analysis. The sensitivity of well leakage to CO₂ density, formation pressure and plug length are similar with a slightly nonlinear relationship for all three parameters. The leakage rate is largely insensitive to the permeability and thickness of the Nisku formation.

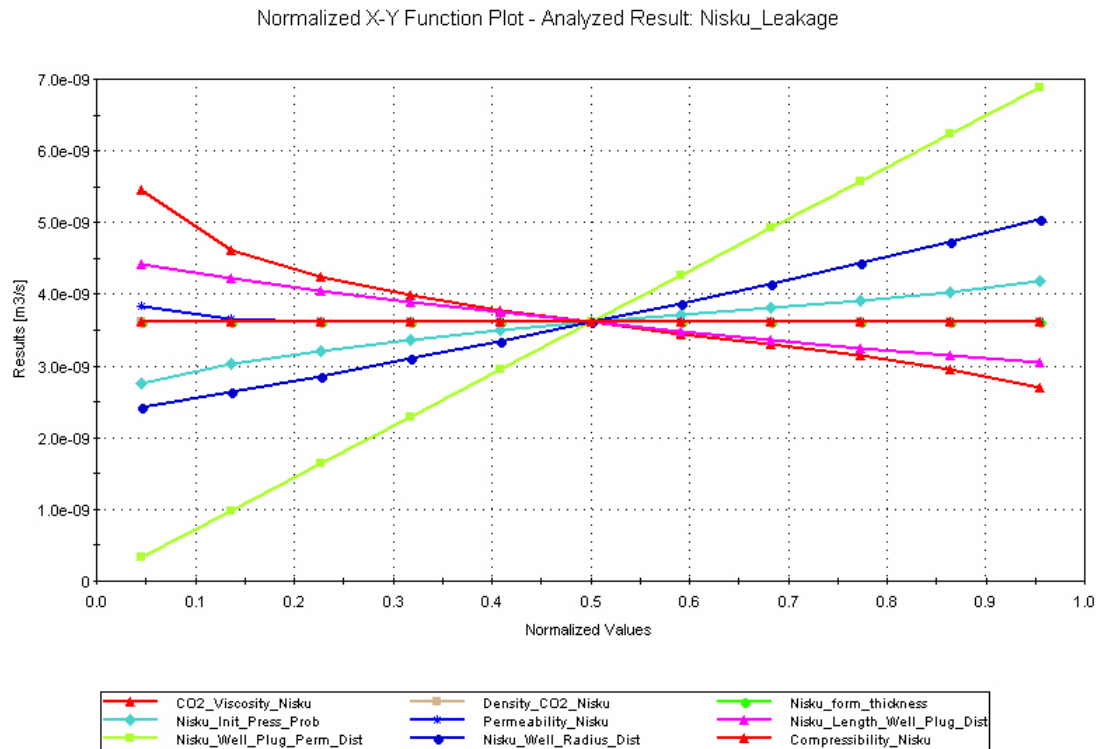
Figure 22: Tornado Plot of the Sensitivity Analysis Results for Leakage Through Abandoned Nisku Well





WASP RISK-BASED LEAKAGE MODEL

Figure 23: X-Y Function Chart of Sensitivity Results for Leakage through Abandoned Nisku Well



6.2 Leakage in Banff Abandoned Well

The parameters identified as potentially having a strong influence on the leakage in the Banff abandoned well are:

- the abandoned well parameters associated with leakage through the plug between the Banff and the surface;
- the Banff formation hydrogeological parameters;
- the abandoned well parameters associated with leakage through the conduit plug between the Nisku and Banff formations; and
- the Nisku formation hydrogeological parameters.

The results of the sensitivity analyses for the leakage through an abandoned well in the Banff formation are shown in Figures 24 and 25. The results are similar to the leakage in the Nisku abandoned well (Section 6.1). The parameter with the strongest influence on well leakage is plug permeability with a linear relationship between permeability and the leakage rate. The CO₂ viscosity and abandoned well radius are the next to parameters with the greatest influence on the leakage rate. The CO₂ viscosity relationship is nonlinear at the lower range of the distribution included in the sensitivity analysis. The sensitivity of well leakage to CO₂ density, formation pressure and plug length are similar with a slightly nonlinear relationship for all three parameters. The leakage rate is largely insensitive to the permeability and thickness of the Nisku formation.



WASP RISK-BASED LEAKAGE MODEL

Figure 24: Tornado Plot of the Sensitivity Analysis Results for Leakage Through Abandoned Banff Well

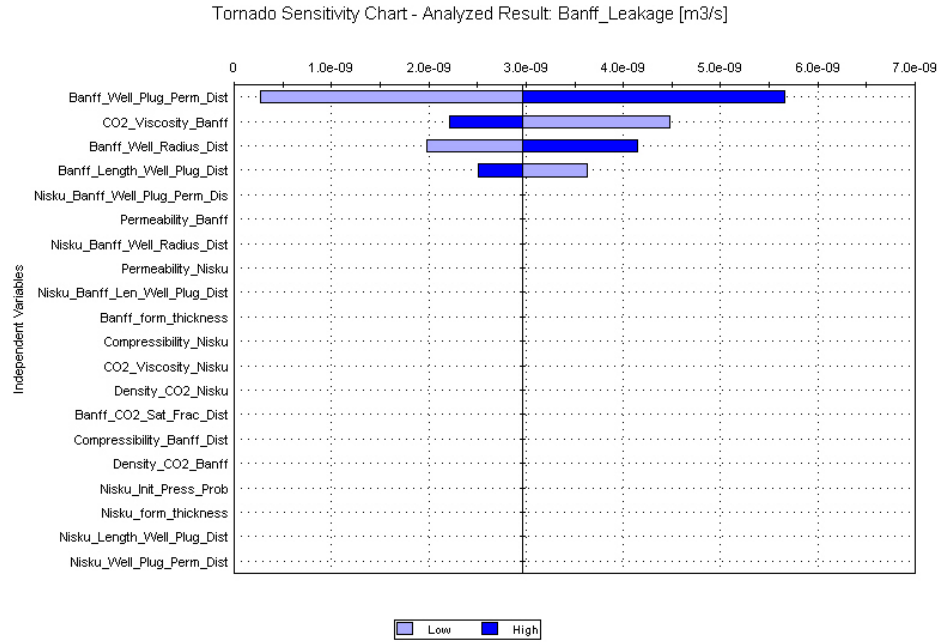
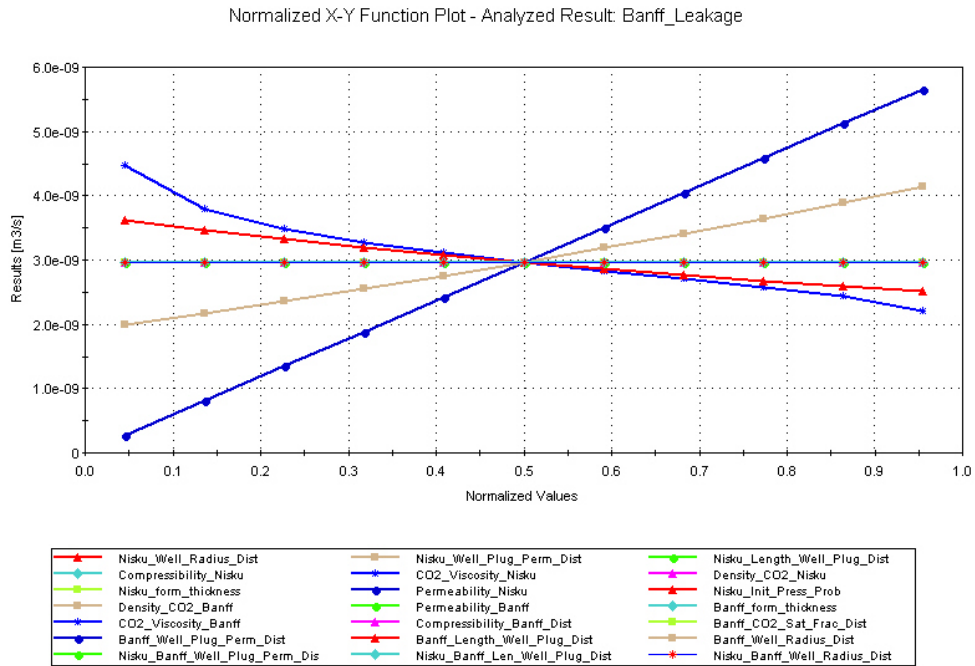


Figure 25: X-Y Function Chart of Sensitivity Results for Leakage through Abandoned Banff Well





6.3 CO₂ Plume Migration in the Nisku

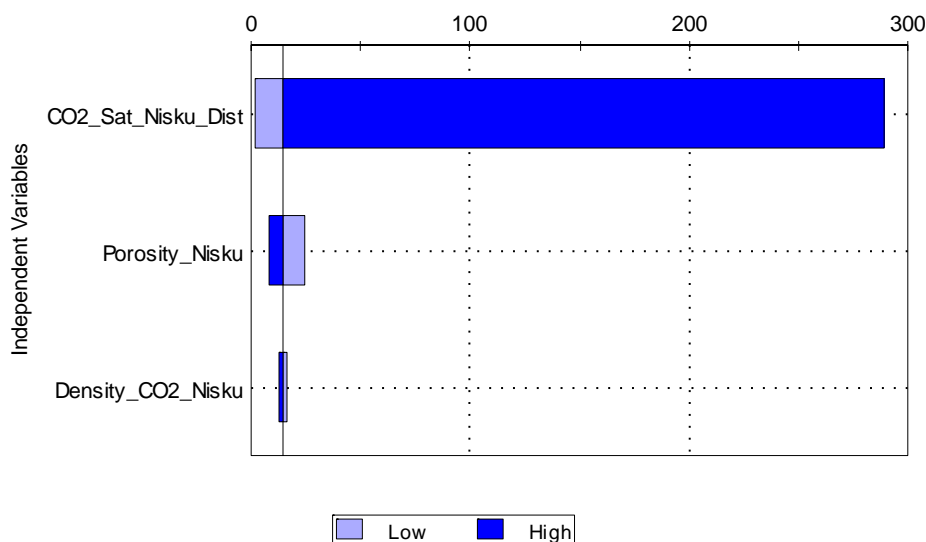
The parameters identified as potentially having a strong influence on the maximum radial extent of the plume and plume arrival time in the Nisku abandoned well are:

- the saturation fraction of CO₂ in the Nisku;
- the porosity of the Nisku; and
- the CO₂ density in the Nisku.

The results of the sensitivity analyses for the leakage through an abandoned well in the Banff formation are shown in Figures 26 and 27. The parameter with the strongest influence on plume radius is the CO₂ saturation ratio with a highly nonlinear relationship between the ratio and plume radius. The Nisku porosity is the next parameter with the greatest influence on the plume migration but has a significantly smaller influence than the CO₂ saturation ratio. The sensitivity of the plume radius to CO₂ density is relatively small.

Figure 26: Tornado Plot of the Sensitivity Analysis Results for Plume Migration in the Nisku

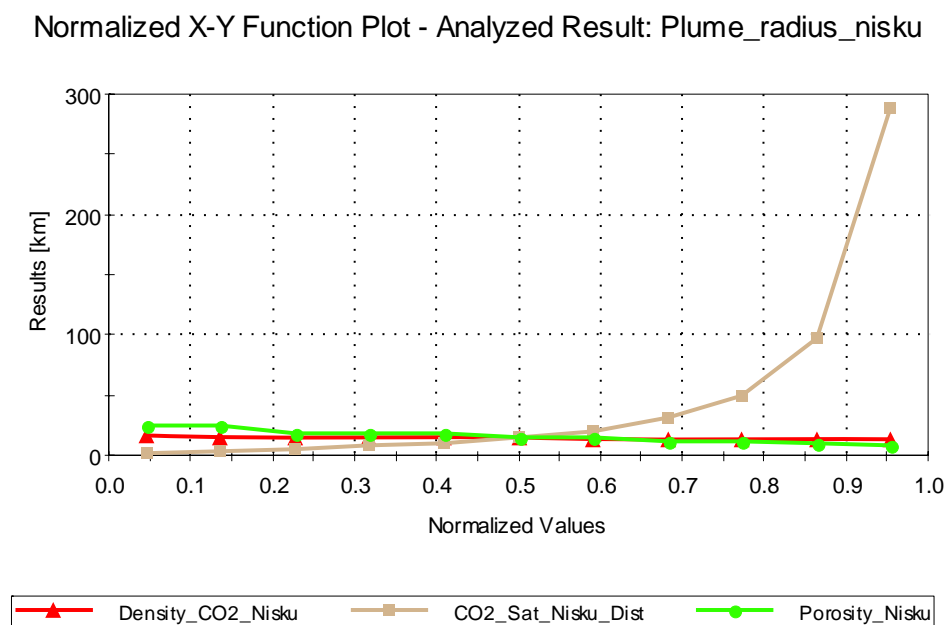
Tornado Sensitivity Chart - Analyzed Result: Plume_radius_nisku [km]





WASP RISK-BASED LEAKAGE MODEL

Figure 27: X-Y Function Chart of Sensitivity Results for Leakage Plume Migration in the Nisku





7.0 SUMMARY AND RECOMMENDATIONS

Golder Associates have developed a probabilistic analytical simulator capable of evaluating alternative leakage scenarios associated with legacy wells in multiple formations. The simulator can be used to evaluate the simplest scenario of leakage to the surface via a single abandoned well in the Nisku formation and the more complicated scenario of leakage through a combination of wells in the Nisku and Banff formations. The mathematical models are based to a large extent on the analytical solutions developed by Nordbotten et al., (2004, 2005). The use of analytical expressions in the simulator allows the uncertainty in the input parameters to be explicitly represented and propagated in the model calculations using the Monte Carlo simulation method. The simulator is scalable and can be expanded to represent CO₂ release through additional leakage pathways such as faults, fracture networks and spill points.

The simulator includes a user interface for defining the input parameters and describing different release scenarios (i.e., 'what if' analysis) that are fundamental in CO₂ sequestration risk analysis and useful for developing a diagnostic understanding of the different leakage scenarios. The interface contains a number of predefined model outputs including time histories of formation pressure, CO₂ plume migration within the injection formation, and CO₂ flux rates through the abandoned wells. The preliminary set of input parameters in the simulator that describe Nisku and Banff formation properties and the characteristics of the potential leakage pathways up the abandoned wells were developed by members of the WASP research team.

The reference input parameters were used to perform sensitivity analyses to identify those that most strongly influence the projected CO₂ plume migration and potential leakage through abandoned wells. The results from the sensitivity analysis can be used to prioritize site characterization data needs for reducing the overall uncertainty in the performance of a potential CCS site.

The conceptual model that forms the basis for the simulator can be expanded to include other potential pathways (e.g., faults and spill points) and multiphase flow. These features can be accommodated by adding additional modules to the existing model. Prior to further development or using the simulator for guiding site characterization activities, Golder recommends the current version of the simulator be thoroughly tested by the WASP research team in order that any errors or omissions are addressed. Furthermore, while the simulator has been benchmarked against independent calculations, the large number of input parameters and calculations as well as the imbedded logic in the simulator calls for additional testing. For example, the simulator could be more thoroughly benchmarked using an established reservoir simulator such as TOUGH2 (Preuss, 2009). For these reasons, the simulator should be considered a prototype until this testing has taken place and the model has been revised as appropriate.



8.0 REFERENCES

- AAPG, 1996. *Hydrocarbon Migration and Its Near-Surface Expression*, Ed. D Schumacher and AA Abrams, AAPG Memoir 66, AAPG Press, Oklahoma, OK, 1996.
- Anton, 1984. *Elementary Linear Algebra*, 4th Edition, H Anton, J Wiley & Sons, New York, 1984.
- Aziz and Settari, 1979. *Petroleum Reservoir Engineering*, K Aziz and A Settari, Applied Science Publishers Ltd., London, 1979.
- Celia, 2008. *Implications of Abandoned Wells for Site Selection*, MA Celia, Princeton University, and *Risk of Leakage versus Depth of Injection*, Presentation by MA Celia, Princeton University, http://www.princeton.edu/cee/people/data/c/celia/profile/the-darcy-lecture-outline/?_toolbar=1, 2009
- CO₂-PENS, 2007. *CO₂-PENS: A System Model for the Geological Sequestration of Carbon Dioxide*, PH Stauffer, HS Viswanthan, RJ Pawar and GD Guthrie, GoldSim User Conference, San Francisco, October, 2007.
- CONRAD, 2006. *Risk Assessment of Potential Oil Sands Coke Combustion in the Final Storage Landscape*, report prepared by Golder Associates for CONRAD, May, 2006.
- Eisinger, 2009. Spreadsheet of WASP Formation Parameters, C Eisinger, private communication, March, 2009;
- Freeze and Cherry, 1979. *Groundwater*, RA Freeze and JA Cherry, Prentice-Hall, Englewood Cliffs, NJ, 1979.
- Gasda et al, 2004. SE Gasda, S Bachu and MA Celia, *Spatial characterization of the location of potentially leaky wells penetrating a deep saline aquifer in a mature sedimentary basin*, Environmental Geology, Vol 46, pp707-720, (2004).
- Ghaderi, 2009. *CO₂ Injection into Saline Aquifers Containing H₂S (Sour Aquifers): The Wabamun Area CO₂ Sequestration Project*, S Ghaderi, M Shevalier, Y Leonenko, B Mayer, I Hutcheon, R Lavoie and D Keith, Proceedings of the AAPG/SEG/SPE Hedberg Conference, Vancouver, 2009.
- Gautsch and Cahill, 1964. W Gautsch and WF Cahill, *Exponential Integral and Related Functions*, Chapter 5, *Handbook of Mathematical Functions with Formulas, Graphs, and Mathematical Tables*, Ed. M Abramowitz and IA Stegun, National Bureau of Standards, Washington DC, 1964.
- GoldSim, 2006. *Risk-Based Decision Support For Housing Development On Undermined Land*, Andrew McGoey-Smith, Ray Predika, Jack Crooks, and Ian Miller, GoldSim Users Conference, Vancouver, June, 2006.
- GoldSim, 2009. GoldSim, *Monte Carlo Simulation Software for Decision and Risk Analysis*, www.goldsim.com.
- IPCC, 2007. Chapter 5, *Underground geological storage*, Intergovernmental Panel on Climate Change (IPCC), United Nations Environmental Program, 2007, http://www.ipcc.ch/pdf/special-reports/srccs/srccs_chapter5.pdf.
- IUPAC, 2006. IUPAC Goldbook on-line corrected version, <http://goldbook.iupac.org/S05921.html>
- Ghaderi et al, 2009. S Ghaderi, M Shevalier, Y Elonenko, B Mayer, I Hutcheon, R Lavoie, and D Keith, *CO₂ Injection into Saline Aquifers Containing H₂S (Sour Aquifers): The Wabamun Area Sequestration Project*, AAPG/SEG/SPE Hedberg Conference, Vancouver, BC, Aug 16-19, 2009



WASP RISK-BASED LEAKAGE MODEL

- Lavoie, 2008. *Analytical Plume Size and CO₂ Injectivity*, Presentation, Wabamun Lake CO₂ Sequestration Project Kick-off Meeting, R Lavoie, February 22nd, 2008.
- Lavoie, 2009. Excel Spreadsheet of WASP Plume Radius Model, R Lavoie, private communication, 2009.
- Morgan and Henrion, 1990. *Uncertainty: A Guide to Dealing with Uncertainty in Quantitative Risk and Policy Analysis*, MG Morgan and M Henrion, Cambridge University Press, New York, 1990.
- Nordbotten et al. 2004. JM Nordbotten, MA Celia and S Bachu, *Analytical solutions for leakage rates through abandoned wells*, Water Resources Research, Vol. 40, W04204, pp1-10, 2004.
- Nordbotten et al., 2005a. JM Nordbotten, MA Celia and S Bachu, *Injection and Storage of CO₂ in Deep Saline Aquifers: Analytical Solution for CO₂ Plume Evolution During Injection*, Transp. Porous Med. Vol. 58, pp339-360, 2005.
- Nordbotten et al., 2005b. JM Nordbotten, MA Celia and S Bachu, and H Dahle, *Semianalytical Solution of CO₂ Leakage from an Abandoned Well*, Environ. Sci. Technol. Vol. 39, pp602-611, 2005.
- Nordbotten et al., 2009. JM Nordbotten, D Kavetski, MA Celia and S Bachu, *Model for CO₂ Leakage Including Multiple Geological Layers and Multiple Leaky Wells*, Environ. Sci. Technol., Vol. 43, pp743-749, 2009.
- Nygaard, 2009. *Status of Well Completion for WASP*, private communication, R Nygaard, February, 2009.
- Numerical Recipes, 1997. *Numerical Recipes in C: The Art of Scientific Computing*, 2nd Edition, WH Press, WT Vetterling, SA Teukolsky and BP Flannery, Cambridge University Press, Cambridge, MA, 1997.
- Preuss, 2009. *TOUGH2, A General-purpose Numerical Simulation Program for Multi-phase Fluid and Heat Flow in Porous and Fractured Media*, K Preuss, Lawrence Berkley Laboratory, <http://esd.lbl.gov/TOUGH2>
- Static Model, 2008. Presentation on the *Static Model*, WASP Sponsors Meeting, C Eisinger and Jerry Jensen, 26th September, 2008.



Report Signature Page

GOLDER ASSOCIATES LTD.

Kevin Heal, B.Comm.
Project Manager

Charles F Voss, MS
Principal

KH/CFV/SL

<http://capws/if11028wabamunareasequestrationproject/phases and tasks/report/draft report/wasp draft report ver12.docx>



APPENDIX A

Conversion from Hydraulic Head to Pressure



WASP RISK-BASED LEAKAGE MODEL

The following relationships hold linking hydraulic head h to pressure p , transmissivity T to hydraulic conductivity K , hydraulic conductivity to permeability k and storability S to compressibility c :

$$h = \frac{p}{\rho g} \quad (A1)$$

$$T = Kb \quad (A2)$$

$$K = \frac{\rho g}{\mu} k \quad (A3)$$

$$S = \rho g b c \quad (A4)$$

Therefore the standard well pumping equation (Nordbotten et al., 2004)

$$h(r, t) - h_{mit} = \frac{Q_w}{4\pi T} W(u) \quad (A5)$$

where $W(u) = E_1(u)$ becomes

$$p(r, t) - p_{mit} = \frac{\mu Q_w}{4\pi k b} W(u) \quad (A6)$$

where

$$u = \frac{c \mu r^2}{4 k b t} \quad (A7)$$

and the well pumping function $E_1(u)$ is the exponential integral function:

$$E_1(u) = -\gamma - \ln(u) - \sum_{n=1}^{\infty} \frac{(-1)^n u^n}{n \cdot n!} \quad (A8)$$

Where $\gamma = 0.577$ is Euler's constant.

The starting point for the mathematical model of leakage is equation (2) from Nordbotten et al. (2004) which is (A6). This is the pressure equation for single injection into the storage formation (CO₂ reservoir), without leakage outwards:

$$h(r, t) - h_{mit} = \frac{Q_w}{4\pi T} W(u) \quad (A9)$$

here h denotes hydraulic head (as defined in Darcy's equation for flow in a porous medium)

r denotes the distance between the injection well;

t denotes time since start of injection;

h_{mit} is the hydraulic head of the target formation prior to injection; and

Q_w denotes volumetric flow rate (injection rate for an injection well and later, leakage rate for an abandoned well), which is assumed to be constant; and u is given by (A7).



APPENDIX B

Nordbotten et al. Equations for Multiple Wells and Multiple Layers



WASP RISK-BASED LEAKAGE MODEL

The Nordbotten et al. equations for M multiple active and N abandoned wells, where the abandoned wells

penetrate L multiple formation layers, are given by equation (7) of (Nordbotten et al., 2004) where the substitutions (A1) to (A3) have been made, the weight of the CO_2 has been included as was the case in (Nordbotten et al., 2005b), and the partial derivative replaced as per the discussion in 2.3 of (Nordbotten et al., 2004). They are a set of L coupled algebraic equations:

$$p_{i,l}(r, t) - p_{i,l}^{\text{init}} = \mu / (4\pi k_{i,l} b_{i,l}) \sum_{i=1}^M Q_{i,l}(r, t) W(u) - r_{i,l}(t) + \mu / (4\pi k_{i,l} b_{i,l}) \sum_{i=M+1}^{M+N} Q_{i,l}(r, t) \quad \text{(A12)}$$

where

$$Q_{i,l}^+(r) = \frac{\pi r_{w,l}^2 k_{w,l} [p_{\text{top}} - p_{i,l}(r, t)]}{\mu D_{w,l}} \quad \text{(A13)}$$

is the vertical leakage flux (out) of the l^{th} layer to a top layer above (could be the adjacent layer or the surface), $D_{w,l}$ is the length of porous material in the well bore through which leakage can occur, $L_{w,l}$ is the distance between the storage formation and the top layer and

$$Q_{i,l}^-(r) = \frac{\pi r_{w,l}^2 k_{w,l} [p_{i-1}(r, t) - p_{i,l}(r, t)]}{\mu D_{w,l}} \quad \text{(A14)}$$

is the leakage in to the l^{th} layer from the adjacent $(l-1)^{\text{th}}$ layer below and $\gamma=0.92$. Note γ is not the same here as the Euler constant.

For N abandoned wells, the pressure is evaluated at a total of N times at the appropriate radial distance from each abandoned well. This results in NL equations in NL unknowns in block tri-diagonal form which can be solved by standard linear equation solving techniques, as discussed earlier in this document.



APPENDIX C

Leakage Flux for One Injection Well and One Abandoned Well with One Aquifer Penetration



WASP RISK-BASED LEAKAGE MODEL

For the case of 1 injection well and 1 abandoned well, we have $M=1$ and $N=1$ which reduces (A12) down to one

equation in 1 unknown for evaluating the pressure at the abandoned well location. Note that the second term and third terms in equation (A12) are singular if we evaluate them at the middle of the injection well. Therefore we evaluate the expression with an offset equal to the abandoned well radius $\bar{r}_1 = r_1 + r_{w1}$ which results in a finite W -value. Since we are interested in leakage from the storage formation through the wellbore directly to the surface only, we have

$$p(\bar{r}_1, t) - p_{init} = \frac{\mu}{4\pi k_1 b_1} Q_0 W[u(\bar{r}_1 - r_0, t)] + \frac{k_{1s} r_{w1}^2}{4k_1 b_1 D_{1s}} [p_s - p(\bar{r}_1, t)] W[u(\bar{r}_1, \gamma t)] \quad (A15)$$

where, in general,

$$\bar{r}_1 = r_1 + r_{w1} \quad (A16)$$

and D_{1s} is the vertical length associated with the porous material between the storage formation, L_{1s} is the

distance from the storage formation to the surface, ρ is the density of CO_2 in the reservoir, k_{1s} is the permeability of porous material between the storage formation and the surface along the wellbore, and p_s is the pressure at the surface (atmospheric pressure).

Rearranging (A15), and using (6), the following two equations are obtained for estimating surface leakage through a single abandoned well:

$$Q_{1s}(t) = \frac{\pi r_{w1}^2 k_{1s} [p_s - p(\bar{r}_1, t)]}{\mu D_{1s}} \quad (A17)$$

where

$$p(\bar{r}_1, t) = \frac{p_{init} + \frac{\mu Q_0 W[u(\bar{r}_1, t)]}{4\pi k_1 b_1} + \frac{k_{1s} r_{w1}^2 p_s W[u(\bar{r}_1, \gamma t)]}{4k_1 b_1 D_{1s}}}{\left(1 + \left[\frac{k_{1s} r_{w1}^2 W[u(\bar{r}_1, \gamma t)]}{4k_{1s} k_1 b_1 D_{1s}}\right]\right)} \quad \square$$

Note that for wells in 'good condition', the cement permeability k_{1s} is low (of the order of 10^{-11} m^2 or less) and the cement plug length is high (larger than 10m), hence the denominator term is close to unity. We can then approximate (A18) with

$$p(\bar{r}_1, t) \approx p_{init} + \frac{\mu Q_0 W[u(\bar{r}_1, t)]}{4\pi k_1 b_1} + \frac{k_{1s} r_{w1}^2 p_s W[u(\bar{r}_1, \gamma t)]}{4k_1 b_1 D_{1s}} \quad \square \quad (A19)$$



APPENDIX D

Leakage Flux for One Injection Well and Two Abandoned Wells with Two Aquifer Penetrations



WASP RISK-BASED LEAKAGE MODEL

The starting point for the single injection well and 2 abandoned well penetrations, with 1 penetration in the storage formation, and one penetration in a less deep formation close to the storage formation, is equation (A12). This situation corresponds to a single injection into the Nisku formation and 1 abandoned well penetration in and Nisku formation and a second well penetration in the Banff formation. We assume negligible leakage occurs between the Nisku and the surface.

We evaluate this equation for each layer and at each abandoned each well location, offset by well distance r_{wj} so that the W -values are non-singular. Given that we know the pressure at the surface, we have 3 equations in 3 unknowns.

In the Nisku layer, the pressure at the foot of the first abandoned well is a sum of the initial pressure prior to injection, the pressure flow due injection and the loss of pressure through a pathway in the first abandoned well. The injection pressure can be calculated by applying the Theis equation which accounts for the vertically averaged radial flow in the Nisku formation from the foot of the injection well to the foot of the first abandoned well. The pressure lost through the abandoned well is calculated using the Theis type equation, except with injection replaced by the vertical flux from the Nisku to the Banff layers. Here the well function is evaluated at a distance equal to the well radius which accounts for pressure loss through the cement in the well casing.

Similarly, the pressure in the Banff formation at 1st abandoned well is the sum of the initial formation pressure prior to injection, the pressure gained from leakage through the 1st abandoned well and the pressure lost through leakage through the 2nd abandoned well. The well leakage pressure is computed by multiplying the leakage fluxes by an appropriate well function.

In conceptual terms we have a summation of four different well functions times three vertical fluxes

$$\begin{aligned}
 p_1(\bar{r}_1) &= p_1^{init} + W_{inj\ well-1}^{rad\ flow} \cdot Q_{inj} + W_{1-2}^{well1} \cdot Q_{1-2} \\
 p_1(\bar{r}_2) &= p_2^{init} - W_{1-2}^{ab\ well1} \cdot Q_{1-2} \\
 p_2(\bar{r}_2) &= p_2^{init} - W_{well1-well2}^{rad\ flow} \cdot Q_{1-2} + W_{2-s}^{well2} \cdot Q_{2-s}
 \end{aligned}$$

Which in our standard mathematical notation becomes:

$$p_1(\bar{r}_1) = p_1^{init} + \frac{\mu Q_0}{4\pi k_1 b_1} W[u_1(\bar{r}_1), t] + \frac{k_{12} r_{12}^2}{4b_1 k_1 D_{12}} [p_2(\bar{r}_1) - p_1(\bar{r}_1)] \cdot W[u_1(r_{w1}, \gamma t)] \quad (A19)$$

$$p_2(\bar{r}_1) = p_2^{init} - \frac{k_{12} r_{12}^2}{4b_2 k_2 D_{12}} [p_2(\bar{r}_1) - p_1(\bar{r}_1)] \cdot W[u_2(r_{w1}, \gamma t)] \quad (A20)$$

$$p_2(\bar{r}_2) = p_2^{init} - \frac{k_{12} r_{12}^2}{4b_2 k_2 D_{12}} [p_2(\bar{r}_2) - p_1(\bar{r}_2)] \cdot W[u_2(\bar{r}_2), \gamma t] + \frac{k_{2s} r_{2s}^2}{4b_2 k_2 D_{2s}} [p_s - p_2(\bar{r}_2)] \cdot W[u_2(r_{w2}, \gamma t)] \quad (A21)$$

where

$$u_l(r, t) = \frac{cH_l r^2}{4k_l t} \quad (A22)$$

And $l=1$ or 2 .

These equations (A19) to (A21) can be arranged into the following matrix equation where the dot (\cdot) denotes matrix multiplication. The matrix formulation will be used in the next section for solving the pressure for N wells and L layers.



WASP RISK-BASED LEAKAGE MODEL

$$\begin{bmatrix} a_1 & b_1 & c_1 \\ a_2 & b_2 & c_2 \\ a_3 & b_3 & c_3 \end{bmatrix} \cdot \begin{bmatrix} p_1(r_1) \\ p_2(r_1) \\ p_3(r_2) \end{bmatrix} = \begin{bmatrix} d_1 \\ d_2 \\ d_3 \end{bmatrix}$$

Where the matrix coefficients are given by:

$$a_1 = 1 + \frac{k_{12} r_{12}^2 W[u_1(r_{12}, \gamma t)]}{4b_1 k_1 D_{12}} \quad (A24)$$

$$b_1 = -\frac{k_{12} r_{12}^2 W[u_2(r_{12}, \gamma t)]}{4b_1 k_1 D_{12}} \quad (A25)$$

$$c_1 = 0 \quad (A26)$$

$$a_2 = -\frac{k_{12} r_{12}^2 W[u_1(r_{12}, \gamma t)]}{4b_2 k_2 D_{12}} \quad (A27)$$

$$b_2 = 1 + \frac{k_{12} r_{12}^2 W[u_2(r_{12}, \gamma t)]}{4b_2 k_2 D_{12}} \quad (A28)$$

$$c_2 = 0 \quad (A29)$$

$$a_3 = -(k_{12} r_{12}^2 W[u_1(r_{12}, \gamma t)] / [4(b_1 k_1)_{12}])_{12}$$

$$b_3 = \frac{k_{12} r_{12}^2 W[u_2(r_{12}, \gamma t)]}{4b_3 k_3 D_{13}} \quad (A31)$$

$$c_3 = 1 + \frac{k_{23} r_{23}^2 W[u_2(r_{23}, \gamma t)]}{4b_3 k_3 D_{23}} \quad (A32)$$

And the d -vector elements are:

$$\begin{aligned} d_1 &= p_1^{init} + (uQ_{10} W[u_1(r_{10}, \gamma t)] / [4\pi k_1]_{10})_{10} \\ d_2 &= p_2^{init} \end{aligned} \quad (A34)$$

$$d_3 = p_3^{init} + \frac{k_{23} r_{23}^2 W[u_2(r_{23}, \gamma t)]}{4b_3 k_3 D_{23}} p_3 \quad (A35)$$

The matrix equation can easily be solved using Cramer's rule from matrix algebra (Anton, 1984) to give

$$p_1(r_1) = \frac{(b_2 d_1 - b_1 d_2)_{11}}{[(a_1 b_2 - a_2 b_1)]_{11}} \quad (A36)$$

$$p_2(r_1) = \frac{[(a_1 d_2 - a_2 d_1)]_{11}}{[(a_1 b_2 - a_2 b_1)]_{11}} \quad (A37)$$

$$p_3(r_2) = \frac{(a_1 b_3 - a_3 b_2) d_1 + (b_1 a_3 - a_1 b_3) d_2 + (a_1 b_2 - a_2 b_1) d_3}{(a_1 b_2 - a_2 b_1) c_3} \quad (A38)$$

for the three pressure terms.

The leakage rate of CO₂ to the surface is given by Darcy's equation through the abandoned well is given by:



WASP RISK-BASED LEAKAGE MODEL

$$Q_{2s}(t) = \frac{k_{2s}\pi r_{2s}^2}{\mu D_{2s}} \left[p_s - \frac{(a_2 b_3 - a_3 b_2) d_1 + (b_1 a_3 - a_1 b_3) d_2 + (a_1 b_2 - a_2 b_1) d_3}{[(a_1 b_2 - a_2 b_1) c_3]} \right] \quad (A39)$$

and the flux between the two formations through the abandoned well is given by

$$Q_{12}(t) = \frac{\pi r_{12}^2 k_{12} [p_2(\bar{r}_1) - p_1(\bar{r}_1)]}{\mu D_{12}} \quad (A40)$$

which substituting for the two pressure terms becomes

$$Q_{12}(t) = \frac{k_{12}\pi r_{12}^2 [(a_1 + b_1) d_2 - (a_2 + b_2) d_1]}{\mu D_{12} [(a_1 b_2 - a_2 b_1) c_3]} \quad (A41)$$

These equations will be implemented in the simulation model to provide estimates of CO₂ surface through the abandoned wells.

Note that the pressure equations reduce to a simpler form by making some approximations. First the determinant $\det(A)$ can be closely approximated by unity when the well plug permeability terms are low ($k_{wp} < 10^{11} \text{ m}^2$)

$$\det(A) = (a_1 b_2 - a_2 b_1) c_3 \approx 1$$

because the first term resulting from the multiplication of all three diagonal terms (each in turn close to unity) of matrix A dominates the determinant.

Second we note that the terms c_1 and c_2 are identically zero

$$c_1 = c_2 = 0$$

Finally, we note that the diagonal terms of the A -matrix are close to unity for abandoned wells in a state of good completion:

$$a_1 \approx 1,$$

$$b_2 \approx 1 \quad \text{and}$$

$$c_3 \approx 1$$

so that

$$p_1(\bar{r}_1) \approx p_1^{int} + \frac{\mu Q_0}{4\pi k_1 b_1} W[u(\bar{r}_1 - r_0), t] + b_1 d_s \quad (A42)$$

where the sum of the first two terms are equal to the pressure in the reservoir after injection and the third term accounts for leakage from the reservoir to the surface since it depends on leakage flux from the first to the second formation multiplied by leakage flux from the second formation to the surface. Note that the third term in the equation is negative.

$$p_2(\bar{r}_1) \approx p_1^{int} - a_2 \quad (A43)$$

and

$$p_2(\bar{r}_1) \approx p_1^{int} - a_2 d_1 + b_2 [(p_s - d_1)] \quad (A44)$$

At Golder Associates we strive to be the most respected global group of companies specializing in ground engineering and environmental services. Employee owned since our formation in 1960, we have created a unique culture with pride in ownership, resulting in long-term organizational stability. Golder professionals take the time to build an understanding of client needs and of the specific environments in which they operate. We continue to expand our technical capabilities and have experienced steady growth with employees now operating from offices located throughout Africa, Asia, Australasia, Europe, North America and South America.

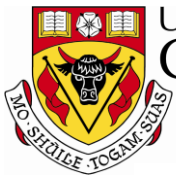
Africa	+ 27 11 254 4800
Asia	+ 852 2562 3658
Australasia	+ 61 3 8862 3500
Europe	+ 356 21 42 30 20
North America	+ 1 800 275 3281
South America	+ 55 21 3095 9500

solutions@golder.com
www.golder.com



Golder Associates Ltd.
102, 2535 - 3rd Avenue S.E.
Calgary, Alberta, T2A 7W5
Canada
T: +1 (403) 299 5600





Recommendations for Injection and Storage Monitoring

WABAMUN AREA CO₂ SEQUESTRATION PROJECT (WASP)

Authors

Don Lawton

Bernhard Mayer

Rob Lavoie

Jerry Jensen

David Keith

Rev.	Date	Description	Prepared by
1	November 25, 2009	Draft	Don Lawton
2	January 10, 2010	Final	Don Lawton after edits by all

Table of Contents

INTRODUCTION.....	3
1. WASP II CO ₂ INJECTION PROGRAM.....	3
2. WASP II PROPOSED MONITORING PROGRAM	4
2.1 Stage I.....	4
2.2 Stage II.....	4
2.3 Stages III & IV	5
2.3.1 Near-Surface and Atmospheric Baseline Surveys.....	6
2.3.2 Subsurface Baseline Surveys	6
2.4 Stage IV	7
2.4.1 Continuous Monitoring	7
2.4.2 Periodic Monitoring	7
2.5 Stage V	8
REFERENCES.....	9

INTRODUCTION

Studies completed under WASP Phase I have characterized the Nisku Formation over an area of slightly greater than 5,000 km². Various reports describe the development of a geologic static model (Eisinger and Jensen), regional geochemistry (Shevalier, et al.), regional geophysics (Alshuhail et al.), geomechanical modelling and analysis (Goodarzi and Settari), reservoir simulation (Ghaderi and Leonenko), well design and integrity (Nygaard) and water disposal well analysis, including those wells that experienced lost circulation (Lavoie). Log data and cores from wells in the area are sparse and reservoir models are poorly constrained in terms of porosity and permeability trends. Some 3D seismic surveys in the area provided additional trends of interpreted physical properties of the Nisku reservoir and overlying formations.

Programs for site monitoring during and after injection of CO₂ have two principle objectives:

- (a) identifying and tracking the injected CO₂ plume in the storage reservoir, if possible; and
- (b) early detection of CO₂ breaches through the caprock of the storage reservoir and upward migration of CO₂ into overlying stratigraphic units, shallow groundwater, soil or into the atmosphere.

Of paramount importance to carbon capture and storage (CCS) is the ability to track CO₂ plume movement on a best effort basis to assess whether the CO₂ flow is consistent with model predictions, and to optimise safeguards for early leak detection. These goals are vital for public acceptance of CCS, particularly during early projects as the technology becomes implemented at commercial scale. Comprehensive yet affordable monitoring protocols thus need to be established. A wide range of technologies have been developed for monitoring CO₂ injection and storage, including surface and subsurface measurements, but continued research and development is required for next generation technologies that will enable effective monitoring programs to be implemented.

Within the WASP project area, the Nisku Formation is between 1,600 and 2,000 m below ground surface. The Nisku aquifer pressure is approximately 16 MPa, therefore the injected CO₂ will remain in a supercritical phase in the reservoir.

1. WASP II CO₂ INJECTION PROGRAM

The recommended monitoring program for WASP II CO₂ injection would be staged in accord with the overall program implementation. This technical component of this program may consist of:

- Stage I** Site selection for a test well, based on models developed from WASP Phase I, or a continuation of the approach used in Phase I over a larger region.
- Stage II** Local geological, geophysical, hydrogeological and geomechanical characterization of the selected site using existing data (possibly additional to WASP Phase I database).
- Stage III** Drilling of a well to test Nisku reservoir connectivity and CO₂ injectivity with site specific characterization based on a comprehensive core analysis program (including caprock), full geochemical evaluation of the reservoir fluids and a detailed suite of geophysical logs from the well, followed by an update of the static geological model.
- Stage IV** Further characterization of the reservoir via a period of pressure transient testing using brine production or injection as the pressure disturbance mechanism. The pressure disturbance could take the form of either an extended drawdown (production of brine) followed by a buildup period (shut-in) or, ideally, simply conducting a long period of

drawdown while monitoring the flowing bottom hole pressure (via surface recording sensors located below an electrical submersible pump [ESP]). This would serve as a reservoir limits test. Either way, the objective would be two fold; i) to assess the bulk average reservoir permeability-thickness over an extended distance away from the well and ii) assess the distance at which reservoir boundaries are experienced. Brine from the extended period of production would need to be disposed of. This could be done by completing a second well, not too far away from the test well, and pumping into either the Banff or Wabamun aquifers. Brine disposal into these shallower aquifers would provide additional reservoir characterization of potential brine disposal locations should pressure plume management prove to be required during a commercial CO₂ storage project.

If the Nisku Formation in the test well meets predetermined performance metrics, then a CO₂ injection pilot would be established at the site with injection of up to 100 t of CO₂ per day for a period long enough to establish important CO₂ injectivity parameters as well as provide sufficient CO₂ plume development to be observed using geophysical methods (e.g., cross-well, vertical seismic profiles and time-lapse borehole logging). In particular, geophysical tests would be used to monitor the shape of this CO₂ plume over time in order to further characterize the vertical permeability near the test well. Prior to initiation of CO₂ injection, baseline geophysical, geochemical and shallow groundwater sampling surveys would be undertaken. At least one (preferably two) fully instrumented observation well would be required for Stage IV, with both surface and subsurface monitoring programs initiated. Details about the various surveys are provided below.

Stage V If the Pilot CO₂ injection program is successful, Stage V consists of up-scaling the injection program to the 1 Mt/year target. Appropriate monitoring programs to be deployed would be designed, based on results from Stage IV of the program. Pipelining of the CO₂ from the source would be required but this is not covered in this report.

2. WASP II PROPOSED MONITORING PROGRAM

The monitoring programs recommended are specific for the Nisku target, based on WASP Phase I reports, and are also drawn from best practices recommended by the US Department of Energy National Energy Laboratory (Srivastava et al., 2009).

2.1 Stage I

Site selection would be made by the operator (i.e., TransAlta), assisted by information provided in the WASP Phase I reports. Regional characterization of the Nisku aquifer may be required over areas additional to those covered by WASP I, depending on available data.

2.2 Stage II

Once a test injection site has been selected, local site characterization should be undertaken using available well and trade seismic data (2D or 3D). It is recommended that the local characterization cover an area of up to 25 square km (5 km × 5 km) and would include the following activities:

- interpretation of 2D and 3D seismic data not previously available in WASP I;
- detailed core and log analyses from wells in the local site characterization area;

- geochemical analyses from production wells in the local site characterization area;
- groundwater sampling surveys to characterize shallow aquifers in the local site characterization area; and
- development of a local geological static model from the ground surface to the Nisku Fm.

2.3 Stages III and IV

Design of the test injection well could be undertaken by the WASP team (e.g., Runar Nygaard) or a selected engineering services company. A full well-logging suite should be run in the well, including caliper, gamma-ray, resistivity, sonic-scanner, neutron, density, and cement bond logs from base of surface casing to total depth, with FMI and formation tester logs at selected intervals. Once the well has been completed, the brine injection or production test would be undertaken to characterize the reservoir around the injection well, and if successful, this would be followed by a CO₂ injection test and pilot. During the drilling operations, a full core from the well should be obtained through the Calmar Formation (caprock) and the complete Nisku Section through to the underlying Ireton Shale. In order to refine a subsequent monitoring program, the following core analyses are required for both caprock and reservoir rocks:

- mineralogy;
- petrophysical properties, including static and dynamic moduli and formation factor;
- porosity and permeability measurements;
- V_p and V_s measurements on reservoir core at RTP for CO₂ saturations from 0 to 100%;
- sampling and analysis of reservoir fluids; and
- sampling and characterization of shallow aquifers intersected by the well (above Colorado Group).

Once these data have been collected, then the following tasks should be undertaken:

- update of the local-scale static geological model;
- update of the local-scale geomechanical model;
- simulation of CO₂ injection and plume development in the Nisku formation; and
- geochemical modelling of CO₂-rock interaction.

If the brine injection/production program and CO₂ injectivity tests are successful, then a number of observation wells (at least three) should be drilled to penetrate the Nisku Formation in order to monitor the CO₂ plume in the reservoir directly. These wells would all be capable of being instrumented with retrievable monitoring tools, permanent pressure and temperature gauges, and should allow sampling of the Nisku reservoir fluids as well as from deep and shallow aquifers. The location of the monitoring wells would be guided by the results of simulation of CO₂ plume development, but it is anticipated that the first observation well to be drilled should be between 200 m and 500 m from the injection well in order for microseismic monitoring and cross-well seismic surveys to be effective. If the Nisku Fm is to be stimulated in the injection well, then the first two observation wells should be completed so that the frac can be monitored with the microseismic arrays.

In conjunction with the completion of the observation wells, baseline monitoring programs should be undertaken prior to start of CO₂ injection, and these could be completed during construction of the pilot plant infrastructure. The recommended baseline surveys consist of the following.

2.3.1 Near-Surface and Atmospheric Baseline Surveys

These surveys would consist of the following.

- soil and vadose zone surveys to determine baseline CO₂ concentrations and isotopic compositions in the near-surface soil and shallow groundwater;
- flux accumulation chambers to determine background CO₂ flux from the soil near the proposed injection well and observation wells;
- groundwater surveys to determine baseline chemical and isotopic composition of groundwater in the local site characterization area. Samples would be obtained from available wells; the drilling of additional groundwater monitoring wells may be necessary;
- surface tiltmeter array to measure transient ground motion during injection (if warranted by geomechanical modelling);
- surface monuments for high-accuracy differential GPS measurements and for microgravity surveys; and
- establishment of a network of INSAR reflectors for baseline surface strain state. Areal coverage should be no less than 50 km².

2.3.2 Subsurface Baseline Surveys

These surveys would consist of the following.

- Instrumentation of the observation wells, including the following.
 - Pressure and temperature gauges at reservoir level in the overlying Wabamun Formation and at the top of the Colorado Formation.
 - Microseismic arrays, either permanent or retrievable. The recommended array is made up of sixteen three-component geophones spaced at 15 m intervals, with the deepest geophone assembly just below the base of the Nisku Formation.
 - In-situ down-hole sampling of fluids from the reservoir, from formations above the caprock and shallower aquifers (above Colorado Gp) for baseline aqueous geochemistry.
- Well logs to establish near-well resistivity and porosity characteristics. If steel casing is used, resistivity measurements may be problematic, so pulsed-neutron logs may need to be used instead. If fiberglass casing is used, standard oilfield induction resistivity measurements are the resistivity measurement of choice.
- 3D multi-component seismic survey to fully map the subsurface structure and stratigraphy within the local site characterization area and to detect faults or other possible natural leakage paths to shallow aquifers or the ground surface. All surface shots of the survey should also be recorded by the downhole array in the observation well.
- Walkaway vertical seismic profiles (VSPs) to provide high-resolution baseline images of the Nisku Formation around the injection well (retrievable array). Walkaway shotlines should extend up to 2 km south and east of the well with shot spacing of 50 m. The VSP surveys should be run from base of surface casing to total depth, with a shuttle interval of 15 m. This is important since the WASP I geophysical program indicates that surface seismic data will be challenged to track the CO₂ plume within the Nisku reservoir.
- A baseline cross-well seismic survey to characterize the in-situ seismic properties of the Nisku Formation between the injection and at least one of the observation wells.

2.4 Stage IV

Monitoring undertaken during fluid production and injection would consist of continuous and periodic programs. Those programs are as follows.

2.4.1 Continuous Monitoring

Continuous monitoring would consist of the following.

- Pressure and temperature monitoring in the injection and observation wells, with automated data logging and cell-based transmission to monitoring office;
- Microseismic monitoring from the downhole geophone arrays in the observation wells, with automated event detection and transmission to monitoring office;
- Tiltmeter array monitoring for mapping transient surface deformation associated with fracture development in the injection reservoir.

2.4.2 Periodic Monitoring

Over the two-year Stage IV program, time-lapse or periodic surveys are proposed:

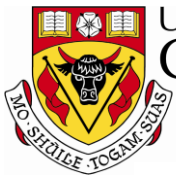
- Induction resistivity (depending on the casing type) and neutron logs in the observation wells from surface to TD.
- Multicomponent surface seismic survey at the end of Stage IV to assess effectiveness of surface seismic surveys to monitor the CO₂ plume and detect any upward migration of the CO₂ into shallower zones.
- Walkaway VSP surveys at the end of Stage IV to monitor CO₂ plume behavior around the injection well.
- Time-lapse geochemical surveys from the observation wells to investigate plume migration and breakthrough, study rock-fluid interactions in the reservoir, and the geochemistry of fluids from the Wabamun Formation which overlies the caprock.
- Time-lapse geochemical surveys of shallow groundwater wells to monitor for changes in groundwater chemistry including CO₂ contents and dissolved carbon species.
- Time-lapse geophysical logging of the observation well closest to the injector to map the vertical distribution of CO₂ within the Nisku Formation and to identify possible microchannel leakage paths through the well casing.
- Time-lapse INSAR surveys (recommended each year) to monitor surface strain resulting from pressure plume associated with CO₂ injection in the Nisku Formation.
- Differential GPS and microgravity surveys at fixed monuments every six months (four surveys in total) to monitor ground strain and subsurface density changes.
- Time-lapse soil, casing gas and flux accumulation surveys to monitor for CO₂ leakage into the vadose zone.
- Time-lapse atmospheric CO₂ monitoring surveys, particularly near existing wells in the Pilot site area.

2.5 Stage V

If the Pilot Project is successful then a full review of the monitoring programs conducted in Stage IV should be undertaken before the monitoring program for Stage V is designed. The review should include updating the geomechanical and geochemical models of the test site area and reservoir performance simulation to history match CO₂ breakthrough at the observation wells. Results of the review will indicate which monitoring programs should either be discontinued or enhanced for scale-up.

REFERENCES

Srivastava, R.D., Brown, B., Carr, T.R., Vikara, D., McIlvried, H., 2009, Monitoring, Verification and Accounting of CO₂ stored in deep geological formations: DOE/National Energy Technology Laboratory-311/081508, 132 pp.



UNIVERSITY OF
CALGARY

Energy &
Environmental
Systems

EES

iseee



Energy and Environmental Systems Group

Institute for Sustainable Energy, Environment and Economy (ISEEE)

Regulatory and Legal Review

WABAMUN AREA CO₂ SEQUESTRATION PROJECT (WASP)

Author

Nigel Bankes

Rev.	Date	Description	Prepared by
1	November 3, 2009	Regulatory and Legal Review	Nigel Bankes

Table of Contents

INTRODUCTION.....	3
1. THE PROPERTY ISSUES	4
2. REGULATORY ISSUES.....	5
2.1 Well Licences.....	5
2.2 Scheme Approval.....	6
2.3 Sour Gas Issue	7
3. CREDITING ISSUES.....	8
CONCLUSION	8
REFERENCES.....	9

INTRODUCTION

The WASP project aims to examine the feasibility of storing 20 Mt-CO₂/year for 50 years within 30 km of Wabamun, Alberta. Several of the science studies for this project identify issues that are relevant to a legal analysis of the project. Perhaps the most important in this context is the contribution of Ghaderi and Leonenko (2009). That paper highlights the geographical scale of the project (the saturation plume and the pressure plume) but also discusses the implications of injecting carbon dioxide (CO₂) into brines that are potentially saturated with hydrogen sulphide (H₂S), with the degree of saturation is as yet unknown. The first is important in terms of identifying the property rights and consents that a project operator might require; the second is significant in terms of the level of regulatory scrutiny (from the Energy Resources Conservation Board [ERCB]) and public concern that a carbon capture and storage (CCS) project of this nature will likely generate.

Ghaderi and Leonenko (2009) examine the number of wells that might be required to achieve the target volume and also estimate the size of the saturation and pressure plumes following injection over a period of fifty years, taking account of modelled reservoir properties, and without exceeding fracture pressure. The results of their work include the following:

- The rate at which CO₂ can be injected without exceeding fracture pressure is a more significant limitation on reaching the project goal of 20 Mt-CO₂/year than is the available pore space.
- Using single vertical injector wells with an injection rate of 1Mt/year, the saturation plume for each well will have a diameter of about 4.6 km with a pressure plume of about 65 km.
- In order to reach the target volume (1 Gt over 50 years) the authors suggest that the project would require 25 vertical wells, 8 km apart.
- Additional wells do not provide much additional injectivity after the first 15–20 wells.
- By the 50th year individual pressure plumes (as opposed to the saturation plume) will tend to merge creating a large scale pressure disturbance (hundred kms).
- Drilling horizontal wells may increase injectivity by up to 50%.

Goodarzi and Settari (2009) address the question of injectivity. They suggest that injection in the Nisku zone at or below fracture pressure is not likely to cause any significant surface heave and is not likely to have any environmental impact associated with surface deformations (at 21). They estimate that, with an injection rate of 20 Mt-CO₂/year for fifty years, vertical displacement at the surface should be approximately 2 mm (at 6). They further note that injection above the fracture pressure will have the potential to increase the well injectivity, but also the possibility of fracturing the caprock. Thermal effects of cold CO₂ injection will reduce the fracture pressure and enhance vertical fracture propagation through caprock. In light of this, and consistent with the idea of using a pilot project to enhance our understanding of CCS, the authors suggest (at 22) using variable injection rates, including injection at a higher rate than fracture pressure in order to initiate the fracture, and then use micro-seismic to measure the extent of the fracture.

This brief review deals with some of the property and regulatory issues that a CCS project in the Nisku would need to resolve. It concludes with a short discussion of crediting issues in the context of Alberta's *Climate Change and Emissions Management Act* and the regulations. The paper does not deal with liability issues.

1. THE PROPERTY ISSUES

The focus area includes large areas of private surface lands but also significant areas of private mineral titles. Private mineral titles are not evenly distributed though the study area. None of the townships have more than 50% private mineral lands. In five of the nine townships there are private mineral titles to between 16 and 18 of the 36 sections in the township (R2, T49 and T47; R3, T48 and T49; and R1, T48). The townships with the least amount of private mineral title are R3, T46 in the south east of the study area (only 2 sections) and R2 T48 (1.5 sections). There are no Indian reserve lands within the focus area although there are some Indian reserve lands (surface and mineral estate) to the south east of the study area. Based on mapping of October 7, 2008 there are significant areas of open Crown land available throughout the study area except in R3 T48 (in the northwest of the study area) where only 7.5 sections (out of 36) are open.

We do not have additional data on the breakdown of the private mineral titles. However, it is reasonable to assume that in any one section where there are private lands that the mineral title will be broken into several tracts (i.e., there will not be a single title for the entire section but multiple tracts with different acreages), and that in some cases there will be split estates as to the minerals (with one party holding, say, natural gas rights, and another party holding, say, petroleum and coal rights). In some cases these private lands may be under petroleum and natural gas leases.

There is considerable uncertainty in Canadian law as to the ownership of aquifer pore space for the purposes of disposal. There are two main possibilities. One possibility is that pore space ownership follows surface ownership. The other possibility is that pore space ownership follows ownership of the mineral title. It is also possible that ownership of the aquifer (or more specifically the water in the aquifer) may be significant given the initial importance of solubility trapping. In Alberta, formation water is owned by the Crown (*Water Act*).

American law generally awards ownership of pore space for natural gas storage purposes to the surface owner. Canadian jurisdictions have not followed this model and have preferred to recognize that pore space for storage purposes is owned by the mineral owner. Alberta amended the *Mines and Minerals Act* (1994) to clarify that natural gas storage rights are owned by the owners of the petroleum and natural gas rights (Acorn and Ekelund, 1995). However, this amendment did not deal explicitly with the use of pore space for disposal purposes of a substance that is not a by-product of hydrocarbon production (Banks et al, 2008).

In Canada, a few provinces have chosen (New Brunswick, Quebec and Nova Scotia) to vest gas storage rights in the Crown, while British Columbia has a mechanism for vesting storage rights in the Crown on a case-by-case basis. Some of the jurisdictions that recognize the possibility of private ownership of pore space for storage or disposal purposes have enacted schemes for dealing with holdout (or assembly) problems (i.e., to deal with private owners who refuse to contribute land to a storage scheme). Ontario and British Columbia offer different models for dealing with holdouts (Banks and Gaunce, in prep). Alberta has no legislation to deal with holdout problems in relation to storage projects (Acorn and Ekelund, 1995) and *a fortiori* to deal with CCS disposal projects.

Given uncertainties as to ownership of pore space for disposal purposes, and given the absence of legislation to deal with private holdout problems or any provincial legislation clarifying pore ownership rights in favour of the Crown, early CCS projects may wish to avoid private mineral lands if possible, both in terms of the spud and bottom hole location of the well, but also in terms of the projected extent of at least the saturation plume for the period of active injection. Early projects may also wish to avoid active Crown leases to avoid concerns that may be raised as to resource sterilization.

The right to dispose of a substance in Crown lands can be obtained by means of a letter of consent from the Department of Energy under the terms of s.56 of the *Mines and Minerals Act* (Bankes et al, 2008). An operator who requires greater certainty might seek to acquire a so-called Crown agreement under s.9 of that same Act (issued by the Minister with the approval of the Lieutenant Governor in Council (Storage Council Interim Report, 2008)) although arguably the section will need to be amended to cover injection for disposal purposes (Bankes, 2008: 16). In either case, the Crown can be expected to address resource sterilization issues (i.e., the potential for a CCS project or other disposal project to prejudice the recovery of other resources) as part of its decision to grant or withhold the requested consent letter or tenure.

2. REGULATORY ISSUES

Alberta does not yet have specific regulatory rules to deal with the review and approval of CCS projects. The Energy Resources Conservation Board takes the view that an application for a CCS project could be accommodated within the existing well licensing and scheme approval provisions of the *Oil and Gas Conservation Act* (OGCA) and the Board's various Directives. More specifically, the Board suggests that the rules pertaining to acid gas disposal projects are equally applicable to CCS projects. The relevant Directives include: Directive 8 on Surface Casing; Directive 20 on Abandonment; Directive 51 (on the classification of wells including disposal wells), Directive 56 on Energy Development Applications (including general consultation, well licences, and special conditions in relation to sour gas), Directive 65 on Resources Applications (including applications for "scheme approval for acid gas disposal projects) and Directive 71, Emergency Preparedness and Response Requirements for the Petroleum Industry. Most of these Directives are discussed in Zeidouni, Moore and Keith (2009) and in Bankes et al. (2008). The Board does not intend to issue a new Directive to govern CCS projects but may issue a Bulletin indicating how it intends to use existing Directives to review CCS projects (WASP meeting with ERCB, May 26, 2009). Zeidouni et al (2009) emphasize that one particular weakness of the current directives is they do not make provision for post-closure monitoring.

An applicant that proposes to drill a well to conduct tests in the Nisku to validate the hypotheses generated in this study will require a well licence (OGCA, s.11; Directive 56). An applicant that proposes to inject CO₂ or any other liquid or gas into an underground formation will require Board approval for that disposal scheme under s.39(1)(d) of the OGCA. I discuss each in turn and then add a note in relation to sour gas issues.

2.1 Well Licences

A party seeking to drill a well for either exploration (testing, evaluation) or injection purposes (see OGCA definition of "well") will need a well licence from the ERCB. Prior to applying for a well licence, the applicant must engage in notification and consultation with the affected parties including surface owners and those owning offsetting acreage (Directive 65, at 17–18; Directive 56). The notification and consultation should be designed to provide appropriate information about the proposed project and, if possible, resolve all concerns of affected parties so that the application can be dealt with administratively (routine) and without the need for a Board hearing. If the concerns cannot be resolved even after invoking the Board's Appropriate Dispute Resolution Mechanisms (ERCB Information Letter, 2001) the matter may be referred for a public hearing as a result of which the Board will issue a reasoned decision granting or denying the application. While matters set down for public hearing are frequently settled where an applicant can satisfy the concerns of a party who may be directly and adversely affected by the application, it

would not be unreasonable to expect early applications for CCS projects to attract significant public attention and a public hearing on a licence application or scheme approval application.

In addition, an applicant for a well licence must also be able to demonstrate (*OGCA*, s16) that it has the right to drill the well for the specified purpose (i.e., for disposal purposes). In the case of an oil and gas exploration well, an applicant would be expected to hold a lease and have any necessary pooling agreements in place for the rights for the prescribed “spacing unit” for that type of well (oil or gas) and target formation. Well spacing varies for different pools and formations in the province, but the default spacing units for gas and oil wells are one section and one quarter section respectively (Oil and Gas Conservation Regulations, s. 4.020). Neither the *Act* nor the Regulations specify spacing for the purposes of an injection well.

In the absence of a concept such as spacing in relation to a disposal well it is unclear how broad (geographically) an area of “authorization” the Board will require. Will it be confined to the bottom whole location of the well? Or will the area currently prescribed for an AGD project provide the model (for an AGD project the relevant area is the disposal section plus adjoining offsetting sections up to a 1.6 km radius)? Or, will it extend to the projected saturation plume or even the area of pressure influence?

Directive 56, Energy Development Applications, currently provides (at s.7.10.11) that: “Water source and injection/disposal wells do not require the acquisition of a complete DSU. A letter authorizing the activity from the mineral rights lessee or, in the case of undisposed minerals, the Alberta Department of Energy, is sufficient to demonstrate the right to produce or operate the well.” The Directive does not indicate what authorization will suffice when there is a freehold mineral title (rather than active or undisposed of Crown lands); nor is it clear that the Board will take such an approach where the scale of the solution plume will be as large as projected by Ghaderi and Leonenko (2009).

2.2 Scheme Approval

As stated above, an applicant that wishes to go beyond testing and evaluating the target formations will also need the Board’s approval under s.39 of the *OGCA* for a disposal scheme. An applicant for a disposal scheme approval must comply with the requirements of Unit 4.2 of Directive 65, which requires the applicant to provide information in relation to: (1) containment “to determine that there will be containment of the disposal fluid within a defined area and geologic horizon to ensure that there is no migration to hydrocarbon-bearing zones or groundwaters”, (2) the reservoir —to ascertain “the impact of the disposal fluid on the reservoir rock matrix, native fluid” and “address phase behaviour, pressure, and migration issues”, (3) hydraulic isolation (cross-referencing Guide 51 on well classification) – to ensure “hydraulic isolation between the disposal fluid and any other wellbores drilled into or through the disposal zone”; and (4) equity and safety (including, in relation to equity, proof of the right to dispose of acid gas in the formation and in the case of an aquifer the “disposal section and the adjoining offset sections up to a 1.6 km radius ...”; and in relation to safety, the Board will require an emergency response plan if the injected fluid contains any H₂S.) The Board can also be expected to address potential resource sterilization issues as part of its determination of whether the project is in the public interest.

In the case of AGD projects the Board chooses to specify MMV requirements, injection rates, cementing and casing requirements, logging requirements, and operating parameters (including injection pressures) in the terms and conditions of scheme approvals rather than through general Directives or regulations. The Board will likely see this as a model to use in the context of CCS projects although it would be necessary to add to existing terms and conditions for scheme approval

to provide for both a closure plan and post closure monitoring. One advantage of this approach is that it allows the Board to tailor all of the above requirements to individual projects and that it permits experimentation and learning by doing. The downside of this approach is that in the early going it does not offer much certainty to applicants. In addition, scheme approvals may well be a good method of communicating with a proponent but they are a poor method of communicating with the public about the rules for CCS projects.

2.3 Sour Gas Issue

A CCS project may give raise concerns in relation to sour gas in at least two ways. First, it is possible that the injection fluid might contain H₂S. Second, as Ghaderi and Leonenko (2009) point out, the result of introducing CO₂ into the Nisku formation (assuming the brine in the formation was saturated with H₂S or even saturated to some degree), is to sweep the H₂S to the edge of the plume and to increase the H₂S concentrations at the edge of the plume. Specifically, the authors suggest (at 25) that “simulation results indicated that injection of pure CO₂ into a saline aquifer that is initially saturated with H₂S causes the vaporization and release of dissolved H₂S into the expanding CO₂ plume. Moreover, the expanding CO₂ plume delivers all of the vaporized H₂S progressively towards the leading edge of the plume.” The authors further note that H₂S concentrations at the leading edge of the pool may reach “a significantly high concentration” which depends on the initial level of H₂S saturation.

The Board has rules to deal with sour gas wells and other facilities in several Directives including ERCB Directive 71, Emergency Preparedness and Response Requirements for the Petroleum Industry and Directive 56, Energy Development Applications. Directive 56 classifies wells for H₂S purposes on the basis of projected H₂S content, H₂S release rates and proximity to the public. The classification of the well triggers different (and progressively more stringent) consultation, notification and consultation requirements (Directive 56, s.7.4 and Table 1), special drilling requirements (*id.*, s.7.10) and may trigger the need for an emergency planning zone (EPZ) and the preparation of a site-specific emergency response plan (ERP) (*id.*, s.7.10.2). Directive 71 deals with calculating EPZs for H₂S and refers to is a software program (ERCBH2S) that calculates site-specific EPZs using thermodynamics, fluid mechanics, atmospheric dispersion, and toxicology modelling. Calculations for a well are based on absolute open flow rates. While this Directive does deal with injection wells it is possible that it may require some adaptation to be applied in the scenario contemplated. Directive 71 also creates an additional and broader area known as an Emergency Awareness Zone.¹

Board Directive 56 indicates that in preparing its well licence application “the applicant must base the category type on the maximum wellhead, cumulative drilling, producing, or completion H₂S release rate. *Applicants must review available production data and consider future production operations that may result in a reservoir originally not containing H₂S gas evolving to gas containing H₂S*” [emphasis supplied].

A project proponent will need to review carefully the implications of the work by Ghaderi and Leonenko (2009) in light of the Board’s requirements in preparing its application and in consulting with potentially affected owners and residents. There will likely be significant public concerns with respect to potential acid gas issues and applicant can expect the Board to carefully scrutinize any application in relation to this issue and to take a precautionary approach.

¹ The implications of Directive 71 for requiring the Board to give standing to request a hearing to parties residing in EPZs and PAZs was recently considered by the Court of Appeal in *Kelly v. Alberta (Energy Resources Conservation Board)* 2009 ABCA 349, October 28, 2009.

3. CREDITING ISSUES

A CCS project proponent will expect to receive credit for the volumes of CO₂ injected as part of a disposal project. In other words, the project proponent will expect the project to generate performance credits or offset credits within the meaning of the Specified Gas Emitters Regulations (SGERs). Allocation of the credit with the CCS chain as between the capture entity, the transportation entity and the storage entity will likely be a matter of commercial negotiation between the parties. While the SGERs provide the basic rules for determining who is a covered entity, the emission reduction obligations of the covered entity and the different ways in which a covered entity can meet its obligations, some parts of the scheme appear to be better developed than other parts. For example, there is a well developed procedure for developing and claiming offset credits (and protocols have been developed for enhanced oil recovery and acid gas injection projects but not for CCS projects) but the procedure for claiming performance credits is not as well developed nor transparent. In particular it is not clear how proponents should allocate responsibility for CO₂ emissions that occur between the boundary of a covered facility and injection and storage. These uncertainties need to be resolved both to afford guidance to project proponents but also to provide assurances to the public as to the environmental integrity of the emissions reduction program.

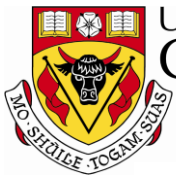
CONCLUSION

The literature (including government task force reports and the like) all suggest that it will be important for governments and regulators to establish a clear legal and regulatory framework in order to facilitate the adoption of commercial scale CCS projects. The government of Alberta (Department of Energy with respect to tenure rules and the clarification of ownership and holdout issues and the Department of the Environment with respect to crediting issues) and the ERCB (with respect to regulatory approval) have yet to establish a clear regulatory framework. This means that early project proponents will face considerable uncertainty.

Proponents may seek to manage the property uncertainties by trying to confine their projects to Crown lands. It will be more difficult for a proponent to manage the regulatory uncertainties. For the time being, proponents should follow the regulatory roadmap for AGD projects. Where the application raises issues that are not covered by the existing Directives proponents should draw these issues to the Board's attention since the failure to do so may result in delays in processing an application.

REFERENCES

- Acorn, G. and Ekelund M. (1995) “An Overview of Alberta’s Recent Legislation on Natural Gas Royalty Simplification and Gas Storage” 33 Alberta Law Review 342.
- Banks, N and Gaunce J. (in prep), “Natural Gas Storage Regimes in Canada: A Survey”.
- Banks, N. (2008), “Legal Issues Associated with the Adoption of Commercial Scale CCS Projects”, 32 pp <http://pubs.pembina.org/reports/ccs-discuss-legal.pdf> paper prepared for Carbon Capture and Storage Forum, A Pembina-ISEEE Thought Leaders Forum, November 10, 2008, Calgary.
- Banks, N. et al (2008) “The Legal Framework for Carbon Capture and Storage in Alberta” 44 Alberta Law Review 585–630.
- Climate Change and Emissions Management Act, SA 2003, c. C-16.7, as amended.
- ERCB Directive 8 on Surface Casing, last revised October 1997,
<http://www.ercb.ca/docs/documents/directives/directive008.pdf>
- ERCB Directive 20 on Abandonment, last revised December 7, 2007,
<http://www.ercb.ca/docs/documents/directives/Directive020.pdf>
- ERCB Directive 51 on the classification of wells including disposal wells, last revised March 2004,
<http://www.ercb.ca/docs/documents/directives/Directive051.pdf>
- ERCB Directive 56 on Energy Development Applications, late revised June 16, 2008,
<http://www.ercb.ca/docs/documents/directives/directive056.pdf>
- ERCB Directive 65 on Resources Applications, last revised, October 7, 2009,
<http://www.ercb.ca/docs/documents/directives/Directive065.pdf>
- ERCB Directive 71, Emergency Preparedness and Response Requirements for the Petroleum Industry, last revised, November 18, 2008
<http://www.ercb.ca/docs/documents/directives/Directive071.pdf>
- ERCB Information Letter.
- Ghaderi S and Leonenko Y. (2009) “Reservoir Modelling” (this volume).
- Goodarzi and Settari (2009) (this volume).
- Oil and Gas Conservation Act, Revised Statutes of Alberta, 2000, chapter O-6,
http://www.ercb.ca/docs/requirements/actsregs/ogc_act.pdf
- Oil and Gas Conservation Regulations, Alberta Regulation, 151/171 as amended,
http://www.ercb.ca/docs/requirements/actsregs/ogc_reg_151_71_ogcr.pdf
- Specified Gas Emitters Regulation, Alberta Regulation, 139/2007.
- Storage Council.
- Water Act, Revised Statutes of Alberta, 2000, chapter.
- Zeidouni M., Moore M., and Keith D., (2009) SPE 121000 “Guidelines for a Regulatory Framework to Accommodate Geological Storage of CO₂ in Alberta” paper prepared for presentation at the 2009 SPE Americas E & P Environmental and Safety Conference, San Antonio, Texas, 23–25 March, 2009.



Project Cost Estimate

Wabamun Area CO₂ Sequestration Project (WASP)

Author

Runar Nygaard

Rob Lavoie

Rev.	Date	Description	Prepared by
1	December 23, 2009	Economics and Costs	Runar Nygaard and Rob Lavoie

Table of Contents

INTRODUCTION.....	5
1. PROJECT COSTING METHODOLOGY AND SOURCES	5
1.1 Fifty Years of Injection	5
1.2 Cost Model Development	6
1.2.1 Site Planning and Preparation	7
1.2.2 Injection Well Costs	8
1.2.3 Well Abandonment Costs	8
1.2.4 Monitoring	10
2. COST MODEL RESULTS	14
2.1 Cost Items.....	14
2.2 Monte Carlo Simulations.....	16
CONCLUSION	18
REFERENCES.....	19

List of Tables

Table 1: Total injected volume of CO ₂ and plume size for each 50-year scenario.....	6
Table 2: Cost estimates for site planning and preparation.	7
Table 3: Cost estimates for drilling and completion of injection wells.....	8
Table 4: Cost estimate for plugging and abandonment.	9
Table 5: Cost for monitoring wells.....	10
Table 6: Cost for monitoring equipment installed in wells.....	11
Table 7: Annual operating cost for monitoring wells.	11
Table 8: Cost for surface monitoring.....	12
Table 9: 4D seismic costs for vertical injection well scenario (without fracture stimulation).....	13
Table 10: Other cost items for surface monitoring techniques.	13
Table 11: Cost summary for the four scenarios including total cumulative injection.	14

List of Figures

Figure 1: Comparison of different cost items for all four different scenarios.	15
Figure 2: Comparison of different cost items for A) Vertical well without hydraulic fracturing stimulation (Scenario 1), and B) Horizontal wells with hydraulic fracturing stimulation (Scenario 4).	16
Figure 3: Cost per ton of stored CO ₂ calculated based on Monte Carlo simulations for the vertical injection well scenario (Scenario 1).	17
Figure 4: Cost per ton for stored CO ₂ calculated using the Monte Carlo simulation method for all four scenarios.	17

INTRODUCTION

This chapter evaluates the cost of sequestering CO₂ into the porous brine-filled Nisku formation in the Wabamun Lake area.

Deep aquifers have been identified as having the potential to store very large volumes of CO₂. However, the typical benchmark rate for CO₂ injection is only 1 Mt/year when studying storage performance. This rate is very low when considering the scale needed by storage technology to play a significant role in managing global emissions. As a result, the reservoir modelling effort for the WASP project addressed the feasibility of injecting large volumes of CO₂ into the Nisku aquifer, which is a deep aquifer located in the Wabamun Lake area. Because of injection limitations in the aquifer, several injection scenarios were modelled to improve the volume of CO₂ injected. The scenarios include vertical or horizontal injection wells as follows:

- Scenario 1—vertical injection wells only.
- Scenario 2—vertical wells with hydraulically fractured stimulation.
- Scenario 3—horizontal injection wells only.
- Scenario 4—horizontal wells with hydraulic fracture stimulation.

The total injection cost for all four scenarios is addressed in this section.

The objective of this report is to estimate the cost per ton for sequestering CO₂ for large sequestration projects, such as the Wabamun Area CO₂ Storage Project. The cost estimate takes into account all of the costs incurred from the wellhead down into the formation and includes the cost of a CO₂ monitoring program. The cost for capturing, transporting and pressurizing CO₂ to get it to the injection site are outside the scope of these analyses. An injection period of 50 years and a total volume of CO₂ ranging from 0.21 to 0.43 GTons (GT) were assumed for the four different reservoir analyses.

1. PROJECT COSTING METHODOLOGY AND SOURCES

1.1 Fifty Years of Injection

In the reservoir model, a practical estimate for the storage capacity was determined using the maximum amount of CO₂ that can be injected in a given period of time (50 years) in a localized injection area (~ 30 km × 90 km) without exceeding the breakdown pressures for the formation (see Reservoir Model section for further details). Based on four different types of injection wells, the total CO₂ that could be stored ranged from 0.21 to 0.43 GT (Table 1). The lowest volume of injected CO₂ was from vertical injection wells without stimulation (Scenario 1) and the largest volume from hydraulically fractured stimulated horizontal wells (Scenario 4). The reservoir injection model also showed that injecting CO₂ using fracture stimulated vertical wells (Scenario 2) provided a higher total of stored volume than horizontal wells without stimulation (Scenario 3).

Table 1: Total injected volume of CO₂ and plume size for each 50-year scenario.

Scenario		CO ₂ (GTons)	CO ₂ Plume Radius (km)	CO ₂ Plume Area (km)
1	Vertical Injection Wells	0.21	5	785
2	Vertical Injection Wells with Fracture Stimulation	0.34	11	1,272
3	Horizontal Injection Wells	0.31	11	1,159
4	Horizontal Injection Wells with Fracture Stimulation	0.43	13	1,608

1.2 Cost Model Development

The objective of the cost model is to estimate the total cost for CO₂ sequestration, which has been defined as the cost for operating CO₂ injection from the wellhead into the formation. The model includes the costs associated with evaluating and preparing the site for injection, as well as all capital expenditures and operating costs for conducting injection for a period of 50 years. Project costs also include CO₂ monitoring during the injection phase and the two phases of post-injection. During the first 10 years a rigorous verification monitoring program is likely, followed by 90 years of monitoring to fulfill anticipated regulatory requirements. The model does not include the costs for pipelining CO₂ to the wellhead or any related acquisition or pressurization costs. Costs have been estimated using a variety of sources, and reflect as accurately as possible current 2009 dollars. Uncertainty in the estimates is addressed by adding a high and low estimate for each actual cost item based on a judgment of the uncertainty of the values. Monte Carlo simulations are used to obtain probability distributions for the cost per ton of CO₂ sequestered.

The cost items in the model are grouped into

- site planning and preparation;
- injection well costs;
- well injection operating costs;
- well abandonment costs;
- surface monitoring well costs;
- 4D seismic costs;
- monitoring operating expenditure;
- surface monitoring; and
- other cost, such as surface lease, project management, administration, and engineering services, and equipment replacement.

Below are the details of the individual cost groups broken into individual cost items.

1.2.1 Site Planning and Preparation

The site planning and preparation cost estimate is shown in Table 2. Geological site characterization includes the work needed to identify, secure and plan an injection site and to complete the data gathering and analyses required to prepare the permit application. The analyses include geological, geophysical, geochemical, geomechanical, reservoir injection well design, and the monitoring program. Hourly employee rates are from the Canadian National Occupational Classification (NOC) database, and time estimates are based on the experience of the individuals conducting the WASP project. Other estimates are based on expert judgment within team member expert area(s) or by soliciting advice from other experts. The total cost for conducting site planning and preparation is ~ \$1.6 million CAD. Typical research-related tasks that are included in pilot studies have not been included in this cost estimate, since the purpose of the exercise is to come up with a realistic cost estimate for a commercial project.

Table 2: Cost estimates for site planning and preparation.

Categories	High (CAD)	Actual (CAD)	Low (CAD)	Source
Geological site characterization	260,700	208,560	156,420	1 year FTE * 1920 h/year * 2.5 fully loaded FTE cost * hourly rate NOC code 2113 @ \$43.45.
Conventional core laboratory work	6,667	5,000	3,333	Assume 3 samples per active well, 10 wells, cost for sample \$100–200 USD per EPA (2008). USD/CAD = .9.
Geochemical analysis	130,350	104,280	78,210	0.5 year FTE * 1920 h/year * 2.5 fully loaded FTE cost * hourly rate NOC code 2113 @ \$43.45 + laboratory samples.
Geochemical laboratory costs	601,020	601,020	601,020	6 samples per active well, 1 well per township, cost for sample \$1350 CAD + 40% overhead.
Geophysics	260,700	208,560	156,420	1 year FTE * 1920 h/year * 2.5 fully loaded FTE cost * hourly rate NOC code 2113 @ \$43.45.
2D seismic line	20,000	–	–	Estimate.
Geomechanical analysis of leakage risk	130,350	104,280	78,210	0.5 year FTE * 1920 h/year * 2.5 fully loaded FTE cost * hourly rate NOC code 2145 @ \$43.45 (USD per hour 96.4 SPE).
Geomechanical laboratory costs	37,500	30,000	27,000	5 different horizons cost per test set (5 tests) \$6000 CAD.
Reservoir engineering and injection design	260,700	208,560	156,420	1 year FTE * 1920 h/year * 2.5 fully loaded FTE cost * hourly rate NOC code 2145 @ \$43.45.
Leakage risk of existing wells	54,313	43,450	32,588	100 wells * 4 h * 2.5 fully loaded FTE cost * hourly rate NOC code 2145 @ \$43.45.
Risk analysis	65,175	52,140	39,105	3/12 FTE * 1920 h/year * 2.5 fully loaded FTE cost * hourly rate NOC code 2145 @ \$43.45.
Total Cost	1,827,474	1,565,850	1,328,726	

1.2.2 Injection Well Costs

A total of 10 injector wells were included in the cost model. The well costs for the vertical injection wells in Scenario 1 were based on the detailed cost estimate for drilling and completing a vertical injection well as described in the Well Integrity section of this report. Vertical wells with a total length of 1960 m and production packing set at 1890 m was used for the base case. Since the Nisku formation dips down towards the west and the reservoir top depth varies between 1680 m and 2480 m, the depth of the 10 injection wells were evenly distributed to account for these factors. The lowest cost for an injection well within the Nisku formation top is at 1680 m and is shown in Table 3 (middle column).

For injection Scenario 2, vertical wells using hydraulic fracturing stimulation included a one-stage fracture estimated at a cost of \$50,000 CAD for each well. For the two scenarios involving horizontal wells, the initial cost model was modified to include a 2500 m-long horizontal injection section within the Nisku formation. Well depths for the two horizontal injection scenarios were evenly distributed for the 10 injection wells. For Scenarios 3 and 4, the difference is an estimated \$360,000 CAD for four hydraulic fracturing stimulations, which has been included in Scenario 4. The cost of the most expensive well from Scenario 4 with hydraulic fracturing stimulation and a Nisku formation top depth of 2480 m is ~ \$3.5 million CAD (see Table 3, last column). The annual cost for the daily operation of the wells is estimated to be \$83,000 CAD plus \$1 CAD per metre of well depth.

Table 3: Cost estimates for drilling and completion of injection wells.

Injection Well Cost	Cost of Vertical Well (no stimulation)	Cost of Horizontal Well (with stimulation)
<i>Drilling Cost</i>		
Well fixed costs	168,920	168,920
Fixed depth-based well costs	154,463	346,361
Variable depth-based well costs	219,772	317,415
Time-based drilling cost per day	297,849	1,496,259
Fixed drilling cost	33,000	89,000
<i>Completion Cost</i>		
Completion fixed costs	38,000	73,513
Depth based completion costs	74,545	22,402
Time-based completion costs	138,840	208,260
Five-day injection test	65,000	114,275
Stimulation fracture	0	360,000
Total well cost	1,190,389	3,196,405
Total well cost plus 5% contingency	1,249,909	3,356,225

1.2.3 Well Abandonment Costs

The well integrity study identified 15 wells in the overall study area that needed to be abandoned or re-abandoned. Three of the wells are suspended, but have not been properly abandoned. The cost to abandon these wells is taken from PSAC (2008) and is shown in Table 4. The 12 wells identified in the well integrity analysis are in need of a workover with the well re-entered and new cement plugs

installed in the Nisku reservoir interval. The existing plugs will be drilled out and new cement plugs installed for a proper abandonment. Table 4 gives the cost for re-entering, plugging and abandoning these 12 wells. The cost is based on the injection well cost model and added abandonment cost from PSAC (2008). The wells should be abandoned before the area is pressurized, since the integrity of the existing casing is unknown and may not have the integrity for holding elevated pressures (see Well Integrity section). To avoid the pressure plume that would be encountered when entering these wells, it is assumed that two wells will be abandoned each year in the first years of the project.

Table 4: Cost estimate for plugging and abandonment.

Year Abandoned	High Monitoring Well Cost	Actual Monitoring Well Cost	Low Well Cost	Monitoring Well Type
2010	31,500	21,000	15,750	suspended
2010	437,422	218,711	109,355	old
2011	31,500	21,000	15,750	suspended
2011	437,422	218,711	109,355	old
2012	31,500	21,000	15,750	suspended
2012	437,422	218,711	109,355	old
2013	437,422	218,711	109,355	old
2013	437,422	218,711	109,355	old
2014	437,422	218,711	109,355	old
2014	437,422	218,711	109,355	old
2015	437,422	218,711	109,355	old
2015	437,422	218,711	109,355	old
2016	437,422	218,711	109,355	old
2016	437,422	218,711	109,355	old
2017	437,422	218,711	109,355	old
Total Cost	5,343,559	2,687,530	1,359,515	

1.2.4 Monitoring

The monitoring program is a combination of four functions: installing a limited set of monitoring wells with access to the injection horizon, conducting surface monitoring, detecting surface CO₂ leakage and CO₂ movement in the subsurface, and performing 4D seismic monitoring. In the cost model, it is assumed that there will be the same number of injection and monitoring wells, and half of the monitoring wells will be existing wells that have been converted. The cost to drill and complete new wells or convert existing wells is shown in Table 5 and were obtained by modifying the well injection cost model. The cost for the monitoring equipment for surface fluid sampling and downhole measurement is given in Table 6. Downhole equipment for measuring temperature and pressure, as well as downhole CO₂ gauges (when available), is included. Micro-seismic phones will be installed downhole to locate CO₂ movement in the subsurface caused by the injection process. A VSP run is included for improving the 4D seismic resolution. The annual operating cost for the monitoring wells is shown in Table 7.

The objective of the surface monitoring program is to detect CO₂ leakage and CO₂ movement in the subsurface. Direct measurement of CO₂ flux to the surface can be detected using ground-surface accumulation chambers. Chemical and isotope signatures can also be detected, which can determine the source of the CO₂ (Oldenburg and Lewicki, 2003). The disadvantage with discrete measurement is that point leakage can go undetected if there is no measurement near the leakage. Atmospheric detection of CO₂ would be a mitigation that would require continuous field-wide measurement. Any ground water well in the injection area is assumed to be regularly monitored to identify potential leakage into potable water. Surface monitoring can also be used to identify CO₂ plume movement by using surface gravity measurement and satellite data for satellite interferometry and satellite land topography. See Table 8 for a summary of the cost for surface monitoring.

Table 5: Cost for monitoring wells.

Type	Year Installed	Drill and Complete New Monitoring Well (CAD)	Converting Existing Well to Monitoring Well (CAD)	Well Depth (m)	High Monitoring Well Cost (CAD)	Actual Monitoring Well Cost (CAD)	Low Well Cost (CAD)
New	2010	1,059,678	–	1600	1,335,986	1,183,845	1,094,687
Converted	2011	–	678,260	1600	1,187,730	802,426	427,123
New	2012	1,127,815	–	1800	1,410,936	1,251,981	1,159,417
Converted	2013	–	735,734	1800	1,273,941	859,901	455,860
New	2014	1,195,951	–	2000	1,485,886	1,320,118	1,224,147
Converted	2015	–	793,208	2000	1,360,152	917,375	484,597
New	2016	1,264,088	–	2200	1,560,837	1,388,255	1,288,877
Converted	2017	–	850,683	2200	1,446,364	974,849	513,335
New	2018	1,332,225	–	2400	1,635,787	1,456,391	1,353,607
Converted	2019	–	908,157	2400	1,532,575	1,032,324	542,072
Total Cost		5,979,757	3,966,042		14,230,195	11,187,465	8,543,723

Table 6: Cost for monitoring equipment installed in wells.

Type of measurement	Objective	High (CAD)	Actual (CAD)	LOW (CAD)	Source
VSP	Improve 4D seismic and identify changes in velocity profile near wellbore with time	14,300	13,000	11,700	\$1000 m * \$13/m for regular well logging (PTAC 2008).
Fluid sampling equipment	To identify changes of composition in formation fluids	37,500	30,000	22,500	Estimate from EPA (2008).
Wireline logging		–	–	–	Cost included in the well design.
Dual pressure and temperature quartz gauges	Changes in pressure and temperature during and after injection	19,040	18,667	18,293	Quote from leading manufacturer.
Down hole CO ₂ concentration gauge	Measure change in CO ₂ concentration in wellbore fluid	40,000	20,000	10,000	Estimate of sensors currently being developed.
Micro-seismic phones	Measure micro-seismic events	59,500	42,500	25,500	\$20,000 per well + \$22,500 in surface equipment per well (estimate)
Total Cost		170,340	124,167	87,993	

Table 7: Annual operating cost for monitoring wells.

Type of Measurement	Objective	Description	High (CAD)	Actual (CAD)	Low (CAD)	Source
Continuous well monitoring: analytical costs	Fate of CO ₂ in target formation	Direct measurement of carbon content in reservoir fluids obtained from five observation wells	17,640	16,800	15,960	Analytical cost per sample \$850 plus field work \$150/sample = \$1000 times # of samples.
Continuous well monitoring	Identify changes of composition in formation fluids	Pressure, temperature, CO ₂ and fluid sampling	10,863	8,690	6,518	1/12 FTE *1920 h/year * 2.5 fully loaded FTE cost * hourly rate NOC code 2145 @ \$43.45.
Micro-seismic events	Measure the micro-seismic events to identify areas with movement in reservoir and caprock		5,431	4,345	3,259	0.25 months engineer time per year – 2/12 FTE *1920 h/year * 2.5 fully loaded FTE cost * hourly rate NOC code 2145 @ \$43.45.
Reporting to authorities			5,431	4,345	3,259	0.25 months FTE *1920 h/year * 2.5 fully loaded FTE cost * hourly rate NOC code 2145 @ \$43.45.
Total Cost			39,365	34,180	28,995	

Table 8: Cost for surface monitoring.

Type of measurement	Objective	Description	Test Frequency (year)	High (CAD)	Actual (CAD)	Low (CAD)	Source
Surface CO ₂ baseline	Leaked CO ₂ to surface	Direct measurement of CO ₂ concentration in the air and vadose zone above the reservoir. Use ground-surface accumulation chambers.	2	3,551,016	1,775,508	–	\$19,000 USD per unit, 1 unit per 1000 measurement, density 100 m × 100 m grid over 25% of 4987 km + Prof. Awuah-Offei pers. comm., 3,4 or 5 measurements per hour, NOC code 2254 @ \$19.21.
Surface gravity measurement	Plume movement	Performed over whole study area	2	935,063	748,050	561,038	\$150 per km ² (estimate) over whole WASP area 4987 km ² .
Topographic heave satellite interferometry	Measure topographic heave	Satellite interferometry	2	41,165	39,204	37,244	\$4000 USD/0.9 USD CAD per 100 km × 100 km radarsat image 2 times per year * 2/12 FTE *1920 h/year * 2.5 fully loaded FTE cost * hourly rate NOC code 2145 @ \$43.45.
Topographic heave	Measure topographic heave	Satellite land topography mapping	2	623,375	498,700	374,025	\$100 per km ² (estimated) over whole WASP area 4987 km ² .
Atmospheric detection	Measure CO ₂ in the atmosphere	By airplane or balloons	1	623,375	498,700	374,025	\$50 per km ² (estimated) over whole WASP area 4987 km ² .
Shallow Groundwater baseline and monitoring	CO ₂ leakage into potable aquifers	Direct measurement of C species in groundwater obtained from drinking water wells	1	117,600	112,000	106,400	Analytical cost per sample \$850 plus field work \$150/sample = \$1000 times # of samples.
Annual total cost during injection and the following 10 years				740,975	610,700	480,425	
Bi-annual total cost during injection and the following 10 years				5,891,593	3,672,162	1,452,732	
90 years after injection (annually)				370,488	305,350	240,213	

The cost for 4D seismic monitoring is included in Table 9. A 3D seismic survey is assumed to be conducted every second year during the fifty-year injection period and every fifth year for the ten years after injection stops. The cost will be higher for the other scenarios, since the area of the plume will be larger for each scenario.

Table 9: 4D seismic costs for vertical injection well scenario (without fracture stimulation).

	High (CAD)	Actual (CAD)	Low (CAD)	Source
Bi-annual total	26,179,939	21,816,616	13,089,969	\$15,000–30,000 USD km ² , exchange rate 0.9, EPA (2008) equal plume size for each scenario.
10 years after injection (every fifth year)	52,359,878	43,633,231	26,179,939	
90 years after injection	–	–	–	

Other cost, such as project organization, well licenses and legal fees, is shown in Table 10. In addition, an equipment replacement cost of 2% of the total equipment cost is included annually.

Table 10: Other cost items for surface monitoring techniques.

	High (CAD)	Actual (CAD)	Low (CAD)	Source
Project organization during injection	861,466	717,888	646,099	4 FTE * \$1920 h/year * 2.5 fully loaded FTE cost * hourly rate NOC code 2145 @ \$43.45, 1 FTE NOC code 2254.
10 year after injection	180,461	150,384	135,346	10 year after injection.
90 year after injection	30,077	25,064	22,558	90 year after injection.
Licenses	16,000	4,000	2,000	Cost per well.
Legal fees per well	17,000	8,500	4,250	0.5% of injection well cost annually.

2. COST MODEL RESULTS

2.1 Cost Items

The total cost of the storage project is estimated to be between \$0.7 billion CAD for the injection scenario with the ten vertical injection wells and \$1.1 billion CAD for the injection scenario with the ten hydraulically fractured horizontal injection wells (see Table 11). All values in the table are shown in 2009 dollars. Table 11 shows that the vertical fractured scenario is more costly than the horizontal injection wells because of the 4D seismic costs relating to the size of the plume (see Figure 1). Table 1 also gives the total injection volume for the four scenarios, which is less than the results from the reservoir model. The small reduction in storage volume is caused by the assumption that there will be two new injector wells started each year and it will take five years before full injection is reached. Figure 1 gives the cost breakdown and shows that the largest expense for all scenarios is 4D seismic. The 4D seismic costs increases with plume size both in actual numbers and as a percentage of the total project cost (see Figure 2). With the suggested monitoring scheme, the cost of monitoring will make up approximately 75% of the project's total cost (Figure 2).

Table 11: Cost summary for the four scenarios including total cumulative injection.

Cost Item Groups	Scenario 1	Scenario 2	Scenario 3	Scenario 4
	Vertical (\$1000 CAD)	Vertical Fracture Stimulated (\$1000 CAD)	Horizontal (\$1000 CAD)	Horizontal fracture stimulated (\$1000 CAD)
Site planning and preparation	1,566	1,566	1,566	1,566
Injection well cost	13,862	14,569	27,538	31,738
Injection well operations	79,085	79,085	79,085	79,085
Well re-abandonment	3,108	3,108	3,108	3,108
Surface monitoring cost	162,090	162,090	162,090	162,090
4D seismic costs	316,341	512,171	466,979	647,746
Monitoring wells costs	11,187	11,187	11,187	11,187
Monitoring well operations	22,046	22,046	22,046	22,046
Equipment replacement	28,786	29,571	43,948	48,610
Surface lease and lease insurance	6,938	6,938	6,938	6,938
Project management, administration, and engineering	39,654	39,654	39,654	39,654
Total Cost	684,662	881,984	864,138	1,053,767

Cumulative Injectivity (Million Tons)	200	309	282	391
--	------------	------------	------------	------------

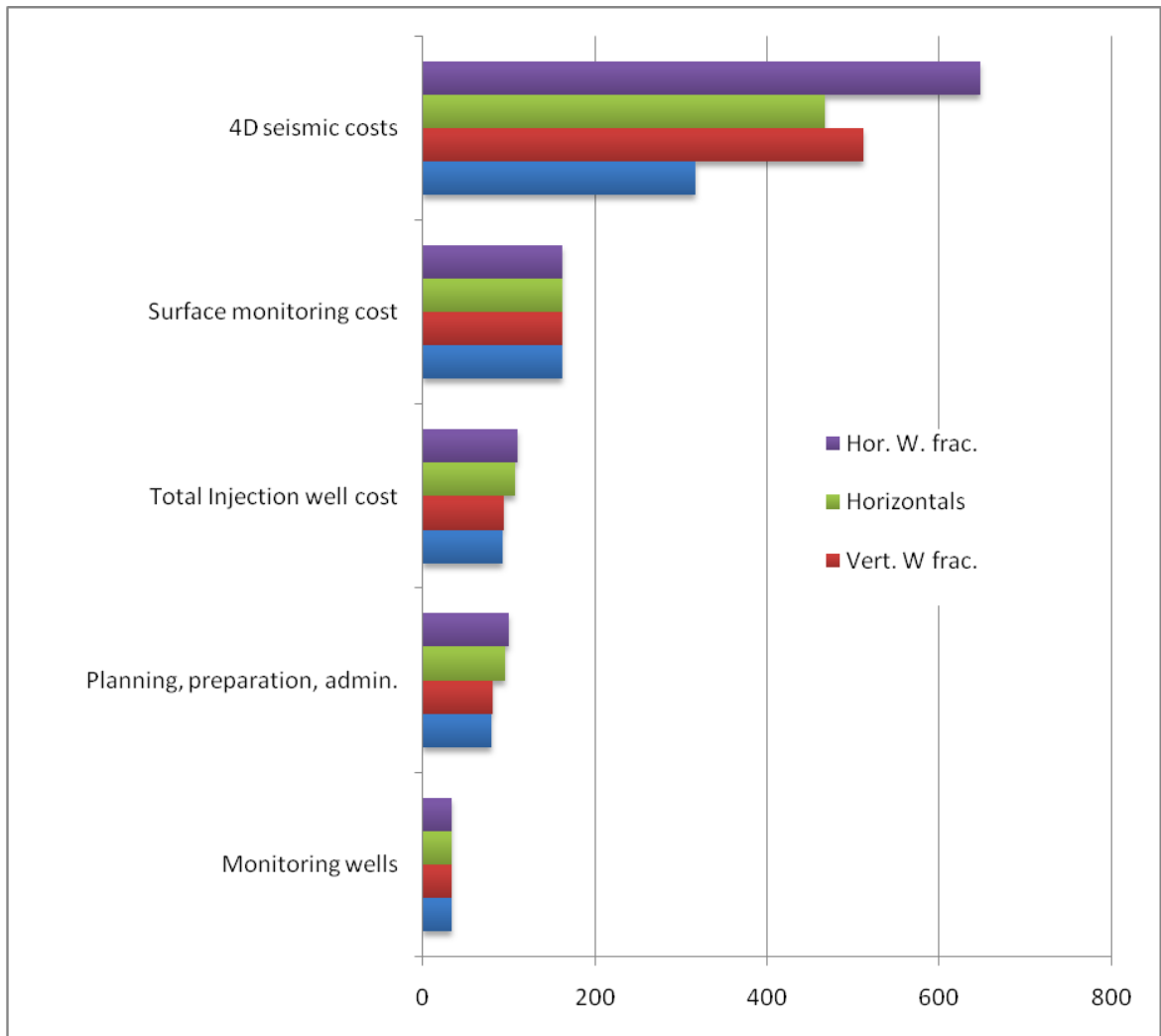


Figure 1: Comparison of different cost items for all four different scenarios.

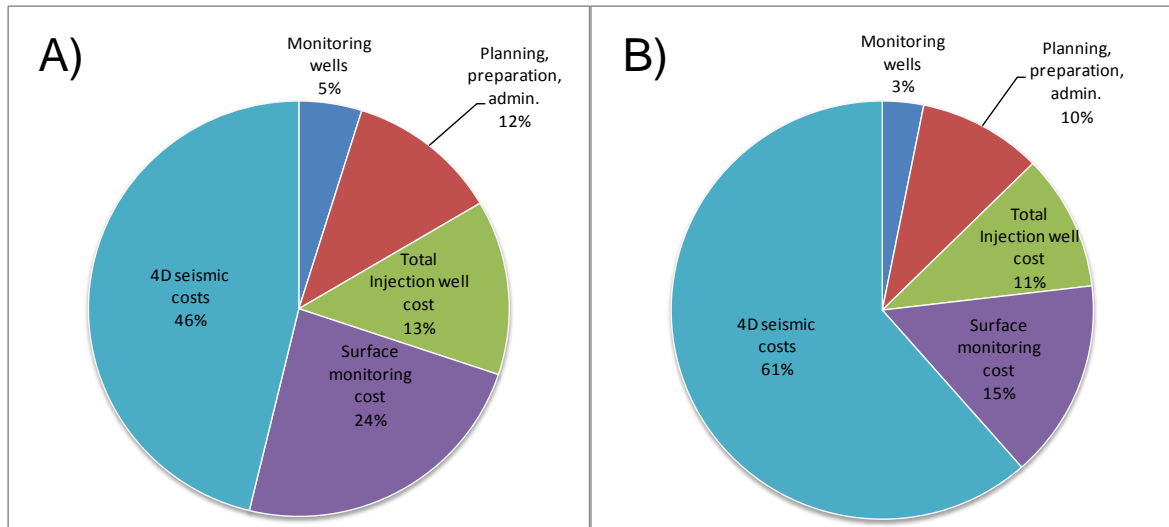


Figure 2: Comparison of different cost items for A) Vertical well without hydraulic fracturing stimulation (Scenario 1), and B) Horizontal wells with hydraulic fracturing stimulation (Scenario 4).

2.2 Monte Carlo Simulations

To estimate the cost per ton of CO₂ injection, Monte Carlo simulations were performed for all four scenarios. Figure 3 shows the results for the vertical scenario and indicates that the storage cost will be below \$3.55 CAD/ton (95 percentile) with a mean cost of \$3.38 CAD/ton of CO₂. A model with full co-variance between the cost items was also conducted, which gave a similar mean of \$3.35 CAD/ton of CO₂ and a larger spread of the 5 and 95 percentile results (\$3.92 CAD/ton of CO₂ for the 95 percentile). It is not expected that the different cost items will be correlated, since there are different driving mechanisms for the uncertainty in cost for the different cost items. Figure 4 shows the cost for the four different scenarios. The mean value varies from \$2.65 CAD/ton of CO₂ for the horizontal injection wells with hydraulic fracture stimulation to \$3.38 CAD/ton of CO₂ for the vertical injection wells scenario.

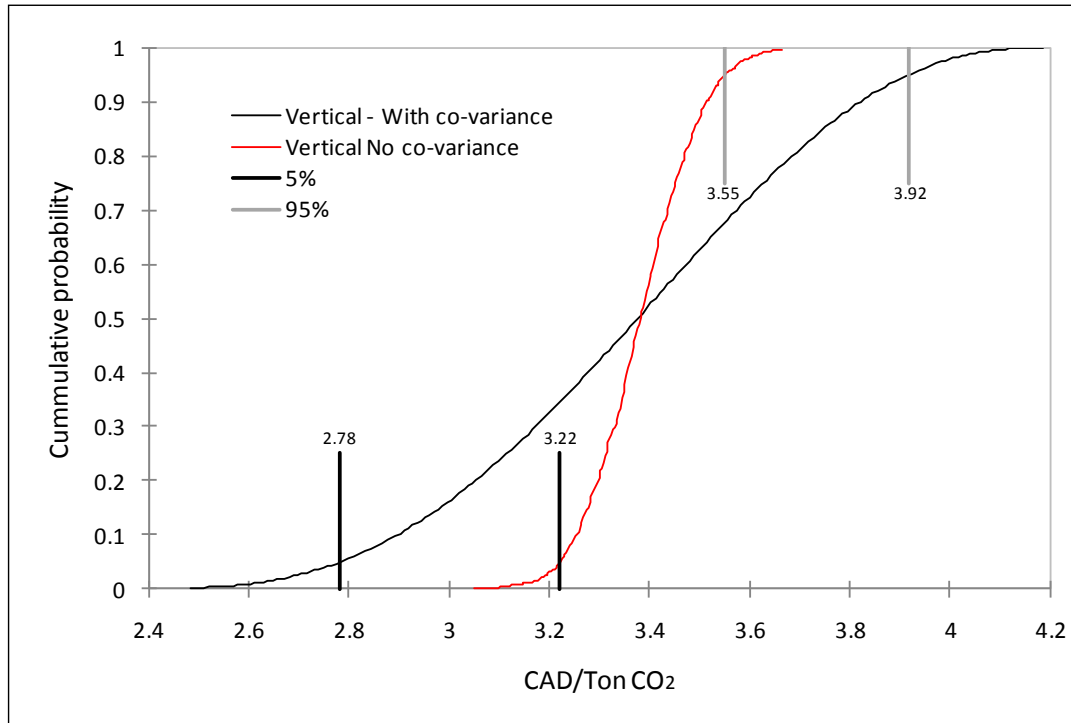


Figure 3: Cost per ton of stored CO₂ calculated based on Monte Carlo simulations for the vertical injection well scenario (Scenario 1).

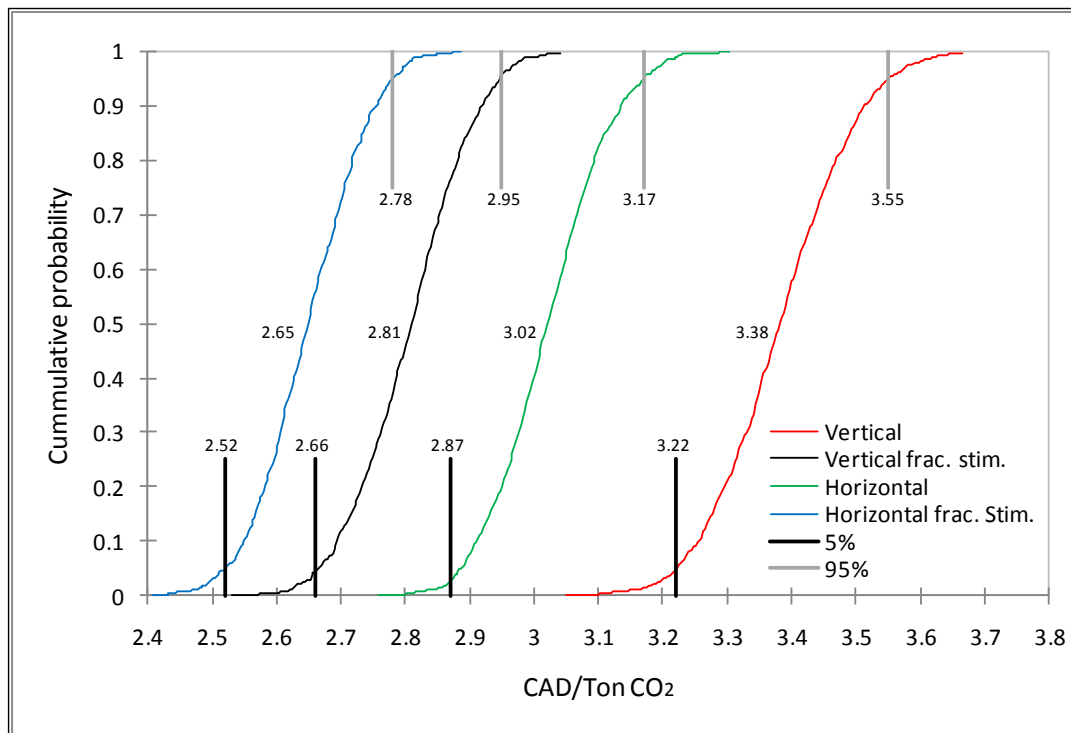


Figure 4: Cost per ton for stored CO₂ calculated using the Monte Carlo simulation method for all four scenarios.

CONCLUSION

A cost model for the Wabamun area CO₂ sequestration project was developed. From that model it was determined that the overall cost for the storage project was between \$0.7 billion CAD for the injection scenario with ten vertical injection wells and \$1.1 billion CAD for the injection scenario with 10 hydraulically fractured horizontal injection wells. All values are shown in 2009 dollars.

The mean cost for storing a ton of CO₂ was estimated to be in the range of \$2.65 to \$3.38 CAD/ton, which depends upon the configuration of the injection wells. The lowest cost per ton was the scenario with the largest amount of CO₂ stored.

In the cost model the highest cost was for monitoring at around 75% of the total cost, with the majority of the monitoring cost comprising 4D seismic. The high cost of repeatedly conducting seismic surveys questions the benefit of conducting the 4D seismic surveys.

REFERENCES

EPA, 2008, United States Environmental Protection Agency, Geological CO₂ sequestration Technology and Cost Analysis, Technical Support Document.

NOC, 2009, National Occupational Classification wage info, <http://www.alis.gov.ab.ca>.

Oldenburg, C.M., and J.L. Lewicki. 2003. Near-Surface Monitoring Strategies for Geologic Carbon Dioxide Storage Verification, Lawrence Berkeley National Laboratory Report LBNL-54089.

PSAC, 2008. Petroleum Services of Canada Report, 2008 Well Cost Study Summer Costs.